Formation of Ozone and Growth of Aerosols in Young Smoke Plumes from Biomass Burning

by

Matthew James Alvarado

B.S. Chemical Engineering, Massachusetts Institute of Technology (2000)

Submitted to the Department of Earth, Atmospheric, and Planetary Sciences
in partial fulfillment of the requirements for the degree of

Doctor of Philosophy in Climate Physics and Chemistry

at the

MASSACHUSETTS INSTITUTE OF TECHNOLOGY

June 2008

Signature of Author .....
Department of Earth, Atmospheric, and Planetary Sciences
2 May 2008

Certified by .....
Ronald G. Prinn
TEPCO Professor of Atmospheric Chemistry
Thesis Supervisor

Accepted by .....
Maria T. Zuber
E.A. Griswold Professor of Geophysics
Head, Department of Earth, Atmospheric and Planetary Sciences

Formation of Ozone and Growth of Aerosols in Young Smoke Plumes from Biomass Burning

by

Matthew James Alvarado

Submitted to the Department of Earth, Atmospheric, and Planetary Sciences
on 2 May 2008, in partial fulfillment of the
requirements for the degree of
Doctor of Philosophy in Climate Physics and Chemistry

Abstract

The combustion of biomass is a major source of atmospheric trace gases and aerosols. Regional- and global-scale models of atmospheric chemistry and climate take estimates for these emissions and arbitrarily "mix" them into grid boxes with horizontal scales of 10-200 km. This procedure ignores the complex non-linear chemical and physical transformations that take place in the highly concentrated environment of the young smoke plumes. In addition, the observations of the smoke plume from the Timbavati savannah fire [*Hobbs et al.*, 2003] show much higher concentrations of ozone and secondary aerosol matter (nitrate, sulfate, and organic carbon [OC]) in the smoke plume than are predicted by current atmospheric chemistry models. To address these issues, we developed a new model of the gas- and aerosol-phase chemistry of biomass burning smoke plumes called ASP (Aerosol Simulation Program). Here we use ASP to simulate the gas-phase chemistry and particle dynamics of young biomass burning smoke plumes and to estimate the errors introduced by the artificial mixing of biomass burning emissions into large-scale grid boxes. This work is the first known attempt to simultaneously simulate the dynamics, gas-phase chemistry, aerosol-phase chemistry, and radiative transfer in a young biomass burning smoke plume.

We simulated smoke plumes from three fires using ASP combined with a Lagrangian parcel model. We found that our model explained the formation of ozone in the Otavi and Alaska plumes fairly well but that our initial model simulation of the Timbavati smoke plume underestimated the formation of ozone and secondary aerosol matter. The initial model simulation for Timbavati appears to be missing a source of OH. Heterogeneous reactions of NO_2 and SO_2 could explain the high concentrations of OH and the rapid formation of ozone, nitrate and sulfate in the smoke plume if the uptake coefficients on smoke aerosols are large [O(10^{-3}) and O(10^{-4}), respectively]. Uncharacterized organic species in the smoke plume were likely responsible for the rapid formation of aerosol OC. The changes in the aerosol size distribution in our model simulations were dominated by plume dilution and condensational growth, with coagulation and nucleation having only a minor effect.

We used ASP and a 3D Eulerian model to simulate the Timbavati smoke plume. We ran two test cases. In the reference chemistry case, the uncharacterized organic species were assumed to be unreactive and heterogeneous chemistry was not included. In the expanded chemistry case, the uncharacterized organic compounds were included, as were heterogeneous reactions of NO_2 and SO_2 with uptake coefficients of 10^{-3} and 2×10^{-4}, respectively. The 3D Eulerian model matched the observed plume injection height, but required a large minimum horizontal diffusion coefficient to match the observed horizontal dispersion of the plume. Smoke aerosols reduced the modeled photolysis rates within and beneath the plume by 10%-20%. The expanded chemistry case provided a better match with observations of ozone, OH, and secondary aerosol matter than the reference chemistry case, but still underestimated the observed concentrations. We find that direct mea-

surements of OH in the young smoke plumes would be the best way to determine if heterogeneous production of HONO from NO_2 is taking place, and that these measurements should be a priority for future field campaigns.

Using ASP within an Eulerian box model to evaluate the errors that can be caused by the automatic dilution of biomass burning emissions into global model grid boxes, we found that even if the chemical models for smoke plume chemistry are improved, the automatic dilution of smoke plume emissions in global models could result in large errors in predicted concentrations of O_3, NO_x and aerosol species downwind of biomass burning sources. The thesis discusses several potential approaches that could reduce these errors, such as the use of higher resolution grids over regions of intense biomass burning, the use of a plume-in-grid model, or the use of a computationally-efficient parameterization of a 3D Eulerian plume chemistry model.

Thesis Supervisor: Ronald G. Prinn
Title: TEPCO Professor of Atmospheric Chemistry

Contents

List of Figures

List of Tables

Acknowledgements

I've always thought it was a little unfair that thesis acknowledgements usually ignore our teachers prior to graduate school. So in that spirit, I'd like to thank Mrs. Nelson, who taught me my times tables all the way to 12; Mrs. Williamson, who taught me what $\frac{dx}{dt}$ meant; Mrs. Markley, who taught me how to diagram a sentence; and Dr. Mohr, who taught me everything I remember about chemical engineering.

Thanks to everyone who advised, guided, and supported me as I worked on this thesis. My advisor, Ron Prinn, supported me as I picked a project outside of the norm and guided me through the ins and outs of a scientific career. Chien Wang guided me through the maze of computer codes and beowulf clusters. The other members of my thesis committee, Greg McRae and Kerry Emanuel, provided guidance and feedback throughout the project, bringing new ideas to every discussion. The other students and post-docs in the Prinn Group helped guide my education and research and helped bang my ideas and presentations into shape. I should give special thanks to those who shared an office with me: Elke Hodson (who also helped revise this thesis), Arnico Panday, Xue Xiao and Eun Jee Lee. Special thanks also goes to Donnan Steele, who created the MELAM model. I owe a debt of gratitude to many other scientists for patiently explaining their models and measurements to me: Rob Griffin (UNH), Bill Carter (UCR), Robert Yokelson (University of Montana), Song Gao (Hong Kong University of Science and Technology), Brian Magi (University of Washington), Jörg Trentmann (MPI-Mainz), and Sasha Madronich (NCAR).

I'd like to thank my mother and father for their constant love and support throughout my education. My mother was my first and best teacher, and listened to all of my worries throughout the thesis work. My father made sure I knew that my potential was unlimited, and gave me the confidence to reach it.

To my wife Anne, who reassured me every step of the way that her love wasn't dependent on whether the model ran or not: I love you more than soda pop. You legally own half this thesis and all of my heart.

And to my son, who will be born shortly after this writing: Thanks, little guy. Without you, Daddy would have taken a lot longer to finish.

My doctoral studies and thesis research were supported by an NSF Graduate Fellowship, a Martin Family Fellowship in Sustainability, an MIT Norman B. Leventhal Presidential Fellowship, NSF Grant ATM-0120468, DOE Grant DE-FG02-94ER61937, and the industrial and foundation sponsors of the MIT Joint Program on the Science and Policy of Global Change.

Chapter 1

Introduction

1.1 Background and Motivation

The combustion of biomass is a major source of atmospheric trace gases and aerosols which can impact global atmospheric chemistry and climate [*Crutzen and Andreae*, 1990; *IPCC*, 2001]. Emissions of NO_x and non-methane organic compounds (NMOCs) from biomass burning can lead to enhancements of tropospheric ozone [*Andreae and Merlet*, 2001; *Crutzen and Andreae*, 1990; *Levine*, 1994], while primary and secondary aerosols from biomass burning can affect the climate directly by the scattering or absorption of sunlight and indirectly through their effects on cloud droplet number concentration, cloud albedo, and cloud precipitation efficiency [*IPCC*, 2001]. In general, regional- and global-scale models of atmospheric chemistry and climate take estimates for the primary emissions of trace gases and aerosols from biomass burning and arbitrarily "mix" them into much larger-scale grid boxes (*e.g.* with 10-200 km horizontal scales) before performing any calculations of gas-phase chemistry, aerosol-phase chemistry, or aerosol dynamics (see Figure 1-1). This procedure ignores the substantial non-linear chemical and physical transformations (*e.g.*, gas-phase chemistry, coagulation of aerosols, condensation of vapors, *etc.*) that can take place in the highly concentrated environment of young biomass burning smoke plumes [*Andreae and Merlet*, 2001; *Jost et al.*, 2003b]. These transformations can lead to significant changes in the gas phase composition of the smoke and the number, size, composition, and shape of the emitted particles [*Jost et al.*, 2003b; *Hobbs et al.*, 2003; *Li et al.*, 2003; *Liousse et al.*, 1995; *Posfai et al.*, 2003; *Reid et al.*, 2005a, b]. As these changes are not correctly included in large-scale models, these large-scale models may misrepresent the true impacts of biomass burning smoke on atmospheric chemistry and climate [*Jost et al.*, 2003b].

In addition, there are several unresolved questions about the chemical and physical changes

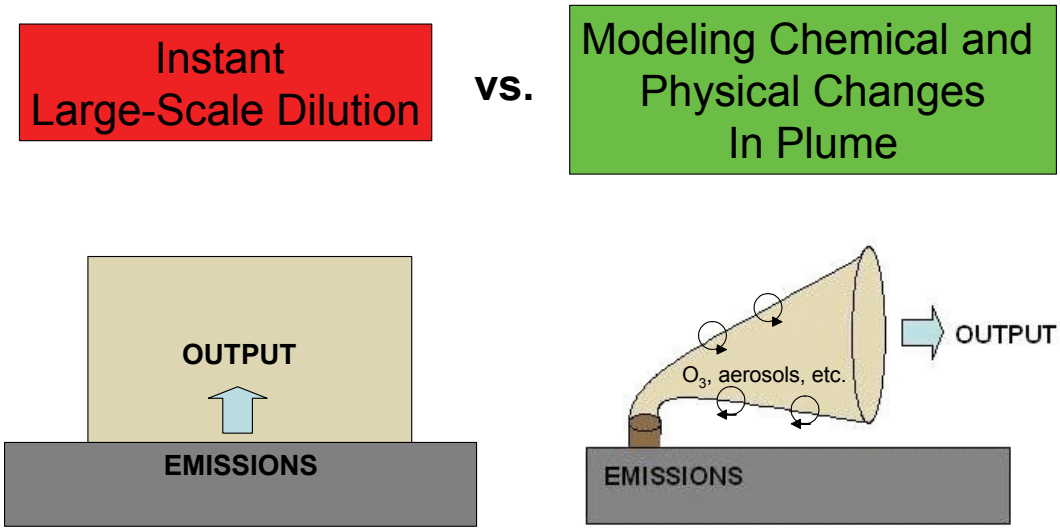

Figure 1-1: A cartoon of the current method for including biomass burning emissions in global atmospheric chemistry models (GACMs) versus the modeling method used in this thesis. In most current GACMs, emissions from biomass burning plumes are automatically diluted in large-scale grid boxes, ignoring the chemical and physical changes that can take place in the concentrated plumes. In this thesis, these non-linear chemical and physical changes are explicitly modeled. Such a model could be used in future GACMs to include the effects of plume-scale chemistry on the effective emissions from biomass burning.

that take place within young biomass burning smoke plumes (defined here as plumes less than 4 hours downwind from the fire source). Figure 1-2 shows the measurements of ozone, aerosol mass concentration, and aerosol number concentration in the smoke plume from the Timbavati savannah fire in South Africa, which was studied as part of the Southern African Regional Science Initiative 2000 (SAFARI 2000) field project [*Hobbs et al.*, 2003]. The observations show rapid formation of ozone within the smoke plume. Previous modeling studies of the gas phase chemistry in the Timbavati smoke plume [*Trentmann et al.*, 2005; *Mason et al.*, 2006] have not been able to simulate this chemistry. The observations also show a large increase in the normalized mass concentrations of secondary aerosol matter (nitrate, sulfate, and organic carbon) as the smoke moves downwind. In addition, *Hobbs et al.* [2003] suggested that the initial reduction in total aerosol number concentration in the plume was due to particle coagulation, while the increase in number concentration further downwind was due to particle nucleation. However, there have been no previous modeling studies to explore the growth and chemical transformation of aerosols in the Timbavati smoke plume due to the formation of secondary aerosol matter, coagulation, and nucleation.

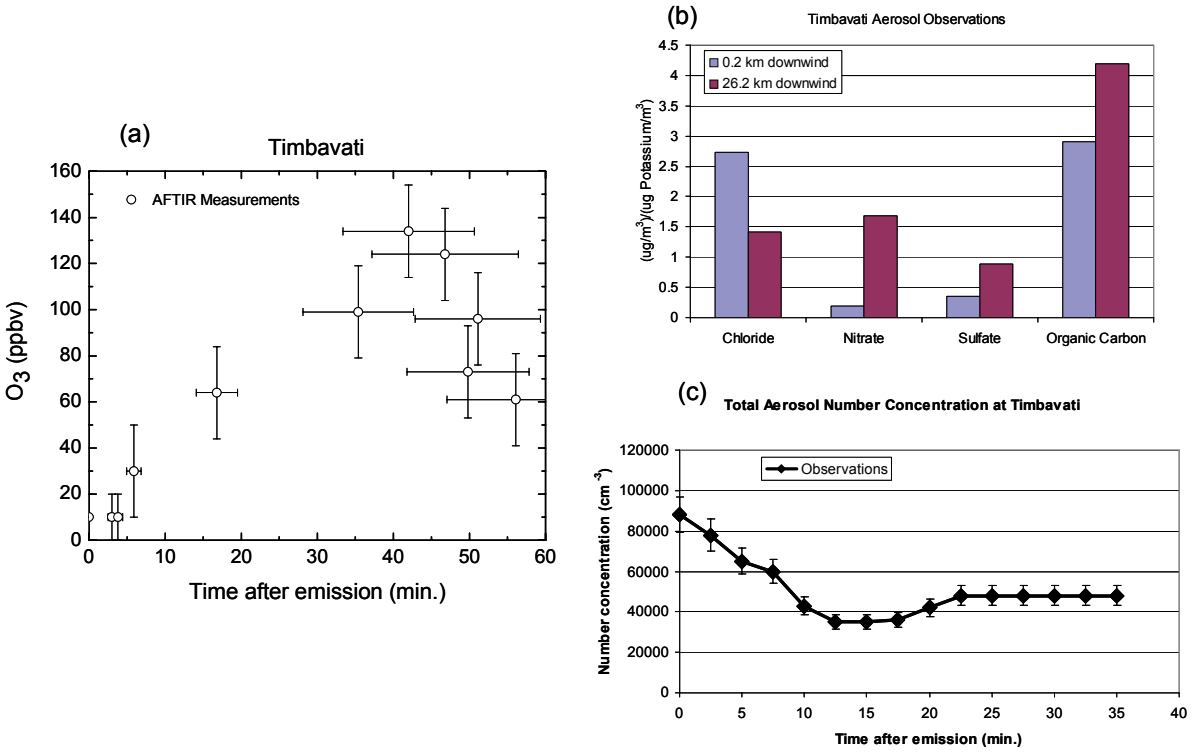

Figure 1-2: Observations of the smoke plume from the Timbavati savannah fire [*Hobbs et al.*, 2003]. (a) Ozone (O_3) mixing ratios in the Timbavati smoke plume as measured by airborne FTIR. The horizontal error bars represent the uncertainty in the Lagrangian age of the smoke plume due to uncertainties in the horizontal wind speed. (b) Mass concentrations of aerosol chloride, nitrate, sulfate and organic carbon (normalized by the mass concentration of potassium) at 0.2 km and 26.2 km downwind from the fire source. (c) Observations of total aerosol number concentration (particle diameters between 3 nm and 3 μm) in the Timbavati smoke plume.

The goals of this thesis are to model the growth of smoke particles within young biomass burning plumes, evaluate the impact of these particles on the gas-phase chemistry and formation of ozone within the plume, and to evaluate the errors caused by the automatic dilution of plume emissions in global atmospheric chemistry models (GACMs). For this thesis, we developed a small scale model capable of simulating the chemical and physical changes of both trace gases and aerosols within smoke plumes. The review of *Reid et al.* [2005b] concluded that such models are "extremely important to our future understanding of the [smoke] aging process". Such models can assist in explaining combustion plume observations, planning field observation studies of biomass burning smoke plumes, and in predicting the regional and global scale impacts of biomass burning smoke. In this thesis we present a new model of the gas and aerosol chemistry of biomass burning smoke plumes called ASP (Aerosol Simulation Program). We have used ASP to simulate the gas-phase chemistry and particle dynamics of young biomass burning smoke plumes in both Lagrangian and Eulerian frameworks, and have used it to estimate the errors introduced into the calculation of the effective emissions from biomass burning plumes by the automatic dilution of emissions within a large-scale grid box, as is done in many current GACMs. To our knowledge this work represents the first attempt to simultaneously simulate the fluid dynamics, radiative transfer, gas-phase chemistry, and aerosol-phase chemistry of a young biomass burning smoke plume.

1.1.1 Outline of the Thesis

Section 1.2 contains a review of the literature on the impacts of biomass burning emissions on climate, the observed and modeled transformations of trace gases and aerosols in smoke plumes, and previous efforts to model the fluid dynamics of buoyant pollution plumes. Based on this literature review, we identify several unanswered questions about the evolution of trace gases and aerosols in biomass burning smoke plumes in Section 1.3, and restate the goals of the thesis.

Chapter 2 describes ASP, the gas- and aerosol-phase chemical model used in this work. The chemical model can simulate the formation of ozone, the formation of secondary aerosol matter (both organic and inorganic), and aerosol growth from coagulation. The model also calculates the average optical properties of the aerosol.

In Chapter 3 we use ASP within a Lagrangian parcel model to study the gas- and aerosol-phase chemistry of young smoke plumes from three fires: the Otavi East African savannah fire [*Jost et al.*, 2003b], the Alaskan forest fire B309 [*Goode et al.*, 2000], and the Timbavati South African savannah fire [*Hobbs et al.*, 2003]. We find that our model explains the formation of ozone in the Otavi and Alaska plumes fairly well but that our initial model simulation of the Timbavati smoke plume

underestimated the formation of ozone and secondary aerosol matter. We then explore several hypotheses to explain the disagreement between the model and observation for the Timbavati plume.

In Chapter 4 we use ASP with the 3D Eulerian cloud resolving model of *Wang and Chang* [1993] and *Wang and Prinn* [2000] to perform the first known simultaneous simulation of the gas- and aerosol-phase chemistry, radiative transfer, and fluid dynamics of a young smoke plume (the Timbavati savannah fire plume). Based on the results of our Lagrangian study, we run two chemistry cases for the Timbavati smoke plume. In the reference chemistry case, the uncharacterized organic species were assumed to be unreactive and heterogeneous chemistry was not included. In the expanded chemistry case, the uncharacterized compounds were included, as were heterogeneous reactions of NO_2 and SO_2. We find that the expanded chemistry case provides a better match with observations of ozone, OH, and secondary aerosol matter than the reference chemistry case, but still underestimated the observed concentrations. We find that direct measurements of OH in the young smoke plumes would be the best way to determine if heterogeneous production of HONO from NO_2 is taking place, and that these measurements should be a priority for future field campaigns.

In Chapter 5 we use ASP in an Eulerian box model to evaluate the errors introduced into the calculation of the effective emissions from biomass burning plumes by the automatic dilution of emissions within a large-scale grid box, as is done in many current GACMs. We find that the automatic dilution approach can result in large errors in the predicted concentrations of O_3, NO_x, and aerosol species within the young smoke plume. We then make recommendations for the inclusion of young plume-scale chemical and physical processes in future GACMs.

Chapter 6 summarizes the major conclusions of this work, discusses the limitations of current data and theory, and makes suggestions for future research on the chemistry and dynamics of young biomass burning plumes.

1.2 Literature Review

In this thesis, we simultaneously model the gas-phase chemistry, aerosol-phase chemistry, and fluid dynamics within the smoke plume in order to better predict the impacts of biomass burning on global chemistry and climate. Here we review the literature on the impacts of biomass burning emissions on climate (Section 1.2.1), the observed and modeled transformations of trace gases and aerosols in young smoke plumes (Section 1.2.2), and the fluid dynamics of buoyant pollution plumes

(Section 1.2.3).

1.2.1 Impact of Biomass Burning Emissions on Climate

There are three classes of biomass burning emissions that can impact the global climate. First, biomass burning emits well-mixed greenhouse gases, such as CO_2, CH_4, and N_2O. Second, biomass burning emits large amounts of CO, NO_x, and NMOCs, which react in the troposphere to produce ozone, another greenhouse gas. Finally, biomass burning is a large source of primary and secondary aerosol particles, which impact climate directly by scattering and absorbing solar radiation and indirectly by altering the albedo and precipitation efficiency of clouds. In this subsection, we review the literature on the impacts of these three classes of biomass burning emissions on global atmospheric chemistry and climate in order to determine what chemical and physical processes should be included in our young plume model.

Well-mixed Greenhouse Gases

Biomass burning is a significant source of the long-lived greenhouse gases CO_2, CH_4, and N_2O, and thus can cause a positive radiative forcing, tending to warm the climate [*IPCC*, 2001]. While biomass burning is not the predominant source of these gases to the atmosphere, biomass burning may have a large impact on the interannual variability of the emissions of these gases. For example, the Indonesian wildfires of 1997 are believed to have made a large contribution to the leap in atmospheric carbon dioxide levels in 1997-1998, emitting between 0.8–2.6 Pg of carbon as CO_2 in 1997 [*Page et al.*, 2002; *Langenfelds et al.*, 2002]. Other large catastrophic fires, like the 12 million acre Chinese/Soviet Union forest fire of 1987, may have had similar impacts on the atmospheric budgets of carbon dioxide [*Levine*, 1994]. However, emissions of these long-lived species are unlikely to be affected by chemistry taking place within young smoke plumes, and so they are not considered further in this thesis.

Ozone Precursors

Biomass burning releases large amounts of CO, NO_x, and NMOCs. These emissions can react within the troposphere to the produce ozone (O_3), a greenhouse gas [*Andreae and Merlet*, 2001; *Crutzen and Andreae*, 1990; *Levine*, 1994]. Tropospheric ozone has a shorter atmospheric lifetime than CO_2 or CH_4, and is not well-mixed in the atmosphere. Transport of the biomass burning smoke can lead to enhanced ozone levels over large, continental-size regions [*Chan et al.*, 2001]. *Marfu et al.* [2000] estimated that on a global scale, $\sim$9% of tropospheric ozone is related to biomass burning.

The creation of tropospheric ozone by biomass burning emissions is especially important in the tropics, where biomass burning can be the predominant source of ozone precursors. Ozone profiles in Brazil and the Congo show dramatic enhancements between 1 km and 4 km during the dry seasons, with the highest concentrations ranging between 50 ppb to 100 ppb [*Andreae and Merlet*, 2001]. These ozone levels are dramatically higher than those of the relatively clean air over the equatorial Pacific, which are generally 10 ppb at the same altitude. This dramatic enhancement of ozone levels over the tropics causes a positive radiative forcing for the region, tending to increase surface temperatures.

The formation of tropospheric ozone by biomass burning emissions is not limited to Africa and Brazil. For example, *Chan et al.* [2001] showed that the enhanced ozone levels observed over Hong Kong in 1997 (up to 130 ppb) were caused by the 1997 Indonesian wildfires. Using data obtained from the Total Ozone Mapping Spectrometer, *Chan et al.* [2001] found that these strong ozone enhancements extended over all of tropical Southeast Asia and subtropical south China. These ozone enhancements led to an additional radiative forcing of 0.26 to 0.48 W m^{-2} over Hong Kong, on top of the normal ozone forcing of 0.48 and 0.39 W m^{-2} in October and December. Similarly, *McKeen et al.* [2002] report that the 1995 Canadian wildfires led to enhanced ozone levels over most of the eastern and central United States. The maximum enhancement was near 30 ppb, but enhancements of 10 ppb were found as far south as Mississippi and as far east as Maryland. In addition, the model results of *Leung et al.* [2007] suggest that enhanced boreal forest fires in 1998 increased surface ozone concentrations by 5-6 ppb near the fires, and enhanced ozone at 500 hPa by 6-10 ppbv north of 45°N and by as much as 20 ppbv over northeast Canada and Russia.

Since the formation of O_3 in the troposphere from biomass burning emissions depends greatly on the emissions of NO_x and NMOCs, and since NO_x and NMOCs react rapidly within young biomass burning smoke plumes, it is necessary to include the chemistry of these species in our model of young biomass burning smoke plumes. Our model predicts the formation of O_3 and the oxidation of NO_x and NMOCs within the young smoke plume in order to better predict the impact of ozone precursors from biomass burning on the global and regional environment.

Aerosol Particles

Particles are directly emitted by biomass burning (primary particulate matter) and can also form from the reaction and condensation of gaseous compounds in the smoke plume (secondary particulate matter) [*Lobert and Warnatz*, 1993; *Andreae and Merlet*, 2001]. The primary particles are mixtures of black carbon (soot), organic compounds, salts (primarily potassium chloride) and

various trace elements and heavy metals, such as phosphorus, iron, lead, and potassium [*Artaxo et al.*, 1993]. While aerosol particles have shorter lifetimes in the atmosphere than the well-mixed greenhouse gases, the small size of biomass burning aerosols (mass mean radius of 0.1 - 0.2 μm) implies that they can travel long distances in the atmosphere, and thus affect climate on regional and global scales [*Kaufman et al.*, 1998]. Indeed, organic tracers for biomass burning have been found in atmospheric particulate matter over the ocean, confirming the long-range transport of smoke aerosols off of the continents [*Simoneit and Elias*, 2001].

Aerosols can affect climate in many ways, generally leading to a negative radiative forcing. The most basic effect of aerosols is the absorption and scattering of sunlight known as the direct effect [*IPCC*, 2001]. In principle, the direct effect of aerosols can be determined from four quantities as a function of wavelength: the extinction cross-section (m^2/g), the functional dependence of light scattering on relative humidity, the single scattering albedo, and the asymmetry parameter. However, the inhomogeneous composition of biomass burning aerosols, along with uncertainty in the number and size distribution of aerosols emitted and their distribution in the atmosphere, makes it difficult to calculate accurately their direct radiative forcing. The IPCC Third Assessment Report estimates the direct radiative effect of biomass burning aerosols as –0.3 W m^{-2} with an uncertainty range from –0.1 to –0.5 W m^{-2} [*IPCC*, 2001]. *Hobbs et al.* [1997], using the results of the SCAR-B experiment, estimate the globally averaged direct radiative forcing due to smoke as no lower than –0.3 W m^{-2}. The review of *Reid et al.* [2005a] notes that the global estimates of direct forcing from biomass burning aerosols vary widely, ranging from near zero to -1 W/m^2, and that most of this difference can be traced to varying assumptions on the optical properties of smoke particles.

In addition to their direct effects, aerosols from biomass burning can affect climate indirectly through their effects on clouds [*IPCC*, 2001]. Observations of forest fires [*Hobbs and Radke*, 1969; *Eagan et al.*, 1974] have shown that biomass burning aerosols can act as cloud condensation nuclei (CCN), thereby altering the microstructure of clouds. This can have two effects on climate. First, the addition of biomass burning CCN can change the size distribution of cloud particles, thereby altering cloud albedo (the first indirect effect) [*IPCC*, 2001]. An analysis of satellite data over the Amazon Basin and Cerrado performed by *Kaufman and Fraser* [1997] found that biomass burning smoke increased cloud albedo from 0.35 to 0.45, while reducing average droplet size from 14 to 9 μm. *Kaufman and Fraser* [1997] estimate this indirect forcing at –2 W m^{-2} for the region during three months of the dry season (July through September).

Second, biomass burning aerosols can alter the precipitation efficiency of clouds (the second indirect effect) [*IPCC*, 2001]. *Eagan et al.* [1974] have reported that the emission of CCN by

forest fires tends to narrow the cloud droplet size distribution, and might therefore reduce the ability of clouds to produce rain through the coalescence of cloud particles. *Rosenfeld* [1999] used satellite observations of the Tropical-Rainfall-Measuring Mission (TRMM) to show that the warm rain convective processes in convective tropical clouds are dramatically inhibited by the addition of forest fire smoke. Estimates of the magnitude of this effect on radiative forcing are highly uncertain, and are the subject of much current research [*IPCC*, 2001].

In addition, the presence of black carbon (soot) in biomass burning aerosols allows the aerosols to absorb sunlight as well as scatter it. The absorbed sunlight would lead to a warming of the atmosphere around the aerosols, while the aerosols would cool the surface due to the reduction of incoming solar radiation. However, *Ackerman et al.* [2000] have proposed that solar absorption by black carbon aerosols might reduce cloud cover levels (by suppressing condensation and suppressing convection below the layer), which could offset the surface cooling effects of the aerosols. Estimates of the total top of atmosphere (TOA) climate forcing from black carbon vary from +0.25 W/m^2 [*IPCC*, 2001] to +0.5 W/m^2 [*Jacobson*, 2001] to +0.5 - +1.0 W/m^2 [*Hansen and Sato*, 2001].

In order to predict the regional and global effects of biomass burning particle emissions on climate, it is necessary to have accurate information on the size distribution and chemical composition of the aerosol [*IPCC*, 2001]. As the size and composition of biomass burning aerosol can be significantly altered within biomass burning plumes, we need to assess the physical and chemical transformation of biomass burning aerosol in the plumes prior to their spreading to large scales. Our model predicts the changes in the aerosol size distribution and chemical composition within the young smoke plumes in order to better understand the impact of these emissions on global atmospheric chemistry and climate.

1.2.2 Physical and Chemical Transformations in Combustion Plumes

Our model of the gas- and aerosol-phase chemistry of young biomass burning smoke plumes is based on the results of previous observational and modeling studies of the physical and chemical transformations of trace gases and aerosols in combustion plumes. This subsection summarizes the major result of these previous studies. Most previous modeling studies of biomass burning plumes have focused on gas-phase chemistry and the formation of ozone [*Trentmann et al.*, 2003a; *Jost et al.*, 2003b; *Mason et al.*, 2001; *Mauzerall et al.*, 1998; *Mason et al.*, 2006], while most models of aerosol dynamics in plumes have focused on the sulfate and nitrate emissions of power plants [*Lazaridis et al.*, 2001; *Hudischewskyj and Seigneur*, 1989; *Bassett et al.*, 1981]. In contrast, our model is designed to model the gas-phase chemistry and aerosol dynamics in young biomass burning smoke

plumes simultaneously. In the following sections we discuss the previous observations and modeling of the gas-phase chemistry within young biomass burning plumes, summarize recent observations of the physical and chemical transformations of aerosols within young biomass burning plumes, and discuss the previous modeling studies of aerosol dynamics in plumes from industrial smoke stacks.

Gas-Phase Chemistry in Young Biomass Burning Smoke Plumes

Most previous observational and modeling studies of young biomass burning smoke plumes has focused on the gas-phase chemistry within these plumes. Here we summarize the results of these studies.

Mauzerall et al. [1998] analyzed the photochemistry occurring in biomass burning plumes over the tropical south Atlantic using data collected during the Transport and Atmospheric Chemistry Near the Equator - Atlantic (TRACE-A) campaign in September 1992, during the tropical dry season. They found that O_3 was produced in biomass burning plumes over at least a one week period; that the formaldehyde (CH_2O) found in biomass burning plumes is primarily emitted during the fire or formed shortly thereafter, and is subsequently lost as the plume ages; and that the acetone found in the plumes is formed after emission as the plume ages. In a case study of a large biomass burning plume, *Mauzerall et al.* [1998] found elevated concentrations of peroxy acetyl nitrate (PAN) in the fresh plume, and that the subsequent degradation of PAN helped maintain NO_x concentrations. Ozone production in the plume was NO_x-limited. *Mauzerall et al.* [1998] suggested that the majority of O_3 production in the tropical south Atlantic is formed in biomass burning plumes.

Mason et al. [2001] used a Lagrangian parcel model to study the effect of including the direct emissions of oxygenated organic species on simulations of the gas-phase photochemistry in a smoke plume. They calculated the photolysis rate constants assuming clear-sky conditions and used the NCAR Master Mechanism for the gas phase chemistry. They found that the concentration of NO_x drops rapidly, and that conditions within the plume are NO_x-limited thereafter, consistent with the conclusions of *Mauzerall et al.* [1998]. They found that the addition of oxygenated compounds to the simulation could either increase or decrease net O_3 production, depending on the initial ratio of NO to CO. Oxygenates were found to always increase H_2O_2 and organic hydroperoxide production due to increased rates of radical-radical reactions. *Mason et al.* [2001] suggested this was the result of the accelerated removal of NO_x from the smoke plume due to the increased radical concentrations resulting from the photolysis of oxygenates (mainly CH_2O) and the high reactivity of the oxygenates.

Jost et al. [2003b] used a Lagrangian parcel model to examine the mechanisms behind the production of O_3 and acetone observed in the plume from the Otavi savannah fire in Northern Namibia during the SAFARI 2000 experiment on September 13, 2000. Fast production of O_3 and acetone was observed in the plume over the first two hours of plume aging. Following *Mason et al.* [2001], *Jost et al.* [2003b] included the primary emissions of short-lived oxygenated hydrocarbons and calculated actinic flux and photolysis reaction rates under clear sky conditions. In addition, two heterogeneous reactions on smoke aerosol were taken into account: hydrolysis of N_2O_5 to produce HNO_3 (uptake coefficient $\gamma_{N_2O_5} = 0.1$) and formation of HONO from NO_2 ($\gamma_{NO_2} = 10^{-6}$). The box model reproduced the fast O_3 production observed, but underestimated acetone mixing ratios in the aging plume. After examining several possible routes of secondary acetone production, they suggest that the acetone formation may be coming from one or more compounds not currently identified in biomass burning emissions and/or not currently included in tropospheric chemical mechanisms.

Trentmann et al. [2003a] used a three-dimensional plume model to investigate the photochemical evolution of a biomass-burning plume during the first tens of minutes after emission. They simulated the Quinault prescribed fire studied during the SCAR-C experiment. They used the three-dimensional non-hydrostatic plume model ATHAM, originally designed for the study of volcanic plumes [*Oberhuber et al.*, 1998; *Herzog et al.*, 1998], to simulate transport, turbulent diffusion, and radiation within the plume. In contrast to *Mason et al.* [2001] and *Jost et al.* [2003b], *Trentmann et al.* [2003a] included the interaction of smoke particles with solar radiation in their calculation of photolysis frequencies, using measurements of aerosol composition [*Martins et al.*, 1996] and size distribution [*Hobbs et al.*, 1996; *Gasso and Hegg*, 1998] in the aged smoke (1-2 hours old) from the Quinault fire. However, they did not simulate the growth of aerosol particles within the plume; the particle sizes and composition were not allowed to evolve with time [*Trentmann et al.*, 2002]. In addition, two heterogeneous reactions were included: hydrolysis of N_2O_5 to produce HNO_3 and formation of HONO from NO_2 ($\gamma_{N_2O_5} = 0.1$ and $\gamma_{NO_2} = 10^{-6}$). *Trentmann et al.* [2003a] found that their modeled O_3 concentrations were close to observations, but found that omitting the emissions of oxygenated volatile organic compounds led to unrealistically low ozone concentrations. The main nitrogen reservoir species downwind of the fire were HNO_3 (60%) and PAN (30%). Photolysis of formaldehyde emitted by the fire was found to be the primary source of radicals in the plume. In addition, *Trentmann et al.* [2003a] performed sensitivity simulations which found that the addition of a non-absorbing aerosol and/or a lower emission of NO_x enhanced the radical concentration, photochemical O_3 formation and the oxidation efficiency of the plume.

Trentmann et al. [2005] used a Lagrangian parcel model to study the chemical processes within the Timbavati smoke plume [*Hobbs et al.*, 2003]. The field measurements showed significant production of ozone and acetic acid; however, the model significantly underestimated the ozone production rate, and no significant production of acetic acid was observed in the model. *Trentmann et al.* [2005] concluded that the ozone discrepancy could be caused by the neglect of unmeasured emissions or by a heterogeneous reaction of methanol with NO_2 first proposed by *Tabazedeh et al.* [2004]. *Trentmann et al.* [2005] also concluded that no known gas-phase reactions could produce sufficient acetic acid on the 1 hour time scale of the observations.

Mason et al. [2006] presented the results of an intercomparison of the State University of New York (SUNY-Fredonia) model of *Mason et al.* [2001] and the Mainz model of *Trentmann et al.* [2005] in simulating the chemical evolution of two biomass burning plumes: the Timbavati savannah fire and the Alaskan black spruce forest/shrub/bog fire B309 [*Goode et al.*, 2000]. They found that the differences between the two smoke plume models were significantly smaller than the uncertainties of the available photokinetic data and field measurements, with most of the deviations between models attributable to differences in oxidative photochemical mechanisms rather than the calculation of photolysis frequencies.

In general, these previous studies of the chemistry of young smoke plumes have not accounted for the transformations of the aerosol particles in the smoke, or their potential impact on the gas-phase chemistry within the smoke plume. Those studies that have looked at the impacts of the aerosol particles on the gas-phase chemistry, either through heterogeneous chemistry or the scattering and absorption of sunlight, have used fixed aerosol size distributions and optical properties, ignoring the impact of aerosol growth in the smoke plumes on the aerosol properties. In contrast, we model the evolution of the gas and aerosol phases simultaneously, and explicitly model the impact of the growing aerosol particles on the gas-phase chemistry within the young smoke plume.

Observations of Aerosol Transformations in Young Biomass Burning Smoke Plumes

We have not been able to find any previous modeling studies of the growth of aerosol particles in young biomass burning smoke plumes. However, there have been several observational studies of the chemical and physical transformations of smoke aerosols in biomass burning plumes. Here we summarize these previous studies and discuss how our aerosol model is designed to capture the important transformations of biomass burning particles.

Aerosol changes within biomass burning smoke plumes are driven by the coagulation of existing particles, the growth of existing particles due to gas-particle partitioning of material, chemical

reactions within or on the surface of existing particles, and the nucleation of new particles from the gas phase [*Bassett et al.*, 1981]. *Liousse et al.* [1995] studied the effect of aging on the optical properties of savannah biomass burning aerosols during the FOS-DECAFE experiment at Lamato, Ivory Coast in January 1991. They found that the main altered physical parameter of the smoke mix is the size distribution, as rapid coagulation occurs within the first 100 m of the fire, reducing the number of sub-micron carbonaceous particles and increasing the number of larger particles. Plume dispersion reduced both particle number concentration and water vapor concentration, leading to a decrease in aerosol optical depth. The ratio of black carbon (soot) to total particle carbon increased, suggesting that particulate organic material was lost as the particles aged.

Hobbs et al. [1996], *Martins et al.* [1996], and *Gasso and Hegg* [1998] studied the particle size distributions, composition, and optical properties of smoke emitted from three proscribed fires in the Pacific Northwest during the Smoke, Clouds and Radiation - California (SCAR-C) experiment. *Hobbs et al.* [1996] reported that CO_2-normalized peak particle concentrations in the Quinault plume were dramatically reduced over the first two hours due to coagulation, with the mode CO_2-normalized number concentration changing from 3,900 $cm^{-3}(ppm\ CO_2)^{-1}$ to 2,000 $cm^{-3}(ppm\ CO_2)^{-1}$, the particle number mode diameter shifting from 0.16 to 0.28 μm and the particle volume mode diameter shifting from 0.25 to 0.38 μm. *Hobbs et al.* [1996] suggest that, as the ratio of SO_2 to excess CO_2 decreased by 60% over an interval of 1.8 hr., some of the observed increase in particle mode size was produced by the oxidation of SO_2 and the subsequent condensation of the produced sulfate. Total particle volume increased by a factor of 2 over the 1.8 hour period, due to the absorption of water vapor and/or gas-to-particle conversion (*i.e.*, the formation and condensation of sulfate and condensed organic matter (OM)). In addition, the CO_2-normalized light scattering coefficient (units $km^{-1}(ppm\ CO_2)^{-1}$) increased with time, suggesting that the increase in particle size has a stronger influence on the scattering coefficient than the reduction in particle number concentration.

Reid and Hobbs [1998] and *Reid et al.* [1998] studied the physical, chemical, and optical properties of young smoke and regional hazes dominated by smoke in Brazil as part of the Smoke, Clouds, and Radiation-Brazil (SCAR-B) experiment during the 1995 burning season. They found that as smoke particles aged, their sizes increased significantly due to coagulation and the formation of secondary aerosol matter (ammonium, organic acids and sulfate). Aerosol mass increased by approximately 20-40% due to condensation and gas-to-particle conversion of inorganic and organic vapors. They suggested that a third to a half of this mass growth occurs in the first few hours of aging due to the condensation of large organic molecules, with the remainder of the mass growth

likely associated with photochemical and cloud-processing mechanisms operating over several days.

Posfai et al. [2003] and *Li et al.* [2003] studied the composition, size distribution and aging of carbonaceous and inorganic particles, respectively, emitted by biomass burning in southern Africa during the SAFARI 2000 campaign. *Posfai et al.* [2003] found three distinct types of carbonaceous particles in smoke: organic particles with inorganic salt inclusions, "tar ball" particles, and soot particles. Soot was a minor constituent in all plumes studied, consistent with studies of the primary emissions from burning of Asian biomass, where elemental carbon was found to be 0.6% to 11.4% of the fine particle mass [*Sheesley et al.*, 2003]. The concentration of soot in the emissions was twice as high in flaming combustion as in smoldering combustion. Organic particles dominated young smoke, and appeared to have been hydrated prior to analysis. Soot particles were generally not mixed with organic particles in young smoke. The predominant salts in young smoke were KCl, K_2SO_4 and KNO_3. The Cl/S ratio depended both on fuel and the type of combustion, with flaming combustion favoring KCl, and smoldering combustion favoring K_2SO_4.

In the slightly aged (1 - 2 hr.) smoke, tar ball particles begin to outnumber the organic particles within the first hour of aging [*Posfai et al.*, 2003]. *Posfai et al.* [2003] suggest that this may be due to the nucleation or condensation of organic matter. In addition, aged carbonaceous particles appear to contain more C and S and less K and Cl than young smoke, possibly due to the condensation of organic matter and sulfate. *Li et al.* [2003] point out that the KCl found in the young smoke is quickly (16 km downwind) transformed to KNO_3 and K_2SO_4, likely due to the oxidation of SO_2 and NO_x. *Li et al.* [2003] suggest that the transformation of KCl to KNO_3 and K_2SO_4 may change the hygroscopic properties of the smoke particles. In addition, *Li et al.* [2003] found that the chain-like soot aggregates present in young smoke break down into more closely packed, spherical particles as the smoke ages, possibly due to collisions or the condensation of water onto the soot particles.

In the background haze layers, *Posfai et al.* [2003] found that the higher haze layers ($>$ 3km) were more affected by smoke emissions than the lower haze layers. The lower haze consisted primarily of ammonium sulfate particles, whereas the upper haze layers consist of mixed organic/sulfate, soot/sulfate, and organic/soot/sulfate particles which have a more uniform composition (*i.e.* are closer to an internal mixture) than in young smoke. *Posfai et al.* [2003] suggest that the mixtures in the upper haze layers could be formed either by coagulation or the heterogeneous nucleation of sulfate on preexisting organic and soot particles. In general, the particles in the upper haze layers are larger than in young or slightly aged smoke, the concentration of tar ball particles is relatively low, and externally mixed sulfate particles may exist alongside the smoke particles *Abel et al.* [2003] reported an increase in the bulk aerosol single-scattering albedo with time during SAFARI 2000,

going from 0.84 near the source to 0.90 in regional hazes that have aged 5 hours. They suggested that the condensation of scattering material (*e.g.*, OM and sulfate) from the gas phase accounts for most of the change, with the transformation of soot from a chain-like to a clump-like structure having little effect on the bulk aerosol single scattering albedo.

Reid et al. [2005b] reviewed the available literature on smoke particle size, chemistry, thermodynamic properties and emission factors. They report that fresh smoke particles are generally internally mixed, with a core of black carbon and KCl coated with organic compounds. The hydrocarbons in fresh smoke are predominantly long chain alkanes, with carbohydrates and organic acids accounting of 10-20% of the particle mass each. Aged smoke particles are generally larger and more spherical than fresh smoke particles, and the aged particles have a narrower size distribution (lower geometric standard deviations). Aged smoke particles also show a substantial increase in sulfate, nitrate, and ammonium concentration over that of fresh smoke. Organic acids such as oxalate, formate, and acetate are also greatly enriched in aged smoke, along with other semi-volatile organic compounds. *Reid et al.* [2005b] suggest that this increase in organic acids increases the CCN efficiency and hygroscopicity of the smoke particles with time. *Reid et al.* [2005a] also find that the optical properties of smoke can change substantially with aging, with coagulation increasing particle mass scattering efficiency and single scattering albedo, and condensation of vapor increasing particle mass scattering efficiency and single scattering albedo while decreasing particle mass absorption efficiency. *Reid et al.* [2005b] conclude that the modeling of smoke aging is "extremely important to our future understanding of the aging process" and that future field campaigns would benefit from the inclusion of mesoscale chemistry models during the mission-planning phase.

In this thesis we compare the results of our model to the observations of the Timbavati smoke plume from SAFARI 2000. Based on the above observations, our model is designed to simulate the growth of aerosol in biomass burning smoke plumes due to coagulation and the condensation of inorganic and organic secondary aerosol matter. The model includes the thermodynamics of the inorganic and organic aerosol, including the observed loss of Cl^- to the gas phase as HCl. The organic aerosol includes long chain alkanes, carbohydrates and organic acid species. The optical properties of the aerosol are also calculated and compared to available observations.

Models of Aerosol Dynamics in Industrial Smoke Stack Plumes

As mentioned above, we have not found any previous studies that simultaneously modeled the gas- and aerosol-phase chemistry within young biomass burning smoke plumes. Most modeling work on aerosol dynamics in plumes has focused on inorganic aerosol in plumes from industrial smoke

stacks. Here we summarize these previous studies, and discuss how our aerosol model differs from these studies.

Bassett et al. [1981] developed the first model for simultaneously predicting the evolution of the size distribution and chemical composition of aerosols in a smoke stack plume. They used a simple box model that simulated the dilution of plume emissions using the Pasquill-Gifford parameters to estimate the rate of plume dilution. *Bassett et al.* [1981] used an internally-mixed sectional size distribution to simulate the aerosol dynamics. Coagulation, homogeneous nucleation, heterogeneous condensation, aerosol chemical equilibrium and particle-phase chemical reactions (*i.e.*, the oxidation of SO_2 by O_2, catalyzed by Mn^{2+}) were included. The model assumed that the initial aerosols were aqueous solutions of $MnSO_4$, and simulated the formation of sulfate in the plume in a constant relative humidity of 90%. They found that the particles in the plume grew due to coagulation, the liquid-phase oxidation of SO_2 and the condensation of sulfuric acid vapor formed by the gas-phase oxidation of SO_2.

Hudischewskyj and Seigneur [1989] developed a more detailed model to calculate the gas- and aerosol-phase concentrations of sulfur and nitrogen compounds in a plume that undergoes transport, dispersion, and dry deposition in the atmosphere. Instead of the simple box model used by *Bassett et al.* [1981], *Hudischewskyj and Seigneur* [1989] used the PLMSTAR model developed by *Godden and Lurmann* [1983] which uses a two-dimensional array of grid cells moving along a mean wind trajectory to simulate the transport and dispersion of the plume. The Carbon Bond Mechanism, version 3 (CBM-III) [*Killus and Whitten*, 1984] was used to perform the gas-phase chemistry, with the addition of other reactions to simulate the chemistry of sulfate and nitrate formation. As in *Bassett et al.* [1981], aerosols were modeled using an internally-mixed sectional aerosol distribution. Particle growth due to formation of sulfate (gas-phase reaction of SO_2 with OH and aqueous reactions of SO_2 with H_2O_2 and O_2, catalyzed by Mn^{2+} and Fe^{3+}) and nitrate (gas-phase reaction of NO_2 with OH) was included, as was coagulation and dry deposition. Comparisons of the model results with measurements made in the plumes of three power plants and one smelter were satisfactory, although the model tended to underpredict sulfate aerosol concentrations and scattering coefficients.

More recently, *Lazaridis et al.* [2001] used the Reactive Plume Model, version 4 (RPM-IV) [*Morris et al.*, 1992] to study aerosol processes within point source plumes, and compared the results with observations of power plant plumes in Nevada and Arizona. RPM-IV, like PLMSTAR, simulates a two-dimensional Lagrangian grid that follows the mean wind speed. The number of cells in the 2-D grid remains constant, and the cells expand as the plume travels downwind in such a way

that the amount of an inert species remains constant in the cell. The rate of expansion is chosen to match the evolution of a Gaussian point source plume. Aerosols were simulated using an internally-mixed size distribution, which included processes such as nucleation (*i.e.*, binary nucleation of H_2SO_4 and H_2O), coagulation, condensation and deposition. Aerosols were assumed to consist of elemental carbon (EC), organic carbon (OC), crustal material, water, ammonium, chloride, nitrate, and sulfate. The inorganic multicomponent equilibrium model SEQUILIB [*Pilinis and Seinfeld*, 1987; *Lurmann et al.*, 1997] was used to simulate aerosol equilibrium. Constant percentage yields of condensable organic compounds (COCs) from *Pandis et al.* [1992] were used to estimate the potential production of COCs from oil industry emissions and vehicle emissions. *Lazaridis et al.* [2001] found that secondary organic aerosol formation does contribute to the total aerosol mass concentration in these plumes, but at a much lower level than the oxidation of sulfate.

Our model represents an extension of these above studies. In this thesis we explicitly model the growth of aerosol particles in the smoke plume due to coagulation and the condensation of secondary inorganic and organic aerosol matter using a moving-center sectional size distribution. The yield of organic aerosol matter is determined using the absorptive partitioning theory of *Pankow* [1994a] and *Pankow* [1994b]. The rates of nucleation and aqueous chemistry in biomass burning smoke plumes are also evaluated through simple scale analyses. The aerosol chemistry model is used in both a (single-box) Lagrangian parcel model and a 3D Eulerian dynamics model, and model results are compared to the observations of the Timbavati smoke plume.

1.2.3 Model Simulations of the Fluid Dynamics of Biomass Burning Plumes

Since the non-linear chemistry within smoke plumes can be greatly affected by the fluid dynamics of the buoyant plume, we want to model the chemistry and dynamics within the young smoke plume simultaneously. Much work has been done previously on modeling the effective plume rise and horizontal dispersion of buoyant plumes in the atmosphere. Here, we summarize this previous work and discuss how we model plume rise and dispersion in our 3D Eulerian plume model.

Most of the past work on the effective plume rise of buoyant plumes has focused on buoyant jets emitted from smoke stacks. Many empirical formulas have been presented to predict the effective rise of the plume above the top of the chimney as a function of wind speed, heat emission rate, atmospheric stability and distance downwind of the chimney. For example, Table 18.3 of *Seinfeld and Pandis* [1998] presents the formulas of *American Society of Mechanical Engineers (ASME)* [1973] and *Briggs* [1969] for plumes dominated by buoyant forces and plumes dominated by momentum forces. More theoretical models for plume rise from a smoke stack have also been

proposed. For example, *Schatzmann* [1979] developed an integral model of plume rise, deriving a new function for atmospheric entrainment into the plume from the mean kinetic energy equation and the integral form of the streamwise momentum equation. While this model is based on the fundamental physics of the buoyant plume, the entrainment function includes 5 empirically-fitted coefficients.

More recently, mesoscale Eulerian models have been used to investigate the plume rise and horizontal dispersion of plumes from biomass burning. For example, *Trentmann et al.* [2002] modified the 3-dimensional (3D) Eulerian volcanic plume model ATHAM [*Oberhuber et al.*, 1998; *Herzog et al.*, 1998] to successfully simulate the injection height (250-600 m) and horizontal extent (4 km) of the plume from the Quinault prescribed fire studied during SCAR-C. *Trentmann et al.* [2003b] and *Trentmann et al.* [2003a] used this simulation to investigate the actinic flux and gas-phase chemistry, respectively, within the Quinault smoke plume.

Trentmann et al. [2006] and *Luderer et al.* [2006] used the ATHAM model to investigate the injection of biomass smoke into the lower stratosphere by the Chisholm forest fire in Alberta, Canada in 2001. The Chisholm fire initiated deep convection, creating a pyro-cumulonimbus cloud that injected smoke to an altitude of 13 km, above the tropopause at 11.2 km. The reference model simulation of *Trentmann et al.* [2006] showed that the main smoke outflow from the pyro-convection occurred at about 10.6 km, but that about 8% of the smoke aerosol was transported above the tropopause. In contrast to regular deep convection, the region of maximum updraft for the pyro-cumulonimbus cloud was near the surface above the fire, with updraft velocities of greater than 10 m/s at the cloud base. *Luderer et al.* [2006] found that the pyro-convection simulations were very sensitive to the background meteorology and the release of sensible heat by the fire. The injection height of the plume was not very sensitive to emissions of water vapor, but water vapor did affect the amount of smoke transported above the tropopause level. In contrast to other studies, *Luderer et al.* [2006] did not find any enhancement of convection by the presence of aerosols, although the microphysical structure of the cloud was sensitive to the aerosol burden. *Luderer et al.* [2007] further investigated the pyro-cumulonimbus cloud created by the Chisholm fire, concluding that the small-scale mixing processes near the tropopause were enhanced by the formation and breaking of a stationary gravity wave induced by the overshooting dome of the cloud. This small-scale mixing significantly enhanced the penetration of smoke into the stratosphere.

Recently, *Freitas et al.* [2007] proposed a method for including the sub-grid scale plume rise of vegetation fires in low-resolution 3D Eulerian atmospheric models, such as GACMs. They imbedded a 1D cloud-resolving model in each column of the 3D host model. The host model provides the

environmental conditions, and the plume rise is calculated explicitly using the 1D model. The simulated plume rise is then used to determine the effective injection height of emissions in the host model. The lower boundary condition for the 1D model is based on a virtual source of buoyancy with known or estimated convective energy flux and radius. These parameters are used with similarity formulas to determine the vertical velocity and temperature of the buoyant plume at the surface. The final plume rise height is determined as the height where the vertical velocity of the plume drops below 1 m/s. This scheme improved the match between observed and modeled CO concentrations by increasing the modeled CO concentration in the free troposphere and decreasing it in the boundary layer. They found that plume rise was sensitive to the environmental parameters supplied by the 3D host model, but was less sensitive to the uncertainty in the fire size and heat flux.

In this thesis, we simultaneously model the chemistry and fluid dynamics in a young biomass burning smoke plume using the 3D Eulerian model CRM6 [*Wang and Chang*, 1993; *Wang and Prinn*, 2000], which we have modified to include a surface source of sensible heat, trace gases, and aerosol particles. CRM6 calculates the plume rise and horizontal dispersion of the buoyant smoke plume by solving the nonhydrostatic momentum equations using the first order turbulence closure scheme of *Klassen and Clark* [1985]. The comparison of the results of the modified CRM6 model and the observations for the Timbavati smoke plume are presented in Chapter 4.

1.3 Goals of the Thesis

Based on the above literature review, we find that several major questions remain about the evolution of trace gases and aerosols in young biomass burning plumes.

First, the mechanisms by which biomass burning aerosols grow in size and change in composition are uncertain. These changes could be caused by coagulation of preexisting particles, by the condensation of products from the gas-phase oxidation of precursor compounds, by the nucleation of new particles, or by heterogeneous or particle-phase chemistry taking place on the surface of or within the particles, respectively. We would like to determine the major mechanisms for the growth of aerosol particles and the formation of secondary particle matter within smoke plumes.

Second, the effect of aerosols on gas-phase photochemistry within biomass burning plumes needs to be further investigated. Aerosols can effect gas-phase photochemistry by altering the actinic flux within the plume by adsorbing or reflecting radiation or by heterogeneous reactions taking place on the surface of the particles. Although some work has been done on these issues (*e.g.*, *Trentmann*

et al. [2003b]), further laboratory and modeling work is needed to determine the impact of the emitted particles on the gas-phase chemistry of young combustion source plumes.

In addition, most GACMs model the climate impacts of combustion plume emissions by automatically diluting the emissions into large-scale grid boxes, ignoring the chemical and physical changes that can take place in the concentrated plume. This assumption could impact the ability of GACMs to simulate the effect of these emissions on atmospheric chemistry and climate.

Thus, the goals of this thesis are first, to simulate the evolution of particles within the plume to determine what processes are important in the growth of particles and the formation of secondary aerosol matter; second, to evaluate the impact of the particles on the gas-phase chemistry within the plume, especially the formation of ozone; and third, to compare the results of the full plume model with the GACM assumption of automatic dilution of emissions within a large-scale grid box, and make recommendations for the inclusion of young plume-scale chemical and physical processes in GACMs.

Chapter 2

Description of the Chemical Model

2.1 Overview of the Aerosol Simulation Program (ASP)

The gas- and aerosol-phase chemical model developed for this work (ASP - Aerosol Simulation Program) uses the model framework and routines developed by *Steele* [2004] for the Mixed Eulerian-Lagrangian Aerosol Model (MELAM). We have extensively added to and modified the original MELAM model, including new and modified routines for gas-phase and heterogeneous chemistry (Section 2.2), a moving-center sectional aerosol size distribution (Section 2.3), the thermodynamics of solid electrolytes, hydrophobic organic species, and aqueous organics (Section 2.4), kinetic, flux-limited condensation of H_2SO_4 and organic species (Section 2.5), a hybrid gas-to-particle mass transfer scheme (Section 2.6), a semi-implicit coagulation routine (Section 2.7), and a core-in-shell Mie calculation of aerosol optical properties (Section 2.8). These routines are described in detail in the corresponding sections below. The model results are compared to experimental data, other model predictions, and analytical solutions where available. Here, we give a brief overview of the components of the model.

The gas-phase chemistry in the model is based on the Caltech Atmospheric Chemistry Mechanism (CACM) of *Griffin et al.* [2002b], including the modifications made by *Griffin et al.* [2005]. The CACM includes state-of-the-art treatment of O_3 formation with the explicit prediction of the formation of semi-volatile compounds that can form SOA. The original CACM was modified in this work to (1) integrate all radical species rather than assuming steady state, (2) fit the reaction rates calculated by the group-contribution method of *Kwok and Atkinson* [1995] to an Arrhenius temperature dependence, and (3) explicitly calculate heterogeneous reaction rates based on the aerosol surface area concentration using the method of *Jacob* [2000].

Aerosols are represented in the model as a moving-center sectional size distribution, based on

the work of *Jacobson* [1997, 2002, 2005]. In this representation, the distribution is divided into a series of size bins. Size bin boundaries remain fixed while the particle size within the bin is allowed to change with time. When the particle size reaches the bin boundary, all of the particle mass and number concentration is moved to the adjacent bin. We use a single size distribution, implicitly assuming that all aerosol of the same size have the same composition (*i.e.*, the particles in each size bin are internally mixed). The model can also be run in a thermodynamic bulk mode (where only aerosol mass concentration is tracked) or in a monodisperse mode (where all particles are assumed to have the same size).

Each particle is assumed to consist of an aqueous embryo and an insoluble sphere, following the method of *Gorbunov and Hamilton* [1997]. This assumption allows ASP to reduce to the original MELAM model in the simulation of how insoluble components affect aerosol activation [*Steele*, 2004]. We assume that the aqueous embryo consists of water, inorganic ions, aqueous NH_3, and aqueous organic species. The insoluble core is assumed to include any aerosol black carbon (BC), hydrophobic organics, and solid electrolytes present.

The inorganic thermodynamics routines in ASP are based on those of MELAM, but have been expanded to include the ions Ca^{2+}, Mg^{2+}, and their salts, and to predict the formation of solid salts at low relative humidities. The thermodynamics routines for organic species in the aqueous and hydrophobic organic phases are based on the Model to Predict the Multiphase Partitioning of Organics (MPMPO) of *Griffin et al.* [2003, 2005] and *Pun et al.* [2002]. We assume that an aqueous phase and a mixed hydrophobic organic phase are always present in the aerosol. Partitioning of organics between the gas and hydrophobic phase is governed by Raoult's law, while partitioning of organics into the aqueous phase is governed by Henry's law. Following *Pun et al.* [2002], we assume that (1) there is no interaction between the aqueous phase inorganic ions and the aqueous phase organics, and (2) that the activity coefficients of the organic ions (formed by the dissociation of organic acids) are equivalent to those of the corresponding molecular solute. We further assume that the pH of the aqueous phase is dominated by the strong inorganic acids and bases, and that the pH effects of the dissociating organic acids are negligible. We have expanded on the MPMPO model by allowing all organic species, including surrogates of primary organic aerosol (POA), to partition into the gas, aqueous, and hydrophobic organic phases, and by adding 5 surrogate compounds recommended by *Decesari et al.* [2006] to represent water soluble organic carbon (WSOC) in regions affected by biomass burning. We have also developed a hybrid routine for calculating aerosol water content, which uses the iterative method of MELAM to calculate the water associated with the inorganic ions, then uses the non-iterative ZSR method to calculate the water associated with the

aqueous organics, and combines the two to get the total aerosol water content.

The model can integrate the time-dependent, flux-limited condensation/evaporation of H_2SO_4 and organic species between the gas and particle phases. Attempts to integrate the kinetic condensation equations for NH_3, HNO_3, and HCl simultaneously with those for H_2SO_4 led to numerical instabilities. To resolve this problem, we developed a hybrid mass-transfer scheme, where the kinetic equations governing the condensation/evaporation of H_2SO_4 and organic species are integrated, and NH_3, HNO_3, and HCl are assumed to be in equilibrium between the gas and aerosol phases. Scale analysis suggests that this equilibrium assumption is valid within the concentrated environment of the smoke plume, where the aerosol surface area concentration is very large and mass transfer between phases is rapid.

The coagulation of aerosol is calculated using the semi-implicit scheme of *Jacobson* [2005]. The model includes the convectively enhanced Brownian coagulation kernel and the gravitational collection coagulation kernel; possible enhancement of coagulation by van der Waal's forces are not included.

To calculate the optical properties of the aerosol we assume that the particle consists of a spherical core of BC surrounded by a reflective spherical shell containing the rest of the particle mass. *Reid et al.* [2005a] report that the assumption of spherical particles for the calculation of optical properties is generally justifiable for biomass burning smoke particles. The refractive index of the solution of water and inorganic ions at 550 nm is calculated using the method of *Tang* [1997] and *Tang et al.* [1997]. The average refractive index of the shell is calculated using the volume-average dielectric constant mixing rule [*Jacobson*, 2005]. The core-in-shell Mie calculation is performed using the publicly available program DMiLay, which is based on the work of *Toon and Ackerman* [1981].

2.2 Gas Phase Chemical Mechanism

2.2.1 Overview of the Gas Phase Chemical Mechanism

The gas phase chemical mechanism used in ASP is based on the Caltech Atmospheric Chemistry Mechanism (CACM) [*Griffin et al.*, 2002b, 2005]. CACM was designed to combine a state-of-the-art treatment of ozone formation chemistry with explicit predictions of secondary semi-volatile oxidation products that can act as constituents of secondary organic aerosol (SOA). The treatment of ozone formation in the CACM is based on the Regional Atmospheric Chemistry Mechanism (RACM) of *Stockwell et al.* [1997], the work of *Jenkin et al.* [1997] on the tropospheric degradation

of volatile organic compounds (VOCs), and the Statewide Air Pollution Research Center Mechanism (SAPRC-97 and SAPRC-99, available from W.P.L. Carter at http://helium.ucr.edu/~carter/). CACM has been used to study ozone and SOA formation in the South Coast Air Basin of California (SoCAB) [*Griffin et al.*, 2002b, a; *Vutukuru et al.*, 2006], including the incremental secondary organic aerosol reactivity of VOC species in the SoCAB [*Carreras-Sospedra et al.*, 2005]. A Monte Carlo uncertainty and sensitivity analysis of the CACM for SOA precursors, O_3, HCHO, H_2O_2, and peroxyacetyl nitrate (PAN) was performed by *Rodriguez and Dabdub* [2003].

CACM is a lumped mechanism, where individual organic compounds are combined together into surrogate groups to simplify the chemistry. The lumping in CACM is done in a manner similar to that of *Stockwell et al.* [1997], and is designed to represent the entire array of gas-phase organic species emitted to the atmosphere, including aromatic species, isoprene, and monoterpenes. Table 2.1, reproduced with permission from *Griffin et al.* [2002b], lists the compounds included in the CACM. Below, we briefly review the chemistry included in the CACM. We then compare the results of our gas-phase chemical mechanism with results from the original CACM, and with smog chamber data reported by *Carter et al.* [2005]. The reaction stoichiometries and rate constants for first-, second-, and third-order reactions of the gas-phase chemical mechanism are presented in Appendix A.

Inorganic Chemistry

The inorganic chemistry in the CACM includes the major reactions of O_3, NO_x, and SO_x including (1) the conversion of NO to NO_2 via reaction with O_3, HO_2, and organic peroxy radicals (RO_2); (2) the photolysis of NO_2 to produce $O(^3P)$, which combines with O_2 to make O_3; (3) the photolysis of O_3 to form $O(^3P)$ or $O(^1D)$, the latter of which reacts with H_2O to make OH; (4) the production of OH by the photolysis of HONO and H_2O_2; (5) the production of OH by reaction of O_3 and HO_2; (6) the formation of HONO by the reaction of OH with NO and NO_2 with H_2O; (7) the formation of H_2O_2 by the combination of 2 HO_2; (8) the formation and photolysis of NO_3, N_2O_5, and HNO_4; (8) the formation of HNO_3 from the reaction of NO_2 with OH, HO_2 with NO_3, or the heterogeneous hydrolysis of N_2O_5; and (9) the reaction of SO_2 with OH to make SO_3, which is assumed to rapidly hydrolyze to form H_2SO_4 [*Griffin et al.*, 2002b].

Table 2.1: Compounds Included in CACM (Modified from *Griffin et al., 2002*)

Compound	Description
H_2O	water vapor
O_2	oxygen
M	third body
NO	nitric oxide
NO_2	nitrogen dioxide
O_3	ozone
HONO	nitrous acid
HNO_3	nitric acid
HNO_4	pernitric acid
N_2O_5	nitrogen pentoxide
NO_3	nitrate radical
HO_2	hydroperoxy radical
CO	carbon monoxide
CO_2	carbon dioxide
H_2O_2	hydrogen peroxide
SO_2	sulfur dioxide
OH	hydroxyl radical
$O(^1D)$	O, singlet D
O	O (^3P)
CH_4	methane
ETHE	ethene
OLEL	lumped alkenes C3-C6 (1-pentene)
OLEH	lumped alkenes >C6 (4-methyl-1-octene)
ALKL	lumped alkanes C2-C6 (2-methyl-butane)
ALKM	lumped alkanes C7-C12 (3,5-dimethyl-heptane)
ALKH	lumped alkanes >C12 (n-hexadecane)
AROH	lumped high SOA yield aromatic species (3-n-propyl-toluene)
AROL	lumped low SOA yield aromatic species (1,2,3-trimethyl-benzene)
AROO	lumped phenolic species (2,6-dimethyl-phenol)
ARAL	lumped aromatic monoaldehydes (p-tolualdehyde)
ARAC	lumped aromatic monoacids (p-toluic acid)
PAH	lumped gas-phase polycyclic aromatic hydrocarbons (1,2-dimethyl-naphthalene)
HCHO	formaldehyde

Continued on next page

Table 2.1: (continued)

Compound	Description
ALD2	lumped higher aldehydes (n-pentanal)
KETL	lumped ketones C3-C6 (2-pentanone)
KETH	lumped ketones >C6 (2-heptanone)
MEOH	methanol
ETOH	ethanol
ALCH	lumped higher alcohols (2-hexanol)
ISOP	isoprene
BIOL	lumped low SOA yield monoterpene species (α-terpineol)
BIOH	lumped high SOA yield monoterpene species (γ-terpinene)
MTBE	methyl-tert-butyl ether
ADAC	lumped aromatic diacids (terephthalic acid)
ACID	lumped organic acids <C6
UR1	3-methyl-heptanoic acid
UR2	3-hydroxy-4-methyl-benzoic acid
UR3	2-hydroxy-3-isopropyl-6-keto-heptanoic acid
UR4	2-isopropyl-5-keto-hexanal
UR5	1-methyl-3-hydroxy-4-isopropyl-1,2-cyclohexane epoxide
UR6	2-hydroxy-3-isopropyl-6-methyl-cyclohexanone
UR7	3,7-dimethyl-6-keto-3-octenal
UR8	3-isopropyl-6-keto-3-heptenoic acid
UR9	1-methyl-4-isopropyl-1,2-cyclo-4-hexene epoxide
UR10	3-isopropyl-6-methyl-3-cyclohexenone
UR11	1,2-dimethyl-3-hydroxy-naphthalene
UR12	1,2,3-trimethyl-5-nitro-benzene
UR13	3-n-propyl-4-nitro-toluene
UR14	2-nitro-4-methyl-benzoic acid
UR15	1,2-dimethyl-3-nitro-naphthalene
UR16	2-methyl-2-hydroxy-5-heptanone
UR17	2-hydroxy-3-isopropyl-hexadial
UR18	3-isopropyl-2-pentendial
UR19	1-methyl-2-formyl-naphthalene
UR20	11-hydroxy-8-hexadecanone
UR21	keto-propanoic acid
UR22	2,6-dimethyl-3,4-dinitro-phenol

Continued on next page

Table 2.1: (continued)

Compound	Description
UR23	3-isopropyl-4-hydroxy-2-butenoic acid
UR24	maleic anhydride
UR25	3H-furan-2-one
UR26	4,5-dimethyl-6-keto-2,4-heptadienoic acid
UR27	2-carboxy-acetophenone
UR28	oxalic acid
UR29	4-hydroxy-3,5-dimethyl-2,4-hexadiendioic acid
UR30	2-methyl-5-carboxy-2,4-hexadiendioic acid
UR31	2-(dimethyl-propenoic acid)-benzoic acid
UR32	3-methyl-4-heptanone
UR33	2-isopropyl-5-keto-2-hexenal
UR34	8-hexadecanone
PAN1	peroxy pentionyl nitrate
PAN2	peroxy acetyl nitrate (PAN)
PAN3	unsaturated peroxy propionyl nitrate (PPN)
PAN4	keto-PPN
PAN5	methylene-PPN
PAN6	peroxy nitrate derived from glyoxal
PAN7	peroxy 3-methyl-heptionyl nitrate
PAN8	peroxy 2-hydroxy-3-isopropyl-6-keto-heptionyl nitrate
PAN9	peroxy 3-isopropyl-4-hydroxy-2-butenionyl nitrate
PN10	peroxy nitrate derived from glyoxalic acid
MGLY	methyl glyoxal
MVK	methyl-vinyl-ketone
MCR	methacrolein
RPR1	3-methyl-heptanal
RPR2	3-hydroxy-4-methyl-benzaldehyde
RPR3	2-hydroxy-3-isopropyl-6-keto-heptanal
RPR4	2,6-dimethyl-4-nitro-phenol
RPR5	2-nitro-4-methyl-benzaldehyde
RPR6	benzene-1,4-dialdehyde
RPR7	4-formyl-benzoic acid
RPR8	3-isopropyl-4-hydroxy-2-butenal
RPR9	4-hydroxy-3,5-dimethyl-2,4-hexadiendial

Continued on next page

Table 2.1: (continued)

Compound	Description
RP10	2-methyl-butenalic acid
RP11	4,5-dimethyl-6-keto-2,4-heptadienal
RP12	2-methyl-5-formyl-2,4-hexadiendial
RP13	2-carboxyl-5-methyl-2,4-hexadiendial
RP14	2-(dimethyl-propenal)-benzaldehyde
RP15	2-formyl-acetophenone
RP16	glyoxalic acid
RP17	4-hydroxy-3,5-dimethyl-2,4-hexadienalic acid
RP18	2-methyl-5-formyl-2,4-hexadiendioic acid
RP19	2-(dimethyl-propenal)-benzoic acid
AP1	2-nitrooxymethyl-6-methyl-phenol
AP2	2-methyl-2-hydroxy-5-heptylnitrate
AP3	3-methyl-4-heptylnitrate
AP4	1,2-dimethyl-3-nitrooxymethyl-benzene
AP5	4-nitrooxymethyl-benzaldehyde
AP6	4-nitrooxymethyl-benzoic acid
AP7	1-methyl-1-nitrato-2,3-dihydroxy-4-isopropyl-cyclohexane
AP8	1-methyl-4-nitrato-4-isopropyl-5-hydroxy-cyclohexene
AP9	5-isopropyl-6-nitrato-4-hexen-2-one
AP10	1-methyl-2-nitrooxymethyl-naphthalene
AP11	8-hexadecylnitrate
AP12	8-hydroxy-11-hexadecylnitrate
RO_2T	total organic peroxy radical
RO_28	acetyl peroxy radical
RO_21	methyl peroxy radical from oxidation of CH_4
RO_22	hydroxy alkyl peroxy radical <C6 from oxidation of ETHE, ETOH, OLEL, and ALCH (C4, 1-peroxy, 2-hydroxy)
RO_23	nitrato alkyl peroxy radical <C6 from oxidation of ETHE and OLEL (C4, 1-nitrato, 2-peroxy)
RO_24	aldehydic alkyl peroxy radical from oxidation of ISOP and ETHE (C2)
RO_25	alkyl peroxy radical <C6 from oxidation of KETL, ISOP, ALKL, BIOH, and OLEL (C3, 1-peroxy)
RO_26	acyl radical from aldehydic H abstraction of ALD2

Continued on next page

Table 2.1: (continued)

Compound	Description
$RO_2$7	keto alkyl peroxy radical <C6 from oxidation of ISOP and KETL (C4, 2-keto, 3-peroxy)
$RO_2$9	branched hydroxy alkenyl peroxy radical from oxidation of ISOP (C4 chain, 1-hydroxy, 2-methyl, 2-peroxy)
$RO_2$10	branched hydroxy alkenyl peroxy radical from oxidation of ISOP (C4 chain, 2-methyl, 3-peroxy, 4-hydroxy)
$RO_2$11	branched nitrato alkenyl peroxy radical from oxidation of ISOP (C4 chain, 1-nitrato, 2-methyl, 2-peroxy)
$RO_2$12	branched nitrato alkenyl peroxy radical from oxidation of ISOP (C4 chain, 2-methyl, 3-peroxy, 4-nitrato)
$RO_2$13	keto alkenyl peroxy radical from oxidation of ISOP (C4, 3-keto, 4-peroxy)
$RO_2$14	alkenyl peroxy radical from oxidation of ISOP (C2)
$RO_2$15	ether alkyl peroxy radical from oxidation of MTBE (C5, accounts for attack on both sides of the ether bond)
$RO_2$16	keto alkyl peroxy radical from oxidation of KETH (C7, 2-keto, 3-peroxy)
$RO_2$17	aromatic peroxy radical from side chain oxidation of AROO
$RO_2$18	branched hydroxy alkyl peroxy radical >C6 from oxidation of OLEH and ALKM (C7 chain, 2-methyl, 2-hydroxy, 5-peroxy)
$RO_2$19	branched nitrato alkyl peroxy radical from oxidation of OLEH (C8 chain, 4-methyl, 1-nitrato, 2-peroxy)
$RO_2$20	branched alkyl peroxy radical >C6 from oxidation of OLEH and ALKM (C7 chain, 3-methyl, 4-peroxy)
$RO_2$21	aromatic peroxy radical from side chain oxidation of AROL
$RO_2$22	aromatic peroxy radical from side chain oxidation of ARAL
$RO_2$23	aromatic peroxy radical from side chain oxidation of ARAC
$RO_2$24	cyclic dihydroxy alkyl peroxy radical from OH oxidation of BIOL (C6 cycle, 1-methyl, 1-peroxy, 2, 3-dihydroxy, 4-isopropyl)
$RO_2$25	cyclic hydroxy nitrato alkyl peroxy radical from NO_3 oxidation of BIOL (C6 cycle, 1-methyl, 1-peroxy, 2-nitrato, 3-hydroxy, 4-isopropyl)
$RO_2$26	branched keto hydroxy aldehydic peroxy radical from oxidation of BIOL (C7 chain, 2-hydroxy, 3-isopropyl, 5-peroxy, 6-keto)
$RO_2$27	cyclic hydroxy alkenyl peroxy radical from oxidation of BIOH (C6 cycle, 1-methyl, 1-ene, 4-peroxy, 4-isopropyl, 5-hydroxy)

Continued on next page

Table 2.1: (continued)

Compound	Description
$RO_2$28	cyclic nitrato alkenyl peroxy radical from oxidation of BIOH (C6 cycle, 1-methyl, 1-ene, 4-peroxy, 4-isopropyl, 5-nitrato)
$RO_2$29	branched keto alkenyl peroxy radical from oxidation of BIOH (C6 chain, 1-peroxy, 2-isopropyl, 2-ene, 5-keto)
$RO_2$30	branched keto aldehydic peroxy radical from oxidation of BIOH (C7 chain, 3-isopropyl, 3-ene, 5-peroxy, 6-keto)
$RO_2$31	aromatic peroxy radical from side chain oxidation of PAH
$RO_2$32	alkyl peroxy radical from oxidation of ALKH (8-peroxy)
$RO_2$33	peroxy radical from addition of O_2 to RAD2
$RO_2$34	peroxy radical from addition of O_2 to RAD3
$RO_2$35	peroxy radical from addition of O_2 to RAD4
$RO_2$36	peroxy radical from addition of O_2 to RAD5
$RO_2$37	peroxy radical from addition of O_2 to RAD6
$RO_2$38	peroxy radical from addition of O_2 to RAD7
$RO_2$39	unsaturated acyl peroxy radical from oxidation of ISOP (C3)
$RO_2$40	branched hydroxy keto alkenyl peroxy radical from oxidation of BIOH (C6 chain, 1-hydroxy, 2-isopropyl, 2-ene, 4-peroxy, 5-keto)
$RO_2$41	hydroxy alkyl peroxy radical from oxidation of ALKH (8-hydroxy, 11-peroxy)
$RO_2$42	bicyclic peroxy radical from the O_2 bridging in $RO_2$33
$RO_2$43	bicyclic peroxy radical from the O_2 bridging in $RO_2$34
$RO_2$44	bicyclic peroxy radical from the O_2 bridging in $RO_2$35
$RO_2$45	bicyclic peroxy radical from the O_2 bridging in $RO_2$36
$RO_2$46	bicyclic peroxy radical from the O_2 bridging in $RO_2$37
$RO_2$47	bicyclic peroxy radical from the O_2 bridging in $RO_2$38
$RO_2$48	acyl radical from aldehydic H abstraction of MGLY
$RO_2$49	peroxy radical formed from OH oxidation of MVK
$RO_2$50	acyl radical from aldehydic H abstraction of MCR
$RO_2$51	peroxy radical from OH addition to double bond in MCR
$RO_2$52	peroxy radical from NO_3 addition to double bond in MCR
$RO_2$53	dicarbonyl peroxy radical from MCR/O_3 reaction (C3 chain, 1-peroxy, 2-keto, 3-aldehydic)
$RO_2$54	acyl radical from decomposition of $RO_2$53
$RO_2$55	acyl radical from aldehydic H abstraction of RPR1
$RO_2$56	acyl radical from aldehydic H abstraction of RPR3
$RO_2$57	acyl radical from aldehydic H abstraction of RPR7

Continued on next page

Table 2.1: (continued)

Compound	Description
$RO_2$58	acyl acid peroxy radical from aldehydic H abstraction of RP16 (C2)
RAD1	radical from NO_3 oxidation of AROO
RAD2	hexadienyl radical from OH oxidation of AROO
RAD3	hexadienyl radical from OH oxidation of AROL
RAD4	hexadienyl radical from OH oxidation of AROH
RAD5	hexadienyl radical from OH oxidation of ARAL
RAD6	hexadienyl radical from OH oxidation of ARAC
RAD7	hexadienyl radical from OH oxidation of PAH
RAD8	radical from NO_3 oxidation of RPR4

Organic Chemistry

The organic chemistry in CACM assumes that (1) alkyl peroxy radical reactions with RO_2T form the same products as the corresponding NO to NO_2 conversion reaction, and (2) that alkyl peroxy radical reactions with HO_2 instantaneously form the degradation products of the corresponding intermediate hydroperoxide. Below we briefly discuss the reaction pathways for the primary organic species in CACM. Our discussion follows the more detailed description of the CACM contained in *Griffin et al.* [2002b].

Alkanes Alkanes are oxidized by OH abstraction of an H-atom followed by combination with O_2 to make a alkyl peroxy radical. These alkyl peroxy radicals can react with NO to form the corresponding alkyl nitrate or to form NO_2. Following NO_2 formation, short-chain alkanes (ALKL) form HO_2 and the corresponding aldehyde, while medium and long-chain alkanes (ALKM and ALKH) rapidly isomerize through a 1,5-H shift to produce hydroxy alkyl peroxy radicals, which react like other peroxy radicals to produce either a hydroxy alkyl nitrate or NO_2, HO_2, and a hydroxy ketone. The alkyl nitrates can react with OH and O_2 to produce NO_2 and organic products.

Nonbiogenic Alkenes Alkenes can react with OH, NO_3, O_3 and $O(^3P)$. For ETHE, addition of OH forms a peroxy radical which can undergo all of the reactions already discussed except for formation of an alkyl nitrate due to its low carbon number. The products of this pathway include HCHO, ALD2, and HO_2. Reaction of ETHE with NO_3 proceeds similarly, with addition of the NO_3 radical leading to the formation of a peroxy radical which further reacts to produce HCHO, ALD2,

and HO_2 and release NO_2. The reaction of ETHE with O_3 proceeds by addition to the double bond followed by rapid decomposition into HCHO and a high-energy Criegee biradical, which rapidly decomposes to form ACID, HO_2, CO, OH, HCHO and H_2O. Reaction of ETHE with $O(^3P)$ forms CO, HO_2, and peroxy radicals.

As with ETHE, reactions of OLEL and OLEH with OH and NO_3 form peroxy radicals which react as before to form organic nitrates or the corresponding aldehydes and ketones. Reaction with O_3 leads to the formation of HCHO, ACID, CO, CO_2, OH, HO_2, carbonyl-containing products and peroxy radicals. Reaction of OLEL and OLEH with $O(^3P)$ forms alkanes (which represent a reclassified reactive product), carbonyl compounds and peroxy radicals.

Aldehydes Aldehydes (HCHO, ALD2, MGLY, and some RPR species) are oxidized by OH, NO_3, or photolysis. OH and NO_3 remove the aldehydic H-atom to produce H_2O or HNO_3, respectively; further reaction with O_2 produces an acyl peroxy radical ($RC(O)O_2\bullet$). The acyl peroxy radical can then react with NO, NO_2, HO_2, or RO_2T. Reaction with NO leads to the formation of NO_2 and the decomposition of the remaining radical to form CO_2 and an alkyl radical, which combines with O_2 to form an alkyl peroxy radical. Reaction of the acyl peroxy radical with RO_2T also produces CO_2 and an alkyl peroxy radical. NO_2 can combine with the acyl peroxy radical to produce a peroxy acyl nitrate species (PAN) that can thermally decompose back into an acyl radical and NO_2. Reaction of acyl radicals with HO_2 produces organic acids (ACID).

Photolysis of aldehydes produces CO, H•, and an alkyl radical. H• and the alkyl radical rapidly combine with O_2 to produce HO_2 and an alkyl peroxy radical.

Ketones Ketones (KETL and KETH; $R_1CH_2(O)R_2$) either react with OH or are photolyzed. The reaction with OH proceeds via abstraction of the H-atom $\alpha-$ to the carbonyl. Addition of O_2 gives a keto-alkyl peroxy radical ($R_1CH(O_2\bullet)C(O)R_2$). This radical reacts with NO, HO_2, and RO_2T to form an alkoxy radical which decomposes to produce an aldehyde ($R_1C(O)H$) and an acyl peroxy radical ($R_2C(O)O_2\bullet$).

Photolysis of ketones cleaves the carbon-carbon bond adjacent to the carbonyl, and combination with O_2 produces an alkyl peroxy radical ($R_1CH_2O_2\bullet$) and an acyl peroxy radical ($R_2C(O)O_2\bullet$).

Alcohols Alcohols (MEOH, ETOH, and ALCH) react with OH, which can abstract an H-atom from either the O-H or a C-H bond. For MEOH, the resulting intermediates rapidly combine with O_2 to produce HCHO and HO_2. ETOH can proceed by either pathway; reaction with the O-H bond produces an aldehyde and HO_2, while reaction at the C-H bond can produce either an aldehyde or

a peroxy radical. ALCH is expected to primarily react at the C-H bond sites, producing a peroxy radical.

Aromatics Aromatic compounds in the CACM are divided into 6 subgroups: low-yield aromatics (AROL), high-yield aromatics (AROH), phenolic species (AROO), aromatic aldehydes (ARAL), aromatic acids (ARAC), and polycyclic aromatic hydrocarbons (PAH). We consider each class in turn.

AROL and AROH Low-yield aromatics are those with two or more methyl side groups and no other functional side groups, such as xylenes and trimethylbenzenes [*Odum et al.*, 1996, 1997b; *Griffin et al.*, 2002b]. Reaction of AROL with OH produces AROO, a cyclohexadienyl radical (RAD3) formed by H-atom abstraction of an aromatic hydrogen, or an aromatic peroxy radical ($RO_2$21) formed by H-atom abstraction from a side group. The aromatic peroxy radical reacts to form either a methyl nitroxy substituted aromatic (AP4) or an aromatic aldehyde (ARAL). AP4 can also decompose into ARAL and NO_2. RAD3 can react with NO_2 to form a nitro-aromatic species (UR12), but it predominantly reacts with O_2 to form a cyclohexadienyl peroxy radical ($RO_2$34). $RO_2$34 can either isomerize to form a bicyclic peroxy radical ($RO_2$43) or react with NO, HO_2, or RO_2T to produce RP11 in a ring-cleavage reaction. $RO_2$43 reacts with NO, HO_2, or RO_2T to produce ring cleavage products such as methyl glyoxal (MGLY) and RP10. RP11 reacts with OH to form the corresponding acid (UR26). RP10 can either react with OH to produce the corresponding anhydride (UR24) or photolyze to form the corresponding furan (UR25). MGLY behaves as an aldehyde, following the reactions discussed above.

High-yield aromatics have one or no methyl side groups and no other functional side groups, like toluene [*Odum et al.*, 1996, 1997b; *Griffin et al.*, 2002b]. The chemistry is substantially similar to AROL, with a different yield of ring-fragmentation products and different chemical kinetics.

AROO Both NO_3 and OH can oxidize AROO. NO_3 removes the phenolic H-atom to form RAD1, a dimethyl-benzoxy radical, which is assumed to react with NO_2 to form dimethyl-nitro-phenol (RPR4). Reaction of AROO with OH can proceed by side chain abstraction to produce a peroxy radical ($RO_2$17), or by addition of OH to the ring. The addition reaction can reform AROO or produce a cyclohexadienyl radical (RAD2). The aromatic peroxy radical and the cyclohexadienyl radical follow similar chemistry to that discussed for AROL above.

ARAL ARAL can react with either NO_3 or OH. Reaction with NO_3 removes the aldehydic H-atom. It is assumed that the resulting radical reacts rapidly with HO_2 to produce the corresponding aromatic acid (ARAC) and O_3.

Oxidation of ARAL by OH can proceed by one of three pathways: abstraction of the aldehydic H-atom, abstraction of an H-atom from a methyl side group, or ring addition. As with NO_3, reaction with the aldehydic H-atom produces the corresponding acid. The side-group reaction path forms an aromatic peroxy radical which can form either an aromatic with two aldehyde side groups (RPR6) or an aromatic compound with one aldehyde and one nitrooxy-methyl side chain (AP5). AP5 can be further oxidized to RPR6. RPR6 is assumed to react to form the corresponding aromatic acid RPR7, which can further react to form ADAC.

Addition of OH to the aromatic ring produces a cyclohexadienyl radical, RAD5, which follows similar reaction pathways to those discussed for AROL.

ARAC ARAC can react with OH by side-chain H-atom abstraction to form an aromatic peroxy radical or by addition to the ring to produce a cyclohexadienyl radical. These radicals then follow similar chemistry to that already discussed for AROL.

PAH PAH can react with OH in three ways: abstraction of a side-chain H-atom to produce an aromatic peroxy radical, addition to produce an aromatic cyclohexadienyl radical, or produce a hydroxy -PAH (UR11). The peroxy and cyclohexadienyl radicals then follow similar chemistry to that already discussed for AROL.

Biogenics The biogenic compounds isoprene (ISOP) and low- and high-yield monoterpenes (BIOL and BIOH) are included in the CACM mechanism. Their oxidation pathways are discussed below.

Isoprene Like other alkenes, isoprene can react with either OH, NO_3, O_3, or $O(^3P)$. CACM assumes that OH and NO_3 addition to the double bonds only occurs at the two most probable spots. The preferred OH attack is 66% in the 1-position resulting in a tertiary peroxy radical ($RO_2$9), and 34% in the 4-position resulting in a secondary peroxy radical ($RO_2$10). The reactions of $RO_2$9 with NO, HO_2, and RO_2T produce methyl-vinyl ketone (MVK), HCHO, HO_2, and NO_2. The reactions of $RO_2$10 produce methacrolein (MCR), HCHO, HO_2 and NO_2. The reaction pathway with NO_3 is similar, with the production of nitroxy peroxy radicals $RO_2$11 and $RO_2$12. Upon reactions, these radicals release NO_2 and produce MCR, MVK, HCHO, and HO_2.

The reaction of isoprene with O_3 can produce MCR, MVK, HCHO, OLEL (a reclassified small product), CO, CO_2, ACID, OH, HO_2, and two peroxy radicals, $RO_2$13 and $RO_2$14. $RO_2$13 is a 4-carbon unsaturated peroxy radical that breaks down into HCHO and a 3-carbon, unsaturated acyl peroxy radical ($RO_2$39). $RO_2$39 follows the reactions discussed previously for acyl peroxy radicals, forming $RO_2$14, CO_2, an unsaturated peroxy nitrate compound (PAN3), OLEL, ACID, and O_3. $RO_2$14 is a 2-carbon, unsaturated peroxy radical that is converted to OLEL or $RO_2$7 upon reaction. The reaction of ISOP-O(^{3}P) yields OLEL (a reclassified small product) and ALD2.

MCR and MVK are the major products of isoprene oxidation. MVK can react with OH, O_3, or O(^{3}P). OH adds to the double bond producing a peroxy radical, which subsequently reacts to produce methyl glyoxal (MGLY), HCHO, and HO_2. The MVK-O_3 reaction produces MGLY, HCHO, ACID, UR21, ALD2, CO, CO_2, HO_2, OH, water, and $RO_2$8. The MVK-O(^{3}P) reaction yields KETL (a reclassified small product), $RO_2$4 and $RO_2$8.

MCR reacts with OH and NO_3 by addition to the double bond, leading to MGLY and HCHO, or via H-atom abstraction from the aldehyde, leading to PAN5, ACID, OLEL, and $RO_2$14. The MCR-O_3 reaction produces HCHO, MGLY, OH, CO, HO_2, ACID, and $RO_2$53. $RO_2$53 reacts to form the acyl radical $RO_2$54, which can produce RP16 (glyoxalic acid) and PAN6. RP16 can react by photolysis or abstraction of the aldehydic H-atom, producing PN10 and oxalic acid (UR28).

Monoterpenes CACM includes two monoterpene classes: low-yield (BIOL) and high-yield (BIOH). Like other unsaturated compounds, both are oxidized by either OH, NO_3, O_3, or O(^{3}P). Addition of OH or NO_3 to these compounds produces the corresponding nitroxy compound or the keto-aldehyde ring cleavage product. The O(^{3}P) reactions lead to epoxide and carbonyl species, which are assumed to be unreactive.

Reaction of BIOL with O_3 produces UR3 (a hydroxy-keto-acid) , UR4 (a keto-aldehyde), CO, RPR3 (an aldehyde), HO_2, OH, H_2O_2 and $RO_2$26. Reactions of $RO_2$26 lead to the formation of $RO_2$8 and UR17, a hydroxy dial. Reactions of RPR3 lead to the formation of UR3, UR4, and PAN8.

Reaction of BIOH with O_3 produces UR7, UR8, CO, OH, H_2O_2, $RO_2$29 and $RO_2$30. $RO_2$29 produces either a nitroxy product (AP9) or isomerizes into another peroxy radical ($RO_2$40). AP9 oxidizes to produce an unsaturated keto-aldehyde (UR33). $RO_2$40 decomposes into $RO_2$8 and an unsaturated hydroxy aldehyde (RPR8). $RO_2$30 produces UR18, an unsaturated dial. RPR8 can react by two photolysis pathways, one of which produces CO, HO_2 and $RO_2$9 and another which produces the acyl radical $RO_2$57. $RO_2$57 is also formed by the reaction of RPR8 with OH. $RO_2$57

produces $RO_2$9, CO_2, NO_2, PAN9, UR23, and O_3.

Differences between CACM and this work

We have made a few changes to the original CACM to better represent the chemistry of young biomass burning plumes and to better fit the mechanism into the existing MELAM modeling framework. First, we fully integrate all gas-phase species, including peroxy radicals, rather than assuming steady state for some reactive species as in CACM. Second, we explicitly calculate heterogeneous reaction rates based on the surface area concentration of aerosol within the plume, rather than using three-body reactions with water to approximate heterogeneous chemistry as in the CACM, and have added additional heterogeneous reactions to the mechanism. Third, we have fit the reaction rates calculated by the group-contribution method of *Kwok and Atkinson* [1995] in CACM to an Arrhenius temperature dependence to more easily include these reactions within the MELAM modeling framework.

2.2.2 Comparison to CACM output

Three test simulations were performed to compare the results of the above modified version of the CACM with the output of the original CACM. The test output from CACM was provided by Rob Griffin of the University of New Hampshire, along with the initial conditions and photolysis rates used in the CACM runs. The CACM runs are a subset of the runs performed in *Griffin et al.* [2005], which simulated the formation of secondary organic aerosol in the smog chamber experiments of *Odum et al.* [1996], *Odum et al.* [1997b], and *Griffin et al.* [1999]. The three tests simulations included (1) the oxidation of 300 ppbv of toluene (modeled as AROL) in the presence of 540 ppbv NO_x and 300 ppbv propene (modeled as OLEL), (2) the oxidation of 100 ppbv of terpinene (modeled as BIOH) in the presence of 200 ppbv NO_x, and 300 ppbv propene, and (3) the oxidation of 200 ppbv α-pinene (modeled as BIOL) in the presence of 400 ppbv NO_x. All simulations were performed at a temperature of 298.15K, a pressure of 1000 mbar, and a relative humidity of 1%. The photolysis rates used in the simulations are in Table 2.2. Heterogeneous reaction rates were assumed to be negligible for this comparison.

Figures 2-1, 2-2, and 2-3 show the O_3, NO and NO_2 concentrations predicted by both CACM and our modified version of the mechanism for the AROL, BIOH, and BIOL cases, respectively. The simulations match very closely, with some deviations due to the modifications incorporated into our version of the CACM such as integrating all radical species rather than assuming steady state and fitting the reaction rates calculated by the group-contribution method of *Kwok and Atkinson*

Table 2.2: Photolysis Rates Used in Comparision to CACM

Reaction	Photolysis Rate (s^{-1})
$NO_2 \rightarrow NO + O$	3.995×10^{-3}
$NO_3 \rightarrow NO + O_2$	9.35×10^{-3}
$NO_3 \rightarrow NO_2 + O$	8.5167×10^{-2}
$O_3 \rightarrow O + O_2$	2.285×10^{-4}
$O_3 \rightarrow O(^1D) + O_2$	1.89×10^{-5}
$HONO \rightarrow 0.9\ OH + 0.9\ NO + 0.1\ HO_2 + 0.1\ NO_2$	8.15×10^{-4}
$H_2O_2 \rightarrow OH + OH$	3.765×10^{-6}
$HCHO \rightarrow HO_2 + HO_2 + CO$	1.51×10^{-5}
$HCHO \rightarrow H_2 + CO$	2.315×10^{-5}
$ALD2 \rightarrow CO + HO_2 + RO_25 + RO_2T$[a]	3.675×10^{-6}
$RPR1 \rightarrow CO + HO_2 + RO_220 + RO_2T$	3.675×10^{-6}
$RPR3 \rightarrow CO + 2.0\ HO_2 + UR4$	3.675×10^{-6}
$RPR8 \rightarrow CO + HO_2 + RO_29 + RO_2T$	3.675×10^{-6}
$RPR8 \rightarrow HO_2 + RO_257 + RO_2T$	3.675×10^{-6}
$RP10 \rightarrow UR25$	3.675×10^{-6}.
$KETL \rightarrow RO_25 + RO_28 + 2.0\ RO_2T$	7.9×10^{-7}
$KETH \rightarrow RO_25 + RO_28 + 2.0\ RO_2T$	7.9×10^{-7}
$MGLY \rightarrow CO + HO_2 + RO_28 + RO_2T$	7.1×10^{-5}
$RP16 \rightarrow 2.0\ CO + OH + HO_2$	7.1×10^{-5}

[1995] to an Arrhenius temperature dependence. We conclude that the modified form of the CACM mechanism included in the ASP model is performing as designed.

2.2.3 Comparison to Smog Chamber Data

To evaluate the performance of the gas-phase chemical mechanism in predicting the formation of ozone, several test simulations were performed to compare the results of the mechanism to laboratory smog chamber data. The data used for the comparison came from the EPA chamber of *Carter et al.* [2005]. This chamber consists of two collapsible 90 m^3 FEP Teflon reactors (chambers A and B) mounted on pressure-controlled moveable frameworks inside a temperature-controlled room flushed with purified air. Solar radiation is simulated in the chamber using either a 200 kW Argon arc lamp or multiple blacklights; the arc lamp was used for all experiments considered here.

Table 2.3 shows the temperature and initial reactant concentrations used in our model to simulate each chamber study. All model simulations were performed at a pressure of 1000 mbar, a relative humidity of 0.01%, and a CH_4 concentration of 1800 ppbv. The temperature and concentration data was provided by William P.L. Carter [1]. The EPA chamber runs used an 8 compound

[1] Available for download at http://pah.cert.ucr.edu/ftp/pub/carter/

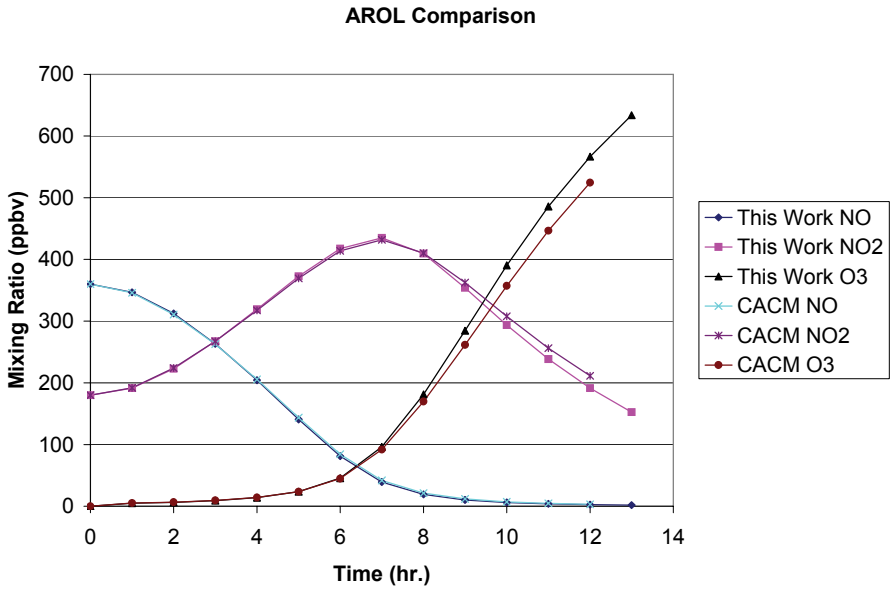

Figure 2-1: Comparison of the O_3, NO and NO_2 concentrations predicted by the ASP model for the oxidation of low-yield aromatic compounds (AROL) versus the predictions of the CACM/MPMPO model of *Griffin et al.* [2005].

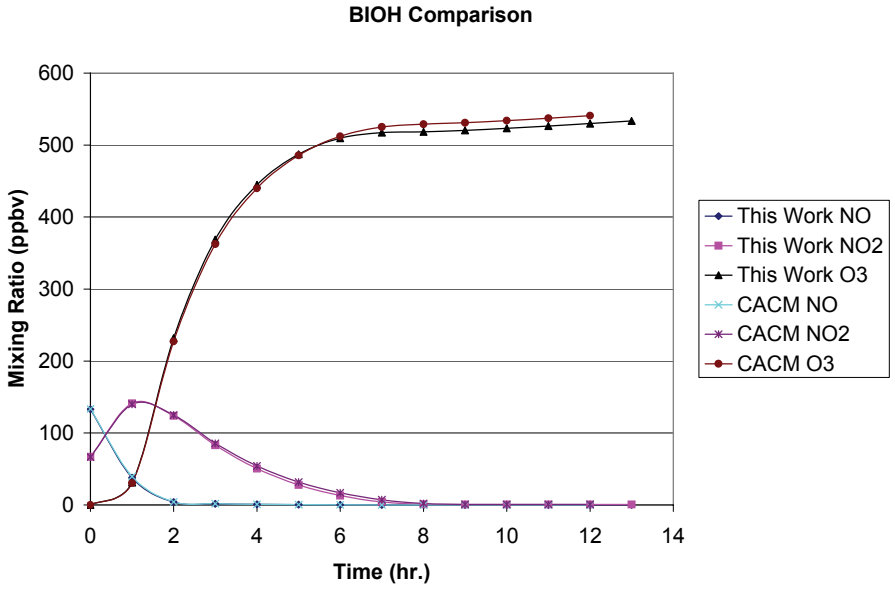

Figure 2-2: Comparison of the O_3, NO and NO_2 concentrations predicted by the ASP model for the oxidation of high-yield biogenic compounds (BIOH) versus the predictions of the CACM/MPMPO model of *Griffin et al.* [2005].

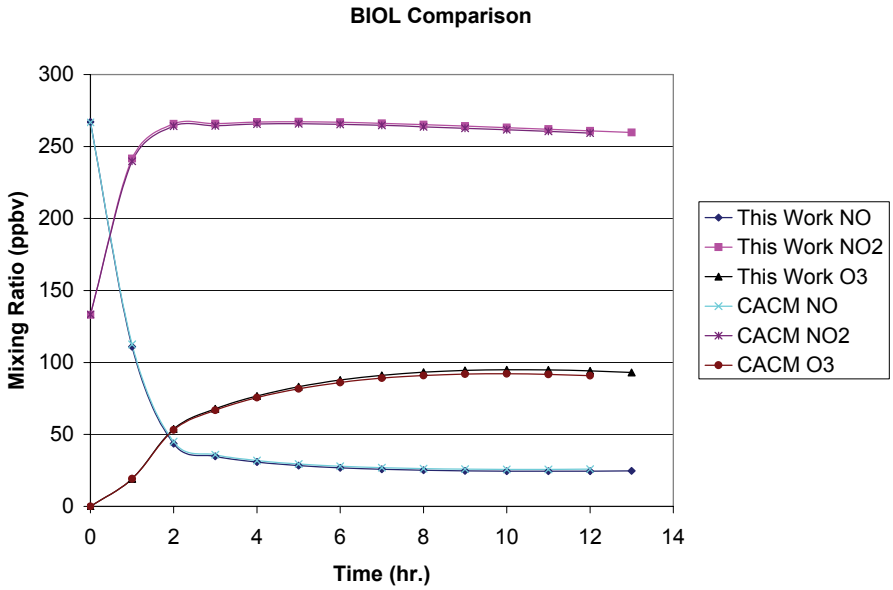

Figure 2-3: Comparison of the O_3, NO and NO_2 concentrations predicted by the ASP model for the oxidation of low-yield biogenic compounds (BIOL) versus the predictions of the CACM/MPMPO model of *Griffin et al.* [2005].

surrogate for ambient VOC concentrations, consisting of formaldehyde (HCHO), ethylene (ETHE), propene (OLEL), trans-2-butene (OLEL), n-butane (ALKL), n-octane (ALKM), toluene (AROH), and m-xylene (AROL) [*Carter et al.*, 2005, 1995]. The concentrations of propene and trans-2-butene were summed into the binned compound OLEL. The initial concentrations of HONO were extrapolated from CO-NO_x and n-butane-NO_x runs to account for the potential chamber radical source [*Carter et al.*, 2005].

Table 2.4 presents the rates of off-gassing, wall reaction rates, and photolysis rates for the chamber experiments considered here. The off-gassing rate for HONO was determined as that rate that enabled the SAPRC-99 chemical mechanism [*Carter*, 2000] to best predict the O_3 formation observed in CO-air, HCHO-air and CO-HCHO-air experiments performed within the chamber [*Carter et al.*, 2005]. The rate in Chamber A was found to be slightly higher than that in Chamber B, so different values are used for the chambers. The off-gassing rate of HCHO was chosen to match the low but measurable amount of formaldehyde found even in pure air and CO-NO_x experiments in the chamber. Heterogeneous wall loss reaction rates for O_3, NO_2, and N_2O_5 were also estimated from reactor observations [*Carter et al.*, 2005]. The photolysis rate of NO_2 in the chambers was measured directly, and scaling factors for the other photolysis rates were calculated by *Carter et al.* [2005] from the relative spectral intensity of the arc lamp.

Table 2.3: Temperature (K) and Initial Concentrations (ppbv except where otherwise noted) for the Comparison of the Gas Chemical Mechanism to Smog Chamber Data

	Temp.	NO	NO_2	HONO (pptv)	CO	HCHO	ETHE	OLEL	ALKL	ALKM	AROH	AROL
96A	303.94	64.13	45.14	2.26	0	21.73	12.29	17.686	62.03	16.15	15.96	15.13
96B	303.94	64.25	46.83	2.34	0	21.73	12.29	17.686	62.03	16.15	15.96	15.13
97A	303.77	3.107	2.175	1.09	0	12.20	8.386	14.254	52.0	11.16	10.59	9.833
97B	303.77	3.168	2.039	1.02	0	12.05	8.208	14.079	52.0	11.28	10.65	10.08
80A	303.65	62.54	29.69	1.48	0	112.30	76.64	120.06	365.7	96.88	90.98	86.35
80B	303.65	62.54	29.69	1.48	0	112.30	76.64	120.06	365.7	96.88	90.98	86.35
81A	303.51	33.47	16.43	0.82	0	59.27	41.41	61.37	187.1	60.08	50.47	46.97
81B	303.51	33.50	16.51	0.82	0	59.01	41.42	61.54	185.7	60.08	49.91	46.70
128A	302.65	30.59	17.03	0.85	0	10.98	8.751	15.382	53.93	12.17	11.67	11.57
83A	303.51	31.69	16.17	0.81	20.67	18.32	26.02	27.65	88.29	24.00	20.23	19.19
84B	303.51	33.61	17.51	0.88	0	24.72	16.34	32.11	100.4	29.00	24.23	22.94

Table 2.4: Wall Reaction and Photolysis Rates Used in Comparision to Smog Chamber Data

Reaction	Rate (s^{-1})
OffGas → HONO	5.5424×10^{-8} (Chamber A) 3.6805×10^{-8} (Chamber B)
Offgas → HCHO	4.33×10^{-8}
O_3 → Wall O_3	1.8×10^{-6}
NO_2 → 0.2 HONO + 0.8 Wall NO_x	2.67×10^{-6}
N_2O_5 → Wall NO_x	4.67×10^{-5}
$NO_2 \rightarrow NO + O$	4.33×10^{-3}
$NO_3 \rightarrow NO + O_2$	8.14×10^{-3}
$NO_3 \rightarrow NO_2 + O$	7.50×10^{-2}
$O_3 \rightarrow O + O_2$	1.72×10^{-4}
$O_3 \rightarrow O(^1D) + O_2$	2.96×10^{-6}
HONO → 0.9 OH + 0.9 NO + 0.1 HO_2 + 0.1 NO_2	9.376×10^{-4}
$H_2O_2 \rightarrow OH + OH$	1.68×10^{-6}
HCHO → HO_2 + HO_2 + CO	4.95×10^{-5}
HCHO → H_2 + CO	1.10×10^{-5}
ALD2 → CO + HO_2 + RO_25 + RO_2T[a]	5.77×10^{-7}
RPR1 → CO + HO_2 + RO_220 + RO_2T	5.77×10^{-7}
RPR3 → CO + 2.0 HO_2 + UR4	5.77×10^{-7}
RPR8 → CO + HO_2 + RO_29 + RO_2T	5.77×10^{-7}
RPR8 → HO_2 + RO_257 + RO_2T	5.77×10^{-7}
RP10 → UR25	5.77×10^{-7}
KETL → RO_25 + RO_28 + 2.0 RO_2T	4.64×10^{-8}
KETH → RO_25 + RO_28 + 2.0 RO_2T	4.64×10^{-8}
MGLY → CO + HO_2 + RO_28 + RO_2T	6.47×10^{-5}
RP16 → 2.0 CO + OH + HO_2	6.47×10^{-5}

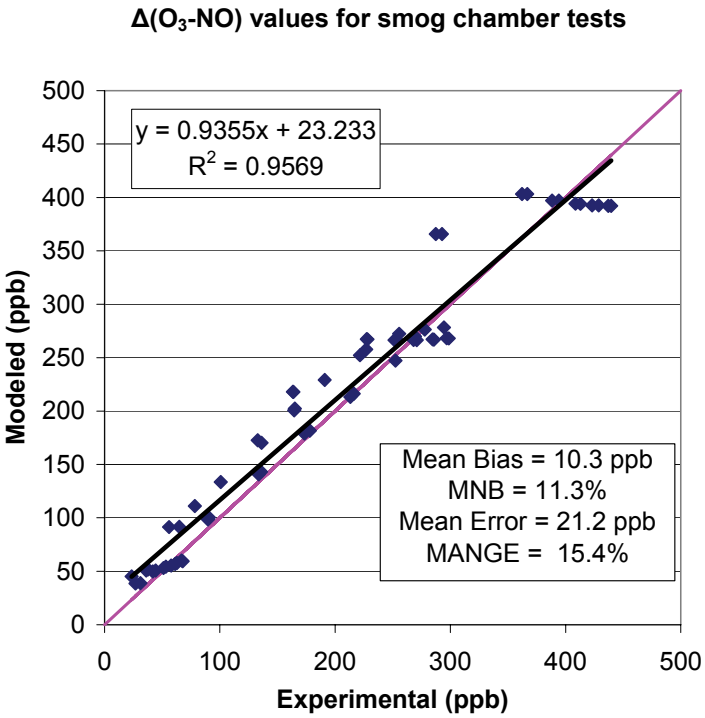

Figure 2-4: Comparison of modeled and measured $\Delta(O_3\text{-NO})$ values for the smog chamber tests.

Following *Carter et al.* [2005], we evaluate the ability of our mechanism to simulate the total amount of NO oxidized and O_3 formed in the experiments, measured as $\left([O_3]_{final} - [NO]_{final}\right) - ([O_3]_{initial} - [NO]_{initial})$, or $\Delta\left([O_3] - [NO]\right)$. The results of the comparisons are presented in Figure 2-4. The model has a slight positive bias, but in general gives a very good match to the observed rates of ozone formation and NO oxidation within the chamber. We conclude that we can use the mechanism to simulate the gas-phase chemistry in young smoke plumes from biomass burning.

2.3 Particle Distribution, Structure and Properties

Aerosol populations within a biomass burning smoke plume can vary greatly in size and composition across space and time. Modeling such populations is a complex multi-dimensional problem and requires making several simplifying assumptions [*Steele*, 2004]. To accomplish this task, several representations of aerosol distributions and dynamics have been developed, including bulk [*Nenes et al.*, 1998], method of moments [*Zhang et al.*, 2002], modal [*Zhang et al.*, 2002], sectional [*Jacobson*, 1997, 2002], Lagrangian [*Steele*, 2004], and mixed sectional-Lagrangian [*Steele*, 2004]. Below, we

discuss the moving-center sectional size distribution used in ASP[2]. We then discuss the assumed particle structure, which consists of an aqueous embryo attached to an insoluble sphere. This representation was chosen to keep MELAM's ability to model the effects of insoluble species on the activation of aerosol particles [*Steele*, 2004]. We then discuss the inorganic and organic compounds included in the aerosol model, the calculation of particle density and size, and the calculation of the surface tension of the aqueous embryo.

2.3.1 Moving-Center Sectional Distribution

In a sectional aerosol distribution, the aerosol size domain is divided into a series of geometrically distributed bins. Generally, particle number concentration and the mass concentration of each chemical component of the particle is tracked for each size bin. Here, we use a moving-center sectional size distribution, where the edges of the size bin are fixed at the beginning of the model run and never change, but the contents of each bin is represented by a single aerosol (the "moving center") that grows or shrinks due to condensation, coagulation, and other processes [*Steele*, 2004; *Jacobson*, 1997, 2002, 2005]. When the moving center crosses the boundary of the size bin into an adjacent bin, all the aerosol number and mass is moved to the adjacent bin[3]. This technique prevents numerical diffusion during condensational growth, and the fixed size bin boundaries simplify the modeling of the advection of particles across grid points of an Eulerian model. Some numerical diffusion still occurs during the coagulation and advection of aerosol particles, but the moving-center scheme can produce quite accurate results when a sufficiently large number of size bins is used (for example, see Sections 2.5.5 and 2.7.3).

In our model, only a single sectional size distribution is used. This implicitly assumes that all particles of the same size have the same composition, *i.e.* that the aerosol within each size bin is internally mixed. The review of *Reid et al.* [2005b] concluded that most biomass burning smoke particles are in fact internally mixed, with a core of BC and KCl surrounded by a coating of organic material. However, *Posfai et al.* [2003] reported observing three separate types of particles in young smoke, including organic-inorganic mixtures, "tar ball" organic particles, and soot particles. The assumption of an internal mixture is made in our work for two reasons. First, in the Timbavati smoke plume studied in this work, only bulk composition data is available [*Hobbs et al.*, 2003] - we cannot initialize externally-mixed size distributions with separate compositions based on this data.

[2]The model can also be run in a thermodynamic bulk mode (where only aerosol mass concentration is tracked) or in a monodisperse mode (where all particles are assumed to have the same size).

[3]In our model, a small number concentration (10^{-4} cm^{-3}) and a proportionally small amount of mass are left in the bin, to prevent numerical issues that may arise when concentrations are near 0.

Second, assuming an internally-mixed size distribution simplifies the model computation and allows for the completion of model runs in a reasonable amount of time. Expanding the model to include many different size distributions would significantly increase the computational time required. For example, the 3D Eulerian runs in Chapter 4, including only 4 aerosol size bins, take 4.5 days to run on our 15 CPU cluster. Expanding the model to represent three aerosol types (e.g., soot, organic particles, and inorganic particles) and their mixtures would require 7 distributions of 4 size bins each, increasing the computational time to at least 30 days. Potential ways to avoid the assumption of an internal mixture in future work are discussed in Section 6.2.

2.3.2 Particle Structure

Steele [2004] followed the work of *Gorbunov and Hamilton* [1997] in assuming that the aerosol particles in MELAM consisted of an aqueous solution embryo attached to an insoluble sphere. This structure allowed *Steele* [2004] to model how the surface properties of the insoluble sphere (represented by the contact angle between the insoluble core and the aqueous embryo) affected the activation of aerosols to cloud droplets. In updating MELAM to accommodate organic species and solid salts, we preserved this structure to ensure that our updated model could be reduced to the original MELAM model, if desired. The particle structure is illustrated in Figure 2-5. The aqueous solution embryo consists of water, dissolved inorganic ions, and dissolved organic species. The insoluble sphere is composed of the hydrophobic organic phase, the solid salts, and black carbon (BC). As the relative humidity increases, the solid salts deliquesce, producing aqueous phase ions, and the insoluble sphere consists of hydrophobic organics and BC. The density and radius of the aqueous embryo and insoluble sphere are calculated as presented in Section 2.3.4.

2.3.3 Chemical Composition

The chemical composition of aerosol in our model includes both inorganic and organic species, some of which are also present in the gas phase. Table 2.5 lists the inorganic compounds included in our aerosol model, including aqueous ions and solid electrolytes. The phases the compounds can be present in are also listed. The list is based on the compounds included in *Kim et al.* [1993a, b] and *Kim and Seinfeld* [1995], and is similar to the list of compounds included in ISORROPIA II [*Fountoukis and Nenes*, 2007]. The thermodynamics of these compounds are discussed in Section 2.4.2.

Table 2.6 lists the condensable organic species included in the model. The list of compounds includes black carbon (BC), 10 surrogate compounds for secondary organic aerosol (SOA) [*Griffin*

Table 2.5: Inorganic Chemical Species included in ASP

Species	Molecular Weight (g/mol)	Phases
H_2O	18.016	Gas, Aqueous
HNO_3	63.018	Gas
NH_3	17.034	Gas, Aqueous
HCl	36.458	Gas
H_2SO_4	98.076	Gas
H^+	1.008	Aqueous
NH_4^+	18.042	Aqueous
Na^+	22.990	Aqueous
K^+	39.0983	Aqueous
Ca^{2+}	40.078	Aqueous
Mg^{2+}	24.305	Aqueous
SO_4^{2-}	96.06	Aqueous
HSO_4^-	97.068	Aqueous
NO_3^-	62.01	Aqueous
Cl^-	35.45	Aqueous
OH^-	17.008	Aqueous
NH_4Cl	53.492	Solid
NH_4NO_3	80.052	Solid
$(NH_4)_2SO_4$	132.144	Solid
NH_4HSO_4	115.110	Solid
$(NH_4)_3H(SO_4)_2$	247.254	Solid
NaCl	58.44	Solid
$NaNO_3$	85.0	Solid
Na_2SO_4	142.0395	Solid
$NaHSO_4$	120.058	Solid
NaOH	39.998	Solid
KCl	74.5483	Solid
KNO_3	101.1083	Solid
K_2SO_4	174.2566	Solid
$KHSO_4$	136.1663	Solid
KOH	56.1063	Solid
$MgCl_2$	95.205	Solid
$Mg(NO_3)_2$	148.325	Solid
$MgSO_4$	120.365	Solid
$Mg(HSO_4)_2$	218.441	Solid
$Mg(OH)_2$	58.321	Solid
$CaCl_2$	110.978	Solid
$Ca(NO_3)_2$	164.098	Solid
$CaSO_4 \cdot 2H_2O$	172.17	Solid
$Ca(HSO_4)_2$	234.214	Solid
$Ca(OH)_2$	74.094	Solid

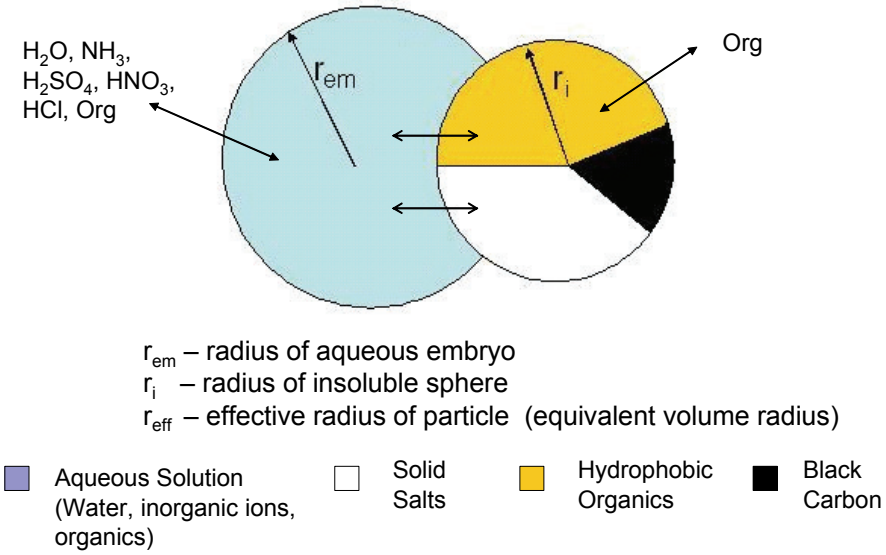

Figure 2-5: Cartoon of particle composition and structure

et al., 2002b, 2005], and 8 surrogates for primary organic aerosol (POA) [*Griffin et al.*, 2002b, 2005]. We also include 5 compounds identified by *Decesari et al.* [2006] as model compounds to represent the chemical composition of the water-soluble organic carbon (WSOC) present in biomass burning aerosols measured during the LBA-SMOCC 2002 experiment, including levoglucosan (LEVO) and cellobiosan (CBIO). The chemical structures are shown in Figure 2-6 for the SOA surrogates, in Figure 2-7 for the POA surrogates, and in Figure 2-8 for the biomass burning compound surrogates. The organic species, except for BC, are all allowed to be present in the gas, aqueous, and/or hydrophobic organic phases. This is different than in the MPMPO, where the POA surrogates are assumed to be involatile [*Griffin et al.*, 2002b, 2005].

The CACM predicts the gas-phase concentrations of 37 condensable organic compounds. The mass of these compounds are assigned to the 10 SOA surrogates to reduce the number of equations for the thermodynamic partitioning of these compounds between the gas and aerosol phases [*Pun et al.*, 2002; *Griffin et al.*, 2002b, 2005]. Table 2.6 lists which condensable species predicted by the CACM are assigned to which SOA surrogate. The lumping of condensable species proceeds as described by *Pun et al.* [2002] by converting the molecular concentrations of condensable gas-phase species (molecules cm^{-3}) to mass concentrations ($\mu g\ m^{-3}$). These mass concentrations are then summed for each surrogate compound; at the same time, the mass fraction that each gas-phase

Table 2.6: Organic Chemical Species included in ASP

Species	MW (g/mol)	No. of C	Included Gas Phase Compounds	Structure Reference
BC	200[a]	-	-	-
SOA1	90	2	UR21, UR28	1,2
SOA2	184	8	RP13, RP17, RP18, UR26, UR29, UR30	1,2
SOA3	154	8	RPR9, RP12	1,2
SOA4	186	9	UR3, UR8, UR23	1,2
SOA5	186	10	UR7, UR17	1,2
SOA6	211	9	AP1, AP6, UR31	1,2
SOA7	178	10	ADAC, ARAC, RPR7, RP14 RP19, UR2, UR14, UR27	1,2
SOA8	217	12	AP10, UR11, UR15	1,2
SOA9	303	16	AP11, AP12, UR20, UR34	1,2
SO10	217	10	AP7, AP8, UR5, UR6	1,2
POA1	408	29	-	1,2
POA2	118	4	-	1,2
POA3	216	12	-	1,2
POA4	276	22	-	1,2
POA5	412	30	-	1,2
POA6	166	8	-	1,2
POA7	284	18	-	1,2
POA8	390	28	-	1,2
LEVO	162.1	6	-	3
CBIO	324.3	12	-	3
CPD1	330.3	18	-	3
CPD2	332.4	19	-	3
CPD3	730.7	36	-	3

[a]The molecular weight for BC is an approximation. The value doesn't affect the results.
References: 1, *Griffin et al.* [2003]; 2, *Griffin et al.* [2005], 3, *Decesari et al.* [2006]

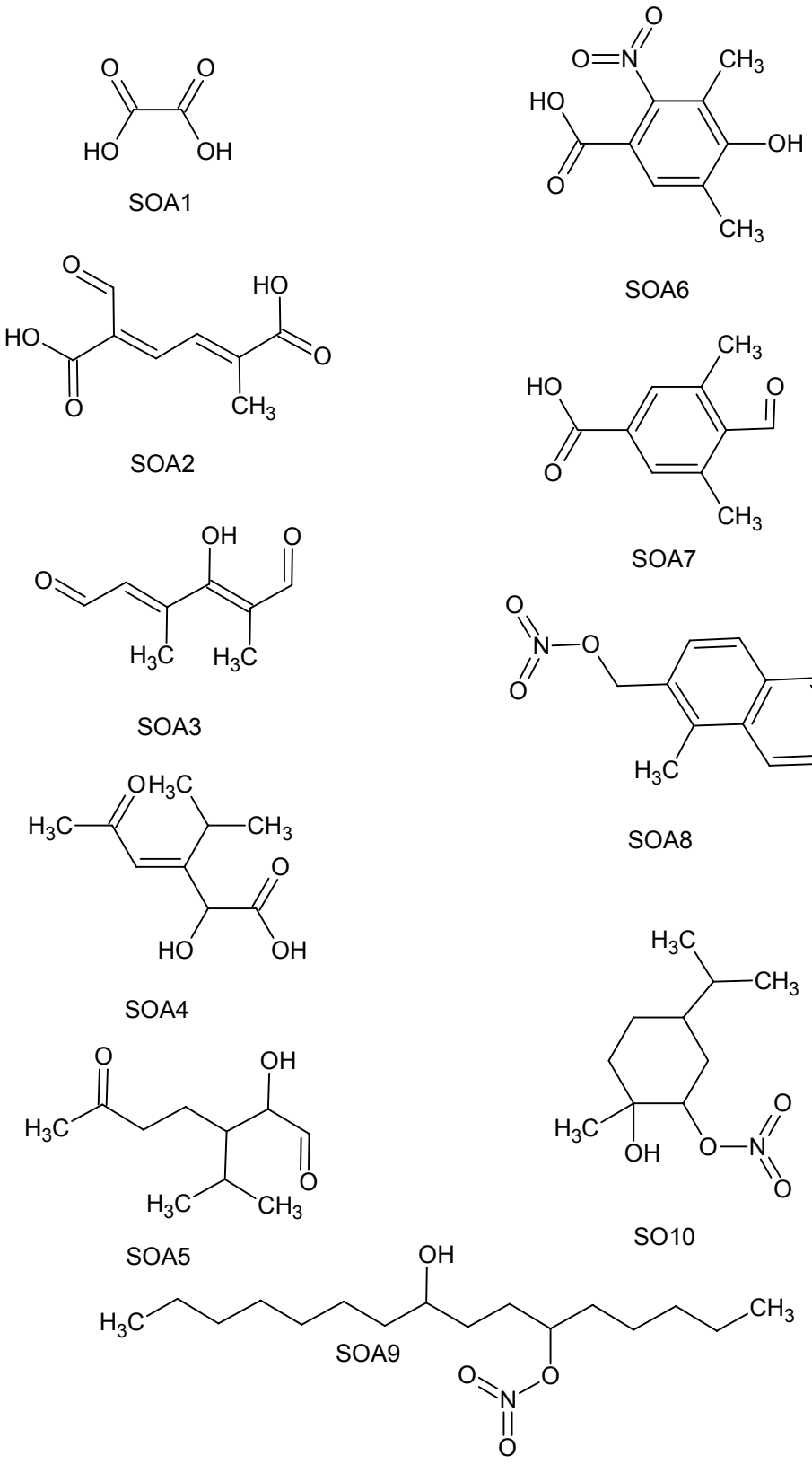

Figure 2-6: Chemical structures for the surrogates for secondary organic aerosol.

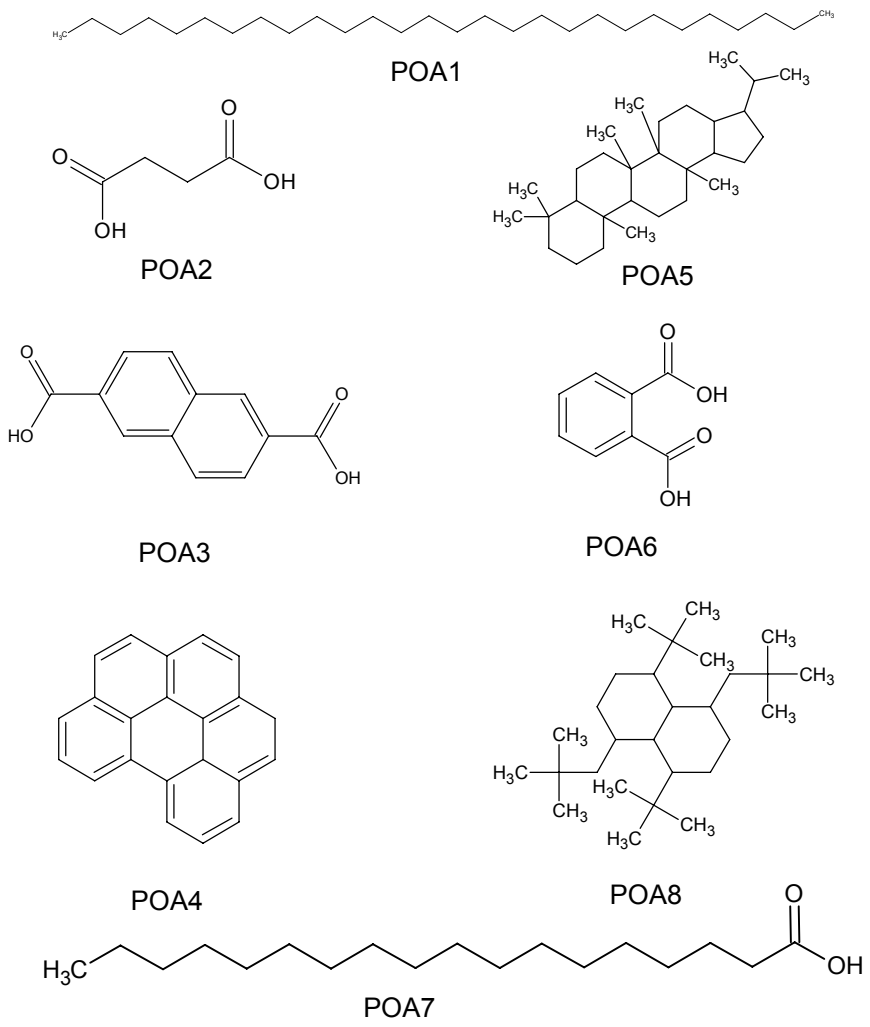

Figure 2-7: Chemical structures of the surrogates for primary organic aerosol.

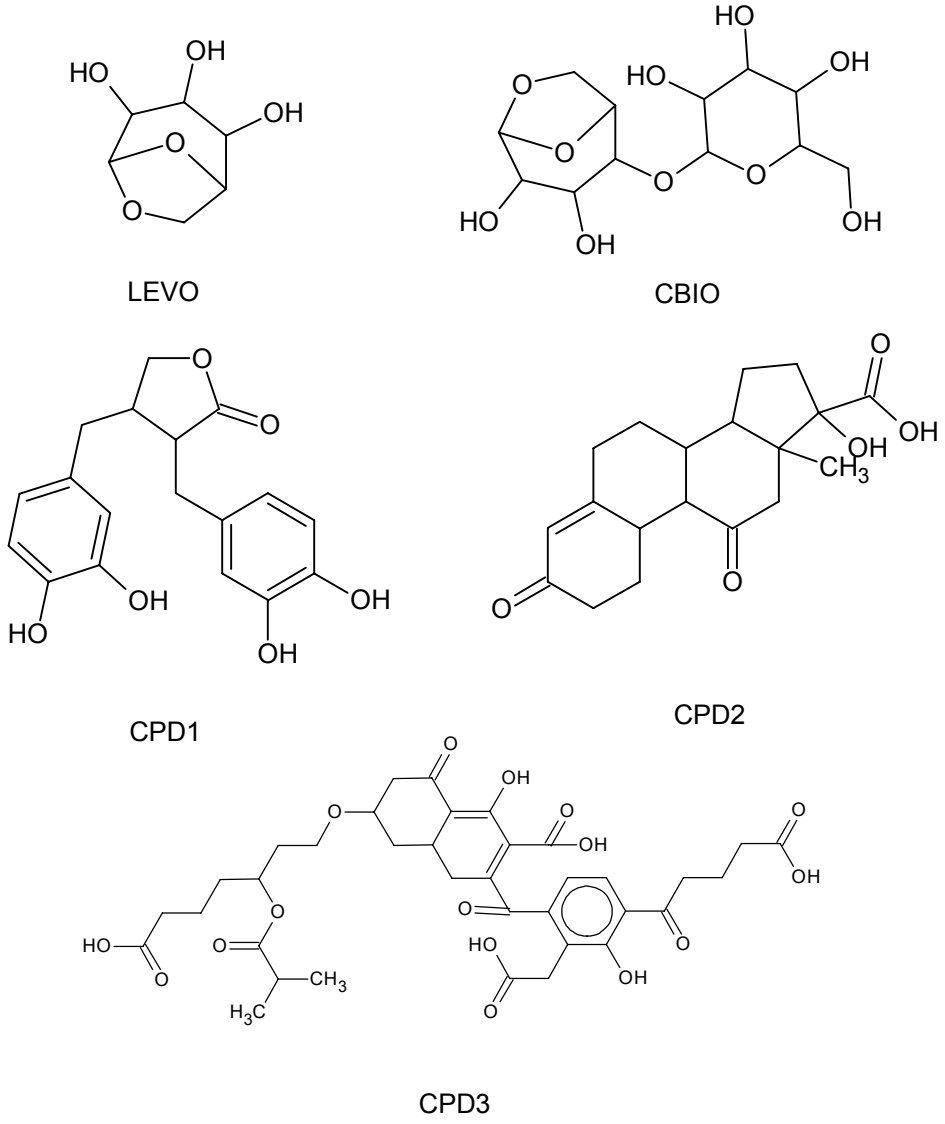

Figure 2-8: Chemical structures for the surrogates of biomass burning organic aerosol compounds.

species contributes to the surrogate (χ_q) is calculated and stored. The molecular weight of the surrogate is then used to calculate the molecular concentration of the surrogate. The partitioning model is then called. Upon completion, an updated gas-phase concentration is available for the surrogate. These surrogate concentrations are then multiplied by the appropriate χ_q values to update the individual gas-phase concentrations needed by the gas-phase mechanism [*Pun et al.*, 2002].

2.3.4 Density and Size

Many important aerosol properties depend on the size and density of the aerosol. For our aerosol, which is assumed to consist of a spherical aqueous embryo attached to an insoluble sphere, we must calculate the size and density of the embryo and insoluble sphere as well as the average density and size of the whole particle. Below, we describe how we calculate (1) the density of the mixture of water and inorganic ions, ignoring the effects of aqueous organics $\left(\rho_{water-ion}\right)$, (2) the density of the aqueous solution, including water, inorganic ions, and aqueous organics $\left(\rho_{sol,i}\right)$, (3) the density of the insoluble fraction of the aerosol (solid salts, hydrophobic organics, and black carbon) $\left(\rho_{insol,i}\right)$, (4) the average density of the particle (ρ_i), (5) the volume-equivalent radius of the aqueous solution embryo ($r_{i,em}$), and (6) the volume-equivalent radius of the insoluble sphere ($r_{i,insol}$), and (7) the effective (volume-equivalent) radius of the whole particle ($r_{i,eff}$).

Density of water-inorganic ion solution

Following *Steele* [2004] and *Resch* [1995], the binary density of a single electrolyte IJ in water, ρ^o_{IJ}, is parameterized as

$$\rho^o_{IJ} = \wp^{(0)}_{ij} + e^{-\wp^{(1)}_{ij}\mathbf{m}_{IJ}}\left(\rho_{H_2O} - \wp^{(1)}_{ij}\right) \tag{2.1}$$

where $\mathbf{m}_{IJ}$ is the molality of electrolyte IJ in solution, ρ_{H_2O} is the density of pure water, and $\wp^{(0)}_{ij}$ and $\wp^{(1)}_{ij}$ are two electrolyte-specific parameters that are determined by regressing Equation 2.1 against the solution density data found in *Lobo* [1989]. The values of the parameters used in this work are given in Table 2.7. The density of the water-ion solution $\rho_{water-ion}$ is then calculated using the Patwardhan and Kumar mixing rule [*Patwardhan and Kumar*, 1993]

$$\rho_{water-ion} = \frac{\sum_{ij}\psi_{IJ}}{\sum_{ij}\left(\frac{\psi_{IJ}}{\rho^o_{IJ}}\right)} \tag{2.2}$$

ψ_{IJ} is defined as

$$\psi_{IJ} = (1000 y_{IJ} + \mathbf{m}_{IJ} M_{IJ}) \tag{2.3}$$

where M_{IJ} is the molecular weight of electrolyte IJ and y_{IJ} is defined as [*Patwardhan and Kumar*, 1993]

$$y_{IJ} = \mathbf{F}_I Z_J + \mathbf{F}_J Z_I \tag{2.4}$$

$\mathbf{F}_x$ is the ionic strength fraction of ion I

$$\mathbf{F}_x = \frac{\frac{1}{2}\mathbf{m}_x z_x^2}{\mathbf{I}} \tag{2.5}$$

where $\mathbf{m}_x$ is molality of x in solution, z_x is charge of x and $\mathbf{I}$ is the ionic strength of the solution. Z_x is the charge fraction, defined as

$$Z_x = \frac{\mathbf{m}_x z_x}{\sum_k \mathbf{m}_k z_k} \tag{2.6}$$

where the sum k is over all cations if x is a cation and over all anions if x is an anion.

Solution, Insoluble, and Particle Density

To calculate the average densities of the aqueous embryo, insoluble sphere, and whole particle, we need values for the single compound densities of solid salts and organic species, along with an appropriate mixing rule for calculating average densities in the particle mixtures.

Solid salt densities are given in Table 2.7. The density of BC was set to 2 g/cm^3, the value recommended by *Seinfeld and Pandis* [1998]. The density of all organic compounds was set to 1.5 g/cm^3 in both the aqueous and organic phases, similar to the value of 1.53 g/cm^3 reported for biomass burning aerosol by *Martins et al.* [1996] and *Trentmann et al.* [2002] and the value of 1.48 g/cm^3 reported by *Odum et al.* [1996] for SOA formed from m-xylene, but slightly higher than the range of 1.2-1.4 g/cm^3 recommended for dry smoke particles by *Reid et al.* [2005b].

To calculate the density of the aqueous solution $\left(\rho_{sol,i}\right)$ when both inorganic ions and aqueous organics are present, we assumed that the volumes of the aqueous organics and the water-ion solution are unaffected by mixing. We also assumed that the volumes of dissociated organics are similar to those of the parent species. $\rho_{sol,i}$ can then be calculated as the total solution mass $\mathcal{M}_{sol}$ (g/particle) divided by $\mathcal{V}_{sol}$ (cm^3/particle), which is the sum of the volumes contributed by the

Table 2.7: Solution and Solid Salt Density Parameters for Inorganic Electrolytes

Species	$\wp_{ij}^{(0)a}$	$\wp_{ij}^{(1)}$	Solid Salt Density[b]
H_2O	0.	0.	NA
HNO_3	1.455	0.0702	NA
NH_3+H_2O	1.540	-0.110	NA
HCl	1.382	0.0416	NA
H_2SO_4	1.696	0.0906	NA
NH_4Cl	1.190	0.0717	1.53
NH_4NO_3	1.353	0.0812	1.69
$(NH_4)_2SO_4$	1.361	0.198	1.769
NH_4HSO_4	3.204	0.0176	1.78
$(NH_4)_3H(SO_4)_2$	-	-	1.5[b]
NaCl	1.728	0.0517	2.163
$NaNO_3$	1.732	0.0715	2.257
Na_2SO_4	1.557	0.230	2.698
$NaHSO_4$	0	-	2.742
NaOH	1.602	0.0648	2.130
KCl	2.512	0.0278	1.988
KNO_3	1.746	0.0138	1.915
K_2SO_4	1.884	0.0151	2.662
$KHSO_4$	0	-	2.35
KOH	1.751	0.0664	2.044
$MgCl_2$	1.6783	0.1120	2.325
$Mg(NO_3)_2$	1.7694	0.1412	1.82
$MgSO_4$	1.8675	0.1387	2.66
$Mg(HSO_4)_2$	0	-	1.5[b]
$Mg(OH)_2$	0	-	3.258
$CaCl_2$	1.8259	0.1079	2.152
$Ca(NO_3)_2$	1.9590	0.1128	2.36
$CaSO_4{\cdot}2H_2O$	0	-	2.32
$Ca(HSO_4)_2$	0	-	1.5[b]
$Ca(OH)_2$	0	-	2.2

[a] Density parameters for Na^+, K^+, and NH_4^+ salts are from *Steele* [2004].
Density parameters for Ca^{2+} and Mg^{2+} salts are from this work, calculated from data in *Lobo* [1989]. Cases with 0 are those with no density data, and are assumed to have little effect on the solution density that is not accounted for by the other electrolyte pairs.
[b] Solid salt densities from *Green and Maloney* [1997] if available; assumed to be 1.5 g/cm^3 otherwise.

water-ion solution and the aqueous organics (*i.e.* the total volume of the aqueous embryo). Thus,

$$\rho_{sol,i} = \frac{\mathcal{M}_{sol}}{\mathcal{V}_{sol}} = \frac{M_{H_2O}c_{H_2O,i} + \sum_{\text{inorg ions}} M_q c_{q,i} + \sum_{\text{aq orgs}} M_q c_{q,i}}{\frac{M_{H_2O}c_{H_2O,i} + \sum_{\text{inorg ions}} M_q c_{q,i}}{\rho_{water-ion}} + \sum_{\text{aq orgs}} \frac{M_q c_{q,i}}{\rho_q}} \tag{2.7}$$

where M_q is the molecular weight (g/mol) of species q, $c_{q,i}$ is the concentration of species q in size bin i (mol/particle), and ρ_q is the density of pure species q. Note that the volume of the water-inorganic ion mixture is calculated using $\rho_{water-ion}$, so that the interaction effects of the inorganic species on the aqueous volume are included.

The density of the insoluble sphere, including solid salts, organic species and BC, are calculated by assuming that the volumes of the individual species are unaffected by mixing. $\rho_{insol,i}$ can then be calculated as

$$\rho_{insol,i} = \frac{\mathcal{M}_{insol}}{\mathcal{V}_{insol}} = \frac{M_{BC}c_{BC,i} + \sum_{\text{solid salts}} M_q c_{q,i} + \sum_{\text{hydrophobic orgs}} M_q c_{q,i}}{\frac{M_{BC}c_{BC,i}}{\rho_{BC}} + \sum_{\text{solid salts}} \frac{M_q c_{q,i}}{\rho_q} + \sum_{\text{hydrophobic orgs}} \frac{M_q c_{q,i}}{\rho_q}} \tag{2.8}$$

where $\mathcal{M}_{insol}$ (g/particle) is the total mass in the insoluble sphere, and $\mathcal{V}_{insol}$ (cm^3/particle) is the sum of the volumes contributed by each species in the insoluble sphere. The average particle density ρ_i is then calculated as

$$\rho_i = \frac{\mathcal{M}_{sol} + \mathcal{M}_{insol}}{\mathcal{V}_{sol} + \mathcal{V}_{insol}} \tag{2.9}$$

Radius Calculations

The radius of the aqueous embryo ($r_{i,em}$) is calculated from $\mathcal{V}_{sol}$ as

$$r_{i,em} = \left(\frac{3}{4\pi}\mathcal{V}_{sol}\right)^{1/3} \tag{2.10}$$

The radius of the insoluble sphere ($r_{i,insol}$) is calculated from $\mathcal{V}_{insol}$ as

$$r_{i,insol} = \left(\frac{3}{4\pi}\mathcal{V}_{insol}\right)^{1/3} \tag{2.11}$$

The effective, volume-equivalent radius for the size bin ($r_{i,eff}$) is then calculated as

$$r_{i,eff} = \left[\frac{3}{4\pi}\left(\mathcal{V}_{sol} + \mathcal{V}_{insol}\right)\right]^{1/3} \tag{2.12}$$

Note that the particle radius, which is used to calculate diffusive flux rate, coagulation coefficients, optical properties, *etc.*, is proportional to $\mathcal{V}^{1/3}$, or $\rho^{-1/3}$, and is thus a weak function of density. For example, a 10% error in the calculated particle density would lead to only a 3.2% error in the predicted particle radius.

2.3.5 Surface Tension

The surface tension of the aqueous embryo is needed to calculate the Kelvin effect for the aqueous phase (see Equation 2.39). Following *Steele* [2004], we use the Li and Lu approach to calculate the surface tension of the solution of water and inorganic electrolytes [*Li and Lu*, 2001]

$$\sigma_{ion} = \sigma_{H_2O} + RT \sum_{ij} \zeta_{ij} \ln \left(1 - \frac{K^a_{ij} a_{ij}}{1 + \sum_{kl} K^a_{kl} a_{kl}} \right) \tag{2.13}$$

where a_{ij} is the mean activity for ion pair ij (see Section 2.4.2). Values for ζ_{ij} and K^a_{ij} are given in Table 2.8.

To include the effect of aqueous organics on the surface tension of the aqueous phase, we use Equation 16.34 of *Jacobson* [2005], which is taken from *Facchini et al.* [1999]:

$$\sigma = \sigma_{ion} - 0.0187 T \ln \left(1 + 628.14 \mathbf{m}_c \right) \tag{2.14}$$

where σ is the surface tension of the aqueous solution of electrolytes and organics in dyn cm^{-1}, σ_{ion} is the ion-corrected surface tension calculated above, T is the temperature in Kelvin, and $\mathbf{m}_c$ is the molality of carbon dissolved in the aqueous phase (moles carbon per kilogram of water).

As $\mathbf{m}_c$ gets large (such as at very low RH), Equation 2.14 can lead to a negative surface tension. To prevent this, we fix a minimum aqueous surface tension of 28.21 dyn cm^{-1}, corresponding to the surface tension of benzene at 298K (see Table 10.2 of *Seinfeld and Pandis* [1998]).

2.4 Inorganic and Organic Aerosol Thermodynamics

In order to simulate the formation or loss of aerosol mass in the atmosphere, we must be able to calculate the thermodynamic properties and equilibrium concentrations of inorganic and organic species in both the gas and particle phases. This section discusses the routines used in our model to calculate the activities and equilibrium concentrations of inorganic and organic species in the gas and particle phases. The model includes the gas phase, an aqueous phase that contains both inorganic ions and organic species, a hydrophobic organic phase, and solid salts (see Figure 2-5

Table 2.8: Surface Tension Parameters for Inorganic Compounds

Species	ζ_{ij} (mol m^{-2})	K^a_{ij}
H_2O	0	-
HNO_3	8.05×10^{-7}	1.06×10^{-1}
NH_3+H_2O	0	-
HCl	4.12×10^{-7}	4.68×10^{-3}
H_2SO_4	-6.75×10^{-8}	1.65×10^{3}
NH_4Cl	-1.01×10^{-6}	1.30
NH_4NO_3	-3.08×10^{-6}	4.89×10^{-1}
$(NH_4)_2SO_4$	-8.79×10^{-7}	3.84×10^{1}
NH_4HSO_4	0	-
$(NH_4)_3H(SO_4)_2$	0	-
NaCl	-1.05×10^{-6}	1.20
$NaNO_3$	-1.66×10^{-6}	1.25
Na_2SO_4	$-8.37\text{x}10^{-7}$	7.57×10^{1}
$NaHSO_4$	0	-
NaOH	-1.13×10^{-6}	1.17
KCl	-7.31×10^{-7}	4.16
KNO_3	-2.38×10^{-6}	1.02
K_2SO_4	-7.05×10^{-6}	9.58
$KHSO_4$	0	-
KOH	-5.44×10^{-7}	8.00
$MgCl_2$	$-2.49x10^{-7}$	2.27×10^{2}
$Mg(NO_3)_2$	0	-
$MgSO_4$	-1.25×10^{-4}	3.79
$Mg(HSO_4)_2$	0	-
$Mg(OH)_2$	0	-
$CaCl_2$	-4.88×10^{-7}	1.50×10^{1}
$Ca(NO_3)_2$	0	-
$CaSO_4$*$2H_2O$	0	-
$Ca(HSO_4)_2$	0	-
$Ca(OH)_2$	0	-

Reference: *Li and Lu* [2001].
Zero is used for electrolyte pairs with no data. This implicitly assumes that the surface tension effects can be represented by the other ions pairs without further correction.

above).

Inorganic thermodynamics is calculated in ASP using routines originally developed for MELAM [*Steele*, 2004] which have been significantly extended to include additional species and the formation of solid salts. Organic thermodynamics is calculated using procedures based on the MPMPO model of *Griffin et al.* [2005], which has been extended to include additional organic compounds found in biomass burning aerosol. In addition, our model allows each condensing organic species to partition into either the gas phase, the hydrophobic organic phase, or the aqueous phase. This means that the POA surrogates are allowed to volatilize, unlike in the MPMPO. Following *Pun et al.* [2002] and *Griffin et al.* [2005], we assume that (1) the aqueous organic and inorganic species do not interact, (2) that the activity coefficients of organic ions are equivalent to those of the corresponding molecular solute, and (3) that a separate hydrophobic organic and aqueous phase are always present. These assumptions simplify the calculation of aerosol thermodynamics by allowing us to treat the inorganic and organic species as independent, and represent an advance on models that only calculate inorganic aerosol equilibrium. However, interactions between inorganic and organic species, such as the formation of ammonium-organic ion salts, cannot be accounted for with this procedure [*Pun et al.*, 2002].

Section 2.4.1 outlines the Mass Flux Iteration (MFI) method [*Jacobson*, 2005] that is used in ASP to calculate equilibrium concentrations of organic and inorganic species. Sections 2.4.2 and 2.4.3 discuss the calculation of activities and equilibrium constants for inorganic and organic species, respectively. Section 2.4.4 discusses the calculation of the equilibrium water content of the aerosol due to the presence of aqueous organic and inorganic species. Sections 2.4.5 and 2.4.6 compare the results of our aerosol equilibrium model with those of the inorganic aerosol model ISORROPIA [*Nenes et al.*, 1998] and the organic aerosol model CACM/MPMPO [*Griffin et al.*, 2005], respectively.

2.4.1 Mass Flux Iteration (MFI) Method

The iterative equilibrium routines used in our model are based on the routines developed for MELAM [*Steele*, 2004]. These routines use the Mass Flux Iteration (MFI) method to solve for the gas- and aerosol-phase concentrations at equilibrium for a given reaction (*Jacobson* [2005], Section 17.11). The MFI procedure is described below.

Consider a general equilibrium reaction of the form

$$v_A A + v_B B + \ldots \rightleftharpoons v_C C + v_D D + \ldots \tag{2.15}$$

First, we find the concentration of the limiting product and reactant by scaling the concentrations by the stoichiometric coefficients and selecting the minimum. Let Q_{r} be the scaled concentration of the limiting reactant and Q_p be the scaled concentration of the limiting product. Then

$$Q_r = \min\left(\frac{c_A}{v_A}, \frac{c_B}{v_B}, \ldots\right) \quad ; \quad Q_p = \min\left(\frac{c_C}{v_C}, \frac{c_D}{v_D}, \ldots\right) \tag{2.16}$$

Next, we calculate an initial value for the tracking parameter ($\mathcal{Z}_1$) and the mass flux parameter (Δx_1) where the subscript refers to the iteration number.

$$\mathcal{Z}_1 = \frac{Q_r + Q_p}{2} \tag{2.17}$$

$$\Delta x_1 = Q_r - \mathcal{Z}_1 = \frac{Q_r - Q_p}{2} \tag{2.18}$$

To go from iteration l to iteration $l+1$, the mass flux parameter Δx_l is then subtracted from the reactants and added to the products, after being scaled by the appropriate stoichiometric coefficient

$$c_{A,l+1} = c_{A,l} - v_A \Delta x_l \qquad c_{B,l+1} = c_{B,l} - v_B \Delta x_l \tag{2.19}$$

$$c_{C,l+1} = c_{C,l} + v_C \Delta x_l \qquad c_{D,l+1} = c_{D,l} + v_D \Delta x_l \tag{2.20}$$

We then check to see if equilibrium has been achieved by calculating the ratio F of the current activities to the equilibrium coefficient. For example, for Equation 2.15,

$$F = \frac{a_C^{v_C} a_D^{v_D}}{a_A^{v_A} a_B^{v_B} K_{eq}(T)} \tag{2.21}$$

If F is equal to 1 within the prescribed error, the procedure has converged and the concentrations are at equilibrium with respect to the given reaction. If the procedure has not converged, the tracing parameter is updated as $\mathcal{Z}_{l+1} = 0.5\mathcal{Z}_l$. If F is greater than 1, $\Delta x_{l+1} = -\mathcal{Z}_{l+1}$. Otherwise, $\Delta x_{l+1} = \mathcal{Z}_{l+1}$.

To calculate gas-particle equilibrium, each reaction is iterated for each particle size bin. In general, the iteration is continued until all size bins are in equilibrium with all reactions. However, there are some conditions where this procedure can take a very long time to converge or, in some cases, not converge at all [*Steele*, 2004]. In these cases, special criteria are used to exit the iteration

routine and prevent an infinite loop. These special criteria are noted below.

2.4.2 Inorganic Thermodynamics

The inorganic equilibrium routines originated in the MELAM model of *Steele* [2004], but have been extended to include an expanded set of species (*e.g.*, Ca^{2+}, Mg^{2+}, and their salts), and to calculate the equilibrium between solid salts and aqueous ions. The inclusion of the formation of solid salts from aqueous ions in the new thermodynamic routines represents a significant advance over MELAM.

First, we discuss how the model calculates thermodynamic activities for inorganic compounds. We then consider ion-electrolyte equilibrium reactions (*i.e.*, reactions between aqueous ions and solid or liquid electrolytes) and gas-particle reactions (*i.e.*, reactions between inorganic gas-phase species and solid- or liquid-phase species) in turn.

Thermodynamic Activities

The mean activity of an electrolyte ij dissociating into ions i and j is defined as

$$a_{ij} \equiv a_i^{v_i} a_j^{v_j} = \mathbf{m}_i^{v_i} \mathbf{m}_j^{v_j} \gamma_{ij}^{v_i+v_j} \tag{2.22}$$

where $\mathbf{m}_i$ is the molality of ion i in aqueous solution (mol/kg H_2O), v_i is the number of ions i in electrolyte ij, and γ_{ij} is the mean activity coefficient for ion pair ij, defined as

$$\gamma_{ij} \equiv \left(\gamma_i^{v_i} \gamma_j^{v_j}\right)^{\frac{1}{v_i+v_j}} \tag{2.23}$$

Our model uses the routines developed for MELAM to calculate activity coefficients for inorganic species. MELAM uses the Kusik-Meissner method for calculating binary activity coefficients and the activity coefficients of multi-component inorganic systems, and contains a number of extensions to deal with partially dissociating electrolytes and other cases [*Steele*, 2004].

Binary Activity Coefficients: Kusik-Meissner Method When data for the binary activities of an ion pair are available, we can use the Kusik-Meissner method to estimate binary activity coefficients [*Kusik and Meissner*, 1978; *Steele*, 2004]. First, we define the reduced mean activity coefficient Γ_{ij} as

$$\Gamma_{ij} \equiv \gamma_{ij}^{\frac{1}{|z_i z_j|}} \tag{2.24}$$

where z_i is the charge of ion i. The binary reduced mean activity coefficient is then approximated as

$$\Gamma_{ij}^{o} = \log_{10}\left(1 + [0.75 - 0.065q]\left[\{1 + 0.1\mathbf{I}\}^{q} - 1\right]\right) - \frac{0.5107\sqrt{\mathbf{I}}}{1 + C\sqrt{\mathbf{I}}} \tag{2.25}$$

where $\mathbf{I}$ is the ionic strength of the solution and C and q are calculated as:

$$C = 1.0 + 0.055q\exp\left[-0.023\mathbf{I}^3\right] \tag{2.26}$$

$$q = q_r\left(1 + q_T\frac{T - T_r}{z_i z_j}\right) \tag{2.27}$$

Only the parameters q_r, the Kusik-Meissner parameter at the reference temperature, and q_T, the linear dependence of q on temperature, must be determined experimentally. In general, there is not enough data to constrain q_T, so a default value of -0.0027 proposed by *Meissner* [1980] is used. Table 2.9 contains the values for q_r and q_T used in this work.

Table 2.9: Kusik-Meissner Parameters for Selected Electrolytes

Electrolyte	q_r	q_t	Ref.
HNO_3	2.017	-0.0027	[*Steele*, 2004]
HCl	6.00	-0.0027	[*Wexler and Seinfeld*, 1991]
H_2SO_4	-0.10	-0.0027	[*Kim et al.*, 1993a]
H-HSO_4	8.00	-0.0027	[*Kim et al.*, 1993a]
NH_4Cl	0.82	-0.0027	[*Kusik and Meissner*, 1978]
NH_4NO_3	-1.15	-0.0027	[*Kusik and Meissner*, 1978]
$(NH_4)_2SO_4$	-0.25	-0.0027	[*Kusik and Meissner*, 1978]
NaCl	2.290	0.00707	[*Steele*, 2004]
$NaNO_3$	-0.39	-0.0027	[*Kusik and Meissner*, 1978]
Na_2SO_4	-0.19	-0.0027	[*Kusik and Meissner*, 1978]
NaOH	3.00	-0.0027	[*Kusik and Meissner*, 1978]
KCl	0.92	-0.0027	[*Kusik and Meissner*, 1978]
KNO_3	-2.33	-0.0027	[*Kusik and Meissner*, 1978]
K_2SO_4	-0.25	-0.0027	[*Kusik and Meissner*, 1978]
KOH	4.77	-0.0027	[*Kusik and Meissner*, 1978]
$MgCl_2$	2.90	-0.0027	[*Kusik and Meissner*, 1978]
$Mg(NO_3)_2$	2.32	-0.0027	[*Kusik and Meissner*, 1978]
$MgSO_4$	0.15	-0.0027	[*Kusik and Meissner*, 1978]
$CaCl_2$	2.40	-0.0027	[*Kusik and Meissner*, 1978]
$Ca(NO_3)_2$	0.93	-0.0027	[*Kusik and Meissner*, 1978]

When binary activity coefficient data are not available, mean activity coefficients are constructed using an appropriate combination of other mean activity coefficients [*Steele*, 2004]. The model automatically scans for appropriate combinations of activity coefficients for any reaction for which the Kusik-Meissner parameters are not available. For example, for the reaction $NH_3+H_2O \leftrightarrow NH_4^+ + OH^-$, the mean activity $\gamma^2_{(NH_3+H_2O)}$ is calculated as

$$\gamma^2_{(NH_3+H_2O)} = \gamma_{NH_4^+}\gamma_{OH^-} = \frac{\left(\gamma_{NH_4^+}\gamma_{NO_3^-}\right)\left(\gamma_{K^+}\gamma_{OH^-}\right)}{\gamma_{K^+}\gamma_{NO_3^-}} = \frac{\gamma^2_{NH_4NO_3}\gamma^2_{KOH}}{\gamma^2_{KNO_3}} \tag{2.28}$$

To account for bisulfate, a "place-holder" species, H-HSO_4, is used to describe the activity of the sulfuric acid to bisulfate transition [*Steele*, 2004; *Kim et al.*, 1993a].

The activity coefficient of $(NH_4)_3H(SO_4)_2$ cannot be calculated using the Kusik-Meissner formula, as it is not a simple ion pair. The activity coefficient is instead calculated using the formula of *Kim et al.* [1993a]:

$$\gamma_{(NH_4)_3H(SO_4)_2} = \left(\gamma^3_{(NH_4)_2SO_4}\gamma_{H_2SO_4}\right)^{1/4} \tag{2.29}$$

Mean Activity Coefficients in Multicomponent Mixtures Following *Resch* [1995] and *Steele* [2004], we use the mixing rule of *Kusik and Meissner* [1978] to calculate the mixed reduced mean activity coefficient for the ion pair of cation I and anion J

$$\log_{10}\Gamma_{IJ} = \frac{z_I \sum_j \mathbf{F}_j \frac{(z_I+z_j)^2}{2|z_I z_j|}\log_{10}\Gamma^o_{Ij} + z_J \sum_i \mathbf{F}_i \frac{(z_i+z_J)^2}{2|z_i z_J|}\log_{10}\Gamma^o_{iJ}}{z_I + z_J} \tag{2.30}$$

where j indicates a summation over all anions and i indicates a summation over all cations, and $\mathbf{F}_i$ is the ionic strength fraction of ion i from Equation 2.5. This mixing rule is based on Brønsted's proposal that activity coefficients are primarily influenced by interactions with ions of opposite charges, and interactions with ions of like charges can be ignored [*Steele*, 2004].

Ion-Electrolyte Equilibrium

The data used to calculate equilibrium constants for ion-electrolyte reactions are given in Table 2.10. The temperature dependence of $K_{eq}(T)$ is given by the equation ($T_o = 298.15K$)

$$K_{eq}(T) = \exp\left(-\frac{\Delta G^o_{rxn}}{RT_o}\right) \tag{2.31}$$

$$= K_{eq}(T_o)\exp\left[-\frac{\Delta H^o_{rxn}}{RT_o}\left(\frac{T_o}{T}-1\right) - \frac{\Delta C^o_{p,rxn}}{R}\left(1-\frac{T_o}{T}+\ln\frac{T_o}{T}\right)\right] \tag{2.32}$$

Table 2.10: Equilibrium Constants of Electrolyte Equilibrium Reactions

Reaction	$K_{eq}\,(298\,\mathrm{K})$	$-\frac{\Delta H^o_{rxn}}{RT_o}$	$-\frac{\Delta C^o_{p,rxn}}{R}$	Units	Ref.
$H_2O \leftrightarrow H^+ + OH^-$	1.01×10^{-14}	-22.52	26.92	mol kg^{-1}	J
$HNO_3 \leftrightarrow H^+ + NO_3^-$	∞	-	-	-	
$NH_3 + H_2O \leftrightarrow NH_4^+ + OH^-$	1.805×10^{-5}	-1.50	26.92	mol kg^{-1}	C
$HCl \leftrightarrow H^+ + Cl^-$	∞	-	-	-	
$H_2SO_4 \leftrightarrow H^+ + HSO_4^-$	∞	-	-	-	
$HSO_4^- \leftrightarrow H^+ + SO_4^{2-}$	1.015×10^{-2}	8.85	25.14	mol kg^{-1}	K93
$NH_4Cl \leftrightarrow NH_4^+ + Cl^-$	1.96×10^{1}	-6.13	16.92	mol^2 kg^{-2}	J
$NH_4NO_3 \leftrightarrow NH_4^+ + NO_3^-$	1.49×10^{1}	-10.40	17.56	mol^2 kg^{-2}	J
$(NH_4)_2SO_4 \leftrightarrow 2\ NH_4^+ + SO_4^{2-}$	1.82	-2.65	38.57	mol^3 kg^{-3}	J
$NH_4HSO_4 \leftrightarrow NH_4^+ + HSO_4^-$	1.38×10^{2}	-2.87	15.83	mol^2 kg^{-2}	J
$(NH_4)_3H(SO_4)_2 \leftrightarrow 3\ NH_4^+ + HSO_4^- + SO_4^{2-}$	2.93×10^{1}	-5.19	54.40	mol^5 kg^{-5}	J
$NaCl \leftrightarrow Na^+ + Cl^-$	3.61×10^{1}	-1.61	16.90	mol^2 kg^{-2}	J
$NaNO_3 \leftrightarrow Na^+ + NO_3^-$	1.20×10^{1}	-8.22	16.01	mol^2 kg^{-2}	J
$Na_2SO_4 \leftrightarrow 2\ Na^+ + SO_4^{2-}$	4.80×10^{-1}	0.98	39.50	mol^3 kg^{-3}	J
$NaHSO_4 \leftrightarrow Na^+ + HSO_4^-$	2.84×10^{2}	-1.91	14.75	mol^2 kg^{-2}	J
$NaOH \leftrightarrow Na^+ + OH^-$	∞	-	-	-	
$KCl \leftrightarrow K^+ + Cl^-$	8.68	-6.94	19.95	mol^2 kg^{-2}	J
$KNO_3 \leftrightarrow K^+ + NO_3^-$	8.72×10^{-1}	-14.07	19.39	mol^2 kg^{-2}	J
$K_2SO_4 \leftrightarrow 2\ K^+ + SO_4^{2-}$	1.57×10^{-2}	-9.59	45.81	mol^3 kg^{-3}	J
$KHSO_4 \leftrightarrow K^+ + HSO_4^-$	2.4×10^{1}	-8.42	17.96	mol^2 kg^{-2}	J
$KOH \leftrightarrow K^+ + OH^-$	∞	-	-	-	
$MgCl_2 \leftrightarrow Mg^{2+} + 2\ Cl^-$	9.557×10^{21}	-	-	mol^3 kg^{-3}	K95
$Mg(NO_3)_2 \leftrightarrow Mg^{2+} + 2\ NO_3^-$	2.507×10^{15}	-	-	mol^3 kg^{-3}	K95
$MgSO_4 \leftrightarrow Mg^{2+} + SO_4^{2-}$	1.079×10^{5}	-	-	mol^2 kg^{-2}	K95
$Mg(HSO_4)_2 \leftrightarrow Mg^{2+} + 2\ HSO_4^-$	∞	-	-	-	
$Mg(OH)_2 \leftrightarrow Mg^{2+} + 2\ OH^-$	∞	-	-	-	
$CaCl_2 \leftrightarrow Ca^{2+} + 2\ Cl^-$	7.974×10^{11}	-	-	mol^3 kg^{-3}	K95
$Ca(NO_3)_2 \leftrightarrow Ca^{2+} + 2\ NO_3^-$	6.067×10^{5}	-	-	mol^3 kg^{-3}	K95
$CaSO_4{*}2H_2O \leftrightarrow Ca^{2+} + SO_4^{2-} + 2\ H_2O$	4.319×10^{-5}	-	-	mol^2 kg^{-2}	K95
$Ca(HSO_4)_2 \leftrightarrow Ca^{2+} + 2\ HSO_4^-$	∞	-	-	-	
$Ca(OH)_2 \leftrightarrow Ca^{2+} + 2\ OH^-$	∞	-	-	-	

References: C, *Clegg and Brimblecombe* [1989]; K93, *Kim et al.* [1993a];
K95, *Kim and Seinfeld* [1995]; J, *Jacobson* [2005].
A reaction with an equilibrium constant of ∞ means only the
product is allowed to exist; the reactant completely dissociates.

There is one canonical form of the equilibrium constant for ion-electrolyte reactions and four special cases. The canonical case is for a reaction between a solid electrolyte and a pair of aqueous ions (*e.g.*, $NH_4Cl \leftrightarrow NH_4^+ + Cl^-$). In this case, the equilibrium constant and F ratio are

$$K_{eq}\,(T) = \mathbf{m}_i^{v_i}\mathbf{m}_j^{v_j}\gamma_{ij}^{v_i+v_j} \quad F = \frac{\mathbf{m}_i^{v_i}\mathbf{m}_j^{v_j}\gamma_{ij}^{v_i+v_j}}{K_{eq}\,(T)} \tag{2.33}$$

where $\mathbf{m}_i$ is the molality of ion i in aqueous solution (mol/kg H_2O), v_i is the number of ions i in

electrolyte ij, and γ_{ij} is the mean activity coefficient for ion pair ij calculated above.

The first special case is the reaction $(NH_4)_3H(SO_4)_2 \leftrightarrow 3\ NH_4^+ + HSO_4^- + SO_4^{2-}$, where

$$K_{eq}(T) = \mathbf{m}^3_{NH_4^+}\mathbf{m}_{HSO_4^-}\mathbf{m}_{SO_4^{2-}}\gamma^5_{(NH_4)_3H(SO_4)_2} \quad F = \frac{\mathbf{m}^3_{NH_4^+}\mathbf{m}_{HSO_4^-}\mathbf{m}_{SO_4^{2-}}\gamma^5_{(NH_4)_3H(SO_4)_2}}{K_{eq}(T)} \tag{2.34}$$

The second special case is the hydrate-forming reaction $CaSO_4{*}2H_2O \leftrightarrow Ca^{2+} + SO_4^{2-} + 2\ H_2O$. For this case,

$$K_{eq}(T) = \mathbf{m}_{Ca^{2+}}\mathbf{m}_{SO_4^{2-}}\gamma_{CaSO_4}a_w^2 \quad F = \frac{\mathbf{m}_{Ca^{2+}}\mathbf{m}_{SO_4^{2-}}\gamma_{CaSO_4}a_w^2}{K_{eq}(T)} \tag{2.35}$$

where a_w is the activity of water and v_w is the number of molecules of water in the hydrate.

Third, the reaction of the bisulfate ion ($HSO_4^- \leftrightarrow H^+ + SO_4^{2-}$) is included using the formula (see the extensive discussion in *Steele* [2004], Section 4.4.3)

$$K_{eq}(T) = \frac{\mathbf{m}_{H^+}\mathbf{m}_{SO_4^{2-}}}{\mathbf{m}_{HSO_4^-}}\frac{\gamma^3_{H_2SO_4}}{\gamma^2_{H-HSO_4}} \tag{2.36}$$

The final special case is the reaction $NH_3 + H_2O \leftrightarrow NH_4^+ + OH^-$, where

$$K_{eq}(T) = \frac{\mathbf{m}_{NH_4^+}\mathbf{m}_{OH^-}\gamma^2_{(NH_3+H_2O)}}{\mathbf{m}_{NH_3}a_w} \tag{2.37}$$

Table 2.11 gives the deliquescence relative humidities (DRH) for the solid electrolytes. The DRH is the relative humidity at which the pure electrolyte first takes on water and dissolves into an ionic solution. When the relative humidity is above the DRH for a solid electrolyte, the solid electrolyte is not allowed to form. The crystallization relative humidity (CRH), the relative humidity at which a pure ionic solution first crystallizes to form solid electrolytes, is not included in ASP, and thus ASP cannot be used to study the phase hysteresis of inorganic particles. The temperature dependence of the DRH is calculated using the equation

$$DRH(T) = DRH\,(298\,\mathrm{K})\exp\left[\alpha\left(\frac{1}{T} - \frac{1}{298K}\right)\right] \tag{2.38}$$

where $\alpha = -\frac{M_w\mathbf{m}_s L_s}{1000R}$, M_w is the molecular weight of water, m_s is the molality of the saturated solution at 298 K, and L_s is the latent heat of fusion for a salt from a saturated solution [*Fountoukis and Nenes*, 2007].

Steele [2004] found that in some cases, reactions that redistributed minor constituents or that

Table 2.11: Electrolyte Deliquesence Relative Humidities

Electrolyte	DRH (298 K)	α	Ref.
NH_4Cl	0.7710	239	K93
NH_4NO_3	0.6138	852	K93
$(NH_4)_2SO_4$	0.7997	80	K93
NH_4HSO_4	0.40	984	K93, N
$(NH_4)_3H(SO_4)_2$	0.69	-	K93
NaCl	0.7528	25	K93
$NaNO_3$	0.7379	304	K93
Na_2SO_4	0.93	80	K93, N
$NaHSO_4$	0.52	-45	K93, N
NaOH	0	-	
KCl	0.8426	179	K95
KNO_3	0.9248	-	K95
K_2SO_4	0.9751	36	K95
$KHSO_4$	0.52	-45	Assumed equivalent to $NaHSO_4$
KOH	0	-	
$MgCl_2$	0.328412	-1860	K95
$Mg(NO_3)_2$	1.0	0	
$MgSO_4$	0.8613	-714	K95
$Mg(HSO_4)_2$	0	-	
$Mg(OH)_2$	0	-	
$CaCl_2$	0.2830	-1121	K95
$Ca(NO_3)_2$	0.4906	-431	K95
$CaSO_4$*$2H_2O$	0.97	-	K95
$Ca(HSO_4)_2$	0	-	
$Ca(OH)_2$	0	-	

References: K93, *Kim et al.* [1993a]; K95, *Kim and Seinfeld* [1995];
N, *Nenes et al.* [1998].
A DRH of 0 means the solid electrolyte is never allowed to form.
A DRH of 1.0 means that solid may always form, if thermodynamically favorable.

had very large or very small equilibrium constants would keep the system from converging to equilibrium in a reasonable amount of time. To address this computational issue, Steele implemented a scheme in MELAM would defer the equilibration of these minor reactions until the end of the equilibration step [*Steele*, 2004]. This scheme is included in our model.

In addition, a few other computational checks are included to ensure the iterative scheme does not enter an infinite loop. For equilibrium between a solid electrolyte and aqueous ions, the iteration of the equilibrium reaction is stopped when the solution is subsaturated but the electrolyte concentration is approaching 0. In addition, when the aerosol is very acidic, the concentration of SO_4^{2-} can approach 0, preventing equilibration of reactions involving this ion. The iteration of these reactions are stopped when SO_4^{2-} approaches 0.

Gas-Particle Reactions

When modeling equilibrium between gas and particle phases, we must account for the fact that the vapor pressure over a curved surface is higher than the vapor pressure over a flat surface - the Kelvin effect. For compounds dissolving into the aqueous phase of particles in size bin i, the ratio of the vapor pressure over the curved surface of the aqueous embryo to the vapor pressure over a flat surface, $S_{aq,i}$, is [*Seinfeld and Pandis*, 1998]

$$S_{aq,i} = \frac{P_{curved}^{SAT}}{P_{flat}^{SAT}} = \exp\left(\frac{2\sigma_i M_{H_2O}}{RT\rho_{sol,i} r_{i,em}}\right) \tag{2.39}$$

where σ_i is the surface tension of the aqueous solution, including contributions from both inorganic ions and organic solutes (see Section 2.3.5), M_{H_2O} is the molecular weight of water, $\rho_{sol,i}$ is the density of the aqueous solution and $r_{i,em}$ is the radius of the aqueous embryo of the particle. The embryo radius is used so that the current model remains consistent with the original MELAM studies of *Steele* [2004] of the activation of particles containing both a soluble species and an insoluble core.

There are several types of reactions where inorganic gases are in equilibrium with the particle phase. Thermodynamic data for these reactions are listed in Table 2.12. Acid gases such as HCl and HNO_3 are in equilibrium with their constituent ions. For example, for the reaction $HCl_{(g)} \leftrightarrow H^+ + Cl^-$, the equilibrium constant (units of $mol^2\ kg^{-2}\ atm^{-1}$) has the form

$$K_{eq}(T) = \frac{S_{aq,i}\gamma_{HCl}^2 \mathbf{m}_{H^+}\mathbf{m}_{Cl^-}}{P_{HCl}} \tag{2.40}$$

where P_{HCl} is the partial pressure of HCl.

Table 2.12: Equilibrium Constants of Inorganic Gas-Particle Reactions

Reaction	$K_{eq}\,(298\,\mathrm{K})$	$-\frac{\Delta H^o_{rxn}}{RT_o}$	$-\frac{\Delta C^o_{p,rxn}}{R}$	Units	Ref.
$H_2SO_{4(g)} \leftrightarrow 2\ H^+ + SO_4^{2-}$	∞	-	-	-	-
$HCl_{(g)} \leftrightarrow H^+ + Cl^-$	1.97×10^6	30.19	19.91	$\mathrm{mol^2\ kg^{-2}\ atm^{-1}}$	B
$HNO_{3(g)} \leftrightarrow H^+ + NO_3^-$	2.51×10^6	29.17	16.83	$\mathrm{mol^2\ kg^{-2}\ atm^{-1}}$	B
$NH_{3(g)} + H^+ \leftrightarrow NH_4^+$	1.03×10^{11}	34.81	-5.39	$\mathrm{atm^{-1}}$	J
$NH_{3(g)} \leftrightarrow NH_{3(aq)}$	57.64	13.79	-5.39	$\mathrm{mol\ kg^{-1}\ atm^{-1}}$	C
$NH_{3(g)} + HCl_{(g)} \leftrightarrow NH_4Cl_{(s)}$	9.208×10^{15}	71.00	-2.40	$\mathrm{atm^{-2}}$	N
$NH_{3(g)} + HNO_{3(g)} \leftrightarrow NH_4NO_{3(s)}$	1.740×10^{16}	74.38	-6.12	$\mathrm{atm^{-2}}$	N

References: B, *Brimblecombe and Clegg* [1988, 1989]; C, *Clegg and Brimblecombe* [1989]; J, *Jacobson* [2005]; N, *Nenes et al.* [1998]

A reaction with an equilibrium constant of ∞ means only the product is allowed to exist; the reactant saturation vapor pressure is assumed to be 0.

The reaction of $H_2SO_{4(g)} \leftrightarrow 2\ H^+ + SO_4^{2-}$ is a special case of this type of reaction. As in other equilibrium aerosol models (*e.g.*, ISORROPIA of *Nenes et al.* [1998]) it is assumed that at equilibrium, all of the sulfate is present in the particle phase, and the gas-phase concentration is 0. However, this assumption does not determine how much of the gas-phase sulfate should go to each particle size bin. We assume that the transfer of sulfate from the gas to the particle phase is a diffusion-limited process, and that the fraction of the sulfate that goes to each size bin (f_{i,H_2SO_4}) is given by the ratio of the number-concentration weighted mass transfer coefficient for that size bin to the sum of the number-concentration weighted mass transfer coefficients over all size bins:

$$f_{i,H_2SO_4} = \frac{\bar{k}_{i,H_2SO_4} n_i}{\sum_i \bar{k}_{i,H_2SO_4} n_i} \tag{2.41}$$

where n_i is the number concentration in size bin i ($\mathrm{cm^{-3}}$), and $\bar{k}_{i,H_2SO_4}$ is the mass transfer coefficient ($\mathrm{cm^3\ s^{-1}}$) for sulfate described in Section 2.5.1 below.

The dissolution of ammonia into the aqueous phase is modeled using two equilibrium reactions. The first reaction, $NH_{3(g)} \leftrightarrow NH_{3(aq)}$, has the equilibrium constant

$$K_{eq}(T) = \frac{S_{aq,i}\mathbf{m}_{NH_3}}{P_{NH_3}} \tag{2.42}$$

The second reaction, $NH_{3(g)} + H^+ \leftrightarrow NH_4^+$, has the equilibrium constant

$$K_{eq}(T) = \frac{S_{aq,i}\mathbf{m}_{NH_4^+}}{\mathbf{m}_{H^+} P_{NH_3}} \frac{\gamma^2_{(NH_3+H_2O)}}{\gamma^2_{H_2O}} \tag{2.43}$$

Finally, there are two reactions where ammonia and an acid gas are in equilibrium with a solid

salt. For example, the reaction $NH_{3(g)}$ + $HCl_{(g)}$ $\leftrightarrow NH_4Cl_{(s)}$ has an equilibrium constant of the form

$$K_{eq}(T) = \frac{1}{P_{NH_3} P_{HCl}} \tag{2.44}$$

As with sulfate, the equilibrium constant for these reactions determines the total amount of NH_3 and HCl in the gas phase, but does not determine the fraction that evaporates from or condenses to each size bin. We assume that the transfer of these gases is a diffusion-limited process, and that the fraction evaporating from or condensing to each size bin is equal to the ratio of the surface area concentration in that size bin to the total surface area concentration summed over all size bins.

2.4.3 Organic Thermodynamics

. In our model, all condensing organic species are allowed to be present in the gas phase, the hydrophobic organic phase, and the aqueous phase. The equilibrium calculation between the condensed and gas-phase organic species is described below.

Hydrophobic Phase

As discussed in Section 2.3.2, the hydrophobic organic phase is assumed to be present in a spherical insoluble core attached to the aqueous embryo. The radius and curvature of this insoluble core is different from that of the aqueous embryo, and so we need a different approximation for the effect of curvature on the vapor pressure of hydrophobic organic compounds. We define $S_{org,i}$ as

$$S_{org,i} = \exp\left(\frac{2\sigma_{org} M_{org}}{RT\rho_{insol,i} r_{i,insol}}\right) \tag{2.45}$$

where σ_{org} is the surface tension of the hydrophobic organic phase, M_{org} is the average molecular weight of the organic phase, and $\rho_{insol,i}$ and $r_{i,insol}$ are the density and radius of the insoluble sphere, respectively. $\rho_{insol,i}$ and $r_{i,insol}$ are calculated as discussed in Section 2.3.4. σ_{org} is assumed to be constant at 28.21 dyn cm^{-1}, the surface tension of benzene at 298 K [*Seinfeld and Pandis*, 1998, p. 522]. M_{org} is assumed to be 200 g/mol. This calculation for $S_{org,i}$ is of course an approximation, but the above procedure is more realistic than ignoring the effect of curvature on the vapor pressure of hydrophobic organics.

Following the absorptive partitioning theory of *Pankow* [1994a, b], the vapor pressure of the

hydrophobic organics over particles in size bin i is calculated from Raoult's law

$$P_{q,i}^{eq} = S_{org,i} x_{q,i} \gamma_{q,i} P_q^{SAT} \tag{2.46}$$

where $S_{org,i}$ is the curvature correction defined above, $x_{q,i}$ is the mole fraction of species q in the hydrophobic organic phase, $\gamma_{q,i}$ is the activity coefficient of species q in the hydrophobic organic phase, and P_q^{SAT} is the vapor pressure of pure species q. The F factor for the MFI scheme is thus

$$F = \frac{S_{org,i} x_{q,i} \gamma_{q,i} P_q^{SAT}}{P_q} \tag{2.47}$$

where P_q is the partial pressure of species q in the gas phase.

As in the MPMPO, P_q^{SAT} is calculated using the method of *Myrdal and Yalkowsky* [1997], as reproduced in *Schwarzenbach et al.* [2003] and modified in *Griffin et al.* [2005]. The formula is

$$P_q^{SAT}\,(\text{mbar}) = \frac{1000}{CF} \exp\left(-\left(21.2 + 0.3\tau + 177.0 HBN\right)\left(\frac{T_b}{T} - 1\right) + \left(10.8 + 0.25\tau\right) \ln \frac{T_b}{T} \right) \tag{2.48}$$

where T_b is the boiling point at atmospheric pressure of species q. Data for T_b was taken from *Griffin et al.* [2005] or was estimated from the compound structure using ACD/Labs software v.9.00 (Advanced Chemistry Development, Inc., 2005).

τ is the effective number of torsional bonds, calculated as

$$\tau = \sum \left(SP3 + 0.5 SP2 + 0.5 RING\right) - 1 \tag{2.49}$$

where SP3 and SP2 are the number of non-ring, non-terminal sp^3 and sp^2 atoms, respectively, in the molecule and RING is the number of independent ring systems in the compound.

HBN is the hydrogen bond number, calculated as

$$HBN = \frac{\sqrt{OH + COOH} + 0.33\sqrt{NH_2}}{MW} \tag{2.50}$$

where MW is the molecular weight of the compound and OH, COOH, and NH_2 are the number of alcohols, carboxylic acids, or primary amines, respectively, in the molecule.

CF is an empirical correction factor applied to some species by *Griffin et al.* [2005] to better match the results of smog chamber experiments of secondary organic aerosol formation. The properties for each organic species are listed in Table 2.13.

Table 2.13: Vapor Pressure Parameters for Organic Compounds

Species	T_b (K)	Ref.	τ	HBN	Correction Factor CF^a
SOA1	560.0	[*Griffin et al.*, 2005]	0	1.57×10^{-2}	1
SOA2	698.0	[*Griffin et al.*, 2005]	2.5	7.68×10^{-3}	1
SOA3	575.0	[*Griffin et al.*, 2005]	2	6.49×10^{-3}	33
SOA4	679.0	[*Griffin et al.*, 2005]	3.0	7.60×10^{-3}	3.3
SOA5	615.0	[*Griffin et al.*, 2005]	5.0	5.37×10^{-3}	15
SOA6	685.3	[*Griffin et al.*, 2005]	0.5	6.70×10^{-3}	1.5
SOA7	634.0	[*Griffin et al.*, 2005]	0.5	5.61×10^{-3}	1.4
SOA8	645.5	[*Griffin et al.*, 2005]	2.0	0	2.4
SOA9	672.2	[*Griffin et al.*, 2005]	14.5	3.30×10^{-3}	1.0
SO10	566.3	[*Griffin et al.*, 2005]	1	4.61×10^{-3}	66
POA1	714 ± 8	ACD	26	0	-
POA2	509 ± 13	ACD	2	1.20×10^{-2}	-
POA3	710 ± 25	ACD	0.5	6.55×10^{-3}	-
POA4	797 ± 45	ACD	0	0	-
POA5	731 ± 12	ACD	0.5	0	-
POA6	651 ± 25	ACD	0.5	8.52×10^{-3}	-
POA7	633 ± 5	ACD	15.5	3.52×10^{-3}	-
POA8	710 ± 12	ACD	5.5	0.	-
LEVO	657 ± 42	ACD	0	1.069×10^{-2}	-
CBIO	914 ± 55	ACD	2	7.55×10^{-3}	-
CPD1	929 ± 50	ACD	2.5	6.055×10^{-3}	-
CPD2	850 ± 50	ACD	0	4.25×10^{-3}	-
CPD3	1232 ± 65	ACD	16.5	3.35×10^{-3}	-

[a] From *Griffin et al.* [2005]
ACD - Boiling point estimated using ACD/Labs software v.9.00
(Advanced Chemistry Development, Inc., 2005)

As in the MPMPO, the Raoult's law activity coefficients for the organic species are calculated using the UNIFAC group contribution method, originally presented in *Fredenslund et al.* [1975] and refined in *Fredenslund et al.* [1977]. A summary of the method, including example calculations, is contained in Section 11-5 of *Lyman et al.* [1990]. While UNIFAC was not designed for use with highly polar compounds such as those considered here, we follow *Pun et al.* [2002] in assuming that the UNIFAC group contribution parameters can be applied to our surrogate condensed organic compounds. The UNIFAC group contribution parameters are taken from *Lyman et al.* [1990].

Aqueous Phase

As in the MPMPO, we assume that (1) there is no interaction between the aqueous phase inorganic ions and the aqueous phase organics, and (2) that the activity coefficients of the organic ions (formed by the dissociation of organic acids) are equivalent to those of the corresponding molecular solute [*Pun et al.*, 2002]. With these assumptions, the vapor pressure of organic species q over the aqueous embryo of particles in size bin i can be estimated using Henry's law

$$P_{q,i}^{eq} = \frac{S_{aq,i}\gamma_{q,i}^{HL}\mathbf{m}_{q,i}}{H_{q,i}^{eff}} \tag{2.51}$$

where $S_{aq,i}$ is the curvature correction for the aqueous embryo, $\mathbf{m}_{q,i}$ is the molality of species q in the aqueous solution, $\gamma_{q,i}^{HL}$ is the Henry's law activity coefficient, and $H_{q,i}^{eff}$ is the effective Henry's law coefficient for species q in units of mol kg^{-1} mbar^{-1}. The F factor for the MFI scheme is thus

$$F = \frac{S_{aq,i}\gamma_{q,i}^{HL}\mathbf{m}_{q,i}}{H_{q,i}^{eff}P_q} \tag{2.52}$$

where P_q is the partial pressure of species q in the gas phase.

Some organic species have one or two carboxylic acid functional groups which are able to dissociate into organic ions, following the schematic reactions

$$H_2A \rightleftharpoons H^+ + HA^- \quad K_1 \tag{2.53}$$

$$HA^- \rightleftharpoons H^+ + A^{2-} \quad K_2 \tag{2.54}$$

To include the effect of these reactions on the partitioning of organic species into the aqueous

phase, we calculate an effective Henry's law constant as

$$H_{q,i}^{eff}(T) = H_q(T)\left(1 + \frac{K_{q,1}(T)}{\mathbf{m}_{H^+,i}} + \frac{K_{q,1}(T)\,K_{q,2}(T)}{\mathbf{m}_{H^+,i}^2}\right) \tag{2.55}$$

where $\mathbf{m}_{H^+,i}$ is the molality of protons, $H_q(T)$ is the Henry's law coefficient for the undissociated acid, and $K_{q,1}(T)$ and $K_{q,2}(T)$ are the acid-dissociation equilibrium constants, in units of mol/kg. We assume that the dissociation of organic acids has a very small effect on the aqueous proton concentration when compared with the strong inorganic acids HCl, HNO_3, and H_2SO_4 and the base gas NH_3, and so the proton concentration is entirely determined by the equilibrium reactions of the inorganic species in the model.

As in the MPMPO, the temperature dependence of the Henry's law coefficient is calculated as

$$H_q(T) = H_q(T_o)\exp\left[-\frac{\Delta H_{rxn}^o}{R}\left(\frac{1}{T} - \frac{1}{T_o}\right)\right] \tag{2.56}$$

where ΔH_{rxn}^o assumed to be 15 kcal/mol for all species [*Griffin et al.*, 2005]. The temperature dependence for the acid-dissociation constants are

$$K_{q,1}(T) = K_{q,1}(T_o)\exp\left[-\frac{\Delta H_{rxn}^o}{R}\left(\frac{1}{T} - \frac{1}{T_o}\right)\right] \tag{2.57}$$

$$K_{q,2}(T) = K_{q,2}(T_o)\exp\left[-\frac{\Delta H_{rxn}^o}{R}\left(\frac{1}{T} - \frac{1}{T_o}\right)\right] \tag{2.58}$$

where ΔH_{rxn}^o assumed to be 0.5 kcal/mol for all species, as in the MPMPO [*Griffin et al.*, 2005]. Values of $H_{org}(298K)$, $K_1(298K)$ and $K_2(298K)$ for the particle-phase organic species are listed in Table 2.14.[4] $H_{org}(298K)$ values were also taken from MPMPO when available. Otherwise, they were calculated using the bond contribution method of HENRYWIN, a program that is part of EPI Software Suite v.3.12 from the EPA (EPA, 2000). The one exception is the humic acid surrogate CPD3, which contained too many bonds to be handled by the software package. In this case, we assumed a large value of $H_{org}(298K)$, similar to that of CBIO and CPD1, to represent CPD3 as a hydrophilic, non-volatile compound.

As in the MPMPO, the activity coefficients for the organic species in the aqueous phase are calculated using the UNIFAC group contribution method. The UNIFAC method calculates Raoult's law activity coefficients, where the activity coefficient equals 1 for the pure organic solvent. However,

[4] The values of $H_{org}(298K)$ in Table 2.14 are in units of $\left(\frac{\mu g\ i/\mu g\ H_2O}{\mu g\ i/m^3\ air}\right)$ to match the values in the MPMPO. To convert to mol kg^{-1} mbar^{-1}, multiply by $\left(\frac{\left(10^9 \frac{\mu g\ H_2O}{kg\ H_2O}\right)\left(\frac{1bar}{10^3 mbar}\right)}{\left(8.314\times10^{-5}\frac{m^3\ air\cdot bar}{mol\ i\cdot K}\right)(298K)}\right)$.

Table 2.14: Henry's Law Constants and Acid Dissociation Constants for Organic Compounds

Species	$H_{org}\,(298K)$ $\left(\frac{\mu g\ i/\mu g\ H_2O}{\mu g\ i/m^3\ air}\right)$	Ref.	$K_1\,(298K)$ (mol/kg)	$K_2\,(298K)$ (mol/kg)	Ref.
SOA1	2.512×10^{-2}	[*Griffin et al.*, 2005]	5.4×10^{-2}	5.2×10^{-5}	[*Griffin et al.*, 2005]
SOA2	22.01	[*Griffin et al.*, 2005]	3.7×10^{-5}	3.9×10^{-6}	[*Griffin et al.*, 2005]
SOA3	1.47×10^{-4}	[*Griffin et al.*, 2005]	0	0	[*Griffin et al.*, 2005]
SOA4	4.89×10^{-2}	[*Griffin et al.*, 2005]	6.52×10^{-4}	0	[*Griffin et al.*, 2005]
SOA5	9.55×10^{-4}	[*Griffin et al.*, 2005]	0	0	[*Griffin et al.*, 2005]
SOA6	1.82×10^{-2}	[*Griffin et al.*, 2005]	1.7×10^{-3}	0	[*Griffin et al.*, 2005]
SOA7	1.202×10^{-4}	[*Griffin et al.*, 2005]	7.33×10^{-5}	0	[*Griffin et al.*, 2005]
SOA8	1.38×10^{-6}	[*Griffin et al.*, 2005]	0	0	[*Griffin et al.*, 2005]
SOA9	2.455×10^{-7}	[*Griffin et al.*, 2005]	0	0	[*Griffin et al.*, 2005]
SO10	2.884×10^{-5}	[*Griffin et al.*, 2005]	0	0	[*Griffin et al.*, 2005]
POA1	2.13×10^{-17}	EPI	0	0	-
POA2	6.85×10^{-2}	EPI	6.17×10^{-5}	2.3×10^{-6}	[*Lide*, 2007]
POA3	1.15×10^{-1}	EPI	1.58×10^{-4}	2.0×10^{-5}	[*Amoco Chem. Ltd*, 1997]
POA4	2.35×10^{-8}	EPI	0	0	-
POA5	2.82×10^{-15}	EPI	0	0	-
POA6	1.12×10^{-2}	EPI	1.29×10^{-3}	3.09×10^{-6}	[*Lide*, 2007]
POA7	5.14×10^{-8}	EPI	7.08×10^{-11}	0	[*Kanicky and Shah*, 2002]
POA8	4.27×10^{-16}	EPI	0	0	-
LEVO	1.72×10^{-1}	EPI	0	0	-
CBIO	1.88×10^{7}	EPI	0	0	-
CPD1	1.77×10^{8}	EPI	0	0	-
CPD2	7.59×10^{-1}	EPI	0^a	0	-
CPD3	1.0×10^{10}	*b*	0^a	0	-

EPI - Calculated using HENRYWIN (Bond Method),
part of EPI Suite v.3.12 (EPA, 2000)

[a] Since the vapor pressure of CPD2 and CPD3 is already very low, the correction due to acid dissociation is ignored for these large, multifunctional molecules.

[b] CPD3 was too large to calculate a Henry's law constant using HENRYWIN. We used an estimated value designed to keep CPD3 nonvolatile and in the aqueous phase.

Henry's law uses a different reference state, and so Henry's law activity coefficients are 1 at infinite dilution in water. The Henry's law activity coefficient can be calculated from the Raoult's law activity coefficients at the current state and at infinite dilution [*Saxena and Hildemann*, 1996]

$$\gamma_{q,i}^{HL} = \frac{\gamma_{q,i}}{\gamma_{q,i}^{\infty}} \tag{2.59}$$

where $\gamma_{q,i}^{HL}$ is the Henry's law activity coefficient, $\gamma_{q,i}$ is the Raoult's law activity coefficient, and $\gamma_{q,i}^{\infty}$ is the Raoult's law activity coefficient at infinite dilution. $\gamma_{q,i}^{\infty}$ is estimated assuming a mole fraction of 10^{-6} for the organic species, with the balance of the solution containing water. The UNIFAC group contribution parameters are taken from *Lyman et al.* [1990].

Equilibrium Between the Hydrophobic and Aqueous Phase

When the gas to particle transfer of organic species is calculated assuming kinetic, diffusion-limited mass-transfer between the gas and aerosol phases, organics are assumed to rapidly equilibrate between the hydrophobic and aqueous particle phases (see Section 2.6). This equilibrium is calculated assuming that the equilibrium saturation vapor pressure over both phases should be equal. The F factor for the MFI procedure in this case is

$$F = \frac{S_{org,i} x_{q,i} \gamma_{q,i} P_q^{SAT} H_{q,i}^{eff}}{S_{aq,i} \gamma_{q,i}^{HL} \mathbf{m}_{q,i}} \tag{2.60}$$

2.4.4 Water Equilibrium

MELAM included an iterative solution routine for the water content of inorganic aerosols based on the Gibbs-Duhem equation [*Steele*, 2004]. This approach gives better results at high relative humidities than the Zdanovskii-Stokes-Robinson (ZSR) method, which assumes that there is no interaction between solute molecules and thus the water contents associated with each solute are additive. However, the MPMPO uses the ZSR method to calculate the combined water content due to inorganic aerosols and aqueous organic species. Thus, we developed a method that would use the iterative scheme from MELAM to calculate the water associated with all inorganic solutes, and then use the ZSR method to calculate the water associated with the aqueous organic species. The total aerosol water content is then calculated as the sum of the water content associated with the inorganic ions and that associated with the aqueous organic species. This hybrid procedure is consistent with the use of the ZSR method for all species in the MPMPO [*Pun et al.*, 2002; *Griffin et al.*, 2005], as the ZSR method assumes that the water content associated with separate

solutes are independent and can be added, and retains the iterative solution routine of MELAM for predominantly inorganic aerosols. Below, we discuss the inorganic and organic water content calculations in turn.

Inorganic Water Content

The water content associated with the inorganic aerosol species is calculated using the iterative method of MELAM, derived in Section 5.5 of *Steele* [2004]. At equilibrium, the relative humidity is related to the activity of water in the aerosol by the equation

$$RH = a_w S_{aq} \tag{2.61}$$

where a_w is the activity of water, S_{aq} is the curvature correction for the aqueous embryo, and RH is the relative humidity (on a scale of 0 to 1). RH is calculated as

$$RH = \frac{P_{H_2O}}{P_{H_2O}^{SAT}} \tag{2.62}$$

where P_{H_2O} is the partial pressure of water and $P_{H_2O}^{SAT}$ is the saturation vapor pressure of water, parameterized as [*Bolton*, 1980; *Jacobson*, 2005]

$$P_{H_2O}^{SAT} = 6.112 \exp\left(17.67 \frac{(T - 273.15)}{(T - 29.65)}\right) \tag{2.63}$$

where T is in K.

The MELAM water equilibrium scheme uses an iterative bisectional search algorithm to find the water content that would minimize the absolute value of the water residual r_w, defined as

$$r_w = a_w S_{aq} - RH \tag{2.64}$$

The water activity is approximated as an average of binary water activities for solutions at the same ionic strength weighted by the Patwardhan and Kumar factor y_{ij} from Equation 2.4:

$$\ln a_w = \sum_{ij} y_{ij} \ln \left(a_w^o\right)_{ij} \tag{2.65}$$

The binary water activities $\left(a_w^o\right)_{ij}$ are calculated using the following formula, derived from the

Gibbs-Duhem equation

$$-55.51 d \log_{10} \left(a_w^o\right)_{ij} = \frac{2\mathbf{I}}{\ln 10 \left|z_i z_j\right|} + 2 \int_0^{\mathbf{I}} \left\{ \mathbf{I}' \frac{d \log_{10} \Gamma_{ij}}{d\mathbf{I}'} \right\} d\mathbf{I}' \tag{2.66}$$

where Γ_{ij} is the reduced mean activity coefficient for electrolyte ij, which in the Kusik-Meissner method is only a function of ionic strength (dummy variable $\mathbf{I}'$) [*Steele*, 2004]. The integrals are evaluated using DGAUS8, a public domain eight step Legendre-Gauss algorithm written by R.E. Jones as part of the SLATEC Fortran library.

Organic Water Content

The water content associated with the aqueous organic species is calculated using the ZSR method, as in the MPMPO. First, UNIFAC is iterated to determine the molality of each organic in a binary mixture with water at the water activities 0, 0.1, 0.2, ..., 0.9, and 1.0. The model linearly interpolates between the given values to determine the molality of organic species q in a binary mixture at the water activity of interest ($m_{q0}\left(a_w\right)$). The total water content associated with the organics is then

$$LWC_{org,i} = \frac{1}{M_{H_2O} n_i} \sum_q \frac{\mathbf{c}_{q,i}}{m_{q0}\left(a_w\right)} \tag{2.67}$$

where $\mathbf{c}_q$ is the molar concentration of species q in the aqueous phase in units of mol q/cm^{3}air, $m_{q0}\left(a_w\right)$ is in units of mol q/g H_2O, M_{H_2O} is the molecular weight of water, n_i is the number of particles in bin i (particles cm^{-3}), and LWC_{org} is the water associated with aqueous organics in units of mol H_2O per particle.

2.4.5 Comparison to ISORROPIA output

To test the performance of our inorganic aerosol equilibrium model, we compared the results of our model to the output of the ISORROPIA model of *Nenes et al.* [1998]. ISORROPIA is an aerosol inorganic equilibrium model that has, due to its computational efficiency, been used in many three-dimensional air quality models, chemical transport models and general circulation models [*Fountoukis and Nenes*, 2007]. Version 1 solves for equilibrium concentrations of Na, NH_3, H_2SO_4, HNO_3, HCl, and H_2O [*Nenes et al.*, 1998]; the recently released Version 2 includes the crustal species K, Ca, and Mg [*Fountoukis and Nenes*, 2007]. ISORROPIA does not keep track of particle number concentration and size. Instead, it uses a bulk approach, calculating the total gas- and aerosol-phase concentrations of each species and ignoring any effects of curvature on vapor pressure. Binary activity coefficients in ISORROPIA are calculated using the Kusik-Meissner method described

above, with multicomponent activity coefficients calculated using Bromley's formula. Water content in ISORROPIA is calculated using the ZSR method, with the water content scaled when the relative humidity is between the mutual deliquescence relative humidity (MDRH) and the DRH of the most hygroscopic salt [*Nenes et al.*, 1998].

For our comparisons, we used ISORROPIA, v. 1.5 (25 Oct 03). Table 2.15 lists the temperatures and concentrations used in the test cases. All simulations were done at a pressure of 1000 mbar. Since ISORROPIA does not calculate curvature effects, S_{aq} was set equal to 1 for all simulations. The remote continental, urban, and marine cases match those from *Nenes et al.* [1998], and represent realistic aerosol concentrations in remote continental, urban, and marine atmospheres. The high concentrations of the NH_3+HCl and NH_3+HCl+HNO_3 cases were used to test how well ASP represented the gas-solid equilibrium of NH_4Cl and NH_4NO_3. The High Sulfate case was designed to test ASP's performance with acidic aerosols, where there is not enough ammonia present to neutralize the sulfate. The comparisons for each case are discussed below. As both models assume that all sodium (Na^+) and sulfate are present in the aerosol phase, we focus our comparison on the predicted total concentrations of NO_3^-, Cl^-,NH_4^+, and H_2O in the aerosol phase.[5]

Table 2.15: Temperature and Total Concentrations Used in the Equilibrium Model Test Cases

		Concentrations (μg m^{-3})				
Case	T (K)	Na^+	NH_3	H_2SO_4	HNO_3	HCl
Remote Continental	298.15	0	4.250	11.270	0.145	0
Urban	298.15	0	3.400	9.143	1.953	0
Marine	278.15	1.967	0.020	0.510	0.163	3.121
NH_3+HCl	278.15	0	49.64	0	0	106.3
NH_3+HCl+HNO_3	298.15	0	99.28	183.6	0	106.3
High Sulfate	298.15	0	5.11	19.61	0	0

Remote Continental Case

The aerosol in the Remote Continental case is predominantly ammonia and sulfate, with a small amount of nitrate. Figure 2-9 shows the aerosol water content predicted by ISORROPIA and ASP for the Remote Continental case over the RH range of 20% to 90%. The predicted water contents match fairly well, with ASP giving a slightly higher deliquescence point than ISORROPIA (75% vs. 71%).

Figure 2-10 shows the comparison for aerosol total ammonia concentration for the Remote Continental case. These values are almost an exact match.

[5] By "total concentration", we mean the total concentration of each ion, summed over each species it is present in, including solid salts.

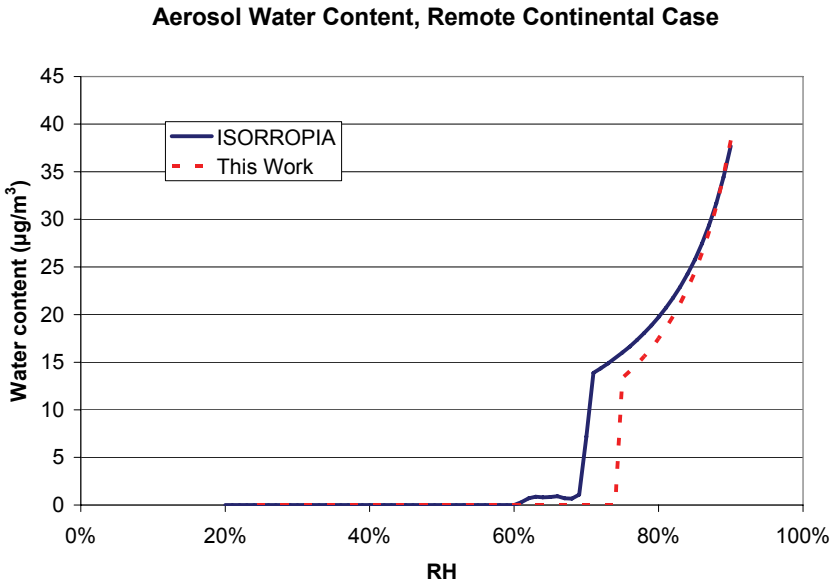

Figure 2-9: Predicted aerosol water content for the Remote Continental case.

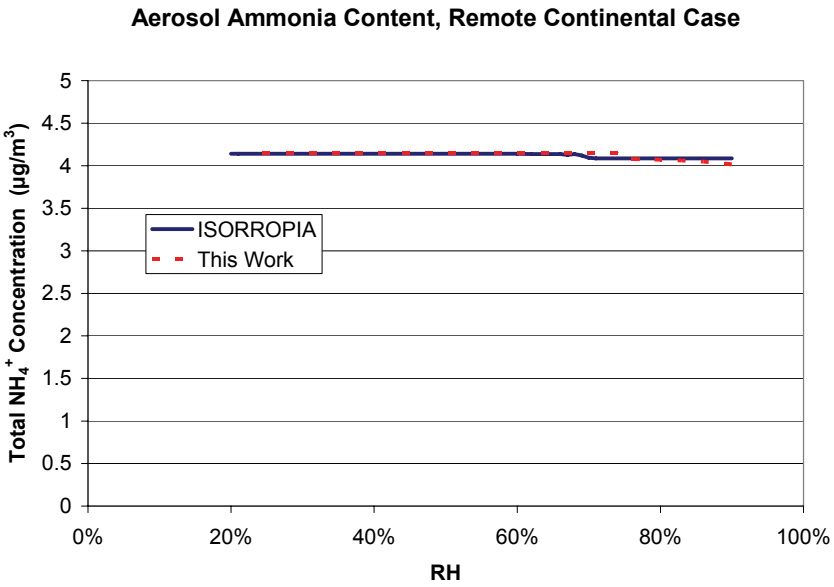

Figure 2-10: Predicted total aerosol ammonia concentration for the Remote Continental case.

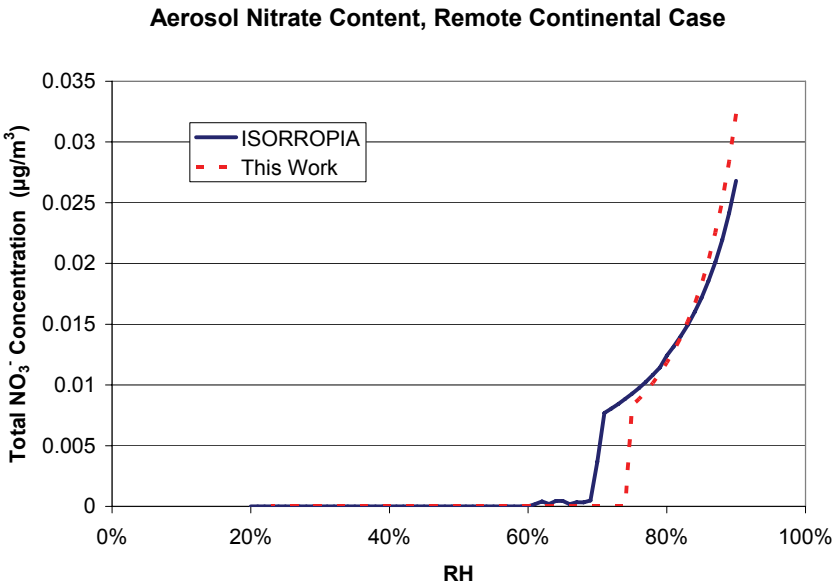

Figure 2-11: Predicted total aerosol nitrate concentration for the Remote Continental case.

Figure 2-11 shows the comparison for aerosol total nitrate concentration for the Remote Continental case. As with the liquid water concentration, there is a fairly good match above the deliquescence point, with the slight difference in the calculated deliquescence points leading to differences in the predicted point where nitrate concentration approaches 0.

Urban Case

The aerosol in the Urban case is also predominantly ammonia and sulfate, with a larger amount of nitrate than the Remote Continental case. Figure 2-12 shows the aerosol water content predicted by ISORROPIA and ASP for the Urban case. As in the Remote Continental case, the predicted water contents match fairly well, with ASP giving a slightly higher deliquescence point (74% vs. 71%). The comparison for the total ammonia concentration is nearly an exact match, and so the figure is not reproduced here.

Figure 2-13 shows the comparison for aerosol total nitrate concentration for the Urban case. As with the Remote Continental case, the match between models is fairly good, with the difference in the predicted deliquescence points accounting for the largest differences.

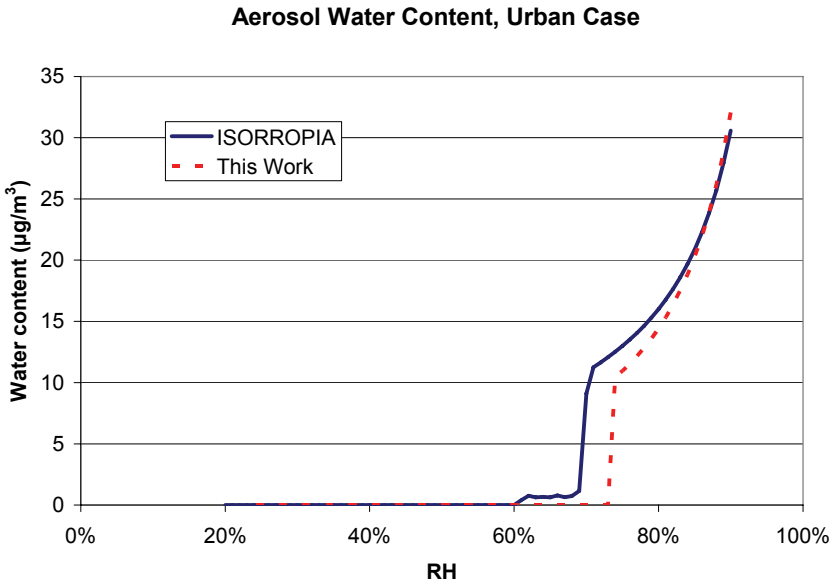

Figure 2-12: Predicted aerosol water content for the Urban case.

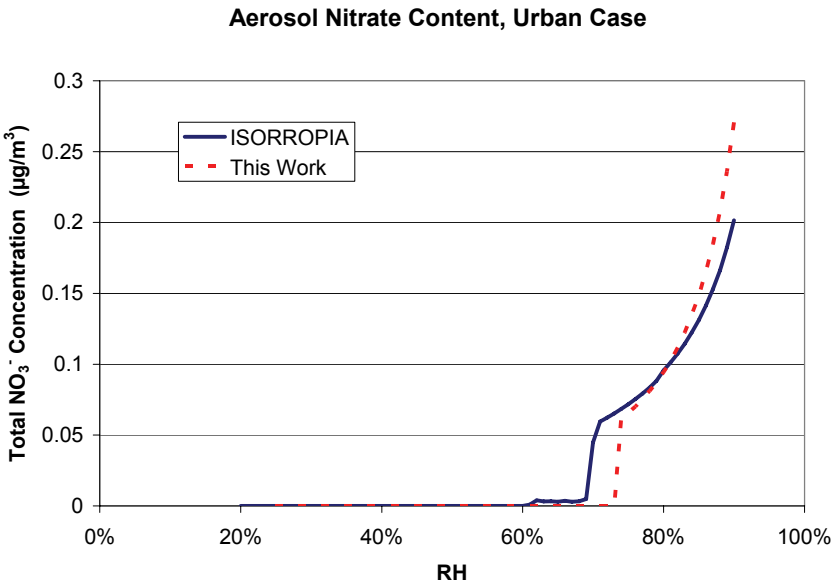

Figure 2-13: Predicted total aerosol nitrate concentration for the Urban case.

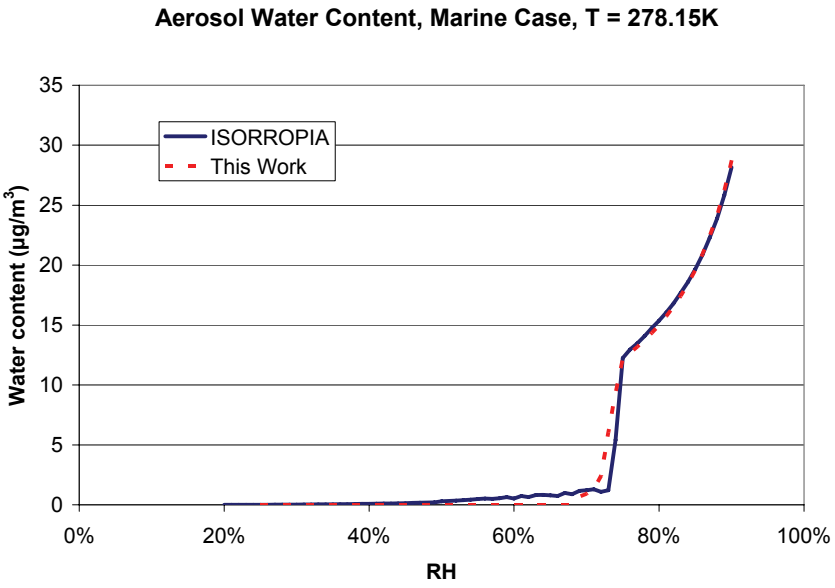

Figure 2-14: Predicted aerosol water content for the Marine case.

Marine Case, T = 278.15 K

The Marine comparison tests the temperature dependence of the inorganic equilibrium component of ASP, as the calculations were performed at a temperature of 278.15 K rather than 298.15 K. The aerosol in this case is predominantly NaCl, with small amounts of nitrate, sulfate, and ammonia present. Figure 2-14 shows the aerosol water contents predicted by ISORROPIA and ASP for the Marine case. The values match very well. Figure 2-15 shows the total aerosol chloride concentration predicted by both models, which are nearly an exact match.

Figures 2-16 and 2-17 show the total aerosol nitrate and ammonia concentrations, respectively, predicted by each model for the Marine case. The match for these minor components is not as good as that for water and chloride, but both models predict similar aerosol concentrations and qualitative behavior as RH changes.

NH_3+HCl Case, T = 278.15 K

This case is designed to test the formation of NH_4Cl from gas-phase NH_3 and HCl in ASP. The temperature was set to 278.15 K to test the temperature dependence of ASP. Figures 2-18 and 2-19 show that the total aerosol chloride and ammonia concentrations, respectively, predicted by each model match very well. Figure 2-20 shows that the predicted aerosol water contents also match

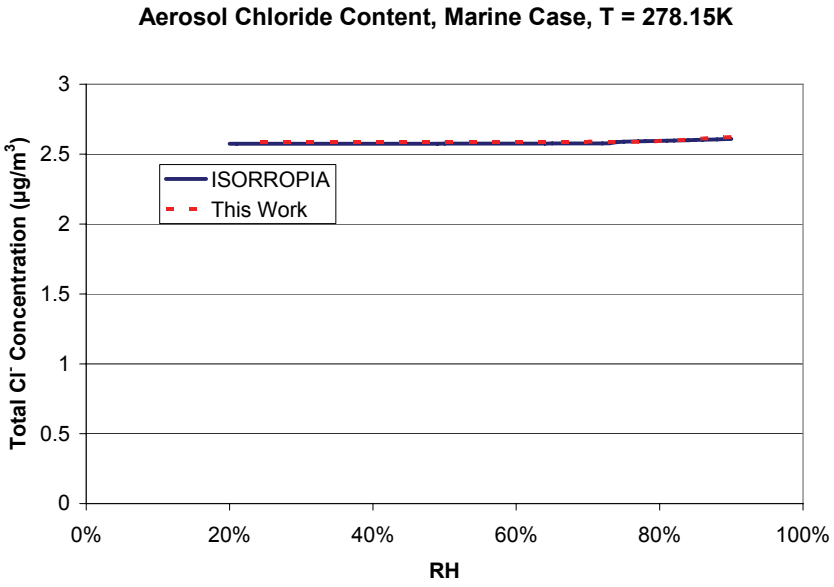

Figure 2-15: Predicted total aerosol chloride concetration for the Marine case.

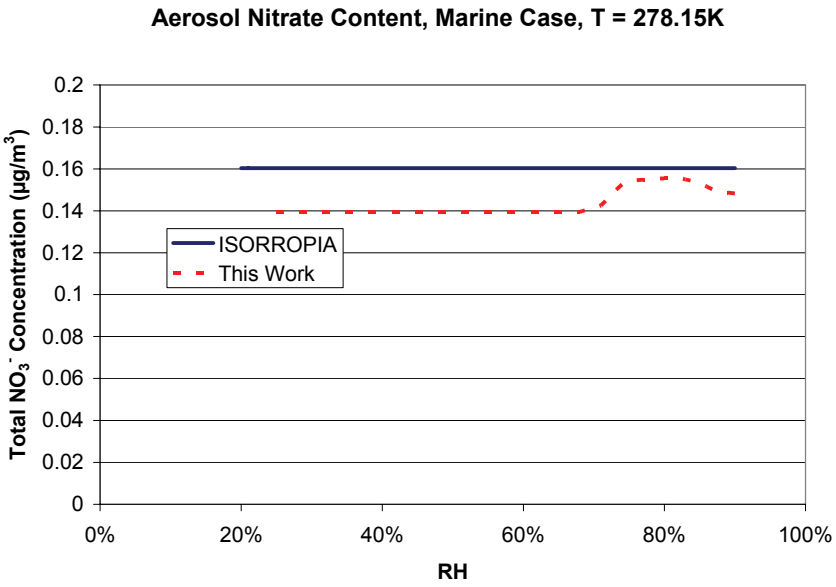

Figure 2-16: Predicted total aerosol nitrate concentration for the Marine case.

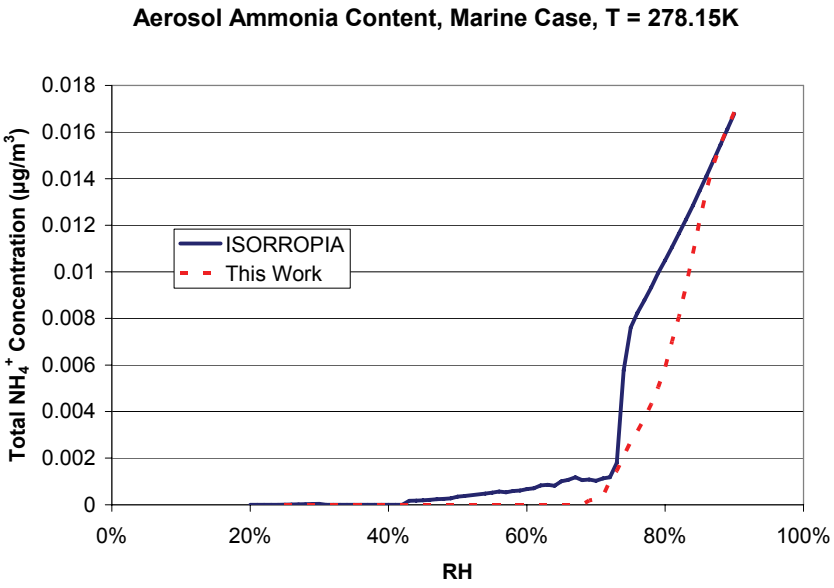

Figure 2-17: Predicted total aerosol ammonia concentration for the Marine case.

well, with ISORROPIA predicting a slightly higher deliquescence point than our model (82% vs. 78%).

NH_3+HCl+HNO_3 Case

This case was designed to test the simultaneous equilibration of solid NH_4Cl and NH_4NO_3 with gas-phase NH_3, HCl, and HNO_3 in ASP. The comparison of predicted aerosol liquid water content in Figure 2-21 shows that ISORROPIA v.1.5 had difficulty with this system, predicting no aerosol above a RH of 78%. However, the two models match fairly well at RH $<$ 78%.

Figures 2-22, 2-23, and 2-24 show the comparisons for aerosol ammonia, chloride, and nitrate concentration, respectively, for the NH_3+HCl+HNO_3 case. The ISORROPIA predictions are more "noisy", in that the predicted concentrations can rapidly change with relative humidity, resulting in the peaks and drops seen in the graphs. In contrast, ASP displays a more gradual change with relative humidity. However, both models reach the same equilibrium solution at low relative humidities.

High Sulfate Case

This case was designed to test how ASP behaves under acidic conditions, where there is not enough ammonia present to neutralize all of the sulfate. The total aerosol ammonia concentrations for

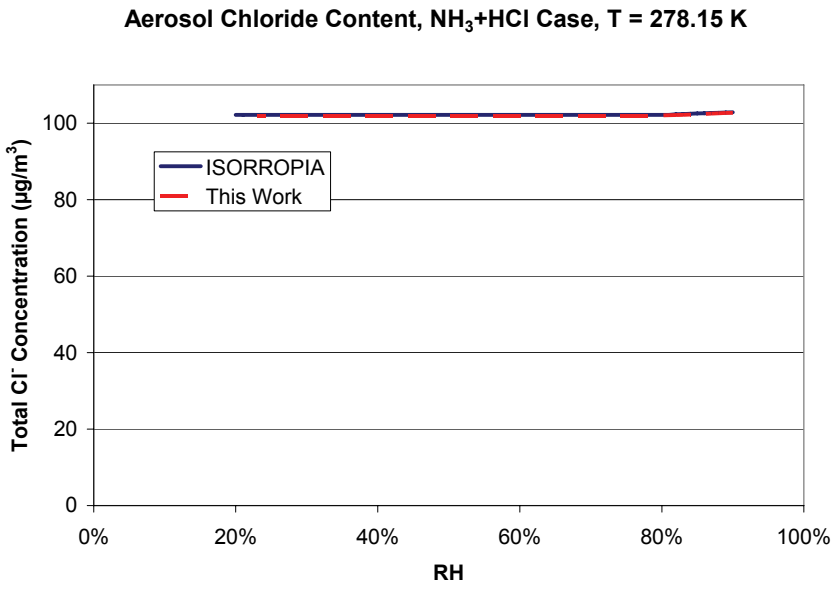

Figure 2-18: Predicted total aerosol chloride concentration for the NH_3+HCl case.

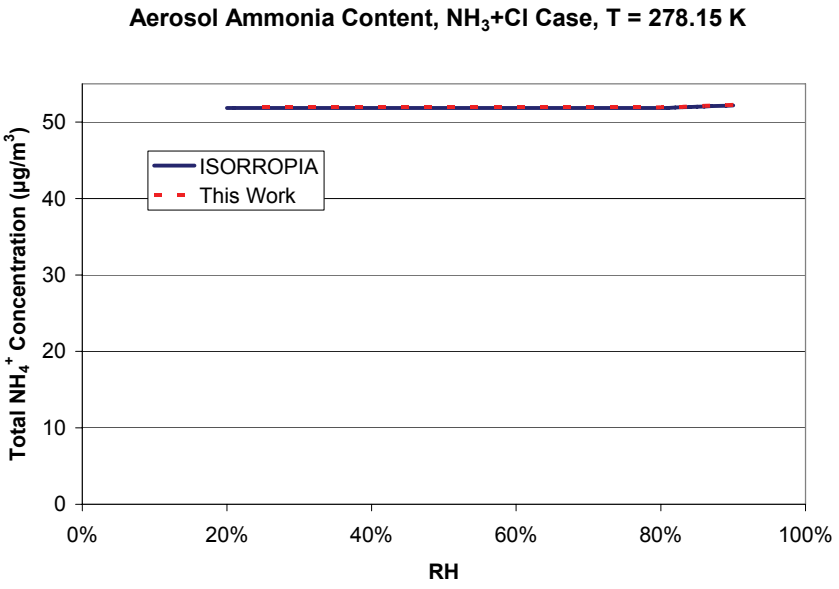

Figure 2-19: Predicted total aerosol ammonia concentration for the NH_3+HCl case.

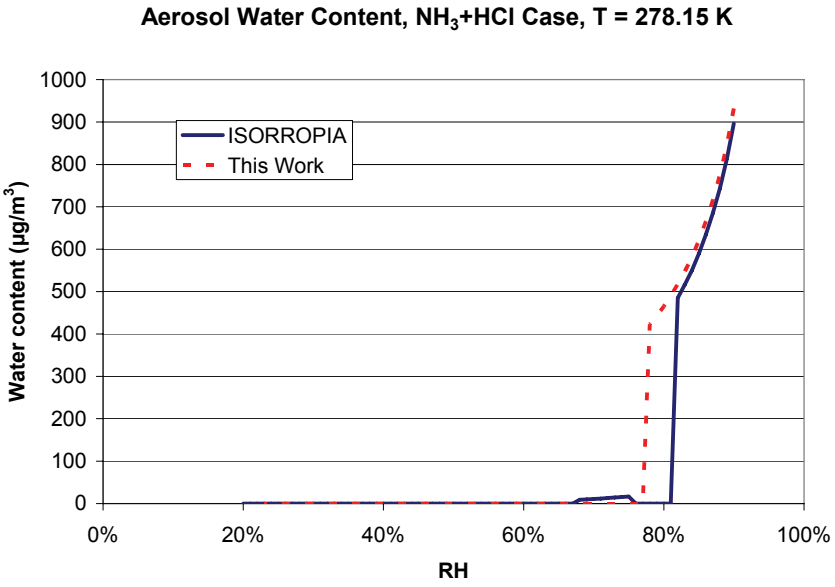

Figure 2-20: Predicted aerosol water content for the NH_3+HCl case.

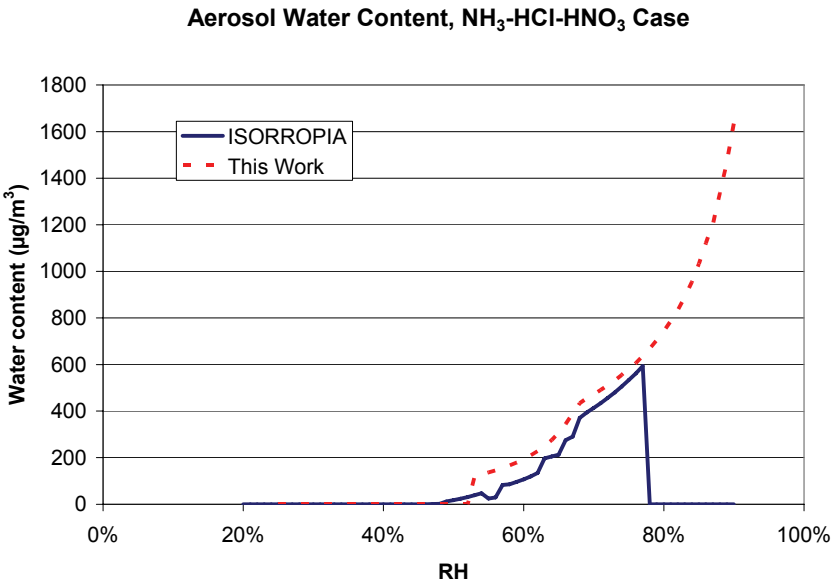

Figure 2-21: Predicted aerosol water content for the NH_3+HCl+HNO_3 case.

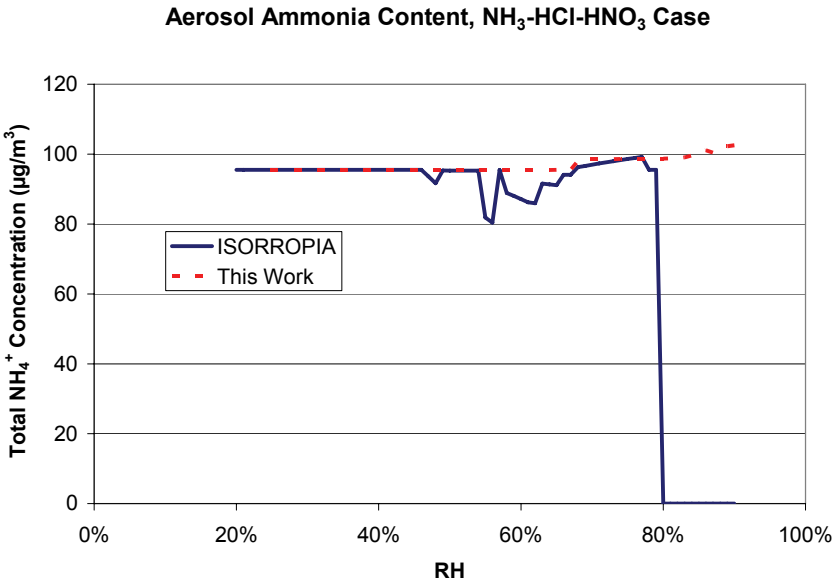

Figure 2-22: Predicted total aerosol ammonia concentration for the NH_3+HCl+HNO_3 case.

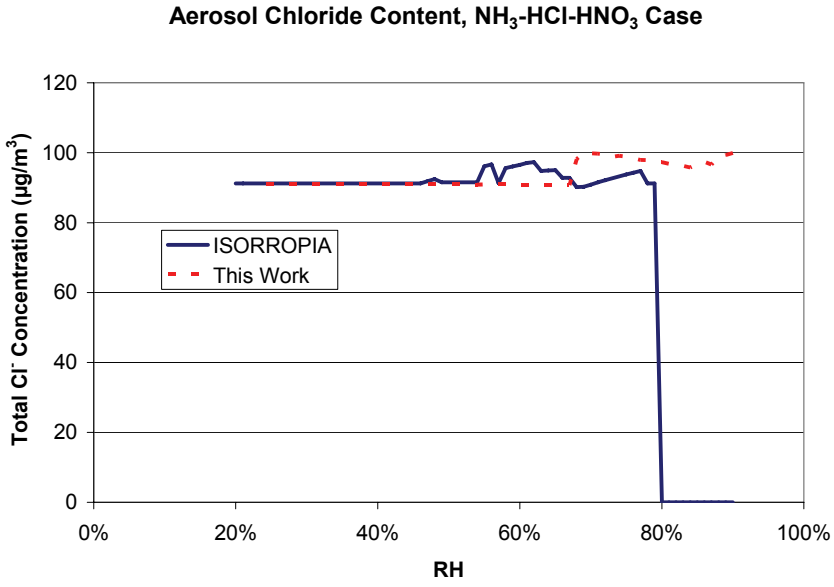

Figure 2-23: Predicted total aerosol chloride concentration for the NH_3+HCl+HNO_3 case.

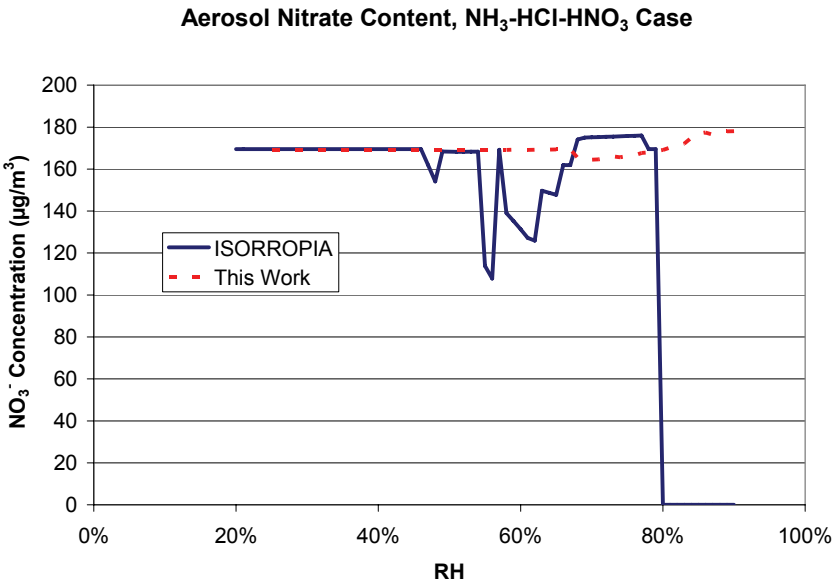

Figure 2-24: Predicted total aerosol nitrate concentration for the NH_4+HCl+HNO_3 case.

this case (not shown) are nearly identical, as all of the ammonia enters the aerosol phase. Figure 2-25 shows the aerosol liquid water contents predicted by ISORROPIA and ASP for this case. Our model predicts a slightly higher water content for RH > 68%. The ISORROPIA results show a sharp deliquescence at RH=68% (close to 69%, the DRH of $(NH_4)_3H(SO_4)_2$), while ASP loses water at a more gradual rate, finally drying at RH = 39% (close to 40%, the DRH of NH_4HSO_4). It appears that the difference is caused by ISORROPIA predicting the formation of $(NH_4)_3H(SO_4)_2$ for RH < 68%, while our model forms less $(NH_4)_3H(SO_4)_2$, with some NH_4^+ and HSO_4^- remaining aqueous until the DRH of NH_4HSO_4 is reached.

The difference in the predicted water content is likely related to the difference in how the models approach the sulfate-bisulfate equilibrium. *Steele* [2004] showed that MELAM and ISORROPIA differ significantly from each other in their predictions of sulfate-bisulfate equilibrium for pure H_2SO_4 aerosols, and that neither model provides a good match to the available experimental data, with both models predicting higher concentrations of bisulfate than is observed (see Figure 4-6 of *Steele* [2004]). Figure 2-26 shows the mass ratio of bisulfate to sulfate predicted by ISORROPIA and our model for the High Sulfate case. We can see that ISORROPIA predicts a much higher ratio of bisulfate to sulfate for RH > 68%, which would result in a prediction of greater $(NH_4)_3H(SO_4)_2$ formation, and the sharp deliquescence observed in Figure 2-25.

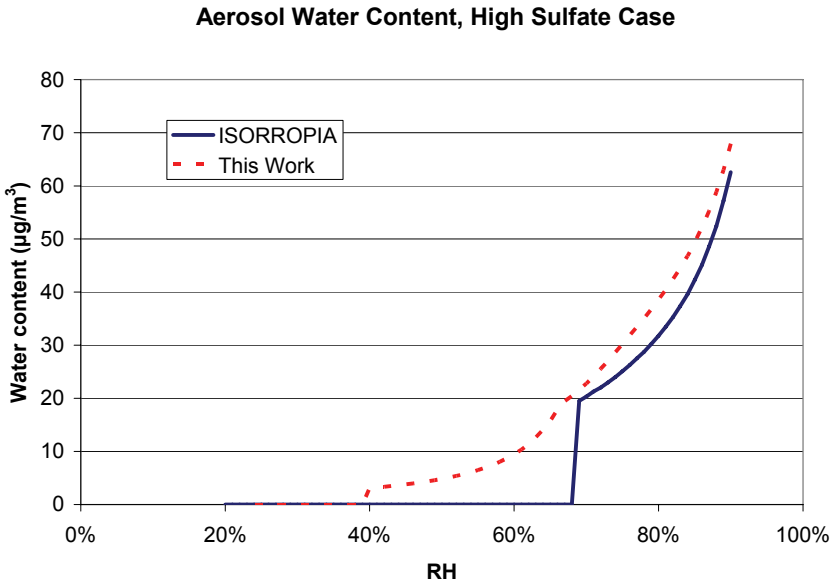

Figure 2-25: Predicted aerosol water content for the High Sulfate case.

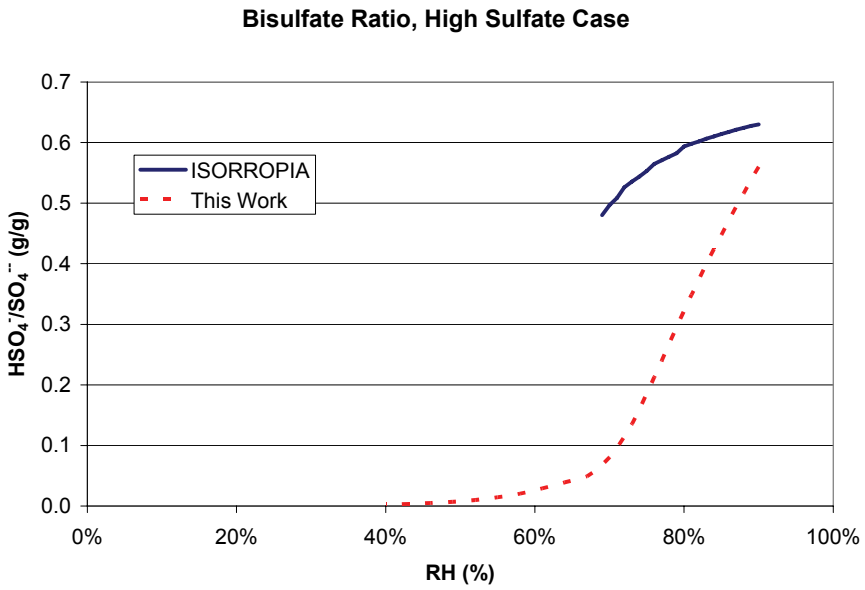

Figure 2-26: Predicted ratio of bisulfate to sulfate (g/g) for the High Sulfate case.

Summary

The above comparisons show that our inorganic aerosol equilibrium model compares well with the results of the ISORROPIA. The models match very well for the Remote Continental, Urban, and Marine cases. The largest differences are noticed for the NH_3+HCl+HNO_3 and High Sulfate cases. ISORROPIA appears to have problems solving for equilibrium concentrations in the NH_3+HCl+HNO_3 case; ASP has no such difficulty, and both models reach the same equilibrium state at low relative humidities. The difference in predicted aerosol water concentration for the High Sulfate case appears to be related to different predictions of the bisulfate-sulfate equilibrium. Based on these results, we conclude that we can use ASP to study the inorganic aerosol equilibrium in biomass burning smoke plumes.

2.4.6 Comparison to CACM/MPMPO output

To test the performance of our organic aerosol equilibrium model, we compared the results of ASP to the output of the CACM/MPMPO model of *Griffin et al.* [2005]. The three test cases are the ones that were used above to check the performance of the gas-phase chemical mechanism (see Section 2.2.2).

The experimental conditions for these comparison simulations were noted previously in Section 2.2.2. Figure 2-27 shows the amount of secondary organic aerosol (SOA) predicted by ASP and the amount predicted by the CACM/MPMPO model. The predictions are nearly identical, showing that the organic aerosol equilibrium model is performing as designed.

Furthermore, based on these successful comparisons and the fact that our gas-phase chemical mechanism and organic aerosol equilibrium model are based on the CACM/MPMPO model, we can expect our model to perform as well in comparisons to laboratory chamber data of SOA formation as the CACM/MPMPO model has. As reported in *Griffin et al.* [2005], the CACM/MPMPO model shows the correct qualitative behavior when compared to laboratory chamber data. The yield of SOA from the oxidation of AROL and AROH in the CACM/MPMPO was found to fall slightly above the lower limit of the yields of SOA from aromatic species reported by *Odum et al.* [1997a]. The yield of SOA from the oxidation of BIOL in CACM/MPMPO matched the yield reported by *Odum et al.* [1996] for α-pinene, while the yield from BIOH fell above the yields reported for α-pinene but below those reported for terpinenes by *Griffin et al.* [1999]. Thus, we conclude that we can use ASP to study the formation of SOA in biomass burning smoke plumes.

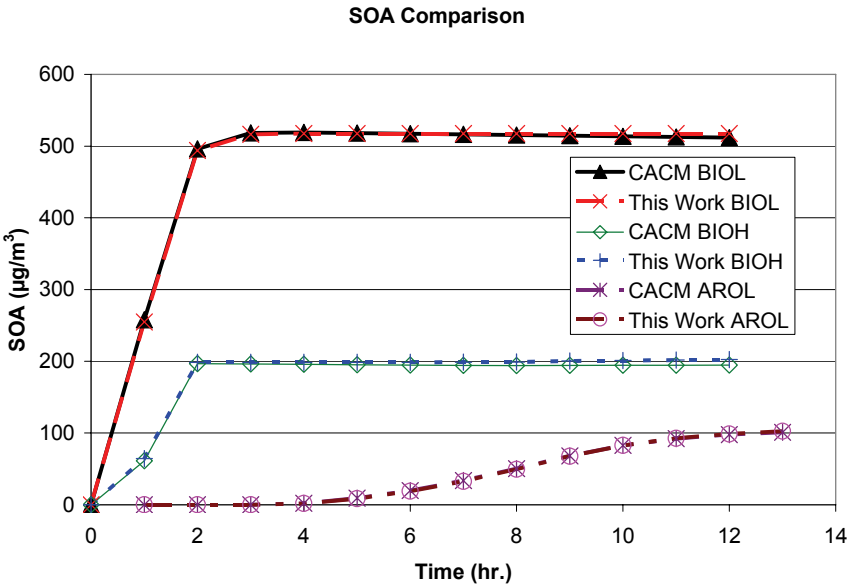

Figure 2-27: Comparison of model predictions for the formation of secondary organic aerosol versus the predictions of the CACM/MPMPO model of Griffin et al., 2005.

2.5 Kinetic Flux-Limited Condensation

Aerosol equilibrium models cannot be used to study systems where the transfer of material between the gas and particle phases can take a long time relative to the time scale of interest. In addition, exploring the nucleation of new particles requires a model capable of predicting the non-equilibrium concentrations of sulfate and organic acids present in the gas phase at a given time. Kinetic models, where the differential equations describing the transfer of material between the gas and particle phases are integrated directly, address these issues. Here, we describe a kinetic model for the condensation/evaporation of H_2SO_4 and condensable organics. The model is based on the assumption that the transfer of mass between phases is limited by the diffusive flux to the particle surface. The mass transfer differential equations for each species are integrated using the publicly available Livermore Solver for Ordinary Differential Equations - Single Precision (LSODES).[6]

The kinetic condensation of NH_3, HNO_3, and HCl is not included in the model. The kinetic model developed by *Steele* [2004] for these gases, where each gas was integrated separately, was found to give widely varying results for different time steps, due to the strong dependence of the equilibrium of these gases on pH. A combined kinetic model that integrated H_2SO_4, NH_3,

[6]LSODES is available at http://www.netlib.org/alliant/ode/prog/lsodes.f.

HNO_3, and HCl simultaneously using LSODES was developed, but the scheme became numerically unstable when solid salts were allowed to form, leading to negative concentrations and in some cases crashing the model. Thus, the fully kinetic model for these gases was abandoned in favor for equilibrating NH_3, HNO_3, and HCl at each time step after the condensation of H_2SO_4 is calculated. While this hybrid scheme does not account for the rate limitations of diffusion for these gases, scale analysis (see Section 2.6.2) suggests that the equilibrium assumption is valid in the concentrated, polluted environment of the smoke plume, where the high surface area concentration leads to fast mass transfer between the gas and particle phases. For more details on the gas to particle mass transfer of NH_3, HNO_3, and HCl, see the description of the hybrid mass transfer routine in Section 2.6.

Section 2.5.1 describes the calculation of the mass transfer rate constants for each species, with special attention to corrections to the gas-phase diffusivity of the condensing gas due to collisional geometry, sticking probability, and wake entrainment of vapor. Sections 2.5.2, 2.5.3, and 2.5.4 present the equations governing the mass transfer of sulfate, organics to the hydrophobic phase, and organics to the aqueous phase, respectively. To validate the condensation routine, Section 2.5.5 compares the results of ASP to an analytical solution for aerosol growth by condensation.

2.5.1 Flux-limited Mass Transfer Rate Constants

The calculation of the mass transfer rate constants is based on the procedure used in MELAM (see Section 5.7 of *Steele* [2004]). For the condensation of gas q (not water)[7] onto particle bin i, the mass transfer rate constant (in units of cm^3/s) is

$$\bar{k}_{i,q} = 4\pi r_{i,eff} D_q^{'} \tag{2.68}$$

where $D_q^{'}$the corrected diffusion coefficient for gas-phase species q, given by the formula [*Jacobson*, 2005]

$$D_q^{'} = D_q \varpi_{q,i} F_{q,L,i} \tag{2.69}$$

where D_q is the uncorrected diffusivity of species q in air, calculated using Equation A.6.

$\varpi_{q,i}$ represents the corrections to the molecular diffusivity due to collisional geometry and sticking probability; this factor accounts for the growth of small particles outside the continuum

[7] The rate constant for the condensation of water includes an additional factor to account for the latent heat of water (see Equation 5.34 of *Steele* [2004]). This factor is assumed to be negligible for gases other than water [*Jacobson*, 2005, p. 541].

regime, and for the fact that not all molecules that diffuse to the surface will be able to stick to the particle. The combined effects can be represented using the equation [*Jacobson*, 2005; *Pruppacher and Klett*, 1998]

$$\varpi_{q,i} = \left(1 + \left\{\frac{1.33 + 0.71Kn_{q,i}^{-1}}{1 + Kn_{q,i}^{-1}} + \frac{4\,(1 - \alpha_{q,i})}{3\alpha_{q,i}}\right\} Kn_{q,i}\right) \tag{2.70}$$

where $\alpha_{q,i}$ is the mass accommodation coefficient of gas q (the probability that a molecule of gas q colliding with particle i will stick to the surface) and $Kn_{q,i}$ is the Knudsen number of the condensing gas, given by the formula

$$Kn_{q,i} = \frac{\lambda_q}{r_{i,eff}} \tag{2.71}$$

λ_q is the mean free path of gas q, calculated using the formula [*Jacobson*, 2005]

$$\lambda_q = \frac{64 D_q}{5\pi \overline{c}_q} \left(\frac{M_{air}}{M_{air} + M_q}\right) \tag{2.72}$$

where M_{air} is the molecular weight of air, M_q is the molecular weight of the condensing gas, and $\overline{c}_q$ is the average thermal speed of a molecule of gas q, calculated using Equation A.7.

$F_{q,L,i}$ represents the corrections to molecular diffusivity due to the entrainment of vapors by the turbulent wakes behind large aerosol particles. It is calculated using the formula [*Jacobson*, 2005; *Pruppacher and Klett*, 1998]

$$F_{q,L,i} = \begin{array}{ll} 1 + 0.108 x_{i,q}^2 & : \quad x_{i,q} \leq 1.4 \\ 0.78 + 0.308 x_{i,q} & : \quad x_{i,q} > 1.4 \end{array} \qquad x_{i,q} = \mathrm{Re}_i^{1/2}\, Sc_q^{1/3} \tag{2.73}$$

where Re_i is the Reynolds number for particle i (calculated using Equation 2.117 below) and Sc_q is the Schmidt number for the condensing gas, calculated as

$$Sc_q = \frac{\eta_a}{\rho_a D_q} \tag{2.74}$$

where ρ_a is the density of air and η_a is the viscosity of air, calculated using Equation 2.102 below.

2.5.2 H_2SO_4 Condensation

For the condensation of $H_2SO_{4(g)}$, we assume that at equilibrium, all of the sulfate will be present in the aerosol phase. The accommodation coefficient is assumed to be 0.65 [*Poschl et al.*, 1998].

The rate equations are

$$\frac{dC_{H_2SO_{4(g)}}}{dt} = -\sum_{i=1}^{N_B} \bar{k}_{i,H_2SO_4} n_i \left(C_{H_2SO_{4(g)}} \right) \tag{2.75}$$

$$\frac{dc_{SO_4^{2-},i}}{dt} = \bar{k}_{i,H_2SO_4} \left(C_{H_2SO_{4(g)}} \right) \tag{2.76}$$

$$\frac{dc_{H^+,i}}{dt} = 2\bar{k}_{i,H_2SO_4} \left(C_{H_2SO_{4(g)}} \right) \tag{2.77}$$

where $C_{H_2SO_{4(g)}}$ is the gas-phase concentration of H_2SO_4 (molecules/cm^3), N_B is the number of aerosol size bins, $c_{SO_4^{2-},i}$ is the concentration of sulfate ion in size bin i (molecules/particle), $c_{H^+,i}$ is the concentration of protons in size bin i (molecules/particle), $\bar{k}_{i,H_2SO_4}$ is the mass transfer rate constant for size bin i from Equation 2.68 (cm^3/s), and n_i is the number concentration of particles in size bin i (particles/cm^3).

2.5.3 Hydrophobic Phase Organics

For hydrophobic phase organics, we assume that at equilibrium they follow Raoult's law. The rate equations are

$$\frac{dC_{q_{(g)}}}{dt} = -\sum_{i=1}^{N_B} \bar{k}_{i,q} n_i \left(C_{q_{(g)}} - C_{q_{(g)},i}^{SAT} \right) \tag{2.78}$$

$$\frac{dc_{q_{(org)},i}}{dt} = \bar{k}_{i,q} \left(C_{q_{(g)}} - C_{q_{(g)},i}^{SAT} \right) \tag{2.79}$$

where $C_{q_{(g)}}$ is the gas-phase concentration of species q (molecules/cm^3), $c_{q_{(org)},i}$ is the concentration of species q in the organic phase of size bin i (molecules/particle), $\bar{k}_{i,q}$ is the mass transfer rate constant for size bin i (cm^3/s), n_i is the number concentration of particles in size bin i (particles/cm^3), and $C_{q_{(g)},i}^{SAT}$ is the gas-phase concentration of species q in equilibrium with the particles in size bin i.

In the absence of species specific accommodation coefficient values for organic species, we assume that the accommodation coefficient for the organics is 0.1 in both the hydrophobic and aqueous phases. This assumption gives organic vapors similar accommodation coefficients to the inorganic gases H_2SO_4 (0.65 [*Poschl et al.*, 1998]), NH_3 (0.04 [*Leriche et al.*, 2000]), HNO_3 (0.054 [*Leriche et al.*, 2000]), and HCl (0.064 [*Leriche et al.*, 2000]) on aqueous surfaces, and results in relatively rapid condensation of organic vapors; a lower assumed value would increase the equilibrium time for the organic vapors, but would not change the final equilibrium. For comparison, *Donaldson*

et al. [2005] reports a value of 6×10^{-3} for naphthalene and 1,2,3-trichlorobenzene condensing onto oleic acid surfaces. The effect of the assumed accommodation coefficient on the results for the Timbavati savannah fire smoke plume is explored in Chapter 3 (p. 165).

Using Raoult's law (Equation 2.46), the ideal gas law, and accounting for the curvature of the insoluble sphere, $C^{SAT}_{q_{(g)},i}$ is calculated as

$$C^{SAT}_{q_{(g)},i} = \bar{S}_{org,i}\left(\frac{P^{SAT}_q \gamma_{q,i} x_{q,i}}{RT}\right) \tag{2.80}$$

where R is the universal gas constant, T is temperature in K, $\bar{S}_{org,i}$ is the curvature correction for the hydrophobic organic phase (see Equation 2.45), P^{SAT}_q is the saturation vapor pressure of species q (estimated using Equation 2.48), $\gamma_{q,i}$ is the activity coefficient of species q in the organic phase and $x_{q,i}$ is the mole fraction of species q in the hydrophobic organic phase. $x_{q,i}$ and $c_{q_{(org)},i}$ are related by the equation

$$x_{q,i} = \frac{c_{q_{(org)},i}}{\sum\limits_q c_{q_{(org)},i}} \tag{2.81}$$

2.5.4 Aqueous Phase Organics

For aqueous phase organics, we assume that at equilibrium they follow Henry's law and that their accommodation coefficient is 0.1. The rate equations are

$$\frac{dC_{q_{(g)}}}{dt} = -\sum_{i=1}^{N_B} \bar{k}_{i,q} n_i \left(C_{q_{(g)}} - C^{SAT}_{q_{(g)},i}\right) \tag{2.82}$$

$$\frac{dc_{q_{(aq)},i}}{dt} = \bar{k}_{i,q}\left(C_{q_{(g)}} - C^{SAT}_{q_{(g)},i}\right) \tag{2.83}$$

where $C_{q_{(g)}}$ is the gas-phase concentration of species q (molecules/cm^3), $c_{q_{(aq)},i}$ is the concentration of species q in the aqueous phase of size bin i (molecules/particle), $\bar{k}_{i,q}$ is the mass transfer rate constant for size bin i (cm^3/s), n_i is the number concentration of particles in size bin i (particles/cm^3), and $C^{SAT}_{q_{(g)},i}$ is the gas-phase concentration of species q in equilibrium with the particles in size bin i.

Using Henry's law (Equation 2.51), the ideal gas law, and accounting for the curvature of the aqueous embryo, $C^{SAT}_{q_{(g)},i}$ is calculated as

$$C^{SAT}_{q_{(g)},i} = \frac{\bar{S}_{aq,i}\gamma^{HL}_{q,i}\mathbf{m}_{q(aq),i}}{\bar{H}^{eff}_{q,i} RT} \tag{2.84}$$

where R is the universal gas constant, T is temperature in K, $\bar{S}_{aq,i}$ is the curvature correction for

the aqueous embryo (see Equation 2.39), $\bar{H}_{q,i}^{eff}$ is the effective Henry's law constant for species q in size bin i (see Equation 2.55), $\gamma_{q,i}^{HL}$ is the activity coefficient of species q in the organic phase (see Equation 2.59) and $\mathbf{m}_{q(aq),i}$ is the molality of species q in the aqueous phase (mol q/kg H_2O). $\mathbf{m}_{q(aq),i}$ and $c_{q_{(aq)},i}$ are related by the equation

$$\mathbf{m}_{q(aq),i} = \frac{c_{q_{(aq)},i}\left(10^3 \frac{g}{kg}\right)}{c_{H_2O,i} M_{H_2O}} \tag{2.85}$$

where $c_{H_2O,i}$ is the concentration of water in size bin i (molecules/particle), and M_{H_2O} is the molecular weight of water.

2.5.5 Comparison to Analytical Solution

The flux-limited kinetic condensation routine and the moving-center sectional size distribution of ASP were tested by comparing the results of ASP to an analytical solution for aerosol growth by condensation. Section 12.2.1 of *Seinfeld and Pandis* [1998] solves the condensation equation for an initially log-normal aerosol distribution with total number concentration N_o, initial geometric mean diameter $\overline{D}_{pg}$ and standard deviation σ_g, assuming that the accommodation coefficient is unity, the aerosols are in the continuum regime, and there is a constant gas-phase supersaturation. The solution is given in Equation 12.27[8] of *Seinfeld and Pandis* [1998]:

$$n\left(D_p, t\right) = \frac{D_p}{\left(D_p - 2At\right)} \frac{N_o}{\sqrt{2\pi}\ln\sigma_g} \exp\left(-\frac{\ln^2\left[\left(D_p - 2At\right)^{\frac{1}{2}} / \overline{D}_{pg}\right]}{2\ln^2\sigma_g}\right) \tag{2.86}$$

A is given by the formula:

$$A = \frac{4 D_q M_q \left(p_q - p_{eq,q}\right)}{RT\rho_p} \tag{2.87}$$

where D_q is the diffusion coefficient for species q in air, M_q is its molecular weight, p_q is its partial pressure, $p_{eq,q}$ is the partial pressure of species q at equilibrium, R is the ideal gas constant, T is the temperature, and ρ_p is the density of the particles.

For the comparison, $N_o = 1000$ cm^{-3}, $\overline{D}_{pg} = 0.2$ μm, and $\sigma_g = 1.5$. In the model simulations, temperature was set to 298.15 K, pressure to 1000 mbar, and relative humidity to 1%. The particles were composed of POA1 (long-chain alkanes), which was also used as the condensing gas. This choice gives a constant particle density of 1.5 g/cm^3 and a molecular weight of 408 g/mol. The uncorrected diffusivity of POA1 in air is calculated using Equation A.6 above, giving a value of

[8] Note that the original equation had a typo, placing a square root in the denominator of the first factor.

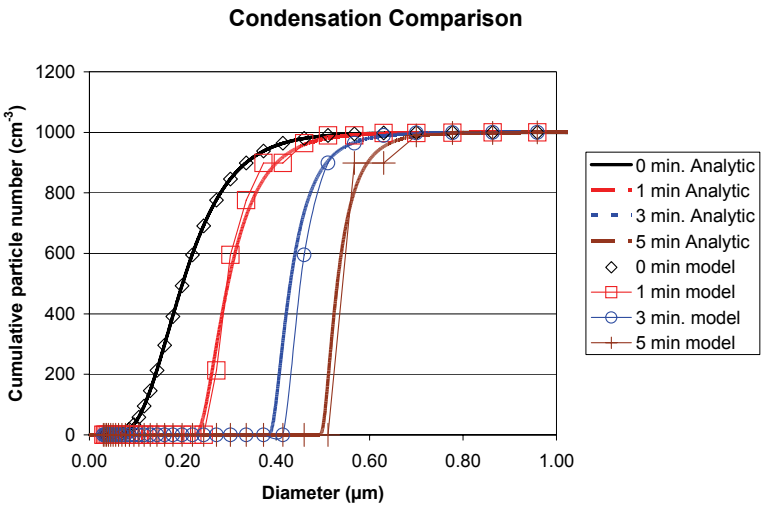

Figure 2-28: Comparison between the model predictions and analytical solution of condensational growth of an initially log-normal size distribution. The conditions for the model simulation are noted in the text.

9.2×10^{-6} m^2/s. The gas-phase concentration of POA1 was set at 1.009881 ppbv, giving a constant supersaturation of 1 ppbv. Corrections to the gas-phase diffusivity and the Kelvin effect were ignored, and the accommodation coefficient for POA1 was set to unity. 44 size bins were used, with 42 arrayed between 15 nm and 1 μm in radius.

Figure 2-28 compares the cumulative size distributions predicted by the model simulation at 0, 1, 3, and 5 minutes with the analytical solution. The results of ASP and the analytical solution match well, although we can see some places where the moving-center size distribution has left a size bin empty, causing a flat patch in the cumulative size distribution. The good match gives us confidence that the flux-limited kinetic condensation routine is working properly.

2.6 Hybrid Mass-Transfer Routine

As mentioned in Section 2.5, attempting to simultaneously integrate the flux-limited mass-transfer equations for H_2SO_4, NH_3, HNO_3, and HCl using LSODES gave a numerically unstable routine that could not be used for atmospheric modeling. Instead, we used a hybrid approach where the mass transfer of H_2SO_4 and condensable organic species was calculated using a kinetic model, while NH_3, HNO_3, and HCl are assumed to be in equilibrium between the gas and particle phases. Section 2.6.1 describes the hybrid mass transfer routine used in this model. Section 2.6.2 contains a scale analysis to examine the validity of the equilibrium assumption for NH_3, HNO_3, and HCl

in young smoke plumes. Finally, Section 2.6.3 compares the results of the hybrid mass transfer routine to the equilibrium solution calculated using the techniques from Section 2.4.

2.6.1 Description

Figure 2-29 shows a flow chart for the hybrid mass transfer routine. The routine first checks to see if the relative humidity is below 98%. If it is (as it is for all cases considered in this thesis), the aerosol water concentration is calculated using the equilibrium routine described in Section 2.4.4. Otherwise, the change in water is calculated using the kinetic condensation routine of *Steele* [2004].

The model then calculates the mass transfer of H_2SO_4 from the gas to the particle phase using the kinetic condensation routine described in Section 2.5.2. The gas-to-particle equilibrium reactions of NH_3, HNO_3, and HCl are then iterated using the MFI method until they are in equilibrium. Next, the equilibrium between the aqueous ions and the solid salts is calculated, completing the inorganic portion of the hybrid routine.

The model then calculates the kinetic mass transfer of organics between the gas and hydrophobic organic phases using the method described in Section 2.5.3. The kinetic mass transfer of organics between the gas and aqueous phases is then calculated using the method described in Section 2.5.4. We assume that mass transfer of organics between the aqueous and hydrophobic particle phases is rapid, and thus equilibrate organics between the hydrophobic and aqueous phases using the method described in Section 2.4.3. Finally, the mass and number concentration of any size bin that has grown or shrunk past its boundaries is redistributed to the neighboring size bin to maintain the moving center size distribution.

2.6.2 Equilibrium Assumption Scale Analysis

It is valid to assume equilibrium between the gas and particle phases when the time scale of mass-transfer between the phases is small compared to the time scale of interest. We can perform a simple scale analysis to see if this assumption is valid for the young smoke plumes considered in this work. Since the aerosol surface area concentrations in the plume are large, we expect mass transfer to be fast. For example, for HNO_3, the gas-phase kinetic equation is

$$\frac{dC_{HNO_{3(g)}}}{dt} = -\sum \bar{k}_{i,HNO_3} n_i \left(C_{HNO_{3(g)}} - C^{SAT}_{HNO_3,i} \right) \tag{2.88}$$

where $\bar{k}_{i,HNO_3}$ is the mass transfer coefficient defined in Equation 2.68, n_i is the number concentration in bin i, $C_{HNO_{3(g)}}$ is the gas phase concentration of HNO_3 and $C^{SAT}_{HNO_3,i}$ is the saturation

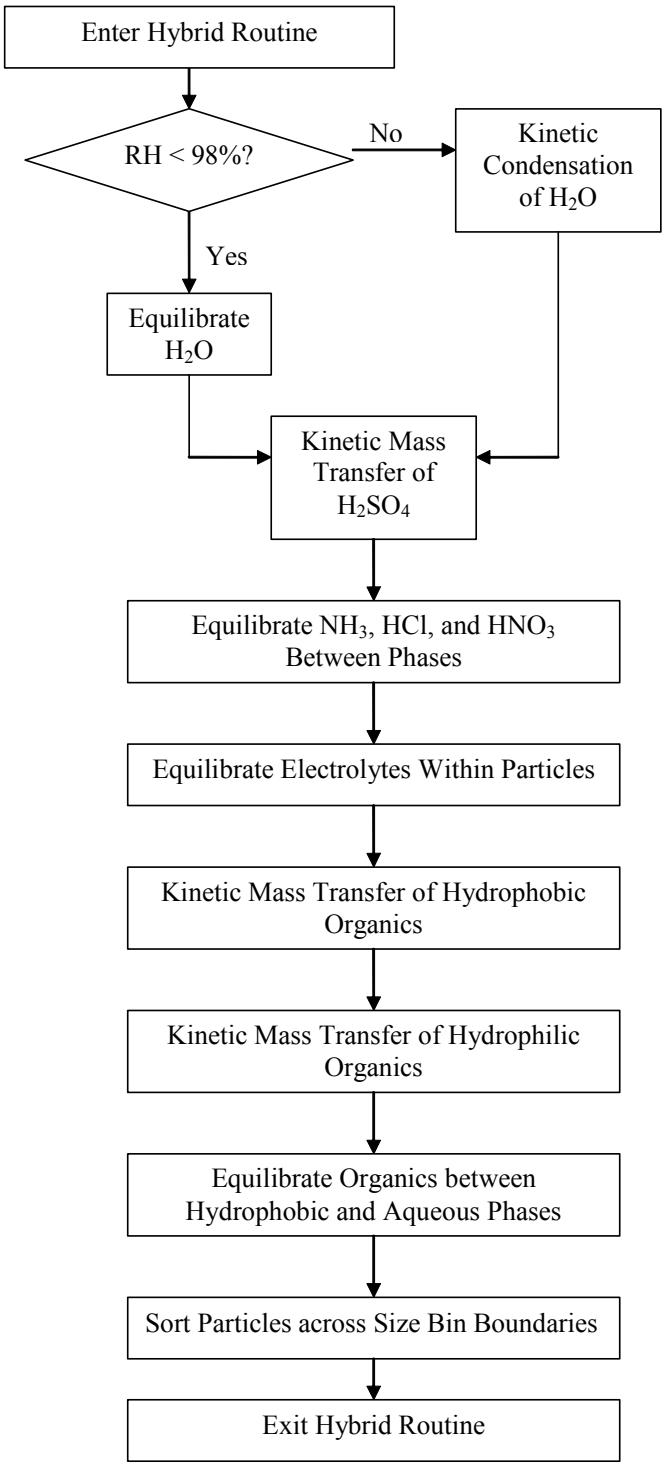

Figure 2-29: Flow chart for the hybrid mass-transfer routine

gas-phase concentration of HNO_3 for size bin i. Assuming an accommodation coefficient of 0.054 [*Leriche et al.*, 2000], a monodisperse aerosol of radius 0.1 μm, a pressure of 900 mbar, a temperature of 288.15 K and a relative humidity of 45% - the conditions of the Timbavati savannah fire smoke plume [*Hobbs et al.*, 2003; *Trentmann et al.*, 2005; *Mason et al.*, 2006] gives a value for $\bar{k}_{i,HNO_3}$ of 1.3×10^{-6} cm^3/s. The total number concentration of aerosol in the Timbavati plume varies from 100,000 cm^{-3} to 10,000 cm^{-3}. Thus the time scale for equilibrium $\left(\frac{1}{\bar{k}_{i,HNO_3} n_i}\right)$ varies from 8 to 80 s, comparable to the 20 s time step used for mass transfer in the Lagrangian model and the 60 s time step used in the Eulerian model. Thus, we expect the error involved in assuming equilibrium for NH_3, HNO_3, and HCl to be small in the concentrated environment of the plume.

Outside of the plume, the aerosol number concentration can be much lower. For example, a number concentration of 1,000 cm^{-3} would give an equilibrium time-scale of 800s, or about 13 minutes. This suggests that our equilibrium assumption is less valid outside of the plume. However, the chemical changes in the background are also expected to be more gradual, and are not the focus of this thesis. Thus, with the aforementioned caveats, we can use our hybrid mass-transfer routine to describe the changes in aerosol composition in young smoke plumes from biomass burning.

2.6.3 Comparison between Equilibrium and Hybrid Routines

To check the performance of the hybrid mass transfer routine, we compared the results of the hybrid routine with the results of the equilibrium routine of Section 2.4. We present here two test cases; the conditions and initial concentrations for each case are given in Table 2.16. In the $(NH_4)_2SO_4$ case, H_2SO_4, NH_3, and POA6 condense onto a monodisperse (*i.e.* single size bin) aerosol that is initially composed of Na_2SO_4 and POA1. In the KCl case, H_2SO_4, HNO_3, NH_3, and POA6 condense onto a monodisperse aerosol that is composed of KCl, NH_4Cl, POA1 and CBIO. The aerosol composition in the KCl case was chosen to mimic the initial composition of biomass burning aerosols found in the Timbavati savannah fire smoke plume (see Chapter 3). The time step of the hybrid scheme was 1 minute for both tests. A number concentration of 100 cm^{-3} was chosen for each test, as this low number concentration allows us to see the gradual, flux-limited condensation of H_2SO_4 and organic species. The results of each test are discussed below.

$(NH_4)_2SO_4$ Case

Figure 2-30 shows the aerosol concentrations of total POA, sulfate, ammonia, and water predicted by the equilibrium and hybrid mass transfer routines for the $(NH_4)_2SO_4$ case. Figure 2-31 shows the gas phase concentrations of POA6, H_2SO_4, and NH_3 predicted by each routine. In this case,

Table 2.16: Conditions and Initial Concentrations for the Comparison of the Equilibrium and Hybrid Mass Transfer Routines

	$(NH_4)_2SO_4$ Case	KCl Case
Temperature (K)	298.15	298.15
Pressure (mbar)	1000.0	1000.0
RH (%)	40.0	40.0
$NH_{3(g)}$ (ppbv)	30.0	3.0
$H_2SO_{4(g)}$ (ppbv)	10.0	1.0
$HNO_{3(g)}$ (ppbv)	0	2.0
$HCl_{(g)}$ (ppbv)	0	0
$POA6_{(g)}$ (ppbv)	10.0	1.0
Number Conc. (cm^{-3})	100	100
Na_2SO_4 ($\mu g/m^3$)	1.0	0
KCl ($\mu g/m^3$)	0	3.0
NH_4Cl ($\mu g/m^3$)	0	5.0
POA1 ($\mu g/m^3$)	1.0	3.0
POA6 ($\mu g/m^3$)	0	0
CBIO ($\mu g/m^3$)	0	6.0

the excess NH_3, H_2SO_4 and POA6 condense onto the aerosol, forming $(NH_4)_2SO_4$ and additional organic aerosol. The results of the hybrid model at long times match the results of the equilibrium model (plotted at 25 minutes) very well, giving us confidence that the hybrid scheme approaches the correct equilibrium solution at long times. The hybrid model also successfully models the time it takes for POA6 and H_2SO_4 to reach equilibrium, which for this low aerosol number concentration is 10-15 minutes. NH_3 also approaches the equilibrium solution on the same time scale - however, NH_3 is not modeled kinetically in the hybrid scheme, but is instead assumed to be in equilibrium with the aerosol at each time step. The gradual increase in aerosol NH_4^+ is driven by the kinetic condensation of H_2SO_4, and is unrelated to any flux limitations there may be on the condensation of NH_3.

KCl Case

Figure 2-32 shows the aerosol concentrations of total POA, sulfate, water, ammonia, nitrate, and chloride predicted by the equilibrium and hybrid mass transfer routines for the KCl case. Figure 2-33 shows the gas phase concentrations of POA6, H_2SO_4, HNO_3, HCl, and NH_3 predicted by each routine. In this case, the condensation of H_2SO_4 leads to a loss of chloride from the aerosol to the gas-phase, and very little of the HNO_3 condenses as aerosol nitrate. The hybrid mass transfer routine successfully approaches the correct equilibrium solution at long times. As before, the gradual change in time of HCl, HNO_3, NH_3 and water is not due to mass-transfer limitations

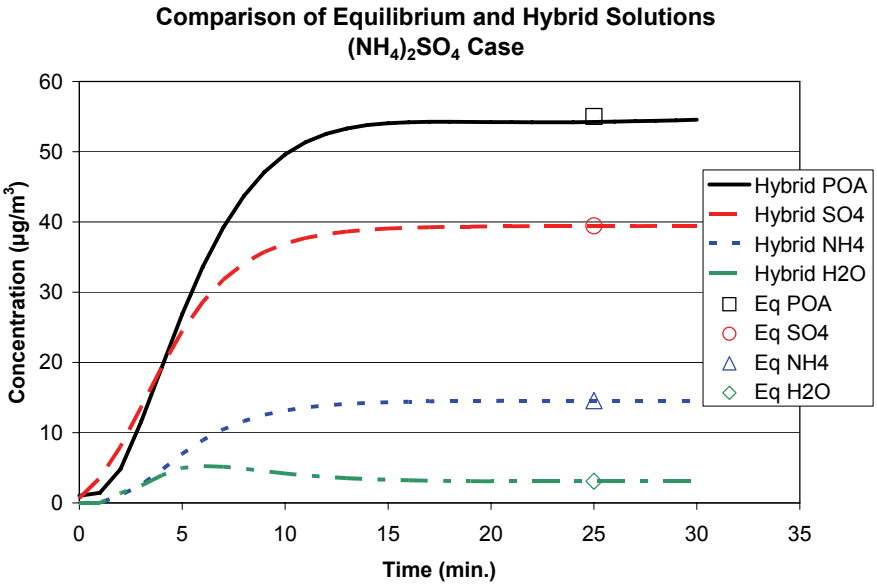

Figure 2-30: Aerosol concentrations predicted by the equilibrium and hybrid mass transfer routines for the $(NH_4)_2SO_4$ case.

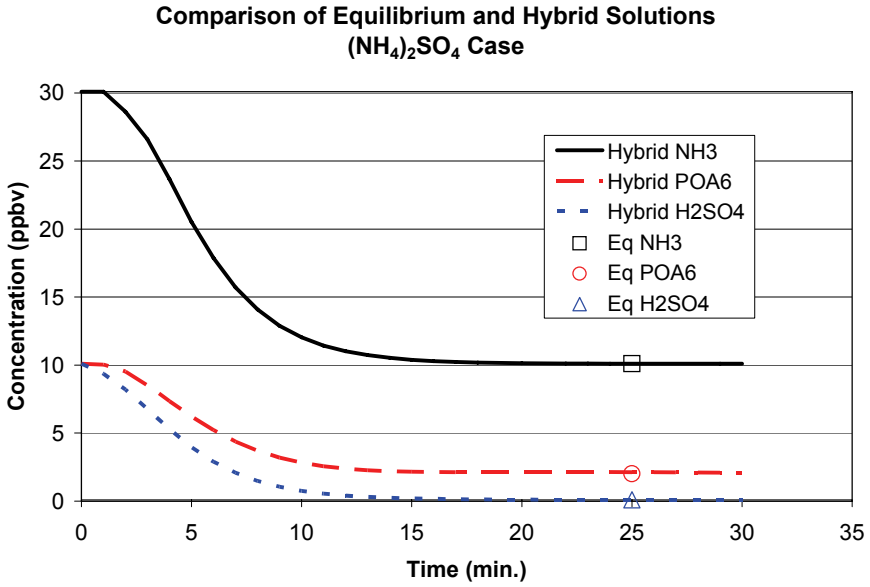

Figure 2-31: Gas concentrations predicted by the equilibrium and hybrid mass transfer routines for the $(NH_4)_2SO_4$ case.

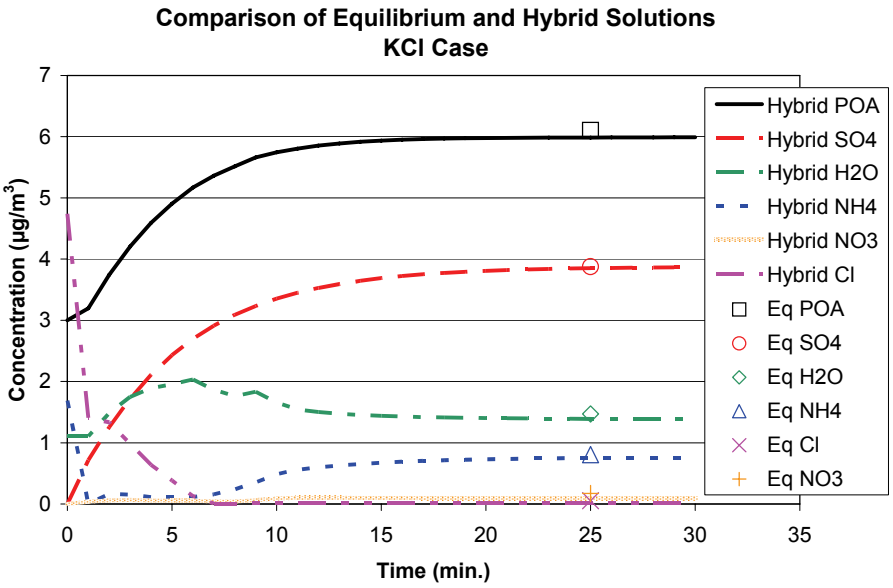

Figure 2-32: Aerosol concentrations predicted by the equilibrium and hybrid mass transfer routines for the KCl case.

on these species in the model, but is rather driven by the gradual condensation of H_2SO_4.

2.7 Coagulation

In addition to growing through the condensation of material from the gas-phase, aerosol particles can grow through coagulation, which is where aerosol particles collide and stick to form larger particles. In contrast to condensation, where the number concentration is constant but the aerosol mass increases, coagulation has no effect on the aerosol mass but leads to a decrease in the number concentration.

Coagulation is included in our model using the semi-implicit coagulation method of *Jacobson* [2005]. This method is described in Section 2.7.1. Section 2.7.2 presents the calculation of the coagulation kernels included in the model, such as those for Brownian motion and gravitational collection. Finally, Section 2.7.3 compares the results of the semi-implicit coagulation routine to an analytical solution for aerosol growth due to coagulation.

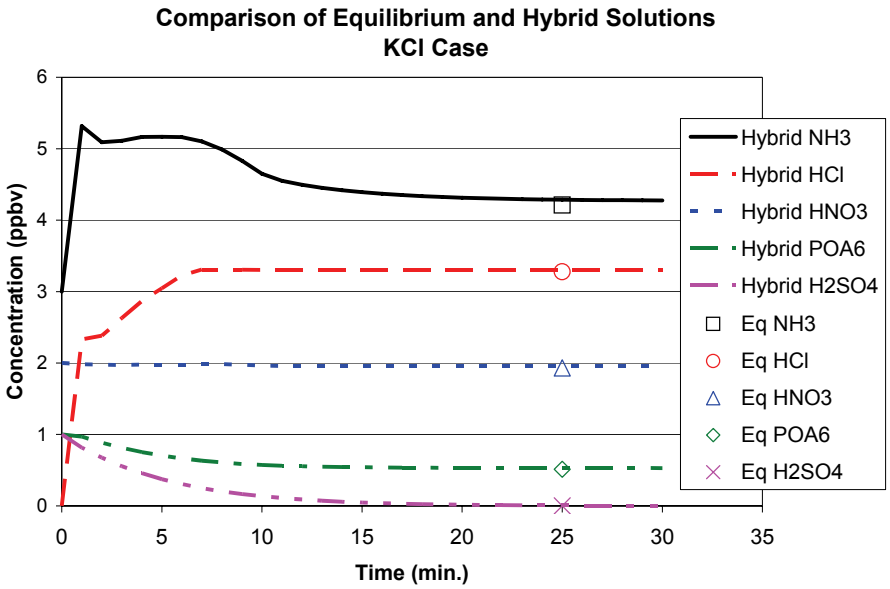

Figure 2-33: Gas concentrations predicted by the equilibrium and hybrid mass transfer routines for the KCl case.

2.7.1 Semi-implicit Coagulation Routine

The coagulation routine follows Equations 15.9 through 15.14 of *Jacobson* [2005]. First, the volume concentration of species q in size bin i, $\mathbf{v}_{q,i}$ (cm^3 q/cm^3 air), is calculated using the formula

$$\mathbf{v}_{q,i} = \frac{c_{q,i} n_i M_q}{\rho_q} \tag{2.89}$$

where $c_{q,i}$ is the concentration of q in size bin i (mol/particle), n_i is the number concentration of particles in size bin i (particles/cm^3 air), M_q is the molecular weight of q (g/mol), and ρ_q is the density of q in the particle phase (g/cm^3). For solid salts, hydrophobic organics, and aqueous organics, ρ_q is a constant across all particles (see Section 2.3.4). For water and aqueous ions, however, the solution density can vary slightly between size bins. It was found that using each size bin's solution density in calculating volume concentration failed to conserve mass for water and aqueous ions. To correct this, an average solution density, $\overline{\rho}_{solution}$, is used to calculate the volume concentrations of water and the aqueous ions

$$\overline{\rho}_{solution} = \frac{\sum_{i}^{N_B} \rho_{i,solution}}{N_B} \tag{2.90}$$

N_B is the number of size bins and $\rho_{i,solution}$ is the solution density for particle i, calculated as shown in Section 2.3.4. Using the average solution density strictly conserves the mass of water and aqueous ions in the aerosol phase.

The moving-center coagulation solution begins with defining $V_{i,j}$ (cm^3/particle), the volume of the particle that results when a particle in size bin i collides with a particle in size bin j, as

$$V_{i,j} = \nu_i + \nu_j \tag{2.91}$$

where the single particle volume ν_i (cm^3/particle) for particles in each size bin is calculated as

$$\nu_i = \frac{4}{3}\pi r_{i,eff}^3 \tag{2.92}$$

and $r_{i,eff}$ is the effective particle radius, calculated as shown in Section 2.3.4.

The intermediate particle has a volume that is between the volume of particles in size bin k and $k+1$. The fraction of $V_{i,j}$ to be placed in each bin ($f_{i,j,k}$) is calculated as

$$f_{i,j,k} = \begin{array}{ccc} \left(\frac{\nu_{k+1}-V_{i,j}}{\nu_{k+1}-\nu_k}\right)\frac{\nu_k}{V_{i,j}} & \nu_k \le V_{i,j} < \nu_{k+1} & k < N_B \\ 1 - f_{i,j,k-1} & \nu_{k-1} < V_{i,j} < \nu_k & k > 1 \\ 1 & V_{i,j} \ge \nu_k & k = N_B \\ 0 & \text{all other cases} & \end{array} \tag{2.93}$$

We can now calculate the change in the number concentration of particles, n_i (particles/cm^3), in each bin. First, we calculate the initial total volume concentration in each size bin

$$\mathbf{v}_{k,t-\Delta t} = \nu_i n_{i,t-\Delta t} \tag{2.94}$$

where $\mathbf{v}_i$ has units of (cm^3/cm^3 air). The change in total volume concentration due to coagulation is then calculated as (see Equation 15.12 of *Jacobson* [2005])

$$\mathbf{v}_{k,t} = \frac{\mathbf{v}_{k,t-\Delta t} + \Delta t_{coag} \sum_{j=1}^{k} \left(\sum_{i=1}^{k-1} f_{i,j,k} K_{i,j} \mathbf{v}_{i,t} n_{j,t-\Delta t} \right)}{1 + \Delta t_{coag} \sum_{j=1}^{N_B} \left(1 - f_{k,j,k}\right) K_{k,j} n_{j,t-\Delta t}} \tag{2.95}$$

where Δt_{coag} is the coagulation time step in seconds and $K_{i,j}$ is the total coagulation kernel for size bins i and j (cm^3/s). The method for calculating $K_{i,j}$ is discussed in Section 2.7.2 below. The

equations are solved in the order of $k = 1, ..., N_B$, so that all $\mathbf{v}_{i,t}$ terms are known when $\mathbf{v}_{k,t}$ is calculated. The new number concentration is then calculated as

$$n_{i,t} = \frac{\mathbf{v}_{i,t}}{\nu_i} \tag{2.96}$$

The change in volume concentration for component q in each size bin is calculated similarly to Equation 2.95 with

$$\mathbf{v}_{q,k,t} = \frac{\mathbf{v}_{q,k,t-\Delta t} + \Delta t_{coag} \sum_{j=1}^{k} \left(\sum_{i=1}^{k-1} f_{i,j,k} K_{i,j} \mathbf{v}_{q,i,t} n_{j,t-\Delta t} \right)}{1 + \Delta t_{coag} \sum_{j=1}^{N_B} \left(1 - f_{k,j,k}\right) K_{k,j} n_{j,t-\Delta t}} \tag{2.97}$$

and $c_{q,i}$ is recalculated as

$$c_{q,i} = \frac{\mathbf{v}_{q,i} \rho_q}{n_i M_q} \tag{2.98}$$

At the end of the coagulation calculation, the moving-center size distribution is checked for any size bins that may have grown beyond their boundaries, and the particle number and mass is moved to the appropriate size bin.

2.7.2 Coagulation Kernels

The coagulation kernel in Equations 2.95 and 2.97 is calculated as

$$K_{i,j} = E_{coal} \left(K_{i,j}^{B} + K_{i,j}^{DE} + K_{i,j}^{GC} \right) \tag{2.99}$$

where $K_{i,j}^{B}$, $K_{i,j}^{DE}$, and $K_{i,j}^{GC}$ are the collision coefficients (cm^3/s) for Brownian diffusion, convective enhancement, and gravitational collection, respectively. Each of these is discussed further below. E_{coal} is the coalescence efficiency, which represents the fraction of collisions that result in the formation of a new particle as the initial two particles join or coalesce. Here, we assume $E_{coal} = 1.0$ throughout, which is consistent with the small sizes of particles we are considering here (see *Jacobson* [2005], Section 15.6.8).

Brownian Collision Coefficient

Brownian coagulation is the process by which particles collide and coalesce in the atmosphere due to the Brownian motion of the particles [*Jacobson*, 2005]. The Brownian coagulation kernel (cm^3

particle^{-1} s^{-1}) is

$$K_{i,j}^{B} = 4\pi \left(r_{i,eff} + r_{j,eff}\right)\left(D_i + D_j\right)\beta_{i,j} \tag{2.100}$$

where $r_{i,eff}$ is the effective radius of the particles in size bin i, D_i is the Brownian diffusivity of particles in size bin i, and $\beta_{i,j}$ is the Fuchs form of the correction to the coagulation kernel for non-continuum effects.

The Brownian diffusivity of particles is given by

$$D_i = \frac{k_b T C_{s,i}}{6\pi\eta_a r_{i,eff}} \tag{2.101}$$

where k_b is Boltzmann's constant.

η_a is the dynamic viscosity of air (g cm^{-1} s^{-1}) and is calculated using Sutherland's equation (Equation 4.54 of *Jacobson* [2005], which cites *List* [1984])

$$\eta_a = 1.8325 \times 10^{-4}\left(\frac{416.16}{T+120}\right)\left(\frac{T}{296.16}\right)^{1.5} = 1.4963 \times 10^{-5}\frac{T^{1.5}}{T+120} \tag{2.102}$$

$C_{s,i}$ is the Cunningham slip correction factor, calculated as (from *Fuchs* [1964], cited in Table 12.1 of *Seinfeld and Pandis* [1998])

$$C_{s,i} = \left(\frac{5 + 4Kn_i + 6Kn_i^2 + 18Kn_i^3}{5 - Kn_i + (8+\pi)\,Kn_i^2}\right) \tag{2.103}$$

where Kn_i is the particle Knudsen number, the ratio between the mean free path of air and the particle radius (see *Jacobson* [2005], Equations 15.23 to 15.25)

$$Kn_i = \frac{\lambda_a}{r_{i,eff}} \tag{2.104}$$

The mean free path of air, λ_a is given by

$$\lambda_a = \frac{2\eta_a}{\rho_a \overline{c}_a} \tag{2.105}$$

where $\overline{c}_a$ is the average thermal speed of an air molecule, calculated as

$$\overline{c}_a = \sqrt{\frac{8k_bT}{\pi\left(\frac{M_a}{A_v}\right)}} \tag{2.106}$$

where M_a is the molecular weight of air, and A_v is Avogadro's number.

The density of the moist air ρ_a is calculated as

$$\rho_a = \frac{P}{R_{dry}T}\frac{(1+\omega_v)}{(1.+\omega_v/\epsilon)} \tag{2.107}$$

where R_{dry} is the gas constant for dry air, $\epsilon = 0.622$ is the ratio between the molecular weight of water vapor and the molecular weight of dry air, and the mass mixing ratio of water vapor ω_v (kg water/kg dry air) is given by

$$\omega_v = \frac{\epsilon P_{H_2O}}{[P - P_{H_2O}]} \tag{2.108}$$

where P_{H_2O} is the vapor pressure of water.

A correction factor, $\beta_{i,j}$, has to be applied for the transition and free molecular regimes. To calculate the Fuchs form of $\beta_{i,j}$ [*Fuchs*, 1964], we first calculate the particle mass m_i (g/particle)

$$m_i = \sum_q M_q c_{q,i} \tag{2.109}$$

where M_q is the molecular weight of q (g/mol) and $c_{q,i}$ is the concentration of q in size bin i (mol/particle).

The mean free path of the particle is calculated as (see Table 12.1 of *Seinfeld and Pandis* [1998] and Equations 15.33 and 15.34 of *Jacobson* [2005])

$$l_i = \frac{8D_i}{\pi\overline{c_i}} \tag{2.110}$$

where $\overline{c_i}$ is the root mean speed of the particle, calculated as

$$\overline{c_i} = \sqrt{\frac{8k_bT}{\pi m_i}} \tag{2.111}$$

g_i is calculated as (see Table 12.1 of *Seinfeld and Pandis* [1998] and Equations 15.33 and 15.34 of *Jacobson* [2005])

$$g_i = \frac{1}{6r_{i,eff}l_i}\left[(2r_{i,eff}+l_i)^3 - \left(2r_{i,eff}^2 + l_i^2\right)^{1.5}\right] - 2r_{i,eff} \tag{2.112}$$

Finally, the Fuchs form of $\beta_{i,j}$ is [*Fuchs*, 1964; *Seinfeld and Pandis*, 1998; *Jacobson*, 2005]

$$\beta_{i,j} = \left(\frac{r_{i,eff}+r_{j,eff}}{r_{i,eff}+r_{j,eff}+\left(g_i^2+g_j^2\right)^{1/2}} + \frac{4\left(D_1+D_2\right)}{\left(\overline{c_i}^2+\overline{c_j}^2\right)^{1/2}\left(r_{i,eff}+r_{j,eff}\right)}\right)^{-1} \tag{2.113}$$

Convective Enhancement to Brownian Collision Coefficient

Eddies in the wake of large falling particles can enhance the diffusion of other particles to the surface, enhancing the coagulation rate [*Jacobson*, 2005]. *Pruppacher and Klett* [1998] provide a formula for calculating this enhancement, which is reproduced as Equation 15.35 of *Jacobson* [2005]

$$K_{i,j}^{DE} = \begin{array}{ll} K_{i,j}^{B} 0.45\, \mathrm{Re}_j^{1/3}\, Sc_i^{1/3} & \mathrm{Re}_j \leq 1, r_j \geq r_i \\ K_{i,j}^{B} 0.45\, \mathrm{Re}_j^{1/2}\, Sc_i^{1/3} & \mathrm{Re}_j > 1, r_j \geq r_i \end{array} \tag{2.114}$$

where the particle Reynold's number, Re_i, and Schmidt number, Sc_i, are calculated as follows.

Reynold's Number The calculation of the Reynold's number for aerosol particles is discussed in Section 20.1 of *Jacobson* [2005]. *Beard* [1976] studied the fall speeds of cloud drops and raindrops in air and found that a correction factor for the terminal velocity and Reynold's number for such large particles ($\mathrm{Re} \geq 0.01$, corresponding to a radius greater than 10 μm), could be parameterized as a function of the properties of the drops and their surroundings. The procedure has two steps. In the first, we calculate an estimated particle Reynolds number Re_i^{est} as

$$\mathrm{Re}_i^{est} = \frac{2 r_{i,eff} \rho_a V_{f,i}^{est}}{\eta_a} \tag{2.115}$$

where the estimated terminal velocity, $V_{f,i}^{est}$, is calculated as

$$V_{f,i}^{est} = \frac{2 r_{i,eff}^2 C_{s,i} \left(\rho_{p,i} - \rho_a\right) g}{9 \eta_a} \tag{2.116}$$

where $\rho_{p,i}$ is the particle density. If Re_i^{est} is less than 0.01, the true Reynolds number (Re_i) is the same as the estimated value. If not, further corrections are applied. The corrections are summarized in Equation 2.117

$$\mathrm{Re}_i = \begin{array}{cc} \mathrm{Re}_i^{est} & \mathrm{Re}_i^{est} < 0.01 \\ C_{s,i} \exp\left(B_o + B_1 X + B_2 X^2 + ...\right) & 0.01 \leq \mathrm{Re}_i^{est} < 300 \\ N_P^{1/6} C_{s,i} \exp\left(E_o + E_1 Y + E_2 Y^2 + ...\right) & \mathrm{Re}_i^{est} \geq 300 \end{array} \tag{2.117}$$

The B and E coefficients are given in Table 2.17. X and Y are calculated as

$$X = \ln\left[\frac{32 r_{i,eff}^3 \left(\rho_{p,i} - \rho_a\right) \rho_a g}{3 \eta_a^2}\right] \qquad Y = \ln\left[\frac{4}{3} N_{Bo} N_P^{1/6}\right] \tag{2.118}$$

N_{Bo} is the Bond number, calculated as [*Jacobson*, 2005]

$$N_{Bo} = \frac{4r_{i,eff}^2 \left(\rho_{p,i} - \rho_a\right) g}{\sigma} \tag{2.119}$$

where σ is the surface tension of the aqueous particle. N_P is the physical-property number defined as

$$N_P = \frac{\sigma^3 \rho_a^2}{\eta_a^4 \left(\rho_{p,i} - \rho_a\right) g} \tag{2.120}$$

Once the Reynold's number is known, the terminal velocity is calculated as

$$V_{f,i} = \frac{\mathrm{Re}_i \, \eta_a}{2 r_{i,eff} \rho_a} \tag{2.121}$$

Note that since all of the aerosol considered in this thesis will have radii much less than 10 μm, the Beard corrections are not used in this thesis.

Table 2.17: Coefficients for Beard's Correction to Reynold's Number

$B_o = -3.18657$	$E_o = -5.00015$
$B_1 = 0.992696$	$E_1 = 5.23778$
$B_2 = -1.53193 \times 10^{-3}$	$E_2 = -2.04914$
$B_3 = -9.87059 \times 10^{-4}$	$E_3 = 0.475294$
$B_4 = -5.78878 \times 10^{-4}$	$E_4 = -0.0542819$
$B_5 = 8.55176 \times 10^{-5}$	$E_5 = 2.38449 \times 10^{-3}$
$B_6 = -3.27815 \times 10^{-6}$	

References: *Beard* [1976]; *Jacobson* [2005]

Schmidt Number

The particle Schmidt number, $Sc_{p,i}$, is the ratio of the viscous forces to the diffusive forces, and is calculated following Equation 15.36 of *Jacobson* [2005].

$$Sc_{p,i} = \frac{\eta_a}{\rho_a D_i} \tag{2.122}$$

Gravitational Collection Collision Coefficient

When two particles of different sizes fall, the faster particle may collide with the slower one, leading to an enhancement of coagulation [*Jacobson*, 2005]. We can account for the coagulation caused by differential fall speeds with the gravitational collection coagulation coefficient, calculated as (See

Equation 15.37 of *Jacobson* [2005])

$$K_{i,j}^{GC} = E_{\text{col},i,j}\pi \left(r_{i,eff} + r_{j,eff}\right)^2 \left|V_{f,i} - V_{f,j}\right| \tag{2.123}$$

where the terminal velocity, $V_{f,i}$, is calculated using Equation 2.121.

The collision efficiency, $E_{\text{col},i,j}$, is calculated as [*Ludlum*, 1980; *Jacobson*, 2005]

$$E_{\text{col},i,j} = \frac{60E_{V,i,j} + E_{A,i,j}\,\text{Re}_j}{60 + \text{Re}_j} \qquad r_j \geq r_i \tag{2.124}$$

where $E_{V,i,j}$ is the limit of the collision efficiency at $\text{Re} \ll 1$ and $E_{A,i,j}$ is the limit at $\text{Re} \gg 1$.

$E_{V,i,j}$ is calculated as

$$E_{V,i,j} = \begin{array}{ll} \left[1 + \frac{0.75\ln(2St_{i,j})}{St_{i,j}-1.214}\right]^{-2} & St_{i,j} > 1.214 \\ 0 & St_{i,j} \leq 1.214 \end{array} \tag{2.125}$$

where $St_{i,j}$ is the dimensionless Stokes number, calculated as

$$St_{i,j} = \frac{V_{f,i}\left|V_{f,j} - V_{f,i}\right|}{r_{j,eff}g} \qquad r_j \geq r_i \tag{2.126}$$

$E_{A,i,j}$ is calculated as

$$E_{A,i,j} = \frac{St_{i,j}^2}{\left(St_{i,j} + 0.5\right)^2} \tag{2.127}$$

2.7.3 Comparison to Analytical Solution

The semi-implicit coagulation routine and the moving-center size distribution model of ASP were tested by comparing the results of ASP to an analytical solution for aerosol growth by coagulation. Equation 5.10 of *Resch* [1995] gives an analytical solution for the growth of an initial exponential size distribution $\left(n\left(v\right) = \frac{N_o}{v_o}\exp\left(-\frac{v}{v_o}\right)\right)$, where N_o is the initial total number concentration of the distribution and v_o is the initial mean volume, in the case where the coagulation kernel K_o is constant.[9] The solution is:

$$n\left(v,t\right) = \frac{N_o}{v_o\left(1-\tau\right)^2}\exp\left(-\frac{v}{v_o\left(1+\tau\right)}\right) \tag{2.128}$$

[9]For consistency, I am using K_o as the symbol for the coagulation coefficient, rather than β_o as used in [*Resch*, 1995].

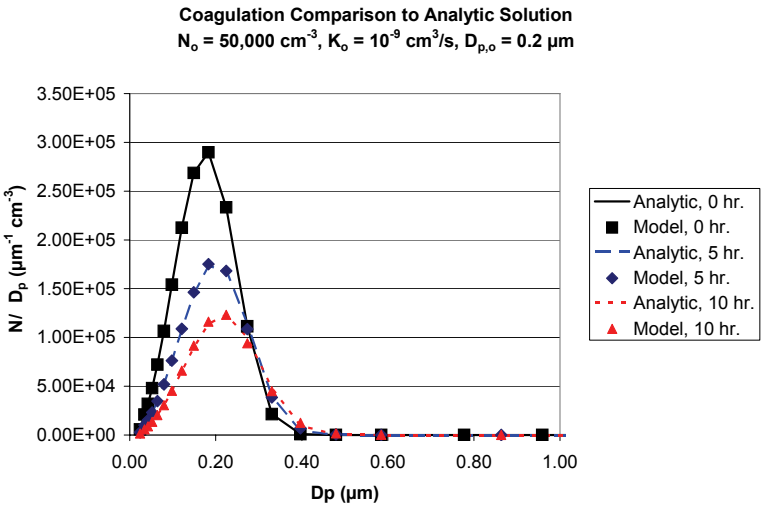

Figure 2-34: Comparison of model results to the analytical solution for growth by coagulation. Conditions for the model simulation are described in the text.

where $\tau = \frac{1}{2} N_o K_o t$ is the dimensionless coagulation time constant. Recognizing that $v = \frac{\pi}{6} D_p^3$ and $n(D_p) = \frac{\pi}{2} D_p^2 n(v)$ gives

$$n\left(D_p, t\right) = \frac{3 D_p^2 N_o}{D_{p,o}^3 \left(1-\tau\right)^2} \exp\left(-\frac{D_p^3}{D_{p,o}^3 \left(1+\tau\right)}\right) \tag{2.129}$$

Figure 2-34 compares the size distribution predicted by the model simulations at 0, 5 and 10 hours with the analytical solution. In the model simulations, nonvolatile Na_2SO_4 was used for the particle composition and the coagulation coefficients were forced to be constant, rather than calculated. We used N_o = 50,000 cm^{-3}, $K_o = 10^{-9}$ cm^3/s, and $D_{p,o} = 0.2$ μm. The relative humidity was set to 40% at 298.15K. The model used 22 size bins, with 20 arrayed between 15 nm and 1 μm in radius. The match is very good, giving us confidence in the performance of the semi-implicit coagulation scheme.

2.8 Optical Properties

Aerosol particles can have a substantial impact on the radiative field in the atmosphere by scattering and absorbing radiation. This can in turn affect gas phase chemistry by changing the rates of photolysis reactions. To model the radiative impact of aerosols on the gas-phase chemistry within the smoke plume, we have to calculate the optical properties (extinction coefficient, single scattering

albedo, and asymmetry parameter) of the aerosols.

Our model calculates the optical properties of the aerosol by assuming that the aerosols are stratified spheres, with black carbon forming the absorbing core of the particle and the other components forming a reflective shell - the core-in-shell model. Section 2.8.1 describes the on-line calculation of refractive indices at 550 nm and 10 μm based on particle composition. Section 2.8.2 describes the core-in-shell Mie calculation of aerosol average optical properties.

2.8.1 Refractive Index at 550 nm and 10 μm

The refractive index of the ionic solution (water and inorganic ions) at 550 nm is calculated from molar refraction using the approach of *Tang* [1997] and *Tang et al.* [1997]. The refractive index of the ionic solution is then combined with aqueous organics, solid salts, and hydrophobic organics using a volume-average dielectric constant mixing rule.

Water and Ions: Molar Refraction

The real refractive index for the solution of water with inorganic ions at 550 nm is calculated using the molar refraction R of the water-ion solution, defined as [*Tang*, 1997; *Tang et al.*, 1997]

$$R = \frac{V\left(n^2 - 1\right)}{\left(n^2 + 2\right)} \tag{2.130}$$

where n is the real part of the refractive index and V is the molal volume of the solution ($\mathrm{cm}^3/\mathrm{mol}$). The molal refraction of the solution is calculated as

$$R = \sum_{ions} y_i R_i + y_{H_2O} R_{H_2O} \tag{2.131}$$

where y_i and y_{H_2O} are the mole fractions of the ions and water, respectively, in the ion-water solution and R_i and R_{H_2O} are the molar refraction of the ions and water [*Tang*, 1997; *Tang et al.*, 1997]. The values of R_i are given in Table 2.18.

V is calculated as [*Tang*, 1997; *Tang et al.*, 1997]

$$V = \frac{\sum_{ions} y_i M_i + y_{H_2O} M_{H_2O}}{\rho_{water-ion}} \tag{2.132}$$

where M_i and M_{H_2O} are the molecular weights of the ions and water, respectively, and $\rho_{water-ion}$ is the density of the water-ion solution, as calculated in Section 2.3.4. The real refractive index at

Table 2.18: Molar Refraction Values

Species	Molar Refraction (R_i)
H_2O	3.717
NH_4^+	5.01
K^+	3.21
Na^+	0.86
Ca^{2+}	0.03
Mg^{2+}	1.93
HSO_4^-	13.44
SO_4^{2-}	13.44
NO_3^-	10.36
Cl^-	8.09

References: *Tang* [1997]; *Tang et al.* [1997]

550 nm is then calculated from Equation 2.130. The imaginary part of the refractive index at 550 nm is assumed to be the 1.0×10^{-9}, as for water [*Jacobson*, 2005]. Since we are mainly interested in the effect of the aerosol on photolysis rates and thus on the solar spectrum, we assume that the ionic solution has the refractive index of pure water at 10 μm.

Volume Average Dielectric Constant Mixing Rule

Once the refractive index of the water and inorganic ion solution has been calculated as above, the average refractive index of all species in the shell (hydrophobic organics, aqueous organics, solid salts, and the water and inorganic ion solution) is calculated using the volume average dielectric constant mixing rule [*Jacobson*, 2005]. Here, the complex dielectric constant of each species in the shell at wavelength λ is calculated as

$$\varepsilon_{r,\lambda,q} = n_{r,\lambda,q}^2 - n_{i,\lambda,q}^2 \tag{2.133}$$

$$\varepsilon_{i,\lambda,q} = 2n_{r,\lambda,q}n_{i,\lambda,q} \tag{2.134}$$

where $\varepsilon_{r,\lambda,q}$ and $\varepsilon_{i,\lambda,q}$ are the real and imaginary parts of the dielectric constant for species q at wavelength λ, and $n_{r,\lambda,q}$ and $n_{i,\lambda,q}$ are the real and imaginary parts of the refractive index for species q at wavelength λ.[10] The average dielectric constant for the shell is then weighted by species volume

[10] Note that the water and inorganic ion mixture is considered here as one species, with a real refractive index calculated from molal refraction as described in Section 2.8.1.

fraction in the shell as

$$\varepsilon_{r,\lambda} = \sum_q \frac{\mathbf{v}_q}{\mathbf{v}_{shell}} \varepsilon_{r,\lambda,q} \tag{2.135}$$

$$\varepsilon_{i,\lambda} = \sum_q \frac{\mathbf{v}_q}{\mathbf{v}_{shell}} \varepsilon_{i,\lambda,q} \tag{2.136}$$

where $\mathbf{v}_q$ is the volume of species q in the size bin (cm^3 q/cm^3 air) and $\mathbf{v}_{shell}$ is the total shell volume concentration in the size bin (cm^3 shell/cm^3 air). ($\mathbf{v}_{shell}$ is equal to the total volume concentration in the size bin minus the volume concentration of the BC core.) The shell-average real and imaginary refractive indices can then be calculated as [*Jacobson*, 2005]

$$n_{r,\lambda} = \sqrt{\frac{\sqrt{\varepsilon_{r,\lambda}^2 + \varepsilon_{i,\lambda}^2} + \varepsilon_{r,\lambda}}{2}} \tag{2.137}$$

$$n_{i,\lambda} = \sqrt{\frac{\sqrt{\varepsilon_{r,\lambda}^2 + \varepsilon_{i,\lambda}^2} - \varepsilon_{r,\lambda}}{2}} \tag{2.138}$$

The refractive indices at 550 nm and 10 μm that are used in the model are given in Table 2.19. Due to a lack of species specific data, several assumptions had to be made. All organic compounds are assumed to have the same refractive index, regardless of phase. Sulfate salts are assumed to have the refractive index of $(NH_4)_2SO_4$, while all other solid salts are assumed to have the refractive index of NaCl. Aqueous NH_3 is assumed to have the same refractive index as water. These assumptions allow us to model the impact of aerosol absorption and scattering on the rates of photolysis reactions in the gas phase in the absence of more species specific data.

Table 2.19: Refractive Index Values

Species	Refractive Index (550 nm)	Refractive Index (10 μm)
H_2O	$1.34+1.0\times10^{-9}i$	$1.22+0.05i$
$(NH_4)_2SO_4$	$1.52+0.0005i$	$2.15+0.02i$
NaCl	$1.45+0.00015i$	$1.53+0.033i$
Organics	$1.45+0.001i$	$1.77+0.12i$
BC	$1.82+0.74i$	$2.40+1.00i$

Reference: *Jacobson* [2005]

2.8.2 Core-in-Shell Mie Calculation

The optical properties of the aerosol particles are calculated using DMiLay, a publicly available[11] software package which computes the electromagnetic scattering of a stratified sphere - that is, a particle consisting of a spherical core surrounded by a spherical shell, where the core and shell have different refractive indices [*Toon and Ackerman*, 1981]. The core is assumed to consist of all of the BC in the particle, while the shell consists of all other species. Since CRM6 has 18 radiation bands (6 solar, 12 IR), we perform 18 core-in-shell Mie calculations. In the solar bands, the refractive index of the core and shell at 550 nm is used, while in the IR bands, the refractive index of the core and shell at 10 μm is used. For each band, a proxy wavelength in the middle of the band is assigned for use in the Mie calculation. The wavelength bands and the refractive index and proxy wavelengths used for each band are listed in Table 2.20.

Table 2.20: Wavelength Bands, Refractive Indices, and Proxy Wavelengths

Wavelength Band	Refractive Index	Proxy Wavelength
0.2 - 0.7 μm	Solar (550 nm)	550 nm
0.7 - 1.3 μm	Solar (550 nm)	1.0 μm
1.3 - 1.9 μm	Solar (550 nm)	1.3 μm
1.9 - 2.5 μm	Solar (550 nm)	2.2 μm
2.5 - 3.5 μm	Solar (550 nm)	3.0 μm
3.5 - 4.0 μm	Solar (550 nm)	3.75 μm
2200 - 1900 cm^{-1}	IR (10 μm)	4.79 μm
1900 - 1700 cm^{-1}	IR (10 μm)	5.45 μm
1700 - 1400 cm^{-1}	IR (10 μm)	6.51 μm
1400 - 1250 cm^{-1}	IR (10 μm)	7.57 μm
1250 - 1100 cm^{-1}	IR (10 μm)	8.55 μm
1100 - 980 cm^{-1}	IR (10 μm)	9.65 μm
980 - 800 cm^{-1}	IR (10 μm)	11.35 μm
800 - 670 cm^{-1}	IR (10 μm)	13.71 μm
670 - 540 cm^{-1}	IR (10 μm)	16.72 μm
540 - 400 cm^{-1}	IR (10 μm)	21.76 μm
400 - 280 cm^{-1}	IR (10 μm)	30.36 μm
280 - 0 cm^{-1}	IR (10 μm)	71.43 μm

The core-in-shell Mie calculation gives the extinction efficiency, scattering efficiency, and asymmetry parameter for each particle size bin at each wavelength band. To use this information in the radiative transfer code of CRM6, we must calculate the aerosol extinction coefficient summed over all size bins, and the single scattering albedo and asymmetry parameter averaged over all size bins.

[11] Available by anonymous ftp from climate.gsfc.nasa.gov in directory pub/wiscombe.

The total aerosol extinction coefficient $b_{ext,aero}$ (m^{-1}) is calculated as

$$b_{ext,aero} = \frac{100\,\mathrm{cm}}{\mathrm{m}} \sum_{i=1}^{N_B} n_i \pi r_{i,eff}^2 Q_{ext,i} \tag{2.139}$$

where n_i is the number concentration of particles in bin i (particles cm^{-3}), $r_{i,eff}^2$ is the effective radius of the particle in cm, and $Q_{ext,i}$ is the extinction efficiency from the core-in-shell Mie calculation.

The average aerosol single scattering albedo, ϖ_{aero}, is calculated as the ratio of the total aerosol scattering coefficient and the total aerosol extinction coefficient (see Equation 9.103 of *Jacobson* [2005])

$$\varpi_{aero} = \frac{b_{scat,aero}}{b_{ext,aero}} = \frac{\sum_{i=1}^{N_B} n_i \pi r_{i,eff}^2 Q_{sca,i}}{b_{ext}} \tag{2.140}$$

where $Q_{sca,i}$ is the scattering efficiency from the core-in-shell Mie calculation.

The average aerosol asymmetry parameter, $\langle g \rangle_{aero}$, is calculated as (see Equation 9.117 of *Jacobson* [2005])

$$\langle g \rangle_{aero} = \frac{\sum_{i=1}^{N_B} n_i \pi r_{i,eff}^2 Q_{sca,i} \langle g \rangle_i}{\sum_{i=1}^{N_B} n_i \pi r_{i,eff}^2 Q_{sca,i}} \tag{2.141}$$

The optical properties predicted by the ASP model for the Timbavati savannah fire smoke plume at 550 nm are compared to reported values for fresh savannah smoke in Chapter 3. We find that our predicted single scattering albedo for fresh smoke of 0.866 is within the range of 0.82±0.05 given for fresh savannah smoke by *Reid et al.* [2005a], while our predicted asymmetry parameter for fresh smoke of 0.654 is slightly higher than the range of 0.55±0.06 for fresh grass/savannah smoke recommended by *Reid et al.* [2005a].

Chapter 3

Lagrangian Parcel Model Studies

In this chapter, we use the gas- and aerosol-phase chemistry model from Chapter 2 (Aerosol Simulation Program - ASP) to study the chemical evolution of three young smoke plumes from biomass burning. All of these studies are done in a Lagrangian framework, where the concentrations within a single parcel are tracked over time. Section 3.1 describes the Lagrangian parcel model used in these studies.

The three plumes that are modeled in this chapter are from the Otavi East African savannah fire (Section 3.2), Alaskan boreal forest fire B309 (Section 3.3), and the Timbavati South African savannah fire (Sections 3.4 to 3.6). Gas-phase composition measurements are available for all three smoke plumes, but aerosol-phase composition measurements are only available for the Timbavati smoke plume. Thus, we model the gas-phase chemistry of the Otavi and Alaskan plumes, and model both the gas- and aerosol-phase compositions of the Timbavati plume. The Timbavati study represents the first attempt, to our knowledge, to simultaneously model the gas- and aerosol-phase chemical evolution of a young biomass burning smoke plume. Section 3.7 summarizes the results and conclusions of the Lagrangian studies.

3.1 Description of Lagrangian Parcel Model

For these studies, we used ASP in a Lagrangian parcel model. The Lagrangian parcel model used in this study has been used in several previous studies of the gas-phase chemistry of smoke plumes from biomass burning [*Mason et al.*, 2001; *Jost et al.*, 2003b; *Trentmann et al.*, 2005; *Mason et al.*, 2006]. The derivation of the model is presented in *Mason et al.* [2001]. The model is illustrated in Figure 3-1.

We assume a Lagrangian parcel of fixed height (H) and length, but variable width $y(t)$. The

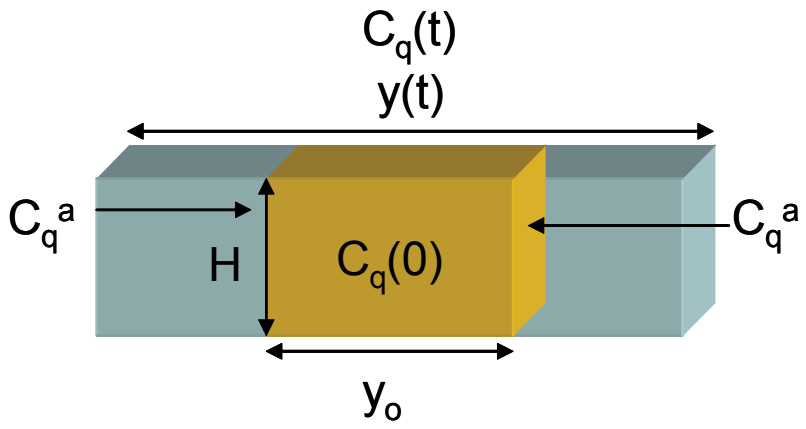

Figure 3-1: Schematic of the Lagrangian parcel model.

temperature and pressure of the parcel are assumed to be constant. The effect of plume dispersion on concentrations is then [*Mason et al.*, 2001]

$$\left(\frac{dC_q}{dt}\right)_{disp} = -\frac{1}{y\left(t\right)}\frac{dy\left(t\right)}{dt}\left(C_q - C_q^a\right) \tag{3.1}$$

where C_q is the concentration of species q within the parcel (molecules/cm^3) and C_q^a is the concentration of species q in the atmosphere outside of the parcel. The form of $y\left(t\right)$ is assumed to be $y\left(t\right) = \left(y_o^2 + 8K_y t\right)^{\frac{1}{2}}$, where y_o is the initial plume width. This expression is derived from the Gaussian solution to the diffusion equation, $\frac{d\sigma}{dt} = \frac{K_y}{\sigma}$, by setting $y\left(t\right)$ equal to twice the Gaussian variance [*Mason et al.*, 2001]. K_y represents the horizontal diffusivity of the atmosphere. The effect of plume dispersion then becomes

$$\left(\frac{dC_q}{dt}\right)_{disp} = -\frac{4K_y}{\left(y_o^2 + 8K_y t\right)}\left(C_q - C_q^a\right) \tag{3.2}$$

The full continuity equations for the Lagrangian parcel model are thus

$$\frac{dC_q}{dt} = -\frac{4K_y}{\left(y_o^2 + 8K_y t\right)}\left(C_q - C_q^a\right) - \frac{v_d}{H}C_q + \left(\frac{dC_q}{dt}\right)_{cond} + \left(\frac{dC_q}{dt}\right)_{chem} \tag{3.3}$$

$$\frac{dn_i}{dt} = -\frac{4K_y}{\left(y_o^2 + 8K_y t\right)}\left(n_i - n_i^a\right) - \frac{v_d}{H}n_i + \left(\frac{dn_i}{dt}\right)_{cond} + \left(\frac{dn_i}{dt}\right)_{coag} \tag{3.4}$$

$$\frac{d\mathbf{c}_{q,i}}{dt} = -\frac{4K_y}{\left(y_o^2 + 8K_y t\right)}\left(\mathbf{c}_{q,i} - \mathbf{c}_{q,i}^a\right) - \frac{v_d}{H}\mathbf{c}_{q,i} + \left(\frac{d\mathbf{c}_{q,i}}{dt}\right)_{cond} + \left(\frac{d\mathbf{c}_{q,i}}{dt}\right)_{coag} + \left(\frac{d\mathbf{c}_{q,i}}{dt}\right)_{chem} \tag{3.5}$$

where C_q is the concentration of gas-phase species (molecules/cm^3 air), n_i is the number concentration of particles in size bin i (particles/cm^3 air) and $\mathbf{c}_{q,i} = c_{q,i} n_i$ is the concentration of aerosol species q in size bin i (mol/cm^3 air).

The first term on the right-hand side of each continuity equation represents the effect of plume dispersion on the concentrations. The second term is the effect of deposition on the concentrations, where H is the height of the parcel (usually the inversion height of the boundary layer) and v_d is the deposition velocity (cm/s). For this thesis, we set the deposition velocity equal to 0 for gas-phase species (assuming that the effects of deposition are small on the 1 to 3 hour time scale of interest here) and use the terminal velocity of the aerosol particles as the deposition velocity for aerosol species. The remaining terms represent the change in gas and particle-phase concentrations due to mass transfer between the gas and aerosol phases (*cond*), coagulation of particles (*coag*), and irreversible and reversible chemistry (*chem*). The calculation of these terms are performed by ASP as described in Chapter 2. The integration of the different terms of the continuity equations is operator split for computational efficiency, with the time step for gas-phase chemistry, plume dispersion, and deposition set at 1 s, the time step for mass transfer and aerosol equilibrium set at 20 s, and the time step for coagulation set at 60 s.

In applying the model to observations of young smoke plumes, the values for y_o are taken from observations of the initial width of the young smoke plume, while the value of K_y is determined by a least-squares fit of Equation 3.2 to the concentrations of a conservative tracer, usually CO (*e.g.*, *Trentmann et al.* [2005]). CO is used as a tracer in these studies because the lifetime of CO (1 to 3 months) is much longer than the time scale of the young smoke plumes, and the high initial concentration of CO means than gas-phase production can be considered negligible. The Lagrangian time for the measurements is derived from the average observed wind speed in the plume and the distance of the sampling location from the fire source. Uncertainty and variation in the wind speed leads to uncertainty in the Lagrangian time of the measurements - this uncertainty is represented in the plots shown in this chapter by horizontal error bars on the measurements (see, for example, Figure 3-9).

The photolysis rates for the Lagrangian parcel model are calculated using the Tropospheric Ultraviolet and Visible (TUV) Radiation Model (v.4.1)[1] of S. Madronich and coworkers for 15 minute increments, which are then linearly interpolated within the model. For the Lagrangian

[1] Available online at
http://cdp.ucar.edu/browse/browse.htm?uri=http://dataportal.ucar.edu
/metadata/acd/software/TUV/v4.4/v4.4.thredds.xml

studies, we assume a "clear sky" radiation field that ignores the effect of aerosol absorption and scattering on photolysis rates. The impact of aerosols on the radiative field and photolysis rates for the Timbavati smoke plume is discussed in the 3D Eulerian studies in Chapter 4.

3.2 Otavi Smoke Plume

The Otavi smoke plume was emitted by a savannah fire near the city of Otavi in Northern Namibia on September 13, 2000. The trace gas composition of the Otavi plume was investigated by *Jost et al.* [2003b] as part of the Southern African Regional Science Initiative 2000 (SAFARI 2000) field campaign using the UK Met Office C-130 aircraft. In addition, *Jost et al.* [2003b] used a Lagrangian parcel model to investigate the formation of ozone within the Otavi smoke plume.

In this section we summarize the observations of the trace gas chemistry within the Otavi smoke plume and present the results of our Lagrangian modeling study of the Otavi plume. Section 3.2.1 summarizes the observations made by *Jost et al.* [2003b] of the Otavi smoke plume. Section 3.2.2 describes the chemical and physical parameters used by our model to simulate the Otavi plume. Section 3.2.3 then compares the results of our model to the available observations and the previous modeling study of *Jost et al.* [2003b].

3.2.1 Summary of Observations

The observations of the trace gas composition of the Otavi smoke plume made by *Jost et al.* [2003b] included high-frequency (0.25-1 Hz) measurements of CO, O_3, acetone and acetonitrile made during 10 transects of the Otavi smoke plume. The plume maximum and average concentration of these species is shown in Table 3.1; the standard deviation of the concentrations within the plume was not reported by *Jost et al.* [2003b]. The Lagrangian age reported for each transect assumes a vertical transport time of 10 min., representing an average updraft speed of 2 m/s to the sampling height at 2.7 km above mean sea level (1.5 km above ground level), and a mean horizontal wind speed of 9 m/s [*Jost et al.*, 2003b]. The uncertainty in the updraft speed was reported as a factor of 2, but no standard deviation for the horizontal wind speed was reported.

CO was measured with a vacuum-UV resonance fluorescence instrument with a measurement frequency of 1 Hz and a reported error of 2.4% [*Gerbig et al.*, 1999]. O_3 mixing ratios were measured using a Thermo Environmental Instruments Inc. (Franklin, MA, USA) UV photometric ozone analyzer model 49. The measurement frequency was 0.25 Hz with a reported precision of 1 ppb. Acetone and acetonitrile were measured with an Atmospheric Pressure Chemical Ionization

Table 3.1: Trace Gas Observations for the Otavi Plume

			CO		CH_3CN		Acetone		O_3	
Leg	Distance (km)	Plume Age (min.)	Max (ppbv)	Avg. (ppbv)	Max (ppbv)	Avg. (ppbv)	Max (ppbv)	Avg. (ppbv)	Max (ppbv)	Avg. (ppbv)
Over fire	0	0	16915	1703	40.947	5.407	91.994	11.541	99.9	86.5
1	4	17	1055	598	2.973	1.563	9.049	4.924	89.2	87.2
2	9	27	704	516	1.790	1.255	13.216	6.722	93.7	88.7
3	14	36	679	548	1.777	1.348	8.734	6.800	99.7	94.2
4	18	43	637	491	2.114	1.286	9.782	6.258	103.6	93.5
5	21	49	514	457	1.458	1.159	10.339	6.020	105.3	96.9
6	33	71	505	424	1.540	1.185	9.401	5.960	101.7	98.8
7	36	77	513	436	1.485	1.107	9.380	6.367	103.6	100.5
8	47	97	459	434	-	-	-	-	105.3	102.3
9	55	112	462	443	-	-	-	-	102.0	100.2
10	62	125	433	417	1.306	1.147	4.753	4.230	102.5	101.0

Data taken from Table 2 of *Jost et al.* [2003b]

Mass Spectrometer (AP-CIMS) with a measurement frequency of 1 Hz and a reported error for acetone of 15% [*Jost et al.*, 2003a].

In addition, two flask samples were taken close to the fire and analyzed following the campaign for nonmethane hydrocarbons (NMHCs) using an automated gas chromatograph with a flame ionization detector. The measured concentrations of NMHCs were used to derive the emission ratios and initial concentrations of NMHCs shown in Table 3.2 below. Also, NO_x emissions from the fire were measured with a Thermo Environmental Instruments Inc. (Franklin, MA, USA) NO_x instrument, model 42C. This instrument has an effective time resolution of 30 s, and the catalyst used to convert NO_2 to NO can also convert other nitrogen species that may be formed in the plume. Thus, *Jost et al.* [2003b] report only NO_x concentrations near the fire, where the sampling time was long enough to get accurate data. These values are shown in Table 3.2 below.

3.2.2 Model Initialization

We initialized our model similarly to the modeling study of *Jost et al.* [2003b]. Table 3.2 shows the initial and background concentrations used to model the Otavi plume. Since our gas-phase chemistry is based on the lumped CACM, several of the NMHCs must be lumped together into the appropriate class in the mechanism. This classification is given in the last column of Table 3.2.

Table 3.3 shows the temperature, pressure, relative humidity, and other parameters used to simulate the conditions of the Otavi smoke plume. Photolysis rates for the Otavi fire were derived using TUV v4.1 at 3 km above sea level. The initial plume width (y_o) was set to 500 m. Least-squares fitting of the plume average CO data gives a value of K_y of 400 m^2 s^{-1} [*Jost et al.*, 2003b].

Table 3.2: Background and Initial Concentrations for the Otavi Plume

Species	Background (ppbv)[a]	Emission Ratio (mol/mol CO)[a]	Initial Conc. (ppbv)[a]	CACM Classification
CO	250	-	1700	-
Acetone	2.8	-	11.5	KETL
O_3	85	-	75.0	-
NO_2	1.3	-	10.0	-
NO	0.7	-	2.0	-
HNO_3	1.3[b]	-	1.3	-
H_2O_2	4.5[b]	-	4.5	-
CH_4	1710[b]	6.2%	1799.9	-
C_2H_6	0.946	0.44%	7.3	ALKL
C_2H_4	0.03	0.33%	4.8	ETHE
C_3H_8	0.056	0.08%	1.2	ALKL
C_3H_6	0.38	0.24%	3.9	OLEL
CH_3OH	2.5[b]	1.16%	19.3	MEOH
$OHCH_2CHO$	0.2	0.8%	11.8	ALD2
HCHO	1.3[b]	2.1%	31.8	HCHO
CH_3CHO	0.2[b]	0.8%	11.8	ALD2
HC(O)OH	0.2[b]	0.56%	8.3	ACID
$CH_3C(O)OH$	1[b]	1.45%	22.0	ACID

[a]Values taken from Table 5 of *Jost et al.* [2003b].
[b]Values are from output of MATCH model (see *Jost et al.* [2003b]).

This is in line with the data and empirical equation of *Gifford* [1982] for horizontal atmospheric diffusion, which predicts K_y of O(100 m^2 s^{-1}) for a lateral standard deviation of O(100 m). *Jost et al.* [2003b] gives values for the total aerosol number concentration and average size, which are included in Table 3.3. However, no heterogeneous chemistry was included in the Otavi simulation presented here.

3.2.3 Results and Comparison to Observations

Figure 3-2 shows the modeled and observed CO concentrations for the Otavi smoke plume. The data points are the plume average measurements reported by *Jost et al.* [2003b]. The vertical error bars represent the reported precision of the measurements. The solid black line is from the Lagrangian parcel model used in this work while the dotted red line is from the model results of *Jost et al.* [2003b]. The K_y value of 400 m^2 s^{-1} gives a good match to the change in the plume-average CO concentrations for the Otavi fire.

Figure 3-3 shows the modeled and observed O_3 concentrations for the Otavi smoke plume. Our model gives a fairly good match to the observed formation of ozone within the Otavi smoke plume, with only a slight underestimate (~5 ppbv) of the downwind concentrations. In addition,

Table 3.3: Time, Location, and Atmospheric Parameters for the Otavi Plume

Parameter		Value[a]
Date (dd/mm/yyyy)		13/09/2000
Latitude		-19.7°
Longitude		17.6°
Temperature (K)		290
Pressure (mbar)		730
Relative Humidity		10%
Surface Albedo		0.15
Ozone Column (DU)		349.13
Aerosol Number Conc.[b] (cm^{-3})		3.1×10^4
Aerosol Size[c] (μm)		0.1
Time of Model Start	LT	13:00
	UT	11:00
Model Run Time (hr.)		2.5

[a]Values taken from *Jost et al.* [2003b] unless otherwise stated.
[b]Value taken from *Haywood et al.* [2003].
[c]Assumed size of fresh savannah smoke aerosols.
(Compare to 0.11±0.01 μm reported by *Reid et al.* [2005b].)

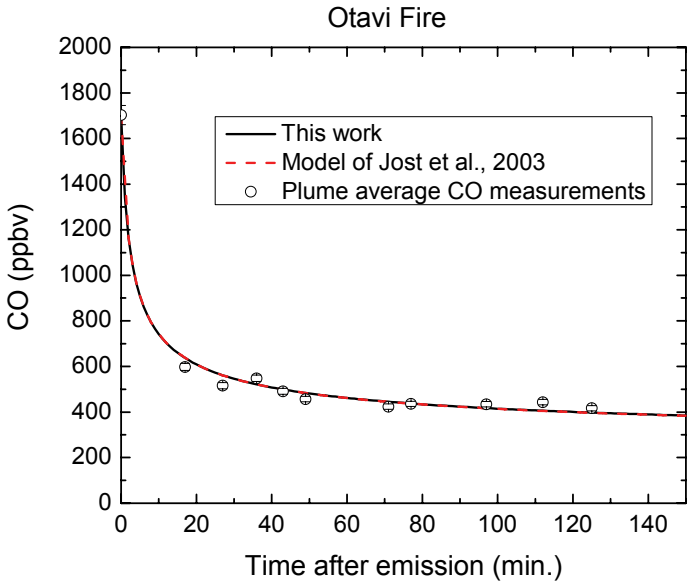

Figure 3-2: Modeled and measured CO concentrations for the Otavi smoke plume. Data points are the plume average measurements reported by *Jost et al.* [2003b].

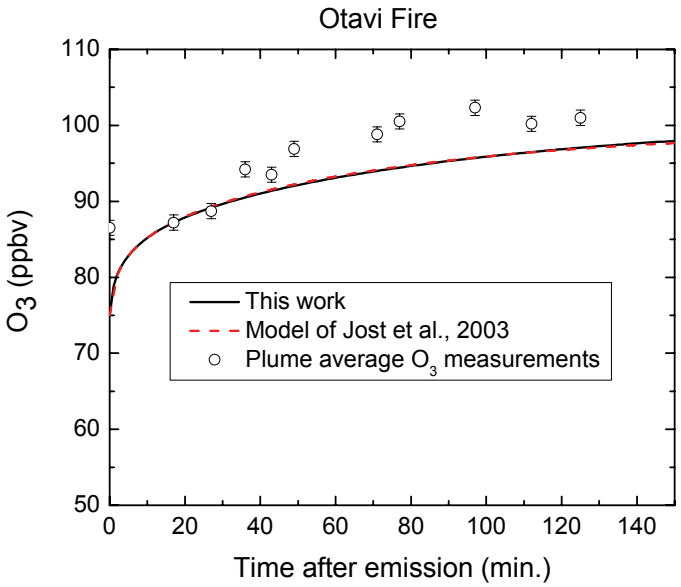

Figure 3-3: Modeled and measured O_3 concentrations for the Otavi smoke plume. Data points are the plume average measurements reported by *Jost et al.* [2003b].

our model matches closely with the model results of *Jost et al.* [2003b] for O_3 formation, showing that our lumped chemical mechanism can represent the formation of ozone in the Otavi smoke plume as well as the species-specific mechanism of *Jost et al.* [2003b]. As reported by *Jost et al.* [2003b], a 25% enhancement of photolysis rates can improve the match with the observed downwind concentrations. This level of enhancement is within the parametric uncertainty for these photolysis rates (see p. 178).

Figure 3-4 shows the observed plume average acetone concentrations for the Otavi smoke plume. The measurements are compared with the acetone concentration from the model of *Jost et al.* [2003b] and the KETL concentrations from our simulation of the Otavi smoke plume. Both models underpredict the level of acetone measured in the plume between 30 and 80 minutes after emission, suggesting that both models are missing a secondary source of acetone within the smoke plume. This secondary source may be an uncharacterized gas-phase compound within the smoke plume, or the result of heterogeneous reactions with the organic smoke aerosol producing secondary gas-phase acetone. Our model shows slightly lower levels of acetone (KETL) than the model of *Jost et al.* [2003b], possibly due to different reaction rates for acetone and KETL between the two models.

Figures 3-5, 3-6, and 3-7 compare the modeled NO, NO_2, and HCHO concentrations from our

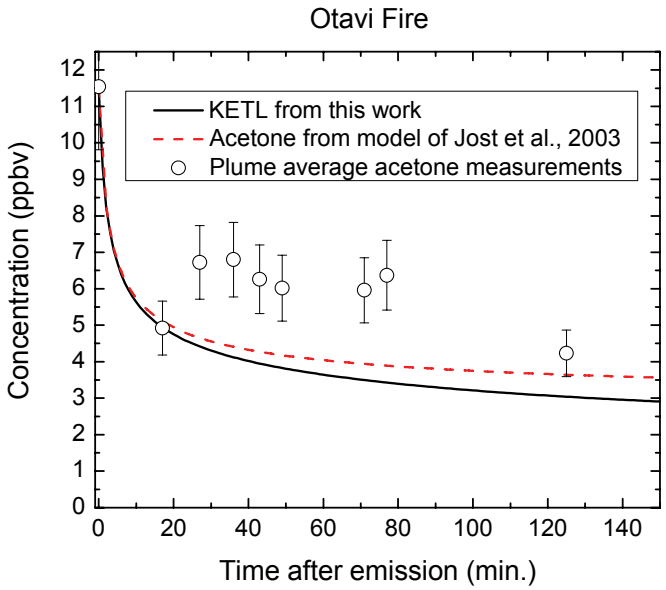

Figure 3-4: Modeled and measured acetone (KETL) concentrations for the Otavi smoke plume. Data points are the plume average measurements of acetone reported by *Jost et al.* [2003b].

model and from the modeling study of *Jost et al.* [2003b]. Data for these species in the Otavi smoke plume are not available. The two models agree very well, showing only slight differences in the predicted concentrations.

3.3 Alaska Smoke Plume

The Alaska smoke plume (emitted by Alaska Fire Service fire B309) was measured by *Goode et al.* [2000] on June 27, 1997 using airborne Fourier transform infrared spectrometry (AFTIR) on a King Air B-90 aircraft. The fire, ignited by lightning, burned within the black spruce forest-shrub-bog mosaic of the Innoko Wildlife Refuge. The gas-phase chemistry for this case has been previously studied in the model intercomparison of *Mason et al.* [2006].

In this section we summarize the observations of the trace gas chemistry within the Alaska smoke plume and present the results of our Lagrangian modeling study of the Alaska plume. Section 3.3.1 summarizes the observations made of the Alaska smoke plume by *Goode et al.* [2000]. Section 3.3.2 describes the chemical and physical parameters used by our model to simulate the Alaska plume. Section 3.3.3 then compares the results of our model to the available observations.

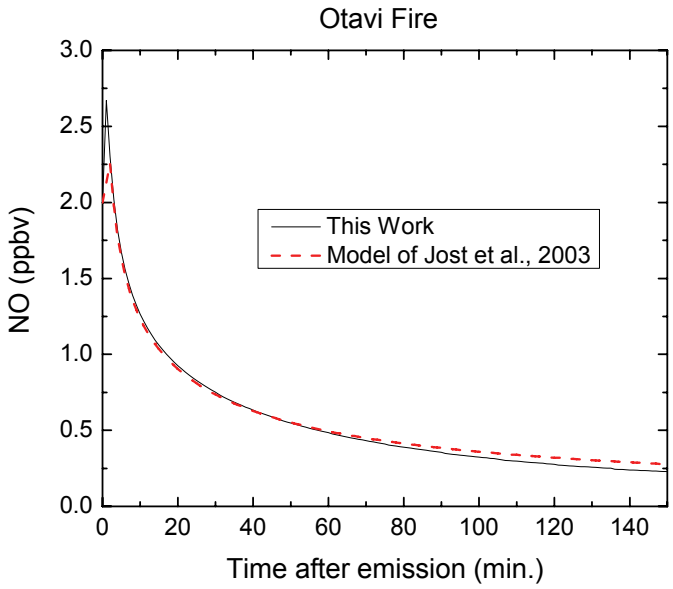

Figure 3-5: Modeled NO concentrations for the Otavi smoke plume.

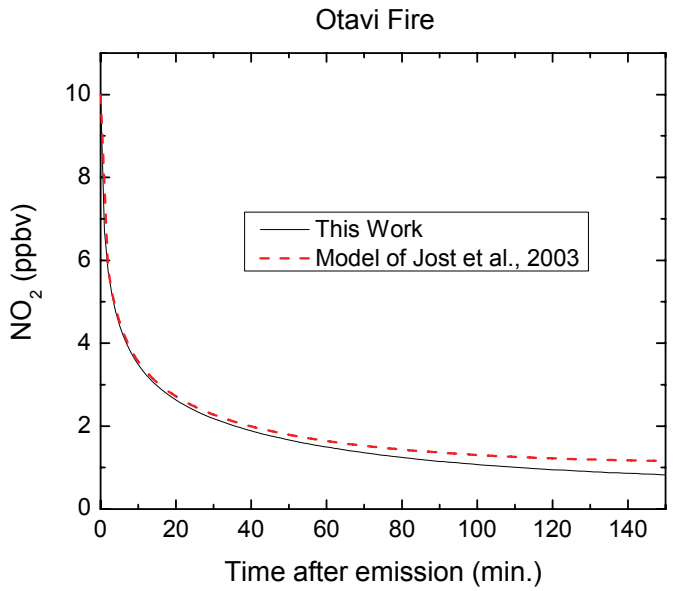

Figure 3-6: Modeled NO_2 concentrations for the Otavi smoke plume.

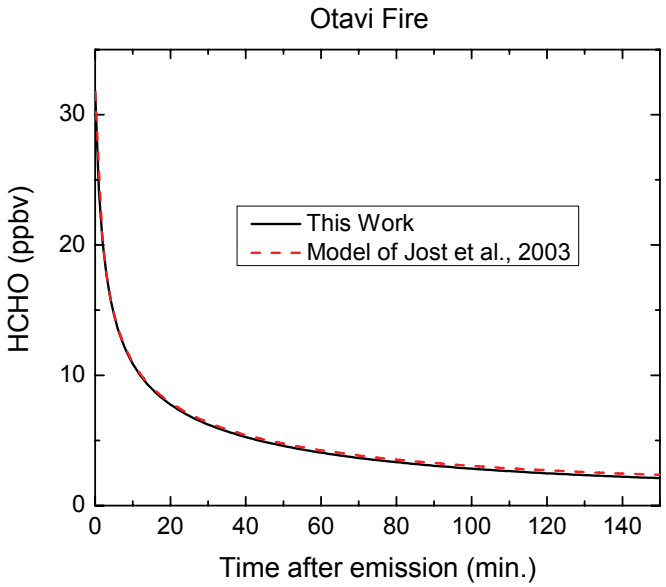

Figure 3-7: Modeled HCHO concentrations for the Otavi smoke plume.

3.3.1 Summary of Observations

Four samples were collected and analyzed by AFTIR during transects of the smoke plume, while an additional three samples were collected and analyzed while flying down the long axis of the smoke plume [*Mason et al.*, 2006]. A detailed description of the AFTIR technique is given in *Goode et al.* [2000]. In general, the sampling time for the AFTIR instrument is 3-5 s, so that these measurements represent point samples rather than plume average values. The measurements are presented in Table 3.4. The Lagrangian age reported for each sample assumes a mean horizontal wind speed of 7.55±2.0 m/s [*Mason et al.*, 2006]; horizontal error bars are used in the data plots below to represent the uncertainty in the Lagrangian age due to the varying horizontal wind speed.

3.3.2 Model Initialization

We initialized our model similarly to the modeling intercomparison of *Mason et al.* [2006]. Table 3.5 shows the initial and background concentrations used to model the Alaska plume, including their CACM classification.

Table 3.6 shows the temperature, pressure, relative humidity, and other parameters used to simulate the conditions of the Alaska smoke plume. Photolysis rates for the Alaska fire were derived using TUV v4.1 at 2 km above sea level. The initial plume width (y_o) was set to 13,735

Table 3.4: Trace Gas Observations for the Alaska Plume

Samples[a]	PP1	XC1 3500'	LAX1-2	LAX1-3	XC2 4000'	XC2 5500'	LAX1-4
Sample Time (LT)	16:53	17:10	17:34	17:37	17:52	17:50	17:39
Latitude	63.57	63.54	63.48	63.43	63.40	63.41	63.42
Longitude	-158.43	-158.06	-157.66	-157.43	-157.42	-157.37	-157.17
Altitude[b] (m)	510.9	1251.9	1897.8	1752.8	1412.7	1842.9	1568.9
Smoke Age[c] (h)	0.00	0.69	1.45	1.93	1.98	2.05	2.40
Distance Downwind (km)	0	18.8	39.4	52.5	53.8	55.8	65.1
CO_2^d (excess ppmv)	49.8	14.7	-	-	-	-	-
CO^d (excess ppmv)	4.40	1.57	1.46	2.60	0.51	1.30	0.56
CH_4^d (excess ppmv)	0.182	-	-	-	-	-	-
$C_2H_4^d$ (excess ppmv)	0.077	0.023	0.022	0.030	-	0.020	-
$C_2H_2^d$ (excess ppmv)	0.012	-	-	-	-	-	-
CH_2O^d (excess ppmv)	0.072	-	-	0.054	-	-	-
CH_3OH^d (excess ppmv)	0.041	-	-	0.022	-	0.011	-
$CH_3C(O)OH^d$ (excess ppmv)	0.048	-	0.029	0.037	-	0.034	-
$HC(O)OH^d$ (excess ppmv)	0.031	-	-	0.028	0.010	0.020	0.016
NH_3^d (excess ppmv)	0.043	0.013	-	0.008	-	-	-
NO^d (excess ppmv)	0.093	0.012	-	-	-	-	-
NO_2^d (excess ppmv)	0.088	0.017	-	0.028	-	-	-
O_3^d (excess ppmv)	-	0.026	0.067	0.110	0.039	0.077	0.039

[a] Data taken from Table I of *Mason et al.* [2006]

[b] Above ground level. Ground at 450 m above mean sea level.

[c] Derived from measured average wind speed of 7.55 $\pm$ 2 m/s.

[d] All concentration data are excess mixing ratios (concentration above background).

Background concentrations are given in Table 3.5.

Table 3.5: Background and Initial Concentrations for the Alaska Plume

Species	Background (ppbv)[a]	Emission Ratio (mol/mol CO)[b]	Initial Conc. (ppbv)	CACM Classification
CO_2	365000	-	414800	-
CO	100	-	4502.00	-
CH_4	1580	5.45%	1819.909	-
C_2H_6	0.8	0.95%	42.619	ALKL
C_2H_4	0.02	1.75%	77.055	ETHE
C_2H_2	0.01	0.25%	11.015	-
C_3H_8	0.011	0.40%	17.619	ALKL
C_3H_6	0.01	0.60%	26.422	OLEL
CH_3OH	0.33	0.93%	41.2686	MEOH
CH_2O	0.2	1.64%	72.3928	HCHO
$OHCH_2CHO$	0.018	0.34%	14.9848	ALD2
CH_3CHO	0.018	0.75%	33.033	ALD2
Acetone	0.3	0.22%	9.9844	KETL
HCOOH	0.0034	0.70%	30.8174	ACID
CH_3COOH	0.0969	1.09%	48.0787	ACID
Isoprene	0.0215	0.16%	7.0647	ISOP
Toluene	0.08	0.11%	4.9222	AROH
MEK	0	1.30%	57.226	KETL
Phenol	0	0.33%	14.5266	AROO
Acetol	0	1.10%	48.422	KETL
H_2O_2	0.8	0.00%	0.8	-
H_2	580	35.00%	2120.7	-
O_3	32.5	-	17.1	-
NO_2	0.0166	1.96%	86.2958	-
NO	0.0052	2.07%	91.1266	-
HNO_3	0.021	0.00%	0.021	-
HONO	0.1	0.78%	34.4356	-
PAN	0.0989	0.00%	0.0989	-
N_2O_5	0.00005	0.00%	0.00005	-
N_2O	320	0.16%	327.0432	-
NH_3	0	0.98%	43.1396	-

[a]Values taken from Table IV of *Mason et al.* [2006]
[b]Values taken from Table V of *Mason et al.* [2006]

m, a much larger initial plume width than in the Otavi case. Least-squares fitting of the available CO data gives a value of K_y of 34,000 m^2 s^{-1} [*Mason et al.*, 2006]. This value is much larger than the value of 400 m^2 s^{-1} used in the Otavi case. The larger diffusivity is related to the larger plume size. As noted by *Gifford* [1982], the bigger the plume is, the faster it spreads. For example, the data and empirical equation of *Gifford* [1982] for horizontal atmospheric diffusion predicts K_y of O(10,000 m^2 s^{-1}) for a lateral standard deviation of O(10 km), in line with the values used here for the Alaska plume. No heterogeneous chemistry was included in the Alaska simulation runs presented in this section.

Table 3.6: Time, Location, and Atmospheric Parameters for the Alaska Plume

Parameter		Value[a]
Date (dd/mm/yyyy)		27/06/1997
Latitude		63.46°
Longitude		-158.65°
Altitude (kmsl)		1.621
Temperature (K)		280.6
Pressure (mbar)		846.5
Relative Humidity		72%
Surface Albedo		0.10
Ozone Column (DU)		320
Time of Model Start	LT	15:52
	UT	0:52
Model Run Time (hr.)		2.75

[a]Values taken from Table III of *Mason et al.* [2006].

3.3.3 Results and Comparison to Observations

Figure 3-8 shows the modeled and observed CO concentrations for the Alaska smoke plume. The vertical error bars represent the reported precision of the AFTIR measurements [*Goode et al.*, 2000] while the horizontal error bars represent the uncertainty in the Lagrangian age of the smoke samples due to the variation in the horizontal wind speed. The solid black line shows the modeled CO concentration for the best-fit value of K_y (34,000 m^2 s^{-1}). As we can see, there is one sample with a significantly higher concentration of CO than is predicted using this value of K_y, and two samples that show significantly lower concentrations of CO. To account for this apparent variability in plume dispersion, we ran two additional models runs, one with a low (slow) K_y of 6,700 m^2 s^{-1} and one with a high (fast) K_y of 134,750 m^2 s^{-1}.

Figure 3-9 shows the modeled and observed concentrations of O_3 for the Alaska plume. Our model gives a fairly good match to the observed O_3 formation in the Alaska plume, covering most

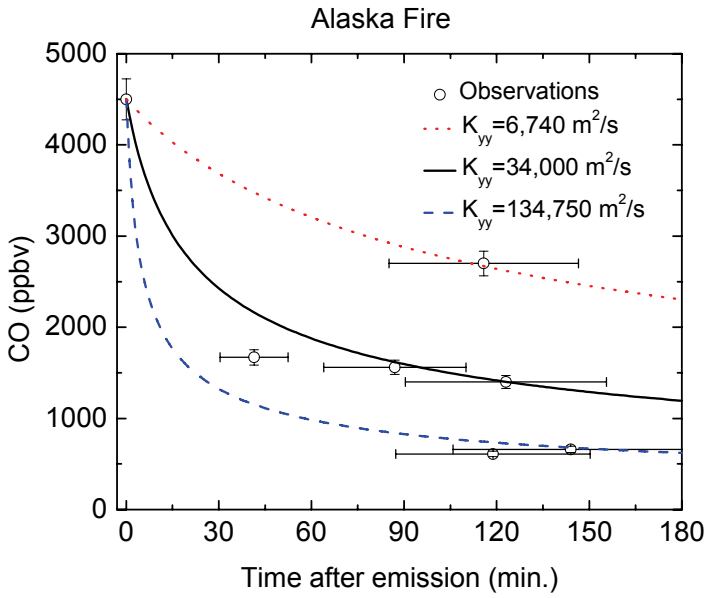

Figure 3-8: Modeled and measured CO concentrations for the Alaska smoke plume.

of the ozone observations within the uncertainty of the plume dispersion rates, Lagrangian age, and measurement precision.

Figures 3-10, 3-11, and 3-12 show the modeled and measured concentrations of NO_x, NO, and NO_2 for the Alaska plume, respectively. In general, the model appears to overestimate the concentrations of nitrogen oxides, although the low number of measurements and high uncertainties make it difficult to draw any definitive conclusions.

Figure 3-13 shows the modeled and measured concentration of HCHO for the Alaska plume. Only two measurements of HCHO are available, and only one downwind. The results show the model may be underestimating HCHO, but again the low number of measurements and high uncertainties make it difficult to draw any specific conclusions.

Figure 3-14 shows the modeled and measured concentration of ethylene (ETHE) for the Alaska plume. The measurements all appear to be in line with the model values, suggesting that the chemistry of ethylene in the Alaska plume is correctly represented in the model.

Figure 3-15 shows the modeled ACID concentration and the sum of the measurements of formic and acetic acid in the Alaska plume. The model underestimates the concentrations of these acids observed in the Alaska smoke plume. This underprediction of secondary acid formation in smoke plumes has also been reported for the Timbavati South African savannah fire [*Trentmann et al.*,

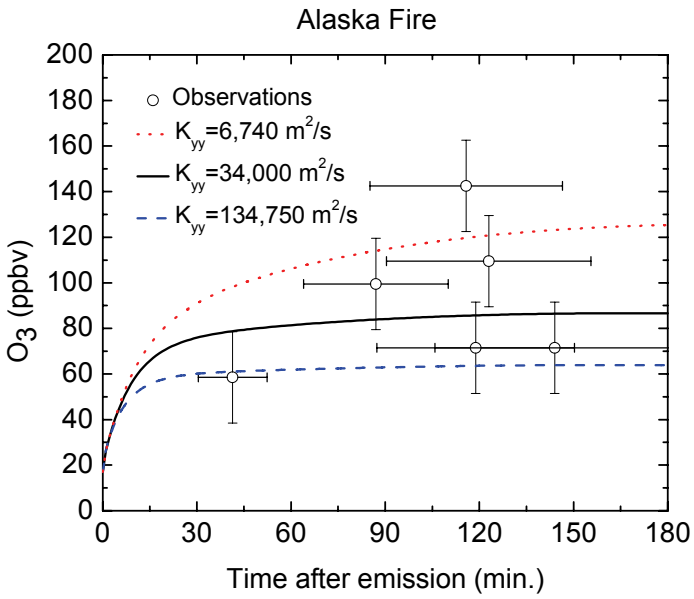

Figure 3-9: Modeled and measured O_3 concentrations for the Alaska smoke plume.

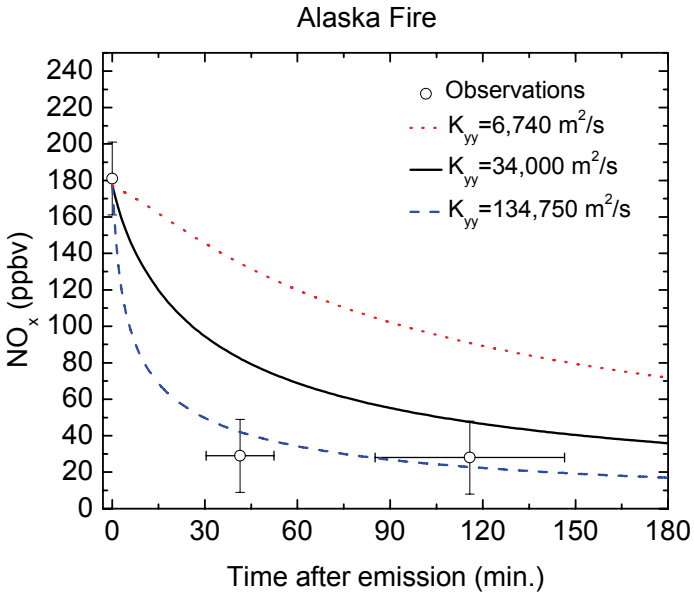

Figure 3-10: Modeled and measured NO_x ($NO+NO_2$) concentrations for the Alaska smoke plume.

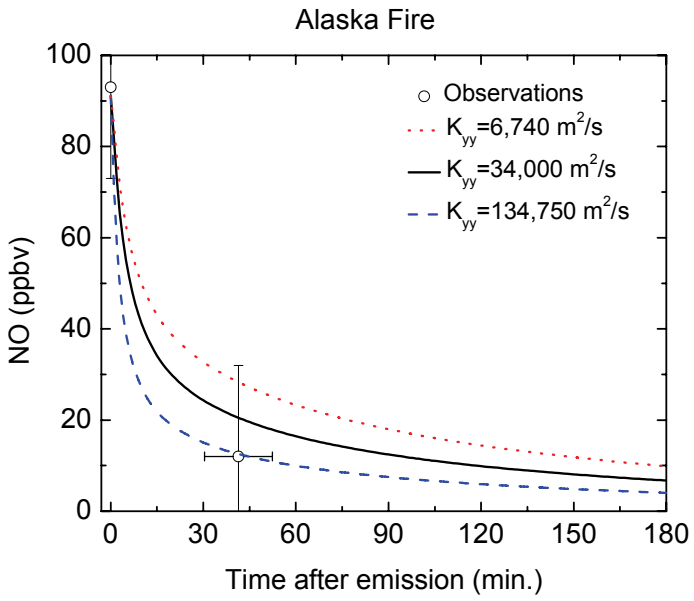

Figure 3-11: Modeled and measured NO concentrations for the Alaska smoke plume.

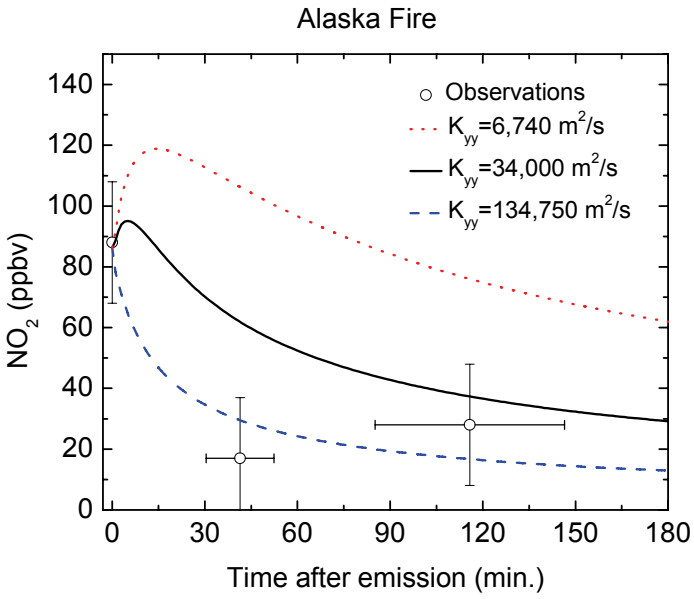

Figure 3-12: Modeled and measured NO_2 concentrations for the Alaska smoke plume.

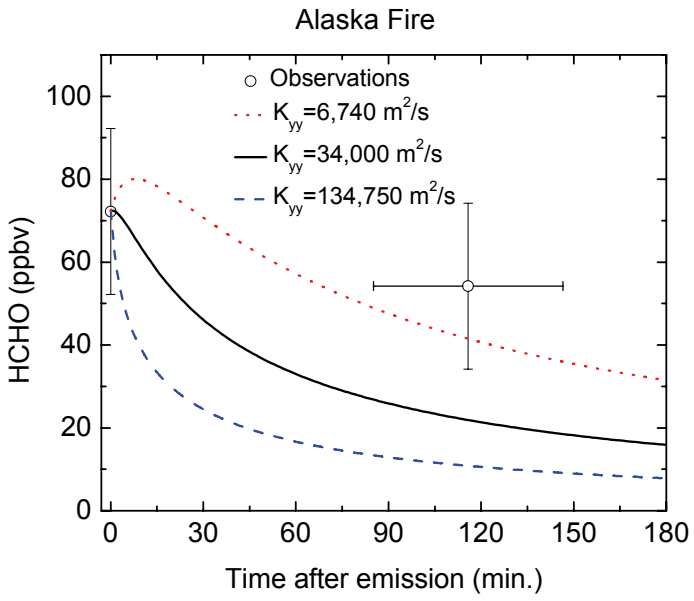

Figure 3-13: Modeled and measured HCHO concentrations for the Alaska smoke plume.

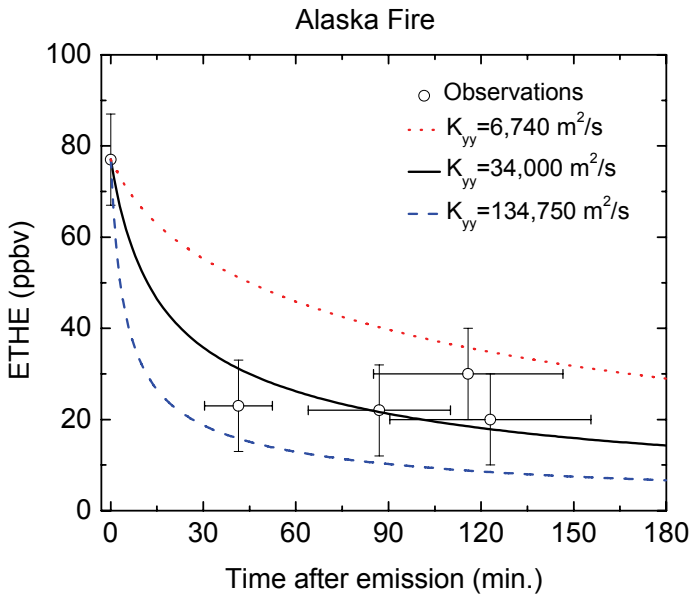

Figure 3-14: Modeled and measured ETHE (ethylene) concentrations for the Alaska smoke plume.

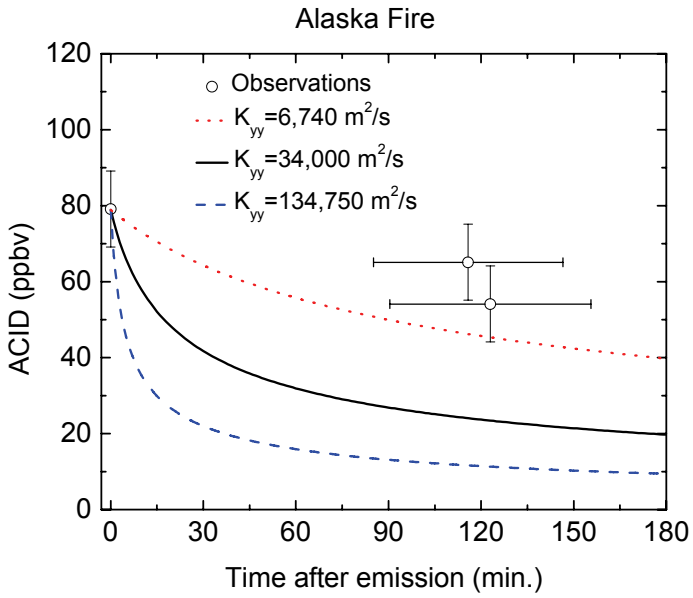

Figure 3-15: Modeled and measured ACID (formic plus acetic acid) concentrations for the Alaska smoke plume. Data points are the sum of measurements for formic and acetic acid.

2005]. The underestimate could be caused by the oxidation of a gas-phase organic species not currently included in our model, or by the heterogeneous oxidation of organic aerosol species to produce gas-phase acids. These possibilities are further explored for the Timbavati smoke plume (see page 187).

3.4 Timbavati Smoke Plume: Summary of Observations

The Timbavati smoke plume in South Africa was sampled by *Hobbs et al.* [2003] on Sept. 7, 2000 as part of the Southern African Regional Science Initiative 2000 (SAFARI 2000) field project. This grass fire was intentionally ignited in the lowveld of South Africa. Measurements of both the gas and aerosol phase composition of the smoke plume were made aboard the University of Washington Convair-580 research aircraft. The gas-phase chemistry for the Timbavati smoke plume has been previously modeled by *Trentmann et al.* [2005] and in the model intercomparison of *Mason et al.* [2006].

Below we summarize the observations of the trace gas and aerosol chemistry within the Timbavati smoke plume and present the results of our Lagrangian modeling study of the plume. This section summarizes the observations made by *Hobbs et al.* [2003]. Section 3.5 describes the chemical

and physical parameters used by our model to simulate the Timbavati plume. Section 3.6 compares the results of our model to the available observations and discusses several hypotheses that could improve the match between the model and observations. Model sensitivity tests and scale analyses are presented to evaluate these hypotheses.

3.4.1 Sample Conditions

Measurements of the Timbavati smoke plume were made by *Hobbs et al.* [2003]. The location, pressure, temperature, and relative humidity for each sampling transect are shown in Table 3.7. Temperature was measured with a Rosemount platinum resistance thermometer. The dewpoint temperature, from which the ambient relative humidity was derived, was measured with a Cambridge chilled-mirror device [*Hobbs et al.*, 2003]. The Lagrangian ages of the samples were estimated by *Trentmann et al.* [2005] assuming an average wind speed of 9.3±1.5 m/s for samples below 1 km in altitude and a wind speed of 7.3±1.5 m/s for samples above 1 km.

Table 3.7: Samples of Smoke From the Timbavati Plume

Sample[a]	Time (UTC)	Lat.	Long.	Dist. (km)	Alt.[b] (m)	Age[c] (min.)	P (hPa)	T (^{o}C)	RH (%)	MCE[d]
1	0843	-24.37	31.22	1.0	598	1.8	941	19	35	0.94
2	0857	-24.36	31.25	0.2	564	0.4	942	19	34	0.93
3	0923	-24.33	31.25	4.9	896	8.8	909	16	40	0.92
4	0939	-24.18	31.12	20.8	1440	47.5	848	14	78	0.91
5	1014	-24.16	31.17	26.2	545	47.0	952	21	34	0.93
a	0843	-24.37	31.26	1.7	616	0	939	21	38	0.93
b	0846	-24.37	31.24	0.1	739	3.0	920	20	36	0.94
c	0855	-24.29	31.27	9.5	710	16.8	942	20	34	0.91
d	0921	-24.36	31.23	1.9	862	5.9	903	17	41	0.88
e	0933	-24.24	31.28	15.7	1710	35.4	843	16	22	0.93
f	0934	-24.21	31.21	17.7	1430	42.0	849	14	32	0.93
g	0940	-24.19	31.21	19.9	1440	46.8	846	15	78	0.91
h	0946	-24.36	31.25	2.0	564	3.8	940	21	35	0.91
i	1015	-24.18	31.09	26.6	545	49.8	943	22	34	0.92
j	1021	-24.17	31.09	27.3	500	51.1	956	23	32	0.91
k	1036	-24.15	31.08	30.1	538	56.1	945	23	28	0.94

[a] Data from Table 1 of *Hobbs et al.* [2003] except where otherwise noted.

[b] Altitude above ground level.

[c] Data from Table 1 of *Trentmann et al.* [2005].

[d] MCE - Modified combustion efficiency $\left(\frac{\Delta[CO_2]}{\Delta[CO_2]+\Delta[CO]}\right)$

3.4.2 Gas Phase Observations

Measurements of the gas-phase composition of the Timbavati plume were made using continuous sampling devices, AFTIR, and electropolished stainless steel canisters which collected samples for laboratory analysis [*Hobbs et al.*, 2003]. SO_2 was measured continuously with a Teco 43S pulsed fluorescence analyzer with a precision of 7% and a detection limit of 1 ppbv.

Table 3.8 shows the measurements performed using the AFTIR instrument of *Yokelson et al.* [2003]. The AFTIR measurements are reported as excess ppbv, or concentration above that of ambient air. The sampling time for the AFTIR was about 3-5 s. After collecting a smoke sample, the samples were analyzed for 2-3 minutes to allow sufficient signal averaging. The detection limit and precision for the measured species were reported by *Yokelson et al.* [2003] and are generally between 5 to 20 ppbv.

Table 3.8: Excess Mixing Ratios (ppbv) Measured by AFTIR for the Timbavati Plume

Species	b	a	d	h	c	e	f	g	i	j	k
CO_2	68,600	79,200	6900	15,600	19,100	13,900	21,300	10,100	6100	6300	7100
CO	4024	5738	911	1592	1776	1042	1625	954	549	644	426
CH_4	214	345	80	67	109	55	117	60	33	28	21
C_2H_4	58	91	12	20	21	bdl	bdl	bdl	bdl	bdl	bdl
C_2H_2	14	19	bdl	bdl	6	bdl	bdl	bdl;	bdl	bdl	bdl
HCHO	74	109	20	25	16	31	37	31	10	10	20
CH_3OH	55	86	20	19	28	10	bdl	7	bdl	9	5
$CH_3(O)OH$	58	75	23	53	14	30	71	36	27	35	32
HC(O)OH	33	33	bdl	6	17	11	bdl	5	bdl	bdl	bdl
NH_3	13	5	bdl	3	bdl	bdl	bdl	bdl	bdl	bdl	bdl
NO	52	57	bdl	bdl	bdl	bdl	bdl	bdl	bdl	bdl	bdl
NO_2	123	137	bdl	51	51	bdl	bdl	bdl	6	bdl	bdl
HCN	29	37	9	bdl	18	8	18	11	bdl	bdl	bdl
O_3	-52	-52	-12	bdl	22	60	98	86	31	54	19

Data from Table 3 of *Hobbs et al.* [2003].

Table 3.9 shows the results for the steel canister samples. A detailed description of the analytical procedure for the canisters is given by *Colman et al.* [2001]. A typical sampling time for the canister measurements was 30 s. The composition of the canisters was analyzed using gas chromatography with flame ionization, electron capture and mass spectrometer detection [*Hobbs et al.*, 2003]. The precision of the measurements is approximately 3%, with a detection limit of 3 pptv [*Hobbs et al.*, 2003]. A laboratory study of emissions from African biomass burning by *Christian et al.* [2003] using similar sampling and detection methods identified only 70% of the carbon emitted as non-methane organic compounds (NMOCs), suggesting that the NMOCs listed in Table 3.9 account for roughly 70% of the carbon released by the Timbavati fire as NMOC [*Trentmann et al.*, 2005]. We

examine the potential effect of these uncharacterized organic compounds on the plume chemistry in Section 3.6.2.

In addition to the measurements listed above, *Hobbs et al.* [2003] estimated the average OH concentration within the Timbavati smoke plume using the observed decay rates of five species (propene, ethylene, 1-butene, ethane and CO) that have various reaction rates with OH but negligible competing loss rates due to O_3. The average derived OH concentration for the first 40 minutes in the Timbavati plume is $(1.7 \pm 0.2) \times 10^7$ radicals cm^{-3}, suggesting a highly oxidizing plume environment.

3.4.3 Aerosol Phase Observations

The total aerosol number concentration in the smoke plume was measured with a TSI 3025A ultrafine condensation particle counter. The instrument has a precision of 10% and a size range of 0.003-3 μm in diameter. Particle size spectra from 0.5 to 3.0 μm in diameter were continuously measured with a TSI 3320 aerodynamic particle sizer. Unfortunately, most aerosol particles from savannah burning have a number mean diameter of only 0.11±0.01 μm [*Reid et al.*, 2005b], so the size distribution measurements available for Timbavati are not very useful for initializing or evaluating the model aerosol size distribution. The light-scattering coefficient of particles was measured continuously using a MS Electron nephelometer.

Aerosol bulk chemical composition was measured by collecting particles on quartz filters (Pallflex 2500 QAT-UP) and Teflon filters (Gleman Sciences Teflon membrane, 2.0 μm pore size) [*Hobbs et al.*, 2003]. The results are presented in Table 3.10. Since the time that it took for the aircraft to cross the smoke plume (O(1 min.)) was too short to pass enough smoke through the filters, a "grab-bag" technique was used where a 2.5 m^3 Velostat plastic bag was filled with smoke in 7-12 s. The sample in the grab bag was then passed through the filters for subsequent analysis. The grab-bag system had an aerosol 50% cut-off diameter of about 4 μm [*Hobbs et al.*, 2003].

The Teflon filters were weighed before and after sampling to determine the mass of dry total particulate matter (TPM) collected on the filters. Afterwards, the Teflon filters were extracted in deionized water and analyzed by ion chromatography for concentrations of chloride, nitrate, sulfate, and organic ions such as oxalate. An Inductively Coupled Plasma-Atomic Emission Spectrometer was used to measure potassium. Details on the Teflon filter analyses are given by *Gao et al.* [2003].

The quartz filters were analyzed by *Kirchstetter et al.* [2003] for particulate carbon. The filters were analyzed for total carbon (TC) content using the evolved gas analysis (EGA) method described by *Novakov* [1981, 1982]. The filters were heated from 50 to 800 ^oC in an oxygen atmosphere. The

Table 3.9: Gas Concentrations (ppbv) in Canister Samples of the Timbavati Plume

Species[a]	Sample 1	Sample 2	Sample 3	Sample 4	Sample 5	Ambient Air
CO_2	427,000	425,000	391,000	397,000	388,000	377,000
CO	3500	3900	1500	2300	1100	220
SO_2	66	25	15	9.4	8.9	1.7
CH_4	1870	1900	1790	1820	1780	1740
CH_3SCH_3	0.028	0.044	0.012	0.014	0.0051	bdl
CH_3Br	0.030	0.034	0.019	0.023	0.014	0.0096
CH_3Cl	3.0	3.4	1.7	2.1	1.2	0.68
CH_3I	0.0054	0.0063	0.0026	0.0035	0.0019	0.00064
CH_3ONO_2	0.018	0.018	0.013	0.0225	0.0089	0.0057
Ethane (C_2H_6)	9.8	13	4.3	7.2	3.3	0.86
Ethene (C_2H_4)	32	35	12	16	6.0	0.32
Propane (C_3H_8)	1.6	2.3	0.72	1.2	0.55	0.11
Propene (C_3H_6)	7.4	8.8	2.6	2.3	0.83	0.031
Acetylene (C_2H_2)	12	12	4.8	7.3	3.1	0.49
i-butane (C_4H_{10})	0.14	0.18	0.054	0.084	0.044	0.009
n-butane (C_4H_{10})	0.36	0.47	0.15	0.24	0.11	0.023
t-2-butene (C_4H_8)	0.31	0.42	0.079	0.097	0.005	bdl
1-butene (C_4H_8)	1.0	1.3	0.35	0.27	0.097	0.023
c-2-butene (C_4H_8)	0.23	0.31	0.063	0.055	0.006	bdl
i-pentane (C_5H_{12})	0.037	0.053	0.019	0.030	0.012	0.006
n-pentane (C_5H_{12})	0.082	0.11	0.037	0.061	0.026	0.009
1,3-butadiene (C_4H_6)	1.2	1.4	0.38	0.086	0.033	bdl
3-methyl-1-butene (C_5H_{10})	0.11	0.13	0.036	0.030	0.010	bdl
t-2-pentene (C_5H_{10})	0.084	0.11	0.023	bdl	bdl;	bdl
2-methyl-2-butene (C_5H_{10})	0.089	0.12	0.019	bdl	bdl	bdl
2-methyl-1-butene (C_5H_{10})	0.11	0.13	0.031	0.013	0.005	bdl
c-2-pentene (C_5H_{10})	0.052	0.067	0.014	bdl	bdl	bdl
n-hexane (C_6H_{14})	0.19	0.22	0.067	0.067	0.027	0.007
Isoprene (C_5H_8)	0.64	0.79	0.15	0.018	0.015	0.018
2-methyl-1-pentene (C_6H_{12})	0.056	0.078	0.016	bdl	bdl	bdl
Heptane (C_7H_{16})	0.074	0.12	0.026	0.022	0.01	0.014
Benzene (C_6H_6)	3.1	3.7	1.2	1.8	0.73	0.096
Toluene (C_7H_8)	2.2	3.1	0.89	1.4	0.47	0.082

[a]Data from Table 2 of *Hobbs et al.* [2003].
Measurements made by gas chromatography [*Colman et al.*, 2001].
Detection limit of 3 pptv.

Table 3.10: Aerosol Mass Concentrations for the Timbavati Plume

Species[a]	Sample 1	Sample 3	Sample 5	Ambient Air
Total Particulate Matter (TPM) (μg/m^3)	1180	232	179	30.1
Organic Carbon (OC) (μg/m^3)	206	57	34	3.6
Black carbon (BC) (μg/m^3)	35	7.7	6.7	0.5
Chloride (μg/m^3)	193	28	5.4	bdl
Nitrate (μg/m^3)	13.6	7.2	9.1	0.78
Sulfate (μg/m^3)	25.0	9.2	8.1	1.2
Potassium (μg/m^3)	70.9	9.5	3.8	0.74

[a]Data from Table 2 of *Hobbs et al.* [2003].
All samples taken using filters via grab bag.
Reported precision for inorganic ions is ±5%. Reported precision for TPM is ±6 μg.

carbon-containing gases that evaporated from the samples were converted to CO_2 over a manganese dioxide catalyst. The CO_2 was then measured with a nondispersive infrared analyzer (Beckman Model 870). The area under the plot of CO_2 concentration versus temperature is proportional to the TC content of the sample. The tandem filter method described by *Turpin et al.* [1994] and *Kirchstetter et al.* [2001] was used to adjust estimates of TC for the positive sampling artifact that results from the adsorption of organic gases on the quartz filters.

Black carbon (BC) concentrations were estimated by *Kirchstetter et al.* [2003] with an optical transmission technique. The method compares the attenuation of white light through a loaded sample filter relative to that of a blank filter. A value of 20 m^2 g^{-1} was used for the mass absorption cross section of BC deposited on quartz based on light absorption and thermal EGA measurements of BC. Aerosol organic carbon (OC) concentration was then estimated as the concentration of TC minus the concentration of BC.

3.5 Timbavati Smoke Plume: Model Initialization

Table 3.11 shows the temperature, pressure, relative humidity, and other parameters used to simulate the conditions of the Timbavati smoke plume. Photolysis rates for Timbavati were derived using TUV v4.1 at 1 km above sea level. The initial plume width (y_o) was set to 2,000 m and K_y was set to 7,000 m^2 s^{-1} [*Trentmann et al.*, 2005].

Tables 3.12 and 3.13 list the gas-phase compounds included in our simulation of the Timbavati smoke plume. Table 3.12 contains the compounds included in the previous modeling study of *Trentmann et al.* [2005]. In addition, Table 3.12 lists the other compounds identified by *Hobbs et al.* [2003] as being present in the Timbavati smoke plume. We include these compounds as well. Furans (at an initial concentration of 18.426 ppbv) were also included in the modeling study of

Table 3.11: Parameters for the Timbavati Plume

Parameter		Value[a]
Date (dd/mm/yyyy)		07/09/2000
Latitude		-24.38
Longitude		31.25
Altitude (kmsl)		0.657
Temperature (K)		288
Pressure (mbar)		900
Relative Humidity		45%
Surface Albedo		0.15
Ozone Column (DU)		288
Time of Model Start	LT	10:45
	UT	8:45
Model Run Time (hr.)		1.00

[a]Values taken from Table III of *Mason et al.* [2006].

Trentmann et al. [2005], but are here assumed unreactive as they are not included in the CACM. The potential sensitivity of ozone formation to furan chemistry is considered in Section 3.6.3 below.

Table 3.13 lists other compounds that have been identified in savannah/grassland smoke but were not listed in the measurements of *Hobbs et al.* [2003]. These compounds might also affect the ozone formation, and thus we add these gas-phase compounds to our model using the emission ratios given by *Andreae and Merlet* [2001].

Table 3.14 shows the initial and background concentrations of aerosols included in the baseline model runs for Timbavati. Since size-distribution data for particles smaller than 0.5 μm in diameter is not available for the Timbavati fire, we must estimate the size distribution for the initial smoke aerosol from literature values. The mean geometric diameter D_g and standard deviation σ for the initial smoke are from *Reid and Hobbs* [1998]. The initial number concentration and aerosol composition were chosen to match the mass concentrations reported for Sample 1 by *Hobbs et al.* [2003]. In the absence of measurements of aerosol ammonium, we assumed that sufficient ammonium was present to neutralize the measured anions. Furthermore, we assumed that the initial aerosol OC was 60% water-soluble organic carbon (WSOC) and 40% insoluble OC, based on *Decesari et al.* [2006] which reports 64% WSOC on average for fine mode biomass burning aerosols in Brazil. Cellobiosan (CBIO) was used as a proxy for the initial WSOC, while long-chain alkanes (POA1) were used as a proxy for the insoluble OC.

The background aerosol number concentration in Table 3.14 matches the value reported by *Hobbs et al.* [2003]. D_g for this mode is for remote continental aerosols [*Seinfeld and Pandis*, 1998], where σ has been increased to match the aerosol mass concentrations reported by *Hobbs et al.* [2003]. The background aerosol mass composition also assumes that sufficient ammonium is

Table 3.12: Background and Initial Gas Concentrations for the Timbavati Plume

Species	Background (ppbv)	Emission Ratio (mol/mol CO as %)	Initial Conc. (ppbv)	CACM Classification
From *Trentmann et al.* [2005], Table 3				
CO	182	-	4900	-
CH_4	1774	5.83	2049.1	-
C_2H_6	0.86	0.3	15.0	ALKL
C_2H_4	0.32	1.6	75.8	ETHE
C_3H_8	0.11	0.0525	2.6	ALKL
C_3H_6	0.031	0.235	11.1	OLEL
C_4H_8	0	0.033	1.6	OLEL
HCHO	0.855	1.87	89.1	-
$OHCH_2CHO$	0.304	0.316	15.2	ALD2
CH_3CHO	0.304	0.678	32.3	ALD2
CH_3OH	2.5	1.45	70.9	MEOH
HC(O)OH	0.225	0.64	30.4	ACID
$CH_3C(O)OH$	0.6	1.46	69.5	ACID
$CH_3C(O)CH_3$	3.6	0.128	9.6	KETL
$C_3H_6O_2$	0	0.33	15.6	KETL
C_6H_5OH	0	0.346	16.3	AROO
$C_6H_5CH_3$	0	0.078	3.7	AROH
C_5H_8	0	0.02	0.9	ISOP
C_3H_6O	0	0.166	7.8	OLEL
$CH_3COC_2H_5$	0	0.286	13.5	KETL
NO	0.296	1.16	55.0	-
NO_2	0.46	2.6	123.1	-
HONO	0	0.122	5.8	-
SO_2	10	1.28	70.4	-
NH_3	0.478	0.16	8.0	-
H_2	540	25.7	1752.5	-
From *Hobbs et al.* [2003], Table 2 (Ambient and Sample 2)				
i-butane	0.009	3.62×10^{-3}	0.18	ALKL
n-butane	0.023	9.47×10^{-3}	0.47	ALKL
trans-2-butene	0	8.90×10^{-3}	0.42	OLEL
cis-2-butene	0	6.57×10^{-3}	0.31	OLEL
i-pentane	0.006	9.96×10^{-4}	0.053	ALKL
n-pentane	0.009	2.14×10^{-3}	0.11	ALKL
butadiene	0	2.97×10^{-2}	1.4	OLEL
3-methyl-1-butene	0	2.76×10^{-3}	0.13	OLEL
trans-2-pentene	0	2.33×10^{-3}	0.11	OLEL
2-methyl-2-butene	0	2.54×10^{-3}	0.12	OLEL
2-methyl-1-butene	0	2.76×10^{-3}	0.13	OLEL
c-2-pentene	0	1.42×10^{-3}	0.067	OLEL
n-hexane	0.007	4.51×10^{-3}	0.22	ALKL
2-methyl-1-pentene	0	1.65×10^{-3}	0.078	OLEL
heptane	0.014	2.25×10^{-3}	0.12	ALKM

Table 3.13: Background and Initial Gas Concentrations for the Timbavati Plume (continued)

Species	Background (ppbv)	Emission Ratio (mol/mol CO as %)	Initial Conc. (ppbv)	CACM Classification
From *Andreae and Merlet* [2001], Table 1 (Savannah and Grassland)				
1-butene	0	6.91E-02	3.26	OLEL
i-butene	0	2.30E-02	1.09	OLEL
1-pentene	0	1.35E-02	0.64	OLEL
2-methyl-butane	0	6.57E-03	0.31	ALKL
cyclopentene	0	7.59E-03	0.36	OLEL
4-methyl-1 pentene	0	2.46E-02	1.16	OLEL
1-hexene	0	1.89E-02	0.89	OLEL
isohexanes	0	2.50E-02	1.18	ALKL
octenes	0	2.11E-03	0.10	OLEH
terpenes	0	4.82E-03	0.23	half BIOL, half BIOH
xylenes	0	1.83E-02	0.86	AROL
ethylbenzene	0	5.28E-03	0.25	AROH
styrene	0	9.93E-03	0.47	OLEL
PAHs	0	6.63E-04	0.03	PAH
ethanol	0	1.03E-02	0.49	ETOH
1-propanol	0	1.79E-02	0.85	ALCH
butanols	0	4.65E-03	0.22	ALCH
cyclopentanol	0	1.60E-02	0.76	ALCH
acrolein	0	6.15E-02	2.90	MCR
propanal	0	6.68E-03	0.32	ALD2
butanals	0	3.17E-02	1.49	ALD2
hexanals	0	5.60E-03	0.26	ALD2
heptanals	0	1.13E-03	0.05	ALD2
2,3-butanedione	0	2.85E-01	13.45	KETL
pentanones	0	7.51E-03	0.35	KETL
heptanones	0	2.27E-03	0.11	KETH
octanones	0	5.05E-03	0.24	KETH
benzaldehyde	0	1.18E-02	0.56	ARAL
methyl formate	0	1.08E-02	0.51	KETL
methyl acetate	0	3.20E-02	1.51	KETL

Table 3.14: Initial and Background Aerosol Concentrations for the Timbavati Plume

Parameter	Initial Concentration	Background Concentration
Number Concentration (cm^{-3})	116,000[a]	1000[e]
D_g	0.11[b]	0.116[f]
σ	1.91[b]	2.0[f]
KCl	16.93%[c]	-
NH_4Cl	25.50%[c]	-
NH_4NO_3	2.19%[c]	10.41%[g]
$(NH_4)_2SO_4$	4.28%[c]	4.13%[g]
K_2SO_4	-	17.00%[g]
BC	4.36%[c]	5.16%[g]
POA1	12.04%[c,d]	-
CBIO	34.69%[c,d]	-
CPD3	-	63.30%[g]

[a] Number concentration chosen to match mass concentrations of Sample 1 in Table 3.10.
[b] Values taken from *Reid and Hobbs* [1998].
[c] Values are mass percentage, chosen to match composition of Sample 1.
[d] Assumes OC is 60% water soluble (modeled as CBIO)
and 40% insoluble (as POA1) [*Decesari et al.*, 2006].
[e] Background number concentration reported by *Hobbs et al.* [2003].
[f] Remote continental size distribution from *Seinfeld and Pandis* [1998] p. 430,
with σ increased to match mass concentrations reported by *Hobbs et al.* [2003].
[g] Values are mass percentage, chosen to match composition reported by *Hobbs et al.* [2003].

present to neutralize the cations, and assumes that the background aerosol OC can be represented by humic acid (CPD3).

3.6 Timbavati Smoke Plume: Results and Comparison to Observations

Figure 3-16 shows the modeled and observed CO concentrations for the Timbavati smoke plume. The vertical error bars represent the reported precision of the AFTIR [*Yokelson et al.*, 2003] and canister [*Colman et al.*, 2001] measurements while the horizontal error bars represent the uncertainty in the Lagrangian age of the smoke samples due to the variation in the horizontal wind speed. The solid black line shows the modeled CO concentration for the best-fit value of K_y (7,000 m^2 s^{-1}). As we can see, there is significant variation in measured CO values about this best-fit line. Figure 3-17 shows similar variability when we plot the sum of the CO and CO_2 concentrations in the smoke plume, suggesting the variability in CO is not due to variability in combustion efficiency, but due to the variability of plume dispersion and the heterogeneity of the plume. Following *Trentmann et al.* [2005], we accounted for this variability in plume dispersion by performing two

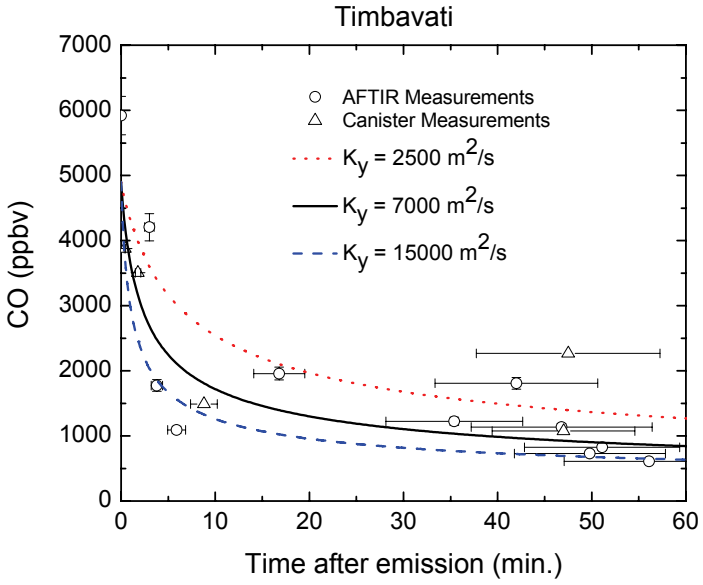

Figure 3-16: Modeled and measured CO concentrations for the Timbavati plume.

additional models runs, one with a low (slow) K_y of 2,500 m^2 s^{-1} and one with a high (fast) K_y of 15,000 m^2 s^{-1}.

Figure 3-18 shows the modeled and measured O_3 concentration for the baseline model run of the Timbavati plume using the three values of K_y discussed above. As in the results of *Trentmann et al.* [2005] and *Mason et al.* [2006], our baseline model underestimates the formation of O_3 within the smoke plume. In addition, the baseline chemistry model runs underestimate the concentration of OH relative to the reported value.

Figure 3-19 compares the observed and modeled aerosol mass concentrations at 47 minutes downwind from the fire source. The observed concentrations are from Sample 5 of Table 3.10, and the model runs all use the baseline chemistry and the medium K_y of 7000 m^2 s^{-1}. We can see that the baseline model run overestimates the concentration of potassium (K^+) downwind, as well as underestimating the ratios of nitrate, sulfate, and OC to potassium.

Given the poor match between the model simulations using the baseline chemistry and the available observations, we explored many hypotheses to attempt to improve the match between the model and observations. Below we discuss several sensitivity tests we performed on the model for the Timbavati smoke plume to address the overestimate of K^+, the underestimate of OC, the underestimate of O_3 and OH, the underestimate of sulfate, and the underestimate of gas-phase

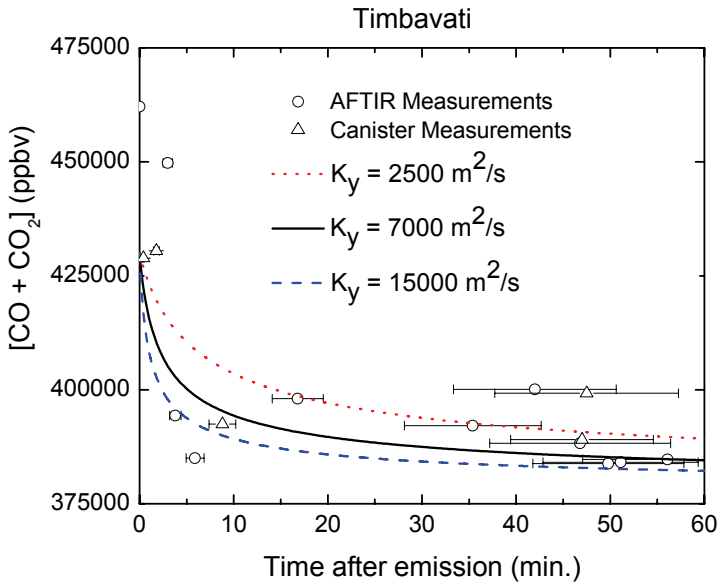

Figure 3-17: Modeled and measured CO_x [CO+CO_2] concentrations for the Timbavati plume.

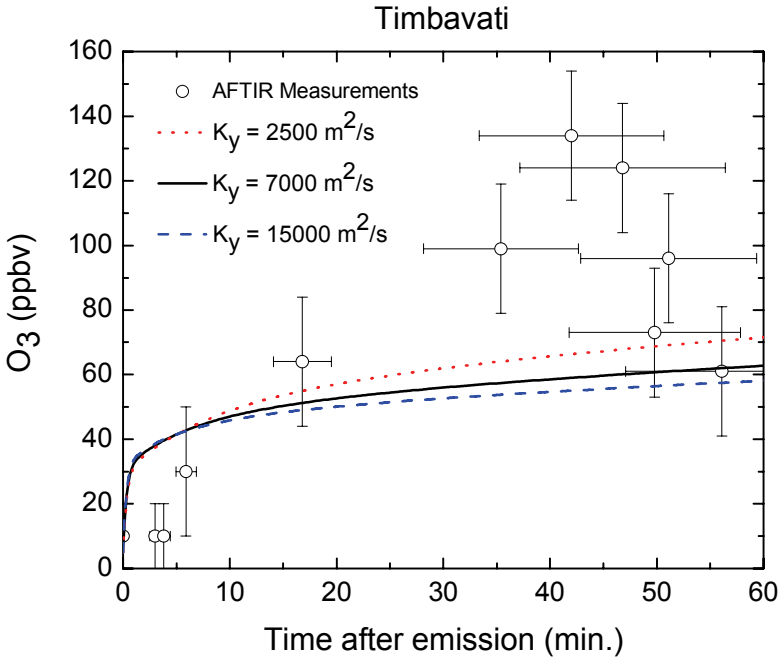

Figure 3-18: Baseline modeled and measured O_3 for the Timbavati smoke plume. The model runs shown here use the baseline model chemistry.

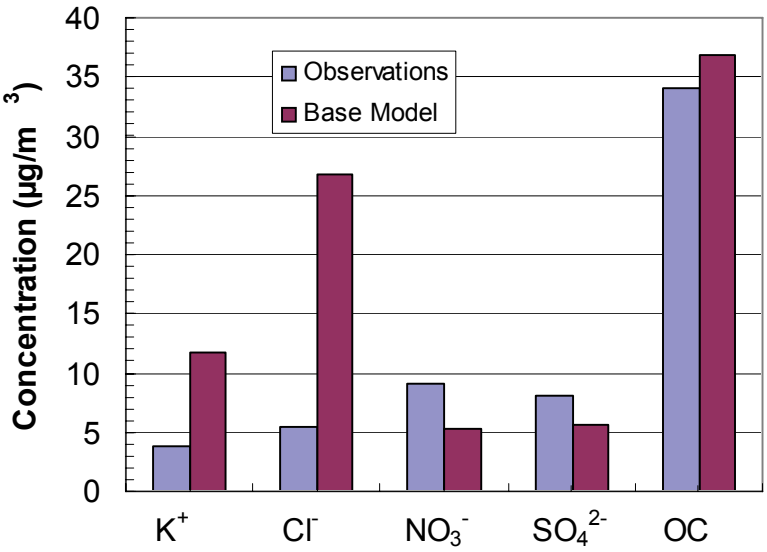

Figure 3-19: Baseline modeled and observed aerosol mass concentrations at 47 minutes downwind from fire source. The observed concentrations are from Sample 5 in Table 3.10 above. Modeled concentrations use the baseline chemistry and K_y of 7000 m^2 s^{-1}.

organic acids. We explore the sensitivity of the modeled aerosol mass concentrations to heterogeneous reactions of NO_2, SO_2, and CH_3OH. We then use these sensitivity tests to design an expanded chemistry case and explore the growth of aerosols, change in aerosol number concentration, and change in aerosol optical properties in the expanded chemistry case.

3.6.1 Potassium (K^+) Concentrations

The model overpredicts the downwind potassium concentration when it is initialized with the potassium value measured 1 km downwind of the fire source (Sample 1 in Table 3.10). In the observations reported by *Hobbs et al.* [2003], the ratio of excess[2] K^+ to excess CO decreases with time, from a value of 21 μg m^{-3} K^+/ppmv CO at a distance of 1 km from the fire source to a value of 6.9 μg m^{-3} K^+/ppmv CO at 5 km downwind and to 3.6 μg m^{-3} K^+/ppmv CO at 26.2 km downwind. However, since the deposition of submicron particles and the chemical loss of CO are both small on the 1 hour time scale considered here, both aerosol K^+ and gas-phase CO should be acting as conservative tracers, with a constant ratio between them as they move downwind.[3]

[2]Here, "excess" refers to the concentration of a substance in the smoke plume minus the concentration of the substance in the background, environmental air.

[3]Note that the deposition velocity of particles is already included in the baseline model simulation.

It is possible that this discrepancy could be explained by different initial ratios of K^+ and CO being produced by the savannah fire. However, the large fluctuations of a factor of 6-7 implied by this explanation, plus the fact that the ratio monotonically decreases, make this explanation seem unlikely. *Hobbs et al.* [2003] address this concern by pointing out that the fire was predominantly flaming and was consistently moving into fresh fuel, with modified combustion efficiency (MCE) values of 0.91-0.94 (except for one outlier of 0.88 in a non-aerosol sample). In addition, if the ratio of K^+ to CO was fluctuating randomly, the odds of a monotonically decreasing sequence would be 1 out of 6 - not impossible, but unlikely.

Instead, we propose that the observed decrease in the ratio is an artifact of the different sampling methods and averaging times of the aerosol and CO measurements made during the Timbavati fire. The canister sampling used to measure CO in this case had an averaging time of approximately 30 s, while the "grab bag" techniques used for the aerosol filter sampling had an averaging time of 7-12 s. Thus, near the source the canister measurements may have sampled a larger proportion of background air than the aerosol measurements, leading to an upward bias in the ratio of excess K^+ to excess CO. As the plume expanded horizontally, this bias decreased, explaining the monotonic decrease of the ratio.

Based on this argument, we reduced the initial aerosol mass concentrations in the model to better match the observed downwind concentration of K^+ while keeping the geometric mean diameter and the standard deviation of the log-normal submicron mode constant. The rescaling reduced the initial aerosol mass concentration by a factor of 3.4. This resulted in a lower initial total number concentration (34,000 cm^{-3}). To keep the initial aerosol number concentration near the observed value of 100,000 cm^{-3}, we added a second small-aerosol log-normal mode with a number concentration of 66,000 cm^{-3}, geometric mean diameter of 0.02 μm, and geometric standard deviation of 1.175. This mode, which starts in the smallest size bin of the model, has the same composition as the sub-micron mode, but its small size means it has a negligible impact on the mass concentrations of the aerosol. The rescaled initial aerosol concentrations are shown in Table 3.15. The rescaled aerosol is used in all of the model runs discussed below.

3.6.2 Organic Carbon (OC) Concentrations

When the initial aerosol is rescaled to reflect the downwind concentration of potassium, the baseline model chemistry underpredicts the secondary formation of aerosol organic carbon (OC) within the Timbavati smoke plume. This suggests that the baseline mode is missing a source of secondary condensed organic matter. The laboratory study of *Christian et al.* [2003] suggested that 30%

Table 3.15: Rescaled Initial and Background Aerosol Concentrations for the Timbavati Plume

Parameter	Initial Concentration		Background Concentration
	Mode 1	Mode 2	
Number Concentration $\left(cm^{-3}\right)$	34,000[a]	66,000	1000[e]
D_g (μm)	0.11[b]	0.02	0.116[f]
σ	1.91[b]	1.175	2.0[f]
KCl	16.93%[c]	16.93%[c]	-
NH_4Cl	25.50%[c]	25.50%[c]	-
NH_4NO_3	2.19%[c]	2.19%[c]	10.41%[g]
$(NH_4)_2SO_4$	4.28%[c]	4.28%[c]	4.13%[g]
K_2SO_4	-	-	17.00%[g]
BC	4.36%[c]	4.36%[c]	5.16%
POA1	12.04%[c,d]	12.04%[c,d]	-
CBIO	34.69%[c,d]	34.69%[c,d]	-
CPD3	-	-	63.30%

[a] Number concentration chosen to match mass concentrations of Sample 1 in Table 3.10.
[b] Values taken from *Reid and Hobbs* [1998].
[c] Values are mass percentage, chosen to match composition of Sample 1.
[d] Assumes OC is 60% water soluble (modeled as CBIO)
and 40% insoluble (as POA1) [*Decesari et al.*, 2006].
[e] Background number concentration reported by *Hobbs et al.* [2003].
[f] Remote continental size distribution from *Seinfeld and Pandis* [1998],
with σ increased to match mass concentrations reported by *Hobbs et al.* [2003].
[g] Values are mass percentage, chosen to match composition reported by *Hobbs et al.* [2003].

of the carbon emitted as non-methane organic compounds (NMOCs) is unidentified by current techniques. If these species reacted to form condensed organic carbon, they could explain the observed formation of OC.

To test this possibility, we included the uncharacterized compounds in our model. Using the NMOC initial concentrations from Tables 3.12 and 3.13, we estimated that 600 ppbv of carbon is uncharacterized in the initial emissions from the Timbavati smoke plume. We used monoterpenes (BIOH) as a proxy compound for these uncharacterized organic species, giving an initial concentration of 60 ppbv BIOH, as monoterpenes have 10 carbons per molecule. Note that we are not saying that the uncharacterized compounds are monoterpenes - we are merely using the BIOH compound class in the model as a proxy for a high molecular weight, reactive organic compound.

Including the uncharacterized compounds in the chemical model as BIOH increased the secondary formation of organic aerosol. Using the rescaled initial aerosol and including the uncharacterized organic compounds, the modeled concentration of organic carbon at 47 minutes downwind is 30.9 μg/m^3, close to the observed value of 34 μg/m^3. This model result is slightly sensitive to our assumed accommodation coefficient (α) for organic vapors of 0.1. Reducing the accommoda-

tion coefficient by a factor of 10 to 0.01 only decreases the modeled organic carbon concentration at 47 minutes downwind from 30.9 $\mu g/m^3$ to 30.3 $\mu g/m^3$, a reduction of about 2%. However, an accommodation coefficient of 10^{-3} reduces the modeled organic carbon concentration at 47 minutes to 21.5 $\mu g/m^3$, a reduction of about 30%.

There are two potential interpretations of the secondary organic aerosol formation from uncharacterized compounds suggested by our work. The first is that these uncharacterized compounds are emitted directly to the gas-phase by the fire, where they react and form secondary compounds that then condense onto the aerosol. The second possibility is that the uncharacterized compounds are intermediate volatility organic compounds as defined by *Robinson et al.* [2007]. In this scenario, the uncharacterized compounds are initially present on the smoke aerosol, but rapidly evaporate into the gas-phase due to the dilution of the smoke emissions in the first minute. These compounds, now in the gas-phase, react and form secondary products that can condense onto the aerosol. Our model results are consistent with both interpretations, but further field and laboratory research is needed to determine the identity, history, and fate of the uncharacterized organic compounds in biomass burning smoke plumes.

3.6.3 O_3 and OH Concentrations

As seen in Figure 3-18, our baseline model chemistry underestimates the formation of ozone observed for the Timbavati smoke plume. We examined four possible explanations: (1) that the oxidation of oxygenated organic species not included in the baseline model is responsible for the high observed O_3 formation; (2) that heterogeneous reactions taking place on the aerosol particles are responsible for the high levels of O_3 observed; (3) that parametric uncertainty in the rate constants of our chemical mechanism are responsible for the underprediction of ozone by the model; and (4) that electrical discharges (lightning) within the plume could have acted as a source of NO_x within the plume, increasing O_3 formation.

Unidentified Oxygenates

The first hypothesis is that oxygenated species, such as ketones, aldehydes, alcohols, or furans, which are not included in the baseline model are responsible for the ozone formation observed in the Timbavati smoke plume. These compounds might not have been identified in previous measurements as these species might react on the walls of the sampling canisters prior to analysis. Thus, they are in addition to the uncharacterized organic compounds we included in the model as BIOH.

To test this hypothesis, we ran sensitivity tests where additional ketones (KETL, KETH), aldehydes (ALD2), alcohols (ALCH), and furans were added to the initial concentrations. As furan chemistry is not included in the CACM, we designed an addition to the mechanism to include the chemistry of furans. This mechanism is shown in Table 3.16. Figure 3-20 shows the assumed structures for the lumped species FURAN, RP20, $RO_2$59 and $RO_2$60 used in the mechanism. The reaction rates for FURAN are based on 2-methylfuran [*Bierbach et al.*, 1995], while those for RP20 are based on butenedial [*Bierbach et al.*, 1994].

Table 3.16: Lumped Chemical Mechanism for Furans Used in this Work

Reaction	A	n	E_a (K)	Ref.
FURAN + OH => HO_2 + RP20	6.2e-11	0	0	1
RP20 + OH => 0.53 $RO_2$59 + 0.47 $RO_2$60 + RO_2T	5.6e-11	0	0	2
RP20 => UR25	-	-	-	3
$RO_2$59 + NO => NO_2 + HO_2 + UR24	2.08e-12	0	180.0	4
$RO_2$59 + HO_2 => OH + HO_2 + UR24	3.14e-13	0	800.2	4
$RO_2$59 + RO_2_T => HO_2 + UR24 + RO_2T	1.0e-15	0	0	4
$RO_2$60 + NO => NO_2 + HO_2 + 2.0 MGLY	2.08e-12	0	180.0	4
$RO_2$60 + HO_2 => OH + HO_2 + 2.0 MGLY	3.14e-13	0	800.2	4
$RO_2$60 + RO_2T => HO_2 + 2.0 MGLY + RO_2T	1.0e-15	0	0	4

References: 1, *Bierbach et al.* [1995]; 2, *Bierbach et al.* [1994]
3, Assumed equal to ALD2
4, Stoichiometry adapted from University of Leeds Master Chemical Mechanism (http://mcm.leeds.ac.uk/) with reaction rates adapted from CACM and *Jenkin et al.* [1997].

Table 3.17 shows the change in the modeled ozone concentration at 60 minutes downwind when 30 ppbv of KETL, KETH, ALD2, and ALCH are added, respectively, and when 18.426 ppbv of FURAN is added using the above mechanism. As we can see, the final ozone concentration at 60 minutes is fairly insensitive to the concentrations of these oxygenated compounds, and the changes observed are not large enough to explain the high concentrations of ozone observed in the Timbavati fire.

Heterogeneous Formation of HONO

Our second hypothesis was that heterogeneous reactions taking place on the aerosol particles are responsible for the high levels of O_3 observed. This was suggested by model runs we performed where we fixed the OH concentration in the model at the reported value of 1.7×10^7 radicals/cm^3 [*Hobbs et al.*, 2003]. As is shown in Table 3.17, fixing the model OH at this level dramatically increased the modeled concentration of O_3 and greatly improved the match between the model and the observations. This suggests that the baseline model chemistry is missing a source of OH.

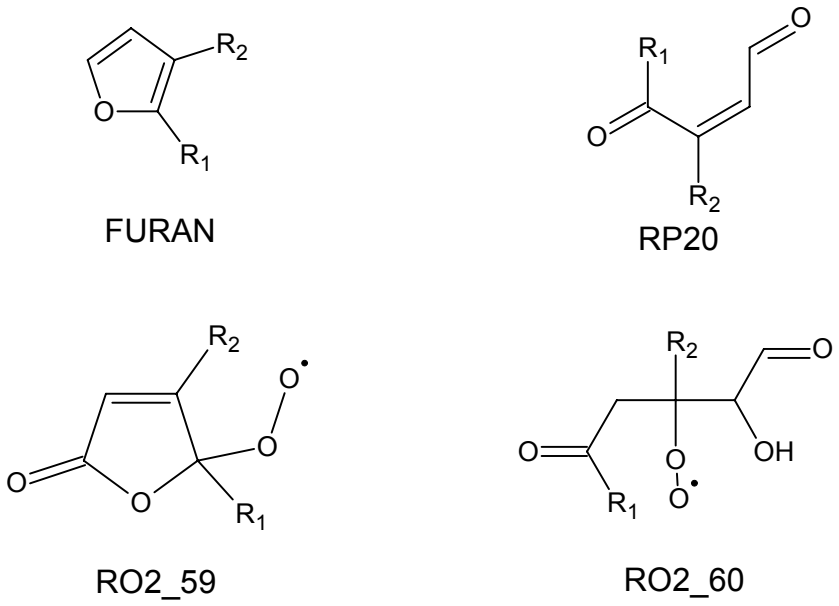

Figure 3-20: Assumed structures for compounds in the furan machanism.

Table 3.17: Results of Ozone Sensitivity Tests

	O_3 (ppbv) at 60 min.	
	K_y = 7000 m^2/s	K_y= 2500 m^2/s
Reference (with 60 ppbv BIOH)	71.8	86.5
+30 ppbv KETL	72.2 (+0.4)	87.1 (+0.6)
+ 30 ppbv KETH	-	87.1 (+0.6)
+30 ppbv ALD2	72.3 (+0.5)	87.3 (+0.8)
+30 ppbv ALCH	-	89.1 (+2.6)
+ Furan Mechanism	-	90.7 (+4.2)
+ CH_3OH-NO_2 Hetero. Rxn (Rate x10)	76.1 (+4.3)	100.4 (+13.9)
+ $\gamma_{NO_2 \rightarrow 0.5HONO+0.5HNO_3} = 10^{-3}$	77.3 (+5.5)	99.5 (+13.0)
+ $\gamma_{NO_2 \rightarrow HONO} = 10^{-3}$	82.6 (+10.8)	110.6 (+24.1)
OH fixed at 1.7×10^7 radicals/cm^3	109.4 (+37.6)	144.4 (+57.9)
Observations	60-135	

We explored the possibility that this missing source of OH came from heterogeneous production of HONO within the smoke plume. In this scheme, NO_2 reacts on the surface of particles to produce HONO, which then photolyzes to produce OH and NO. Heterogeneous production of HONO has been reported to take place on humic acid aerosols [*Stemmler et al.*, 2006, 2007], aqueous aerosols [*Jacob*, 2000], and soot aerosols [*Nienow and Roberts*, 2006]. We investigated two different reaction stoichiometries. The first ($NO_2 \rightarrow$ HONO) was reported by *Stemmler et al.* [2006, 2007] to take placed on light-activated humic acid aerosol surfaces with an uptake coefficient of 10^{-5}-10^{-6}. The second ($NO_2 \rightarrow 0.5$ HONO + 0.5 HNO_3) has been reported by many investigators to take place on aqueous aerosols. The review of *Jacob* [2000] reports uptake coefficients ranging from 10^{-3}-10^{-6}, and recommends a value of 10^{-4} for this reaction.

A third possibility for heterogeneous chemistry was proposed by *Trentmann et al.* [2005]. They found that including the reaction of methanol and NO_2 (CH_3OH + 2 $NO_2 \rightarrow HO_2$ + HCHO + HNO_3 + NO) in their model increased the ozone formation in the Timbavati smoke plume when they increased the reaction rate to 10 times the value originally reported by *Tabazedeh et al.* [2004] for this reaction on cloud droplets.

Figure 3-21 shows the ozone concentration predicted when the three heterogeneous reactions are included. In the figure, an uptake coefficient of 10^{-3} is used for both NO_2 reactions. We found that uptake coefficients lower than this value resulted in negligible changes to O_3 and OH concentrations. In addition, the rate of the methanol reaction has been increased by a factor of 10 as in *Trentmann et al.* [2005]. All runs were performed at the slow horizontal diffusion rate (K_y = 2500 m^2/s) and include the uncharacterized organic compounds as monoterpenes. These impact of these reactions is also shown in Table 3.17. We can see that, with these high uptake coefficients, these three reactions do an equally good job of explaining the formation of O_3 in the Timbavati smoke plume, and still underestimate the highest values of ozone observed.

Of these three cases, including the reaction $NO_2 \rightarrow$ HONO provides the best match to the reported OH concentration (not shown), while including $NO_2 \rightarrow 0.5$ HONO + 0.5 HNO_3 provides the best match to the observed aerosol nitrate concentration (see Figure 3-32). Furthermore, the uptake coefficient of 10^{-3} used above is within the range of reported values for the reaction $NO_2 \rightarrow$ 0.5 HONO + 0.5 HNO_3 on aqueous aerosols, but is outside the range reported for the reaction $NO_2 \rightarrow$ HONO on humic acid aerosols. Thus, of the three heterogeneous reactions considered here the reaction $NO_2 \rightarrow 0.5$ HONO + 0.5 HNO_3 with an uptake coefficient of 10^{-3} is the most consistent with the available observations for the Timbavati fire.

As stated above, including the heterogeneous formation of HONO from NO_2 with an uptake

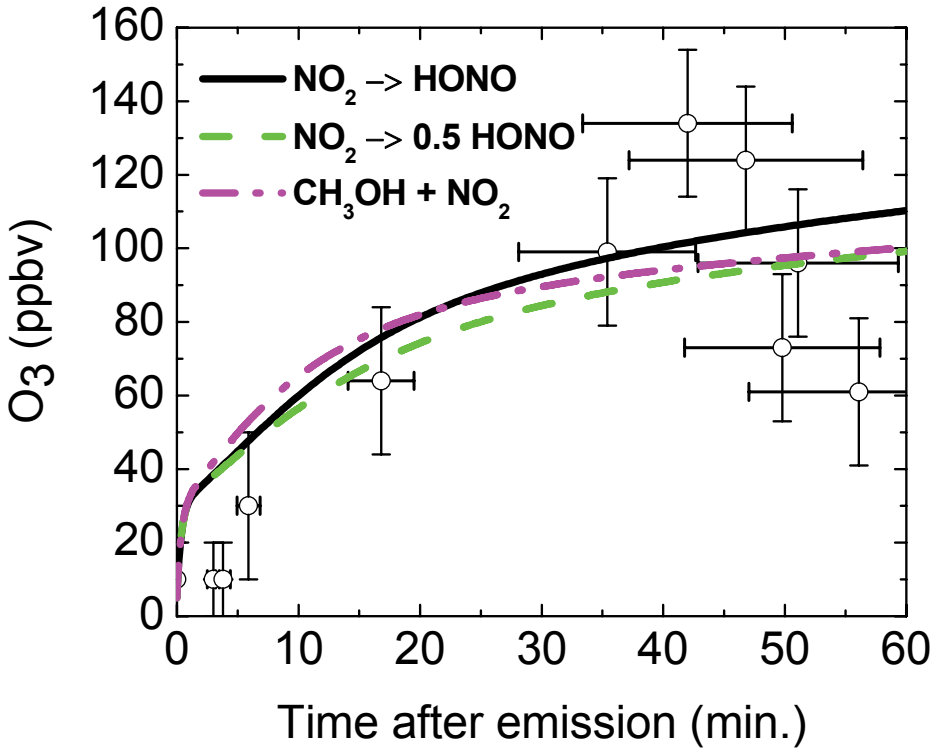

Figure 3-21: Ozone formation predicted when different heterogeneous reactions are included. The uptake coefficients are 10^{-3} for both NO_2 reactions, and the rate of the methanol reaction has been increased by a factor of 10. All runs were performed at slow dilution rate (K_y = 2500 m^2/s) and include the uncharacterized organic compounds as monoterpenes.

coefficient of less than 10^{-3} results in a negligible increase in the modeled ozone concentrations. Reported uptake coefficients for NO_2 on aerosol surfaces vary over several orders of magnitude: measured uptake coefficients on aqueous aerosols vary from 10^{-3} to 10^{-6} [*Jacob*, 2000], while measured uptake coefficients on soot aerosols vary from 10^{-3} to 10^{-8} [*Nienow and Roberts*, 2006]. Given this large uncertainty and variability, the uptake coefficient of NO_2 on biomass burning aerosols deserves further laboratory and field investigation.

In addition, it is possible that the true aerosol surface area concentration is larger than that assumed in our model. Our model determines the aerosol surface area concentration by assuming that all particles are spherical. However, soot particles in young biomass burning smoke can have fractal shapes (see, for example, the pictures of *Posfai et al.* [2003]). For these fractal particles, the actual surface area may be much larger than our calculated value, and could increase the rate of heterogeneous HONO production at lower values of the uptake coefficient. For example, if we assume that the true aerosol surface area is greater than the calculated value by a factor of 10, including the reaction $NO_2 \rightarrow 0.5$ HONO + 0.5 HNO_3 with an uptake coefficient of 10^{-4} gives an ozone concentration at 60 minutes of 99.5 ppbv[4], identical to using the calculated surface area concentration and an uptake coefficient of 10^{-3}.

One may ask how the reaction $NO_2 \rightarrow 0.5$ HONO + 0.5 HNO_3 would change the results for the Otavi and Alaska smoke plumes discussed above. For the Otavi fire, we are able to use measurements of the total aerosol number concentration in this smoke plume to estimate the effect of the heterogeneous production of HONO on ozone formation. We find that the impact of the heterogeneous chemistry is negligible in the Otavi smoke plume, as the initial NO_x concentrations are a factor of 10 lower than in Timbavati and the initial total aerosol number concentration is a factor of 3 lower. For Alaska, no measurements of total aerosol number concentration are available, so we cannot perform a model run to evaluate this case. However, the initial NO_x concentration for the Alaska smoke plume is comparable to Timbavati, suggesting that this heterogeneous chemistry could also boost the modeled ozone formation in the Alaska plume by 10-20 ppbv. As can be seen in Figure 3-9 above, this increase in ozone would give a somewhat better match to the observations than the baseline chemistry model. The increased loss of NO_x due to the heterogeneous reactions would also provide a better match with observations of NO and NO_2 for the Alaska fire. Thus the proposed heterogeneous reaction is consistent with the observations of all three smoke plumes considered in this thesis.

[4]This run uses the slow horizontal diffusion rate of 2500 m^2/s and includes the uncharacterized compounds as BIOH.

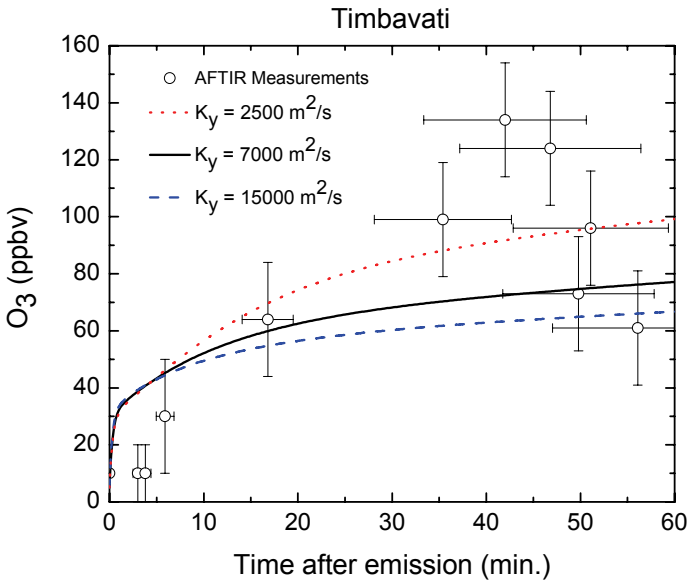

Figure 3-22: Modeled and measured ozone concentrations for the Timbavati smoke plume (expanded chemistry case). Model runs include the heterogeneous reaction $NO_2 \rightarrow 0.5$ HONO + 0.5 HNO_3 ($\gamma_{NO_2} = 10^{-3}$) and include the uncharacterized compounds as BIOH.

Based on the above results, we added the heterogeneous reaction $NO_2 \rightarrow 0.5$ HONO + 0.5 HNO_3 to our model runs, using an uptake coefficient of 10^{-3} and included the uncharacterized compounds as BIOH. We now discuss how this expanded chemistry case compares with the gas-phase composition measurements made in the Timbavati smoke plume.

Figure 3-22 shows the modeled and measured ozone concentrations for our expanded chemistry case. We can see that the addition of heterogeneous formation of HONO has increased the modeled O_3 concentrations above the baseline runs. However, the expanded chemistry case still has difficulty matching the two highest ozone observations for the Timbavati smoke plume.

Figures 3-23 and 3-24 compare the modeled NO and NO_2 concentrations, respectively, for the expanded chemistry case to the available airborne FTIR measurements in the Timbavati plume. Measurements that were below detection limits are plotted at 10 ppbv (half of the detection limit) with an uncertainty from 0 to 20 ppbv. As we can see, the high detection limits mean that all three horizontal diffusion rates modeled are consistent with the available downwind observations of NO_x, which are generally below the detection limit. These large error bars mean that the observations of NO_x don't give us much information on the chemical state of the Timbavati smoke plume.

Figures 3-25 and 3-26 show the modeled concentrations of HONO and OH, respectively, for

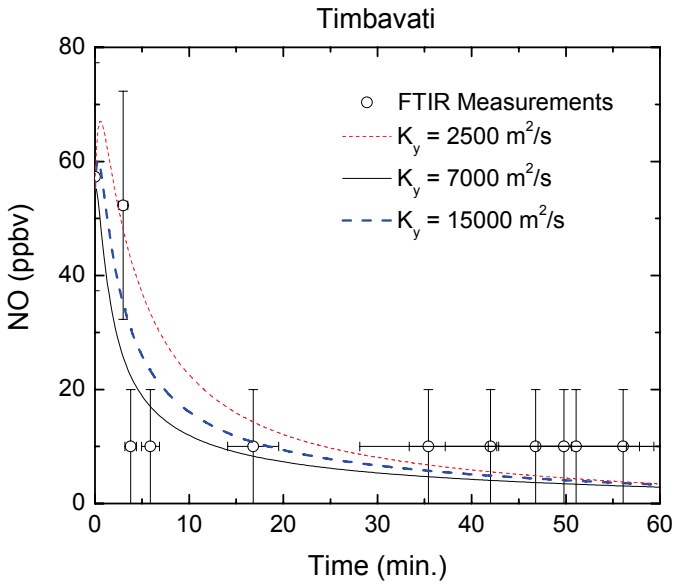

Figure 3-23: Modeled and measured NO concentrations for the Timbavati smoke plume (expanded chemistry case). Model runs include the heterogeneous reaction $NO_2 \rightarrow 0.5$ HONO + 0.5 HNO_3 ($\gamma_{NO_2} = 10^{-3}$) and include the uncharacterized compounds as BIOH.

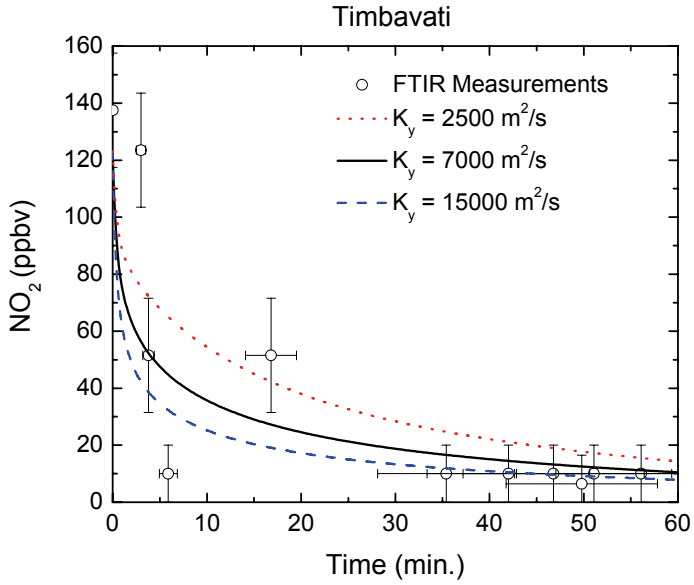

Figure 3-24: Modeled and measured NO_2 concentrations for the Timbavati smoke plume (expanded chemistry case). Model runs include the heterogeneous reaction $NO_2 \rightarrow 0.5$ HONO + 0.5 HNO_3 ($\gamma_{NO_2} = 10^{-3}$) and include the uncharacterized compounds as BIOH.

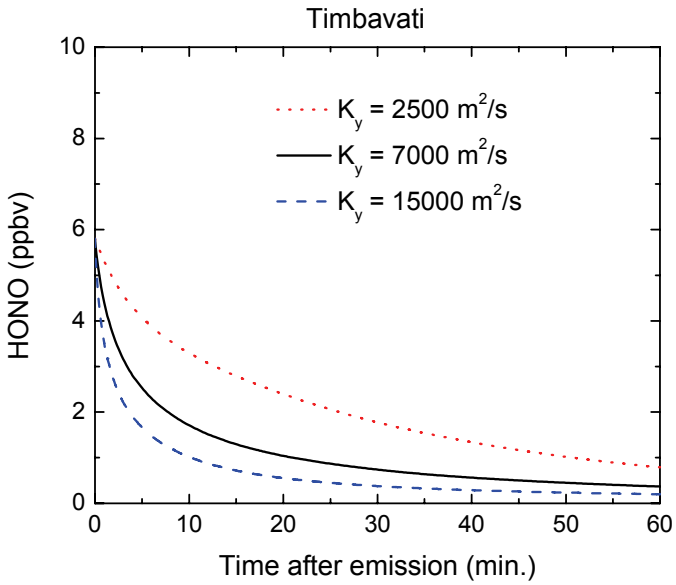

Figure 3-25: Modeled and measured HONO concentrations for the Timbavati smoke plume (expanded chemistry case). Model runs include the heterogeneous reaction $NO_2 \rightarrow 0.5$ HONO + 0.5 HNO_3 ($\gamma_{NO_2} = 10^{-3}$) and include the uncharacterized compounds as BIOH.

the expanded chemistry case. Figure 3-25 shows that the modeled HONO concentration in the expanded case stays between 0.5 ppbv and 6 ppbv over the hour simulated here. These HONO concentrations are well below the detection limit for HONO by AFTIR (~20 ppbv; R. Yokelson, personal communication 2006) and thus the available AFTIR measurements cannot be used to rule in or rule out the possibility of heterogeneous HONO formation. Figure 3-26 shows that the OH concentrations in the expanded chemistry model cases show a maximum of 8×10^6 radicals/cm^3, about half of the reported value of 1.7×10^7 radicals/cm^3.

Figures 3-27, 3-28, 3-29, and 3-30 compare the modeled concentrations of CH_3OH, ETHE, HCHO, and ACID, respectively, for the expanded chemistry case to the available observations. Measurements below the detection limit are plotted at half their detection limit with uncertainty bars covering the range from the detection limit to 0. The observations of ACID in Figure 3-30 represent the sum of the observations of formic and acetic acid. In general, the large uncertainty in the airborne FTIR measurements means that the model runs are consistent with the available observations. The model may be underestimating the concentrations of ETHE, HCHO, and ACID downwind, but the large uncertainty in the AFTIR measurements means that our model is consistent with most of the downwind observations to within the measurement uncertainty.

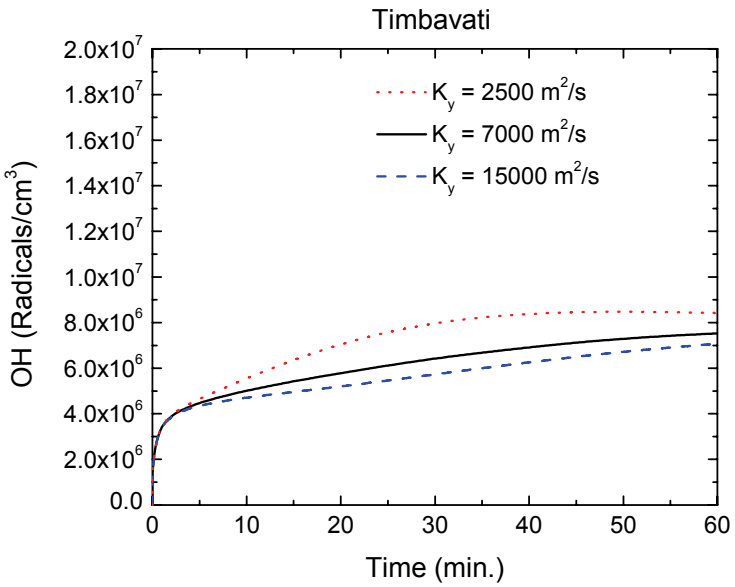

Figure 3-26: Modeled and measured OH concentrations for the Timbavati smoke plume (expanded chemistry case). Model runs include the heterogeneous reaction $NO_2 \rightarrow 0.5$ HONO + 0.5 HNO_3 ($\gamma_{NO_2} = 10^{-3}$) and include the uncharacterized compounds as BIOH.

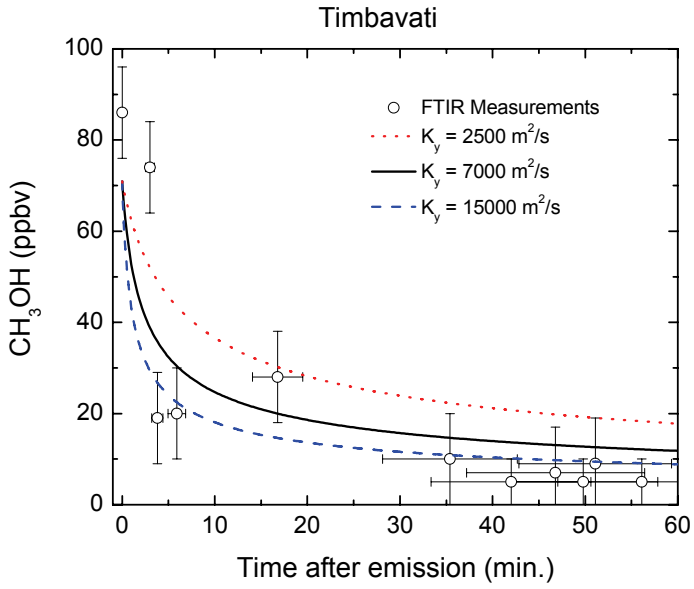

Figure 3-27: Modeled and measured CH_3OH concentrations for the Timbavati smoke plume (expanded chemistry case). Model runs include the heterogeneous reaction $NO_2 \rightarrow 0.5$ HONO + 0.5 HNO_3 ($\gamma_{NO_2} = 10^{-3}$) and include the uncharacterized compounds as BIOH.

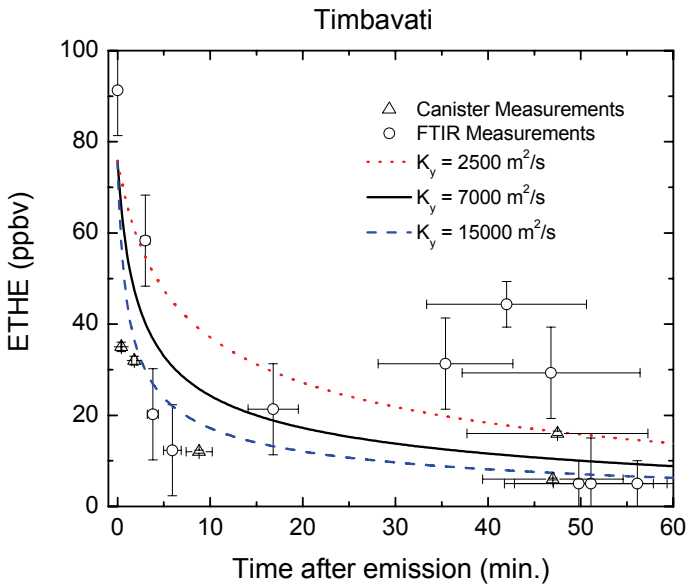

Figure 3-28: Modeled and measured ETHE (ethylene) concentrations for the Timbavati smoke plume (expanded chemistry case). Model runs include the heterogeneous reaction $NO_2 \rightarrow 0.5$ HONO + 0.5 HNO_3 ($\gamma_{NO_2} = 10^{-3}$) and include the uncharacterized compounds as BIOH.

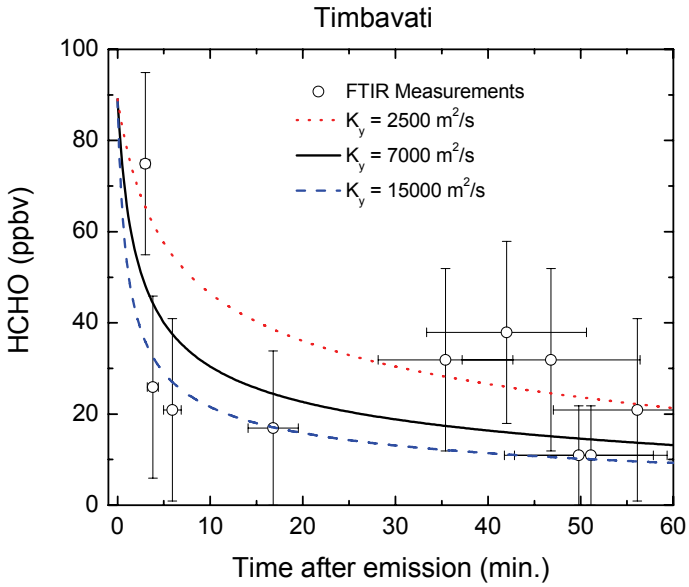

Figure 3-29: Modeled and measured HCHO concentrations for the Timbavati smoke plume (expanded chemistry case). Model runs include the heterogeneous reaction $NO_2 \rightarrow 0.5$ HONO + 0.5 HNO_3 ($\gamma_{NO_2} = 10^{-3}$) and include the uncharacterized compounds as BIOH.

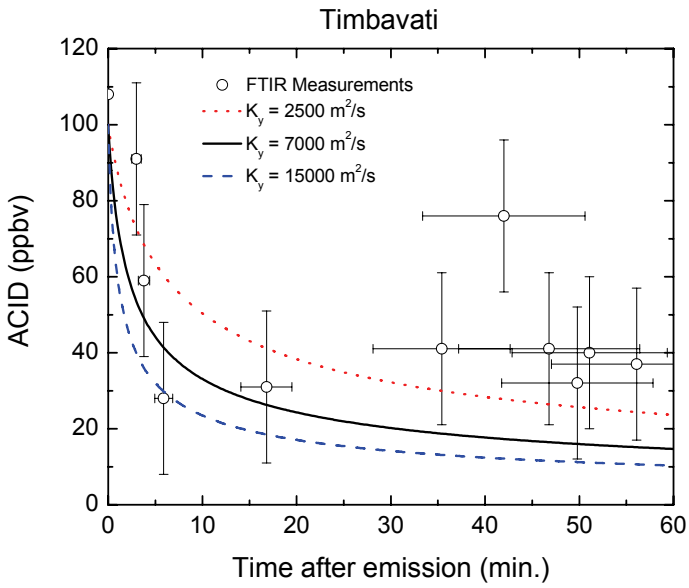

Figure 3-30: Modeled and measured ACID (formic plus acetic acid) concentrations for the Timbavati smoke plume (expanded chemistry case). Model runs include the heterogeneous reaction $NO_2 \rightarrow 0.5$ HONO + 0.5 HNO_3 ($\gamma_{NO_2} = 10^{-3}$) and include the uncharacterized compounds as BIOH.

Uncertainty in Reaction Rate Constants

Our third hypothesis was that parametric uncertainty in the reaction rate constants of our gas-phase chemical mechanism might explain the difference between the modeled and observed concentration of ozone. To test this hypothesis, we performed a limited first-order sensitivity study to assess the uncertainty in the modeled ozone concentration due to the uncertainty in the gas-phase chemical rate constants. Following the method of *Lucas* [2003], we assume that our uncertain rate constants are independent and uncorrelated, and that they are log-normally distributed. Thus, the parameter uncertainties can be expressed using a multiplicative uncertainty factor ϕ. We define C_{O_3} as the concentration of ozone and p_j as the value of parameter (rate constant) j. The first-order local sensitivity coefficient ($z_{O_3,j}$) for C_{O_3} to p_j is defined as

$$z_{O_3,j} = \frac{\partial C_{O_3}}{\partial p_j} \tag{3.6}$$

Because rate constants will have different units based on the order of the reaction, the first-order local sensitivity coefficients will also have different units. To compare sensitivity coefficients, they are normalized by

$$\frac{\partial \eta_{O_3}}{\partial \rho_j} = \frac{\partial \log\left(C_{O_3}\right)}{\partial \log\left(p_j\right)} = \frac{p_j}{C_{O_3}} z_{O_3,j} \tag{3.7}$$

which uses the log-scaled concentration of ozone η_{O_3} and the log-scaled rate constant ρ_j. Note that the standard deviation of the log-scaled rate constant $\sigma_j = \log \phi_j$. The total variance of ozone due to the uncertainty of the rate constant is then given by the equation (see Equation 3.21 of *Lucas* [2003])

$$\sigma_{O_3}^2 \approx \sum_{j=1}^{M} \left(\frac{\partial \eta_{O_3}}{\partial \rho_j} \right)^2 \sigma_j^2 \tag{3.8}$$

where σ_j^2 is the variance of ρ_j. Each term on the right-hand side represents the contribution of parameter j to the total variance. This equation is valid if the parameters p_j are independent and uncorrelated.

Table 3.18 shows the reactions included in our sensitivity study along with their uncertainty factors and reference values for the Timbavati fire. They include the 7 reactions reported by *Rodriguez and Dabdub* [2003] to account for $\geq 5\%$ of the uncertainty in O_3 in their Monte Carlo uncertainty and sensitivity analysis of the CACM chemical mechanism. Together, they account for 54-62% for the uncertainty in O_3 prediction for the Los Angeles Basin, depending on the VOC/NO_x

ratio [*Rodriguez and Dabdub*, 2003]. They include 4 photolysis rates, gas-phase nitrate formation, and 2 reactions of the peroxy acyl radical RO_26 (formed by the abstraction of aldehydic H atom from ALD2). The uncertainty factors for these reactions are taken from *Pun* [1998] and IUPAC Kinetic Data Sheets (http://www.iupac-kinetic.ch.cam.ac.uk).

Table 3.18: Reactions Included in Ozone Senistivity Study and their Uncertainty Factors

Reaction	Uncertainty Factor (ϕ)	Ref.[a]	Reference Value for Timbavati	Values used for Sensitivity Study
$NO_2 + h\nu \rightarrow NO + O(^3P)$	1.3	1	9.4x10^{-3} [b]	7.2×10^{-3} [b] 1.2×10^{-2} [b]
$HCHO + h\nu \rightarrow CO + 2\ HO_2$	1.4	1	3.1×10^{-5} [b]	2.2×10^{-5} [b] 4.4×10^{-5} [b]
$ALD2 + h\nu$	1.4	1	5.5×10^{-6} [b]	3.9×10^{-6} [b] 7.7×10^{-6} [b]
$MGLY + h\nu$	1.6	1	1.1×10^{-4} [b]	6.9×10^{-5} [b] 1.8×10^{-4} [b]
$NO_2 + OH + M$	2.0	2	1.0×10^{-11} [c]	5.0×10^{-12} [c] 2.0×10^{-11} [c]
$RO_26 + NO$	1.4	2	2.1×10^{-11} [c]	1.5×10^{-11} [c] 3.0×10^{-11} [c]
$RO_26 + NO_2$	2.5[b]	2	9.2×10^{-12} [c]	3.7×10^{-12} [c] 2.3×10^{-11} [c]

[a] References: 1, *Pun* [1998]; 2, IUPAC Data Sheets (http://www.iupac-kinetic.ch.cam.ac.uk)
[b] Units s^{-1}
[c] Units cm^3 $molecule^{-1}$ s^{-1}
[d] Uncertainty of k_o

Table 3.19 shows the ozone concentrations at 60 minutes after emission for the sensitivity runs, while Table 3.20 shows the contribution to the total variance from each uncertain reaction rate. Runs were performed at both the medium and slow horizontal diffusion rates. These runs were performed including the uncharacterized compounds as BIOH and including the heterogeneous reaction $NO_2 \rightarrow 0.5\ HONO + 0.5\ HNO_3$ with the recommended uptake coefficient on aqueous aerosols of $\gamma_{NO_2} = 10^{-4}$ [*Jacob*, 2000]. Including the heterogeneous reaction with this uptake coefficient has a very small effect on the total ozone formation (+0.5 ppbv and +1.1 ppbv for K_y = 7000 m^2/s and 2500 m^2/s, respectively). The reference ozone formation in each case is 72.3 ppbv and 87.8 ppbv, respectively.

We can see that the formation of ozone in the Timbavati smoke plume is most sensitive to the rate of gas-phase formation of HNO_3 and the photolysis of NO_2 and HCHO, with the other 4 reaction rates making only minor contributions to the total variance. Furthermore, the 1σ uncertainty range due to the uncertainty in these three reaction rates is comparable to the increase in O_3 formation

Table 3.19: Modeled Ozone Concentrations (ppbv) for Rate Constant Sensitivity Studies

Reaction	K_y = 7000 m^2/s		K_y = 2500 m^2/s	
	O_3 (Low)	O_3 (High)	O_3 (Low)	O_3 (High)
$NO_2 + h\nu \rightarrow NO+O(^3P)$	69.0	75.7	83.0	92.7
$HCHO + h\nu \rightarrow CO + 2\ HO_2$	69.4	76.6	83.4	94.3
ALD2 + $h\nu$	71.9	72.9	87.2	88.8
MGLY + $h\nu$	71.7	73.2	87.1	88.9
NO_2 + OH + M	76.5	67.3	93.9	80.4
RO_26 + NO	71.3	73.3	86.4	89.4
RO_26 + NO_2	72.4	72.2	87.9	87.7

Table 3.20: Ozone Variance from Uncertainty in Rate Constants

Reaction	K_y = 7000 m^2/s		K_y = 2500 m^2/s	
	Variance (x10^6) (% of total)	O_3 Variability $10^{\sqrt{\sigma^2}}-1$	Variance (x10^6) (% of total)	O_3 Variability $10^{\sqrt{\sigma^2}}-1$
$NO_2 + h\nu \rightarrow NO+O(^3P)$	427 (25.2%)	4.87%	608 (24.3%)	5.84%
$HCHO + h\nu \rightarrow CO + 2\ HO_2$	433 (25.5%)	4.91%	671 (26.8%)	6.14%
ALD2 + $h\nu$	8.80 (0.5%)	0.69%	15.3 (0.6%)	0.90%
MGLY + $h\nu$	19.4 (1.1%)	1.02%	19.0 (0.8%)	1.01%
NO_2 + OH + M	774 (45.6%)	6.62%	1140 (45.4%)	8.07%
RO_26 + NO	34.0 (2.0%)	1.35%	51.8 (2.1%)	1.67%
RO_26 + NO_2	0.363 (0.02%)	0.14%	0.246 (0.01%)	0.11%
Total	1700	9.95% (79.5-65.8)	2500	12.20% (98.5-78.3)

we see when the heterogeneous reaction $NO_2 \rightarrow 0.5$ HONO + 0.5 HNO_3 is included with an uptake coefficient of 10^{-3}. However, in the sensitivity studies the O_3 concentration increases when the gas-phase formation of HNO_3 decreases. Since our baseline model chemistry underestimates both O_3 and aerosol nitrate, we cannot explain both discrepancies with reference to the parametric uncertainty in the gas-phase formation of HNO_3 - a change that fixes one makes the other worse. The heterogeneous reaction $NO_2 \rightarrow 0.5$ HONO + 0.5 HNO_3, by contrast, produces both additional O_3 and additional aerosol nitrate.

Plume Electricity

Lightning in convective clouds is a significant source of NO_x to the atmosphere. Volcanic eruptions are sometimes accompanied by lightning, thought to be caused by volcanic dust particles colliding and building up static charges [*Anderson et al.*, 1965; *Thomas et al.*, 2007]. If a similar process were taking place in biomass burning plumes, the lightning within the smoke plume could act as a source of NO_x, potentially increasing the formation of O_3. However, the observations of *Hobbs et al.* [2003] do not mention any lightning flashes observed within the Timbavati smoke plume. In addition, we have been unable to find any record of lighting discharges within biomass burning smoke plumes except in the cases where the the fire induced the formation of a cumulonimbus cloud [*Rosenfeld et al.*, 2007] or where smoke was entrained into cumulonimbus clouds [*Latham*, 1991; *Lyons et al.*, 1998; *Murray et al.*, 2000][5]. Thus, it seems unlikely that plume electricity is responsible for the ozone formation observed at Timbavati.

[5] A small digression into studies of lightning in smoke-contaminated clouds is in order here. It has been observed by many investigators [*Latham*, 1991; *Lyons et al.*, 1998; *Murray et al.*, 2000; *Rosenfeld et al.*, 2007] that lightning flashes from smoke-contaminated clouds tend to be more positively-polarized than average (*i.e.*, the lighting brings positive charges down to the surface, rather than negative charges). Two hypotheses have been suggested to explain this polarization effect. *Vonnegut et al.* [1995] found that biomass burning lead to the formation of a negative space charge within the smoke plume, as the background atmospheric electrical field led to the release of negative ions into the smoke and tended to keep the positive ions in the ash. This negative space charge, when entrained into a cumulonimbus cloud, could lead to an inverted (negative) dipole within the cloud, resulting in positive cloud-to-ground lightning flashes.

Jungwirth et al. [2005] suggested a chemical explanation. Their molecular dynamics simulations of graupel found that when the graupel contains sulfate anions, the ammonium cations are closer to the surface of the graupel, and are preferrentialy transferred to the light ice particles. This leads to the formation of a positive dipole, and a negative charge at the base of the cloud. However, when the graupel contains monovalent anions (Cl^- or NO_3^-), the anions are closer to the surface than the cations. This would create a negative cloud dipole with positive charge at the cloud base and positive cloud-to-ground lightning flashes. Since fresh biomass burning smoke contains large amounts of KCl, this could lead to the observed increase in positive cloud-to-ground lightning flashes from smoke-contaminated clouds.

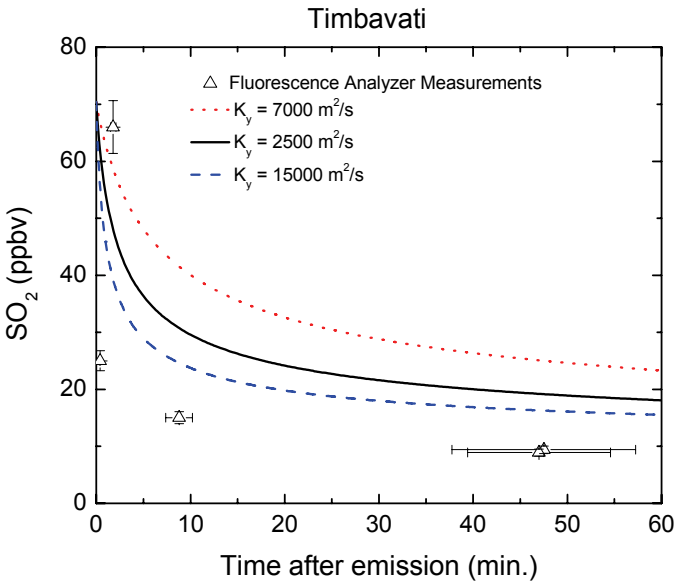

Figure 3-31: Modeled and measured SO_2 concentrations for the Timbavati smoke plume (expanded chemistry case). Model runs include the heterogeneous reaction $NO_2 \rightarrow 0.5$ HONO + 0.5 HNO_3 ($\gamma_{NO_2} = 10^{-3}$) and include the uncharacterized compounds as BIOH.

3.6.4 Sulfate Concentrations

Gas-phase formation of sulfate is included in the baseline model chemistry, but produces a sulfate concentration at 47 minutes downwind of only 3.1 $\mu g/m^3$, much lower than the observed value of 8.1 $\mu g/m^3$. In addition, as is shown in Figure 3-31, the downwind SO_2 concentration is overestimated relative to the observations. We examined three possible explanations for the discrepancy: (1) uncertainty in the gas-phase formation rate of sulfate, (2) aqueous oxidation of sulfate taking place within plume aerosol particles, and (3) heterogeneous oxidation of SO_2 on the aerosol surface.

Uncertainty in the Gas-Phase Formation Rate

The IUPAC kinetic data evaluation for the gas-phase formation of SO_2 (available at http://www.iupac-kinetic.ch.cam.ac.uk) states this reaction rate is uncertain by a factor of 2. Doubling the reaction rate increased the predicted sulfate concentration at 47 minutes downwind from 3.1 $\mu g/m^3$ to 4.2 $\mu g/m^3$, still about a factor of 2 lower than the observed value of 8.1 $\mu g/m^3$. We also explored if the low formation rate of sulfate could be explained by the model underpredicting the OH concentration within the plume. Fixing the OH concentration to the average value of 1.7×10^7 radicals/cm^3

reported by *Hobbs et al.* [2003] increased the predicted sulfate concentration at 47 minutes downwind from 3.1 μg/m^3 to 5.0 μg/m^3. Thus, an improved model prediction of OH still would not be sufficient to explain the observed secondary sulfate formation.

Another possibility is that other sulfur oxides, such as SO or SO_3, could have been present in the plume. The gas-phase oxidation of these compounds could then lead to the enhanced sulfate concentration seen in the Timbavati plume. As no measurements of the concentration of these species were made in the Timbavati plume, we cannot use the available observations to test this hypothesis directly. However, we can estimate the lifetimes of SO and SO_3 within the Timbavati smoke plume.

SO_3 reacts primarily with H_2O to form sulfuric acid.

$$SO_3 + H_2O \rightarrow H_2SO_4 \tag{3.9}$$

IUPAC (Data sheet SOx47, Nov. 2001) gives a preferred value for the rate of this reaction as 5.7×10^4 s^{-1} at 298 K and 50% relative humidity. *Reiner and Arnold* [1994] estimated the second-order rate constant for the reaction as $1.2\pm0.2 \times 10^{-15}$ cm^3 molecules^{-1} s^{-1} at 298 K. For the conditions of the Timbavati smoke plume, the H_2O concentration is 1.9×10^{17} molecules cm^{-3}, giving a rate of 230 s^{-1} and a lifetime of 4.3×10^{-3} s. The data of *Jayne et al.* [1997] suggest a mechanism for Reaction 3.9 that is first-order in SO_2 and second-order in H_2O, with a rate constant of

$$k_{SO_3}\left(s^{-1}\right) = (3.9 \pm 0.8) \times 10^{-41} \exp\left(\frac{6830}{T}\right) C^2_{H_2O_{(g)}} \tag{3.10}$$

which for the conditions of the Timbavati plume gives a lifetime of SO_3 of approximately 4×10^{-5} s.[6] Thus, for the conditions of the Timbavati smoke plume we expect any SO_3 present to be rapidly converted to H_2SO_4 in the first few seconds after emission, and not to cause the gradual increase of sulfate we see downwind in the Timbavati plume.

SO reacts with O_2 to produce SO_2 by the reaction (IUPAC, October 2006)

$$SO + O_2 \rightarrow SO_2 + O \tag{3.11}$$

with the reaction rate

$$k_{SO}\left(s^{-1}\right) = 1.6 \times 10^{-13} \exp\left(\frac{-2280}{T}\right) C_{O_2} \tag{3.12}$$

[6] This is consistent with Figure 10a of *Jayne et al.* [1997], which gives a lifetime of of SO_3 of 10^{-6} s near the surface. However, the quadratic dependence on water vapor concentration means that the lifetime increases rapidly with altutude, to a value of 100 s at 25 km and 10^4 s at 35 km.

For the Timbavati plume, this gives a lifetime of SO of $3{\times}10^{-3}$ s, so any SO emitted by the fire would be rapidly converted to SO_2, and thus is not responsible for the downwind formation of aerosol sulfate.

Aqueous Chemistry of SO_2

One possible explanation for the underestimate of secondary sulfate formation is aqueous chemistry taking place on the surface of the particles. However, the low relative humidities observed in the Timbavati plume make this unlikely, as only a very small amount of condensed water was present in the smoke plume.

A simple scale analysis helps to illustrate this point. We use the results of a model run that (1) sets $K_y = 7000$ m^2/s, (2) included the uncharacterized organic compounds using BIOH as a proxy species, and (3) includes the heterogeneous reaction $NO_2 \rightarrow 0.5$ HONO + 0.5 HNO_3 with an uptake coefficient of 10^{-3}. In this case, the maximum water concentration is the initial value of 19 μg/m^3. The maximum SO_2, O_3, and H_2O_2 concentrations are 70 ppbv, 78 ppbv, and 0.09 ppbv, respectively. The pH of the aerosol aqueous solution is generally in the range of 2.3 to 2.4, with a maximum ionic strength of 30 M. Using these parameters, we can estimate the rate of sulfate formation by the aqueous reaction of, first, SO_2 and H_2O_2, and second, SO_2 and O_3, and compare it to the gas-phase formation rate.

H_2O_2 is a very effective oxidant of aqueous S(IV), since it is very soluble in water. The rate expression is [*Seinfeld and Pandis*, 1998]

$$R_{H_2O_2} = -\frac{d\left[S\left(IV\right)\right]}{dt} = \frac{k\left[H^+\right]\left[H_2O_2\right]\left[HSO_3^-\right]}{1+K\left[H^+\right]} = \frac{kH_{H_2O_2}P_{H_2O_2}H_{SO_2}K_{s1}P_{SO_2}}{1+K\left[H^+\right]} \tag{3.13}$$

with $k = 7.5 \times 10^7$ M^{-2} s^{-1}, and K = 13 M^{-1} at 298 K. The reaction rate is practically independent of pH, as $1 + K\left[H^+\right] \simeq 1$ for pH greater than 2. From *Seinfeld and Pandis* [1998]

$$H_{H_2O_2}\left(288K\right) = 1.74 \times 10^5 \text{ M atm}^{-1} \tag{3.14}$$

$$H_{O_3}\left(288K\right) = 1.52 \times 10^{-2} \text{ M atm}^{-1} \tag{3.15}$$

$$H_{SO_2}\left(288K\right) = 1.77 \text{ M atm}^{-1} \tag{3.16}$$

$$K_{s1}\left(288K\right) = 1.66 \times 10^{-2} \text{ M} \tag{3.17}$$

$$K_{s2}\left(288K\right) = 7.5 \times 10^{-8} \text{ M} \tag{3.18}$$

Thus, for $P_{H_2O_2} = 8.1 \times 10^{-11}$ atm and $P_{SO_2} = 6.3 \times 10^{-8}$ atm, $R_{H_2O_2} = 1.96 \times 10^{-6}$ M/s. Multiplying by the liquid water concentration of 19 μg/m^3 gives 3.74×10^{-14} mol/m^3 air/s, or 2.24x10^4 molecules/cm^3 air/s. By comparison, the modeled OH concentration in this case is about 6×10^6 radicals/cm^3, with SO_2 at 1.6×10^{12} molecules/cm^3/s and $k_{SO_2+OH} \simeq 1\times10^{-12}$ cm^3/molecule/s, giving a gas-phase formation rate for H_2SO_4 of 9.6×10^6 molecules/cm^3 air/s, over 400 times larger than the rate from aqueous reaction of SO_2 and H_2O_2. Thus the aqueous reaction of SO_2 and H_2O_2 is expected to be negligible compared to the gas-phase formation of sulfate, and cannot explain the observed secondary sulfate formation.

The reaction of aqueous S(IV) with O_3 has been studied by many investigators. The reaction rate in a dilute solution is from *Seinfeld and Pandis* [1998]:

$$R_{O_3,o} = -\frac{d\left[S\left(IV\right)\right]}{dt} = \left(k_o + k_1\left[HSO_3^-\right] + k_2\left[SO_3^{2-}\right]\right)\left[O_3\right] \tag{3.19}$$

The rate constants at 298 K are taken from the mean values reported by Hoffman and Calvert *Hoffmann and Calvert* [1985], and are $k_o\,(298\text{ K}) = 2.4 \times 10^4$ M^{-1}s^{-1}, $k_1\,(298\text{ K}) = 3.7 \times 10^5$ M^{-1}s^{-1}, and $k_2\,(298\text{ K}) = 1.5\times10^9$ M^{-1}s^{-1}. As the relative concentrations of aqueous SO_2, HSO_3^- and SO_3^{2-} depend strongly on pH, the reaction rate of aqueous S(IV) with O_3 is a strong function of pH, with the reaction rate at a pH of 6 approximately 6 orders of magnitude faster than the reaction rate at a pH of 2 *Seinfeld and Pandis* [1998]. In addition, *Lagrange et al.* [1994] found that the rate of the S(VI)-O_3 reaction varies linearly with ionic strength according to the equation

$$R_{O_3} = \left(1 + F\mathbf{I}\right) R_{O_3,o} \tag{3.20}$$

where $\mathbf{I}$ is in M and F (M^{-1}) depends on the supporting electrolyte. For example, F is 1.59 ± 0.3 for NaCl, and is 3.71 ± 0.7 for Na_2SO_4, and is less than 1.1 for $NaClO_4$ and NH_4ClO_4.

Using a pH of 2.4 gives

$$\left[H^+\right] = 0.004 \text{ M} \quad (3.21)$$

$$[SO_2 \cdot H_2O] = 1.11 \times 10^{-7} \text{ M} \quad (3.22)$$

$$\left[HSO_3^-\right] = \frac{K_{s1}\left[SO_2 \cdot H_2O\right]}{\left[H^+\right]} = 4.6 \times 10^{-7} \text{ M} \quad (3.23)$$

$$\left[SO_3^{2-}\right] = \frac{K_{s2}\left[HSO_3^-\right]}{\left[H^+\right]} = 8.7 \times 10^{-12} \text{ M} \quad (3.24)$$

$$P_{O_3} = 7.2 \times 10^{-8} \text{ atm} \quad (3.25)$$

$$[O_3] = H_{O_3} P_{O_3} = 1.1 \times 10^{-9} \text{ M} \quad (3.26)$$

Thus, $R_{O_3,o} = 2.04 \times 10^{-10}$ M/s. Adding in the maximum ionic strength correction, using 3.71 for F and an ionic strength of 30 gives a rate of 2.3×10^{-8} M/s, about 80 times lower than the H_2O_2 aqueous reaction and about 10,000 times lower than the gas-phase reaction rate when the low concentration of liquid water is taken into account. Although there is of course some uncertainty in the concentrations of O_3, H_2O_2 and aerosol water, we have in this scale analysis chosen values designed to maximize the impact of aqueous sulfate formation, and still find the rate 400 to 10,000 time slower than gas-phase formation. Thus, we find that aqueous SO_2 formation within the plume was likely negligible compared to gas-phase chemistry, and that aqueous chemistry cannot explain the rapid formation of sulfate observed in the Timbavati fire.

Heterogeneous Chemistry of SO_2

With gas-phase formation of sulfate too slow and aqueous-phase formation even slower, it is still unclear what caused the rapid secondary formation of sulfate in the Timbavati smoke plume. *Buzcu et al.* [2006] had similar problems explaining the rapid formation of secondary sulfate they observed in a wood smoke pollution event over Texas. After ruling out gas-phase and aqueous-phase chemistry, they proposed a heterogeneous reaction where SO_2 is oxidized on the surface of particles to form sulfate:

$$SO_2 \rightarrow H_2SO_4 \quad (3.27)$$

They found a good match between their model and observations when they assumed that the uptake coefficient for this reaction was 10^{-2}. The possibility of heterogeneous chemistry of SO_2 is also consistent with the results of *Lammel and Leip* [2005], who found that the observed rate of sulfate formation in the cloud-free Berlin urban plume was much faster than could be explained by

gas-phase chemistry alone.

Using the same procedure as *Buzcu et al.* [2006], we found that including the Reaction 3.27 with an uptake coefficient of 2×10^{-4} increased the predicted sulfate concentration at 47 minutes downwind from 3.1 $\mu g/m^3$ to 6.9 $\mu g/m^3$, closer to the observed value of 8.1 $\mu g/m^3$.

While there is little data for SO_2 uptake on biomass burning aerosols, the heterogeneous chemistry of SO_2 on soot aerosols has been studied by many investigators. In the 1970s, *Novakov et al.* [1974] established that soot could catalyze the oxidation of SO_2 in the presence of water or oxygen. However, other researchers found that the rate of this reaction decreased with time as the formation of insoluble sulfur species poisoned the catalyst [*Nienow and Roberts*, 2006]. Reported values for the uptake coefficient on soot vary over several orders of magnitude from 3×10^{-5} to 10^{-8} [*Britton and Clarke*, 1980]. The necessary value for the Timbavati fire of 2×10^{-4} is higher than this range, but as mentioned before our procedure of assuming spherical particles may be underestimating the true surface area concentrations of the fresh aerosol particles. Based on these results, we conclude that heterogeneous chemistry of SO_2 is a more likely explanation for the observed high rate of sulfate formation than aqueous chemistry or the uncertainty in gas-phase chemistry. Thus, the uptake coefficient of SO_2 on biomass burning smoke aerosol deserves further laboratory investigation.

3.6.5 Gas-Phase Organic Acid Concentrations

Measurements of acetic acid in both the Alaska and Timbavati smoke plumes suggest that there is secondary production of acetic acid in biomass burning smoke plumes. *Trentmann et al.* [2005] found that known gas-phase reactions of known emissions could not explain the secondary production of acetic acid. They proposed two potential explanations: first, that there may be as yet undetected gas-phase emissions with properties similar to 2,3-dimethyl-2-butene which could be the source of the secondary acetic acid; and second, that particulate-phase chemistry, either on the surface or in the bulk of the particles, might contribute to the secondary production of acetic acid.

Figure 3-30 compares our model prediction of ACID concentrations versus observations of formic and acetic acid. In this case, the uncharacterized compounds are included as BIOH and the heterogeneous reaction $NO_2 \rightarrow 0.5$ HONO + 0.5 HNO_3 is included with an uptake coefficient of 10^{-3}. We can see that most of the AFTIR measurements are above the model values, although the large uncertainty in the airborne FTIR measurements does cross the modeled concentrations.

We used our model to evaluate the possibility that heterogeneous reactions at the surface of the aerosol may be responsible for the secondary formation of acetic acid. We assumed that O_3 could be reacting on the surface of the particle with compounds structurally similar to 2,3-dimethyl-

2-butene to produce acetic acid. We represented this chemistry with the schematic first-order heterogeneous reaction $O_3 \rightarrow$ ACID. As with the uptake coefficients for NO_2 and SO_2, reported values for the uptake coefficient of O_3 can vary widely. For example, values from 10^{-3} to 10^{-8} have been reported for soot aerosols [*Nienow and Roberts*, 2006]. We tested two different values for the O_3 uptake coefficient: 2×10^{-4} and 10^{-3}.

Table 3.21 shows the effect of including this heterogeneous formation of ACID by O_3 on the modeled concentrations of O_3 and ACID. For these runs, the uncharacterized compounds are included as BIOH, the heterogeneous reaction $NO_2 \rightarrow 0.5$ HONO + 0.5 HNO_3 is included with an uptake coefficient of 10^{-3} and the heterogeneous reaction $SO_2 \rightarrow H_2SO_4$ is included with an uptake coefficient of 2×10^{-4}. When the uptake coefficient for O_3 is set to 2×10^{-4}, we see only a slight increase in modeled ACID concentrations. This slight increase does not significantly improve the match between the model and observations for ACID. In fact, the reduction in O_3 for this case means that the match between model and observations is made worse when this reaction is included. Increasing the uptake coefficient for O_3 to 10^{-3} improves the match between model and observations for ACID, but results in a very low O_3 concentration. Thus, heterogeneous reactions of O_3 with the particles to produce acetic acid seem like an unlikely pathway for secondary production of acetic acid. However, this pathway might be viable if the reaction produced other organic species or oxidizers in addition to ACID, which could compensate for the direct loss of O_3.

Table 3.21: Modeled Ozone and ACID Concentrations (ppbv) for ACID Sensitivity Studies

	O_3			ACID		
	Obs. 60 to 135 (±20)			Obs. 30 to 80 (±20)		
K_y (m^2/s)	2500	7000	15000	2500	7000	15000
$\gamma_{O_3} = 0$	100.8	77.9	67.1	23.5	14.6	10.3
$\gamma_{O_3} = 2\times10^{-4}$	92.8 (-8.0)	74.1 (-3.8)	65.0 (-2.1)	32.5 (+9.0)	18.8 (+4.2)	12.5 (+2.2)
$\gamma_{O_3} = 10^{-3}$	68.4 (-32.4)	61.2 (-16.7)	57.5 (-9.6)	60.5 (+37.0)	33.0 (+18.4)	20.5 (+10.2)

3.6.6 Aerosol Mass Concentrations

Figure 3-32 shows the observed and modeled aerosol mass concentrations at 47 minutes downwind for the Timbavati smoke plume. These model runs all use the rescaled initial aerosol from Table 3.15, include the uncharacterized organic compounds as BIOH, and used the medium horizontal diffusion value of 7000 m^2/s. The model runs differ in the heterogeneous chemistry that was included. We can see that the rescaled initial aerosol improves the match between the modeled and measured potassium (K^+) concentrations. Including the uncharacterized compounds as BIOH

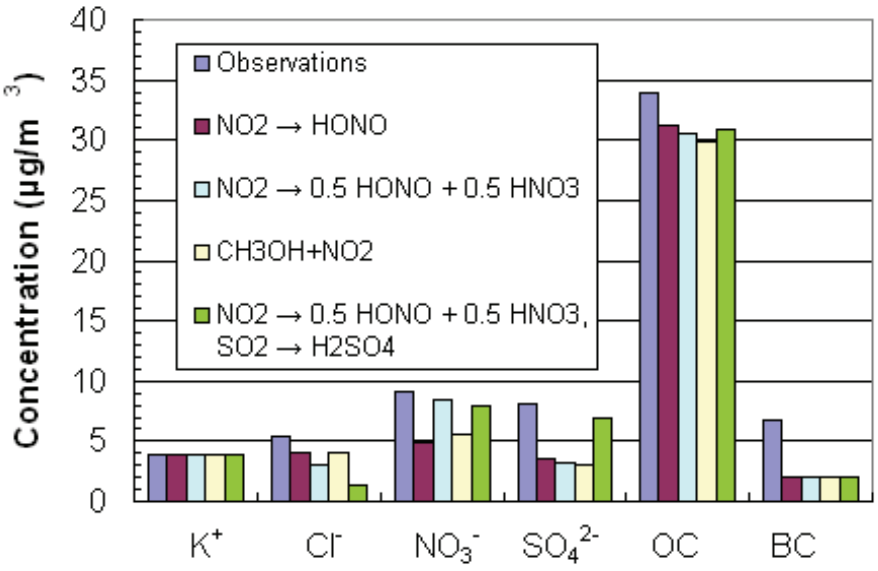

Figure 3-32: Aerosol mass concentrations at 47 minutes downwind in the Timbavati smoke plume when heterogeneous chemistry is added. All model runs use the rescaled inital aerosol from Table 3.15, set $K_y = 7000$ m$^2/s$ and include the uncharacterized compounds as BIOH.

improves the match between the modeled and measured OC concentrations. The model consistently underpredicts the measured concentration of BC. The model treats BC as a conservative tracer; however, the measurements of BC were based on an optical absorption technique. It is possible that some of the secondary organic carbon absorbs in the visible spectrum, and may lead to an overestimate of BC concentration in the measurements.

We can see that the cases that include the heterogeneous reaction $NO_2 \rightarrow 0.5$ HONO + 0.5 HNO_3 with an uptake coefficient of 10^{-3} give the best match to the observed aerosol nitrate concentration, while the run that includes $SO_2 \rightarrow H_2SO_4$ with an uptake coefficient of 2×10^{-4} gives the best match to the observed aerosol sulfate concentration. However, this final case (in green in Figure 3-32) underpredicts the concentration of aerosol chloride relative to the observations. This suggests that our aerosol chemical model may not be capturing the correct partitioning between the gas and aerosol phase for these inorganic species. Unfortunately, since the measurements of the Timbavati smoke plume did not include gas-phase measurements of HCl and HNO_3, we cannot use those measurements to evaluate the partitioning calculated by our thermodynamic model.

Figures 3-33 and 3-34 illustrate the gas to aerosol partitioning of chloride and nitrate, respectively, at 47 minutes downwind in our model runs for the Timbavati smoke plume. Figure 3-33 shows that the total concentration of chloride in the model is the same for all model runs, but

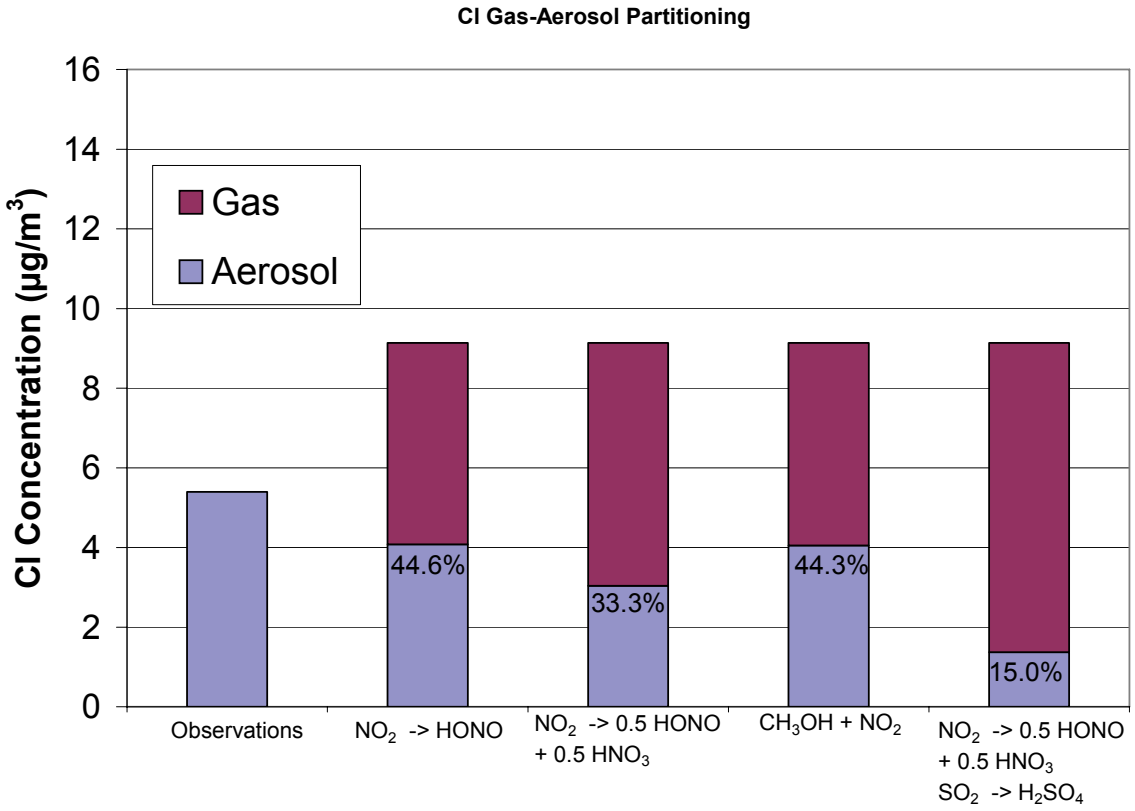

Figure 3-33: Gas and aerosol mass concentrations of chloride (as Cl) at 47 minutes downwind in the Timbavati smoke plume when heterogeneous chemistry is added. All model runs use the rescaled inital aerosol from Table 3.15, set $K_y = 7000$ m$^2/s$ and include the uncharacterized compounds as BIOH. Percentages refer to percent of total chloride that is in the aerosol phase.

that the partitioning between the gas and aerosol phases is greatly affected when heterogeneous production of nitrate and sulfate is included in the model. The behavior of the chloride partitioning follows Le Chatlier's principle: when more strong acids such as sulfate and nitrate are produced and condense into the aerosol phase, this increases the aerosol H^+ concentration. The system responds by pushing chloride out into the gas phase as HCl, reducing aerosol H^+.

Figure 3-34 shows that the total concentration of nitrate (gas + aerosol) in the model varies greatly when different heterogeneous chemistry is considered, and that the heterogeneous chemistry can also slightly effect the gas to aerosol partitioning of nitrate. Total nitrate concentrations are higher when heterogeneous production of nitrate is included in the model. Including heterogenous chemistry for SO_2 increased the total nitrate production further, likely by removing SO_2 as a competing sink for OH. The partitioning in the four cases shown here is relatively constant, with

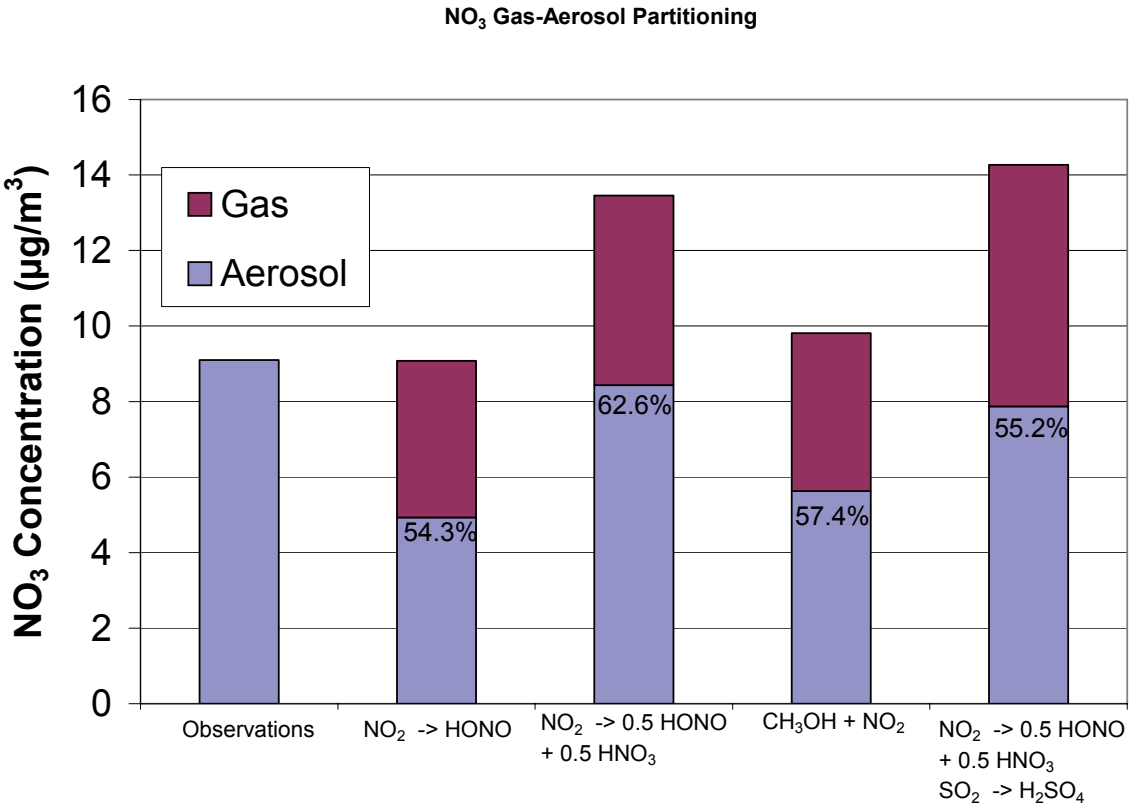

Figure 3-34: Gas and aerosol mass concentrations of nitrate (as NO_3) at 47 minutes downwind in the Timbavati smoke plume when heterogeneous chemistry is added. All model runs use the rescaled inital aerosol from Table 3.15, set $K_y = 7000\ m^2/s$ and include the uncharacterized compounds as BIOH. Percentages refer to percent of total nitrate that is in the aerosol phase.

54%-63% of the total nitrate mass residing in the aerosol phase.

Figure 3-35 shows that the total concentration of condensable organic compounds (gas + aerosol) in the model doesn't vary greatly with the heterogeneous chemistry, nor does the partitioning. In general about 90% of the condensable organic carbon is found in the aerosol phase.

The lack of gas-phase measurements of HCl and HNO_3 represents a major limitation on our ability to simulate and understand the evolution of the aerosol composition in the Timbavati smoke plume. This conclusion is similar to the conclusions of the uncertainty analysis of *San Martini* [2004], which compared modeled and measured inorganic aerosol composition using data gathered in the Mexico City metropolitan area in February 2004. *San Martini* [2004] concluded that, where possible, gas-phase NH_3, HCl, and HNO_3 should be measured simultaneously with aerosol phase NH_4^+, NO_3^-, and Cl^-, but that if this were not possible, it would be best to focus measurement

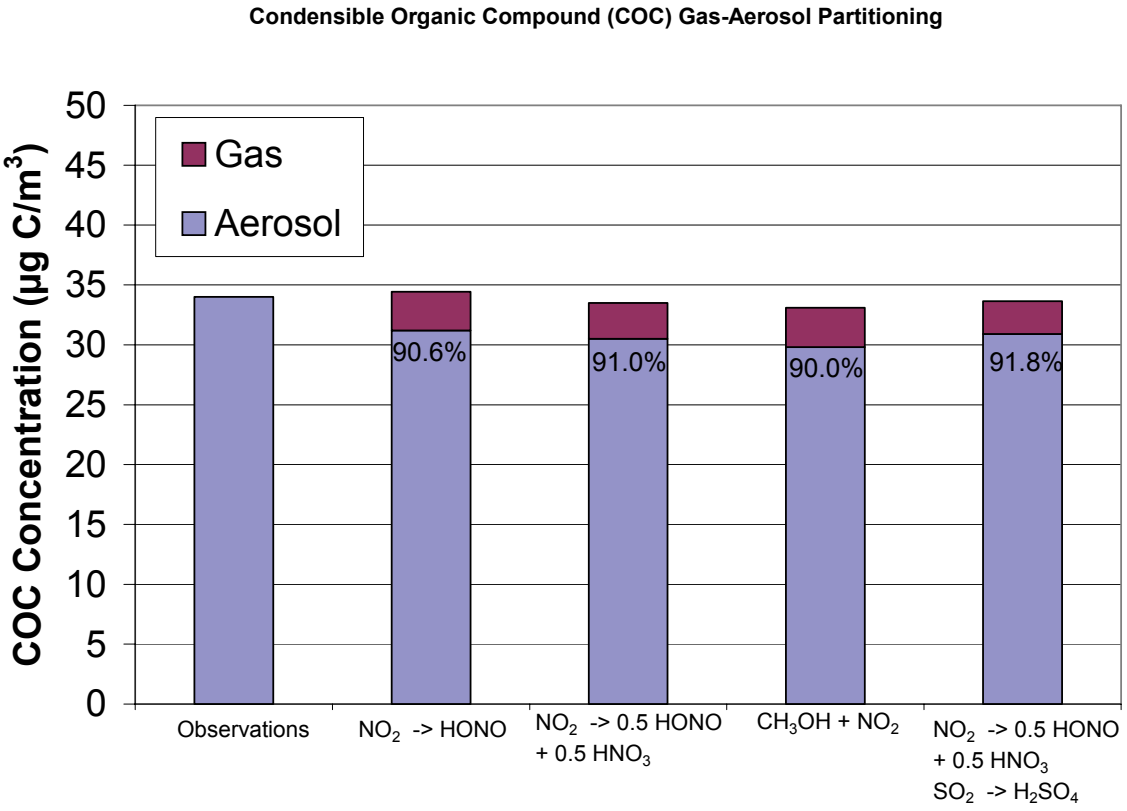

Figure 3-35: Gas and aerosol mass concentrations of condensible organic compounds (COC as μg C/m^3) at 47 minutes downwind in the Timbavati smoke plume when heterogeneous chemistry is added. All model runs use the rescaled inital aerosol from Table 3.15, set $K_y = 7000$ m$^2/s$ and include the uncharacterized compounds as BIOH. Percentages refer to percent of total COC concentration that is in the aerosol phase.

efforts on the gas-phase species with the smallest *a priori* uncertainty. Similarly, we suggest that future work should try to measure ammonia, nitrate and chloride in both the gas and aerosol phase simultaneously. This would help to close the mass balance for Cl and N atoms in the smoke plume, and help to evaluate aerosol thermodynamic models.

3.6.7 Aerosol Growth and Dilution

Figure 3-36[7] shows the normalized aerosol size distributions at the beginning of the model run and at 47 minutes downwind for two cases: one where coagulation is included in the model (blue dashed line) and one where it is not (red dotted line). These number concentrations are normalized to the concentration of a hypothetical conservative tracer (initial concentration 1000 ppbv, background concentration 0 ppbv) to remove the effects of dilution on the number concentration. We can see that condensational growth, due to the secondary formation of sulfate, nitrate, and condensable organic carbon, dominates the growth of the aerosol size distribution, with coagulation having only a minor impact.

The black line and data points in Figure 3-37 shows the total aerosol number concentration measured in the Timbavati smoke plume as the plane flew towards the fire source. The observations were made with the condensation particle counter, which counted particles in the size range of 3 nm to 3 μm in diameter. The blue dashed line and the red dotted line show the modeled total aerosol number concentration for K_y values of 7000 m^2/s and 2500 m^2/s, respectively. We can see that the model does a good job of representing the decrease of the aerosol number concentration in the first 10 minutes after emission. This decrease is primarily due to plume dilution in our model runs, with coagulation having only a minor effect. This is in contrast to the discussion of *Hobbs et al.* [2003] which attributed the initial decrease to coagulation of the highly concentrated particles. One possible explanation for the discrepancy is that *Hobbs et al.* [2003] attempted to account for plume dilution by interpolating canister measurements of CO taken during transects of the plume. These observations are not necessarily comparable with the number concentration data, which were measured continuously as the plane flew along the length of the plume at a different time. Our procedure, which uses both canister and airborne FTIR measurements of CO to calculate a range of horizontal diffusion rates, may better represent the effects of plume dilution on the total aerosol number concentration.

[7] All model runs in this subsection use the rescaled initial aerosol concentrations from Table 3.15 and include the heterogeneous reaction $NO_2 \rightarrow 0.5$ HONO + 0.5 HNO_3 ($\gamma_{NO_2} = 10^{-3}$), the heterogeneous reaction $SO_2 \rightarrow H_2SO_4$ ($\gamma_{SO_2} = 10^{-3}$) and the uncharacterized compounds as BIOH.

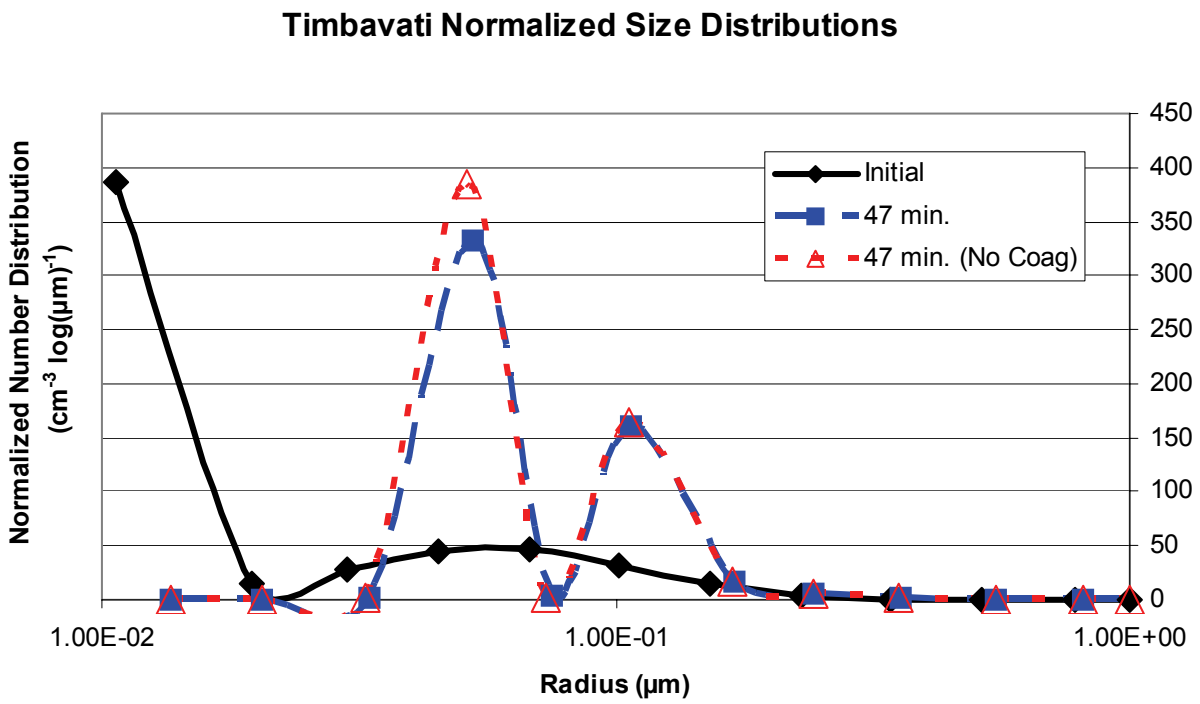

Figure 3-36: Normalized aerosol size distributions for the Timbavati case. Number concentrations have been normalized to remove the effect of dilution ($K_y = 7000$ m^2/s). Model runs include the heterogeneous reaction $NO_2 \rightarrow 0.5$ HONO + 0.5 HNO_3 ($\gamma_{NO_2} = 10^{-3}$), the heterogeneous reaction $SO_2 \rightarrow H_2SO_4$ ($\gamma_{SO_2} = 10^{-3}$) and include the uncharacterized compounds as BIOH.

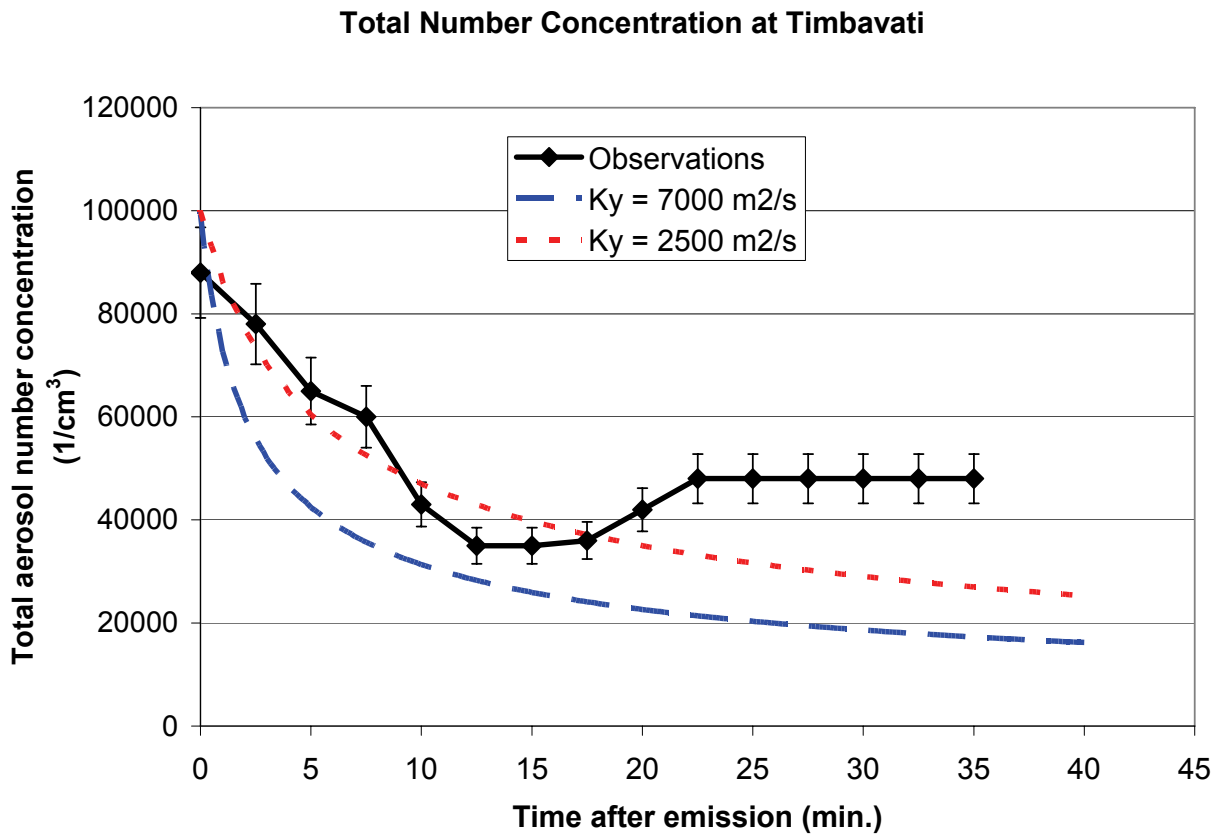

Figure 3-37: Modeled and measured total aerosol number concentrations (cm^{-3}) for the Timbavati smoke plume. Observations are from *Hobbs et al.* [2003].

We find that our model does not match the observed increase in total aerosol number concentration seen beyond 10 minutes downwind in Figure 3-37. *Hobbs et al.* [2003] suggested that this increase could be due to the production of new particles by gas-to-particle conversion (nucleation). Other possible explanations for the observed increase are that very small particles, initially below the size cut off of the condensation particle counter, may have grown by condensation into the detectable size range, increasing the measured total aerosol number concentration, or that the plane may have moved relative to the centerline of the smoke plume during the measurement flight.

To evaluate whether nucleation could account for the increase in total aerosol number concentration observed in the Timbavati smoke plume, we performed a scale analysis of the nucleation of new particles by sulfuric acid and condensable organic vapors. We used the parameterized nucleation scheme of *Fan et al.* [2006], which accounts for the enhanced nucleation effect of secondary condensable organics. This scheme generally gives a higher nucleation rate than the binary H_2SO_4-H_2O parameterization of *Kulmala et al.* [1998]. The parameterization is

$$J_r = C \cdot P_{H_2SO_4} \cdot \sum_i P_{i,org} \tag{3.28}$$

where C = 3×10^{-19} cm^3/s is inferred from the typical nucleation rate measured in a urban atmosphere (1-10 cm^{-3} s^{-1}) and the concentrations of H_2SO_4 and condensable organics are predicted by the model *Fan et al.* [2006]. For our study, $P_{H_2SO_4} \approx 2 \times 10^7$ molecules/cm^3 (0.8 pptv) and $\sum_i P_{i,org} \approx 2.3 \times 10^{10}$ molecules/cm^3 (1 ppbv), giving $J_r = 0.138$ particles/cm^3/s. Thus, over 1 hour, this nucleation rate would increase the modeled number concentration by only 500 particles/cm^3, not enough to explain the high number concentration of particles observed downwind of the Timbavati fire. This suggests that either the growth of small particles and/or variability of concentrations within the smoke plume are responsible for the observed increase.

3.6.8 Aerosol Optical Properties

The optical properties of the smoke aerosol change greatly with time as the smoke grows due to the condensation of secondary organic carbon, sulfate, and nitrate onto the particles. For example, the radius of the black carbon core is 31% of the effective particle radius for the fresh smoke aerosols in our model, but the radius of the black carbon core is only 8.5% and 20-30% of the effective particle radius for the small and large particle modes, respectively, at 47 minutes downwind.

Table 3.22[8] shows the modeled optical properties at a wavelength of 550 nm for both the initial

[8] All model runs in this subsection use the rescaled initial aerosol concentrations from Table 3.15, set $K_y = 7000$

Table 3.22: Aerosol Optical Properties for the Timbavati Fire

Parameter	Fresh Smoke		Aged Smoke	
(at 550 nm)	Model[a]	Reported Range	Model[a]	Reported range
Single Scattering Albedo ϖ_{aero}	0.866	0.82±0.05[b]	0.902	0.86±0.05[b]
Asymmetry Parameter $\langle g \rangle_{aero}$	0.654	0.55±0.06[b]	0.609	0.58±0.06[b]
Mass Scattering Efficiency α_s (m^2/g)	2.77	3.6±0.4[b] 3.6±1.0[c]	2.35	4.0±0.4[b] 3.6±1.1[c]
Mass Absorption Efficiency α_a (m^2/g)	0.429	0.8±0.3[b] 0.54±0.2[c]	0.255	0.65±0.3[b] 0.45±0.2[c]
Humidification Factor $f(RH)$	2.88	1.70-1.79[d]	1.22	1.40[d]

[a] These runs use the rescaled initial aerosol concentrations
and include the uncharacterized compounds as BIOH,
the heterogeneous reaction $NO_2 \rightarrow 0.5$ HONO + 0.5 HNO_3 ($\gamma_{NO_2} = 10^{-3}$)
and the heterogeneous reaction $SO_2 \rightarrow H_2SO_4$ ($\gamma_{SO_2} = 2 \times 10^{-4}$).
Aged smoke is at 1 hour after emission.
[b] Range reported for grassland and savannah smoke by *Reid et al.* [2005a].
[c] Range recommended for biomass burning smoke by IPCC. (See *Reid et al.* [2005a]).
[d] Measurements made for Timbavati smoke plume by *Magi and Hobbs* [2003].

smoke aerosol and for the smoke aerosol aged for 1 hour within the smoke plume. The model values are compared with the range of reported values for fresh and aged savannah fire smoke, respectively. The model values for single scattering albedo ϖ_{aero} fall within the ranges for fresh and aged savannah fire smoke reported by *Reid et al.* [2005a]. The model value for the asymmetry parameter $\langle g \rangle_{aero}$ for fresh smoke is slightly higher than the reported range, but the model value for the aged smoke agrees well with the range reported by *Reid et al.* [2005a].

The aerosol mass scattering efficiency α_s (m^2/g) is calculated using the formula

$$\alpha_s = \frac{b_{ext,aero} \varpi_{aero}}{\mathbf{c}_{aero}} \tag{3.29}$$

where $\mathbf{c}_{aero}$ is the total aerosol mass concentration in g/m^3. For our fresh smoke, we calculate α_s at 550 nm as 2.77 m^2/g, below the range of 3.6±0.4 m^2/g recommended by *Reid et al.* [2005a] for fresh grassland and savannah smoke, but within the range recommended by the IPCC for fresh smoke (3.6±1.0 m^2/g). *Reid et al.* [2005a] also notes that typical values for fresh smoke can vary between 2.8 to 4.2 m^2/g, putting us near the bottom of that range. For the aged smoke, our modeled α_s of 2.35 m^2/g is also below the ranges given by *Reid et al.* [2005a] and the IPCC for aged smoke, although it matches the IPCC range better. Furthermore, we see a decrease in α_s with time, while the review of *Reid et al.* [2005a] suggests that this parameter increases with time.

m^2/s, and include the heterogeneous reaction $NO_2 \rightarrow 0.5$ HONO + 0.5 HNO_3 ($\gamma_{NO_2} = 10^{-3}$), the heterogeneous reaction $SO_2 \rightarrow H_2SO_4$ ($\gamma_{SO_2} = 10^{-3}$) and the uncharacterized compounds as BIOH.

The aerosol mass absorption efficiency α_a (m^2/g) is calculated using the formula

$$\alpha_a = \frac{b_{ext,aero}(1 - \varpi_{aero})}{\mathbf{c}_{aero}} \tag{3.30}$$

Our modeled value of 0.429 m^2/g for fresh smoke is slightly lower than the range of 0.8±0.3 m^2/g recommended by *Reid et al.* [2005a] for fresh grassland and savannah smoke, but is within the range recommended by the IPCC (0.54±0.2 m^2/g). For the aged smoke, our model value of α_a is 0.255 m^2/g, near the bottom of the range reported by the IPCC and just below the range reported by *Reid et al.* [2005a]. It should be noted that since the production of black carbon is closely related to the combustion efficiency of the fire, fires of different combustion efficiencies can produce aerosol with very different mass absorption efficiencies, which may account for the low values observed here.

To see if our model was correctly representing the scattering of radiation due to the smoke aerosols, we compared the model calculated values for the aerosol scattering coefficient (m^{-1}) with the nephelometer measurements made during transects of the Timbavati smoke plume. The nephelometer-measured scattering coefficient within the Timbavati smoke plume varied across the plume, but the maximum values reported were about 2.2×10^{-3} m^{-1} near the fire source and 4.0×10^{-4} m^{-1} at 26.2 km downwind from the source. Our model gives a (plume average) initial value of $7.0\times10^{-4} m^{-1}$ and a value of 2.1 $\times10^{-4}$ m^{-1} at 47 min. downwind (26.2 km), roughly in line with the observations.

The humidification factor $f(RH)$ is calculated as

$$f(RH) = \frac{(b_{sca,aero})\,|_{RH=80\%}}{(b_{sca,aero})\,|_{RH>35\%}} = \left(1 - \frac{RH}{100}\right)^{-\alpha} \tag{3.31}$$

and represents the relative increase in aerosol scattering as the relative humidity is increased from 30% to 80%. The reported values of $f(RH)$ given in Table 3.22 are from the measurements made by *Magi and Hobbs* [2003] in the Timbavati smoke plume. Our value of $f(RH)$ for fresh Timbavati smoke of 2.88 is much higher than the values of 1.70 and 1.79 reported by *Magi and Hobbs* [2003]. Figure 3-38 compares our model results for the relative scattering increase over the RH range of 30-80% with the measurements of *Magi and Hobbs* [2003] for the fresh smoke. We can see that the model and measurements agree well up to a relative humidity of 66%, at which point the model aerosol takes on much more water than the measurements would suggest. Below 66%, the aerosol water uptake is primarily due to the WSOC (modeled as CBIO). The large increase in water content for the model aerosol comes from the deliquescence of aerosol NH_4Cl. Since all of

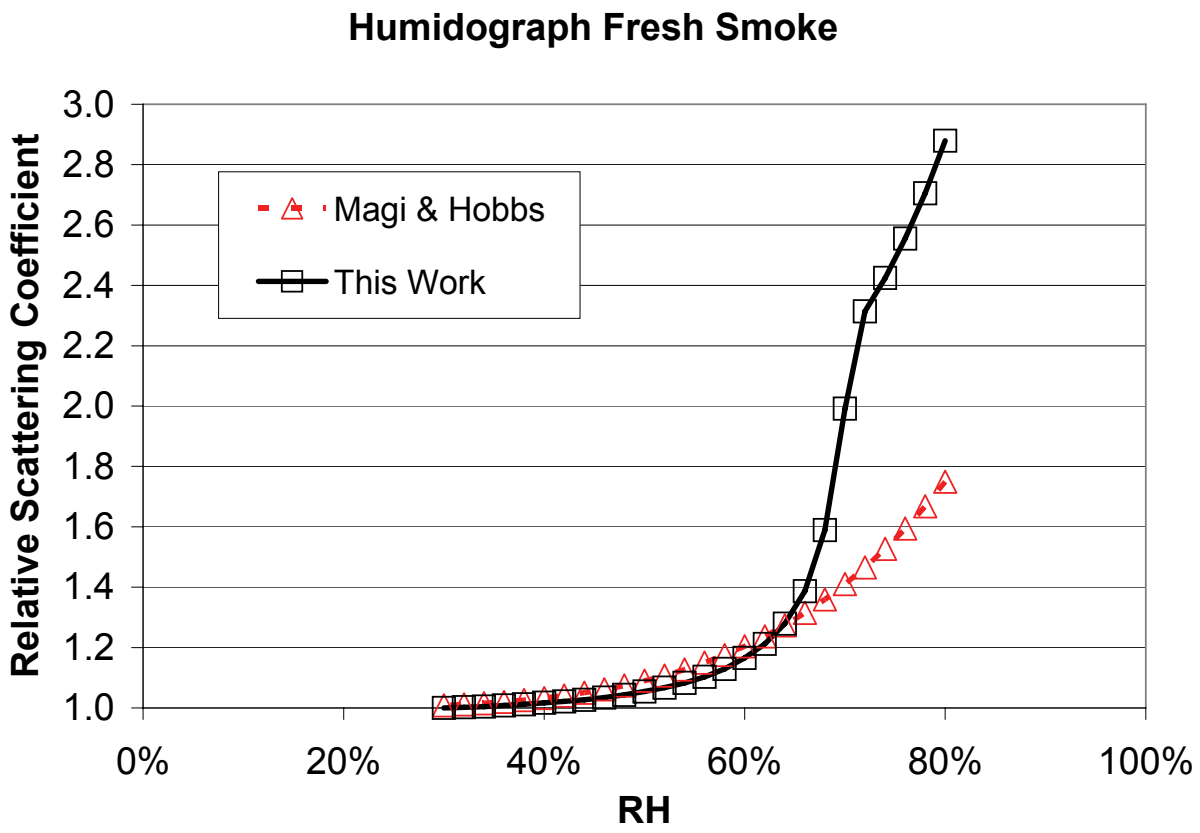

Figure 3-38: Humidograph for the Timbavati fresh smoke. The dashed red line is the observed change in the relative scattering coefficient versus as measured by *Magi and Hobbs* [2003]. The black line is the model result.

the model runs considered in this thesis take place at a relative humidity of less than 50%, the agreement between model and observation is adequate for our purpose. However, further work is necessary to determine how to correctly represent water uptake by fresh biomass burning aerosols at high relative humidities.

Figure 3-39 compares our model results for the relative scattering increase over the relative humidity range of 30-80% with the measurements of *Magi and Hobbs* [2003] for the aged smoke. Both the model and the measurements show that $f(RH)$ decreases as the smoke ages, and neither shows a sharp deliquescence point below 80% RH. The model agrees with the measurements up to a relative humidity of 50%, at which point the aged model aerosol takes up less water than is suggested by the measurements. This suggests that the organic surrogates used to represent aerosol organic carbon are not reflecting the water uptake properties of the true aged organic aerosol mixture.

The Angstrom exponent $\alpha_{\lambda_1=550nm,\lambda_2}$ can be calculated as

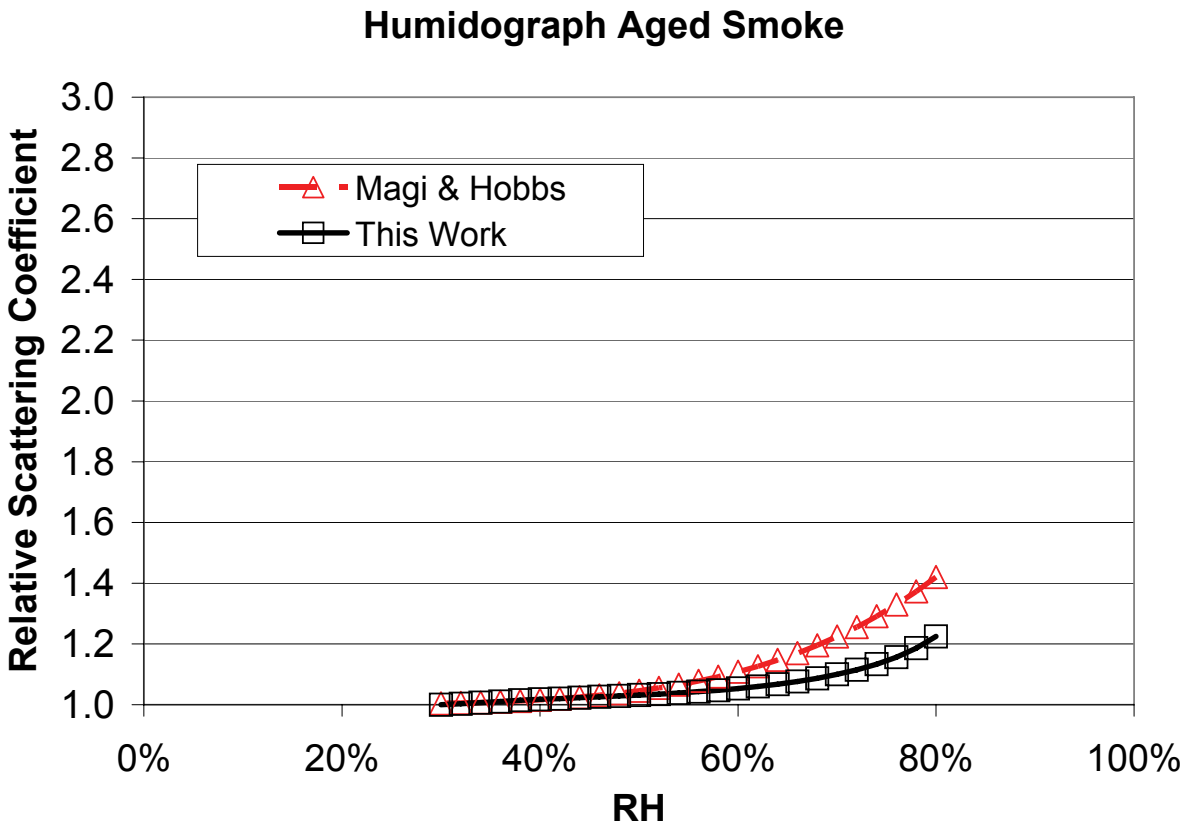

Figure 3-39: Humidograph for the Timbavati aged smoke. The dashed red line is the observed change in the relative scattering coefficient versus as measured by *Magi and Hobbs* [2003]. The black line is the model result for smoke aged 1 hour.

$$\alpha_{\lambda_1,\lambda_2} = -\frac{\ln\left(\tau_{\lambda_1}/\tau_{\lambda_2}\right)}{\ln\left(\lambda_1/\lambda_2\right)} = -\frac{\ln\left(b_{ext,\lambda_1}/b_{ext,\lambda_2}\right)}{\ln\left(\lambda_1/\lambda_2\right)} \tag{3.32}$$

At 30% RH, $\alpha_{\lambda_1=550nm,\lambda_2}$ for the modeled fresh smoke varies from 1.70-2.36 for the solar wavelengths, near the range of 2.0-2.5 for fresh smoke reported by *Reid et al.* [2005a]. This suggests that our assumption of a constant refractive index in the solar regime does not greatly impact our ability to simulate the wavelength dependence of aerosol extinction, as this is mainly a function of aerosol and wavelength size. For our aged model smoke, $\alpha_{\lambda_1=550nm,\lambda_2}$ varies from 1.92-2.57 for the solar wavelengths; we do not observe the decrease in $\alpha_{\lambda_1=550nm,\lambda_2}$ with aging reported by *Reid et al.* [2005a].

Sensitivity to Refractive Indices of OC and BC Table 3.23 shows the results for our sensitivity studies of the optical properties of the modeled fresh smoke. Varying the real refractive index of BC between 1.62-2.02 (not shown) has very little effect on the modeled optical properties for fresh smoke. Varying the imaginary refractive index of BC in the range of $0.54i$ to $0.94i$ has little effect on the asymmetry parameter $\langle g \rangle_{aero}$ or the mass scattering efficiency α_s, but a lower value reduces the mass absorption efficiency α_a and increases the single scattering albedo ϖ_{aero}. Similarly, increasing (or decreasing) the imaginary refractive index of OC by a factor of 10 has little effect on the asymmetry parameter or the mass scattering efficiency, but does slightly decrease (increase) the single scattering albedo and increase (decrease) the mass absorption efficiency. None of these changes significantly alter the scattering coefficient b_{sca}.

Table 3.23: Sensitivity of Fresh Smoke Optical Properties to the Refractive Indices of OC and BC

Parameter		n_{BC}		n_{OC}			
(at 550 nm)	Reference	1.82+0.94i	1.82+0.54i	$1.45+10^{-2}$i	$1.45+10^{-4}$i	$1.25+10^{-3}$i	$1.65+10^{-3}$i
ϖ_{aero}	0.866	0.843	0.892	0.844	0.868	0.838	0.885
$\langle g \rangle_{aero}$	0.654	0.646	0.662	0.657	0.654	0.677	0.625
α_s (m^2/g)	2.77	2.71	2.84	2.72	2.77	1.98	3.66
α_a (m^2/g)	0.429	0.505	0.342	0.504	0.421	0.384	0.477
b_{sca} (m^{-1})	7.0×10^{-4}	6.9×10^{-4}	7.2×10^{-4}	6.9×10^{-4}	7.0×10^{-4}	7.2×10^{-4}	9.2×10^{-4}

[a] These runs use the rescaled initial aerosol concentrations,
and include the uncharacterized compounds as BIOH,
the heterogeneous reaction $NO_2 \rightarrow 0.5$ HONO + 0.5 HNO_3 ($\gamma_{NO_2} = 10^{-3}$)
and the heterogeneous reaction $SO_2 \rightarrow H_2SO_4$ ($\gamma_{SO_2} = 2 \times 10^{-4}$).

The modeled optical properties are most sensitive to changes in the real refractive index assumed for OC. Increasing the real refractive index of OC to 1.65 from our reference value of 1.45

increases the mass scattering efficiency and scattering coefficient by 32%, increases the aerosol mass absorption efficiency by 11%, reduces the asymmetry parameter by 4.5% and increases the single scattering albedo by 2.2%. Increasing the real refractive index for OC would be consistent with the experimental work of *Hungershofer et al.* [2007], who reported a mean effective refractive index for smoke particles emitted from the combustion of savanna grass as $1.60+10^{-2}i$. The increase improves the match with the reported values for mass scattering efficiency and asymmetry parameter for fresh savannah and grassland smoke, but increases the single scattering albedo to slightly above the reported range.

Table 3.24 shows the impact of increasing the real refractive index of OC to 1.65 on the optical properties for the aged aerosol. As for the fresh aerosol, increasing the OC real refractive index increases the mass scattering and absorption efficiencies, improving the agreement with reported values, while increasing the single scattering albedo above the reported range for aged savannah aerosols.

Table 3.24: Sensitivity of Aged Smoke Optical Properties to the Refractive Index of OC

Parameter (at 550 nm)	Reference	n_{OC} $1.65+10^{-3}$i
ϖ_{aero}	0.902	0.922
$\langle g \rangle_{aero}$	0.609	0.560
α_s (m^2/g)	2.35	3.48
α_a (m^2/g)	0.255	0.294
b_{sca} (m^{-1})	2.1×10^{-4}	2.8×10^{-4}

[a] These runs use the rescaled initial aerosol concentrations, and include the uncharacterized compounds as BIOH, the heterogeneous reaction $NO_2 \rightarrow 0.5$ HONO + 0.5 HNO_3 ($\gamma_{NO_2} = 10^{-3}$) and the heterogeneous reaction $SO_2 \rightarrow H_2SO_4$ ($\gamma_{SO_2} = 2 \times 10^{-4}$).

3.7 Summary and Conclusions

We have combined the gas and aerosol phase chemical model ASP with a Lagrangian parcel model to simulate the aging of smoke in three young smoke plumes from biomass burning. For the Otavi and Alaska smoke plumes, we simulated the gas phase chemistry, while for the Timbavati smoke plume we simulated the gas- and aerosol-phase chemistry simultaneously.

We found that our model can explain the formation of ozone in the Otavi and Alaska plumes fairly well, but has difficulty explaining the formation of ozone and growth of aerosols observed in the Timbavati smoke plume. We investigated several hypotheses to explain the overestimate of

K^+, the underestimate of OC, the underestimate of O_3 and OH, the underestimate of gas-phase organic acids, and the underestimate of sulfate and nitrate in the baseline model simulation for Timbavati.

The lack of size distribution measurements for particles with diameters less than 0.5 μm for the Timbavati plume meant that we had to estimate the initial aerosol size distribution from the literature. We found that the overestimate of potassium downwind in the baseline model simulation was most likely related to an overestimate of the initial aerosol concentration caused by the differing averaging times of the aerosol and gas-canister measurements. We rescaled our initial aerosol mass concentrations to match the downwind observations of K^+ and added a second small mode to keep the initial aerosol number concentration near the observed value.

We found that the 30% of gas-phase carbon that is currently uncharacterized in canister measurements of smoke plumes may be a source of aerosol organic carbon. Including these compounds in the model (using the proxy compound BIOH) greatly improves the match between the model and the observations for aerosol OC. These uncharacterized compounds may be directly emitted by the fire into the gas phase, or may be intermediate volatility organic compounds that are initially present on the smoke particles as in the theory of *Donahue et al.* [2006] and *Robinson et al.* [2007].

Fixing the model OH concentration at the reported value for the Timbavati smoke plume greatly improved the model's match with the observed concentration of ozone. This suggests that the model may be missing a source of OH. We found that a heterogeneous reaction of NO_2 to make HONO could be the missing OH source if the uptake coefficient on smoke aerosols is large [$O(10^{-3})$]. This chemistry appears consistent with the observations of the three smoke plumes considered in this chapter. We found that the modeled ozone concentration was sensitive to the rate of formation of HNO_3 and the rate of photolysis of NO_2 and HCHO. However, while reducing the rate of HNO_3 formation increases the rate of ozone formation, it also decreases the formation of aerosol nitrate, so the uncertainty of this reaction rate cannot explain the available observations for ozone and aerosol nitrate simultaneously. Adding additional oxygenated compounds to the model simulation did not significantly increase the ozone formation.

We found that heterogeneous reactions of NO_2 and SO_2 could explain the rapid formation of nitrate and sulfate if the uptake coefficient on smoke aerosols is large [$O(10^{-3})$ and $O(10^{-4})$, respectively]. Our scale analysis suggests that the aqueous formation of sulfate was negligible in the dry conditions of the Timbavati smoke plume.

We found that a heterogeneous reaction of O_3 to produce acetic acid cannot explain the observations for the Timbavati smoke plume at any value of the accommodation coefficient. A value large

enough to significantly increase secondary production of acetic acid greatly decreases the modeled ozone concentration.

We found that the changes in the aerosol size distribution are dominated by plume dilution and condensational growth. Coagulation has only a minor effect on the aerosol size distribution. In our model, the reduction of aerosol number concentration observed in the first 10 minutes downwind of the Timbavati fire is caused by plume dilution, not by coagulation as suggested by *Hobbs et al.* [2003]. Our scale analysis of nucleation suggests that nucleation was negligible in the Timbavati smoke plume. The growth in aerosol number concentration observed after 15 minutes downwind may have been caused by small particles (< 3 nm in diameter) growing into the detectable size range of the condensation particle counter, or by a sampling artifact caused by the plane's motion relative to the plume centerline.

The model aerosol matches reported values of single scattering albedo and asymmetry factor, underestimates the mass scattering efficiency and has difficulty matching the observed humidification factors. The mass scattering efficiency is most sensitive to the value of the real refractive index for organic carbon. Increasing the real refractive index from 1.45 to 1.65 improves the match between modeled and reported values for mass scattering efficiency, but results in an overestimate of the aerosol single scattering albedo.

Chapter 4

3D Eulerian Investigation of the Timbavati Plume

In this chapter, we present a 3-dimensional Eulerian simulation of the fluid dynamics, gas-phase chemistry, aerosol chemistry, and the scattering and absorption of radiation within the Timbavati biomass burning smoke plume. To our knowledge, this is the first time all of these processes have been simulated simultaneously for a young biomass burning smoke plume. The 3D Eulerian simulation allows us to evaluate the impact of plume buoyancy and dynamics on the formation of ozone and growth of aerosols within the smoke plume and the impact of the aerosol particles on the actinic flux and photolysis rates within the smoke plume. In addition, the 3D Eulerian model allows us to determine how the observed gas and aerosol concentrations might change due to different sampling heights during plume transects and to make suggestions for future measurement campaigns.

The results of the Lagrangian simulation of the Timbavati plume from Chapter 3 are used to design two test cases for the Eulerian simulations. In the reference chemistry case, the uncharacterized organic species are assumed to be unreactive and heterogeneous chemistry is not included. In the expanded chemistry case, the uncharacterized compounds are included using BIOH (monoterpenes) as a proxy and the heterogeneous reactions of NO_2 and SO_2 discussed in Chapter 3 are included.

Section 4.1 describes the 3D Eulerian model used to simulate the dynamics of the Timbavati smoke plume. The dynamical model is a modified version of the cloud resolving model of *Wang and Chang* [1993]. Section 4.2 describes the meteorological and chemical fields used to initialize the model simulations. Section 4.3 presents the results of the model simulations and compares them to

the observations of *Hobbs et al.* [2003]. The conclusions of the 3D Eulerian study of the Timbavati plume are in Section 4.4.

4.1 Description of the Eulerian Model

To simulate the fluid dynamics of the smoke plume, we use an updated version of the Cloud Resolving Model (CRM6) of *Wang and Chang* [1993]. CRM6 was used by *Wang and Prinn* [2000] to simulate the impact of deep convection on tropospheric chemistry. The dynamical prognostic equations in CRM6 include the nonhydrostatic momentum equations, the continuity equations for water vapor and air mass density, the thermodynamic equation, and the equation of state [*Wang and Chang*, 1993; *Wang and Prinn*, 2000]. CRM6 evaluates the subgid turbulent fluxes using the first-order turbulence closure of *Klassen and Clark* [1985]. CRM6 was modified for this thesis work to include a source of sensible heat, trace gases, and particles at the surface to simulate the various emissions from the fire. The model solves the advection-diffusion equations for all modeled gas and aerosol phase species. The equations of CRM6 are discussed in more detail in Appendix B.

A δ-four-stream radiation module based on the model of *Fu and Liou* [1993] is included in the CRM6 model. We modified this module to include the radiative effects of aerosol particles. CRM6 takes the aerosol optical properties (extinction coefficient, single-scattering albedo, and asymmetry parameter) provided by the Aerosol Simulation Program (ASP) and calculates the average optical depth, single-scattering albedo, and phase function within each model grid box. The first four expansion coefficients of the aerosol phase function (ζ_i, $i = 1..4$) for the aerosols are calculated from the asymmetry parameter using the Henyey-Greenstein formula [*Fu and Liou*, 1993]

$$\zeta_1 = 3 \langle g \rangle_{aero} \tag{4.1}$$

$$\zeta_2 = 5 \langle g \rangle_{aero}^2 \tag{4.2}$$

$$\zeta_3 = 7 \langle g \rangle_{aero}^3 \tag{4.3}$$

$$\zeta_4 = 9 \langle g \rangle_{aero}^4 \tag{4.4}$$

The *Fu and Liou* [1993] module calculates the total upward and downward irradiances (in units of W m^{-2}) for each of the 16 radiation bands shown in Table 2.20. However, as noted by *Madronich* [1987], the magnitudes of the irradiance and the actinic flux are not the same. The relationship between them can be derived from the definitions of the actinic flux F (W m^{-2}) and irradiance E, which are calculated by integrating the radiance $L(\theta, \phi)$ (W m^{-2} steradian^{-1}) over all angles with

different weighting functions:

$$F \equiv \int_{\phi}\int_{\theta} L(\theta,\phi)\sin\theta d\theta d\phi \tag{4.5}$$

$$E \equiv \int_{\phi}\int_{\theta} L(\theta,\phi)\cos\theta\sin\theta d\theta d\phi \tag{4.6}$$

As the angle of incidence of the radiation changes, the energy incident upon a layer (the irradiance) decreases, but the actinic flux remains unchanged [*Madronich*, 1987]. The exact relationship between the actinic flux and the irradiance depends on the specific angular dependence of the radiance $L(\theta,\phi)$. For collimated light (*i.e.*, light where the rays are essentially parallel and the light originates from a very small solid angle $\Delta\omega_o$), such as the direct solar beam, the relationship is [*Madronich*, 1987]

$$E_{direct} = F_{direct}\cos\theta_z \tag{4.7}$$

For the upward and downward diffuse radiation, if we assume that these fluxes are isotropic, then $L(\theta,\phi)$ is a constant in each hemisphere (*e.g.*, $L(\theta,\phi) = L_{\downarrow}$). Thus,

$$F_{\downarrow} = L_{\downarrow}\int_{\phi=0}^{2\pi}\int_{\theta=0}^{\frac{\pi}{2}}\sin\theta d\theta d\phi = 2\pi L_{\downarrow} \tag{4.8}$$

$$E_{\downarrow} = L_{\downarrow}\int_{\phi=0}^{2\pi}\int_{\theta=0}^{\frac{\pi}{2}}\cos\theta\sin\theta d\theta d\phi = \pi L_{\downarrow} \tag{4.9}$$

and the relationship between irradiance and actinic flux is [*Madronich*, 1987]

$$E_{\downarrow,diff} = 0.5F_{\downarrow,diff} \tag{4.10}$$

$$E_{\uparrow,diff} = 0.5F_{\uparrow,diff} \tag{4.11}$$

Thus, the total actinic flux (F_{tot}) can be calculated from the downward direct, downward diffuse, and upward diffuse irradiances using the formula

$$F_{tot} = \frac{E_{direct}}{\cos\theta_z} + 2E_{\downarrow,diff} + 2E_{\uparrow,diff} \tag{4.12}$$

Since the radiation module of *Fu and Liou* [1993] does not separate the downward direct irradiance from the downward diffuse irradiance, we used the results of simulations with TUV v.4.1 to calculate the fraction of the downward irradiance due to the downward diffuse irradiance for 10 zenith angles between 0° and 86°. CRM6 then linearly interpolates those values to get the fraction of the downward flux due to the diffuse flux at the current zenith angle.

Table 4.1 compares the values of the irradiance and actinic flux estimated for the wavelength range 290 nm-800 nm by the CRM6 model and the TUV v.4.1 model for the Timbavati smoke plume at a zenith angle of 40°.[1] The values match fairly well, with CRM6 predicting a slightly smaller actinic flux.

Table 4.1: Irradiances and Actinic Fluxes Calculated by TUV and CRM6 (W/m^2)

Surface, Zenith = 40°				
	CRM6 (290 nm-800 nm)		TUV v4.1 (290 nm-800 nm)	
	Actinic Flux[a]	Irradiance	Actinic Flux	Irradiance
Total	801	548	864	592
Direct Beam	556.4	-	600	460
Total Up	143	71.5	155	77
Total Down	657.9	477	709.5	515
Total Diffuse	244.5	-	264	132
Diffuse Up	143	71.5	154.5	77
Diffuse Down	101.5	-	110.	55.

[a] Estimated assuming that the downward irradiance is 89.36% direct beam, 10.64% diffuse downward based on TUV results for surface.

Table 4.2 compares the photolysis rates calculated by the CRM6 model and TUV v.4.1 at 1 km in altitude at a zenith angle of 43.4-43.6°. The photolysis rates calculated by the two methods are generally within 25%, with CRM6 giving lower values. An error of 25% is on the same order as the parametric uncertainty for these photolysis reactions. The two exceptions are the reactions $NO_3 \rightarrow NO + O_2$ and $HCHO \rightarrow H_2 + CO$, where the CRM6 calculated values are only 65% and 51%, respectively, of the TUV calculated values. However, these reactions are unlikely to have a significant impact on the chemistry. The concentration of NO_3 is very low in the daytime and the other photolysis pathway for NO_3 is dominant. For the second HCHO pathway, H_2 and CO are fairly unreactive on the 1 hour time scale of interest here, and so should not significantly impact the chemistry within the smoke plume.

The gas and aerosol chemistry for the Eulerian simulations is calculated using the ASP model described in Chapter 2. Figure 4-1 illustrates the interface between CRM6 and the ASP model. Every 60 seconds, the CRM6 model passes the current gas and aerosol phase concentrations at each Eulerian grid point to the ASP model, along with the calculated values for photolysis rates, temperature, pressure, and relative humidity. The ASP model then integrates the gas-phase chemistry, gas-to-aerosol mass transfer, aerosol thermodynamics, and aerosol coagulation to calculate updated gas and aerosol concentrations, as well as updated aerosol optical properties. These values are then

[1] See the discussion of photolysis rate calculations in Appendix A.

Table 4.2: Photolysis Rates Calculated by TUV and CRM6

Reaction	CRM6 (Zenith = 43.53^o)	TUV v4.1 (Zenith = 43.4^o)	CRM6/TUV
NO_2	7.21×10^{-3}	7.76×10^{-3}	92.9%
$O_3 \rightarrow O(^1D)$	2.02×10^{-5}	2.39×10^{-5}	84.5%
$O_3 \rightarrow O(^3P)$	4.18×10^{-4}	3.84×10^{-4}	108.8%
H_2O_2	4.86×10^{-6}	5.96×10^{-6}	81.5%
$NO_3 \rightarrow NO + O_2$	1.28×10^{-2}	1.96×10^{-2}	65.3%
$NO_3 \rightarrow NO_2 + O$	1.49×10^{-1}	1.53×10^{-1}	97.4%
HONO	1.59×10^{-3}	1.71×10^{-3}	93.0%
MGLY	8.73×10^{-5}	9.17×10^{-5}	95.2%
CH_3CHO	3.79×10^{-6}	4.58×10^{-6}	82.8%
$CH_3C(O)CH_3$	4.18×10^{-7}	5.44×10^{-7}	76.8%
$HCHO \rightarrow 2\ HO_2 + CO$	1.99×10^{-5}	2.62×10^{-5}	75.9%
$HCHO \rightarrow H_2 + CO$	2.03×10^{-5}	4.00×10^{-5}	50.8%

Photolysis rates calculated for Timbavati fire location at 1 km in altitude.
Effect of aerosol on the radiative field was not included.

passed to the CRM6 model, which integrates the dynamics of the smoke plume for 60 seconds before calling the ASP model again. To maintain charge balance during advection and diffusion, the inorganic ions in the aerosol are paired into hypothetical electrolyte pairs by the ASP model before being passed to the CRM6 model. CRM6 then solves the advection-diffusion equations for these electrolyte pairs, and the concentrations of the pairs are passed back to the ASP model, which recalculates the aqueous ion concentrations using the inorganic thermodynamic routines described in Chapter 2.

4.2 Model Initialization

Figure 4-2 shows the Eulerian domain and resolution used for the simulations of the Timbavati smoke plume. The x direction is set as the direction of the surface wind (160° for Timbavati). The total model domain size was 52.5 km × 20 km × 4 km with a resolution of 500 m × 1 km × 100 m. The width of the rectangular fire source was set at 2 km based on observations [*Hobbs et al.*, 2003], with a downwind thickness of 500 m. The time-step for the integration of the dynamical equations was 1 s, while the radiation module and the ASP gas and aerosol model was called every 60 s. The model was allowed to "spin up" for 10 minutes before the fire source was turned on, after which the model was run for 60 minutes. All of the results shown in Section 4.3 are at 60 minutes after the ignition of the fire source. In the rest of this section we discuss the initial meteorological (Section 4.2.1) and chemical (Section 4.2.2) model state for the Timbavati plume simulation, describe the fire emissions of heat, trace gases, and particles (Section 4.2.3), and describe the two chemistry

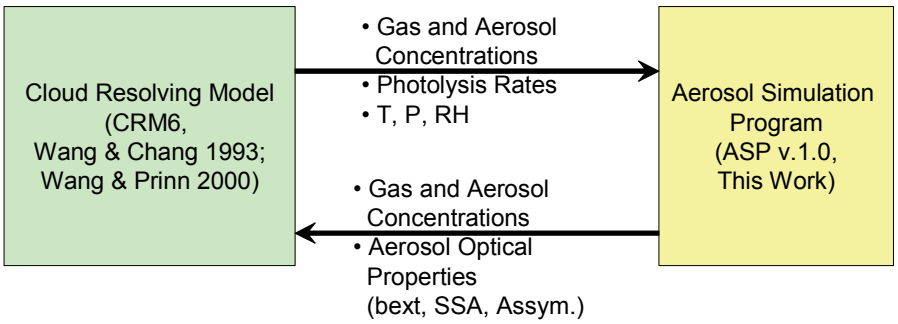

Figure 4-1: Schematic of the interface between the 3D Eulerian dynamics model CRM6 and the gas and aerosol chemical model ASP.

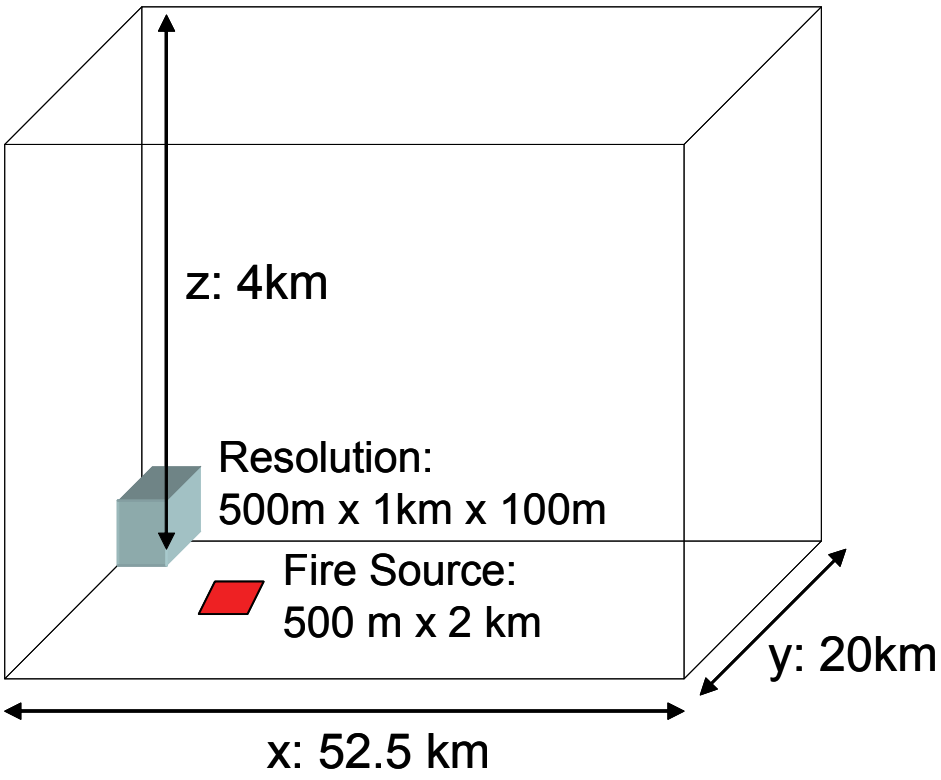

Figure 4-2: Domain size and resolution for the 3D Eulerian simulations of the Timbavati smoke plume.

cases used in our study (Section 4.2.4).

4.2.1 Meteorology

The profiles for temperature, relative humidity, and horizontal winds used to initialize the Timbavati model simulations are shown in Figure 4-3. Initial vertical profiles for temperature, relative humidity, horizontal wind speed and horizontal wind direction between 600 m and 3300 m in altitude are taken from the vertical profiles measured by *Hobbs et al.* [2003] for the Timbavati fire between 0829 and 0840 UTC. The data were binned and averaged for every 100 m in altitude. The direction of the x-axis and u wind was set to 160°, the measured wind direction at 600 m in altitude. For altitudes below 600 m, temperature was calculated assuming a dry adiabatic lapse rate and q_v (kg H_2O/kg moist air) was assumed to be constant. The wind direction below 600 m was held constant at 160° while the wind speed was assumed to follow the logarithmic profile

$$\frac{u(z)}{u_*} = \frac{1}{\kappa} \ln \frac{z}{z_o} \tag{4.13}$$

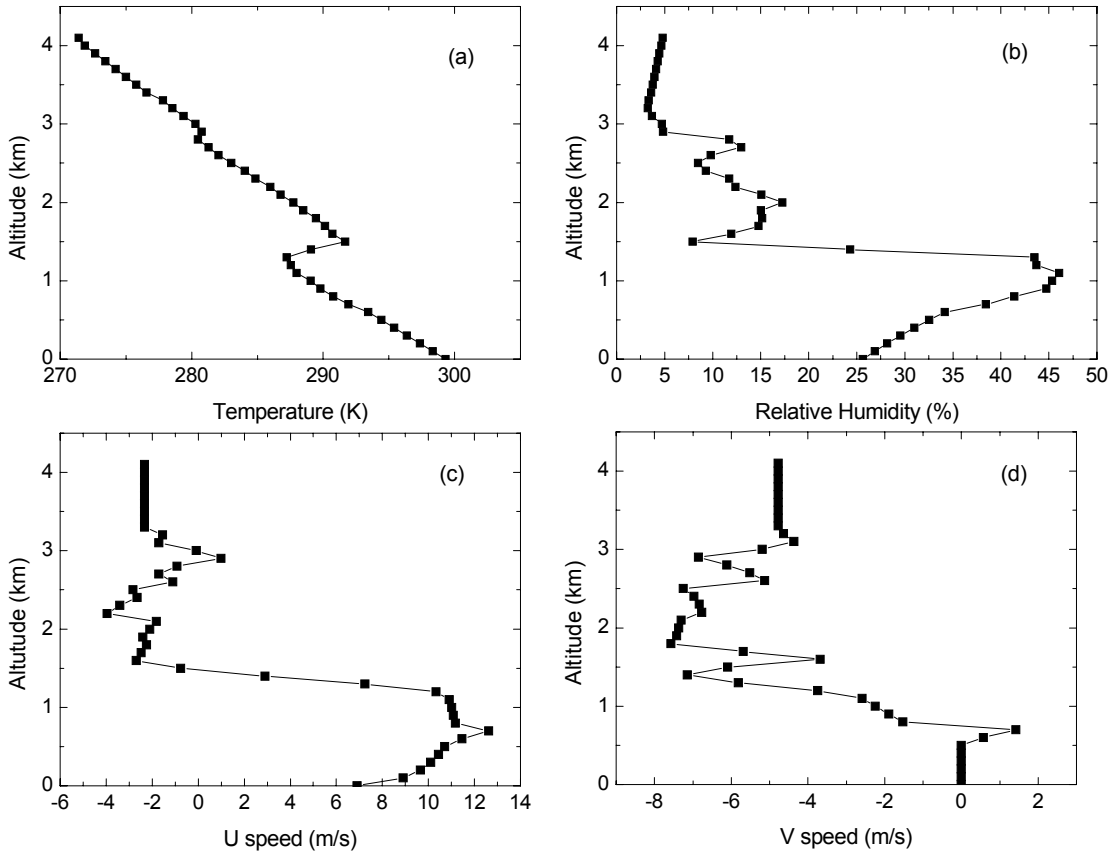

Figure 4-3: Initial meteorological profiles used in the 3D Eulerian simulations of the Timbavati smoke plume. Data between 600 m and 3300 m is from *Hobbs et al.* [2003], and has been binned and averaged for every 100 m. The rest of the profile is extrapolated from the available data as described in the text.

where $\kappa = 0.4$ and $z_o = 0.1$ m (the value for fully grown root crops) [*Seinfeld and Pandis*, 1998]. A value of 0.5 m/s for u_* was used to match the profile to the observed wind speed at 600 m. Above 3300 m, wind direction and speed were held constant, as was q_v. Temperature was calculated assuming that the observed lapse rate below 3300 m stayed constant with height to 4000 m. Pressure was calculated from the temperature and relative humidity profiles using the hydrostatic equation. The data show a strong temperature inversion between 1.3 and 1.5 km in altitude, with corresponding rapid changes in other variables.

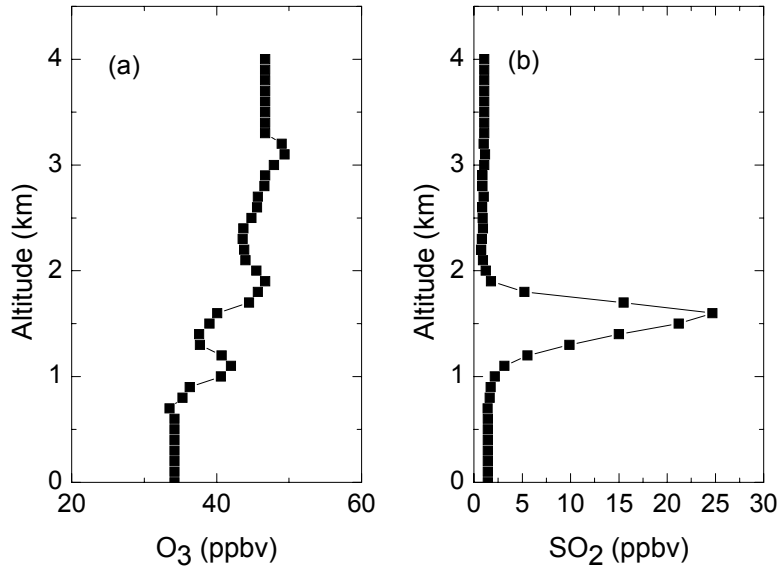

Figure 4-4: Inital mixing ratios of (a) O_3 and (b) SO_2 versus height for the Timbavati smoke plume.

4.2.2 Gas and Aerosol Concentrations

Hobbs et al. [2003] measured the background vertical profiles of O_3 and SO_2 for Timbavati between 0829 and 0840 UTC. This data was binned every 100 m and averaged to provide initial vertical profiles of O_3 and SO_2 for the Eulerian model simulations. The profiles are shown in Figure 4-4. The mixing ratios are assumed to be constant below 600 m and above 3300 m in altitude.

All other gas-phase species were assumed to have a constant mixing ratio versus altitude, with the mixing ratio chosen to match the background concentrations given in Tables 3.12 and 3.13. To prevent numerical problems, all compounds with a background concentration of 0 were assumed to be present at a constant initial mixing ratio of 1 pptv.

The initial vertical profile of aerosol in the model was calculated assuming an exponential decay of aerosol concentration with height [*Seinfeld and Pandis*, 1998]. The decay length scale was set to 700 m, a value within the range reported for remote continental aerosols [*Seinfeld and Pandis*, 1998]. The aerosol number and mass concentrations at 1 km in altitude were set to the values given for the background aerosol in Table 3.15. The initial aerosol number concentration versus height for the Timbavati simulations is shown in Figure 4-5. The aerosol was simulated using a 4 bin size distribution, with 2 of the bins between 0.015 μm and 1 μm in radius. This is the smallest

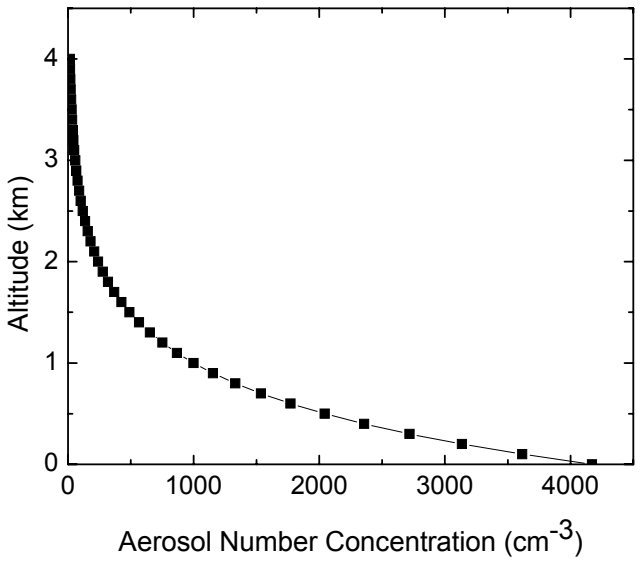

Figure 4-5: Initial aerosol number concentration versus height for the Timbavati smoke plume.

number of bins that could be used and still have the aerosol size distribution represent the optical properties of the 12 bin size distribution used in the Lagrangian experiments in Chapter 3. A small number concentration (0.01 particles cm^{-3} at 1 km) was added to the largest aerosol size bin to prevent numerical problems.

4.2.3 Fire Emissions

According to *Hobbs et al.* [2003], the Timbavati fire burned for 3 hours, covering an area of 1000 ha. The fuel load was 0.48 kg m^{-2} and approximately 80% of the fuel exposed to fire was combusted, corresponding to 3.8×10^6 kg of biomass burned.

In our model simulations, we assume the fire front moved in the downwind direction at a constant speed. The observed total area burned and the width of the fire front corresponds to an average fire front speed of about 0.5 m/s. This is consistent with a fuel of moisture content of 20% and a surface wind speed of 6.9 m/s according to the empirical parameterization of *Mell et al.* [2007] for the rate of spread of grassland fires. Using a value of 18,700 kJ/kg for the heat of combustion of biomass [*Trentmann et al.*, 2006] gives a total heat release of 6.6×10^9 W. Some fraction of this heat is lost to radiation while the rest contributes to the buoyancy of the smoke plume. Commonly accepted values of this fraction are 0.4 to 0.8 [*Trentmann et al.*, 2002]. Following *Trentmann et al.*

[2002], we assume that 55% of the heat released by the fire contributes to the buoyancy of the smoke plume, giving a buoyant heat release of 3.6×10^9 W.

To calculate the emission of CO from the Timbavati fire, we used the USDA Fire Service Fire Emission Production Simulator (FEPS) v.1.1.0. For the reported conditions of the Timbavati fire, FEPS estimated a CO release rate of 49.5 kg CO/s. The emission rate of water vapor was calculated using an emission factor of 0.5 kg H_2O/kg dry fuel [*Freitas et al.*, 2007]. The emissions of all other smoke gases and particles were calculated using the emission ratios of these compounds to CO. The emission ratios for trace gases are given in Tables 3.12 and 3.13, while the emission ratios for aerosol species were calculated from the rescaled initial smoke aerosol concentrations given in Table 3.15.

4.2.4 Reference and Expanded Chemistry Cases

The results of the Lagrangian modeling for the Timbavati plume from Chapter 3 showed that the reference model simulation did not provide a good match with the observed formation of O_3 and growth of aerosols in the Timbavati smoke plume. We found that modeling the uncharacterized organic species in the smoke as a reactive species (BIOH) and adding heterogeneous reactions of NO_2 and SO_2 improved the match between the model and observations.

Based on these results, we performed two simulations of the Timbavati smoke plume using the 3D Eulerian model described above. In the first (hereafter the "reference chemistry" case) we assumed that the uncharacterized organic species were unreactive, and did not include any heterogeneous reactions of NO_2 or SO_2. In the second (hereafter the "expanded chemistry" case) we modeled the chemistry of the uncharacterized organic species using monoterpenes (BIOH) as a proxy for high-carbon number reactive organic species that form organic aerosol. We also included the heterogeneous reactions $NO_2 \rightarrow 0.5$ HONO + 0.5 HNO_3 and $SO_2 \rightarrow H_2SO_4$ with uptake coefficients of 10^{-3} and 2×10^{-4}, respectively. The results of both simulations are presented below.

4.3 Model Results and Comparison to Observations

In this section we present the 3D Eulerian model results for fluid dynamics and CO concentrations (Section 4.3.1), O_3, OH, and NO_x concentrations (Section 4.3.2), aerosol number and mass concentrations (Sections 4.3.3 and 4.3.4, respectively), aerosol optical properties (Section 4.3.5), and solar radiation and photolysis rates (Section 4.3.6). All of the results shown in this section are at 60 minutes after the ignition of the fire source.

4.3.1 Fluid Dynamics and CO Concentrations

Since the lifetime of CO (1 - 3 months) is very long compared to the 1 hour timescale simulated here, we can use the modeled concentration field for CO to evaluate how well the model simulates the injection height and horizontal dispersion of the Timbavati smoke plume. Figure 4-6 shows the modeled CO concentrations along the centerline of the plume (y = 0) and at 800 m in altitude. CO mixing ratios below 200 ppbv represent the background environmental air outside of the plume, while values above 200 ppbv represent the smoke plume. Figures 4-6(a) and 4-6(c) show the modeled CO concentrations when the minimum horizontal diffusion coefficient for chemical tracers ($K_{\min}$) is set at 45 m^2/s.[2] The modeled plume injection height of 0.6 km - 1.0 km is fairly close to the observed injection height of the Timbavati smoke plume: *Hobbs et al.* [2003] reported that most of the smoke was found between 0.5 - 0.9 km in altitude, with some puffs as high as 1.4 - 1.7 km. This injection height seems to be primarily determined by the strong temperature inversion between 1.3 and 1.5 km in altitude for the Timbavati smoke plume. However, the modeled horizontal plume width of 6 km is well below the 10 - 15 km width (at 26.2 km downwind) reported by *Hobbs et al.* [2003].

There are two potential explanations for the underestimate of the horizontal dispersion of the Timbavati smoke plume. First, the first order turbulent closure used in the model may be underestimating the subgrid scale turbulent mixing of the plume. The effect of subgrid scale turbulent mixing can be seen by observing the effect of increasing $K_{\min}$. Figures 4-6(b) and 4-6(d) show the results of increasing $K_{\min}$ to 450 m^2/s. In this case, the horizontal plume width is approximately 10 km, providing a closer match to the observed value of 10 - 15 km. For this reason, we set $K_{\min}$ to 450 m^2/s for all the simulations discussed below.

The second potential explanation is that the model is missing the effects of large-scale variability of the horizontal winds on the horizontal dispersion of the plume. In the model, the boundary conditions for the horizontal winds are held constant. However, the actual boundary layer winds may fluctuate with time on the scale of the smoke plume, increasing the horizontal spread of the smoke emissions. For example, the horizontal velocity spectra for a mixed boundary layer show a peak near a wavelength slightly larger than the height of the mixed layer, which for Timbavati is 1.3-1.5 km [*Kaimal et al.*, 1972; *Stull*, 1988]. These and longer-wavelength fluctuations could increase the dispersion of the smoke plume. Since this effect is not included in the model, the model may underestimate the horizontal dispersion of the smoke plume even though it is modeling the

[2] The minimum horizontal diffusion coefficient for momentum is 1/3 of this value [*Wang and Chang*, 1993].

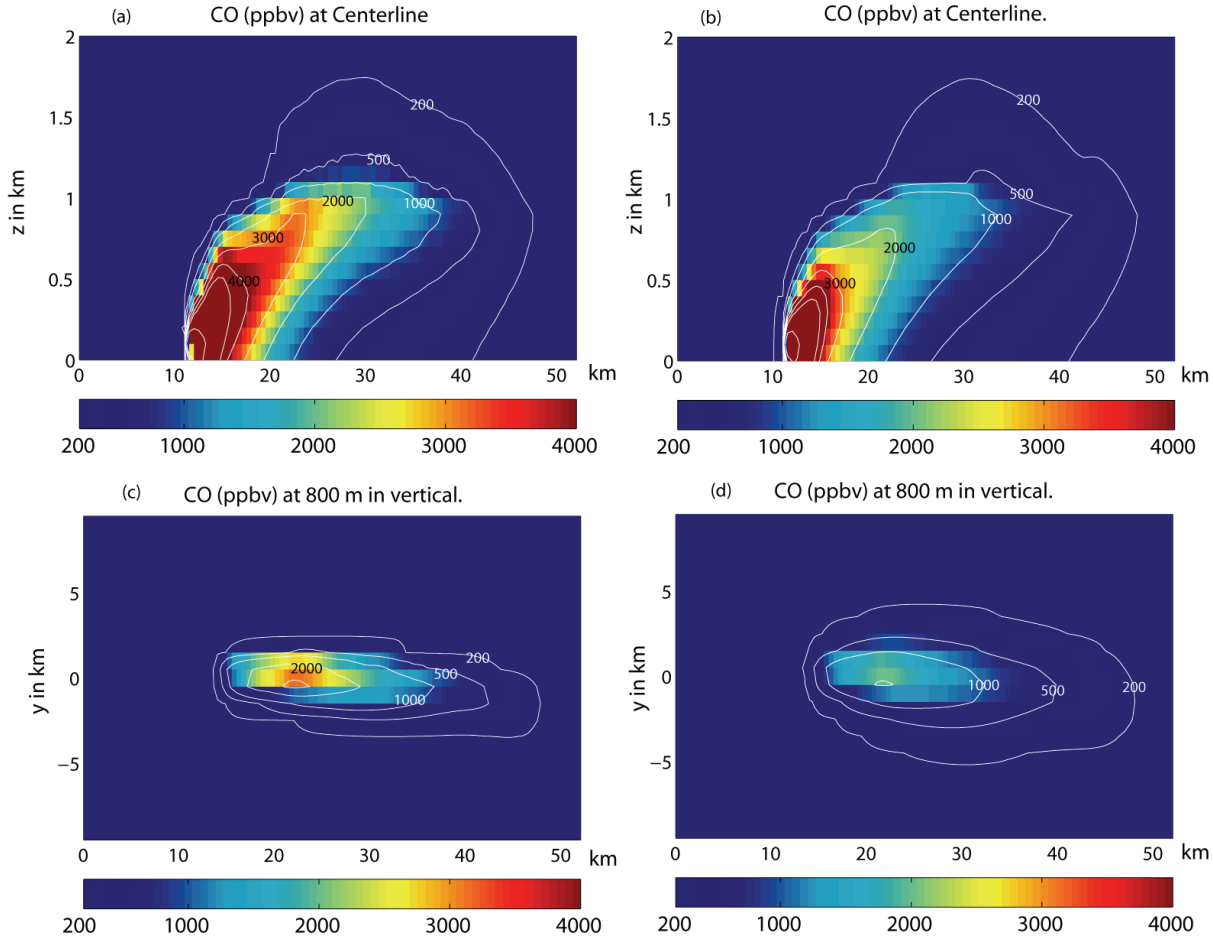

Figure 4-6: CO mixing ratios for the Timbavati smoke plume along the plume centerline ($y = 0$ km) and at 800 m in altitude. Figures (a) and (c) are for the low horizontal diffusion case ($K_{\min} = 45$ m^2/s) while Figures (b) and (d) are for the high horizontal diffusion case ($K_{\min} = 450$ m^2/s).

effect of the subgrid scale eddies correctly.

We can also use the model to explore the time evolution of the circulation induced by the release of sensible heat from the fire. Figure 4-7 shows the wind vectors for the Timbavati smoke plume at 0, 15, 30, 45 and 60 minutes after the fire ignition, and Figure 4-8 shows selected streamlines of the circulation at the same times. We can see that the buoyancy from the fire source induces a rising circulation below 1 km in altitude, causing the streamlines starting at 0.25 and 0.5 km in altitude (the blue dashed and red dotted lines in Figure 4-8, respectively) to move upward as we go further in the x direction. This rising motion also induces a low level convergence of surface streamlines, as is shown by the solid black lines in Figure 4-8.The circulation above 1 km, however, does not appear to be affected by this rising motion. Plots of the vertical wind speed (not shown) suggest that at altitudes above 1 km, the vertical wind speed above the smoke plume is generally negative.

Figure 4-9 shows the time evolution of CO concentrations at 15, 30 and 45 minutes after fire ignition. Here we also see the general rising motion of the smoke below 1 km, along with the horizontal expansion of the smoke plume driven by the higher value of $K_{\min}$.

4.3.2 Ozone, OH, and NO_x

Figure 4-10 shows the concentrations of O_3, OH, and HONO along the centerline of the smoke plume for both the reference and expanded chemistry cases, while Figure 4-11 shows the concentrations of these gases along four different horizontal transects through the smoke plume. As expected, the maximum ozone concentration for the reference chemistry case (62.3 ppbv) is at the bottom of the observed range of ozone concentrations (approx. 60 - 135 ppbv) found downwind in the Timbavati plume [*Hobbs et al.*, 2003]. The expanded chemistry case provides a closer match to the observed ozone concentrations, with a maximum O_3 value of 105.6 ppbv. The horizontal transects show that for both cases, the plume concentration of O_3 is significantly higher at $z = 0.6$ km than at $z = 1.0$ km near the source (x = 16 km), but the concentration at z = 1.0 km is higher than that at z = 0.6 km further downwind (x = 36 km). Downwind, the maximum O_3 varies by 5 to 10 ppbv with altitude, showing that differences in the sample height can affect the measured O_3 concentration. However, this variation is smaller than the 20 ppbv uncertainty of the airborne FTIR measurements of O_3 made for the Timbavati smoke plume [*Yokelson et al.*, 2003].

The higher O_3 concentrations in the expanded chemistry case are primarily from the heterogeneous production of HONO from NO_2, with the uncharacterized organics making a smaller contribution. Figures 4-10 and 4-11 show the impact of including this heterogeneous reaction on the modeled concentrations of OH and HONO. The maximum OH concentration increases from

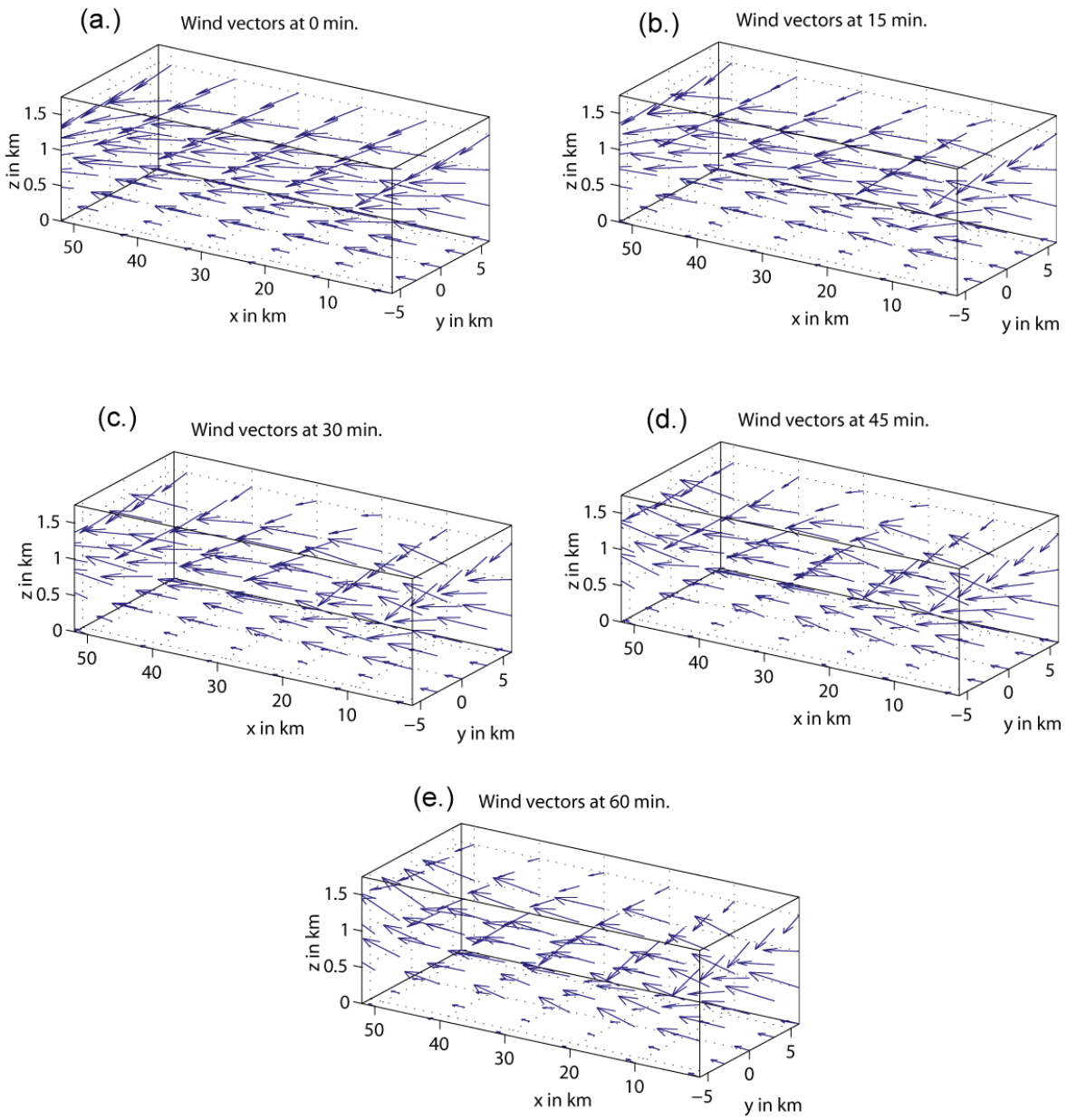

Figure 4-7: Wind vectors for the Timbavati smoke plume simulation. Wind vectors are shown every 15 minutes ($K_{\min} = 450$ m^2/s).

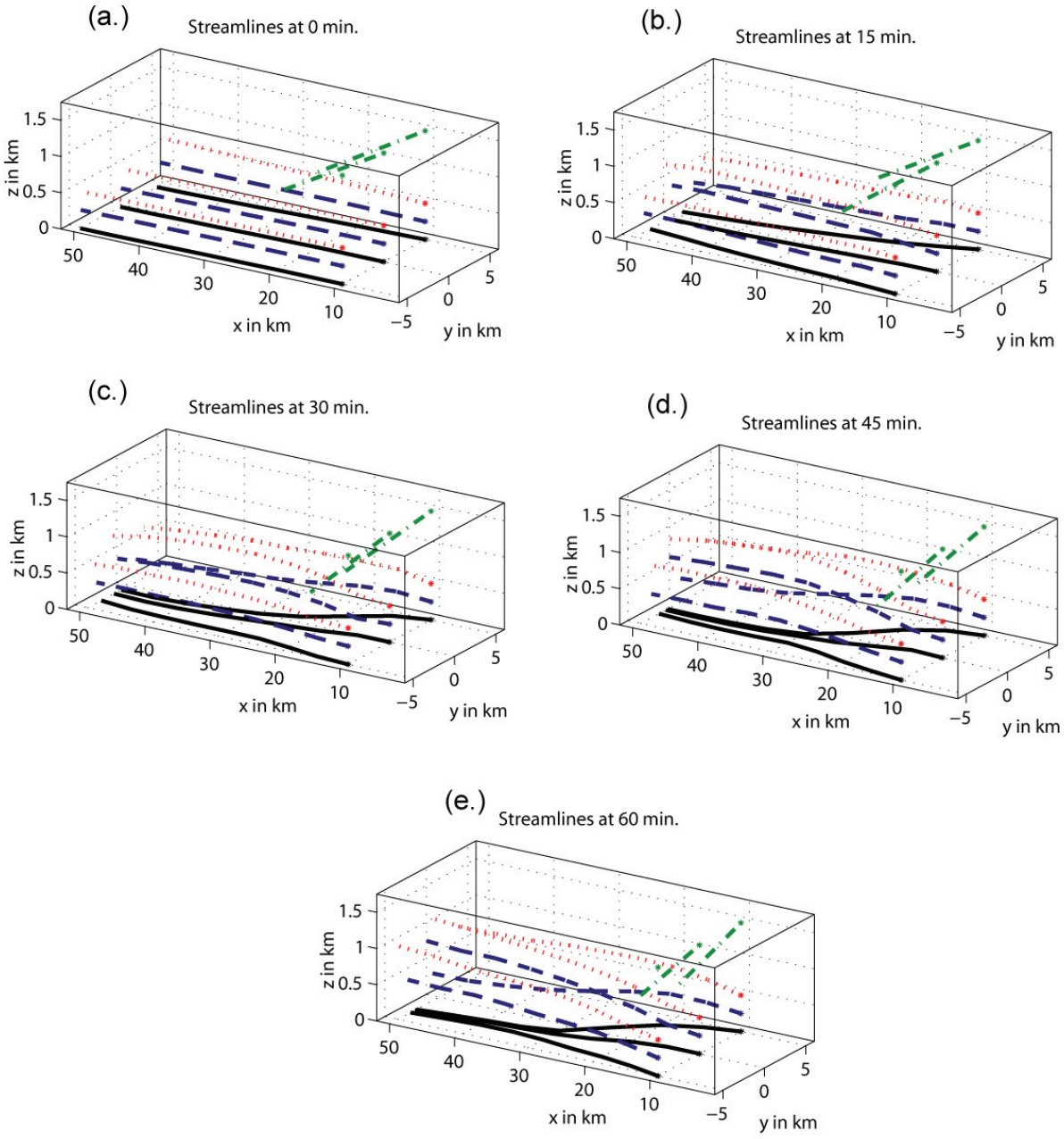

Figure 4-8: Streamlines for the Timbavati smoke plume simulation. Streamlines are shown every 15 minutes ($K_{\min} = 450$ m^2/s).

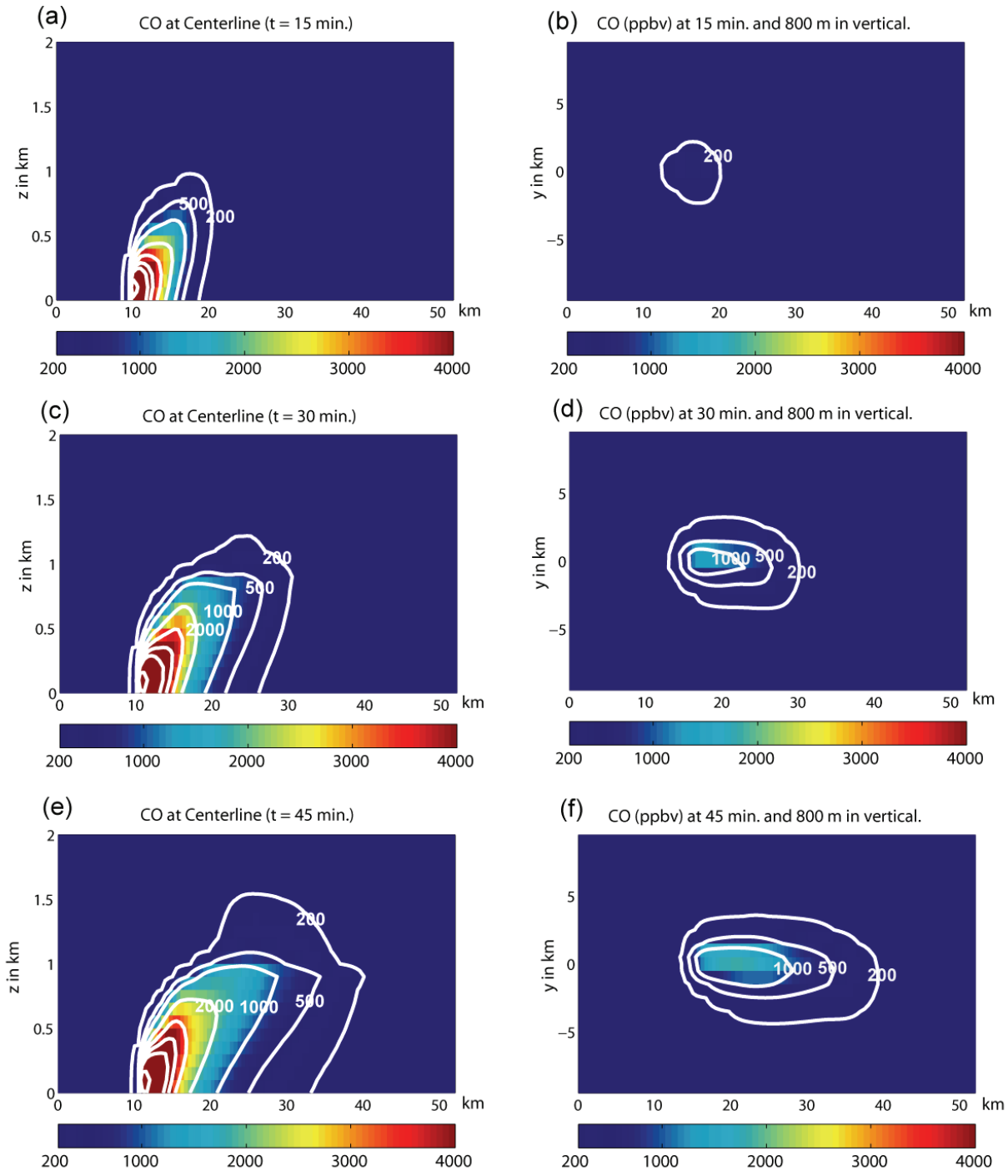

Figure 4-9: CO concentrations (ppbv) at the centerline (y = 0) and at 800 m in altitude at 15, 30 and 45 minutes into the integration ($K_{\min} = 450$ m^2/s).

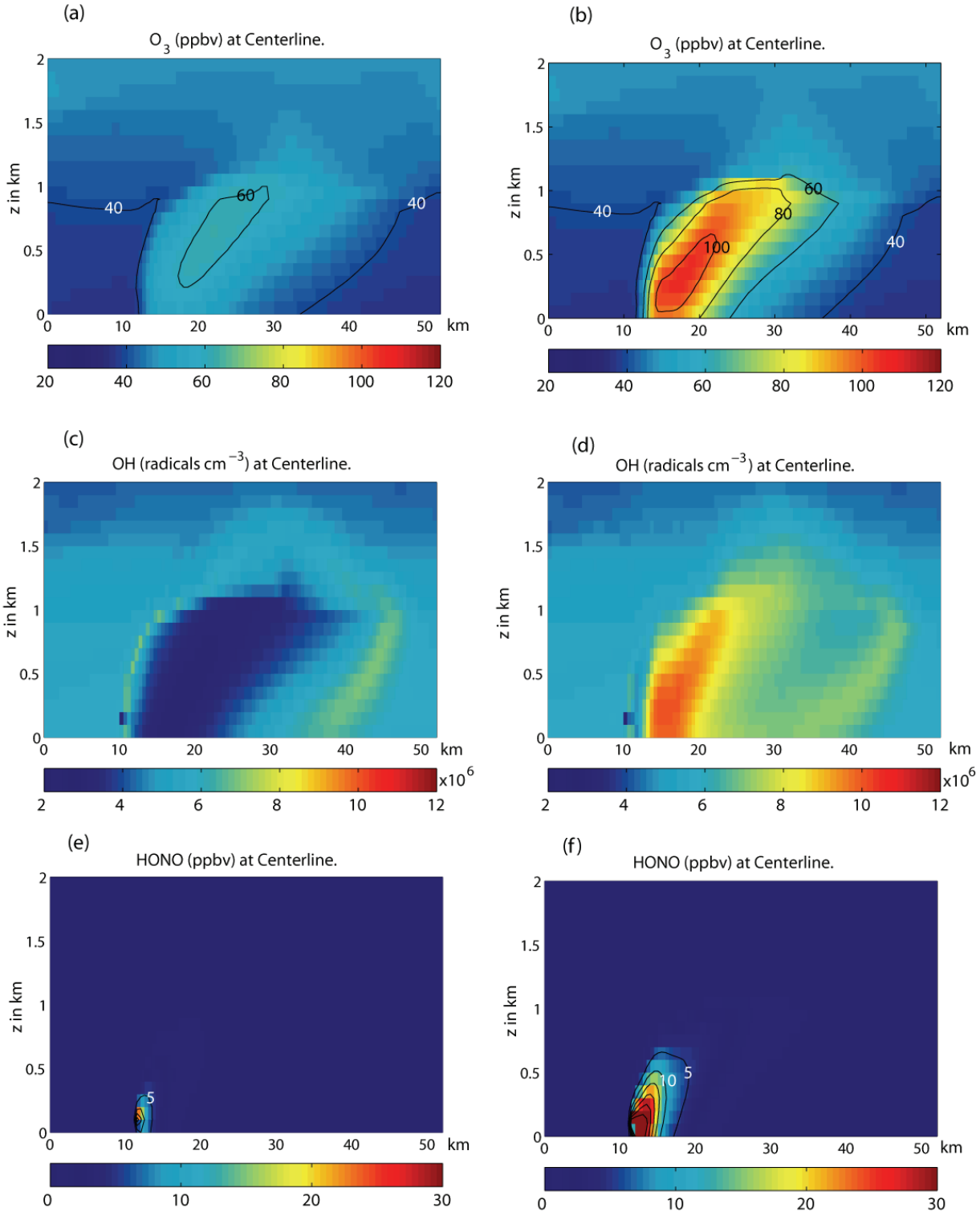

Figure 4-10: Mixing ratios of O_3, OH, and HONO along the centerline of the Timbavati smoke plume ($y = 0$). Figures (a), (c), and (e) are for the reference chemistry case, while Figures (b), (d), and (f) are for the expanded chemistry case.

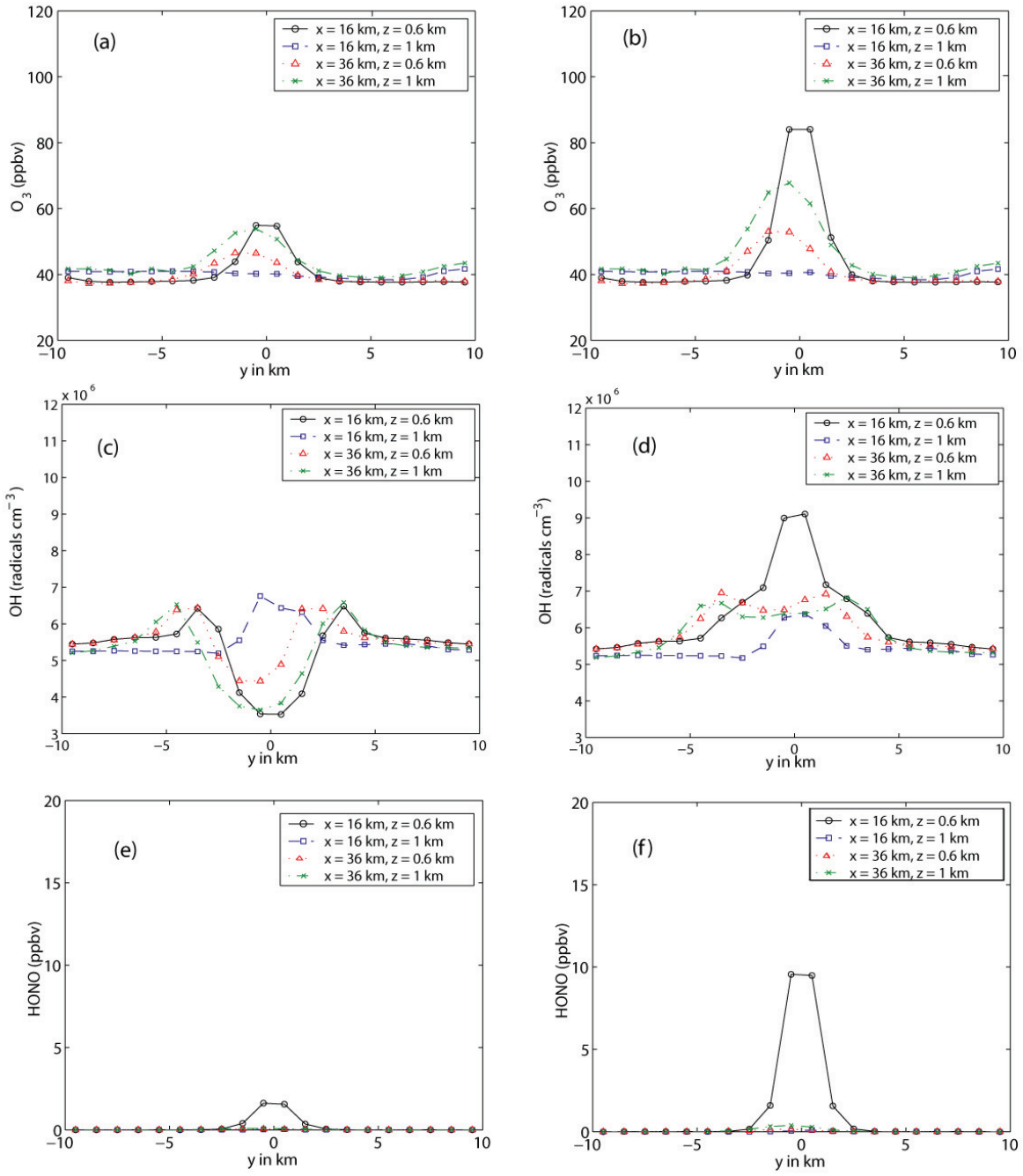

Figure 4-11: Mixing ratios of O_3, OH, and HONO along horizontal transects through the Timbavati smoke plume. Figures (a), (c), and (e) are for the reference chemistry case, while Figures (b), (d), and (f) are for the expanded chemistry case.

7.0×10^6 radicals cm^{-3} to 1.0×10^7 radicals cm^{-3}, but is still well below the inferred plume-average value of $1.7(\pm0.2) \times 10^7$ radicals cm^{-3} reported by *Hobbs et al.* [2003]. In addition, the location of the OH maximum changes. In the reference chemistry case, the maximum OH concentrations are found on the edges of the plume. This can be seen in the "halo" of OH around the smoke plume in Figure 4-10(c) and in the horizontal transects of 4-11(c) which show a dramatic drop in OH concentrations in the center of the smoke plume. This is because the concentrations of the sinks of OH and the absorption of solar radiation by aerosols are highest in the center of the smoke plume, thereby increasing the destruction of OH while reducing its formation from the photolysis of O_3 and HCHO. In the expanded chemistry case (Figures 4-10(d) and 4-11(d)), the concentration of OH is highest in the center of the plume near the source, and is relatively constant through the smoke plume further downwind. This is because the heterogeneous production of HONO is highest in the center of the smoke plume, where the concentrations of NO_2 and aerosol particles are highest. This increased HONO production increases the formation of OH in the smoke plume, counteracting the other effects. This suggests that measurements of OH within the smoke plumes could help to determine if the heterogeneous formation of HONO from NO_2 is responsible for the rapid formation of O_3 observed in young biomass burning smoke plumes.

As expected, the concentration of HONO is higher in the expanded chemistry case due to the heterogeneous formation of HONO. However, the rapid photolysis of HONO to OH and NO keeps the concentration of HONO well below the 20 ppbv detection limit of the airborne FTIR measurements made in the Timbavati smoke plume. In addition, the predicted downwind concentrations of HONO are very small, suggesting that direct measurements of HONO in downwind transects of smoke plumes would have to be very sensitive to determine if the heterogeneous formation of HONO were taking place.

Figure 4-12 shows the concentrations of NO, NO_2, and NO_x along the centerline of the smoke plume for both the reference and expanded chemistry cases, while Figure 4-13 shows the concentrations of these gases along four different horizontal transects through the smoke plume. The horizontal transects in Figure 4-13 are at the same location as those in Figure 4-11. The concentrations of NO_x are lower in the expanded chemistry case. This reduction of NO_x is caused by the heterogeneous reaction of NO_2, which increases the formation of HNO_3 directly (since 1 of every 2 NO_2 molecules that react are converted to HNO_3) and indirectly by increasing the OH concentration, which increases the rate of the gas-phase reaction $OH + NO_2 + M \rightarrow HNO_3 + M$. The downwind (x = 36 km) transects show that the maximum NO_x concentrations for both the reference and expanded chemistry are at or below the airborne AFTIR detection limits for NO and

NO_2 (20 ppbv, [*Yokelson et al.*, 2003]), which is consistent with the observations [*Hobbs et al.*, 2003]. At x = 36 km, the maximum NO_x for the reference chemistry case is 10.0 ppbv and 20.7 ppbv at z = 0.6 km and z = 1.0 km, respectively, while the maximum NO_x for the expanded chemistry case is 6.6 ppbv and 12.6 ppbv, respectively. Thus, the difference between the two cases and the two altitudes are small compared to the 20 ppbv uncertainty in the airborne FTIR measurements. This suggests that a NO_x instrument would need a precision of approximately 1 - 2 ppbv to determine if heterogeneous reactions of NO_2 were taking place, and that slight differences in altitude during the transect flights could cause differences of the same order of magnitude. This would make it difficult to use NO_x measurements to determine if heterogeneous NO_x chemistry is taking place.

4.3.3 Aerosol Number Concentrations

Figure 4-14 shows the total aerosol number concentrations for both the reference and expanded chemistry cases. The results for the two cases are nearly identical. The first set of plots are a vertical slice through the plume centerline. The second set of plots shows the number concentration versus downwind distance along the centerline at three different altitudes. These plots are designed to mimic the flight path taken by *Hobbs et al.* [2003] to produce the observations shown in Figure 3-37. The third set of plots are for three horizontal transects through the smoke plume that were chosen to mimic Samples 2, 3, and 5 of *Hobbs et al.* [2003]; however, the altitudes of the two transects near the source were lowered by 300 m to place them in the center of the modeled plume.

Figures 4-14(c) and (d) show a peak at z = 0.6 km of 6.5×10^4 near the source, with values at 10 and 20 km downwind (x = 20 and 30 km, respectively) varying between 2.1 - 4.3×10^4 and 1.4 - 2.2×10^4 particles cm^{-3}, respectively, depending on altitude. The measurements of *Hobbs et al.* [2003] showed an aerosol number concentration of 8.8×10^4 particles cm^{-3} near the source, decreasing to 3.0×10^4 particles cm^{-3} at 10 km downwind from the fire and increasing to 4.5×10^4 particles cm^{-3} at 20 km downwind. Thus the modeled aerosol number concentration matches the observations well for the first 10 km downwind, but underestimates the observed aerosol number concentration beyond that distance. This result is similar to the result of our Lagrangian studies in Chapter 3, where the Lagrangian model was able to match the initial decrease of number concentration with distance, but could not match the observed increase in number concentration downwind. We showed in Chapter 3 that current nucleation parameterizations would not predict a significant rate of new particle formation in the Timbavati smoke plume, and suggested that the observed increase could be due to the motion of the sampling plane relative to the plume centerline. Figure 4-14 shows that the aerosol number concentration within the plume can vary significantly

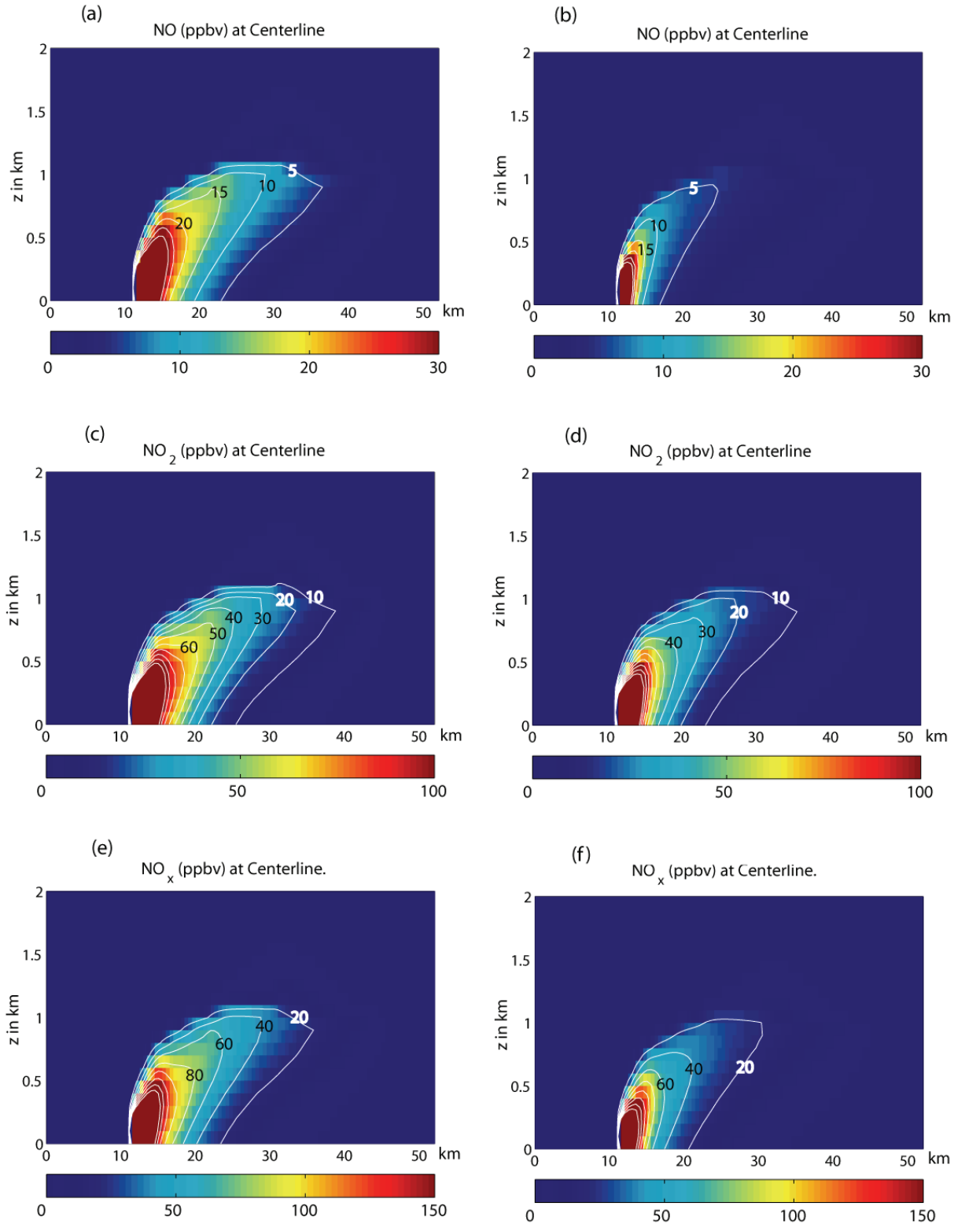

Figure 4-12: Mixing ratios of NO, NO_2, and NO_x along the centerline of the Timbavati smoke plume ($y = 0$). Figures (a), (c), and (e) are for the reference chemistry case, while Figures (b), (d), and (f) are for the expanded chemistry case.

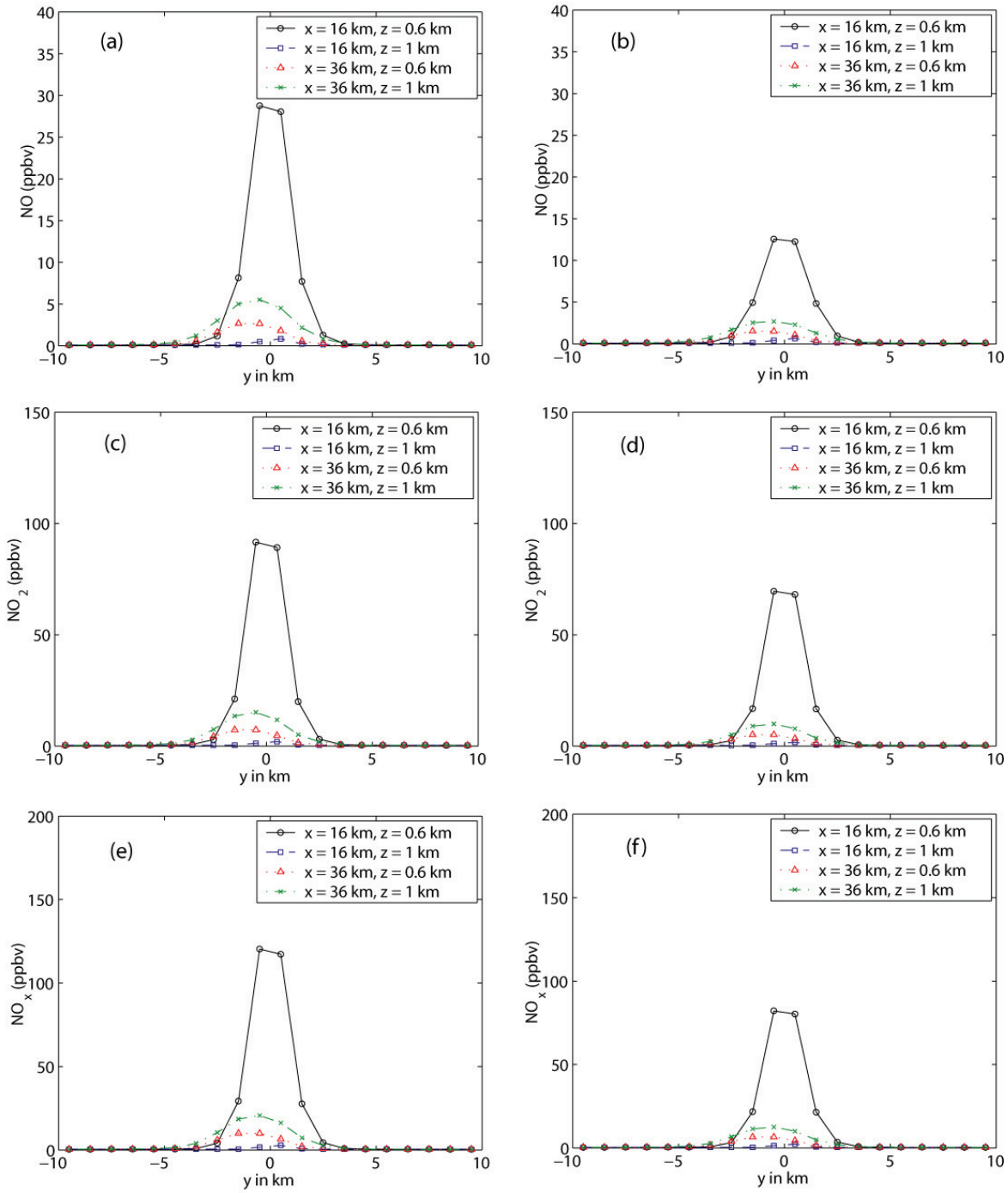

Figure 4-13: Mixing ratios of NO, NO_2, and NO_x along horizontal transects through the Timbavati smoke plume. Figures (a), (c), and (e) are for the reference chemistry case, while Figures (b), (d), and (f) are for the expanded chemistry case.

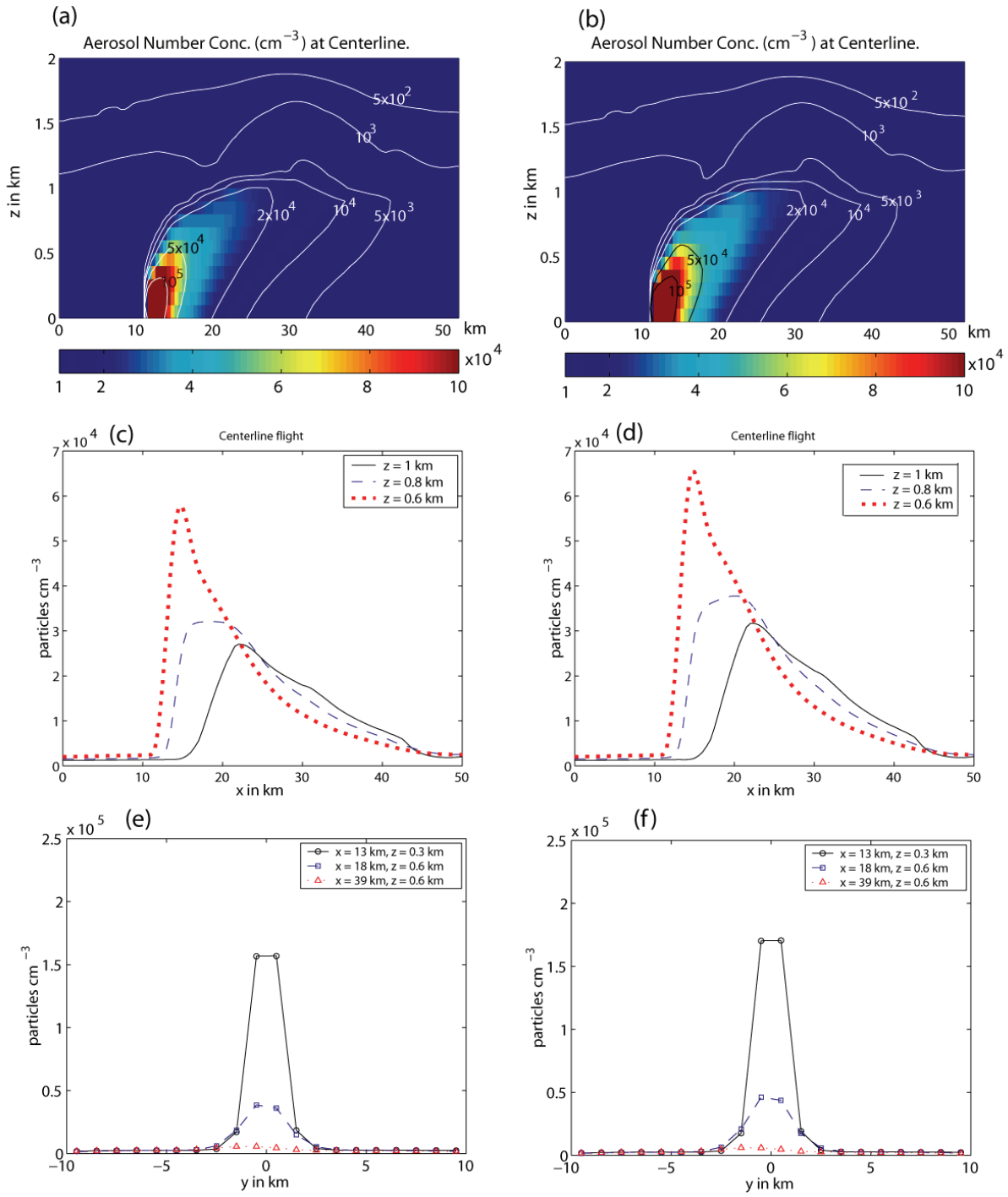

Figure 4-14: Total aerosol number concentration in the Timbavati smoke plume. Figures (a), (c), and (e) are for the reference chemistry case, while Figures (b), (d), and (f) are for the expanded chemistry case. Figures (a) and (b) are vertical slices along the plume centerline ($y = 0$). Figures (c) and (d) show aerosol number concentration versus downwind distance for different altitudes along the plume centerline. Figures (e) and (f) are along horizontal transects of the plume.

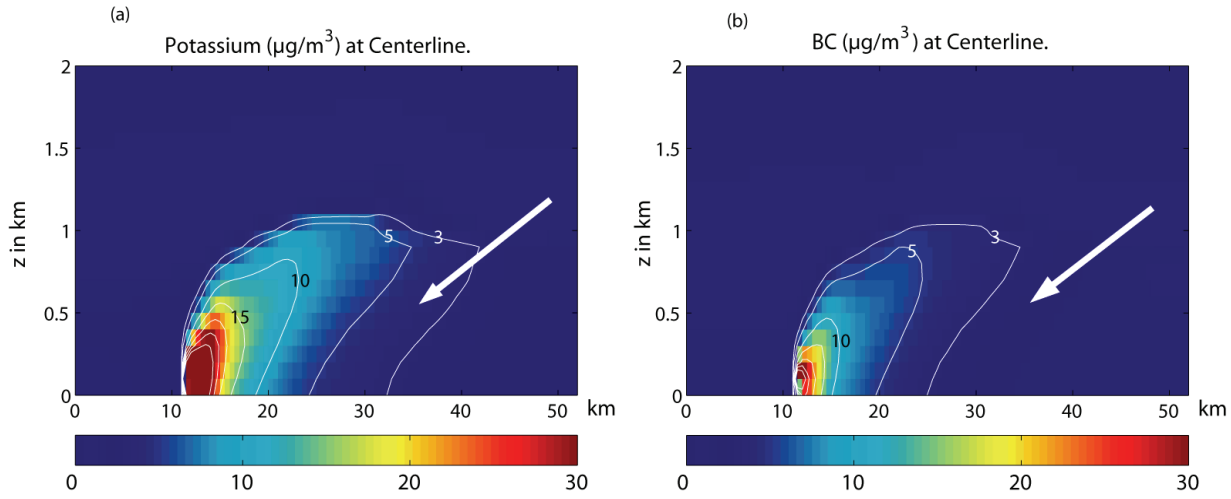

Figure 4-15: Aerosol mass concentrations of potassium (K^+) and black carbon (BC) at the centerline of the Timbavati smoke plume ($y = 0$). The white arrow points to the location of the downwind aerosol measurement from *Hobbs et al.* [2003]. The observed concentrations at this location for K^+ and BC were 3.8 and 6.7 $\mu g/m^3$, respectively.

with altitude, and falls off rapidly with distance from the plume centerline. This result is consistent with our hypothesis that the reported increase in aerosol particle concentrations with downwind distance may be due to the airplane moving relative to the plume centerline.

4.3.4 Aerosol Mass Concentrations

Figure 4-15 shows the mass concentrations of potassium (K^+) and black carbon (BC) at the centerline of the smoke plume. These species are not formed or destroyed within the model, and so act as conservative tracers. The figure shows the results for the expanded chemistry case, which are nearly identical to the reference chemistry case (not shown). The potassium concentration at x = 36 km and z = 0.6 km of 3.5 $\mu g/m^3$ is consistent with the downwind (Sample 5) observation of 3.8 $\mu g/m^3$ reported by *Hobbs et al.* [2003] (see Table 3.10). As in the Lagrangian studies from Chapter 3, the model underestimates the downwind concentration of BC at this location (modeled at 2.2 $\mu g/m^3$ versus the observed concentration of 6.7 $\mu g/m^3$). As discussed in Chapter 3, this discrepancy may be due to the absorption of solar radiation by secondary organic species, which would cause the observed BC concentration, measured by absorption, to be an overestimate that includes some of the light-absorbing OC.

Figure 4-16 shows the mass concentrations of sulfate (SO_4^{2-}) and organic carbon (OC) at the centerline of the smoke plume for the reference and expanded chemistry cases. The expanded

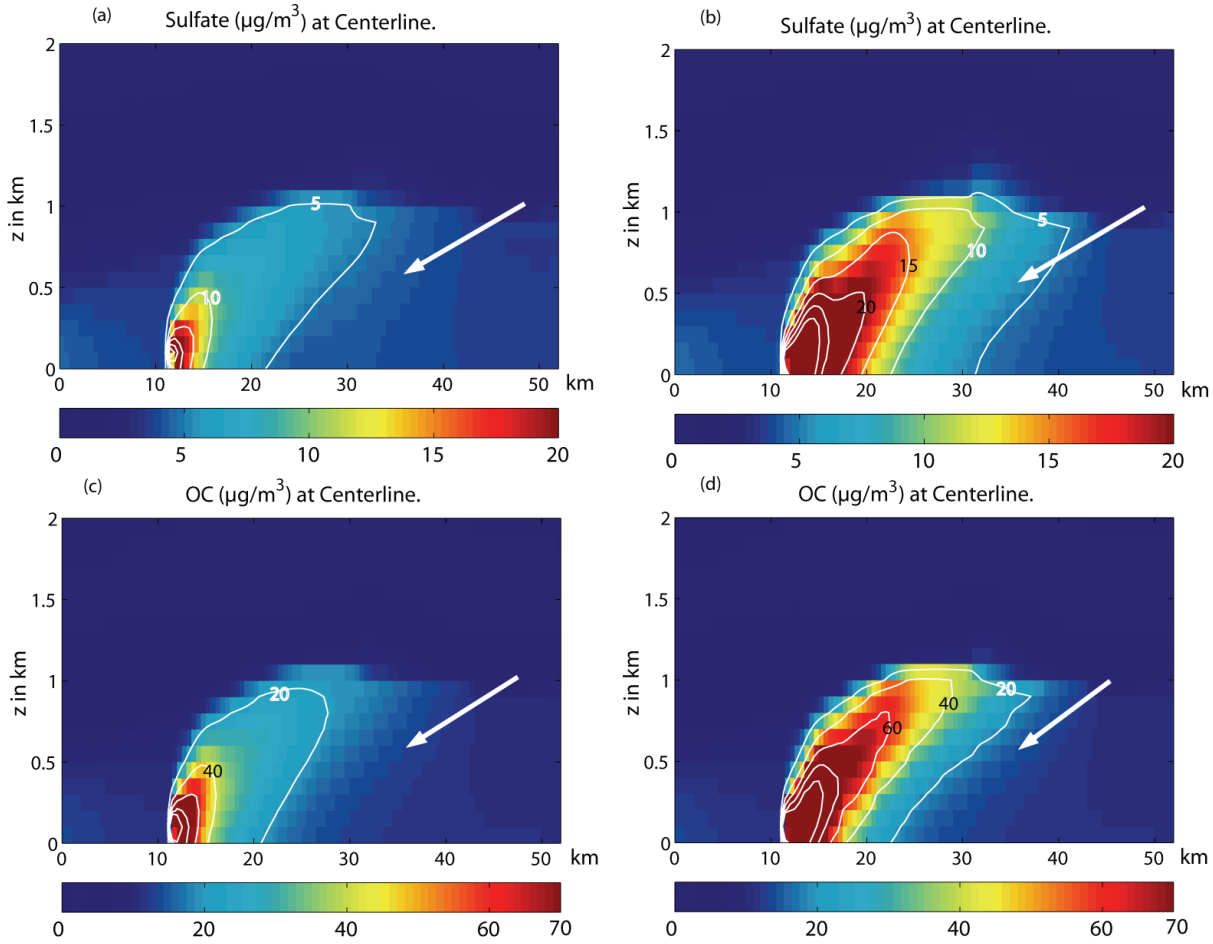

Figure 4-16: Aerosol mass concentrations of sulfate (SO_4^{2-}) and organic carbon (OC) at the centerline of the Timbavati smoke plume ($y = 0$). The white arrow points to the location of the downwind aerosol measurement from *Hobbs et al.* [2003]. The observed concentrations at this location for SO_4^{2-} and OC were 8.1 and 34 μg/m^3, respectively.

chemistry improves the match with observations for these species, but still estimates lower concentrations than reported by *Hobbs et al.* [2003]. For sulfate, *Hobbs et al.* [2003] report a concentration of 8.1 μg/m^3 for Sample 5, while the model gives concentrations (at x = 36 km and z = 0.6 km) of 4.2 and 5.5 μg/m^3 for the reference and expanded chemistry cases, respectively. For OC, *Hobbs et al.* [2003] report a concentration of 34 μg/m^3 for Sample 5, while the model gives concentrations of 13.1 and 14.2 μg/m^3 for the reference and expanded chemistry cases, respectively. However, it is worth noting that at x = 36 km the maximum concentrations of sulfate and OC occur at z = 1 km, with values of 7.5 μg/m^3 SO_4^{2-} and 22.7 μg/m^3 OC, closer to the observed concentrations. This suggests that part of the difference between the model and observation may be due to differences in the height of the maximum smoke concentrations downwind.

Figure 4-17 shows the mass concentrations of chloride (Cl^-) and the mixing ratios of HCl gas for the reference and expanded chemistry cases. Figure 4-18 shows the gas and aerosol chloride concentrations along two horizontal transects at z = 0.6 km, one close to the source and another further downwind. Close to the source, the expanded chemistry case has more of the chloride present in the gas phase as HCl than in the reference chemistry case. This is because more sulfate and nitrate are formed in the expanded chemistry case, and the condensation of these acids onto the aerosol pushes the equilibrium of the chloride toward the gas phase. In both cases, the chloride is almost entirely present in the gas phase at x = 36 km, with aerosol Cl^- concentrations of 0.10 and 0.08 $\mu g/m^3$ for the reference and expanded chemistry cases, respectively. These modeled aerosol Cl^- concentrations are well below the observed downwind Cl^- concentration of 5.4 $\mu g/m^3$. As we discussed in Chapter 3, this underestimate of aerosol Cl^- suggests that our aerosol chemical model may not be capturing the correct partitioning between the gas and aerosol phase for inorganic species. Figure 4-18 shows that total (gas + aerosol) amount of chloride present in the model at x = 36 km is consistent with the observations, but the model predicts that it should be present in the gas phase.

Figure 4-19 shows the mass concentrations of nitrate (NO_3^-) and the mixing ratios of HNO_3 gas for the reference and expanded chemistry cases. Figure 4-20 shows the gas and aerosol nitrate concentrations along two horizontal transects (the same as those in Figure 4-18). The total (gas + aerosol) nitrate concentrations are much higher in the expanded chemistry case than in the reference chemistry case. This is consistent with the increased loss of NO_x in the expanded chemistry case discussed above. The aerosol nitrate concentration at x = 36 km and z = 0.6 km were 1.8 $\mu g/m^3$ and 3.0 $\mu g/m^3$ for the reference and expanded chemistry cases, respectively. These values are much lower than the concentration of 9.1 $\mu g/m^3$ reported by *Hobbs et al.* [2003]. Figure 4-20 shows that the total nitrate concentration at x = 36 km and z = 0.6 km in the expanded chemistry case is below the reported aerosol nitrate value. As was the case for sulfate and OC, the maximum gas and aerosol nitrate concentrations at x = 36 km occur at z = 1 km (4.4 and 6.1 $\mu g/m^3$, respectively). At x = 36 km and z = 1 km the modeled total nitrate concentration is high enough to be consistent with the observations.

4.3.5 Aerosol Optical Properties

Figure 4-21 shows the aerosol scattering coefficient and single scattering albedo at the plume centerline as well as the horizontal distribution of aerosol optical depth for the reference and expanded chemistry cases. Figure 4-22 shows the aerosol scattering coefficient along three horizontal transects

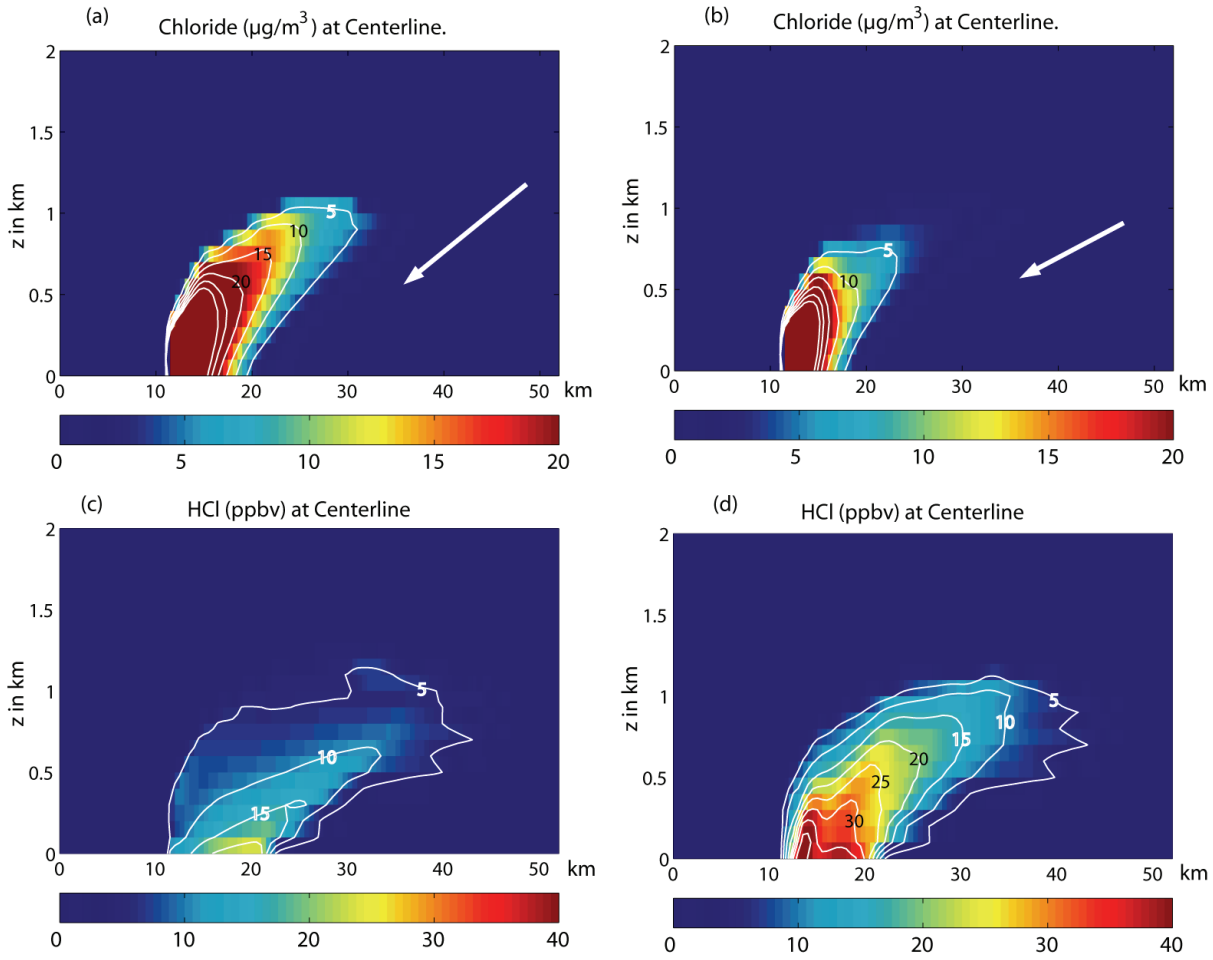

Figure 4-17: Concentrations of gas-phase HCl and aerosol chloride (Cl^-) at the centerline of the Timbavati smoke plume ($y = 0$). Figures (a) and (c) are for the reference chemistry case, while Figures (b) and (d) are for the expanded chemistry case. The white arrow points to the location of the downwind aerosol measurement from *Hobbs et al.* [2003]. The observed Cl^- concentration at this location was 5.4 $\mu g/m^3$.

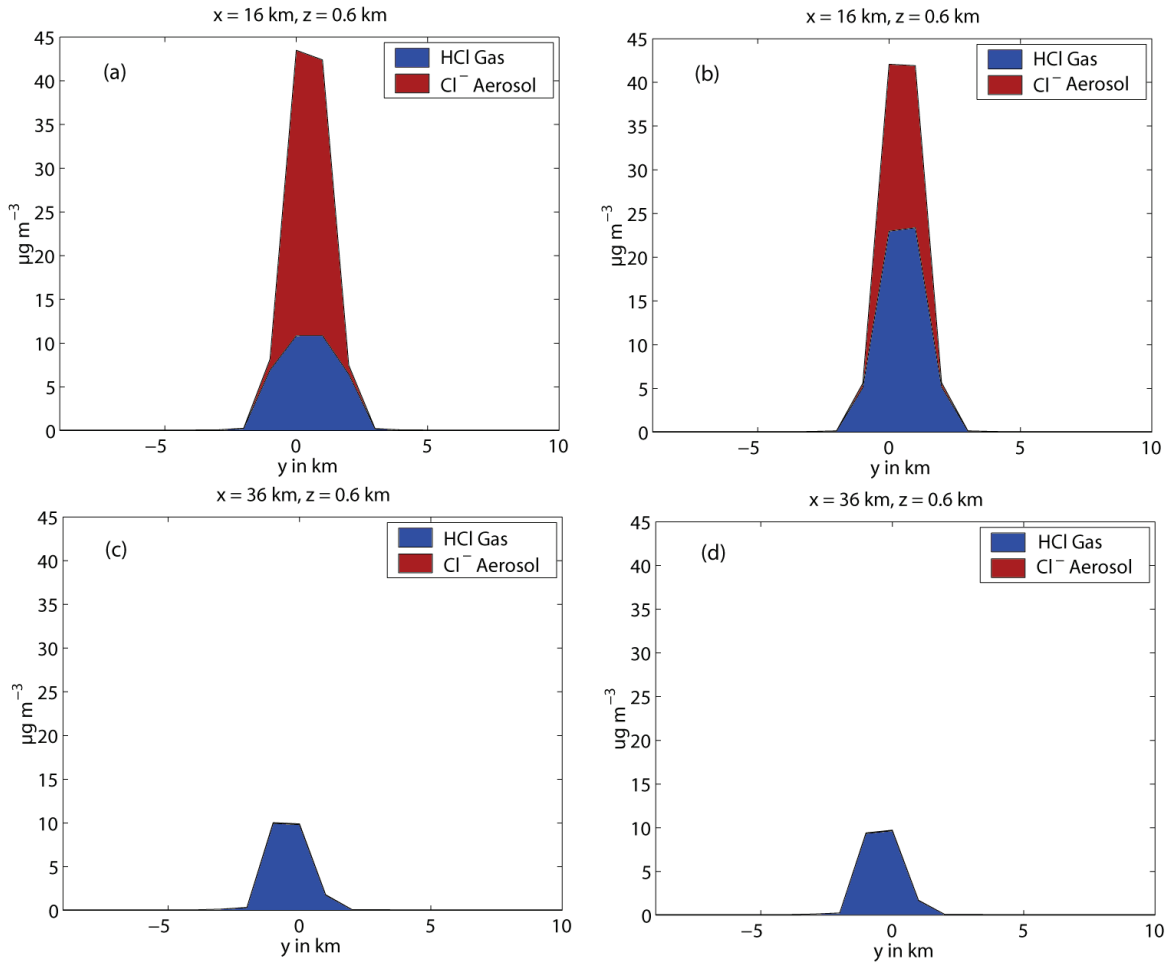

Figure 4-18: Concentrations of gas-phase HCl and aerosol chloride (Cl^-) along two horizontal transects through the Timbavati smoke plume. Figures (a) and (c) are for the reference chemistry case, while Figures (b) and (d) are for the expanded chemistry case.

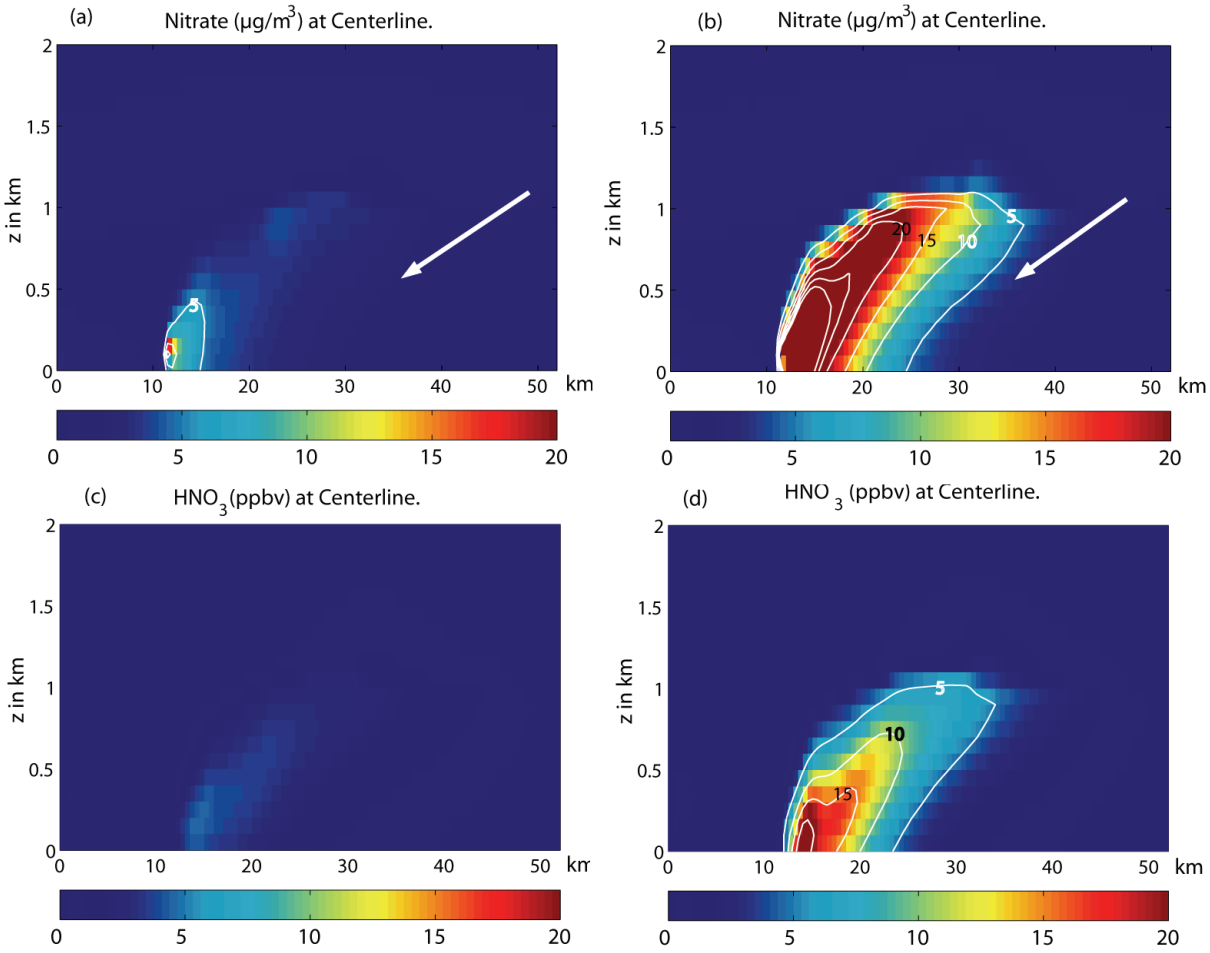

Figure 4-19: Concentrations of gas-phase HNO_3 and aerosol nitrate (NO_3^-) at the centerline of the Timbavati smoke plume ($y = 0$). Figures (a) and (c) are for the reference chemistry case, while Figures (b) and (d) are for the expanded chemistry case. The white arrow points to the location of the downwind aerosol measurement from *Hobbs et al.* [2003]. The observed NO_3^- concentration at this location was 9.1 $\mu g/m^3$.

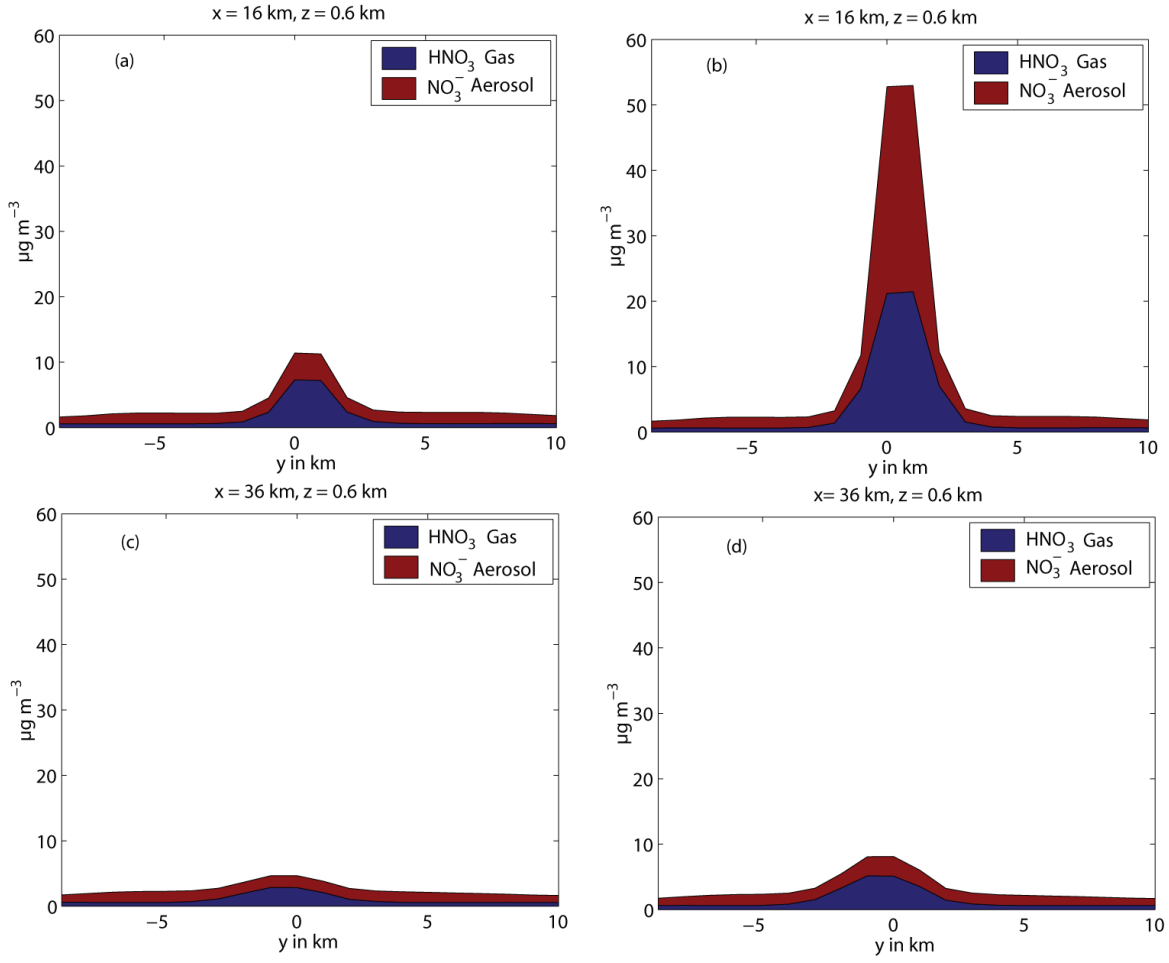

Figure 4-20: Concentrations of gas-phase HNO_3 and aerosol nitrate (NO_3^-) along two horizontal transects through the Timbavati smoke plume. Figures (a) and (c) are for the reference chemistry case, while Figures (b) and (d) are for the expanded chemistry case.

through the smoke plume for the expanded chemistry case; the location of the transects are the same as in Figure 4-14(f). For the expanded chemistry case, the maximum value near the source (x = 13 km, z = 0.3 km) is 1.5×10^{-3} m^{-1}, decreasing to a value of 7.7×10^{-4} m^{-1} (x = 18 km, z = 0.6 km) and 1.1×10^{-4} downwind (x = 39 km, z = 0.6 km). *Hobbs et al.* [2003] reported a peak value of 2.2×10^{-3} m^{-1} for the light scattering coefficient near the source, decreasing to 7.5×10^{-4} m^{-1} at 5 km downwind and to 4.0×10^{-4} m^{-1} at 26 km downwind. These results are similar to the results for the total aerosol number concentration, in that the model is able to reproduce the observed decrease in aerosol scattering coefficient in the first 5 to 10 km downwind, but then underestimates the value further downwind. Thus, the underprediction of the scattering coefficient downwind is likely due to the underprediction of the downwind number concentration.

The aerosol single scattering albedo is larger in the expanded chemistry case than in the reference chemistry case, due to the larger condensation rate of secondary organic and inorganic species onto the aerosol in the expanded chemistry case. The maximum single scattering albedo predicted for the expanded chemistry case is 0.906, near the top of the range of 0.86±0.05 reported by *Reid et al.* [2005a] for aged grassland and savannah smoke. This leads to a larger aerosol scattering coefficient for the expanded chemistry case as well. The aerosol optical depth is also larger for the expanded chemistry case, as the particles have a larger optical cross section than in the reference chemistry case.

4.3.6 Solar Radiation and Photolysis Rates

Figure 4-23 shows the total solar irradiance (the sum of both the upward and downward streams, integrated over 0 - 4 μm in wavelength), the heating rate due to the absorption of solar radiation, and the NO_2 photolysis rate along the plume centerline for the reference and expanded chemistry cases. The values for all three parameters are very similar for the two chemistry cases, with the expanded chemistry case showing a slightly larger upward diffuse irradiance above the plume due to the higher aerosol scattering coefficient in this case. The total solar irradiance is increased above the smoke plume due to the scattering of solar radiation by the smoke aerosols, which increases the upward diffuse irradiance. The solar irradiance within and below the smoke plume is decreased, due to the increased scattering and absorption of solar radiation within the smoke plume, which reduces the upward and downward flux of solar radiation within and beneath the smoke plume. The magnitudes of the increases and decreases of the solar irradiance are approximately 10-20 %. *Hobbs et al.* [2003] reported that the UV flux in the wavelength band 300-390 nm in the center of the plume was about two-thirds of that near the top of the plume. As the smallest wavelength

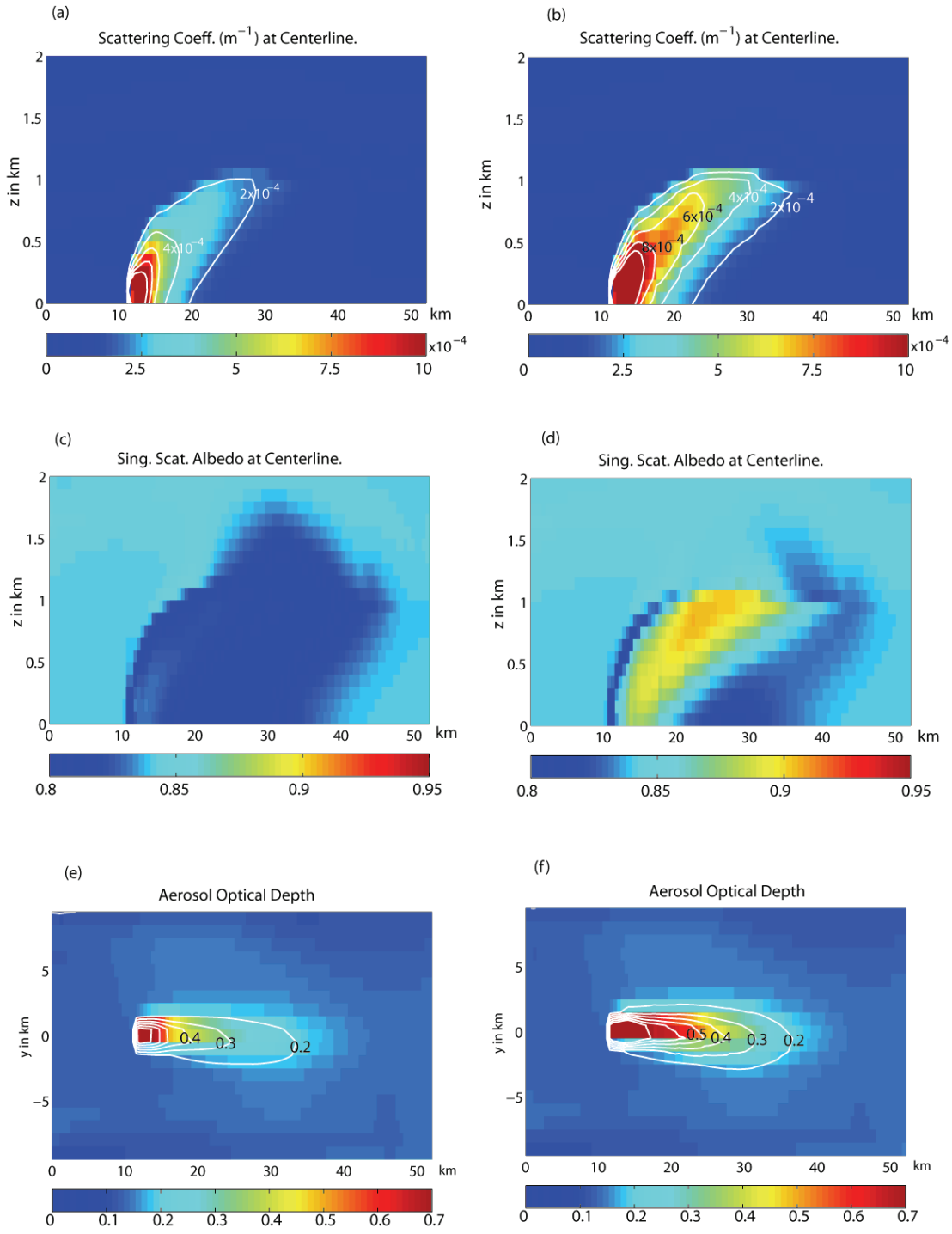

Figure 4-21: Aerosol optical properties at 550 nm for the Timbavati smoke plume. Figures (a), (c), and (e) are for the reference chemistry case, while Figures (b), (d), and (f) are for the expanded chemistry case. Figures (a) and (b) show the aerosol scattering coefficient at the plume centerline ($y = 0$). Figures (c) and (d) show the aerosol single scattering albedo at the plume centerline. Figures (e) and (f) show the aerosol optical depth versus x and y.

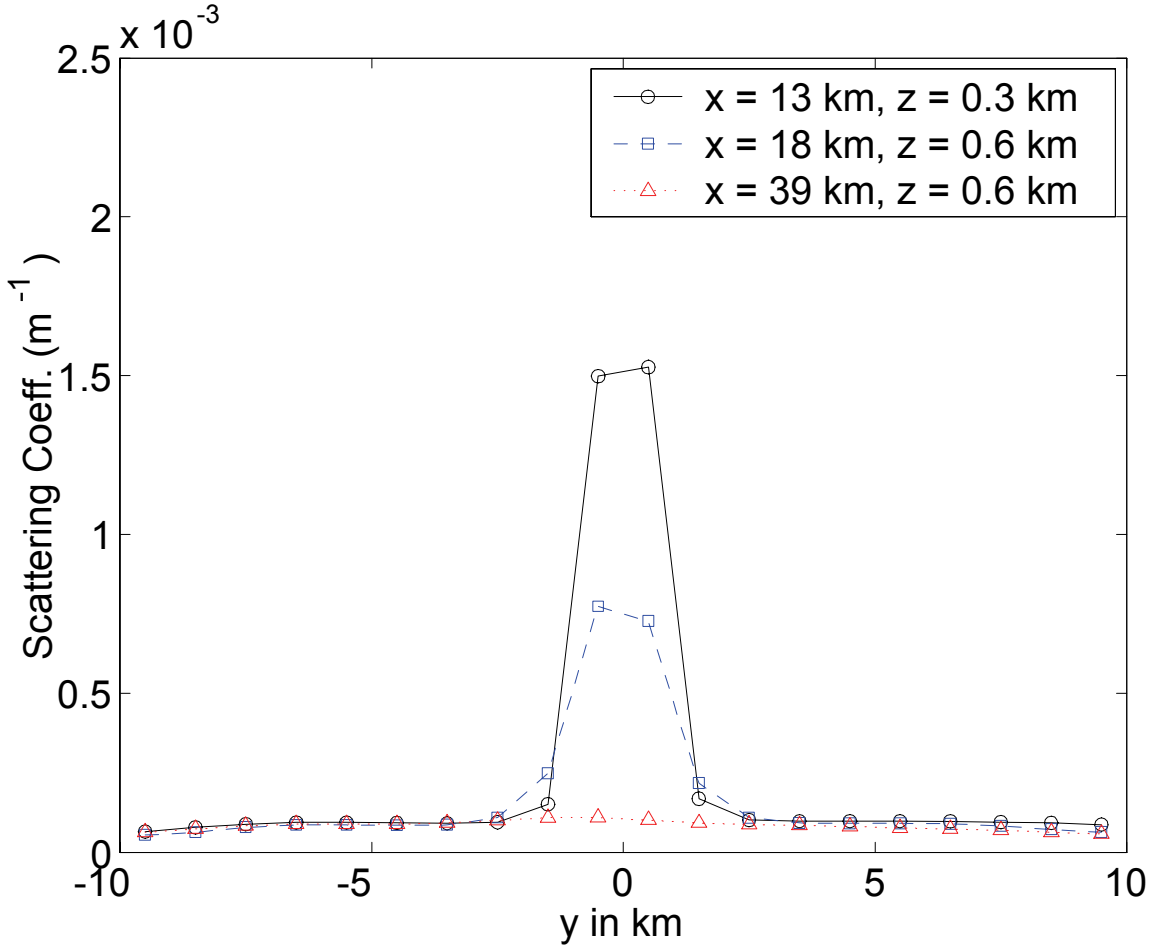

Figure 4-22: Scattering coefficient along three horizontal transects of the Timbavati smoke plume for the expanded chemistry case.

band in our radiation module is from 0-700 nm, we cannot directly compare our model results to this observation. However, the minimum (916 W/m^2) solar irradiance shown in Figure 4-23(b) is 77% of the maximum irradiance (1196 W/m^2). This suggests that the model may be slightly underestimating the absorption of solar radiation by the aerosols in the wavelength band 300 - 390 nm. This additional absorption may be due to secondary organic compounds that absorb radiation, which would also help to explain the underestimate of BC relative to observations.

Hobbs et al. [2003] estimated an instantaneous heating rate of the plume of 7.4 K/day at 20-25 km downwind from the Timbavati fire due to the absorption of solar radiation within the smoke plume. Figures 4-23(c) and 4-23(d) show the solar heating rates predicted for our model simulations. At 20 - 25 km downwind, the modeled heating rate varies from 4 - 6 K/day, slightly lower than the reported value. This is consistent with the observations of BC and UV flux, which also suggest that the model may slightly underestimate the absorption of solar radiation by the smoke aerosols.

Figures 4-23(e) and 4-23(f) show the NO_2 photolysis rate predicted for the two chemistry cases. The results are very similar to the results for solar irradiance, with the photolysis rate being decreased within and below the smoke plume and increased above. The NO_2 photolysis rates are increased and decreased on the order of 10-20%, which is of similar magnitude to the parametric uncertainty of the NO_2 photolysis reaction ($\pm$30%; see Table 3.18).

4.4 Summary and Conclusions

We have presented a 3D Eulerian simulation of the fluid dynamics, gas-phase chemistry, aerosol chemistry, and the scattering and absorption of radiation within the Timbavati biomass burning smoke plume. To our knowledge, this is the first time all of these processes have been simulated simultaneously for a young biomass burning smoke plume. We ran two test cases. In the reference chemistry case, the uncharacterized organic species were assumed to be unreactive and heterogeneous chemistry was not included. In the expanded chemistry case, the uncharacterized compounds were included using BIOH (monoterpenes) as a proxy and heterogeneous reactions of NO_2 and SO_2 were included with uptake coefficients of 10^{-3} and 2×10^{-4}, respectively.

The 3D Eulerian model does a good job matching the observed injection height of the smoke plume, but the initial model run underestimated the horizontal dispersion of the smoke plume. This underestimate may be due to an underestimate of subgrid-scale turbulent mixing or due to the fact that plume-scale fluctuations of the horizontal winds, which may be present in the convective boundary layer, are not included in the model. Increasing the minimum horizontal

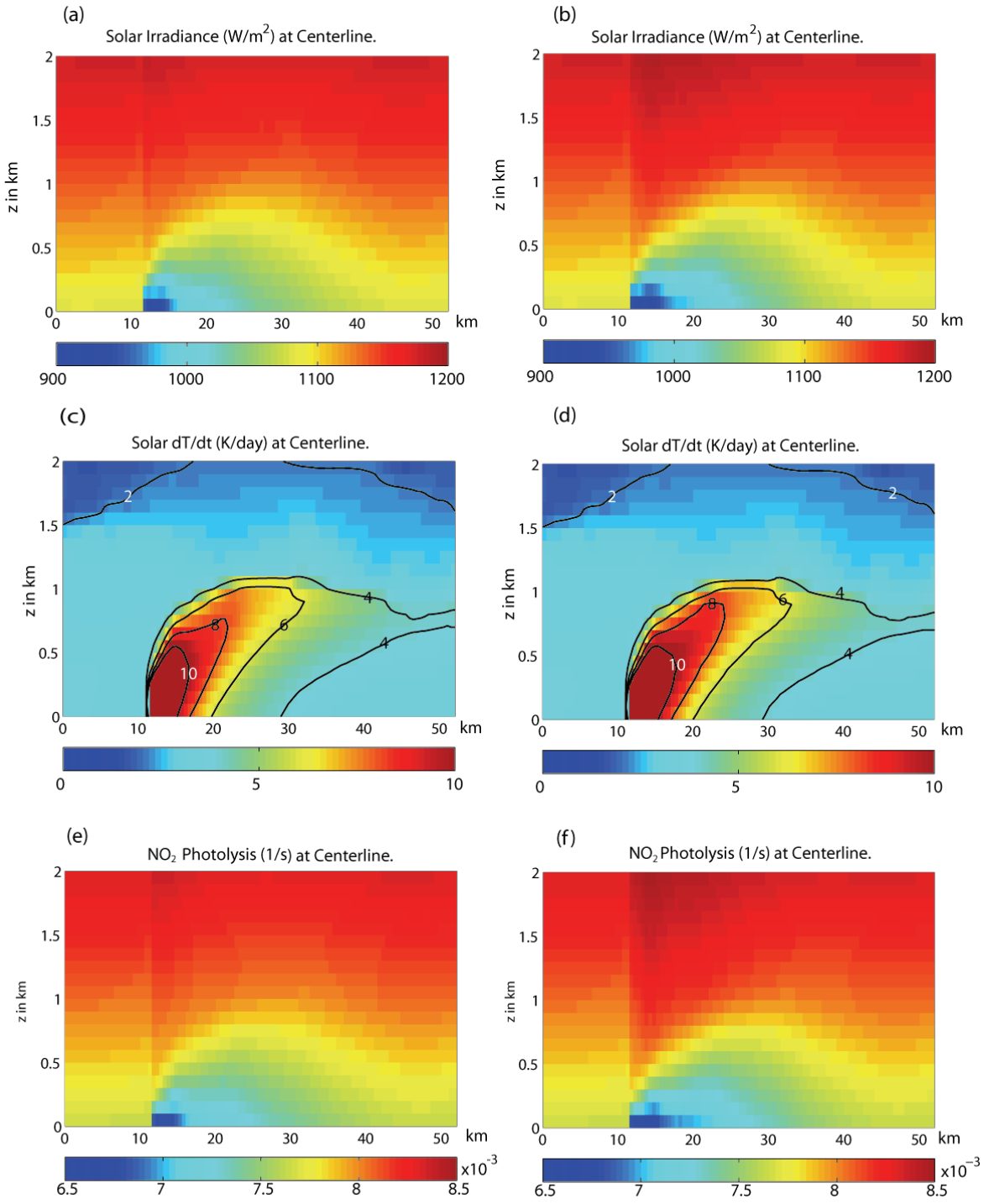

Figure 4-23: Simulated solar radiation field for the centerline of the Timbavati smoke plume. Figures (a), (c), and (e) are for the reference chemistry case, while Figures (b), (d), and (f) are for the expanded chemistry case. Figures (a) and (b) show the solar irradiance (integrated over wavelengths from 0 to 4 μm) at the centerline (y = 0). Figures (c) and (d) show the rate of temperature change due to aborption of solar radiation. Figures (e) and (f) show the NO_2 photolysis rates.

diffusion coefficient in the model provides a better match to the observed horizontal dispersion of the plume.

The reference chemistry case underestimates the observed formation of O_3 while the expanded chemistry case provides a better match with observations. The maximum OH concentration predicted for the expanded chemistry case (1.0×10^7 radicals cm^{-3}) is still well below the reported plume-average OH concentration (1.7×10^7 radicals cm^{-3}), while the concentration of HONO for the expanded chemistry case is well below the detection limit for this species by AFTIR. The expanded chemistry case also gives lower NO_x concentrations than the reference case due to increased production of HNO_3.

The model simulations suggest that direct measurements of OH in the young smoke plumes would be the best way to determine if heterogeneous production of HONO from NO_2 is taking place. An increase in OH while passing through the smoke plume would be consistent with the rapid heterogeneous formation of HONO from NO_2 on smoke particles, while a decrease in OH would suggest other explanations are required for the rapid formation of O_3 and nitrate in young biomass burning plumes. Thus, measurements of OH in young smoke plumes should be a priority for future field campaigns.

The model matches the observed downwind concentration of potassium well, suggesting that the model is correctly reproducing the observed dispersion of the primary aerosol. However, the reference chemistry underestimates the observed secondary formation of OC, nitrate, and sulfate in the smoke plume, and underestimates the amount of chloride observed in the aerosol phase. The expanded chemistry case improves the match with observations, but still underestimates the observed aerosol concentrations. The maximum aerosol concentrations downwind are found at an altitude of 1 km, rather than the altitude of 0.6 km sampled in Timbavati. The total (gas + aerosol) amount of chloride downwind is consistent with the aerosol observations, but in the model the chloride is primarily in the gas phase. The total amount of nitrate downwind is less than the observed aerosol concentration, suggesting that the model is underestimating the formation of nitrate from NO_x even in the expanded chemistry case. Simultaneous measurements of chloride and nitrate in the gas and aerosol phases would help to resolve these discrepancies by allowing us to close the budget for chloride and nitrogen atoms within the smoke plume.

The modeled single scattering albedo for the aerosols in the expanded chemistry case is consistent with reported values for aged savannah smoke aerosols. The modeled aerosol scattering coefficient matches the observations fairly well for the first 10 km downwind from the fire, but underestimates the observed value further downwind. The comparison between modeled and observed

aerosol number concentration is similar, with the model and observations matching fairly well from 0-10 km downwind of the source and then diverging. Thus, the underestimate in aerosol scattering coefficient downwind is likely related to the underestimate of aerosol number concentration downwind.

Smoke aerosols reduce the modeled photolysis rates within and beneath the plume by 10-20%, and increase them above. However, the modeled solar heating due to the absorption of solar radiation is 4-6 K/day at 20-25 km downwind, slightly lower than the reported value of 7.4 K/day, suggesting that the model may underestimate the absorption of solar radiation by the aerosols. This is consistent with the underestimate of BC relative to observations. Both discrepancies may be due to the absorption of solar radiation by secondary organic compounds, leading to an overestimate of BC in the observations and an underestimate of aerosol absorption in the model.

Chapter 5

Comparison to Automatic Dilution Approach

Chapters 3 and 4 have focused on evaluating and improving a model of the gas and aerosol chemistry taking place in young biomass burning smoke plumes, with the goal of improving estimates of the impact of biomass burning emissions on the global environment. The work of *Freitas et al.* [2007] and others is also improving the estimates for biomass burning plume rise in global atmospheric chemistry models (GACMs), allowing us to more accurately determine the effective injection height of biomass burning emissions. However, even if a perfect gas and aerosol chemistry model was incorporated into current GACMs, and plume height were correctly represented in the GACMs, this still may not result in an accurate prediction of the impacts of biomass burning on global atmospheric chemistry and climate. This is because most regional and global atmospheric chemistry models automatically dilute the emissions from biomass burning into large-scale global model grid boxes, which can have a horizontal scale of 10-200 km. Since the chemistry within the smoke plume is highly non-linear, this automatic dilution of emissions may not correctly represent the chemistry taking place within the concentrated smoke plume. Thus, current GACMs may incorrectly estimate the effective emissions of gas and aerosol species from biomass burning to the global environment.

Here, we estimate the errors caused by the automatic dilution approach of GACMs by comparing the results of our 3D Eulerian simulation of the Timbavati smoke plume to the results of a single-box Eulerian model with the same horizontal scale (52.5 km x 20 km) as the full domain of our 3D simulation. This Eulerian box model is used as an analog of the large-scale grid boxes of GACMs. Section 5.1 describes the Eulerian box model used in this work, while Section 5.2 describes the initial conditions and model parameters for the box model simulation of the Timbavati fire. Section 5.3

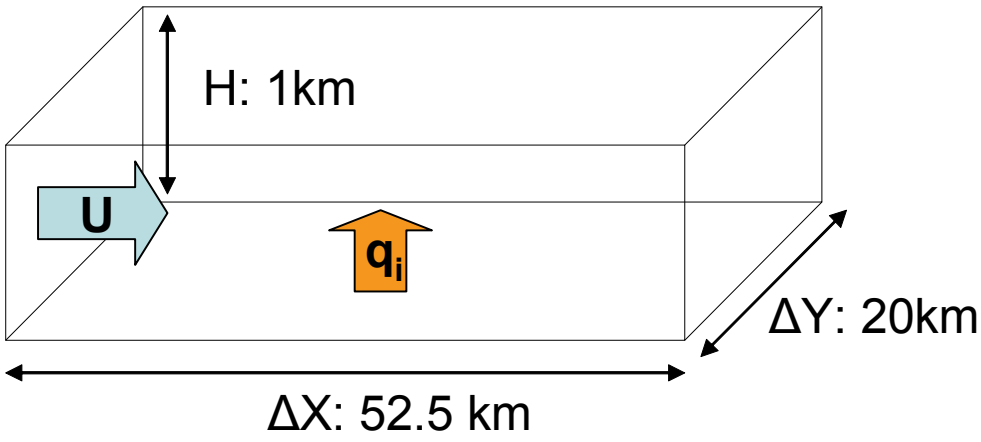

Figure 5-1: Schematic of the Eulerian box model. U is the horizontal wind speed, while q_i is the emissions flux of species i.

discusses the results of the comparison for tracers species, O_3, NO_x, other NO_y species, and aerosol constituents. Section 5.5 summarizes the results of this study and makes recommendations for how GACMs could better represent smoke plume chemistry.

5.1 Eulerian Box Model Description

The goal of this experiment is to evaluate the errors in the effective flux of gas and aerosol species to the global environment caused by the automatic dilution of biomass burning emissions into large-scale global model grid boxes, as is done in many GACMs. We assume that both models will have the same gas and aerosol-phase chemical routines. To perform this comparison, we created an Eulerian box model to use as an analog of a GACM grid box. The model is shown schematically in Figure 5-1. The horizontal scale is the same as the total domain of the 3D Eulerian model used in Chapter 4. The box has a constant height H of 1 km.

The continuity equations for the Eulerian box model are

$$\frac{dC_q}{dt} = \frac{\mathbf{q}_q}{H} - \frac{v_{d,i}}{H} + \frac{U}{\Delta X}\left(C_q^o - C_q\right) + \left(\frac{dC_q}{dt}\right)_{cond} + \left(\frac{dC_q}{dt}\right)_{chem} \quad (5.1)$$

$$\frac{dn_i}{dt} = \frac{\mathbf{q}_i}{H} - \frac{v_{d,i}}{H} + \frac{U}{\Delta X}\left(n_i^o - n_i\right) + \left(\frac{dn_i}{dt}\right)_{cond} + \left(\frac{dn_i}{dt}\right)_{coag} \quad (5.2)$$

$$\frac{d\mathbf{c}_{q,i}}{dt} = \frac{\mathbf{q}_{q,i}}{H} - \frac{v_{d,q,i}}{H} + \frac{U}{\Delta X}\left(\mathbf{c}_{q,i}^o - \mathbf{c}_{q,i}\right) + \left(\frac{d\mathbf{c}_{q,i}}{dt}\right)_{cond} + \left(\frac{d\mathbf{c}_{q,i}}{dt}\right)_{coag} + \left(\frac{d\mathbf{c}_{q,i}}{dt}\right)_{chem} \quad (5.3)$$

where C_q is the concentration of gas-phase species (molecules/cm^3 air), n_i is the number concentration of particles in size bin i (particles/cm^3 air) and $\mathbf{c}_{q,i} = c_{q,i} n_i$ is the concentration of aerosol species q in size bin i (mol/cm^3 air). The first term on the right-hand side of each continuity equation represents the change in concentrations due to emission of species from the fire source, with $\mathbf{q}_q$ representing the flux of species q from the fire source. $\mathbf{q}_q$ (mol/cm^2/s) is calculated from the species emission rate $\mathbf{Q}_q$ (mol/s) as $\mathbf{q}_q = \frac{\mathbf{Q}_q}{\Delta X \Delta Y}$.The second term is the effect of deposition on the concentrations, where v_d is the deposition velocity. As in the Lagrangian studies of Chapter 3, we set the deposition velocity equal to 0 for gas-phase species and use the terminal velocity of the aerosol particles as the deposition velocity for aerosol species. The third term represents the change due to horizontal winds transporting air into and out of the Eulerian box. C_q^o is the concentration of gas q in the background air upwind of the fire site, U is the horizontal wind speed, and ΔX is the horizontal distance in the downwind direction. The remaining terms represent the change in gas and particle-phase concentrations due to mass transfer between the gas and aerosol phases (*cond*), coagulation of particles (*coag*), and irreversible and reversible chemistry (*chem*). The calculation of these terms are performed by the chemical model described in Chapter 2. The integration of the different terms of the continuity equations is operator split for computational efficiency, with the time step for gas-phase chemistry, plume dispersion, and deposition set at 1 s, the time step for mass transfer and aerosol equilibrium set at 20 s, and the time step for coagulation set at 60 s.

The chemical routines for the Eulerian box model and the 3D plume model of Chapter 4 are the same, allowing us to determine the errors caused by the automatic dilution of biomass burning emissions in large-scale grid boxes. However, there are other potentially important differences between the Eulerian box and 3D plume models besides their differences in vertical and horizontal resolution. For example, the Eulerian box model (1) calculates photolysis rates using TUV v.4.1 rather than the CRM6 routines, (2) ignores the effect of aerosol particles on actinic flux and photolysis rates and (3) has no vertical mixing of compounds into or out of the box. Thus the box model is expected to have higher photolysis rates than the 3D Eulerian model as discussed in Section 4.1. The impact of vertical diffusion of compounds on the comparison between the two model is evaluated below by comparing concentrations of different tracer species in the models.

5.2 Box Model Initialization

The temperature and pressure for the box model were set at 288 K and 900 mbar, respectively, as in the Lagrangian studies of the Timbavati smoke plume presented in Section 3.4. The horizontal

wind speed was set at 9.3 m/s [*Trentmann et al.*, 2005]. Photolysis rates were calculated using TUV v.4.1, and are the same as the rates used in the Lagrangian study in Chapter 3.

Initial and upwind concentrations of gases other than SO_2 and O_3 were set to the environmental concentrations for Timbavati as listed in Tables 3.12 and 3.13. Since in the 3D model the concentrations of SO_2 and O_3 varied with height in the bottom 1 km of the model domain (see Figure 4-4), the initial and upwind concentrations were set to the average values of 1.45 ppbv and 35.7 ppbv, respectively, to match the total amount of SO_2 and O_3 initially present in the bottom 1 km of the 3D Eulerian plume model. Similarly, the initial and upwind number concentration of aerosols was set at 2530 cm^{-3} to match the average aerosol concentration present in the bottom 1 km of the 3D Eulerian plume model (see Figure 4-5). As in the 3D Eulerian modeling, 4 aerosol size bins were used, with 2 bins between 0.015 μm and 1 μm in radius. Initial and upwind aerosol chemical composition was taken from the environmental aerosol distribution concentrations for Timbavati listed in Table 3.15.

The emissions of trace gases and aerosols due to the fire source were identical to the emissions for the 3D Eulerian model. The CO emission rate was set to 49.5 kg/s based on the results from the USDA Fire Service Fire Emission Production Simulator (FEPS) v.1.1.0. Emission rates for other species were calculated from their emission ratios to CO, which were calculated using the data from Tables 3.12, 3.13 and 3.15.

The box model was run for two cases, corresponding to the two chemistry cases discussed in Chapter 4. In the "reference chemistry" case we assumed that the uncharacterized organic species were unreactive, and did not include any heterogeneous reactions of NO_2 or SO_2. In the "expanded chemistry" case we modeled the chemistry of the uncharacterized organic species using monoterpenes (BIOH) as a proxy for high-carbon number reactive organic species that form organic aerosol. We also included the heterogeneous reactions $NO_2 \rightarrow 0.5\ HONO + 0.5\ HNO_3$ and $SO_2 \rightarrow H_2SO_4$ with uptake coefficients of 10^{-3} and 2×10^{-4}, respectively. The results of both simulations, and their comparison to the 3D Eulerian plume model results, are presented below.

5.3 Results and Discussion

In order to compare the results of the Eulerian box and 3D models, we define $\mathbf{M}_{q,Box}(t)$ as the total amount of species q (in mol) present in the Eulerian box model at time t and define $\mathbf{M}_{q,3D}(t)$ as the total amount of species q present in the bottom 1 km of the 3D Eulerian plume model at

time t. $\mathbf{M}_{q,Box}(t)$ is calculated from the concentration $C_q(t)$ (mol/cm^3) by the formula

$$\mathbf{M}_{q,Box}(t) = C_q(t)\,\Delta X \Delta Y H \tag{5.4}$$

where $\Delta X = 52.5$ km, $\Delta Y = 20$ km, and $H = 1$ km.

$\mathbf{M}_{q,3D}(t)$ is calculated from the sum

$$\mathbf{M}_{q,3D}(t) = \sum_{i=1}^{105}\sum_{j=1}^{20}\sum_{k=1}^{10} C_q(i,j,k,t)\,\Delta x \Delta y \Delta z \tag{5.5}$$

where $C_q(i,j,k,t)$ is the concentration of species q (mol/cm^3) in grid box (i,j,k) at time t, $\Delta x = 500$ m, $\Delta y = 1000$ m, and $\Delta z = 100$ m. Note that $\frac{\mathbf{M}_{q,3D}(t)}{\Delta X \Delta Y H}$ is the average concentration of species q in the bottom 1 km of the 3D plume model at time t.

For both the box and 3D models, $\mathbf{M}_q$ can be changed by emissions of species q by the fire, reversible and irreversible chemical reactions, and by horizontal transport. $\mathbf{M}_{q,3D}$ can also change due to vertical diffusion of species into or out of the bottom 1 km of the 3D model. In order to estimate the error in the effective flux of biomass burning emissions to the global environment caused by the automatic dilution of emissions in the box model, we calculate the change in $\mathbf{M}_q$ in both models from the ignition of the fire source (t = 0) to the end of the model integration (t = 60 min.):

$$\Delta\mathbf{M}_q = \mathbf{M}_q(60\text{ min.}) - \mathbf{M}_q(0) \tag{5.6}$$

Note that $\frac{\Delta\mathbf{M}_q}{\Delta X \Delta Y H}$ represents the change in the average concentration over 60 minutes of fire emissions.

The bar graphs presented below plot $\Delta\mathbf{M}_q$ for the reference and expanded chemistry runs of the Eulerian box and 3D models. The percentages shown above the bars for the box model represent the normalized difference (ε_q) between the box and 3D model results, calculated using the formula

$$\varepsilon_q = \frac{\Delta\mathbf{M}_{q,Box} - \Delta\mathbf{M}_{q,3D}}{\Delta\mathbf{M}_{q,3D}} \tag{5.7}$$

Appendix C shows the values of $\mathbf{M}_q(0)$, $\mathbf{M}_q(60\text{ min.})$, $\Delta\mathbf{M}_q$ and ε_q for several important gas and aerosol species.

Since both models are spun up for 10 minutes prior to fire ignition, $\mathbf{M}_{q,Box}(0)$ and $\mathbf{M}_{q,3D}(0)$ can be different. The error bars in the figures below represent the differences between the box and

3D model amounts of each species at the fire ignition (δ_q), calculated according to the formula

$$\delta_q = \mathbf{M}_{q,Box}(0) - \mathbf{M}_{q,3D}(0) \tag{5.8}$$

5.3.1 Tracers

As mentioned above, the Eulerian box model does not include the vertical diffusion of species across the top boundary, while the 3D plume model does allow species to diffuse vertically. This can result in differences in $\Delta\mathbf{M}_{q,Box}$ and $\Delta\mathbf{M}_{q,3D}$ even in the absence of non-linear chemistry. To evaluate the importance of this effect, we compared $\Delta\mathbf{M}_{q,Box}$ and $\Delta\mathbf{M}_{q,3D}$ for various tracer species, *i.e.* species whose concentrations are not greatly affected by chemical changes in the model.

Figure 5-2 shows the comparison between the Eulerian box model and the 3D Eulerian plume model for five tracer species. The five species shown are CO, aerosol potassium (K^+), aerosol black carbon (BC), and the total amount of S and Cl atoms, calculated as the sum of the gas and aerosol phase species containing these atoms - $SO_{2(g)}$ and aerosol sulfate (SO_4^{2-}) and $HCl_{(g)}$ and aerosol chloride (Cl^-), respectively. While CO is not strictly a conservative tracer in the model, the chemical production and loss rates for CO are very small compared to the fire emission rates considered here.

The calculated changes in CO in the box and 3D models are nearly identical for both chemistry cases studied, with a maximum $|\varepsilon_{CO}|$ of 0.3%. This close correspondence between the box and 3D models suggests that vertical diffusion of CO across the z = 1 km boundary is unimportant for this species, due to its relatively high background mixing ratio (182 ppbv). For K^+ and BC, $\Delta\mathbf{M}_{q,Box}$ is greater than $\Delta\mathbf{M}_{q,3D}$. This is due to the upward vertical diffusion of these species in the 3D model runs. Since the initial aerosol concentrations in the 3D model decay exponentially with height, turbulence causes these species to mix upward, reducing the concentrations below 1 km. Thus we see that the neglect of vertical diffusion in the box model can lead to positive values of ε_q of up to +10% for aerosol species even in the absence of chemical sources and sinks. The change in the total amount of S atoms ($SO_{2(g)}$ + SO_4^{2-}) is lower in the box model than in the 3D model. This is because the high initial concentration of $SO_{2(g)}$ above 1 km in the 3D model (see Figure 4-4) results in a large downward diffuse flux of SO_2 across the z = 1 km boundary. This downward flux of SO_2 compensates for the upward flux of aerosol sulfate, resulting in a negative value for $\varepsilon_{SO_{2(g)}+SO_4^{2-}}$. The total amount of Cl atoms ($HCl_{(g)}$ + Cl^-) is slightly ($\varepsilon_{HCl_{(g)}+Cl^-}$ =-1% to -6%) smaller in the box model than in the 3D model. The difference between the reference and expanded chemistry results for Cl atoms in the 3D model is likely due to numerical error in solving

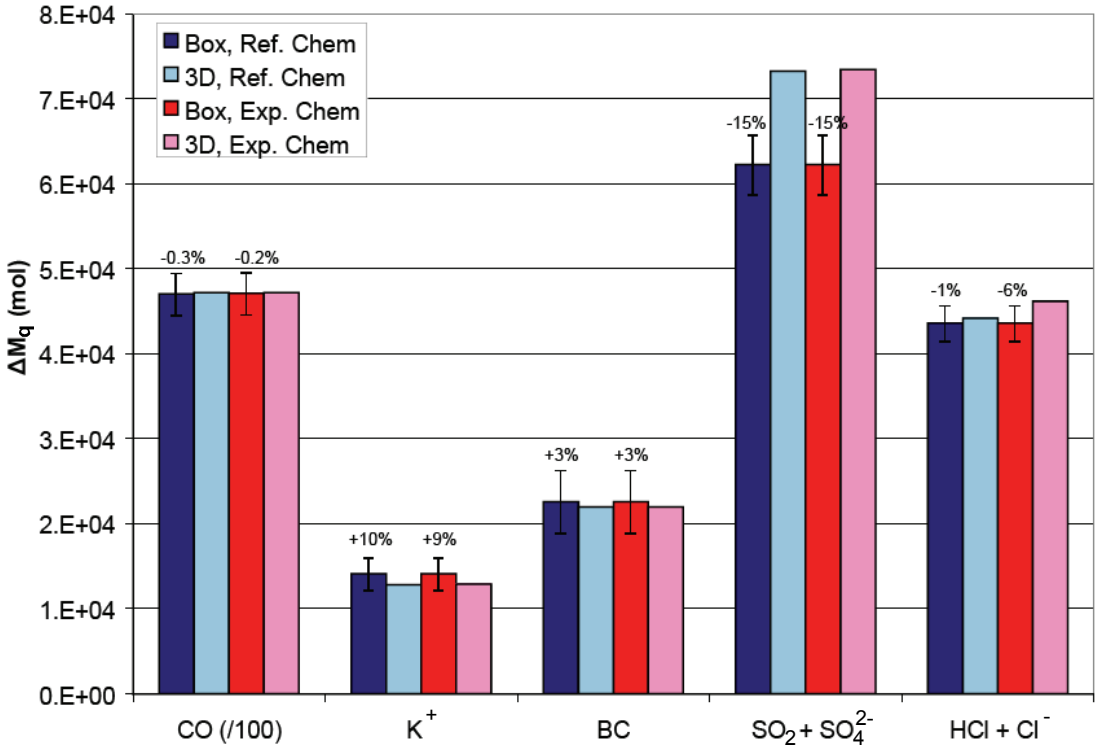

Figure 5-2: Comparison of Eulerian box and 3D model results for conservative tracers. Values plotted represent the change in the total amount of a species (mol) in the lowest 1 km of the model domain from the ignition of the fire source to 60 minutes after ignition ($\Delta \mathbf{M}_q$). Error bars represent the differences between the box and 3D model amounts of each species at the fire ignition (δ_q). The percentages represent the normalized difference of the box model result from the corresponding 3D model result (ε_q). The values for CO have been divided by 100 to fit in the plot.

the advection-diffusion equations for a species with a very low background concentration (~1 pptv) and a very high concentration gradient near the fire source.

Thus, we find that vertical diffusion alone can result in differences of the order of ±1-15% between the box and 3D Eulerian model. The values are larger for species with large vertical gradients in their initial concentrations in the 3D model, such as aerosol species and $SO_{2(g)}$. Thus, we cannot necessarily attribute differences of less than 10 to 15% to the automatic dilution assumption of GACMs. Changes of this size may be due to a combination of vertical diffusion and the error associated with automatically diluting biomass burning emissions.

5.3.2 Ozone and NO_x

Figure 5-3 shows the comparison between the box and 3D models for O_3, NO, NO_2, NO_x (NO + NO_2) and O_x (defined here as NO_2 + O_3). When both models are using the reference chemistry, the models give nearly identical results for NO_x ($\varepsilon_{NO_x} = -1\%$), but the box model gives a higher value for NO ($\varepsilon_{NO} = +46\%$) and a lower value for NO_2 ($\varepsilon_{NO_2} = -16\%$). The differences for NO and NO_2 are consistent with a higher average photolysis rate for NO_2 in the box model. The box model shows larger increases for O_3 ($\varepsilon_{O_3} = +24\%$) and O_x ($\varepsilon_{O_x} = +10\%$) than are seen in the 3D model. This suggests that, when using the reference chemistry, the box model approach results in a more oxidizing atmosphere than in the 3D plume model. This result can be explained by referring to the OH transect plots in Figure 4-11. For the 3D reference chemistry case, the OH concentration drops in the center of the smoke plume, due to the high concentration of OH sinks and the absorption of solar radiation by the smoke aerosols. In the box model reference chemistry case, the sinks of OH are more dilute due to the automatic dilution of smoke emissions and the absorption of solar radiation by the aerosols is ignored. The more dilute sinks of OH result in a higher average OH concentration in the box ($\mathbf{M}_{OH,Box}\,(60\,\text{min}) = 14.06$ mol) than in the 3D model ($\mathbf{M}_{OH,3D}\,(60\,\text{min}) = 9.61$ mol), while the higher rate of NO_2 photolysis in the box model results in more of the created O_x being present as O_3 in the box model than in the 3D model. This result is also consistent with the work of *Lin et al.* [1988], who found that the ozone production efficiency (net ozone production per molecule of NO_x lost) decreased as the NO_x concentration increased from 1 ppbv (as in the box model) to 10 ppbv or higher (as in the 3D plume model). Thus, given the similar loss rates of NO_x in both the box and 3D models, we expect a higher O_3 production rate in the box model.

For the expanded chemistry case, the models match closely for O_3 ($\varepsilon_{O_3} = +0.4\%$) and O_x ($\varepsilon_{O_x} = +3\%$). However, the box model gives a much higher value for NO_x than the 3D model

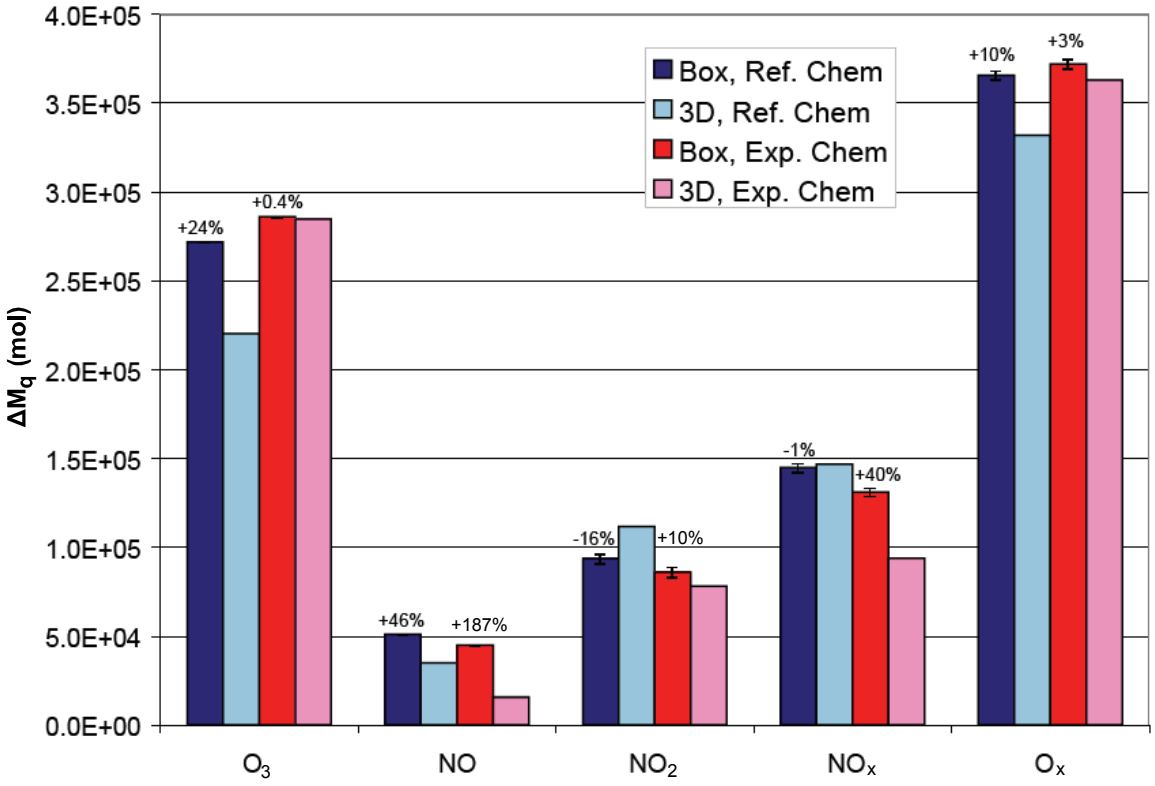

Figure 5-3: Comparison of Eulerian box and 3D model results for O_3, NO, NO_2, NO_x (NO + NO_2) and O_x (NO_2 + O_3). Plotted values are as described in Figure 5-2.

(ε_{NO_x} = +40%). This suggests that, for the expanded chemistry case, the automatic dilution of smoke plume emissions results in an overestimate of effective NO_x emissions from biomass burning sources. This is because the automatic dilution of the smoke emissions in the box model results in lower rates of NO_x loss due to heterogeneous chemistry. In the 3D model, the concentrated plume has high concentrations of NO_2 and aerosol particles, which results in a high rate of heterogeneous formation of HNO_3 and loss of NO_x. In the box model, the automatic dilution of the smoke emissions greatly reduces the concentrations of NO_2 and aerosol particles, and so the heterogeneous reaction rate for NO_2 is much slower.

These results suggest that the GACM approach of automatic dilution can overestimate the effective flux of NO_x to the global environment. This could lead to errors in estimates of the global ozone formation from biomass burning emissions. It also shows that while the addition of heterogeneous reactions of NO_2 improves the match between model and observation for the Lagrangian and 3D Eulerian plume models, simply adding this reaction to GACMs is unlikely to fix the NO_x overestimate, as the automatic dilution of the fire emissions would result in a slower rate of heterogeneous chemistry in GACMs.

5.3.3 Other NO_y Species

Figure 5-4 shows the comparison between the box and 3D models for the NO_y species $HNO_{3(g)}$, aerosol nitrate (NO_3^-), total inorganic nitrate ($HNO_{3(g)}$ + NO_3^-), organic nitrate (AP1 through AP12), PAN species (PAN1 through PN10) and HONO. The total change in species non-NH_3 nitrogen containing species (NO_x plus those listed above) is 10% higher in the box model runs than in the 3D model. This error is consistent with that seen for other tracer species (like K^+), and is due to a combination of upward vertical diffusion of non-NH_3 nitrogen containing species, which have a high emission rate from the fire source but relatively low initial and background concentrations, and the condensation of organic nitrate species onto aerosols. This diffusive error helps to explain why estimates for many nitrogen containing species in the reference chemistry case are higher in the box model while the NO_x concentrations in the two models are very similar.

For the reference chemistry case, the box model gives a much higher change in $HNO_{3(g)}$ ($\varepsilon_{HNO_{3(g)}}$ = +164%) and a much lower change in aerosol nitrate than the 3D model. In fact, the box model shows a reduction in aerosol nitrate with time, while the 3D model shows a small increase. This is because the automatic dilution of emissions in the box model favors evaporation of semivolatile species like nitrate to the gas phase, whereas modeling the concentrated plume results in a region of high $HNO_{3(g)}$ concentration in the smoke plume. Thus more of the total nitrate stays

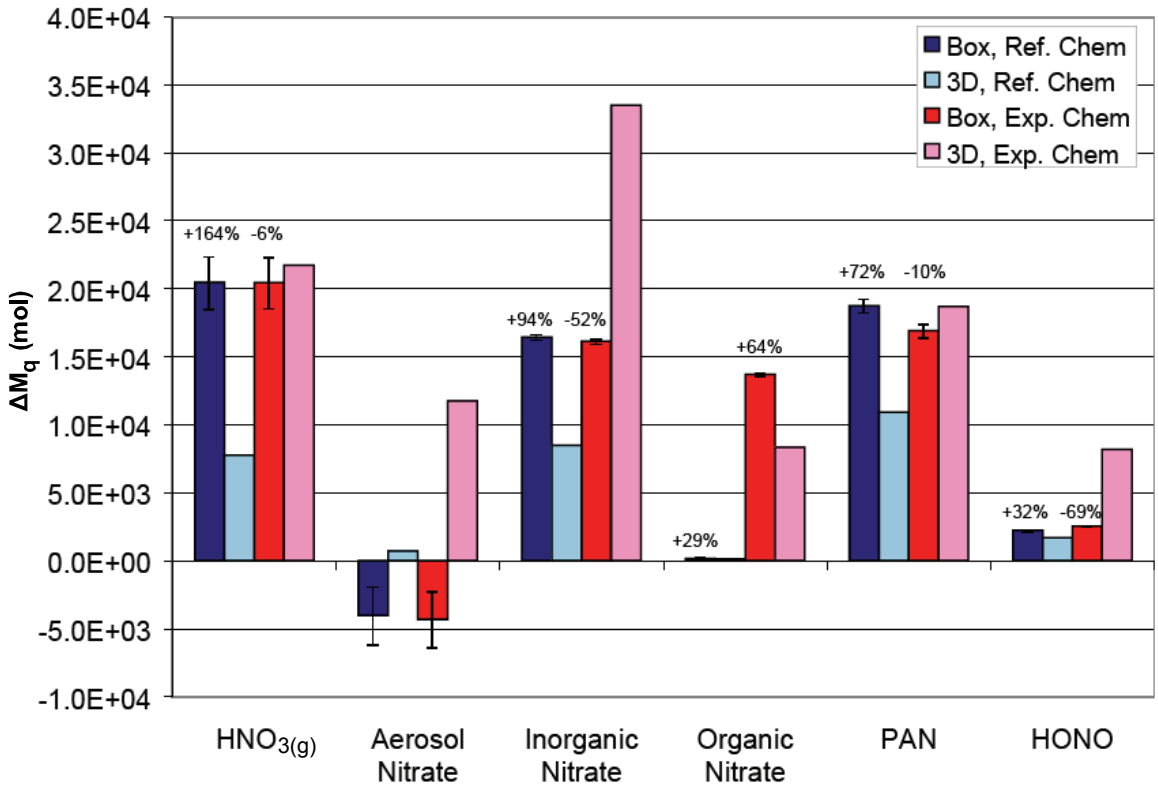

Figure 5-4: Comparison of Eulerian box and 3D model results for NO_y species. Plotted values are as described in Figure 5-2.

in the aerosol phase when the concentrated plume is modeled. The box model also gives a much higher change for total inorganic nitrate ($\varepsilon_{HNO_{3(g)}+NO_3^-} = +94\%$), total PAN ($\varepsilon_{PAN} = +72\%$) and HONO ($\varepsilon_{HONO} = +32\%$). These results are consistent with the higher ozone concentrations seen in the box model than in the 3D model for the reference chemistry case, and are consistent with our previous conclusion that for the reference chemistry the box model approach results in a more oxidizing environment than in the 3D model.

For the expanded chemistry case, the box model gives a much lower change in inorganic nitrate than in the 3D model ($\varepsilon_{HNO_{3(g)}+NO_3^-} = -52\%$). This is due to the much slower rate of heterogeneous HNO_3 formation when the plume emission are automatically diluted in the box model versus the higher rate of heterogeneous reactions in the concentrated smoke plume. This underestimate of the rate of heterogeneous chemistry in the box model also explains the lower change in HONO seen in the box model ($\varepsilon_{HONO} = -69\%$). The formation of organic nitrate is much higher in the expanded chemistry case than in the reference chemistry case due to the addition of BIOH. The concentrations of PAN predicted by the two models are fairly close ($\varepsilon_{PAN} = -10\%$).

5.3.4 Aerosol Species

Figure 5-5 shows the comparison between the box and 3D models for aerosol chloride (Cl^-), aerosol sulfate (SO_4^{2-}), and aerosol organic carbon (OC). For both the reference and expanded chemistry cases, the total change in aerosol chloride is much lower in the box model (ε_{Cl^-} = -84% and -72%, respectively) than in the 3D model. This is consistent with the results for aerosol nitrate above, and is caused by the automatic dilution of fire emissions in the box model. In the concentrated smoke plume, high local concentrations of $HCl_{(g)}$ keep more of the total chloride in the aerosol phase. Automatically diluting the smoke emissions of chloride in the box model results in more of the chloride evaporating into the gas-phase. As the 3D model is already underestimating the amount of aerosol Cl^- relative to observations, the automatic dilution approach of GACMs may result in an even larger underestimate of aerosol Cl concentrations leaving biomass burning smoke plumes.

For the reference chemistry case, the change in aerosol sulfate is larger in the box model than in the 3D model ($\varepsilon_{SO_4^{2-}} = +24\%$), consistent with the results for O_3 and inorganic nitrate which both suggested that for the reference chemistry the box model approach results in a more oxidizing environment than in the 3D model. For the expanded chemistry case, the change in aerosol sulfate is smaller in the box model than in the 3D model ($\varepsilon_{SO_4^{2-}}$ = -45%). This is consistent with the results for NO_x, total inorganic nitrate, and HONO, all of which suggest that the automatic dilution

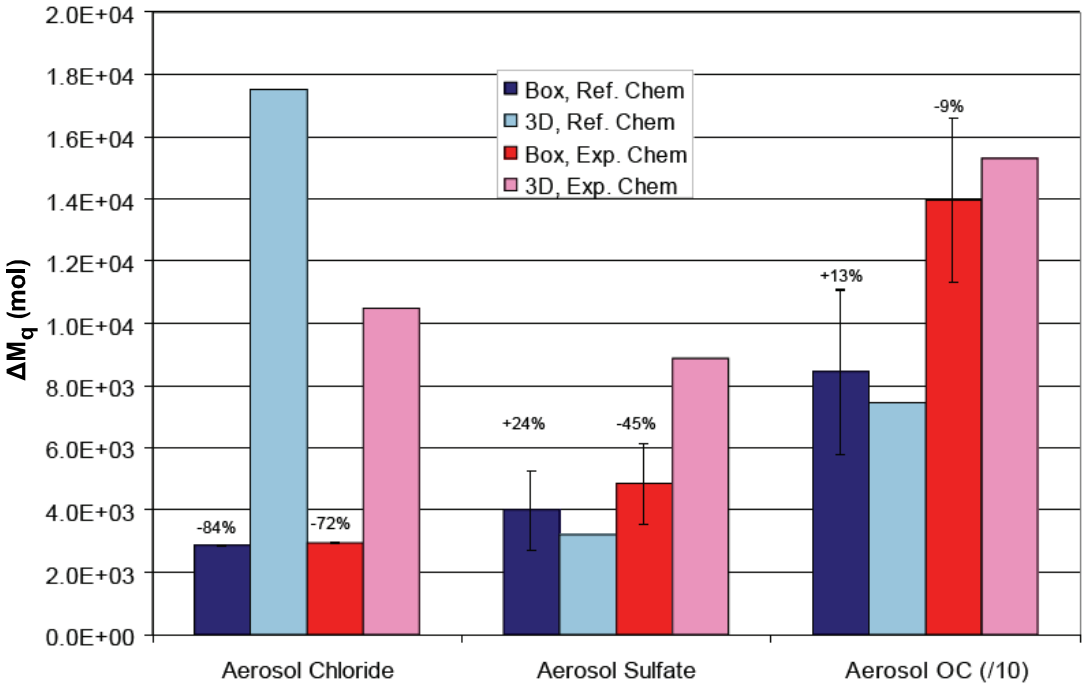

Figure 5-5: Comparison of Eulerian box and 3D model results for aerosol chloride, sulfate, and organic carbon (OC). Plotted values are as described in Figure 5-2. The values for OC have been divided by 10 to fit in the plot.

of smoke emissions in the box model leads to a much lower rate of heterogeneous chemistry in the box model than in the concentrated smoke plume.

Aerosol organic carbon shows similar results to those for aerosol sulfate: the box model shows a smaller change than the 3D model for the reference chemistry case and a larger change for the expanded chemistry case. However, the normalized differences between the box and 3D models for OC (+13% and -9%) are of the same order as the differences due to vertical diffusion in the 3D model, and so it is not clear if the differences due to non-linear chemistry are significant for aerosol OC.

5.4 Effects of Shrinking and Expanding the Eulerian Box

The above discussion suggests two questions. First, since the size of the Eulerian grid box evaluated so far (52.5 km x 20 km) is smaller than the general size of the grid boxes in GACMs, how do the results change when the size of the box is increased? Second, does shrinking the box (for example, by reducing it's scale in the cross-wind direction) reduce the differences between the box model and the 3D plume model?

To answer these questions, we ran two additional box model tests, one where we expanded the box to 100 km x 100 km in the horizontal, and one where we shrunk the cross-wind extent of the box to 52.5 km x 10 km. Figure 5-6 compares the results of these tests with our previous box model and 3D plume results for both the reference and expanded chemistry cases. For the reference chemistry case, shrinking the box generally provides a closer match to the 3D plume model results. The results are more mixed for the expanded chemistry case, where shrinking the box makes the match worse for many species. For both chemistry cases, expanding the box to 100 km x 100 km dramatically increases the predicted formation of O_3, inorganic nitrate, and PAN and the destruction of NO_x relative to the 3D plume model. The differences between the tow chemistry cases for this large box are relatively small. Thus, the large boxes used in global models could substantially overestimate the emission of PAN and O_3 from young smoke plumes, and mask the effects of heterogeneous chemistry within the smoke plumes.

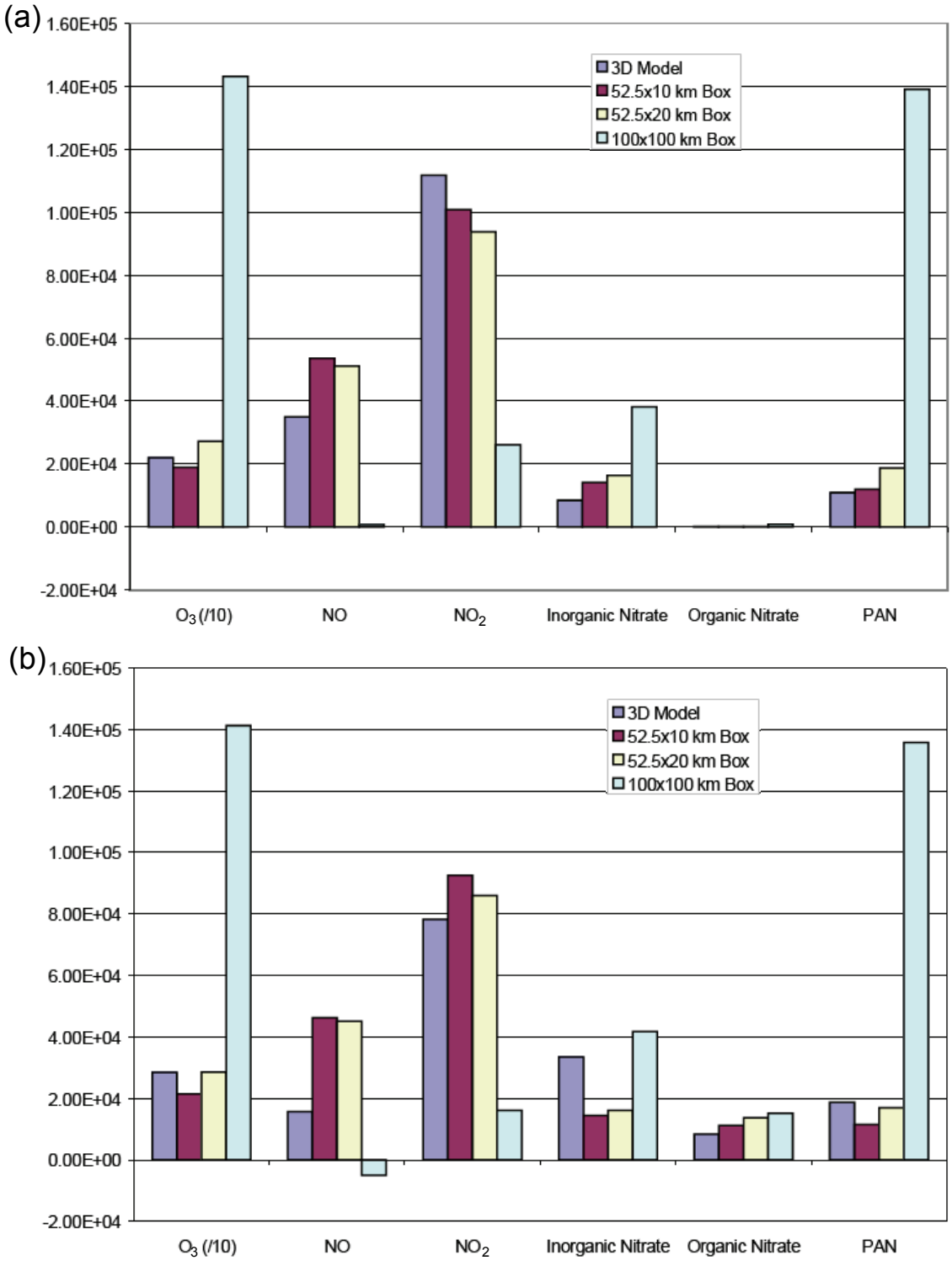

Figure 5-6: Comparison of 3D model results with different size Eulerian box models for the (a) reference and (b) expanded chemistry cases. Values plotted are $\Delta \mathbf{M}_q$ (mol). O_3 values are divided by 10 to fit on plot.

5.5 Conclusions and Recommendations for Global Atmospheric Chemistry Models

We have evaluated the errors in the effective flux of gas and aerosol species to the global environment caused by the automatic dilution of biomass burning emissions into large-scale global model grid boxes. To accomplish this, we compared the results of our 3D Eulerian plume simulation of the Timbavati smoke plume from Chapter 4 to the results of a single-box Eulerian model with the same horizontal scale (52.5 km x 20 km) as the full domain of our 3D simulation. The Eulerian box model was run for the reference and expanded chemistry cases described in Section 4.2.4. We calculated the change in the total amount of each species in the box model and in the bottom 1 km of the 3D plume model over 60 minutes of plume emissions. The differences between the box and 3D model values were used to estimate the error caused by the automatic dilution approach.

We found that the neglect of vertical diffusion of species into and out of the box model could result in errors of the order of $\pm 1 - 15\%$ in the predicted total amounts of tracer species, depending on the initial concentration profile of the species in the 3D model. Thus, changes of this order in other species may be caused by similar differences in advection and diffusion, by differences in non-linear chemistry, or both. For the reference chemistry case, we found that the automatic dilution of emissions in the box model resulted in a more oxidizing environment, with a larger net formation of O_3 (+24%), total (gas plus aerosol) inorganic nitrate (+94%), PAN species (+72%), and aerosol sulfate (+24%). For the expanded chemistry case, the automatic dilution of emissions in the box model results in a lower heterogeneous reaction rate for NO_2 and SO_2. Thus, the automatic dilution of emissions lead to overestimates of NO_x (+40%), while total inorganic nitrate, HONO, and aerosol sulfate are underestimated (-52%, -69%, and -45%, respectively). The O_3 estimates for both models in the expanded chemistry case are very close (within 1%), while the PAN estimates are within 10% of each other. Aerosol organic carbon (OC) shows similar behavior to aerosol sulfate in both chemistry cases (+13% for reference chemistry, -9% for expanded chemistry), but the differences between the box and 3D models are small enough that we cannot rule out the possibility that they are caused by differences in advection and diffusion rather than the effect of dilution on the non-linear chemistry. For both chemistry cases, the automatic dilution of emissions results in more of the total inorganic nitrate and chloride being present in the gas-phase. This is because the automatic dilution of emissions in the box model doesn't capture the localized high concentrations of $HCl_{(g)}$ and $HNO_{3(g)}$ seen in the 3D plume model, which keep more of the chloride and nitrate in the smoke plume within the aerosol phase. Since the 3D model is already underestimating the

amount of aerosol nitrate and chloride downwind relative to emissions, this suggests that the GACM approach could result in substantial underestimates of these semi-volatile aerosol constituents.

This suggests that even if the chemical models for smoke plume chemistry are improved to better match the available observations, the automatic dilution of smoke plume emissions in GACMs could still result in large errors in predicted concentrations of O_3, NO_x and aerosol species downwind of biomass burning sources. These errors could change the predicted impact of biomass burning emissions on global chemistry and climate. For example, the overestimate of NO_x seen in the box model for the expanded chemistry case could result in an overestimate in the amount of global NO_x and O_3 formed by biomass burning emissions.

There are several potential approaches to reduce the errors caused by the automatic dilution of plume emissions in GACMs. GACMs could use nested, higher resolution grids over regions of intense biomass burning to allow them to better capture the non-linear chemistry taking place in concentrated young smoke plumes. These nested grids could be static (fixed in space and time, as in *Kumar and Russell* [1996]) or adaptive, where the grid system changes dynamically with time to meet solution requirements [*Srivastava et al.*, 2001]. One problem with this approach is that the required nested grid resolution may make the global model too computationally expensive to be of great use, especially when detailed gas and aerosol chemistry is included in the model.

Another approach would be the use of a plume-in-grid model, where a subgrid-scale representation of the young smoke plumes is incorporated within the 3D grid system of the GACM. Such plume-in-grid models have already been used to reduce the errors associated with the automatic dilution of smoke-stack emissions in urban and regional air-quality models [*e.g.*, *Karamchandani et al.* [2002]], and the work of *Freitas et al.* [2007] used an imbedded 1-D plume model to predict the effective plume height of biomass burning emissions for use in regional and global-scale models. A more detailed reactive plume model, incorporating a suitable gas- and aerosol-phase chemical model, could be used to estimate not only plume height, but the impact of plume chemistry on the effective emissions of biomass burning to the global environment.

A third approach would be to develop a computationally-efficient parameterization of the 3D Eulerian plume model used in this work, and then to incorporate this parameterization into GACMs. This reduced form model could calculate the net export (effective emissions) of gas- and aerosol-phase species to the global environment from appropriate input parameters. The major inputs for the parameterization would likely include the vertical stability, horizontal turbulence, and chemical composition of the background environment, the initial plume size, and the emission rate of sensible heat, NO_x, HCHO, alkenes, aldehydes, and particles from the fire source. Alkenes, HCHO, and

aldehydes are selected as the most important hydrocarbons in the smoke emissions due to the rapid reaction rate of alkenes and the formation of HO_x radicals by the photolysis of HCHO and aldehydes. This approach is currently used in the MIT Integrated Global Systems Model (IGSM) [*Prinn et al.*, 1999] to account for the impact of urban air chemistry on the effective emissions of several pollutants onto the global atmosphere. *Calbo et al.* [1998] developed a parameterization consisting of a set of analytical expressions to approximate the predictions of the California Institute of Technology - Carnegie-Mellon University (CIT) Urban Airshed Model [*McRae et al.*, 1982] for net export to the environment. The parameterization was derived using the probabilistic collocation method of *Tatang et al.* [1997]. *Mayer et al.* [2000] incorporated this parameterization into the MIT IGSM to study the impact of urban air pollution on global chemistry and climate. All of these approaches would require accurate models of the gas- and aerosol-phase chemistry taking place in a young smoke plume, and would benefit from further research into these chemical models and smoke plume chemistry.

Chapter 6

Conclusions

6.1 Summary and Major Findings

In this thesis, we have investigated the gas and aerosol chemistry of young smoke plumes from biomass burning. Our focus was on explaining the formation of ozone and growth of aerosols within these young smoke plumes in order to better predict the impact that biomass burning emissions have on global atmospheric chemistry and climate. To accomplish this, we developed a new gas- and aerosol-phase chemistry model - the Aerosol Simulation Program (ASP). We used ASP to perform three numerical studies of the chemistry of biomass burning smoke plumes:

- First, we simulated the non-linear chemical and physical changes in three young biomass burning smoke plumes - the Otavi savannah fire in Namibia, an Alaskan boreal forest fire, and the Timbavati savannah fire in South Africa - using ASP combined with a Lagrangian parcel model.

- Second, we used ASP and a 3D Eulerian model to simultaneously simulate the fluid dynamics, gas-phase chemistry, aerosol-phase chemistry, and radiative transfer in the Timbavati smoke plume. This is the first known attempt to simultaneously simulate all of these processes in a young biomass burning smoke plume.

- Third, we used ASP and an Eulerian box model to evaluate the errors that can be caused by the automatic dilution of biomass burning emissions into large-scale (10-200 km) global model grid boxes, as is done in many global atmospheric chemistry models (GACMs).

The major conclusions from these studies are summarized below.

6.1.1 Lagrangian Studies

We used ASP in a Lagrangian parcel model to simulate the formation of ozone and growth of aerosol particles in three young smoke plumes from biomass burning. For the Otavi and Alaska plumes, we simulated the gas-phase chemistry, while for the Timbavati smoke plume we simulated the gas- and aerosol-phase chemistry simultaneously. The Timbavati study is, to our knowledge, the first to look simultaneously at the formation of ozone and growth of aerosols in young biomass burning smoke plumes.

We found that our model explained the formation of ozone in the Otavi and Alaska plumes fairly well, with slight underestimates of ozone formation in both cases. However, our initial model simulation of the Timbavati smoke plume differed greatly from the available observations: the initial model simulation overestimated the concentration of potassium downwind and underestimated the downwind molecular or particle concentrations of ozone, OH, total aerosol, and aerosol organic carbon (OC), sulfate, and nitrate. After eliminating particle deposition as a potential explanation for the potassium overestimate, we believe that the initial aerosol concentration at Timbavati was overestimated relative to CO due to the differing averaging times of the aerosol and gas-canister measurements.

There are four major conclusions to the Lagrangian studies. First, we find that the 30% of gas-phase carbon that is currently uncharacterized in canister measurements of smoke plumes may be responsible for the rapid formation of aerosol OC. Including these compounds in the model (using the proxy monoterpene BIOH) greatly improved the match between the model and the observations for aerosol OC. More work is required to identify these compounds and determine their ability to form secondary organic aerosol.

A second major conclusion of this study is that current models of biomass burning smoke plumes may be missing a source of OH. We found that fixing the model OH concentration at the reported value for the Timbavati smoke plume (1.7×10^7 radicals/cm^3) greatly improved the match between modeled and observed ozone concentrations.

A third major conclusion of this study is that heterogeneous reactions of NO_2 and SO_2 could explain the high concentrations of OH and the rapid formation of ozone, nitrate and sulfate if the NO_2 and SO_2 uptake coefficients on smoke aerosols are large [O(10^{-3}) and O(10^{-4}), respectively]. We found that a heterogeneous reaction of NO_2 to HONO could be the missing OH source in Timbavati if the uptake coefficient on smoke aerosols is large [O(10^{-3})], and that this chemistry is consistent with the observations of the Otavi and Alaska smoke plumes. Based on this, we conclude that the rate of reaction of NO_2 and SO_2 on young biomass burning aerosols deserves further

laboratory and field investigation. Other explanations for the ozone, nitrate and sulfate formation were explored, but did not explain the observations of the Timbavati smoke plume. We found that uncertainty in reaction rates could not simultaneously explain the rapid formation of ozone and aerosol nitrate. In addition, we found that adding additional oxygenated compounds to the model simulation did not significantly increase the ozone formation. Finally, aqueous formation of sulfate was negligible in the dry conditions of the Timbavati smoke plume.

Our fourth major conclusion is that the changes in the aerosol size distribution in the smoke plume are dominated by plume dilution and condensational growth, with coagulation and nucleation having only a minor effect. In our model, the reduction of aerosol number concentration observed in the first 10 minutes downwind of the Timbavati fire is caused by plume dilution, not by coagulation as suggested by *Hobbs et al.* [2003]. In addition, our scale analysis suggests that nucleation was negligible in the Timbavati smoke plume. The growth in aerosol number concentration observed after 15 minutes downwind may have been caused by small particles growing into the detectable size range of the condensation particle counter, or by a sampling artifact caused by the aircraft's motion relative to the plume centerline.

6.1.2 Eulerian Studies

We have presented a 3D Eulerian simulation of the fluid dynamics, gas-phase chemistry, aerosol chemistry, and the scattering and absorption of radiation within the Timbavati biomass burning smoke plume by running two test cases: a reference chemistry case and an expanded chemistry case. In the reference chemistry case, the uncharacterized organic species are assumed to be unreactive and heterogeneous chemistry is not included. In the expanded chemistry case, the uncharacterized compounds are included using BIOH (monoterpenes) as a proxy and the heterogeneous reactions of NO_2 and SO_2 discussed in Chapter 3 are included with uptake coefficients of 10^{-3} and 2×10^{-4}, respectively. The results of the 3D Eulerian model CRM6 matched the observed injection height of the smoke plume, but the initial model run underestimated the horizontal dispersion of the smoke plume. This underestimate may have been due to an underestimate of subgrid-scale turbulent mixing or to plume-scale fluctuations of the horizontal winds which are not included in the model. Increasing the minimum horizontal diffusion coefficient in the model provided a better match to the observed horizontal dispersion of the plume.

There are four main conclusions of our Eulerian studies. First, we find that the expanded chemistry case provides a better match with observations of ozone and OH than the reference chemistry case, but still underestimates the observed concentrations. The maximum OH concen-

tration predicted for the expanded chemistry case (1.0×10^7 radicals cm^{-3}) is still below the reported plume-average OH concentration (1.7×10^7 radicals cm^{-3}), and the maximum ozone concentration in the model (106 ppbv) is below the maximum observed ozone concentration of 135 ppbv.

The second main conclusion of the Eulerian study is that direct measurements of OH in the young smoke plumes would be the best way to determine if heterogeneous production of HONO is taking place. An increase in OH while passing through the smoke plume would be consistent with the rapid heterogeneous formation of HONO from NO_2 on smoke particles, while a decrease in OH would suggest other explanations are required for the rapid formation of O_3 and nitrate in young biomass burning plumes. Thus, measurements of OH in young smoke plumes should be a priority for future field campaigns.

Third, we conclude that simultaneous measurements of chloride and nitrate in the gas and aerosol phases are needed to resolve the discrepancies in the model results for aerosol chloride and nitrate mass concentrations. The model matches the observed downwind concentration of potassium well, suggesting that the model is correctly reproducing the observed dispersion of the primary aerosol. The maximum downwind aerosol concentrations in the model are found at an altitude of 1 km, rather than the altitude of 0.6 km sampled in Timbavati. The expanded chemistry case improves the match with observations for OC, nitrate, and sulfate, but still underestimates the observed aerosol concentrations. The total (gas + aerosol) concentration of chloride downwind is consistent with the aerosol observations, but the total concentration of nitrate downwind is less than the observed aerosol concentration, suggesting that the model is underestimating the formation of nitrate from NO_x even in the expanded chemistry case. Simultaneous measurements of chloride and nitrate in the gas and aerosol phases would allow us to close the budget for chloride and nitrogen atoms within the smoke plume.

Finally, we found that the impact of smoke aerosols on photolysis rates is smaller than the parametric uncertainty in these rates due to uncertainties in absorption coefficient and quantum yield. However, the model may be underestimating the absorption of solar radiation within the smoke plume. The modeled solar heating due to the absorption of solar radiation is 4-6 K/day at 20-25 km downwind, which is slightly lower than the reported value of 7.4 K/day, and suggests that the model may underestimate the absorption of solar radiation by the aerosols. This is consistent with the underestimate of BC relative to observations. Both discrepancies may be due to the absorption of solar radiation by secondary organic compounds. Thus, the light-absorbing properties of this organic matter, especially at the short wavelengths important for photolysis rates, deserve further investigation.

6.1.3 Comparison to "Automatic Dilution" Approach

We have evaluated the errors in the effective flux of gas and aerosol species to the global environment caused by the widely utilized "automatic dilution" of biomass burning emissions into the large-scale surface grid boxes in 3D GACMs. To accomplish this, we compared the results of our 3D Eulerian plume simulation of the Timbavati smoke plume to the results of an Eulerian grid-box model simulation. We calculated the change in the total amount of each species in the box model and in the bottom 1 km of the 3D plume model over 60 minutes of plume emissions. The differences between the grid-box and 3D plume model values were used to estimate the error caused by the automatic dilution approach.

For the reference chemistry case, we found that the automatic dilution of emissions in the box model resulted in a more oxidizing environment, with a larger net formation of O_3 (+24%), total (gas plus aerosol) inorganic nitrate (+94%), PAN species (+72%), and aerosol sulfate (+24%). For the expanded chemistry case, the automatic dilution of emissions in the box model resulted in a lower heterogeneous reaction rate for NO_2 and SO_2, leading to overestimates of NO_x (+40%), while total inorganic nitrate, HONO, and aerosol sulfate are underestimated (-52%, -69%, and −45%, respectively). The O_3 estimates for both models in the expanded chemistry case are very close (within 1%), while the PAN estimates are within 10% of each other. Aerosol organic carbon (OC) shows similar behavior to aerosol sulfate in both chemistry cases (+13% for reference chemistry, -9% for expanded chemistry), but the differences between the box and 3D models are small enough that we cannot rule out the possibility that they are caused by differences in advection and diffusion rather than the effect of dilution on the non-linear chemistry. For both chemistry cases, the automatic dilution of emissions results in more of the total inorganic nitrate and chloride being present in the gas-phase. Since the 3D plume model is already underestimating the amount of aerosol nitrate and chloride downwind relative to emissions, this suggests that the GACM automatic dilution approach could result in substantial underestimates of these semi-volatile aerosol constituents.

The major conclusion of this study is that even if the chemical models for smoke plume chemistry are improved to better match the available observations, the automatic dilution of smoke plume emissions in GACMs would still result in large errors in predicted concentrations of O_3, NO_x and aerosol species downwind of biomass burning sources. The large differences between the Eulerian box and 3D models for O_3, NO_x, NO_y species and aerosol species noted above, even when both models are using identical chemistry, show that the automatic dilution of emissions in GACMs can result in large errors in predicting the non-linear chemical changes within the young smoke plume. These errors could change the predicted impact of biomass burning emissions on global atmospheric

chemistry and climate.

There are several potential approaches to reduce the errors caused by the automatic dilution of plume emissions in GACMs. These include the use of static or dynamic higher resolution nested grids over regions of intense biomass burning, the use of a plume-in-grid model, or the use of a computationally-efficient parameterization of a 3D Eulerian plume chemistry model. All of these approaches would require accurate models of the gas- and aerosol-phase chemistry taking place in a young smoke plume, and would benefit from further research into these chemical models and smoke plume chemistry beyond that achieved in this thesis.

6.2 Limitations of Current Data and Theory

We have presented the first known simultaneous simulation of the fluid dynamics, gas phase chemistry, aerosol chemistry, and radiative transfer in a young biomass burning smoke plume. We have attempted to make this model as comprehensive as possible, but limitations in the available data and theory limit the ability of the current model to fully simulate the chemistry taking place within young smoke plumes. In this section we discuss some of the major limitations of our modeling work, and suggest how these limits could be addressed in the future.

Our current aerosol size distribution model has two major limitations. First, we assumed that the aerosol size distribution is an internal mixture - that is, that all particles of the same size have the same composition. Second, for the purposes of calculating heterogeneous reaction rates, mass-transfer rates, coagulation rates, and optical properties, we assume that all of the particles are spherical. These assumptions are generally true for biomass burning aerosols [*Reid et al.*, 2005b], but some biomass burning aerosols are present as external mixtures of aerosols, which may have substantially different compositions and non-spherical shapes [*Posfai et al.*, 2003]. In future work, the moving-center sectional size distribution could be extended to model an external mixture of multiple aerosol types as a mixture of separate size distributions, as in the work of *Jacobson* [2002]. In addition, non-spherical soot aggregates could be modeled instead as spherically isotropic fractal particles of constant fractal dimension, as in the COSIMA model of *Naumann* [2003]. COSIMA can calculate the available surface area (needed for heterogeneous reaction rate calculations) and the coagulation rates of fractal soot particles. However, the assumption of constant fractal dimension may be unsuitable for soot in combustion plumes. Soot particles in combustion plumes also change their shape with time, going from a fractal structure to a more clumped structure as organic matter and water condenses onto the soot [*Saathoff et al.*, 2003].

The aerosol thermodynamics model has two major limitations. First, we assume that the organic thermodynamics and inorganic thermodynamics can be modeled independently. This assumption was made in the CACM/MPMPO model [*Pun et al.*, 2002; *Griffin et al.*, 2005] and is also included in more recent thermodynamics models such as UHAERO [*Amundson et al.*, 2007]. This assumption ignores organic-inorganic interactions such as the "salting out" effect (where the solubility of an organic species in water is reduced in the presence of inorganic ions) and the formation of ammonium-organic acid salts. However, there is a lack of experimental thermodynamic data on the interactions of organics and inorganic ions, which limits the development of more accurate models [*Raatikainen and Laaksonen*, 2005]. Several researchers are working to improve our understanding and modeling of the thermodynamics of mixtures of organic species, inorganic ions, and water. The work of *Ming and Russel* [2002] provided a first step towards a theory of the interactions between inorganic ions and organic species by combining the Pitzer-Simonson-Clegg approach commonly used for electrolyte mixtures with the UNIFAC approach used for organic mixtures. They provide UNIFAC group interaction parameters for Na^+, NH_4^+, Cl^-, and SO_4^{2-} based on the measurements of the salting out constants of the different ions. *Erdakos et al.* [2006a] and *Erdakos et al.* [2006b] added a Debye-Huckel term to the original UNIFAC activity coefficient equation to estimate activity coefficients for mixtures of organic species with H_2O, Na^+, NH_4^+, Ca^{2+}, NO_3^-, Cl^-, and SO_4^{2-}. Further work is needed to refine these thermodynamic models, and laboratory investigations of the thermodynamics of typical species found in atmospheric aerosol are essential to this effort.

The second major limitation of our aerosol thermodynamic model is the use of group contribution methods to estimate the normal boiling point and vapor pressure of the condensable organic compounds. *Clegg et al.* [2008b] evaluated the uncertainty in vapor pressure predictions for the compounds in the CACM/MPMPO model of *Griffin et al.* [2005]. They found that using different methods for predicting normal boiling point and vapor pressures for organic compounds resulted in uncertainties in the predicted vapor pressures of an order of magnitude or greater. This is because most group contribution methods are based upon data for monofunctional compounds. In addition, vapor pressure is very sensitive to the type and number of functional groups present [*Clegg et al.*, 2008b]. Thus, the lumping of the semi-volatile reaction products into 10 surrogate compound classes increases the uncertainty, as the vapor pressures of compounds within a surrogate class may vary by orders of magnitude. *Clegg et al.* [2008a] conclude that these uncertainties in vapor pressures of organic compounds are large compared to the probable effects of organic-inorganic interactions on activity coefficients, and that further advances in thermodynamic models will require more detailed laboratory and field measurements of the physical properties of atmospheric aerosol mixtures.

The gas- and aerosol-phase chemistry of semi-volatile reactive species in the model needs to be extended. The current version of CACM includes many compounds that are classified as unreactive, but these species will react with atmospheric oxidants like OH over time, leading to second, third, and subsequent generation products. These later-generation products may also be semivolatile and partition between the gas and aerosol phases [*Donahue et al.*, 2006; *Robinson et al.*, 2007]. Further work on this issue would help to improve models of organic aerosol formation. In addition, the current lumping of compounds into compound classes may not correctly capture the impact of these species on ozone formation and the growth of organic aerosol mass. Finally, the model does not include particle-phase reactions of organic species, such as heterogeneous oxidation of organic aerosol by gas-phase species or in-particle oxidation and polymerization reactions.

The major limitation of our work on aerosol optical properties and radiative transfer within the smoke plume is the low spectral resolution of our estimates of complex refractive index and of our radiative transfer model. Higher spectral resolution models are needed to better estimate the impact of biomass burning aerosols on gas-phase photolysis rates. This may include the incorporation of the TUV model into the CRM6 modeling framework to better represent the spectral radiative transfer of solar radiation. In addition, observations of the spectral absorption and scattering of biomass burning aerosol in the laboratory and field and of the spectral complex refractive index for various mixtures common in atmospheric aerosols are necessary to better predict the impact of these aerosols on solar radiation, photolysis rates, and climate. Field measurements of spectral solar irradiance and actinic flux within biomass burning plumes would also help advance this work.

We found that our 3D Eulerian dynamical model had difficulty representing the horizontal dispersion of the young smoke plume. This could have been due to an underestimate of subgrid-scale turbulent mixing or due to plume-scale fluctuations of the horizontal winds which are not included in the model. A better estimate of subgrid-scale turbulent mixing could be obtained by increasing the resolution of the model or improving the turbulent closure scheme used in the model. A one-and-a-half order or higher order turbulence closure scheme that includes prognostic equations for turbulent kinetic energy and velocity covariances could provide a better estimate of the impact of sub-grid scale turbulence on smoke plume dispersion and chemistry. Including fluctuating boundary wind conditions in the CRM6 model could also help better represent plume dispersion due to these fluctuations.

6.3 Suggestions for Future Research

Our work suggests many potential avenues for further research into the chemistry of young biomass burning smoke plumes. Below we summarize our recommendations for field studies (Section 6.3.1), laboratory measurements (Section 6.3.2), and future modeling work (Section 6.3.3).

6.3.1 Field Measurements

One goal of future field campaigns should be to better characterize the dispersion of smoke plumes and the variability of concentrations within the smoke plume. Snapshots or better video of the smoke plume could help better understand the important processes in the plume dispersion. High-frequency measurements (1 Hz) of concentrations during plume transects, as was done for the Otavi smoke plume, would help to characterize the variability of concentrations within the smoke plume. Flight transects of the plume should be made at different altitudes and times at the same downwind distance, to better characterize the temporal and vertical variation of concentrations within the smoke plume.

Direct measurements of OH concentrations in the smoke plumes should be another priority of future field campaigns. Our work suggests that understanding the sources and sinks of OH in the smoke plumes is critical to understanding the rapid formation of ozone in these smoke plumes. Our 3D modeling work suggests that measurements of NO_x and HONO, while desirable, would not be as useful in understanding this chemistry as measurements of OH.

Future field campaigns should also measure simultaneously the gas and aerosol-phase concentrations of semi-volatile species, such as chloride, nitrate and semi-volatile organic compounds (SVOCs), simultaneously during plume transects. Measuring both aerosol nitrate and gaseous HNO_3 would better constrain the total rate of nitrate formation as well as the partitioning of nitrate between the gas and aerosol phases. These measurements should also have a similar sampling or averaging time to help eliminate ambiguities due to sampling artifacts.

Better characterization of the non-methane organic compounds (NMOCs) emitted by biomass burning are needed to understand the formation of ozone and aerosol organic carbon within the young smoke plumes. Our work suggests that the currently uncharacterized organic compounds are responsible for the rapid aerosol OC formation observed in smoke plumes. Understanding the structure and chemistry of these compounds is thus critical to understanding the chemical changes in the young smoke plume.

Measuring the evolution of the aerosol size distribution in young smoke plumes should be a

research priority. Since the mean diameter of aerosol particles in smoke plumes is around 0.1 μm, measurements of aerosol size distribution should be centered on this size. Finally, solar spectral irradiances should be measured in these smoke plumes to help better constrain rates of photolysis within the smoke plume.

6.3.2 Laboratory Measurements

Measuring the rates of heterogeneous uptake of NO_2 and SO_2 on young smoke aerosols, and the products of the reactions, should be a priority for laboratory studies. Our work shows that heterogeneous reactions of NO_2 and SO_2 could explain the rapid formation of ozone, nitrate, and sulfate observed in smoke plumes, but only if the uptake coefficients are large [O(10^{-3}) and O(10^{-4}), respectively]. Laboratory measurements of the rate and products of these reactions would help to determine if this chemistry is taking place within young smoke plumes.

The spectral scattering and absorption of radiation by young and aged biomass particles needs to be better characterized. Knowing how the absorption of radiation by the smoke aerosols changes with wavelength is critical to better assessing the impact of these aerosols on photolysis rates within the smoke plumes. These studies should also strive to connect the optical properties of the smoke aerosols to their composition, and to explain how the optical properties of the aerosol change as the relative humidity of the environment increases.

Lastly, we recommend performing smog-chamber studies of smoke dilution and chemistry. Studying the products of smoke plume chemistry in a controlled environment could help to eliminate many of the uncertainties associated with plume variability and dispersion, making it easier to identify the important chemical processes.

6.3.3 Modeling

The main goal of future modeling work should be to better incorporate plume chemistry into GACMs. As field and laboratory studies identify more NMOCs in smoke plumes, future modeling studies should also incorporate the chemistry of these compounds. These studies should focus on how these newly identified NMOCs could affect the formation of O_3 and aerosol OC within the smoke plumes. However, modeling the chemistry of young smoke plumes will also require methods to model the subgrid scale chemistry of these plumes, such as plume-in-grid models, nested grids, or parameterizations of 3D smoke plume models.

Another potential avenue of future modeling research would be to explore how aerosols and gases from a smoke plume are modified by deep convection during pyro-cumulus events. Most studies of

pyro-cumulus events focus on the height of the smoke injection and the amount of smoke transported to the upper troposphere/lower stratosphere (UT/LS). However, it is also important to know the chemical state of the smoke that is transported to the UT/LS, which could be significantly modified by chemical processes taking place within the pyro-cumulus cloud. Our modeling procedure, which combines a cloud-resolving model with a detailed model of smoke plume chemistry and physics, could be very useful in exploring these questions.

Bibliography

Abel, S. J., J. M. Haywood, E. J. Highwood, J. Li, and P. R. Buseck, Evolution of biomass burning aerosol properties from an agricultural fire in southern Africa, *Geophysical Research Letters*, *30*, 1783, doi:10.1029/2003GL017,342, 2003.

Ackerman, A., O. Toon, D. Stevens, A. Heymsfield, V. Ramanathan, and E. Welton, Reduction of cloudiness by soot, *Science*, *288*, 1042–1047, 2000.

American Society of Mechanical Engineers (ASME), *Recommended Guide for the Prediction of the Dispersion of Ariborne Effluents*, 2nd ed., ASME, New York, 1973.

Amoco Chem. Ltd, National industrial chemicals notification and assessment scheme, full public report, 2,6-naphthalenedicarboxylic acid, Available at http://www.nicnas.gov.au, 1997.

Amundson, N. R., A. Caboussat, J. W. He, A. V. Martynenko, C. Landry, C. Tong, and J. H. Seinfeld, A new atmospheric aerosol phase equilibrium model (UHAERO): Organic systems, *Atmospheric Chemistry and Physics*, *7*, 4675–4698, 2007.

Anderson, R., S. Gathman, J. Hughes, S. Björnsson, S. Jónasson, D. C. Blanchard, C. B. Moore, H. J. Survilas, and B. Vonnegut, Electricity in volcanic clouds, *Science*, *148*, 1179–1189, 1965.

Andreae, M. O., and P. Merlet, Emission of trace gases and aerosols from biomass burning, *Global Biogeochemical Cycles*, *15*, 955–966, 2001.

Artaxo, P., M. Yamasoe, J. Martins, S. Kocinas, S. Carvalho, and W. Maenhaut, Case study of atmospheric measurements in Brazil: Aerosol emissions from Amazon basin fires, in *Fire in the Environment: The Ecological, Atmospheric, and Climatic Importance of Vegetation Fires*, edited by P. J. Crutzen and J. Goldammer, pp. 139–158, John Wiley and Sons, 1993.

Atkinson, P., D. Baulch, R. Cox, J. Hampson, R.S., J. Kerr, and J. Troe, Evaluated kinetic and photochemical data for atmospheric chemistry, *Journal of Physical and Chemical Reference Data*, *21*, 1125–1444, 1992.

Bassett, M., F. Gelbard, and J. H. Seinfeld, Mathematical model for multicomponent aerosol fromation and growth in plumes, *Atmospheric Environment*, *15*, 2395–5406, 1981.

Beard, K., Terminal velocity and shape of cloud and precipitation drops aloft, *Journal of Atmospheric Science*, *33*, 851–864, 1976.

Bierbach, A., I. Barnes, K. H. Becker, and E. Wiesen, Atmospheric chemistry of unsaturated carbonyls: Butenedial, 4-oxo-2-pentenal, 3-hexene-2,5-dione, maleic anhydride, 3h-furan-2-one, and 5-methyl-3h-furan-2-one, *Environmental Science and Technology*, *28*, 715–729, 1994.

Bierbach, A., I. Barnes, and K. Becker, Product and kinetic study of the OH-initiated gas-phase oxidation of furan, 2-methylfuran and furanaldehydes at 300 K, *Atmospheric Environment*, *29*, 2651–2660, 1995.

Bolton, D., The computation of equivalent potential temperature, *Monthly Weather Review*, *108*, 1046–1053, 1980.

Briggs, G., *Plume Rise*, U.S. Atomic Energy Commission Critical Review Series T/D 25075, 1969.

Brimblecombe, P., and S. Clegg, The solubility and behavior of acid gases in the marine aerosol, *Journal of Atmospheric Chemistry*, *7*, 1–18, 1988.

Brimblecombe, P., and S. Clegg, The solubility and behavior of acid gases in the marine aerosol - erratum, *Journal of Atmospheric Chemistry*, *8*, 95, 1989.

Britton, L., and A. Clarke, Heterogeneous reactions of sulfur dioxide and SO2/NO2 mixtures with a carbon soot aerosol, *Atmospheric Environment*, *14*, 829–839, 1980.

Buzcu, B., Z. Yue, M. Fraser, U. Nopmongcol, and D. Allen, Secondary particle formation and evidence of heterogeneous chemistry during a wood smoke episode in texas, *Journal of Geophysical Research*, *111*, D10S13, doi:10.1029/2005JD006,143, 2006.

Calbo, J., W. Pan, M. Webster, R. G. Prinn, and G. J. McRae, Parameterization of urban subgrid scale processes in global atmospheric chemistry models, *Journal of Geophysical Research*, *103*, 3437–3451, 1998.

Carreras-Sospedra, M., R. J. Griffin, and D. Dabdub, Calculations of incremental secondary organic aerosol reactivity, *Environmental Science and Technology*, *39*, 1724–1730, 2005.

Carter, W., D. Luo, I. Malkina, and J. Pierce, Environmental chamber studies of atmospheric reactivities of volatile organic compounds: Effects of varying ROG surrogate and NO_x., *Tech. rep.*, Final Report to Coordinating Research Council, Inc., Project ME-9, California Air Resources Board, Contract A032-0692, and South Coast Air Quality Management District, Contract C91323., 1995, available at http://www.cert.ucr.edu/ carter/absts.htm#rct2rpt.

Carter, W. P., Documentation of the SAPRC-99 chemical mechanism for VOC reactivity assessment, *Tech. rep.*, Draft report to the California Air Resources Board, Contracts 92-329 and 95-308, 2000.

Carter, W. P., and R. Atkinson, Alkyl nitrate formation from the atmospheric photooxidation of alkanes; a revised estimation method, *Journal of Atmospheric Chemistry*, *8*, 165–173, 1989.

Carter, W. P., I. Cocker, David R., D. R. Fitz, I. L. Malkina, K. Bumiller, C. G. Sauer, J. T. Pisano, C. Bufalino, and C. Song, A new environmental chamber for evaluation of gas-phase chemical mechanisms and secondary aerosol formation, *Atmospheric Environment*, *39*, 7768–7788, 2005.

Chan, C., L. Chan, Y. Zheng, J. Harris, S. Oltmans, and S. Christopher, Effects of 1997 Indonesian forest fires on tropospheric ozone enhancement, radiative forcing, and temperature change over the Hong Kong region, *Journal of Geophysical Research*, *106*, 14,875–14,885, 2001.

Christian, T., B. Kleiss, R. Yokelson, R. Holzinger, P. Crutzen, W. Hao, B. Saharjo, and D. Ward, Comprehensive laboratory measurements of biomas-burning emissions: 1. Emissions from Indonesian, African, and other fuels., *Journal of Geophysical Research*, pp. 4719, doi:10.1029/2003JD003,704, 2003.

Clegg, S., and P. Brimblecombe, Solubility of ammonia in pure aqueous and multicomponent solutions, *Journal of Physical Chemistry*, *93*, 7237–7248, 1989.

Clegg, S. L., M. J. Kleeman, R. J. Griffin, and J. H. Seinfeld, Effects of uncertainties in the thermodynamic properties of aerosol components in an air quality model - Part 1: Treatment of inorganic electrolytes and organic compounds in the condensed phase, *Atmospheric Chemistry and Physics*, *8*, 1057–1085, 2008a.

Clegg, S. L., M. J. Kleeman, R. J. Griffin, and J. H. Seinfeld, Effects of uncertainties in the thermodynamic properties of aerosol components in an air quality model - Part 2: Predictions of the vapour pressures of organic compounds, *Atmospheric Chemistry and Physics*, *8*, 1087–1103, 2008b.

Colman, J. J., A. L. Swanson, S. Meinardi, B. C. Sive, D. R. Blake, and F. S. Rowland, Description of the analysis of a wide range of volatile organic compounds in whole air samples collected during PEM-tropics A and B, *Analytical Chemistry*, pp. 3723–3731, 2001.

Crutzen, P. J., and M. O. Andreae, Biomass burning in the tropics: Impact on atmospheric chemistry and biogeochemical cycles, *Science*, *250*, 1669–1678, 1990.

Davis, E., Transport phenomena with single aerosol particles, *Aerosol Science and Technology*, *2*, 121–144, 1983.

Decesari, S., et al., Characterization of the organic composition of aerosols from Rodonia, Brazil, during the LBA-SMOCC 2002 experiment and its representation through model compounds, *Atmospheric Chemistry and Physics*, *6*, 375–402, 2006.

Demore, W., S. Sander, D. Golden, R. Hampson, M. Kurylo, C. Howard, A. Ravishankara, C. Kolb, and M. Molina, *Chemical Kinetic and Potochemical Data for Use in Stratospheric Modeling: Evaluation No. 11 of the NASA Panel for Data Evaluation*, JPL Publication 94-26, 1994.

DeMore, W., et al., *Chemical Kinetic and Photochemical Data for Use in Stratospheric Modeling: Evaluation No. 12 of the NASA Panel for Data Evaluation*, JPL Publication 97-4, 1997.

Donahue, N., A. Robinson, C. Stanier, and S. N. Pandis, Coupled partitioning, dilution, and chemical aging of semivolatile organics, *Environmental Science and Technology*, *40*, 2635–2643, doi:101,021/es052,297c, 2006.

Donaldson, D., B. T. Mmereki, S. R. Chaudhuri, S. Handley, and M. Oh, Uptake and reaction of atmospheric organic vapors on organic films, *Faraday Discussions*, *130*, 227–239, doi:10.1039/b418,859d, 2005.

Dransfield, T. J., K. K. Perkins, N. M. Donahue, et al., Temperature and pressure dependent kinetics of the gas-phase reaction of the hydroxyl radical with nitrogen dioxide, *Geophysical Reserach Letters*, *26*, 687–690, 1999.

Eagan, R. C., P. V. Hobbs, and L. F. Radke, Measurements of cloud condensation nuclei and cloud droplet size distributions in the vicinity of forest fires, *Journal of Applied Meteorology*, *13*, 553–557, 1974.

Erdakos, G. B., W. E. Asher, J. H. Seinfeld, and J. F. Pankow, Prediction of activity coefficients in liquid aerosol particles containing organic compounds, dissolved inorganic salts, and water -

Part 1: Organic compounds and water by consideration of short- and long-range effects using x-UNIFAC.1, *Atmospheric Environment*, *40*, 6410–6421, 2006a.

Erdakos, G. B., E. I. Chang, J. F. Pankow, and J. H. Seinfeld, Prediction of activity coefficients in liquid aerosol particles containing organic compounds, dissolved inorganic salts, and water - Part 3: Organic compounds, water, and ionic constituents by consideration of short-, mid-, and long-range effects using x-UNIFAC.3, *Atmospheric Environment*, *40*, 6437–6452, 2006b.

Facchini, M. C., M. Mircea, S. Fuzzi, and R. J. Charlson, Cloud albedo enhancement by surface-active organic solutes in growing droplets, *Nature*, *401*, 257–259, 1999.

Fan, J., R. Zhang, D. Collins, and G. Li, Contribution of secondary condensible organics to new particle formation: A case study in Houston, Texas, *Geophysical Research Letters*, *33*, L15,802, doi:10.1029/2006GL026,295, 2006.

Fountoukis, C., and A. Nenes, ISORROPIA II: A computationally efficient thermodynamic equilibrium model for K^+-Ca^{2+}-Mg^{2+}-NH_4^+-Na^+-SO_4^{2-}-NO_3^--Cl^--H_2O aerosols, *Athospheric Chemistry and Physics*, *7*, 4639–4659, 2007.

Fredenslund, A., R. Jones, and J. Prausnitz, Group-contribution estimation of activity coefficients in nonideal liquid mixtures, *AIChE Journal*, *21*, 1086–1099, 1975.

Fredenslund, A., J. Gmehling, and P. Rasmussen, *Vapor-Liquid Equilibria Using UNIFAC, A Group Contribution Method*, Elsevier, Amsterdam, 1977.

Freitas, S., et al., Including the sub-grid scale plume rise of vegetation fires in low resolution atmospheric transport models, *Atmospheric Chemsitry and Physics*, *7*, 3385–3398, 2007.

Fu, Q., and K. Liou, Parameterizations of the radiative properties of cirrus clouds, *Journal of the Atmospheric Sciences*, *50*, 2008–2025, 1993.

Fuchs, N., *Mechanics of Aerosols*, Pergamon, New York, 1964.

Gao, S., D. A. Hegg, P. V. Hobbs, T. W. Kirchstetter, B. I. Magi, and M. Sadilek, Water-soluble organic compounds in aerosols associated with savanna fires in southern Africa: Identification, evolution, and distribution, *Journal of Geophysical Research*, *108*, 8491, doi:10.1029/2002JD002,324, 2003.

Gardner, E. P., P. D. Sperry, and J. G. Calvert, Primary quantum yields of NO_2 photodissociation, *Journal of Geophysical Research*, *92*, 6642–6652, 1987.

Gasso, S., and D. A. Hegg, Comparison of columnar aerosol optical properties measured by the MODIS airborne simulator with in situ measurements: A case study, *Remote Sensing of the Environment*, *66*, 138–152, 1998.

Gerbig, C., S. Schmitgen, D. Kley, A. Volz-Thomas, K. Dewey, and D. Haaks, An improved fast-response vacuum-UV resonance fluorescence CO instrument, *Journal of Geophysical Research*, *104*, 1699–1704, 1999.

Gifford, F., Horizontal diffusion in the atmosphere: A lagrangian-dynamical theory, *Atmospheric Envornment*, *16*, 505–512, 1982.

Godden, D., and F. Lurmann, Mathematical modeling of the chemistry and physics of aerosols in plumes, *Tech. rep.*, Southern California Edison Co., Rosemead, CA, 1983.

Goode, J. G., R. J. Yokelson, D. E. Ward, R. A. Susott, R. E. Babbitt, M. A. Davies, and W. M. Hao, Measurements of excess O3, CO2, CO, CH4, C2H4, C2H2, HCN, NO, NH3, HCOOH, CH3COOH, HCHO and CH3OH in 1997 Alaskan biomass burning plumes by airborne fourier transform infrared spectrscopy (AFTIR), *Journal of Geophysical Research*, *105*, 22,147–22,166, 2000.

Gorbunov, B., and R. Hamilton, Water nucleation on aerosol particles containing both soluble and insoluble substances, *Journal of Aerosol Science*, *28*, 239–248, 1997.

Graham, R. A., and H. S. Johnston, The photochemistry of the nitrate radical and the kinetics of the nitrogen pentoxide-ozone system, *Journal of Physical Chemistry*, *82*, 254–268, 1978.

Green, D. W., and J. O. Maloney (Eds.), *Perry's Chemical Engineers' Handbook*, 7th ed., McGraw-Hill, 1997.

Griffin, R. J., D. Dabdub, M. Kleeman, M. Fraser, G. Cass, and J. Seinfeld, Organic aerosol formation from the oxidation of biogenic hydrocarbons, *Journal of Geophysical Research*, *104*, 3555–3567, 1999.

Griffin, R. J., D. Dabdub, M. J. Kleeman, M. P. Fraser, G. R. Cass, and J. H. Seinfeld, Secondary organic aerosol: 3. Urban/Regional scale model of size- and composition-resolved aerosols, *Journal of Geophysical Research*, *107*, 4334, doi:10.1029/2001JD000,544, 2002a.

Griffin, R. J., D. Dabdub, and J. H. Seinfeld, Secondary organic aerosol: 1. Atmospheric chemical

mechanism for production of molecular constituents, *Journal of Geophysical Research*, *107*, 4332, doi:10.1029/2001JD000,541, 2002b.

Griffin, R. J., K. Nguyen, D. Dabdub, and J. H. Seinfeld, A coupled hydrophobic-hydrophilic model for predicting secondary organic aerosol formation, *Journal of Atmospheric Chemistry*, *44*, 171–190, 2003.

Griffin, R. J., D. Dabdub, and J. H. Seinfeld, Development and initial evaluation of a dynamic species-resolved model for the gas phase chemistry and size-resolved gas/particle partitioning associated with secondary organic aerosol formation, *Journal of Geophysical Research*, *110*, D05,304, doi:10.1029/2004JD005,219, 2005.

Hansen, J. E., and M. Sato, Trends of measured climate forcing agents, *Proceedings of the National Academy of Sciences of the United States of America*, *98*, 14,778–14,783, 2001.

Haywood, J., P. Francis, O. Dubovik, M. Glew, and B. Holben, Comparison of aerosol size distributions, radiative properties, and optical depths determined by aricraft observations and sun photometers during SAFARI 2000, *Journal of Geophysical Research*, *108*, 8471, doi:10.1029/2002JD002,250, 2003.

Herzog, M., H.-F. Hraf, C. Textor, and J. M. Oberhuber, The effect of phase changes of water on the development of volcanic plumes, *Journal of Vulcanology and Geothermal Research*, *87*, 55–74, 1998.

Hobbs, P. V., and L. Radke, Cloud condensation nuclei from a simulated forest fire, *Science*, *163*, 279–280, 1969.

Hobbs, P. V., J. S. Reid, J. A. Herring, J. D. Nance, R. E. Weiss, J. L. Ross, D. A. Hegg, R. D. Ottmar, and C. Liousse, Particle and trace-gas measurements in the smoke from proscribed burns of forest products in the Pacific Northwest, in *Biomass Burning and Global Change*, edited by J. S. Levine, pp. 697–715, MIT Press, 1996.

Hobbs, P. V., J. S. Reid, R. A. Kotchenruther, R. J. Ferek, and R. Weiss, Direct radiative forcing by smoke from biomass burning, *Science*, *275*, 1777–1778, 1997.

Hobbs, P. V., P. Sinha, R. J. Yokelson, T. J. Christian, D. R. Blake, S. Gao, T. W. Kirchstetter, T. Novakov, and P. Pilewskie, Evolution of gases and particles from a savanna fire in South Africa, *Journal of Geophysical Research*, *108*, 8485, doi:10.1029/2002JD002,352, 2003.

Hoffmann, M., and J. Calvert, Chemical transformation modules for eulerian acid deposition models, volume 2, the aqueous phase chemistry, *Tech. Rep. EPA/600/3-85/017*, Environemntal Protection Agency, Research Triangle Park, NC, 1985.

Hudischewskyj, A. B., and C. Seigneur, Mathematical modeling of the chemistry and physics of aerosols in plumes, *Environmental Science and Technology*, *23*, 413–421, 1989.

Hungershofer, K., et al., Modelling the optical properties of fresh biomass burning aerosol produced in a smoke chamber: Results from the EFEU campaign, *Atmospheric Chemistry and Physics Discussions*, *7*, 12,657–12,686, 2007.

IPCC, *Climate Change 2001: The Scientific Basis*, Cambridge University Press, Cambridge, UK, 2001.

Jacob, D. J., Heterogeneous chemistry and tropospheric ozone, *Atmospheric Environment*, *34*, 2131–2159, 2000.

Jacobson, M. Z., Development and application of a new air pollution modeling system - II. Aerosol module structure and design, *Atmospheric Environment*, *31*, 131–144, 1997.

Jacobson, M. Z., Strong radiative heating due to the mixing state of black carbon in atmospheric aerosols, *Nature*, *409*, 695–697, 2001.

Jacobson, M. Z., Analysis of aerosol interactions with numerical techniques for solving coagulation, nucleation, condensation, dissolution, and reversible chemistry among multiple size distributions, *Journal of Geophysical Research*, *107*, 4366, doi:10.1029/2001JD002,044, 2002.

Jacobson, M. Z., *Fundamentals of Atmospheric Modeling*, 2nd ed., Cambridge University Press, 2005.

Jayne, J. T., U. Poschl, Y.-M. Chen, D. Dai, L. T. Molina, D. R. Worsnop, C. E. Kold, and M. J. Molina, Pressure and temperature dependence of the gas-phase reaction of so_3 with h_2o and the heterogeneous reaction of so_3 with h_2o/h_2so_4 surfaces, *Journal of Physical Chemistry A*, *101*, 10,000–10,011, 1997.

Jenkin, M. E., S. M. Saunders, and M. J. Pilling, The tropospheric degradation of volatile organic compounds: A protocol for mechanism development, *Atmospheric Environment*, *31*, 81–104, 1997.

Jost, C., D. Spring, T. Kenntner, and T. Reiner, Atmospheric pressure chemical ionization mass spectrometry for the detection of tropospheric trace gases: The influence of clustering on sensitivity and precision, *International Journal of Mass Spectrometry*, *223-224*, 771–782, 2003a.

Jost, C., J. Trentmann, D. Sprung, M. O. Andreae, J. B. McQuaid, and H. Barjat, Trace gas chemistry in a young biomass burning plume over Namibia: Observations and model simulations, *Journal of Geophysical Research*, *108*, 8482, doi:10.1029/2002JD002,431, 2003b.

Jungwirth, P., D. Rosenfeld, and V. Buch, A possible new molecular mechanism of thundercloud electrification, *Atmospheric Research*, *76*, 190–205, 2005.

Kaimal, J., J. Wyngaard, Y. Izumi, and O. Coté, Spectral characteristics of surface layer turbulence, *Quarterly Journal of the Royal Meteorological Society*, *98*, 563–589, 1972.

Kanicky, J. R., and D. O. Shah, Effect of degree, type, and position of unsaturation on the pK_a of long-chain fatty acids, *Journal of Colloid and Interface Science*, *256*, 201–207, 2002.

Karamchandani, P., C. Seigneur, K. Vijayaraghavan, and S.-Y. Wu, Development and application of a state-of-the-science plume-in-grid model, *Journal of Geophysical Research*, *107*, 4403, doi:10.1029/2002JD002,123, 2002.

Kaufman, Y., et al., Smoke, clouds, and radiation-Brazil (SCAR-B) experiment, *Journal of Geophysical Research*, *103*, 31,783–31,808, 1998.

Kaufman, Y. J., and R. S. Fraser, The effect of smoke particles on clouds and climate forcing, *Science*, *277*, 1636–1639, 1997.

Killus, J., and G. Whitten, Technical discussion relating to the use of the carbon-bond mechanism in OZIPM/EKMA, *Tech. Rep. EPA-450/4-84-009*, U.S. Environmental Protection Agency, Research Triangle Park, NC, 1984.

Kim, Y. P., and J. H. Seinfeld, Atmospheric gas-aerosol equilibrium: III. Thermodynamics of crustal elements Ca^{2+}, K^{+} and Mg^{2+}, *Aerosol Science and Technology*, *22*, 93–110, 1995.

Kim, Y. P., J. H. Seinfeld, and P. Saxena, Atmospheric gas-aerosol equilibrium I. Thermodynamic model, *Aerosol Science and Technology*, *19*, 157–181, 1993a.

Kim, Y. P., J. H. Seinfeld, and P. Saxena, Atmospheric gas-aerosol equilibrium II. Analysis of common approximateions and acitivity coefficient calculation methods, *Aerosol Science and Technology*, *19*, 182–198, 1993b.

Kirchstetter, T., C. Corrigan, and T. Novakov, Laboratory and field investigation of the adsorption of gaseous organic compounds onto quartz filters, *Atmospheric Environment*, *35*, 1663–1671, 2001.

Kirchstetter, T. W., T. Novakov, P. V. Hobbs, and B. Magi, Airborne measurements of carbonaceous aerosols in southern africa during the dry biomass burning season., *Journal of Geophysical Research*, pp. 8476, doi:10.1029/2002JD002,171, 2003.

Klassen, G., and T. Clark, Dynamics of the cloud environment interface and entrainment in small cumuli: Two-dimensional simulation in the absense of ambient shear, *Journal of Atmospheric Science*, *42*, 2621–2642, 1985.

Klemp, J. B., and R. B. Wilhelmson, The simulation of three-dimensional convective storm dynamics, *Journal of the Atmospheric Sciences*, *35*, 1070–1096, 1978.

Kulmala, M., A. Laaksonen, and L. Pirjola, Parameterizations for sulfuric Acid/Water nucleation rates, *Journal of Geophysical Research*, *103*, 8301–8307, 1998.

Kumar, N., and A. G. Russell, Multiscale air quality modeling of the northeastern United States, *Atmospheric Environment*, *30*, 1099–1116, 1996.

Kusik, C., and H. Meissner, Electrolyte acitivity coefficients in inorganic processing, in *Fundamental Aspects of Hydrometallurgical Processes, AIChE Symposium Series*, edited by T. Chapman, L. Taularides, G. Hubred, and R. Wellek, pp. 14–20, AIChE, New York, 1978.

Kwok, E. S., and R. Atkinson, Estimation of hydroxyl radical reaction rate constants for gas-phase organic compounds using a structure-reactivity relationship: An update, *Atmospheric Environment*, *29*, 1685–1695, 1995.

Lagrange, L., C. Pallares, and P. Lagrange, Electrolyte effects on aqueous atmnospheric oxidation of sulphur dioxide by ozone, *Journal of Geophysical Research*, *99*, 14,595–14,600, 1994.

Lammel, G., and A. Leip, Formation of nitrate and sulfate in the plume of Berlin, *Environmental Science and Pollution Research*, *12*, 213–220, 2005.

Langenfelds, R. L., R. J. Francey, B. C. Pak, L. P. Steele, J. Lloyd, C. M. Trudinger, and C. E. Allison, Interannual growth rate variations of atmospheric CO_2 and its ^{13}C, H_2, CH_4, and CO between 1992 and 1999 linked to biomass burning, *Global Biogeochamical Cycles*, *16*, 10.1029/2001GB001,466, 2002.

Latham, D., Lightning flashes from a prescribed fire-induced cloud, *Journal of Geophysical Research*, *96*, 17,151–17,157, 1991.

Lazaridis, M., S. S. Isukapalli, and P. G. Georgopoulos, Modeling of aerosol processes in plumes, *Tellus*, *53B*, 83–93, 2001.

Leriche, M., D. Voisin, N. Chaumerliac, A. Monod, and B. Aumont, A model for tropospheric multiphase chemistry: Application to one cloudy event during the CIME experiment, *Atmospheric Environment*, *34*, 5015–5036, 2000.

Leung, J. A., Fok-Yan T. Anf Logan, R. Park, E. Hyer, E. Kasischke, D. Streets, and L. Yurganov, Impacts of enhanced biomass burning in the boreal forests in 1998 on tropospheric chemistry and the sensitivity of model results to the injection height of emissions, *Journal of Geophysical Research*, *112*, D10,313, doi:10.1029/2006JD008,132, 2007.

Levine, J. S., Biomass burning and the production of greenhouse gases, in *Climate Biosphere Interaction: Biogenic Emissions and Environmental Effects of Climate Change*, edited by R. G. Zepp, pp. 139–159, John Wiley and Sons, Inc., New York, 1994.

Li, J., M. Posfai, P. V. Hobbs, and P. R. Buseck, Individual aerosol particles from biomass burning in southern Africa: 2, Compositions and aging of inorganic particles, *Journal of Geophysical Research*, *108*, 8484, doi:10.1029/2002JD002,310, 2003.

Li, Z., and C.-Y. Lu, Surface tension of aqueous electrolyte solutions at high concentrations - representation and prediction, *Chemical Engineering Science*, *56*, 2879–2888, 2001.

Lide, D. R. (Ed.), *CRC Handbook of Chemistry and Physics*, 87th ed., Taylor and Francis, Boca Raton, FL, 2007.

Lin, X., M. Trainer, and S. Liu, On the nonlinearity of the tropospheric ozone production, *Journal of Geophysical Research*, *93*, 15,879–15,888, 1988.

Liousse, C., C. Devaux, F. Dulac, and H. Cachier, Aging of savanna biomass burning aerosols: Consequences on their optical properties, *Journal of Atmospheric Chemistry*, *22*, 1–17, 1995.

List, R. (Ed.), *Smithsonian Meteorological Tables*, 6th ed., Smithsonian Institution Press, Washington, DC, 1984.

Lobert, J., and J. Warnatz, Emissions from the combustion process in vegetation, in *Fire in the Environment: The Ecological, Atmospheric, and Climatic Importance of Vegetation Fires*, edited by P. Crutzen and J. Goldammer, pp. 15–37, John Wiley and Sons, Inc., New York, NY, 1993.

Lobo, V., *Handbook of Electrolyte Solutions, Physical Sciences Data*, vol. 41, Elsevier Science Publishing Company, Inc., New York, 1989.

Lucas, D. D., Mechanistic, sensitivity, and uncertainty studies of the atmospheric oxidation of dimethylsulfide, Ph.D. thesis, Massachusetts Institute of Technology, 2003, available at http://web.mit.edu/cgcs/www/rpts.html.

Luderer, G., J. Trentmann, T. Winterrath, C. Textor, M. Herzog, H. Graf, and M. Andreae, Modeling of biomass smoke injection into the lower stratosphere by a large forest fire (part II): Sensitivity studies, *Atmospheric Chemistry and Physics*, *6*, 5261–5277, 2006.

Luderer, G., J. Trentmann, K. Hungershofer, M. Herzog, M. Fromm, and M. Andreae, Small-scale mixing processes enhancing troposphere-to-stratosphere transport by pyro-cumulonimbus clouds, *Atmospheric Chemistry and Physics Discussions*, *7*, 10,371–10,403, 2007.

Ludlum, F., *Clouds and Storms*, The Pensylvania State University Press, University Park, PA, 1980.

Lurmann, F., A. Wexler, S. Pandis, S. Musarra, N. Kumar, and J. Seinfeld, Modelling urban and regional aerosols - II. Application to California's south coast air basin, *Atmospheric Environment*, *31*, 2695–2715, 1997.

Lyman, W., W. Reehl, and D. Rosenblatt, *Handbook of Chemical Property Estimation Methods: Environmental Behavior of Organic Compounds*, American Chemical Society, Washington, DC, 1990.

Lyons, W. A., T. E. Nelson, E. R. Williams, J. A. Cramer, and T. R. Turner, Enhanced positive cloud-to-ground lightning in thunderstorms ingesting smoke from fires, *Science*, *282*, 77–80, 1998.

Madronich, S., Photodissociation in the atmosphere: 1. Actinic flux and the effects of ground reflections and clouds, *Journal of Geophysical Research*, *92*, 9740–9752, 1987.

Magi, B. I., and P. V. Hobbs, Effects of humidity on aerosols in southern Africa during the biomass burning season, *Journal of Geophysical Research*, *108*, 8495, doi:10.1029/2002JD002,144, 2003.

Marfu, L., F. Dentener, J. Lilieveld, M. Andreae, and G. Helas, Photochemistry of the African troposphere: Influence of biomass burning emissions, *Journal of Geophysical Research*, *105*, 14,513–14, 530, 2000.

Martins, J. V., P. Artaxo, P. V. Hobbs, C. Liousse, H. Cachier, Y. Kaufman, and A. Plana-Fattori, Particle size distributions, elemental compositions, carbon measurements, and optical properties of smoke from biomass burning in the Pacific Northwest of the United States, in *Biomass Burning and Global Change*, edited by J. S. Levine, pp. 716–732, MIT Press, 1996.

Mason, S. A., R. J. Field, R. J. Yokelson, M. A. Kochivar, M. R. Tinsley, D. E. Ward, and W. M. Hao, Complex effects arising in smoke plume simulations due to the inclusion of direct emissions of oxygenated organic species from biomass combustion, *Journal of Geophysical Research*, *106*, 12,527–12,539, 2001.

Mason, S. A., J. Trentmann, T. Winterrath, R. J. Yokelson, T. J. Christian, L. J. Carlson, T. R. Warner, L. C. Wolfe, and M. O. Andreae, Intercomparison of two box models of the chemical evolution in biomass-burning smoke plumes, *Journal of Atmospheric Chemistry*, *55*, 273–297 doi:10.1007/s10,874–006–9039–5, 2006.

Mauzerall, D. L., et al., Photochemistry in biomass burning plumes and implications for tropospheric ozone over the tropical South Atlantic, *Journal of Geophysical Research*, *103*, 8401–8423, 1998.

Mayer, M., C. Wang, M. Webster, and R. G. Prinn, Linking local air pollution to global chemistry and climate, *Journal of Geophysical Research*, *105*, 22,869–22,896, 2000.

McKeen, S., G. Wotawa, D. Parrish, J. Holloway, M. Buhr, G. Hubler, F. Fehsenfeld, and J. Meagher, Ozone production from Canadian wildfires during June and July of 1995, *Journal of Geophysical Research*, *107*, doi:10.1029/2001JD000,697, 2002.

McRae, G., W. Goodin, and J. Seinfeld, Development of a second generation mathematical model of urban air pollution, i., Model formulation, *Atmospheric Environment*, *16*, 679–696, 1982.

Meissner, H., Prediction of activity coefficients of strong electrolytes in aqueous systems, in *Thermodynamics of Aqueous Systems with Industrial Applications*, edited by S. Newamn, pp. 495–511, American Chemical Society, Washington, DC, 1980.

Mell, W., M. A. Jenkins, J. Gould, and P. Cheney, A physics-based approach to modeling grassland fires, *International Journal of Wildland Fire*, p. In press, 2007.

Meller, R., W. Raber, J. Crowley, M. Jenkin, and G. Moortgat, The UV-visible absorption spectrum of methylglyoxal, *Journal of Photochemistry and Photobiology*, *62*, 163–171, 1991.

Ming, Y., and L. M. Russel, Thermodynamic equilibrium of organic-electrolyte mixtures in aerosol particles, *AIChE Journal*, *48*, 1331–1348, 2002.

Molina, L., and M. Molina, Absolute absorption cross sections of ozone in the 185- to 350-nm wavelength range, *Journal of Geophysical Research*, *91*, 14,501–14,508, 1986.

Morris, R. E., E. C. Chang, Z. S. Wang, S. B. Shepard, and M. P. Ligocki, User's guide: Reactive Plume Model IV (RPM-IV), *Tech. Rep. SYSAPP-92/123*, Systems Applications International, San Rafael, CA, 1992.

Murray, N. D., R. E. Orville, and G. R. Huffines, Effect of pollution from central american fires on cloud-to-ground lightning in may 1998, *Geophysical Research Letters*, *27*, 2249–2252, 2000.

Myrdal, P. B., and S. H. Yalkowsky, Estimating pure component vapor pressures of complex organic molecules, *Indunstrial and Engineering Chemistry Research*, *36*, 2494–2499, 1997.

Naumann, K.-H., COSIMA - a computer program simulating the dynamics of fractal aerosols, *Aerosol Science*, *34*, 1371–1397, 2003.

Nenes, A., S. N. Pandis, and C. Pilinis, ISORROPIA: A new thermodynamic equilibrium model for multiphase multicomponent inorganic aerosols, *Aquatic Geochemistry*, *4*, 123–152, 1998.

Nienow, A. M., and J. T. Roberts, Heterogeneous chemistry of carbon aerosols, *Annual Reviews of Physical Chemistry*, *57*, 105–128, 2006.

Novakov, T., Microchemical characterization of aerosols, in *Nature, Aim, and Methods of Microchemistry*, edited by H. Malissa, M. Grasserbaure, and R. Belcher, pp. 141–165, Springer-Verlag, 1981.

Novakov, T., Soot in the atmosphere, in *Particulate Carbon: Atmsopheric Life Cycle*, edited by G. Wolff and R. Klimish, pp. 19–41, Plenum, New York, 1982.

Novakov, T., S. Chang, and A. Harker, Sulfates as pollution particulates: Catalytic formation on carbon (soot) particles, *Science*, *186*, 259–261, 1974.

Oberhuber, J. M., M. Herzog, H.-F. Graf, and K. Schwanke, Volcanic plume simulation on large scales, *Journal of Vulcanology and Geothermal Research*, *87*, 29–53, 1998.

Odum, J. R., T. Hoffman, F. Bowman, D. Collins, R. C. Flagan, and J. H. Seinfeld, Gas/Particle partitioning and secondary organic aerosol yields, *Environmental Science and Technology*, *30*, 2580–2585, 1996.

Odum, J. R., T. Jungkamp, R. J. Griffin, H. Forstner, R. C. Flagan, and J. H. Seinfeld, Aromatics, reformulated gasoline, and atmospheric organic aerosol formation, *Environmental Science and Technology*, *31*, 1890–1897, 1997a.

Odum, J. R., T. Jungkamp, R. J. Griffing, R. C. Flagan, and J. H. Seinfeld, The atmospheric aerosol-forming potential of whole gasoline vapor, *Science*, *276*, 96–99, 1997b.

Page, S. E., F. Siegert, J. O. Rieley, H.-D. V. Boehm, A. Jaya, and S. Limin, The amount of carbon released from peat and forest fires in indonesia during 1997, *Nature*, *420*, 61–65, 2002.

Pandis, S., R. Harley, G. Cass, and J. Seinfeld, Secondary organic aerosol formation and transport, *Atmospheric Environment*, *26*, 2269–2282, 1992.

Pankow, J. F., An absorption model of gas/particle partitioning of organic compounds in the atmosphere, *Atmospheric Environment*, *28*, 185–188, 1994a.

Pankow, J. F., An absorption model of the gas/aerosol partitioning involved in the formation of secondary organic aerosol, *Atmospheric Environment*, *28*, 189–193, 1994b.

Patwardhan, V., and A. Kumar, Thermodynamic properties of aqueous-solutions of mixed electrolytes - a new mixing rule, *AIChE Journal*, *39*, 711–714, 1993.

Pilinis, C., and J. Seinfeld, Continued development of a general equilibrium model for inorganic multicomponent atmospheric aerosols, *Atmospheric Environment*, *21*, 2453–2466, 1987.

Poschl, U., M. Canagaratna, J. T. Jayne, L. T. Molina, D. R. Worsnop, C. E. Kolb, and M. J. Molina, Mass accommodation coefficient of H2SO4 vapor on aqueous sulfuric acid surfaces and gaseous diffusion coefficient of H2SO4 in N2/H2O, *Journal of Physical Chemistry A*, *102*, 10,082–10,089, 1998.

Posfai, M., R. Simonics, J. Li, P. V. Hobbs, and P. R. Buseck, Individual aerosol particles from biomass burning in southern Africa: 1. Compositions and size distributions of carbonaceous particles, *Journal of Geophysical Research*, *108*, 8483, doi:10.1029/2002JD002,291, 2003.

Press, W. H., S. A. Teukolsky, W. T. Vetterling, and B. P. Flannery, *Numerical Recipes in FORTRAN: The Art of Scientific Computing*, 2nd ed., Cambridge University Press, Cambridge, UK, 1992.

Prinn, R., et al., Integrated global system model for climate policy assessment: Feedbacks and sensitivity studies, *Climatic Change*, *41*, 469–546, 1999.

Pruppacher, H. F., and J. D. Klett, *Microphysics of Clouds and Precipitation*, Kluwer Academic Publishers, 1998.

Pun, B. K., R. J. Griffin, C. Seigneur, and J. H. Seinfeld, Secondary organic aerosol, 2, Thermodynamic model for Gas/Particle partitioning of molecular constituents, *Journal of Geophysical Research*, *107*, 4333, doi:10.1029/2001JD000,542, 2002.

Pun, B. K.-L., Treatment of uncertainties in atmospheric chemical systems: A combined modeling and experimental approach, Ph.D. thesis, Massachusetts Institute of Technology, 1998.

Raatikainen, T., and A. Laaksonen, Application of several activity coefficient models to water-organic-electrolyte aerosols of atmospheric interest, *Atmospheric Chemistry and Physics*, *5*, 2475–2495, 2005.

Reid, J. S., and P. V. Hobbs, Physical and optical properties of young smoke from individual biomass fires in Brazil, *Journal of Geophysical Research*, *103*, 32,013–32,030, 1998.

Reid, J. S., P. V. Hobbs, R. J. Ferek, D. R. Blake, J. V. Martins, M. R. Dunlap, and C. Liousse, Physical, chemical, and optical properties of regional hazes dominated by smoke from Brazil, *Journal of Geophysical Research*, *103*, 32,059–32,080, 1998.

Reid, J. S., T. Eck, S. Christopher, R. Koppmann, O. Dubovik, D. Eleuterio, B. Holben, E. A. Reid, and J. Zhang, A review of biomass burning emissions Part III: Intensive optical properties of biomass burning particles, *Atmospheric Chemistry and Physics*, *5*, 827–849, 2005a.

Reid, J. S., R. Koppmann, T. Eck, and D. Eleuterio, A review of biomass burning emissions Part II: Intensive physical properties of biomass burning particles, *Atmospheric Chemistry and Physics*, *5*, 799–825, 2005b.

Reiner, T., and F. Arnold, Laboratory investigations of gaseous sulfuric acid formation via $so_3 + h_2o + m- > h_2so_4 + m$: Measurement of the rate constant and product identification, *Journal of Chemical Physics*, *101*, 7399–7407, 1994.

Resch, T., A framework for modeling suspended multicomponent particulate systems with applications to atmospheric aerosols., Ph.D. thesis, Massachusetts Instutute of Technology, 1995.

Robinson, A. L., N. M. Donahue, M. K. Shrivastava, E. A. Weitkamp, A. M. Sage, A. P. Grieshop, T. E. Lane, J. R. Pierce, and S. N. Pandis, Rethinking organic aerosols: Semivolatile emissions and photochemical aging, *Science*, pp. 1259–1262, doi:10.1126/science.1133,061, 2007.

Rodriguez, M. A., and D. Dabdub, Monte carlo uncertainty and sensitivity analysis of the CACM chemical mechanism, *Journal of Geophysical Research*, *108*, 4443, doi:10.1029/2002JD003,281, 2003.

Rosenfeld, D., TRMM observed first direct evidence of smoke from forest fires inhibiting rainfall, *Geophysical Research Letters*, *26*, 3105–3108, 1999.

Rosenfeld, D., M. Fromm, J. Trentmann, G. Luderer, M. Andreae, and R. Servranckx, The chisholm firestorm: Observed microstructure, precipitation and lightning activity of a pyro-cumulonimbus, *Atmospheric Chemistry and Physics*, *7*, 645–659, 2007.

Saathoff, H., K.-H. Naumann, M. Schnaiter, W. Schock, O. Mohler, U. Schurath, E. Weingartner, M. Gysel, and U. Baltensperger, Coating of soot and (NH4)2SO4 particles by ozonolysis products of alpha-pinene, *Journal of Aerosol Science*, *34*, 1297–1321, 2003.

San Martini, F. M., Decision support tools for urban air quality management, Ph.D. thesis, Massachusetts Institute of Technology, 2004.

Saxena, P., and L. M. Hildemann, Water-soluble organics in atmospheric particles: A critical review of the literature and application of thermodynamics to identify candidate compounds, *Journal of Atmospheric Chemistry*, *24*, 57–109, 1996.

Schatzmann, M., An integral model of plume rise, *Atmospheric Environment*, *13*, 721–731, 1979.

Schwarzenbach, R. P., P. M. Gschwend, and D. M. Imboden, *Environmental Organic Chemistry*, Wiley, Hoboken, NJ, 2003.

Seinfeld, J. H., *Atmospheric Chemistry and Physics of Air Pollution*, Wiley, New York, 1986.

Seinfeld, J. H., and S. N. Pandis, *Atmospheric Chemistry and Physics*, John Wiley and Sons, New York, NY, 1998.

Sheesley, R. J., J. J. Schauer, Z. Chowdhury, G. R. Cass, and B. R. Simoneit, Characterization of organic aerosols emitted from the combustion of biomass indigenous to South Asia, *Journal of Geophysical Research*, *108*, 4285, doi:10.1029/2002JD002,981, 2003.

Simoneit, B. R., and V. Elias, Detecting organic tracers from biomass burning in the atmosphere, *Marine Pollution Bulletin*, *42*, 802–810, 2001.

Srivastava, R., D. McRae, and M. Odman, Simulation of dispersion of a power plant plume using an adaptive grid alogrithm, *Atmospheric Environment*, pp. 4801–4818, 2001.

Staffelbach, T., J. Orlando, G. Tyndall, and J. Calvert, The UV-visible aborption spectrum and photolysis quantum yields of methylglyoxal, *Journal of Geophysical Research*, *100*, 14,189–14,198, doi:10.1029/95JD00,541, 1995.

Steele, H. D., Investigations of cloud altering effects of atmospheric aerosols using a new mixed eulerian-lagrangian aerosol model, Ph.D. thesis, Massachusetts Institute of Technology, 2004, (http://web.mit.edu/cgcs/www/MIT_CGCS_Rpt74.pdf).

Stemmler, K., M. Ammann, C. Donders, J. Kleffmann, and C. George, Photosensitized reduction of nitrogen dioxide on humic acid as a source of nitrous acid., *Nature*, *440*, 195–198, doi:10.1038/nature04,603, 2006.

Stemmler, K., M. Ndour, Y. Elshorbany, J. Kleffmann, B. D'Anna, C. George, B. Bohn, and M. Ammann, Light induced conversion of nitrogen dioxide into nitrous acid on submicron humic acid aerosol, *Atmospheric Chemistry and Physics*, *7*, 4237–4248, 2007.

Stockwell, W. R., F. Kirchner, M. Kuhn, and S. Seefeld, A new mechanism for regional atmospheric chemistry modeling, *Journal of Geophysical Research*, *102*, 25,847–25,879, 1997.

Stull, R. B., *An Introduction to Boundary Layer Meteorology*, Kluwer Academic Publishers, Dordrecht, The Netherlands, 1988.

Tabazedeh, A., R. Yokelson, H. Singh, P. Hobbs, J. Crawford, and L. Iraci, Heterogeneous chemistry involving methanol in tropospheric clouds, *Geophysical Research Letters*, *31*, L06,114, doi:10.1029/2003GL018,775, 2004.

Tang, I. N., Thermodynamic and optical properties of mixed-salt aerosols of atmospheric importance, *Journal of Geophysical Research*, *102*, 1883–1893, 1997.

Tang, I. N., A. Tridico, and K. Fung, Thermodynamic and optical properties of sea salt aerosols, *Journal of Geophysical Research*, *102*, 23,269–23,275, 1997.

Tatang, M. A., W. Pan, R. G. Prinn, and G. J. McRae, An efficient method for parametric uncertainty analysis of numerical geophysical models, *Journal of Geophysical Research*, *102*, 21,925–21,932, 1997.

Thomas, R., P. Krehbiel, W. Rison, H. Edens, G. Aulich, W. Winn, S. McNutt, G. Tytgat, and E. Clark, Electrical activity during the 2006 Mount St. Augustine volcanic eruptions, *Science*, *315*, 1097, 2007.

Toon, O., and T. Ackerman, Algorithms for the calculation of scattering by stratified spheres, *Applied Optics*, *20*, 3657–3660, 1981.

Trentmann, J., M. Andreae, H.-F. Graf, P. Hobbs, R. Ottmar, and T. Trautmann, Simulation of a biomass-burning plume: Comparison of model results with observations, *Journal of Geophysical Research*, *107*, doi:10.1029/2001JD000,410, 2002.

Trentmann, J., M. O. Andreae, and H.-F. Graf, Chemical processes in a young biomass-burning plume, *Journal of Geophysical Research*, *108*, 4705, 2003a.

Trentmann, J., B. Fruh, O. Boucher, T. Trautmann, and M. O. Andreae, Three-dimensional solar radiation effects on the actinic flux field in a biomass-burning plume, *Journal of Geophysical Research*, *108*, 4558, 2003b.

Trentmann, J., R. J. Yokelson, P. V. Hobbs, T. Winterrath, T. J. Christian, M. O. Andreae, and S. A. Mason, An analysis of the chemical processes in the smoke plume from a savannah fire, *Journal of Geophysical Research*, *110*, D12,301, doi:10.1029/2004JD005,628, 2005.

Trentmann, J., G. Luderer, T. Winterrath, M. Fromm, R. Servranckx, C. Textor, M. Herzog, H.-F. Graf, and M. Andreae, Modeling of biomass smoke injection into the lower stratosphere by a large forest fire (Part I): Reference simulation, *Atmospheric Chemistry and Physics*, *6*, 5247–5260, 2006.

Turpin, B., J. Huntzicker, and S. Hering, Investigation of the organic aerosol sampling artifacts in the los angeles basin, *Atmospheric Environment*, *28*, 3061–3071, 1994.

Vonnegut, B., D. Latham, C. Moore, and S. Hunyady, An explanation for anomalous lightning from forest fire clouds, *Journal of Geophysical Research*, *100*, 5037–5050, 1995.

Vutukuru, S., R. J. Griffin, and D. Dabdub, Simulation and analysis of secondary organic aerosol dynamics in the south coast air basin of california, *Journal of Geophysical Research*, *111*, D10S12, doi:10.1029/2005JD006,139, 2006.

Wang, C., and J. Chang, A three-dimensional numerical model of cloud dynamics, microphysics, and chemistry, *Journal of Geophysical Research*, *98*, 14,827–14,844, 1993.

Wang, C., and R. G. Prinn, On the roles of deep convective clouds in tropospheric chemistry, *Journal of Geophysical Research*, *105*, 22,269–22,297, 2000.

Wexler, A., and J. Seinfeld, 2nd-generation inorganic aerosol model, *Atmospheric Environment*, *25*, 2731–2748, 1991.

WMO, *Atmospheric Ozone 1985: Assessment of our Understanding of the Processes Controlling its Present Distribution and Change*, World Meteorological Organization, 1985, report No. 16, 3 vols.

Yokelson, R. J., I. T. Bertschi, T. J. Christian, P. V. Hobbs, D. E. Ward, and W. M. Hao, Trace gas measurements in nascent, aged, and cloud-processed smoke from African savanna fires by airborne fourier transform infrared spectroscopy (AFTIR), *Journal of Geophysical Research*, *108*, 8478, doi:10.1029/2002JD002,322, 2003.

Zhang, Y., R. C. Easter, S. J. Ghan, and H. Abdul-Razzak, Impact of aerosol size representation on modeling aerosol-cloud interactions, *Journal of Geophysical Research*, *107*, 4558, doi:10.1029/2001JD001,549, 2002.

Appendix A

Gas Phase Chemical Mechanism: Reaction Rates and Stoichiometries

A.1 First Order Reactions

A.1.1 Photolysis Reactions

Table A.1 lists the photolysis rates included in the gas-phase chemical mechanism. These photolysis rates are calculated differently in the Lagrangian box model described in Chapter 3 and the 3D Eulerian model described in Chapter 4. In the Lagrangian box model, the photolysis rates are calculated offline using the publicly available radiative transfer model TUV v4.1 of Madronich *et al.*, 2000 (available at http://cprm.acd.ucar.edu/Models/TUV/). This model calculates the radiative transfer through the atmosphere and then calculates photolysis rates k_q $\left(s^{-1}\right)$ based on the formula [*Seinfeld and Pandis*, 1998, p. 142]

$$k_q = \int_{\lambda_2}^{\lambda_1} \sigma_q(\lambda; T, P)\, \phi_q(\lambda; T, P)\, I(\lambda)\, d\lambda \tag{A.1}$$

where $I(\lambda)$ is the spectral intensity (photons cm^{-2} s^{-1} nm^{-1}) at wavelength λ, $\sigma_q(\lambda; T, P)$ is the absorption cross section for gas q (cm^2), and $\phi_q(\lambda; T, P)$ is the quantum yield. Note that both $\sigma_q(\lambda; T, P)$ and $\phi_q(\lambda; T, P)$ may be temperature and/or pressure dependent.

In the Eulerian model (CRM6 - Cloud Resolving Model v.6), photolysis rates are assumed to be proportional to R_{flux}, the total radiative flux between the wavelengths of 200 nm and 4 μm calculated by the radiative transfer scheme of CRM6. The integral from Equation A.1 is calculated between 200 nm and 800 nm for 10 different values of the solar zenith angle θ using data from Table

Table A.1: First Order Photolysis Reactions

Reaction	σ_q, ϕ_q Ref.
$NO_2 \rightarrow NO + O$	TUV v4.1: *Demore et al.* [1994]; *Gardner et al.* [1987] CRM6: *Atkinson et al.* [1992]
$NO_3 \rightarrow NO + O_2$	*Graham and Johnston* [1978]; *Demore et al.* [1994] Madronich, 1988 (unpublished)
$NO_3 \rightarrow NO_2 + O$	*Graham and Johnston* [1978]; *Demore et al.* [1994] Madronich, 1988 (unpublished)
$O_3 \rightarrow O + O_2$	TUV v4.1: *WMO* [1985]; *Molina and Molina* [1986] *DeMore et al.* [1997] CRM6: *Atkinson et al.* [1992] Assumes that ϕ_q for O_3 reactions sum to 1.
$O_3 \rightarrow O(^1D) + O_2$	TUV v4.1: *WMO* [1985]; *Molina and Molina* [1986] *DeMore et al.* [1997] CRM6: *Atkinson et al.* [1992]
$HONO \rightarrow 0.9OH + 0.9NO + 0.1HO_2 + 0.1NO_2$	*DeMore et al.* [1997]
$H_2O_2 \rightarrow OH + OH$	TUV v4.1: *DeMore et al.* [1997] CRM6: *Atkinson et al.* [1992]
$HCHO \rightarrow HO_2 + HO_2 + CO$	TUV v4.1: Madronich, 1991, 1998 (unpublished) CRM6: *Atkinson et al.* [1992]
$HCHO \rightarrow H_2 + CO$	TUV v4.1: Madronich, 1991, 1998 (unpublished) CRM6: *Atkinson et al.* [1992]
ALD2 $\rightarrow$ CO + HO_2 + $RO_2$5 + RO_2T[a]	IUPAC Data Sheet P2 (acetaldehyde) (see http://www.iupac-kinetic.ch.cam.ac.uk/)
RPR1 $\rightarrow$ CO + HO_2 + $RO_2$20 + RO_2T	Assumed equal to ALD2.
RPR3 $\rightarrow$ CO + 2.0 HO_2 + UR4	Assumed equal to ALD2.
RPR8 $\rightarrow$ CO + HO_2 + $RO_2$9 + RO_2T	Assumed equal to ALD2.
RPR8 $\rightarrow$ HO_2 + $RO_2$57 + RO_2T	Assumed equal to ALD2.
RP10 $\rightarrow$ UR25	Assumed equal to ALD2.
KETL $\rightarrow$ $RO_2$5 + $RO_2$8 + 2.0 RO_2T	IUPAC Data Sheet P7 (acetone) (see http://www.iupac-kinetic.ch.cam.ac.uk/)
KETH $\rightarrow$ $RO_2$5 + $RO_2$8 + 2.0 RO_2T	Assumed equal to KETL.
MGLY $\rightarrow$ CO + HO_2 + $RO_2$8 + RO_2T	*Staffelbach et al.* [1995]; *Meller et al.* [1991]
RP16 $\rightarrow$ 2.0 CO + OH + HO_2	Assumed equal to MGLY.

Reaction reference: CACM [*Griffin et al.*, 2002b, 2005]

4.a.4 of *Seinfeld* [1986]. The integral is then divided by the total radiative flux between 200 nm and 800 nm for that zenith angle. These ratios of integrals are then tabulated, and the Eulerian model linearly interpolates the values online for the current zenith angle. To calculate the photolysis rate, the interpolated value is multiplied by $0.5678 R_{flux}$, where the 0.5678 factor accounts for the ratio of the solar flux between 200 nm and 800 nm to that between 200 nm and 4 μm. Note that the final, online calculation treats all solar photons the same - all wavelength dependence is only included in the tabulated integral ratio values. Thus, in the 3D Eulerian model,

$$k_q \approx \int_{200\,\mathrm{nm}}^{800\,\mathrm{nm}} I(\lambda,\theta)\,d\lambda \left(\frac{\int_{200\,\mathrm{nm}}^{800\,\mathrm{nm}} \sigma_q(\lambda;T,P)\,\phi_q(\lambda;T,P)\,I(\lambda,\theta)\,d\lambda}{\int_{200\,\mathrm{nm}}^{800\,\mathrm{nm}} I(\lambda,\theta)\,d\lambda} \right) \tag{A.2}$$

$$\approx 0.5678 R_{flux} \left(\frac{\int_{200\,\mathrm{nm}}^{800\,\mathrm{nm}} \sigma_q(\lambda;T,P)\,\phi_q(\lambda;T,P)\,I(\lambda,\theta)\,d\lambda}{\int_{200\,\mathrm{nm}}^{800\,\mathrm{nm}} I(\lambda,\theta)\,d\lambda} \right) \tag{A.3}$$

The references used for absorption cross section and quantum yield in the Lagrangian and Eulerian models are given in Table A.1. The quantum yield of acetaldehyde is pressure dependent: thus, the ratio of integrals in Equation A.2 was tabulated as a matrix of 10 zenith angles and 11 pressure levels from 0 to 1 bar. The integral ratio was then calculated online through bilinear interpolation [*Press et al.*, 1992]. The quantum yield of acetone is temperature and pressure dependent: thus, the ratio of integrals in Equation A.2 was tabulated for a matrix of 10 zenith angles, 9 temperatures between 215 and 295 K, and for 11 pressure levels from 0 to 1 bar. The integral ratio was then calculated online through trilinear interpolation [*Press et al.*, 1992].

A.1.2 Isomerization Reactions

The reaction rates for the isomerization of cyclohexadienyl peroxy radicals have the form

$$k_{iso} = A T^n \exp\left(\frac{E_a}{T}\right) \tag{A.4}$$

Table A.2 contains the reaction rate parameters for these reactions.

A.1.3 Heterogeneous Reactions

CACM uses reactions with water vapor to approximate the heterogeneous reactions of N_2O_5, NO_2, and HO_2. Since one of the goals of this thesis is to estimate the effect aerosols have on the gas-phase chemistry in a smoke plume, we replace those approximate reactions with explicit calculation of the heterogeneous reaction rates based on particle size and concentration. *Jacob* [2000] gives the

Table A.2: First Order Isomerization Reactions of Cylcohexadienyl Peroxy Radicals

Reaction	A	n	E_a
$RO_2 33 \rightarrow RO_2 42 + RO_2T$	1.97×10^{42}	-11.4	$-9460.0\,K$
$RO_2 34 \rightarrow RO_2 43 + RO_2T$	1.97×10^{42}	-11.4	$-9460.0\,K$
$RO_2 35 \rightarrow RO_2 44 + RO_2T$	1.804×10^{42}	-11.4	$-9460.0\,K$
$RO_2 36 \rightarrow RO_2 45 + RO_2T$	1.97×10^{42}	-11.4	$-9460.0\,K$
$RO_2 37 \rightarrow RO_2 46 + RO_2T$	1.97×10^{42}	-11.4	$-9460.0\,K$
$RO_2 38 \rightarrow RO_2 47 + RO_2T$	1.97×10^{42}	-11.4	$-9460.0\,K$

Reference: CACM [*Griffin et al.*, 2002b, 2005]

formula for calculating a first order heterogeneous reaction rate k_{het} (s^{-1}) as

$$k_{het} = \sum_{i=1}^{N_{bins}} \left(\frac{4\pi r_i^2}{n_i} \right) \left(\frac{r_i}{D_q} + \frac{4}{\gamma \overline{c}_q} \right)^{-1} \tag{A.5}$$

Here, r_i is the radius of particles in bin i, n_i is the number concentration of particles in bin i, D_q is the diffusivity of gas q, $\overline{c}_q$ is the mean molecular speed of gas q, and γ is the dimensionless uptake coefficient.

As in MELAM [*Steele*, 2004], the diffusivity of gas q is calculated using the formula from *Davis* [1983]:

$$D_q = \frac{3}{8 N_A \overline{d_{q,a}^2} \rho_a} \sqrt{\frac{RT M_a \left(M_q + M_a\right)}{2\pi M_q}} \tag{A.6}$$

N_A is Avogadro's number, $d_{q,a}$ is the collision diameter of species q with air (here approximated as 4.5 Å for all species), ρ_a is the air density, R is the universal gas constant, T is temperature, and M_a and M_q are the molecular weights of air and species q, respectively. The mean molecular speed of gas q is then given by

$$\overline{c}_q = \sqrt{\frac{8RT}{\pi \left(MW_q\right)}} \tag{A.7}$$

Table A.3 lists the first-order heterogeneous reaction included in the mechanism. The first four reactions are from *Jacob* [2000], and occur on wet aerosol. The reaction of NO_2 to produce HONO has been found to occur on humic acid surfaces [*Stemmler et al.*, 2006, 2007]. The reaction of SO_2 to produce H_2SO_4 was proposed by *Buzcu et al.* [2006] to account for the formation of sulfate observed during a wood smoke episode in Texas. The last reaction is a hypothetical process that is tested in Chapter 3 to see if heterogeneous reactions of O_3 with organic aerosol surfaces can explain the production of acetic acid observed in the Timbavati fire.

Table A.3: First Order Heterogeneous Reactions

Reaction	γ	MW_q (g/ mol)	Ref.[a]
$NO_2 \rightarrow 0.5$ HONO + 0.5 HNO_3	10^{-4} $\left(10^{-6} - 10^{-3}\right)$	46	1
$HO_2 \rightarrow 0.5$ H_2O_2	0.2 $(0.1 - 1.0)$	33	1
$NO_3 \rightarrow HNO_3$	10^{-3} $\left(2 \times 10^{-4} - 10^{-2}\right)$	62	1
$N_2O_5 \rightarrow 2.0$ HNO_3	0.1 $(0.01 - 1.0)$	108	1
$NO_2 \rightarrow$ HONO	$2 \times 10^{-5} - 6 \times 10^{-6}$	46	2,3
$SO_2 \rightarrow H_2SO_4$	$\sim 10^{-2}$	64	4
$O_3 \rightarrow$ ACID	variable	48	5

[a]Uptake coefficient references: 1, *Jacob* [2000]; 2, *Stemmler et al.* [2006];
3, *Stemmler et al.* [2007]; 4, *Buzcu et al.* [2006]
5, hypothetical reaction explored in this work.

A.1.4 Thermal Degradation of Peroxy Acyl Nitrate (PAN) Radicals

As in the CACM, the rate of thermal degradation of peroxy acyl nitrate (PAN) species k_{deg} (s^{-1}) is calculated from the rate of formation of PAN k_f (cm^3 molecule^{-1} s^{-1}) and the equilibrium constant for PAN formation and degradation K_{eq} (cm^3/molecules) using the formula

$$k_{\text{deg}} = \frac{k_f}{K_{eq}} \tag{A.8}$$

k_f, the rate of the forward, PAN forming three body association reaction is calculated as

$$k_f = \frac{k_o M}{\left(1 + \frac{k_o M}{k_\infty}\right)} F^{\left(1+\left(\log_{10}\left(\frac{k_o M}{k_\infty}\right)\right)^2\right)^{-1}} \tag{A.9}$$

where M is the total concentration of gas molecules, F is a given constant, and k_o and k_∞ are given by the formulas

$$k_o = A_o \left(\frac{T}{300\,\text{K}}\right)^{-n_o} \tag{A.10}$$

$$k_\infty = A_\infty \left(\frac{T}{300\,\text{K}}\right)^{-n_\infty} \tag{A.11}$$

where T is the temperature in Kelvin and A_o, A_∞, n_o, and n_∞ are given constants. K_{eq} is calculated as

$$K_{eq} = \frac{k_f}{k_{\text{deg}}} = B_{eq} \exp\left(\frac{E_{eq}}{T}\right) \tag{A.12}$$

where B_{eq} and E_{eq} are given constants. The PAN degradation reactions and their reaction rate data are listed in Table A.4. Note that all PAN degradation reactions are assumed to have the same rate parameters.

Table A.4: First Order Thermal Degradation Reactions of Peroxy Acyl Nitrates

Reaction	A_o $(\times 10^{29})$	n_o	A_∞ $(\times 10^{12})$	n_∞	B_{eq} $(\times 10^{29})$	E_{eq}	F
PAN1→$RO_2$6+NO_2+RO_2T	9.7	5.6	9.3	1.5	8.62	13954 K	0.6
PAN2→$RO_2$8+NO_2+RO_2T	9.7	5.6	9.3	1.5	8.62	13954 K	0.6
PAN3→$RO_2$39+NO_2+RO_2T	9.7	5.6	9.3	1.5	8.62	13954 K	0.6
PAN4→$RO_2$48+NO_2+RO_2T	9.7	5.6	9.3	1.5	8.62	13954 K	0.6
PAN5→$RO_2$50+NO_2+RO_2T	9.7	5.6	9.3	1.5	8.62	13954 K	0.6
PAN6→$RO_2$54+NO_2+RO_2T	9.7	5.6	9.3	1.5	8.62	13954 K	0.6
PAN7→$RO_2$55+NO_2+RO_2T	9.7	5.6	9.3	1.5	8.62	13954 K	0.6
PAN8→$RO_2$56+NO_2+RO_2T	9.7	5.6	9.3	1.5	8.62	13954 K	0.6
PAN9→$RO_2$57+NO_2+RO_2T	9.7	5.6	9.3	1.5	8.62	13954 K	0.6
PN10→$RO_2$58+NO_2+RO_2T	9.7	5.6	9.3	1.5	8.62	13954 K	0.6

Reference: CACM [*Griffin et al.*, 2002b, 2005]

A.1.5 Thermal Degradation of HNO_4

As in the CACM [*Griffin et al.*, 2002b, 2005], the reaction rate for the thermal degradation reaction HNO_4 →NO_2+HO_2 (k_{HNO_4}, s^{-1}) is calculated using the formula

$$k_{HNO_4} = \frac{k_o M}{\left(1 + \frac{k_o M}{k_\infty}\right)} 0.5^{\left(1.0 + \left(\log_{10}\left(\frac{k_o M}{k_\infty}\right)\right)^2\right)^{-1}} \tag{A.13}$$

where k_o and k_∞ are given by the formulas

$$k_o = 4.1 \times 10^{-5} \exp\left(\frac{-10649.2\,\mathrm{K}}{T}\right) \tag{A.14}$$

$$k_\infty = 5.7 \times 10^{15} \exp\left(\frac{-11172.6\,\mathrm{K}}{T}\right) \tag{A.15}$$

and T is the temperature in Kelvin.

A.1.6 Other First Order Reactions

Following *Griffin et al.* [2002b] and *Griffin et al.* [2005], there are several other first order reactions in the mechanism that have non-canonical reaction rates with complex temperature and pressure dependence. The reactions and their rate formulas are listed below. In all of these formulas T is the temperature in Kelvin.

Thermal degradation of N_2O_5

The reaction rate for the thermal degradation reaction $N_2O_5 \rightarrow NO_2 + NO_3$ ($k_{N_2O_5}$, s^{-1}) is calculated using the formula

$$k_{N_2O_5} = \frac{k_o M}{\left(1 + \frac{k_o M}{k_\infty}\right)} 0.45^{\left(1.0 + \left(\log_{10}\left(\frac{k_o M}{k_\infty}\right)\right)^2\right)^{-1}} \tag{A.16}$$

where k_o and k_∞ are

$$k_o = 1.0 \times 10^{-3} \left(\frac{300.0\,\mathrm{K}}{T}\right)^{3.5} \exp\left(\frac{-11001.5\,\mathrm{K}}{T}\right) \tag{A.17}$$

$$k_\infty = 9.7 \times 10^{14} \left(\frac{T}{300.0\,\mathrm{K}}\right)^{0.1} \exp\left(\frac{-11082.0\,\mathrm{K}}{T}\right) \tag{A.18}$$

Deactivation of $O(^1D)$

The pseudo-first order rate constant for the deactivation of $O(^1D)$ to $O(^3P)$ ($k_{O(^1D)}$, s^{-1}) is given by the formula

$$k_{O(^1D)} = \frac{1.53 \times 10^{11}}{T} \exp\left(\frac{95.6\,\mathrm{K}}{T}\right) \tag{A.19}$$

Pseudo-first order reaction $O(^3P)$ (+ O_2) -> O_3

The pseudo-first order rate constant for the reaction $O(^3P)$ (+ O_2) → O_3 ($k_{O(^3P)}$, s^{-1}) is given by the formula

$$k_{O(^3P)} = \frac{5.53 \times 10^{16}}{T^{4.8}} \tag{A.20}$$

Pseudo-first order reaction of cyclohexadienyl radicals (RAD (+ O_2) -> RO_2)

Table A.5 lists the reactions of cyclohexadienyl radicals with oxygen to form peroxy radicals. All reactions of this type have a common reaction rate (k_{RAD*}, s^{-1}), given by the formula

$$k_{RAD*} = \frac{0.9 * 4.62 \times 10^7}{60T} \tag{A.21}$$

Table A.5: Pseudo-First Order Reactions of Cyclohexadienyl Radicals

Reaction
RAD2 → $RO_2$33 + RO_2T
RAD3 → $RO_2$34 + RO_2T
RAD4 → $RO_2$35 + RO_2T
RAD5 → $RO_2$36 + RO_2T
RAD6 → $RO_2$37 + RO_2T
RAD7 → $RO_2$38 + RO_2T

Reference: CACM [*Griffin et al.*, 2002b, 2005]

A.2 Second Order Reactions

A.2.1 Arrhenius-like Formula

Most second order reactions in CACM follow a modified form of the classic Arrhenius temperature dependence, given by the formula

$$k_q = AT^n \exp\left(\frac{E_a}{T}\right) \tag{A.22}$$

where E_a is the activation energy in K, A is the pre-exponential factor, and n is a constant to represent the secondary temperature tendency of the reaction rate. Tables A.6, A.7, and A.8 list the reaction rate parameters for second-order inorganic, organic and peroxy radical reactions, respectively, that follow Equation A.22.

As noted in Table A.7, the Arrhenius parameters used in this work for some reactions are not used in the CACM of *Griffin et al.* [2002b] and *Griffin et al.* [2005]. In CACM, some organic reaction rates are estimated using the group-contribution method of *Kwok and Atkinson* [1995]. These reactions have a 2 in the reference column of Table A.7. In our mechanism, these estimated reaction rates were fit to an Arrhenius dependence by performing a linear regression of the logarithm of the group-contribution reaction rate versus temperature over the temperature range 220 K - 320 K. Errors were generally less than 1% across this temperature range, and were never greater than 2%, which is much smaller than the expected error in the initial group-contribution method estimate. In addition, in CACM some reaction rates are calculated from the product or ratio of other reactions. These reactions have a 4 in the reference column of Table A.7. Here, we calculated the Arrhenius parameters for those reactions based on the formulas given in *Griffin et al.* [2002b] and *Griffin et al.* [2005].

In addition, in CACM two organic reactions, the reactions of ETOH and ARAL with OH, have a temperature-dependent stoichiometry based on branching ratios calculated using group-contribution methods. The stoichiometry for these reactions was found to vary only slightly over

the temperature range of 280 K- 320 K expected in our smoke plume simulations. Since the MELAM framework requires constant stoichiometry, the stoichiometry for these reactions was approximated as a constant using the values estimated at 300 K from the formulas in CACM. The errors from this approximation are expected to be much smaller than the errors in the original group contribution estimates.

Table A.6: Second Order Inorganic Reactions

Reaction	A	n	E_a (K)
$O + NO_2 \rightarrow NO + O_2$	6.50×10^{-12}	0	119.8
$O_3 + NO \rightarrow NO_2 + O_2$	1.8×10^{-12}	0	−1368.9
$NO_2 + O_3 \rightarrow NO_3 + O_2$	1.4×10^{-13}	0	−2471.1
$NO + NO_3 \rightarrow 2.0\ NO_2$	1.8×10^{-11}	0	110.7
$NO + NO \rightarrow NO_2 + NO_2$	5.09×10^{-18}	−1.0	528.4
$NO_2 + NO_3 \rightarrow NO + NO_2 + O_2$	4.5×10^{-14}	0	−1258.2
$O(^1D) + H_2O \rightarrow OH + OH$	2.2×10^{-10}	0	0
$O_3 + OH \rightarrow HO_2 + O_2$	1.9×10^{-12}	0	−1001.5
$HO_2 + NO \rightarrow NO_2 + OH$	3.41×10^{-12}	0	271.8
$HNO_4 + OH \rightarrow NO_2 + O_2 + H_2O$	1.5×10^{-12}	0	362.4
$HO_2 + O_3 \rightarrow OH + O_2 + O_2$	1.4×10^{-14}	0	−598.9
$NO_3 + HO_2 \rightarrow 0.8\ NO_2 + 0.2\ HNO_3 + 0.8\ OH + O_2$	4×10^{-12}	0	0
$O + O_3 \rightarrow O_2 + O_2$	8×10^{-12}	0	−2058.4
$H_2O_2 + OH \rightarrow HO_2 + H_2O$	2.91×10^{-12}	0	−161
$O + NO \rightarrow NO_2$	6.75×10^{-6}	−2.6	0
$HONO + OH \rightarrow NO_2 + H_2O$	2.7×10^{-12}	0	261.7
$NO_3 + OH \rightarrow NO_2 + HO_2$	2×10^{-11}	0	0
$NO_3 + NO_3 \rightarrow NO_2 + NO_2 + O_2$	8.5×10^{-13}	0	−2450.9
$OH + HO_2 \rightarrow H_2O + O_2$	4.8×10^{-11}	0	251.6

Reference: CACM [*Griffin et al.*, 2002b, 2005]

Table A.7: Second Order Organic Reactions

Reaction	A	n	E_a (K)	Ref.[a]
CH_4 + OH → $RO_2$1 + RO_2T + H_2O	2.66×10^{-12}	0	−1800.2	1
HCHO + OH → HO_2 + CO + H_2O	1.20×10^{-14}	1	286.9	1
HCHO + NO_3 → HNO_3 + CO + HO_2	2.00×10^{-12}	0	−2430.8	1
MEOH + OH → HO_2 + HCHO + H_2O	6.00×10^{-18}	2	170.1	1
ETHE + OH → $RO_2$2 + RO_2T	1.96×10^{-12}	0	437.8	1
ETHE + NO_3 → $RO_2$3 + RO_2T	4.89×10^{-18}	2	−2282.3	1
ETHE + O_3 → 0.63 CO + 0.12 HO_2 + 0.12 OH + 0.37 ACID + 1.0 HCHO + 0.14 H_2O	9.14×10^{-15}	0	−2580.3	1
ETHE + O → 0.6 CO + HO_2 + 0.6 $RO_2$1 + 0.4 $RO_2$4 + RO_2T	7.30×10^{-13}	0	0	1
ETOH + OH → 0.95 HO_2 + 0.95 ALD2 + 0.05 $RO_2$2 +0.05 RO_2T + H_2O	6.18×10^{-18}	2	532	1,3
OLEL + OH → $RO_2$2 + RO_2T	5.86×10^{-12}	0	500.3	1
OLEL + NO_3 → $RO_2$3 + RO_2T	1.00×10^{-13}	0	−800.2	1
OLEL + O_3 → 0.56 CO + 0.2 CO_2 + 0.36 OH + 0.28 HO_2+ 0.5 HCHO + 0.5 ALD2 + 0.24 ACID + 0.1 ALKL + 0.28 $RO_2$5 + 0.28 RO_2T	1.00×10^{-17}	0	0	1
OLEL + O → 0.5 ALKL + 0.4 ALD2 + 0.1 $RO_2$4 + 0.1 $RO_2$5 + 0.2 RO_2T	4.66×10^{-12}	0	0	1
ALKL + OH → $RO_2$5 + RO_2T + H_2O	3.91×10^{-12}	0	0	1
ALD2 + OH → $RO_2$6 + RO_2T + H_2O	6.91×10^{-12}	0	250	1
ALD2 + NO_3 → HNO_3 + $RO_2$6 + RO_2T	3.00×10^{-13}	0	−1427	1
KETL + OH → $RO_2$7 + RO_2T + H_2O	4.91×10^{-12}	0	0	1
ISOP + OH → 0.66 $RO_2$9 + 0.34 $RO_2$10 + RO_2T	2.55×10^{-11}	0	410.2	1
ISOP + NO_3 → 0.66 $RO_2$11 + 0.34 $RO_2$12 + RO_2T	3.02×10^{-12}	0	−445.9	1
ISOP + O_3 → 0.068 CO_2 + 0.461 CO + 0.5 HCHO + 0.664 OH + 0.366 HO_2 + 0.054 OLEL + 0.121 ACID + 0.389 MVK + 0.17 MCR+ 0.271 $RO_2$13 + 0.095 $RO_2$14 + 0.366 RO_2T	7.86×10^{-15}	0	−1912.9	1
ISOP + O → 0.925 OLEL + 0.075 ALD2	3.50×10^{-11}	0	0	1
ALCH + OH → $RO_2$2 + RO_2T + H_2O	6.87×10^{-18}	2	909.16	1,2
KETH + OH → $RO_2$16 + RO_2T + H_2O	2.03×10^{-17}	2	311.1	1,2
AROO + NO_3 → HNO_3 + RAD1	3.77×10^{-12}	0	0	
AROO + OH → 0.16 HO_2 + 0.16 AROO + 0.1 $RO_2$17 + 0.1 RO_2T + 0.74 RAD2 + 0.1 H_2O	2.26×10^{-10}	0	0	1,2
OLEH + OH → $RO_2$18 + RO_2T	1.77×10^{-17}	2	924.46	1,2
OLEH + NO_3 → $RO_2$19 + RO_2T	3.02×10^{-19}	2	−376.04	1,4
OLEH + O_3 → 0.56 CO + 0.2 CO_2 + 0.36 OH + 0.28 HO_2 + 0.5 HCHO + 0.5 RPR1 + 0.12 ACID + 0.12 UR1	3.02×10^{-23}	2	424.16	1,4

Continued on next page

Table A.7: (continued)

Reaction	A	n	E_a (K)	Ref.[a]
+ 0.1 ALKM + 0.28 $RO_2$20 + 0.28 RO_2T				
OLEH + O → 0.5 ALKM + 0.4 RPR1 + 0.1 $RO_2$4	1.41×10^{-17}	2	424.16	1,4
+ 0.1 $RO_2$20 + 0.2 RO_2T				
ALKM + OH → $RO_2$20 + RO_2T + H_2O	1.46×10^{-17}	2	616.95	1,2
AROL + OH → 0.16 HO_2 + 0.16 AROO + 0.1 $RO_2$21 + 0.74 RAD3	3.27×10^{-11}	0	0	1
+ 0.1 RO_2T + 0.1 H_2O				
AROH + OH → 0.16 HO_2 + 0.16 AROO + 0.84 RAD4	3.36×10^{-17}	2	484.94	1,2
ARAL + NO_3 → HNO_3 + O_3 -1.0 HO_2 + ARAC	1.40×10^{-12}	0	−1872.2	1
ARAL + OH → -0.58 HO_2 + 0.16 RPR2 + 0.74 O_3 + 0.74 ARAC	1.29×10^{-11}	0	0	1,3
+ 0.00454 $RO_2$22 + 0.00454 RO_2T				
+ 0.09546 RAD5 + 0.74454 H_2O				
ARAC + OH → 0.16 HO_2 + 0.16 UR2 + 0.1 $RO_2$23 + 0.74 RAD6	1.06×10^{-12}	0	0	1,2
+ 0.1 RO_2T + 0.1 H_2O				
BIOL + OH → $RO_2$24 + RO_2T	1.70×10^{-10}	0	0	1
BIOL + NO_3 → $RO_2$25 + RO_2T	1.46×10^{-11}	0	0	1
BIOL + O_3 → 0.445 CO + 0.055 H_2O_2 + 0.445 HO_2 + 0.89 OH	2.50×10^{-16}	0	0	1
+ 0.055 UR3 + 0.445 UR4 + 0.055 RPR3				
+ 0.445 $RO_2$26 + 0.445 RO_2T				
BIOL + O → 0.75 UR5 + 0.25 UR6	1.35×10^{-10}	0	−500.3	1
BIOH + OH → $RO_2$27 + RO_2T	1.77×10^{-10}	0	0	1
BIOH + NO_3 → $RO_2$28 + RO_2T	2.91×10^{-11}	0	0	1
BIOH + O_3 → 0.445 CO + 0.055 H_2O_2 + 0.89 OH	1.40×10^{-16}	0	0	1
+ 0.055 UR7 + 0.055 UR8				
+ 0.445 $RO_2$29 + 0.445 $RO_2$30 + 0.89 RO_2T				
BIOH + O → 0.75 UR9 + 0.25 UR10	8.59×10^{-11}	0	0	1,4
PAH + OH → 0.16 HO_2 + 0.16 UR11 + 0.1 $RO_2$31 + 0.74 RAD7	7.70×10^{-11}	0	0	1
+ 0.1 RO_2T + 0.1 H_2O				
ALKH + OH → $RO_2$32 + RO_2T + H_2O	6.57×10^{-17}	2	361	1,2
MGLY + OH → $RO_2$48 + RO_2T + H_2O	1.72×10^{-11}	0	0	1
MGLY + NO_3 → HNO_3 + $RO_2$48 + RO_2T	1.40×10^{-12}	0	−1897.3	1
MVK + OH → $RO_2$49 + RO_2T	4.14×10^{-12}	0	452.9	1
MVK + O_3 → 0.56 CO + 0.2 CO_2 + 0.28 HO_2 + 0.36 OH	7.50×10^{-16}	0	−1519.9	1
+ 0.5 MGLY + 0.5 HCHO + 0.12 ACID + 0.1 ALD2				
+ 0.12 UR21 + 0.28 $RO_2$8 + 0.28 RO_2T + 0.2 H_2O				
MVK + O → 0.85 KETL + 0.15 $RO_2$4 + 0.15 $RO_2$8 + 0.3 RO_2T	4.32×10^{-12}	0	0	1
MCR + OH → 0.3 $RO_2$50 + 0.3 H_2O + 0.7 $RO_2$51 + RO_2T	1.86×10^{-11}	0	176.1	1
MCR + NO_3 → 0.3 HNO_3 + 0.3 $RO_2$50 + 0.7 $RO_2$52 + RO_2T	1.50×10^{-12}	0	−1726.2	1

Continued on next page

Table A.7: (continued)

Reaction	A	n	E_a (K)	Ref.[a]
MCR + O_3 → 0.41 CO + 0.41 HO_2 + 0.82 OH + 0.5 HCHO +0.59 MGLY + 0.09 ACID+ 0.41 $RO_2$53 + 0.41 RO_2T	1.36×10^{-15}	0	−2113.7	1
MCR + O → 0.15 CO + 0.15 HO_2 + 0.85 ALD2 + 0.15 $RO_2$7 + 0.15 RO_2T	6.34×10^{-12}	0	0	1
RPR1 + OH → $RO_2$55 + RO_2T + H_2O	5.71×10^{-17}	2	578.8	1,2
RPR1 + NO_3 → HNO_3 + $RO_2$55 + RO_2T	2.48×10^{-18}	2	−1099	1,4
RPR2 + OH → O_3 -1.0 HO_2 + UR2 + H_2O	1.29×10^{-11}	0	0	1
RPR3 + OH → $RO_2$56 + RO_2T + H_2O	4.85×10^{-17}	2	682.75	1,2
RPR3 + NO_3 → HNO_3 + $RO_2$56 + RO_2T	2.11×10^{-18}	2	−994.25	1,4
RPR4 + NO_3 → HNO_3 + RAD8	3.77×10^{-12}	0	0	1
RPR5 + OH → O_3 -1.0 HO_2 + UR14 + H_2O	1.29×10^{-11}	0	0	1
RPR6 + OH → O_3 -1.0 HO_2 + RPR7 + H_2O	1.29×10^{-11}	0	0	1
RPR7 + OH → O_3 -1.0 HO_2 + ADAC + H_2O	1.29×10^{-11}	0	0	1
RPR8 + OH → $RO_2$57 + RO_2T + H_2O	1.15×10^{-10}	0	0	1,2
RPR8 + NO_3 → HNO_3 + $RO_2$57 + RO_2T	4.97×10^{-12}	0	−1677	1,4
RPR9 + OH → O_3 -1.0 HO_2 + RP17 + H_2O	2.41×10^{-10}	0	0	1,2
RP10 + OH → HO_2 + UR24 + H_2O	1.10×10^{-10}	0	0	1,2
RP11 + OH → 0.67 O_3 -0.67 HO_2 + 0.67 UR26 + 0.33 UR24 +0.67 H_2O + 0.33 $RO_2$13	1.96×10^{-10}	0	0	1,2
RP12 + OH → O_3 -1.0 HO_2 + RP13 + H_2O	2.41×10^{-10}	0	0	1,2
RP13 + OH → O_3 -1.0 HO_2 + RP18 + H_2O	2.19×10^{-10}	0	0	1,2
RP14 + OH → O_3 -1.0 HO_2 + RP19 + H_2O	1.45×10^{-10}	0	0	1,2
RP15 + OH → O_3 -1.0 HO_2 + UR27 + H_2O	1.30×10^{-11}	0	0	1,2
RP16 + OH → $RO_2$58 + RO_2T + H_2O	1.72×10^{-11}	0	0	1
RP16 + NO_3 → HNO_3 + $RO_2$58 + RO_2T	1.40×10^{-12}	0	−1897.3	1
RP17 + OH → O_3 -1.0 HO_2 + UR29 + H_2O	2.20×10^{-10}	0	0	1,2
RP18 + OH → O_3 -1.0 HO_2 + UR30 + H_2O	1.97×10^{-10}	0	0	1,2
RP19 + OH → O_3 -1.0 HO_2 + UR31 + H_2O	1.34×10^{-10}	0	0	1,2

References: 1, CACM [*Griffin et al.*, 2002b, 2005]

2, Calculated by regression versus temperature of rates calculated using method of [*Kwok and Atkinson*, 1995]

3, Stoichiometry calculated at 300 K using CACM formulas; stoichiometry held constant in this work

4, Calculated from other reaction rates following CACM formulas

Table A.8: Second Order Radical Reactions

Reaction	A	n	E_a (K)
$RO_2T + HO_2 \rightarrow HO_2$	3.41×10^{-13}	0	800.2
$RO_2T + NO \rightarrow NO$	4.20×10^{-12}	0	181.2
$RO_2T + RO_2T \rightarrow RO_2T$	1.00×10^{-15}	0	0
$RAD1 + NO_2 \rightarrow RPR4$	5.10×10^{-11}	0	0
$RAD2 + NO_2 \rightarrow RPR4 + H_2O$	5.10×10^{-11}	0	0
$RAD3 + NO_2 \rightarrow UR12 + H_2O$	5.10×10^{-11}	0	0
$RAD4 + NO_2 \rightarrow UR13 + H_2O$	5.10×10^{-11}	0	0
$RAD5 + NO_2 \rightarrow RPR5 + H_2O$	5.10×10^{-11}	0	0
$RAD6 + NO_2 \rightarrow UR14 + H_2O$	5.10×10^{-11}	0	0
$RAD7 + NO_2 \rightarrow UR15 + H_2O$	5.10×10^{-11}	0	0
$RO_21 + NO \rightarrow NO_2 + HO_2 + HCHO$	4.09×10^{-12}	0	180.2
$RO_21 + RO_2T \rightarrow HO_2 + HCHO + RO_2T + O_2$	1.00×10^{-15}	0	0
$RO_21 + HO_2 \rightarrow HO_2 + OH + HCHO$	3.41×10^{-13}	0	800.2
$RO_22 + NO \rightarrow NO_2 + HO_2 + HCHO + ALD2$	2.46×10^{-12}	0	180.2
$RO_22 + RO_2T \rightarrow HO_2 + HCHO + ALD2 + RO_2T + O_2$	1.00×10^{-15}	0	0
$RO_22 + HO_2 \rightarrow OH + HO_2 + HCHO + ALD2$	3.41×10^{-13}	0	800.2
$RO_23 + NO \rightarrow 2.0\ NO_2 + HCHO + ALD2$	2.45×10^{-12}	0	180.2
$RO_23 + RO_2T \rightarrow NO_2 + HO_2 + HCHO + ALD2 + O_2 + RO_2T$	1.00×10^{-15}	0	800.2
$RO_23 + HO_2 \rightarrow NO_2 + HO_2 + OH + HCHO + ALD2$	3.41×10^{-13}	0	800.2
$RO_24 + NO \rightarrow NO_2 + CO + HO_2 + HCHO$	3.45×10^{-12}	0	180.2
$RO_24 + RO_2T \rightarrow CO + HO_2 + HCHO + RO_2T + O_2$	1.00×10^{-15}	0	0
$RO_24 + HO_2 \rightarrow CO + HO_2 + OH + HCHO$	3.41×10^{-13}	0	800.2
$RO_25 + RO_2T \rightarrow HO_2 + ALD2 + RO_2T$	1.00×10^{-15}	0	0
$RO_25 + HO_2 \rightarrow HO_2 + OH + ALD2$	3.41×10^{-13}	0	800.2
$RO_26 + NO \rightarrow NO_2 + CO_2 + RO_25 + RO_2T$	1.11×10^{-11}	0	180.2
$RO_26 + HO_2 \rightarrow O_3 + ACID$	9.74×10^{-14}	0	800.2
$RO_26 + RO_2T \rightarrow CO_2 + RO_25 + 2.0\ RO_2T + O_2$	1.00×10^{-15}	0	0
$RO_27 + NO \rightarrow NO_2 + ALD2 + RO_28 + RO_2T$	2.45×10^{-12}	0	180.2
$RO_27 + RO_2T \rightarrow ALD2 + RO_28 + 2.0\ RO_2T + O_2$	1.00×10^{-15}	0	0
$RO_27 + HO_2 \rightarrow OH + ALD2 + RO_28 + RO_2T$	3.41×10^{-13}	0	800.2
$RO_28 + NO \rightarrow NO_2 + CO_2 + RO_21 + RO_2T$	1.11×10^{-11}	0	180.2
$RO_28 + HO_2 \rightarrow O_3 + ACID$	9.74×10^{-14}	0	800.2
$RO_28 + RO_2T \rightarrow CO_2 + RO_21 + 2.0\ RO_2T + O_2$	1.00×10^{-15}	0	0
$RO_29 + RO_2T \rightarrow HO_2 + MVK + HCHO + RO_2T + O_2$	1.00×10^{-15}	0	0
$RO_29 + HO_2 \rightarrow HO_2 + OH + MVK + HCHO$	3.41×10^{-13}	0	800.2
$RO_210 + NO \rightarrow NO_2 + HO_2 + HCHO + MCR$	2.08×10^{-12}	0	180.2
$RO_210 + RO_2T \rightarrow HO_2 + HCHO + MCR + RO_2T + O_2$	1.00×10^{-15}	0	0

Continued on next page

Table A.8: (continued)

Reaction	A	n	E_a (K)
$RO_210 + HO_2 \rightarrow HO_2 + OH + HCHO + MCR$	3.41×10^{-13}	0	800.2
$RO_211 + NO \rightarrow 2.0\ NO_2 + HCHO + MVK$	2.08×10^{-12}	0	180.2
$RO_211 + RO_2T \rightarrow NO_2 + HCHO + MVK + RO_2T + O_2$	1.00×10^{-15}	0	0
$RO_211 + HO_2 \rightarrow NO_2 + OH + HCHO + MVK$	3.41×10^{-13}	0	800.2
$RO_212 + NO \rightarrow 2.0\ NO_2 + HCHO + MCR$	2.08×10^{-12}	0	180.2
$RO_212 + RO_2T \rightarrow NO_2 + HCHO + MCR + RO_2T + O_2$	1.00×10^{-15}	0	0
$RO_212 + HO_2 \rightarrow NO_2 + OH + HCHO + MCR$	3.41×10^{-13}	0	800.2
$RO_213 + NO \rightarrow NO_2 + HCHO + RO_239 + RO_2T$	2.45×10^{-12}	0	180.2
$RO_213 + RO_2T \rightarrow HCHO + RO_239 + 2.0\ RO_2T + O_2$	1.00×10^{-15}	0	0
$RO_213 + HO_2 \rightarrow HCHO + OH + RO_239 + RO_2T$	3.41×10^{-13}	0	800.2
$RO_239 + NO \rightarrow NO_2 + CO_2 + RO_214 + RO_2T$	1.11×10^{-11}	0	180.2
$RO_239 + HO_2 \rightarrow O_3 + 0.5\ OLEL + 0.5\ ACID$	9.74×10^{-14}	0	800.2
$RO_239 + RO_2T \rightarrow CO_2 + RO_214 + 2.0\ RO_2T + O_2$	1.00×10^{-15}	0	0
$RO_214 + RO_2T \rightarrow RO_27 + 2.0\ RO_2T + O_2$	1.00×10^{-15}	0	0
$RO_214 + HO_2 \rightarrow OH + RO_27 + RO_2T$	3.41×10^{-13}	0	800.2
$RO_216 + NO \rightarrow NO_2 + ALD2 + RO_28 + RO_2T$	1.48×10^{-12}	0	180.2
$RO_216 + RO_2T \rightarrow ALD2 + RO_28 + 2.0\ RO_2T + O_2$	1.00×10^{-15}	0	0
$RO_216 + HO_2 \rightarrow OH + ALD2 + RO_28 + RO_2T$	3.41×10^{-13}	0	800.2
$RO_217 + RO_2T \rightarrow HO_2 + RPR2 + RO_2T + O_2$	1.00×10^{-15}	0	0
$RO_217 + HO_2 \rightarrow HO_2 + OH + RPR2$	3.41×10^{-13}	0	800.2
$RO_218 + RO_2T \rightarrow HO_2 + UR16 + RO_2T + O_2$	1.00×10^{-15}	0	0
$RO_218 + HO_2 \rightarrow HO_2 + OH + UR16$	3.41×10^{-13}	0	800.2
$RO_219 + NO \rightarrow 2.0\ NO_2 + HCHO + RPR1$	1.05×10^{-12}	0	180.2
$RO_219 + RO_2T \rightarrow NO_2 + HCHO + RPR1 + RO_2T + O_2$	1.00×10^{-15}	0	0
$RO_219 + HO_2 \rightarrow NO_2 + OH + HCHO + RPR1$	3.41×10^{-13}	0	800.2
$RO_220 + RO_2T \rightarrow RO_218 + 2.0\ RO_2T + O_2$	1.00×10^{-15}	0	0
$RO_220 + HO_2 \rightarrow OH + RO_218 + RO_2T$	3.41×10^{-13}	0	800.2
$RO_221 + RO_2T \rightarrow HO_2 + ARAL + RO_2T + O_2$	1.00×10^{-15}	0	0
$RO_221 + HO_2 \rightarrow HO_2 + OH + ARAL$	3.41×10^{-13}	0	800.2
$RO_222 + RO_2T \rightarrow HO_2 + RPR6 + RO_2T + O_2$	1.00×10^{-15}	0	0
$RO_222 + HO_2 \rightarrow HO_2 + OH + RPR6$	3.41×10^{-13}	0	800.2
$RO_223 + RO_2T \rightarrow HO_2 + RPR7 + RO_2T + O_2$	1.00×10^{-15}	0	0
$RO_223 + HO_2 \rightarrow HO_2 + OH + RPR7$	3.41×10^{-13}	0	800.2
$RO_224 + RO_2T \rightarrow HO_2 + RPR3 + RO_2T + O_2$	1.00×10^{-15}	0	0
$RO_224 + HO_2 \rightarrow HO_2 + OH + RPR3$	3.41×10^{-13}	0	800.2
$RO_225 + NO \rightarrow 2.0\ NO_2 + RPR3$	8.89×10^{-13}	0	180.2
$RO_225 + RO_2T \rightarrow NO_2 + RPR3 + RO_2T + O_2$	1.00×10^{-15}	0	0

Continued on next page

Table A.8: (continued)

Reaction	A	n	E_a (K)
$RO_2 25 + HO_2 \rightarrow NO_2 + OH + RPR3$	3.41×10^{-13}	0	800.2
$RO_2 26 + NO \rightarrow NO_2 + UR17 + RO_2 8 + RO_2T$	8.89×10^{-13}	0	180.2
$RO_2 26 + RO_2T \rightarrow UR17 + RO_2 8 + 2.0\ RO_2T + O_2$	1.00×10^{-15}	0	0
$RO_2 26 + HO_2 \rightarrow UR17 + OH + RO_2 8 + RO_2T$	3.41×10^{-13}	0	800.2
$RO_2 27 + RO_2T \rightarrow HO_2 + 0.3\ UR7 + 0.7\ UR10 + RO_2T + O_2$	1.00×10^{-15}	0	0
$RO_2 27 + HO_2 \rightarrow HO_2 + OH + 0.3\ UR7 + 0.7\ UR10$	3.41×10^{-13}	0	800.2
$RO_2 28 + NO \rightarrow 2.0\ NO_2 + 0.3\ UR7 + 0.7\ UR10$	8.89×10^{-13}	0	180.2
$RO_2 28 + RO_2T \rightarrow NO_2 + 0.3\ UR7 + 0.7\ UR10 + RO_2T + O_2$	1.00×10^{-15}	0	0
$RO_2 28 + HO_2 \rightarrow NO_2 + OH + 0.3\ UR7 + 0.7\ UR10$	3.41×10^{-13}	0	800.2
$RO_2 29 + RO_2T \rightarrow RO_2 40 + 2.0\ RO_2T + O_2$	1.00×10^{-15}	0	0
$RO_2 29 + HO_2 \rightarrow OH + RO_2 40 + RO_2T$	3.41×10^{-13}	0	800.2
$RO_2 40 + NO \rightarrow NO_2 + RPR8 + RO_2 8 + RO_2T$	1.05×10^{-12}	0	180.2
$RO_2 40 + RO_2T \rightarrow RPR8 + RO_2 8 + 2.0\ RO_2T + O_2$	1.00×10^{-15}	0	0
$RO_2 40 + HO_2 \rightarrow OH + RPR8 + RO_2 8 + RO_2T$	3.41×10^{-13}	0	800.2
$RO_2 30 + NO \rightarrow NO_2 + UR18 + RO_2 8 + RO_2T$	8.89×10^{-13}	0	180.2
$RO_2 30 + RO_2T \rightarrow UR18 + RO_2 8 + 2.0\ RO_2T + O_2$	1.00×10^{-15}	0	0
$RO_2 30 + HO_2 \rightarrow OH + UR18 + RO_2 8 + RO_2T$	3.41×10^{-13}	0	800.2
$RO_2 31 + RO_2T \rightarrow HO_2 + UR19 + RO_2T + O_2$	1.00×10^{-15}	0	0
$RO_2 31 + HO_2 \rightarrow HO_2 + OH + UR19$	3.41×10^{-13}	0	800.2
$RO_2 32 + RO_2T \rightarrow RO_2 41 + 2.0\ RO_2T + O_2$	1.00×10^{-15}	0	0
$RO_2 32 + HO_2 \rightarrow OH + RO_2 41 + RO_2T$	3.41×10^{-13}	0	800.2
$RO_2 41 + RO_2T \rightarrow HO_2 + UR20 + RO_2T + O_2$	1.00×10^{-15}	0	0
$RO_2 41 + HO_2 \rightarrow HO_2 + OH + UR20$	3.41×10^{-13}	0	800.2
$RO_2 33 + NO \rightarrow NO_2 + 0.3\ HO_2 + 0.3\ RPR9 + 0.7\ UR35$ $+0.7\ RO_2 1 + 0.7\ RO_2T$	1.25×10^{-12}	0	180.2
$RO_2 33 + RO_2T \rightarrow 0.3\ HO_2 + 0.3\ RPR9 + 0.7\ UR35$ $+ 1.7\ RO_2T + 0.7\ RO_2 1 + O_2$	1.00×10^{-15}	0	0
$RO_2 33 + HO_2 \rightarrow 0.3\ HO_2 + 0.3\ OH + 0.3\ RPR9$ $+ 0.7\ UR35 + 0.7\ RO_2 1 + 0.7\ RO_2T$	3.41×10^{-13}	0	800.2
$RO_2 42 + NO \rightarrow NO_2 + HO_2 + RP10 + MGLY$	1.25×10^{-12}	0	180.2
$RO_2 42 + RO_2T \rightarrow HO_2 + RP10 + MGLY + RO_2T + O_2$	1.00×10^{-15}	0	0
$RO_2 42 + HO_2 \rightarrow HO_2 + OH + RP10 + MGLY$	3.41×10^{-13}	0	800.2
$RO_2 34 + NO \rightarrow NO_2 + 0.3\ HO_2 + 0.3\ RP11$ $+ 0.7\ UR35 + 0.7\ RO_2 1 + 0.7\ RO_2T$	1.05×10^{-12}	0	180.2
$RO_2 34 + RO_2T \rightarrow 0.3\ HO_2 + 0.3\ RP11 + 0.7\ UR35$ $+ 0.7\ RO_2 1 + 1.7\ RO_2T + O_2$	1.00×10^{-15}	0	0
$RO_2 34 + HO_2 \rightarrow 0.3\ HO_2 + 0.3\ OH + 0.3\ RP11$	3.41×10^{-13}	0	800.2

Continued on next page

Table A.8: (continued)

Reaction	A	n	E_a (K)
+ 0.7 UR35 + 0.7 $RO_2$1 + 0.7 RO_2T			
$RO_2$43 + NO → NO_2 + HO_2 + RP10 + MGLY	1.05×10^{-12}	0	180.2
$RO_2$43 + RO_2T → HO_2 + RP10 + MGLY + RO_2T + O_2	1.00×10^{-15}	0	0
$RO_2$43 + HO_2 → HO_2 + OH + RP10 + MGLY	3.41×10^{-13}	0	800.2
$RO_2$35 + NO → NO_2 + 0.5 HO_2 + 0.5 RP11	8.89×10^{-13}	0	180.2
+ 0.5 $RO_2$5 + 0.5 RO_2T + 0.5 UR35			
$RO_2$35 + RO_2T → 0.5 HO_2 + 0.5 RP11 + 0.5 $RO_2$5	1.00×10^{-15}	0	0
+ 0.5 UR35 + 1.5 RO_2T + O_2			
$RO_2$35 + HO_2 → 0.5 HO_2 + 0.5 OH + 0.5 RP11	3.41×10^{-13}	0	800.2
+ 0.5 UR35 + $RO_2$25 + RO_2T			
$RO_2$44 + NO → NO_2 + HO_2 + RP10 + MGLY	8.89×10^{-13}	0	180.2
$RO_2$44 + RO_2T → HO_2 + RP10 + MGLY + RO_2T + O_2	1.00×10^{-15}	0	0
$RO_2$44 + HO_2 → HO_2 + OH + RP10 + MGLY	3.41×10^{-13}	0	800.2
$RO_2$36 + NO → NO_2 + HO_2 + 0.3 RP12 + 0.7 UR35	1.25×10^{-12}	0	180.2
$RO_2$36 + RO_2T → HO_2 + 0.3 RP12 + 0.7 UR35 + RO_2T + O_2	1.00×10^{-15}	0	0
$RO_2$36 + HO_2 → HO_2 + OH + 0.3 RP12 + 0.7 UR35	3.41×10^{-13}	0	800.2
$RO_2$45 + NO → NO_2 + HO_2 + RP10 + MGLY	1.25×10^{-12}	0	180.2
$RO_2$45 + RO_2T → HO_2 + RP10 + MGLY + RO_2T + O_2	1.00×10^{-15}	0	0
$RO_2$45 + HO_2 → HO_2 + OH + RP10 + MGLY	3.41×10^{-13}	0	800.2
$RO_2$37 + NO → NO_2 + HO_2 + 0.3 RP13 + 0.7 UR35	1.25×10^{-12}	0	180.2
$RO_2$37 + RO_2T → HO_2 + 0.3 RP13 + 0.7 UR35 + RO_2T + O_2	1.00×10^{-15}	0	0
$RO_2$37 + HO_2 → HO_2 + OH + 0.3 RP13 + 0.7 UR35	3.41×10^{-13}	0	800.2
$RO_2$46 + NO → NO_2 + HO_2 + RP10 + MGLY	1.25×10^{-12}	0	180.2
$RO_2$46 + RO_2T → HO_2 + RP10 + MGLY + RO_2T + O_2	1.00×10^{-15}	0	0
$RO_2$46 + HO_2 → HO_2 + OH + RP10 + MGLY	3.41×10^{-13}	0	800.2
$RO_2$38 + NO → NO_2 + HO_2 + RP14	6.32×10^{-13}	0	180.2
$RO_2$38 + RO_2T → HO_2 + RP14 + RO_2T + O_2	1.00×10^{-15}	0	0
$RO_2$38 + HO_2 → HO_2 + OH + RP14	3.41×10^{-13}	0	800.2
$RO_2$47 + NO → NO_2 + HO_2 + RP15 + MGLY	6.32×10^{-13}	0	180.2
$RO_2$47 + RO_2T → HO_2 + RP15 + MGLY + RO_2T + O_2	1.00×10^{-15}	0	0
$RO_2$47 + HO_2 → HO_2 + OH + RP15 + MGLY	3.41×10^{-13}	0	800.2
$RO_2$48 + NO → NO_2 + CO_2 + $RO_2$8 + RO_2T	1.11×10^{-11}	0	180.2
$RO_2$48 + HO_2 → O_3 + UR21	9.74×10^{-14}	0	800.2
$RO_2$48 + RO_2T → CO_2 + $RO_2$8 + 2.0 RO_2T + O_2	1.00×10^{-15}	0	0
$RO_2$49 + NO → NO_2 + HO_2 + MGLY + HCHO	2.45×10^{-12}	0	180.2
$RO_2$49 + RO_2T → HO_2 + MGLY + HCHO + RO_2T + O_2	1.00×10^{-15}	0	0
$RO_2$49 + HO_2 → HO_2 + OH + MGLY + HCHO	3.41×10^{-13}	0	800.2

Continued on next page

Table A.8: (continued)

Reaction	A	n	E_a (K)
$RO_2 50 + NO \rightarrow NO_2 + CO_2 + RO_2 14 + RO_2T$	1.11×10^{-11}	0	180.2
$RO_2 50 + HO_2 \rightarrow O_3 + 0.5$ ACID $+ 0.5$ OLEL	9.74×10^{-14}	0	800.2
$RO_2 50 + RO_2T \rightarrow CO_2 + RO_2 14 + 2.0\ RO_2T + O_2$	1.00×10^{-15}	0	0
$RO_2 51 + NO \rightarrow NO_2 + HO_2 + MGLY + HCHO$	2.45×10^{-12}	0	180.2
$RO_2 51 + RO_2T \rightarrow HO_2 + MGLY + HCHO + RO_2T + O_2$	1.00×10^{-15}	0	0
$RO_2 51 + HO_2 \rightarrow HO_2 + OH + MGLY + HCHO$	3.41×10^{-13}	0	800.2
$RO_2 52 + NO \rightarrow 2.0\ NO_2 + MGLY + HCHO$	2.45×10^{-12}	0	180.2
$RO_2 52 + RO_2T \rightarrow NO_2 + MGLY + HCHO + RO_2T + O_2$	1.00×10^{-15}	0	0
$RO_2 52 + HO_2 \rightarrow NO_2 + OH + MGLY + HCHO$	3.41×10^{-13}	0	800.2
$RO_2 53 + NO \rightarrow NO_2 + HCHO + RO_2 54 + RO_2T$	2.91×10^{-12}	0	180.2
$RO_2 53 + RO_2T \rightarrow HCHO + RO_2 54 + 2.0\ RO_2T + O_2$	1.00×10^{-15}	0	0
$RO_2 53 + HO_2 \rightarrow OH + HCHO + RO_2 54 + RO_2T$	3.41×10^{-13}	0	800.2
$RO_2 54 + NO \rightarrow CO_2 + CO + NO_2 + HO_2$	1.11×10^{-11}	0	180.2
$RO_2 54 + HO_2 \rightarrow O_3 + RP16$	9.74×10^{-14}	0	800.2
$RO_2 54 + RO_2T \rightarrow CO_2 + CO + HO_2 + RO_2T + O_2$	1.00×10^{-15}	0	0
$RO_2 55 + NO \rightarrow CO_2 + NO_2 + RO_2 20 + RO_2T$	1.11×10^{-11}	0	180.2
$RO_2 55 + HO_2 \rightarrow O_3 + UR1$	9.74×10^{-14}	0	800.2
$RO_2 55 + RO_2T \rightarrow CO_2 + RO_2 20 + 2.0\ RO_2T + O_2$	1.00×10^{-15}	0	0
$RO_2 56 + NO \rightarrow CO_2 + NO_2 + HO_2 + UR4$	1.11×10^{-11}	0	180.2
$RO_2 56 + HO_2 \rightarrow O_3 + UR3$	9.74×10^{-14}	0	800.2
$RO_2 56 + RO_2T \rightarrow CO_2 + HO_2 + UR4 + RO_2T + O_2$	1.00×10^{-15}	0	0
$RAD8 + NO_2 \rightarrow UR22 + H_2O$	2.30×10^{-11}	0	151
$RO_2 57 + NO \rightarrow CO_2 + NO_2 + RO_2 9 + RO_2T$	1.11×10^{-11}	0	180.2
$RO_2 57 + HO_2 \rightarrow O_3 + UR23$	9.74×10^{-14}	0	800.2
$RO_2 57 + RO_2T \rightarrow CO_2 + RO_2 9 + 2.0\ RO_2T + O_2$	1.00×10^{-15}	0	0
$RO_2 58 + NO \rightarrow CO + CO_2 + NO_2 + OH$	1.11×10^{-11}	0	180.2
$RO_2 58 + HO_2 \rightarrow O_3 + UR28$	9.74×10^{-14}	0	800.2
$RO_2 58 + RO_2T \rightarrow CO + CO_2 + OH + RO_2T + O_2$	1.00×10^{-15}	0	0

Reference: CACM [*Griffin et al.*, 2002b, 2005]

A.2.2 Organic Nitrate Formation

When a peroxy radical reacts with NO, there are two possible outcomes: either the peroxy radical loses an oxygen to NO to form NO_2, or the NO binds to the peroxy radical to form an organic nitrate compound. The branching ratios for these two pathways are estimated in CACM using the formulas of *Carter and Atkinson* [1989].

In CACM, this branching behavior is included by creating one reaction with varying stoi-

chiometries. Since the MELAM framework requires constant stoichiometries, we instead include both reaction pathways separately in our mechanism, and calculate the reaction rates following *Carter and Atkinson* [1989].

The reaction rate for organic nitrate formation, $k_{nitrate}$ (cm^3 molecule^{-1} s^{-1}), is

$$k_{nitrate} = f_{nitrate} k_{overall} \tag{A.23}$$

whereas the reaction rate for the formation of NO_2 is

$$k = (1 - f_{nitrate})\, k_{overall} \tag{A.24}$$

where $k_{overall}$ (cm^3 molecule^{-1} s^{-1}) is the total reaction rate for the peroxy radical and NO, and $f_{nitrate}$ is the branching ratio of the organic nitrate reaction. The reaction rate $k_{overall}$ is calculated from the Arrhenius formula

$$k_{overall} = A \exp\left(\frac{E_a}{T}\right) \tag{A.25}$$

The branching ratio $f_{nitrate}$ is calculated as

$$f_{nitrate} = \frac{R_{nitrate}}{1 + R_{nitrate}} \tag{A.26}$$

where $R_{nitrate} = DX + B$, where D and B are given constants and X is

$$X = C_{scale} \left(\frac{Y_o M \left(\frac{T}{300\,\mathrm{K}}\right)^{-m_o}}{\left(1 + \frac{Y_o M \left(\frac{T}{300\,\mathrm{K}}\right)^{-m_o}}{Y_\infty \left(\frac{T}{300\,\mathrm{K}}\right)^{-m_\infty}}\right)} \right) F^Z \tag{A.27}$$

where M is the total concentration of gas molecules, $F = 0.411$, $m_o = 0.0$, $m_\infty = 8.1$, and $Y_\infty = 0.826$.

The factor C_{scale} equals 0.4 if the peroxy radical is primary, 1.0 if it is secondary, and 0.3 if it is tertiary. Y_o is calculated as

$$Y_o = \alpha \exp(\beta N_c) \tag{A.28}$$

where N_c is the number of carbon atoms in the peroxy radical, $\alpha = 1.94{\times}10^{-22}$, and $\beta = 0.97$. Z is calculated as

$$Z = \left(1 + \left(\log_{10}\left(\frac{Y_o M \left(\frac{T}{300\,\mathrm{K}}\right)^{-m_o}}{Y_\infty \left(\frac{T}{300\,\mathrm{K}}\right)^{-m_\infty}}\right)^2\right)\right)^{-1}$$

Table A.9 lists the peroxy reactions whose rates are calculated using the above formulas.

Table A.9: Second Order Organic Nitrate Formation Reactions

Reaction	Class	A	E_a (K)	N_c	C_{scale}	D	B
$RO_2$5 + NO → ALKL	1	2.91×10^{-12}	180.2	3	0.4	1.0	0.0
$RO_2$5 + NO → NO_2 + HO_2 + ALD2	2	2.91×10^{-12}	180.2	3	0.4	1.0	0.0
$RO_2$9 + NO → OLEL	1	2.08×10^{-12}	180.2	5	0.3	0.5	0.5
$RO_2$9 + NO → NO_2 + HO_2 + HCHO + MVK	2	2.08×10^{-12}	180.2	5	0.3	0.5	0.5
$RO_2$14 + NO → OLEL	1	2.91×10^{-12}	180.2	3	0.3	1.0	1.0
$RO_2$14 + NO → NO_2 + $RO_2$7 + RO_2T	2	2.91×10^{-12}	180.2	3	0.3	1.0	1.0
$RO_2$17 + NO → AP1	1	1.248×10^{-12}	180.2	8	0.4	0.4	0.6
$RO_2$17 + NO → NO_2 + HO_2 + RPR2	2	1.25×10^{-12}	180.2	8	0.4	0.4	0.6
$RO_2$18 + NO → AP2	1	1.25×10^{-12}	180.2	8	1.0	1.0	0.0
$RO_2$18 + NO → NO_2 + HO_2 + UR16	2	1.25×10^{-12}	180.2	8	1.0	1.0	0.0
$RO_2$20 + NO → AP3	1	1.25×10^{-12}	180.2	8	1.0	1.0	0.0
$RO_2$20 + NO → NO_2 + $RO_2$18 + RO_2T	2	1.25×10^{-12}	180.2	8	1.0	1.0	0.0
$RO_2$21 + NO → AP4	1	1.05×10^{-12}	180.2	9	0.4	1.0	0.0
$RO_2$21 + NO → NO_2 + HO_2 + ARAL	2	1.05×10^{-12}	180.2	9	0.4	1.0	0.0
$RO_2$22 + NO → AP5	1	1.25×10^{-12}	180.2	8	0.4	1.0	0.0
$RO_2$22 + NO → NO_2 + HO_2 + RPR6	2	1.25×10^{-12}	180.2	8	0.4	1.0	0.0
$RO_2$23 + NO → AP6	1	1.25×10^{-12}	180.2	8	0.4	1.0	0.0
$RO_2$23 + NO → NO_2 + HO_2 + RPR7	2	1.25×10^{-12}	180.2	8	0.4	1.0	0.0
$RO_2$24 + NO → AP7	1	8.89×10^{-13}	180.2	10	0.3	0.5	0.5
$RO_2$24 + NO → NO_2 + HO_2 + RPR3	2	8.89×10^{-13}	180.2	10	0.3	0.5	0.5
$RO_2$27 + NO → AP8	1	8.89×10^{-13}	180.2	10	0.3	0.5	0.5
$RO_2$27 + NO → NO_2 + HO_2 + 0.3 UR7 + 0.7 UR10	2	8.89×10^{-13}	180.2	10	0.3	0.5	0.5
$RO_2$29 + NO → AP9	1	1.05×10^{-12}	180.2	9	0.4	1.0	0.0
$RO_2$29 + NO → NO_2 + $RO_2$40 + RO_2T	2	1.05×10^{-12}	180.2	9	0.4	1.0	0.0
$RO_2$31 + NO → AP10	1	6.32×10^{-13}	180.2	12	0.4	1.0	0.0
$RO_2$31 + NO → NO_2 + HO_2 + UR19	2	6.32×10^{-13}	180.2	12	0.4	1.0	0.0
$RO_2$32 + NO → AP11	1	3.2×10^{-13}	180.2	16	1.0	1.0	0.0
$RO_2$32 + NO → NO_2 + $RO_2$41 + RO_2T	2	3.2×10^{-13}	180.2	16	1.0	1.0	0.0
$RO_2$41 + NO → AP12	1	3.2×10^{-13}	180.2	16	1.0	1.0	0.0
$RO_2$41 + NO → NO_2 + HO_2 + UR20	2	3.2×10^{-13}	180.2	16	1.0	1.0	0.0

Reference: CACM [*Griffin et al.*, 2002b, 2005]

Heterogeneous Reactions

Tabazedeh et al. [2004] proposed two heterogeneous reactions of methanol to explain the observed drop in methanol concentrations observed when a smoke plume intersected with a cumulus cloud in the SAFARI 2000 field project. *Trentmann et al.* [2005] suggested that these reactions of methanol could also explain the rapid formation of O_3 in the Timbavati smoke plume. Thus, these two potential heterogeneous reactions of methanol are included in our chemical mechanism. Their reaction rates are calculated from the formula:

$$k = k^*_{surf} \sum_{i=1}^{N_{bins}} \left(\frac{4\pi r_i^2}{n_i} \right) \tag{A.29}$$

where k^*_{surf} in units of cm^3*cm/molecule/s, r_i is the radius of particles in bin i, and n_i is the number concentration of particles in bin i. The two body heterogeneous reactions considered in

this work are listed in Table A.10.

Table A.10: Second Order Heterogeneous Reactions

Reaction	k^*_{surf}
MEOH + NO_2 → HO_2 + HCHO + HNO_3 + NO −1.0 NO_2	4.33×10^{-13}
MEOH + OH → HO_2 + HCHO + H_2O	3.68×10^{-8}

References: [*Trentmann et al.*, 2005; *Tabazedeh et al.*, 2004]

A.2.3 Other Second Order Rate Constants

In CACM, some second-order reactions have non-canonical reaction rates. These reaction rates are listed here.

CO + OH

The second order rate constant for the reaction CO + OH → HO_2+CO_2 is given by the equations [*Griffin et al.*, 2002b, 2005]

$$k_1 = 1.3 \times 10^{-13} \tag{A.30}$$

$$k_2 = 3.19 \times 10^{-33} \tag{A.31}$$

$$k_{CO+OH} = k_1 + k_2 M \tag{A.32}$$

where k_{CO+OH} is in units of cm^3 $molecules^{-1}$ s^{-1}.

HO_2 + HO_2

The second order rate constant for the reaction $HO_2 + HO_2 \rightarrow H_2O_2 + O_2$ is given by the equations [*Griffin et al.*, 2002b, 2005]

$$k_1 = 2.2 \times 10^{-13} \exp\left(\frac{598.9\,\mathrm{K}}{T}\right) \tag{A.33}$$

$$k_2 = 1.85 \times 10^{-33} \exp\left(\frac{981.4\,\mathrm{K}}{T}\right) \tag{A.34}$$

$$k_{HO_2+HO_2} = k_1 + k_2 M \tag{A.35}$$

where $k_{HO_2+HO_2}$is in units of cm^3 $molecules^{-1}$ s^{-1}.

HNO_3 + OH

The second order rate constant for the reaction HNO_3 + OH $\rightarrow$ NO_3 + H_2O is given by the equations [*Griffin et al.*, 2002b, 2005]

$$k_1 = 7.2 \times 10^{-15} \exp\left(\frac{785.1\,\mathrm{K}}{T}\right) \quad \text{(A.36)}$$

$$k_2 = 4.1 \times 10^{-16} \exp\left(\frac{1439.4\,\mathrm{K}}{T}\right) \quad \text{(A.37)}$$

$$k_3 = 1.9 \times 10^{-33} \exp\left(\frac{724.7\,\mathrm{K}}{T}\right) \quad \text{(A.38)}$$

$$k_{HNO_3+OH} = k_1 + k_3 M \left(1 + \frac{k_3 M}{k_2}\right) \quad \text{(A.39)}$$

where k_{HNO_3+OH} is in units of cm^3 molecules^{-1} s^{-1}.

A.3 Third Order Reactions

A.3.1 Pseudo-Second Order Rate Constants for Association Reactions

The reaction rates for third order association reactions are calculated by estimating a pressure-dependent pseudo-second order rate constant k_f (cm^3 molecules^{-1} s^{-1}), calculated as

$$k_f = \frac{k_o M}{\left(1 + \frac{k_o M}{k_\infty}\right)} F^{\left(1+\left(\log_{10}\left(\frac{k_o M}{k_\infty}\right)\right)^2\right)^{-1}} \quad \text{(A.40)}$$

where M is the total concentration of gas molecules, F is a given constant, and k_o and k_∞ are calculated from the equations

$$k_o = A_o \left(\frac{T}{300\,\mathrm{K}}\right)^{-n_o} \quad \text{(A.41)}$$

and

$$k_\infty = A_\infty \left(\frac{T}{300\,\mathrm{K}}\right)^{-n_\infty} \quad \text{(A.42)}$$

where A_o, A_∞, n_o, and n_∞ are given constants. Table A.11 lists the third-order association reactions whose reaction rate constants are calculated using this procedure, and their reaction rate parameters.

Table A.11: Third Order Association Reactions

Reaction	A_o	n_o	A_∞	n_∞	F
$O + NO_2 + M \rightarrow NO_3 + M$	9.0×10^{-32}	2.0	2.2×10^{-11}	0.0	0.8
$NO_2 + NO_3 + M \rightarrow N_2O_5 + M$	2.8×10^{-30}	3.5	2.0×10^{-12}	0.2	0.45
$NO + OH + M \rightarrow HONO + M$	7.0×10^{-31}	2.6	3.6×10^{-11}	0.1	0.6
$NO_2 + HO_2 + M \rightarrow HNO_4 + M$	1.8×10^{-31}	3.2	4.7×10^{-12}	0.0	0.6
$OH + SO_2 + M \rightarrow H_2SO_4 + HO_2 + M$	4.1×10^{-31}	3.3	2.0×10^{-12}	0.0	0.45
$RO_26 + NO_2 + M \rightarrow PAN1 + M$	9.7×10^{-29}	5.6	9.3×10^{-12}	1.5	0.6
$RO_28 + NO_2 + M \rightarrow PAN2 + M$	9.7×10^{-29}	5.6	9.3×10^{-12}	1.5	0.6
$RO_239 + NO_2 + M \rightarrow PAN3 + M$	9.7×10^{-29}	5.6	9.3×10^{-12}	1.5	0.6
$RO_248 + NO_2 + M \rightarrow PAN4 + M$	9.7×10^{-29}	5.6	9.3×10^{-12}	1.5	0.6
$RO_250 + NO_2 + M \rightarrow PAN5 + M$	9.7×10^{-29}	5.6	9.3×10^{-12}	1.5	0.6
$RO_254 + NO_2 + M \rightarrow PAN6 + M$	9.7×10^{-29}	5.6	9.3×10^{-12}	1.5	0.6
$RO_255 + NO_2 + M \rightarrow PAN7 + M$	9.7×10^{-29}	5.6	9.3×10^{-12}	1.5	0.6
$RO_256 + NO_2 + M \rightarrow PAN8 + M$	9.7×10^{-29}	5.6	9.3×10^{-12}	1.5	0.6
$RO_257 + NO_2 + M \rightarrow PAN9 + M$	9.7×10^{-29}	5.6	9.3×10^{-12}	1.5	0.6
$RO_258 + NO_2 + M \rightarrow PN10 + M$	9.7×10^{-29}	5.6	9.3×10^{-12}	1.5	0.6

Reference: CACM [*Griffin et al.*, 2002b, 2005]

A.3.2 OH + NO_2 + M

Following the procedure of CACM [*Griffin et al.*, 2002b, 2005], the pseudo-second order reaction rate for the formation of HNO_3 from OH + NO_2 (k_{OH+NO_2},cm^3 molecules^{-1} s^{-1}) is calculated using the following formulas from *Dransfield et al.* [1999]

$$k_{OH+NO_2} = \frac{0.937 k_o M}{\left(1 + \frac{0.937 k_o M}{k_\infty}\right)} \exp\left(\frac{-T}{363\,\mathrm{K}}\right) \left(1 + \left(\frac{\log_{10}\left(\frac{0.937 k_o M}{k_\infty}\right) - 0.12}{0.85 - 0.67 \log_{10}\left(\exp\left(\frac{-T}{363\,\mathrm{K}}\right)\right)}\right)^2\right)^{-1} \quad \text{(A.43)}$$

$$k_o = 2.85 \times 10^{-30} \left(\frac{T}{300\,\mathrm{K}}\right)^{-2.67} \quad \text{(A.44)}$$

$$k_\infty = 3.13 \times 10^{-11} \quad \text{(A.45)}$$

Appendix B

CRM6 Dynamics Model Equations

This appendix describes the dynamic equations solved in the CRM6 3D Eulerian dynamics model used in Chapter 4. All model equations are presented using Einstein's tensor notation. As noted in Chapter 4, we have modified CRM6 to include a source of sensible heat, gases, and particles at the surface. In addition, we have simplified the model dynamics by removing the microphysics of cloud droplets, rain, graupel, and ice crystals.

B.1 Continuity, Momemtum, and Species Conservation Equations

The CRM6 model divides all variables (F) into two parts: the grid scale contribution $\left(\overline{F}\right)$ and the subgrid-scale contribution $\left(F^{'}\right)$, so that

$$F = \overline{F} + F^{'} \tag{B.1}$$

In addition, the grid-scale variable $\overline{F}$ is divided into two parts: the value at a horizontally homogeneous hydrostatic state (F_0) and the deviation from this state (f)

$$\overline{F} = F_0 + f \tag{B.2}$$

For notational convenience, $\overline{F}$ will be simplified to F in the equations below.

The model framework is based on the pseudo-elastic continuity equation of *Klemp and Wilhelmson* [1978]

$$\frac{\partial \pi}{\partial t} = \frac{c^2}{c_p \theta_{v0}^2 \rho_0} \frac{\partial \rho_0 \theta_{v0} u_j}{\partial x_j} \tag{B.3}$$

where t is time, x_j is the spatial coordinate, u_j is the wind speed component along the j axis,

c_p is the specific heat of air at constant pressure, ρ is the air density, θ_v is the virtual potential temperature. c^2 is given by the equation

$$c^2 = \left(\frac{c_p}{c_v}\right) R_d \theta_{v0} \Pi_o \tag{B.4}$$

where c_v is the specific heat of air at constant volume, R_d is the gas constant for dry air, and Π is the non-dimensional pressure, defined as

$$\Pi = \left(\frac{P}{P_o}\right)^{\frac{R_d}{c_p}} \tag{B.5}$$

Note that

$$\pi = \Pi - \Pi_o \tag{B.6}$$

and

$$\theta = \frac{T}{\Pi} \tag{B.7}$$

The momentum equations in flux form for the model are

$$\frac{\partial \rho u_i}{\partial t} + \frac{\partial \rho u_i u_j}{\partial x_j} = -\rho c_p \theta_{v0} \frac{\partial \pi}{\partial x_j} + \left[\frac{\theta}{\theta_0} - 1 + 0.61\left(q_v - q_{v0}\right)\right] g \delta_{i3} + E_{u_i} \tag{B.8}$$

where θ is the potential temperature, g is the acceleration due to gravity, and E_{u_i} is the contribution of the sub-grid scale turbulent mixing of momentum.

The thermodynamic equation is

$$\frac{\partial \rho \theta}{\partial t} + \frac{\partial \rho \theta u_j}{\partial x_j} = E_\theta + S_\theta \tag{B.9}$$

where E_θ is the contribution of the sub-grid scale turbulent mixing of heat and S_θ is the fire source of sensible heat. Note that since we are not considering cloud particles here, the ice-liquid potential temperature used in CRM6 reduces to the potential temperature.

The continuity equations for water vapor (q_v), trace gases (C_q), aerosol number (n_i), and aerosol

mass concentrations ($\mathbf{c}_{q,i}$) are all similar

$$\frac{\partial \rho q_v}{\partial t} + \frac{\partial \rho q_v u_j}{\partial x_j} = E_v + S_v \tag{B.10}$$

$$\frac{\partial C_q}{\partial t} + \frac{\partial C_q u_j}{\partial x_j} = E_q + S_q \tag{B.11}$$

$$\frac{\partial \rho n_i}{\partial t} + \frac{\partial \rho n_i u_j}{\partial x_j} = E_n + S_n \tag{B.12}$$

$$\frac{\partial \rho \mathbf{c}_{q,i}}{\partial t} + \frac{\partial \rho \mathbf{c}_{q,i} u_j}{\partial x_j} = E_m + S_m \tag{B.13}$$

with the E and S terms representing sub-grid scale turbulent mixing and the fire source, respectively.

B.2 Sub-grid Scale Turbulent Mixing Parameterization

The sub-grid scale mixing is parameterized using the first-order closure scheme of *Klassen and Clark* [1985]. For the unsaturated conditions studied in this thesis, the subgrid scale terms in Equations B.8 to B.13 are

$$E_{u_i} = \frac{\partial}{\partial x_j} K_M D_{ij} \tag{B.14}$$

and

$$E_f = \frac{\partial}{\partial x_j} K_H \frac{\partial f}{\partial x_j} \tag{B.15}$$

where f represents all scalar variables expect u_i. D_{ij} is calculated from the flow as

$$D_{ij} = \frac{\partial u_i}{\partial x_j} + \frac{\partial u_j}{\partial x_i} - \frac{2}{3}\delta_{ij}\frac{\partial u_k}{\partial x_k} \qquad (k = i = j \text{ when } i = j) \tag{B.16}$$

andK_M is calculated as

$$K_M = \max\left[\frac{(0.15\Delta)^2}{\sqrt{2}}\left(\frac{1}{2}\sum_{i,j=1}^{3} D_{ij}^2\right) f(R_i), \frac{1}{3}K_{\min}\right] \tag{B.17}$$

where

$$\Delta = \sqrt[3]{\Delta x \Delta y \Delta z} \tag{B.18}$$

$$f(R_i) = \sqrt{1 - R_i} \qquad R_i < 1 \tag{B.19}$$

$$= 0 \qquad R_i \geq 1 \tag{B.20}$$

and R_i is the Richardson number calculated as

$$R_i = \frac{\frac{g}{\theta}\frac{\partial \theta}{\partial x_3}}{\left(\frac{\partial u_i}{\partial x_i}\right)^2} \tag{B.21}$$

Finally, $K_H = \max\left[3K_{M,}K_{\min}\right]$, where $K_{\min}$ is the user-assigned minimum value for the horizontal diffusivity of scalar tracers.

B.3 Fire Source Terms

The fire source terms are only non-zero at the surface of the model and in the horizontal boundaries of the fire source defined by $X_{fire} \leq x \leq X_{fire} + \Delta X_{fire}; Y_{fire} \leq y \leq Y_{fire} + \Delta Y_{fire}$, where ΔX_{fire} and ΔY_{fire} are the downwind and cross-wind dimensions of the fire source and X_{fire} and Y_{fire} are the coordinated of the corner of the fire source. Note that during the simulation X_{fire} moves with the fire front speed (0.5 m/s for Timbavati) while all other parameters of the fire source geometry remain constant.

The source term for potential temperature S_θ (units of K s^{-1}) is derived form the sensible heat release rate of the fire Q_{heat} (units of W) as

$$S_\theta = \frac{Q_{heat}}{\rho c_p \Delta X_{fire} \Delta Y_{fire} \Delta z \Pi} \qquad X_{fire} \leq x \leq X_{fire} + \Delta X_{fire}; Y_{fire} \leq y \leq Y_{fire} + \Delta Y_{fire} \tag{B.22}$$

$$= 0 \qquad \text{Otherwise} \tag{B.23}$$

The source term for trace gases S_q (units of ppbm s^{-1}) are derived from the trace gas emission rate Q_q (kg s^{-1})

$$S_q = \frac{10^9 Q_q}{\rho \Delta X_{fire} \Delta Y_{fire} \Delta z} \qquad X_{fire} \leq x \leq X_{fire} + \Delta X_{fire}; Y_{fire} \leq y \leq Y_{fire} + \Delta Y_{fire} \tag{B.24}$$

$$= 0 \qquad \text{Otherwise} \tag{B.25}$$

The values for Q_q are calculated using the emission rate of CO and the emission ratio of gas q to CO. Similarly, the source term for water vapor S_v (units of kg H_2O (kg air)$^{-1}$ s^{-1}) is

$$S_v = \frac{Q_v}{\rho \Delta X_{fire} \Delta Y_{fire} \Delta z} \qquad X_{fire} \leq x \leq X_{fire} + \Delta X_{fire}; Y_{fire} \leq y \leq Y_{fire} + \Delta Y_{fire} \quad \text{(B.26)}$$

$$= 0 \qquad \text{Otherwise} \quad \text{(B.27)}$$

The source terms for aerosol number and mass concentrations are calculated based on the emission ratio of these species to CO

$$S_n = ER_{n_i/CO} S_{CO} \qquad X_{fire} \leq x \leq X_{fire} + \Delta X_{fire}; Y_{fire} \leq y \leq Y_{fire} + \Delta Y_{fire} \quad \text{(B.28)}$$

$$= 0 \qquad \text{Otherwise} \quad \text{(B.29)}$$

$$S_m = ER_{\mathbf{c}_{i,q}/CO} S_{CO} \qquad X_{fire} \leq x \leq X_{fire} + \Delta X_{fire}; Y_{fire} \leq y \leq Y_{fire} + \Delta Y_{fire} \quad \text{(B.30)}$$

$$= 0 \qquad \text{Otherwise} \quad \text{(B.31)}$$

Appendix C

Results from Comparison of Eulerian Box and 3D Models

C.1 Gases

	Reference Chemistry		Expanded Chemistry	
	Box	3D	Box	3D
$\mathbf{M}_{CO}$ (−10 min.)	7.182×10^{6}	7.443×10^{6}	7.182×10^{6}	7.443×10^{6}
$\mathbf{M}_{CO}$ (0 min.)	7.182×10^{6}	7.432×10^{6}	7.182×10^{6}	7.429×10^{6}
$\mathbf{M}_{CO}$ (60 min.)	1.189×10^{7}	1.215×10^{7}	1.189×10^{7}	1.215×10^{7}
$\Delta\mathbf{M}_{CO}$	4.70×10^{6}	4.72×10^{6}	4.71×10^{6}	4.72×10^{6}
ε_{CO}	−0.3%		−0.2%	
$\mathbf{M}_{O_3}$ (−10 min.)	1.409×10^{6}	1.409×10^{6}	1.409×10^{6}	1.409×10^{6}
$\mathbf{M}_{O_3}$ (0 min.)	1.426×10^{6}	1.421×10^{6}	1.425×10^{4}	1.421×10^{4}
$\mathbf{M}_{O_3}$ (60 min.)	1.698×10^{6}	1.641×10^{6}	1.712×10^{6}	1.706×10^{6}
$\Delta\mathbf{M}_{O_3}$	2.72×10^{5}	2.20×10^{5}	2.87×10^{5}	2.85×10^{5}
ε_{O_3}	+24%		+0.4%	
$\mathbf{M}_{NO}$ (−10 min.)	1.168×10^{4}	1.213×10^{4}	1.168×10^{4}	1.213×10^{4}
$\mathbf{M}_{NO}$ (0 min.)	9.378×10^{3}	8.958×10^{3}	9.278×10^{3}	8.868×10^{3}
$\mathbf{M}_{NO}$ (60 min.)	6.055×10^{4}	4.396×10^{4}	5.432×10^{4}	2.456×10^{4}
$\Delta\mathbf{M}_{NO}$	5.117×10^{4}	3.500×10^{4}	4.504×10^{4}	1.569×10^{4}
ε_{NO}	+46%		+187%	

	Reference Chemistry		Expanded Chemistry	
	Box	3D	Box	3D
$\mathbf{M}_{NO_2}$ (−10 min.)	1.815×10^4	1.887×10^4	1.815×10^4	1.887×10^4
$\mathbf{M}_{NO_2}$ (0 min.)	1.777×10^4	2.056×10^4	1.763×10^4	2.041×10^4
$\mathbf{M}_{NO_2}$ (60 min.)	1.115×10^5	1.323×10^5	1.036×10^5	9.861×10^4
$\Delta\mathbf{M}_{NO_2}$	9.369×10^4	1.117×10^5	8.601×10^4	7.820×10^4
ε_{NO_2}	−16%		+10%	
$\mathbf{M}_{HONO}$ (−10 min.)	0	4.098×10^1	0	4.125×10^1
$\mathbf{M}_{HONO}$ (0 min.)	1.936×10^2	1.181×10^2	2.754×10^2	2.105×10^2
$\mathbf{M}_{HONO}$ (60 min.)	2.445×10^3	1.827×10^3	2.837×10^3	8.396×10^3
$\Delta\mathbf{M}_{HONO}$	2.252×10^3	1.709×10^3	2.562×10^3	8.186×10^3
ε_{HONO}	+32%		−69%	
$\mathbf{M}_{HNO_3}$ (−10 min.)	0	2.095×10^3	0	2.095×10^3
$\mathbf{M}_{HNO_3}$ (0 min.)	7.068×10^3	8.998×10^3	7.162×10^3	9.039×10^3
$\mathbf{M}_{HNO_3}$ (60 min.)	2.754×10^4	1.676×10^4	2.762×10^4	3.079×10^4
$\Delta\mathbf{M}_{HNO_3}$	2.047×10^4	7.762×10^3	2.046×10^4	2.175×10^4
ε_{HNO_3}	+164%		−6%	
$\mathbf{M}_{PAN}$ (−10 min.)	0	1.835×10^2	0	1.835×10^2
$\mathbf{M}_{PAN}$ (0 min.)	1.546×10^3	1.036×10^3	1.557×10^3	1.045×10^3
$\mathbf{M}_{PAN}$ (60 min.)	2.029×10^4	1.197×10^4	1.847×10^4	1.975×10^4
$\Delta\mathbf{M}_{PAN}$	1.875×10^4	1.093×10^4	1.692×10^4	1.871×10^4
ε_{PAN}	+72%		−10%	
$\mathbf{M}_{AP}$ (**−10** min.)	0	1.367×10^2	0	1.367×10^2
$\mathbf{M}_{AP}$ (**0** min.)	1.101×10^1	1.406×10^2	1.105×10^1	1.407×10^2
$\mathbf{M}_{AP}$ (**60** min.)	1.809×10^2	2.721×10^2	1.373×10^4	8.497×10^3
$\Delta\mathbf{M}_{AP}$	1.699×10^2	1.315×10^2	1.372×10^4	8.356×10^3
ε_{AP}	+29%		+64%	

	Reference Chemistry		Expanded Chemistry	
	Box	3D	Box	3D
$\mathbf{M}_{SO_2}$ (**−10** min.)	5.723×10^4	6.100×10^4	5.723×10^4	6.100×10^4
$\mathbf{M}_{SO_2}$ (**0** min.)	5.701×10^4	6.179×10^4	5.686×10^4	6.165×10^4
$\mathbf{M}_{SO_2}$ (**60** min.)	1.153×10^5	1.318×10^5	1.142×10^5	1.262×10^5
$\Delta\mathbf{M}_{SO_2}$	5.824×10^4	7.001×10^4	5.737×10^4	6.455×10^4
ε_{SO_2}	-17%		-11%	
$\mathbf{M}_{HCl}$ (**−10** min.)	0	2.045×10^3	0	2.045×10^3
$\mathbf{M}_{HCl}$ (**0** min.)	0	2.088×10^3	0	2.088×10^3
$\mathbf{M}_{HCl}$ (**60** min.)	4.071×10^4	2.878×10^4	4.064×10^4	3.782×10^4
$\Delta\mathbf{M}_{HCl}$	4.071×10^4 (+%)	2.669×10^4	4.064×10^4	3.573×10^4
ε_{HCl}	$+53\%$		$+14\%$	

C.2 Aerosols

	Reference Chemistry		Expanded Chemistry	
	Box	3D	Box	3D
$\mathbf{M}_{K^+}$ (−10 min.)	5.356×10^4	5.254×10^4	5.356×10^4	5.254×10^4
$\mathbf{M}_{K^+}$ (0 min.)	5.356×10^4	5.164×10^4	5.356×10^4	5.165×10^4
$\mathbf{M}_{K^+}$ (60 min.)	6.768×10^4	6.446×10^4	6.768×10^4	6.457×10^4
$\Delta\mathbf{M}_{K^+}$	1.412×10^4	1.282×10^4	1.412×10^4	1.292×10^4
ε_{K^+}	+10%		+9%	
$\mathbf{M}_{BC}$ (−10 min.)	1.181×10^5	1.156×10^5	1.181×10^5	1.156×10^5
$\mathbf{M}_{BC}$ (0 min.)	1.181×10^5	1.144×10^5	1.181×10^5	1.144×10^5
$\mathbf{M}_{BC}$ (60 min.)	1.407×10^5	1.364×10^5	1.407×10^5	1.364×10^5
$\Delta\mathbf{M}_{BC}$	2.26×10^4	2.20×10^4	2.26×10^4	2.20×10^4
ε_{BC}	+2.7%		+2.7%	
$\mathbf{M}_{NO_3^-}$ (−10 min.)	3.571×10^4	3.496×10^4	3.571×10^4	3.496×10^4
$\mathbf{M}_{NO_3^-}$ (0 min.)	2.925×10^4	2.712×10^4	2.929×10^4	2.723×10^4
$\mathbf{M}_{NO_3^-}$ (60 min.)	2.522×10^4	2.785×10^4	2.497×10^4	3.898×10^4
$\Delta\mathbf{M}_{NO_3^-}$	-4.03×10^3	7.30×10^2	-4.32×10^3	1.175×10^4
$\mathbf{M}_{SO_4^{2-}}$ (−10 min.)	3.563×10^4	3.467×10^4	3.563×10^4	3.467×10^4
$\mathbf{M}_{SO_4^{2-}}$ (0 min.)	3.557×10^4	3.428×10^4	3.571×10^4	3.441×10^4
$\mathbf{M}_{SO_4^{2-}}$ (60 min.)	3.957×10^4	3.751×10^4	4.058×10^4	4.329×10^4
$\Delta\mathbf{M}_{SO_4^{2-}}$	4.00×10^3	3.23×10^3	4.87×10^3	8.88×10^3
$\varepsilon_{SO_4^{2-}}$	+24%		−45%	
$\mathbf{M}_{Cl^-}$ (**−10** min.)	0	4.84×10^1	0	4.82×10^1
$\mathbf{M}_{Cl^-}$ (**0** min.)	1.637×10^1	0.737	1.637×10^1	0.679
$\mathbf{M}_{Cl^-}$ (**60** min.)	2.896×10^3	1.7511×10^4	2.974×10^3	1.0467×10^4
$\Delta\mathbf{M}_{Cl^-}$	2.880×10^3	1.751×10^4	2.958×10^3	1.047×10^4
ε_{Cl^-}	-84%		-72%	

	Reference Chemistry		Expanded Chemistry	
	Box	3D	Box	3D
$\mathbf{M}_{OC}$ (-10 min.)	8.561×10^5	8.378×10^5	8.561×10^5	8.378×10^5
$\mathbf{M}_{OC}$ (0 min.)	8.561×10^5	8.297×10^5	8.561×10^5	8.297×10^5
$\mathbf{M}_{OC}$ (60 min.)	9.406×10^5	9.042×10^5	9.958×10^5	9.826×10^5
$\Delta\mathbf{M}_{OC}$	8.45×10^4	7.45×10^4	1.397×10^5	1.529×10^5
ε_{OC}	$+13\%$		-9%	